The Evolution of Supraglacial Hydrologic Networks on the Greenland Ice Sheet

Lauren Danielle Rawlins

Doctor of Philosophy

University of York

Department of Environment and Geography

June 2023

Abstract

Surface melt and runoff is an important, growing source of mass loss from the Greenland Ice Sheet (GrIS) and its ongoing contribution to global sea level rise (SLR). The transportation, storage and evacuation of surface melt is governed by the supraglacial hydrologic network, consisting of an array of rivers, streams and lakes which fundamentally control the timing and delivery of meltwater outputs, with wider hydro-dynamic implications. Motivated by the need to improve understanding of the spatial distribution, composition and evolution of GrIS-wide hydrology, this thesis expands supraglacial network mapping to understudied and spectrally-complex regions of the GrIS via remotely-sensed and field-acquired imagery over a multitude of temporal and spatial scales.

For the first time, the supraglacial hydrologic network is mapped and quantified over (i) consecutive melt seasons (2016-2020) and (ii) over long, multi-annual timescales (1985-2021) at a major northern outlet glacier, Humboldt (Sermersuaq) Glacier. Work reveals an extensive and complex supraglacial hydrologic network exists, seasonally developing from an inefficient to efficient network in-line with snowline migration up to 1400 m a.s.l, with large-interannual variability attributed to extremes in atmospheric circulation. Over 30+ years, this network is shown to have expanded inland by ~400 m a.s.l and doubled in areal extent, concurrent with increasing air temperatures and amplification of runoff as a result of climatic warming. Field- and commercial-based imagery also reveal small-scale microchannels, inter-stream networks and complex surface facies comprise the spectrally-complex ice marginal region of Russell Glacier (south-western Greenland) and the bare ice zone of Humboldt Glacier.

Collectively, findings from this thesis demonstrate the complex behaviour of the supraglacial hydrologic network, including the variety of sized channels that comprise it and the differing abilities of remotely-sensed data to capture such features. This work provides new insights into the past, present and suggestions of the future nature of this network, with continued hydrologic-research directed towards further mapping of the GrIS and other cryospheric bodies to better predict surface mass balance and SLR contributions now and into the future.

Lay Summary

Since the 1990's, the Greenland Ice Sheet has been losing ice mass at an increasing rate via surface melt (surface mass balance) and iceberg calving (ice discharge) because of increasing air and ocean temperatures. In recent years, increased losses from surface mass balance due to the rapid intensification and expansion of surface meltwater and runoff across the melt-prone margins of the Greenland Ice Sheet has resulted in the presence of an expansive surface drainage network (also known as the supraglacial hydrologic network) during the summer melt season. This drainage network, made up of interconnecting lakes and river channels, store and move meltwater long distances across the ice surface, which ultimately ends up in the ocean; the Greenland Ice Sheet of which contains enough ice to raise global sea levels by 7.4 metres. Even though this surface drainage network is acknowledged to be significant in meltwater transport and storage, it remains largely unmapped and understudied across the Greenland Ice Sheet, with scientific studies over the last two decades focussed around the large melt producing western and south-western regions.

Work conducted in this thesis expands surface drainage mapping to other ice sheet regions, predominately the rapidly changing northern sector. Satellite imagery is used to map, for the first time, the drainage network of a major northern Greenlandic glacier over consecutive melt seasons (2016-2020) and long-term (1985-2021) timescales. Further imagery via commercial-based satellites and an uncrewed aerial vehicle (known as a drone) are also used to reveal small-scale surface features in complex locations. Results from the work conducted reveals the complex nature of this drainage network and provides new insights into the past, present and potential future behaviour of the network and the Greenland Ice Sheet with ongoing climatic warming.

Declaration

The work presented in this thesis is original and my own, composed solely by myself and has not been submitted, either in whole or in part, for any other award or professional qualification. Appropriate credit has been given within the thesis where reference has been made to the work of others.

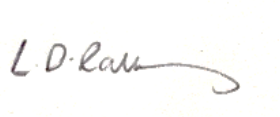

Lauren Rawlins
June 2023

Acknowledgements

First and foremost, I would like to thank my supervisor David Rippin for his encouragement and guidance throughout the PhD, for freedom in exploring various research avenues and my interests in teaching and outreach. Secondly, I thank my co-supervisors Andrew Sole and Stephen Livingstone, who not only provided logistical support for my PhD fieldwork and was welcomed alongside their Polar and Alpine Change (PAC) Masters trip to Greenland, but for their enthusiasm, knowledge and support throughout my PhD, often giving research advice at short notice. I also thank the many PAC students I shared my time in Greenland with, including Emma Lewington – my polar bear watch partner and good friend.

During my PhD, I have received substantial financial support. I thank the Natural Environment Research Council (NERC) for the funding of this PhD research, including my 2019 Greenland field season. I also acknowledge the Royal Geographical Society for the Monica Cole fieldwork grant supporting my 2022 Greenland fieldwork and to the European Space Agency for a third-party imagery grant enabling me use of commercial-based imagery. I am especially grateful for a NERC-DTP placement fund for the opportunity to travel to Canada and undertake a month-long research placement at the University of Calgary, enabling me to gain valuable field experience in UAV research and was a PhD fieldwork highlight.

Throughout this journey, I have been fortunate to meet some incredible and like-minded people who have not only supported me (and each other) through this PhD but for whom I have gained life-long friendships. Whilst at York, I have been lucky to have been part of a fun and encouraging PhD cohort. I met one of my now very best friends, Lucy McMahon, who I am fortunate to have started and ended this PhD journey with, picking each other up when times were tough and cheering each other on as we hit PhD and career milestones. I also extend a huge thank you to Sophie Williams, who too has provided incredible moral support throughout. I treasure both of your friendships greatly. To the rest of the PhD cohort, I thank Katey Valentine, George Day, Alex Burkitt, Ruochan Ma, Abby Mycroft and my many office pals of ENV/134 over the years for copious amounts of tea, PhD cake and laughter in the departmental heart space (+ wine during conference events).

Outside of the office through various glaciological committees and conferences, I have also met a number of wonderful ECRs for whom I have grown strong and loyal friendships. A huge thank you to Isabelle Gapp for our regular online catch ups and for reigniting my passion for ice when imposter syndrome creeped in and I lost my way. You believe in everything I do and no matter where in world you are, I can always count on you. You are an inspiration. Thank you to Penny How - whilst your research-time at York was short before moving to Greenland (envious), your unwavering support and words of wisdom over the years has built my confidence and resilience in showing me the independent and valuable ECR I am. You are a true inspiration to me and for female glacio-ECRs. Additionally, I express my sincere appreciation and thanks to Ellie Bash and Greg McDermid in Canada for hosting me at the University of Calgary in 2022 and providing new fieldwork experiences. My time in Calgary was unforgettable and made possible by your generosity. Memories of my trip to Banff National Park and fieldwork at Athabasca Glacier are truly cherished.

To IGS EGG-ers – I thank Rebecca Schlegel for your comical Whatsapp voice messages which always put a smile on my face and to Nathaniel Baurley for monthly zoom catch ups on the run up to my PhD hand-in and providing great drone chat. To Connor Shiggins and Guy Tallentire, cheers for our regular twitter chats and for ECR collaborations. I also extend my thanks to fellow York ECR glaciologists Adrian Dye and Fran Falcini, who have been great sounding boards and who have provided guidance navigating tricky times.

Outside of my PhD, I have had the ongoing support of close friends and family. A special thanks to my Yorkies, Hannah and Will and to my Leeds folks, Emma, Will, Barbs and Emily, who are always wanting to know what is going on and what exciting things I have lined up next! The many board game and wine nights were great escapes from my PhD brain overloads.

Finally, and most importantly, I want to express my utmost gratitude to my family. To mum, dad and my brother, Kieran – I thank you for your continued interest, enthusiasm, encouragement and support in my pursuit of everything ice-related. As the first family member to go to university, *'your girl did good!'* To the Morris' - Nel, Mark and Polly – I thank you for being my cheerleaders and sending words of motivation and positivity when times were tough.

Finally, to my partner in life and best friend, Dave – my biggest supporter. This PhD journey has had its high and very low moments and you have stood beside me no matter what. I thank you for your continued words of encouragement, reassurance, praise and care

throughout this (and for looking after our dog Eska whilst I galivanted off to Greenland and Canada…). You are my absolute rock!

I did it.

Contents

List of Figures

List of Tables

Abbreviations

Abbreviation	Definition
a.s.l	Above Sea Level
DEM	Digital Elevation Model
dGPS	Differential Global Positioning System
ELA	Equilibrium Line Altitude
ESA	European Space Agency
GBI	Greenland Blocking Index
GCP	Ground Control point
GEE	Google Earth Engine
GIMP	Greenland Ice Mapping Project
GNSS	Global Navigational Satellite System
GPS	Global Positioning System
GrIS	Greenland Ice Sheet
GSD	Ground Sampling Distance
JJA	June, July, August (key melt season months)
NAO	North Atlantic Oscillation
NDWI	Normalised Difference Water Index
$NDWI_{ice}$	Normalised Difference Water Index designed for use on ice
MAQIT	Margin Change Quantification Tool
MAR	Modèle Atmosphérique Régionale (Regional Climate Model)
MODIS	Moderate Resolution Imaging Spectroradiometer satellite-based sensor aboard Terra satellite
PPO	Parsimonious Path Opening
PPP	Precise Point Positioning
RCM	Regional Climate Model

RGB	Red, green and blue colour channels of an image (true colour)
SfM	Structure-from-Motion
SGL	Supraglacial Lake
SLE	Sea Level Equivalent
SLR	Sea Level Rise
UAV	Uncrewed Aerial Vehicle
w.e.	Water Equivalent (equivalent depth of water for a given depth of snow or ice)
WV	Worldview

Statistical Abbreviation	Definition
r	Pearson correlation (measure of linear correlation – parametric test)
R^2	Coefficient of determination (strength of relationship in a linear model)
RMSE	Root mean square error (measure error of a model)
r_s	Spearman rank (summarise strength of relationship between two variables – a non-parametric test)
SE	Standard error (accuracy of a sample mean)
std	Standard deviation (measure of data dispersion)
P	P-value (statistical measure of significance)

"We cannot negotiate with the melting point of ice"

WWF Arctic Programme, 2021

Chapter 1

Introduction

1.1 Motivation

The cryosphere encompasses the portion of Earth's water frozen in ice sheets, ice caps, glaciers, sea and lake ice and seasonally frozen ground (Goodison *et al.*, 2007; Vaughan *et al.*, 2013). In total, it covers ~68 million km^2 in area, together containing the largest reservoirs of freshwater on Earth (Ohmura, 2015; Bolch and Christiansen, 2021). Forming an integral part of the Earth's climate system, the presence of frozen water on land, the ocean surface and within the atmosphere affects various climate feedbacks on both local and global scales (Goodison *et al.*, 2007; Kattsov *et al.*, 2010; Callaghan *et al.*, 2011; Vaughan *et al.*, 2013). From surface energy and moisture fluxes, hydrological conditions and atmospheric and oceanic circulations, to influencing sea level and providing a freshwater resource to high mountain communities (Hock, 2005; Huggel *et al.*, 2015; Clason *et al.*, 2023). The cryosphere exerts fundamental control across various aspects of the physical, biological and social environment (Goodison *et al.*, 2007; Vaughan *et al.*, 2013).

Over recent decades, there has been a surge of scientific interest in glaciers and ice sheets worldwide, owing to the considerable impacts of contemporary climatic change (Cuffey and Paterson, 2010; Hanna *et al.*, 2020). Described as a 'natural thermometer' due to the high sensitivity and integrated response to climate, glaciers and ice sheets are providing some of the most visible signs of climate-driven change (Vaughan *et al.*, 2013; Collins *et al.*, 2019). Anthropogenic-induced warming from greenhouse gas (GHG) emissions has already led to a global average surface temperature increase of 1.1°C above 1880–1900 levels (in 2011-2020), with warming currently increasing at an average of 0.2°C per decade (IPCC, 2021). Of particular concern is the unprecedented effects this is having on the cryosphere, with the IPCC Special Report on the Ocean and Cryosphere in a Changing Climate (SROCC; IPCC, 2019) projecting with *high confidence* that continued mass loss and the extensive retreat of

glaciers worldwide will persist into the future, as well as drive irreversible losses from the two major ice sheets, Greenland and Antarctica (Pattyn *et al.*, 2018).

At present, the Greenland Ice Sheet (GrIS) is experiencing profound mass loss as a result of rising air and ocean temperatures and is now the single largest contributor to global sea level rise (SLR; Vaughan *et al.*, 2013; Albert *et al.*, 2016; van den Broeke *et al.*, 2017; Hofer *et al.*, 2020; IPCC, 2021). Throughout the satellite era, there has been an increasingly positive trend in the extent and duration of GrIS surface melt during the ablation season (Trusel *et al.*, 2018; Noël *et al.*, 2019). To date, surface mass balance (SMB), particularly meltwater runoff, accounts for two thirds of Greenland's total mass loss (Fettweis *et al.*, 2011; Harper *et al.*, 2012; Albert *et al.*, 2016; Fettweis *et al.*, 2021). Surface hydrology, constituting the transportation, storage and evacuation of surface melt through a complex array of supraglacial channels and lakes, is a significant driver of mass loss and dynamical change of the GrIS (Flowers, 2018). These supraglacial features can route surface meltwater across the ice surface, store considerable volumes of meltwater, control the timing and injection of meltwater into the ice sheet via moulins or crevasses, and/or directly drain meltwater off the ice sheet and into proglacial rivers/lakes or the ocean (Rennermalm *et al.*, 2013; Chu, 2014; Flowers, 2018; Pitcher and Smith, 2019). Over the past two decades there has been a significant development in such hydrological research, largely attributed to the increasing availability and resolution of satellite imagery and automated methods for remote sensing studies, generating scientific advances in this field over a short period of time (Chu, 2014; Nienow *et al.*, 2017).

Much of the hydrologic research on the GrIS has focussed within the large melt-producing sectors of the southwestern and central western regions of the ice sheet (Hanna *et al.*, 2008; Lewis and Smith, 2009). Here, extensive hydrologic activity comprised of kilometre-scale turquoise-blue lakes fed by networks of surface rivers and streams are striking in satellite imagery (Figure 1.1), with their disappearance a sign of meltwater delivery to the en- or sub-glacial hydrologic system, which can have a short-lived effect on localised ice velocity (Das *et al.*, 2008; Flowers, 2018). More recently, supraglacial mapping has begun to be expanded to other ice sheet regions (Gledhill and Williamson, 2018; Yang *et al.*, 2019b; Lu *et al.*, 2021) as the ablation zone and subsequent runoff becomes amplified with ongoing warming (Noël *et al.*, 2019). However, much of the morphology, distribution and evolutionary behaviour of supraglacial network across the GrIS remains unmapped and unexplored, with this remaining one of the least studied hydrologic systems on Earth (Yang and Smith, 2013; Smith *et al.*, 2015; Pitcher and Smith, 2019).

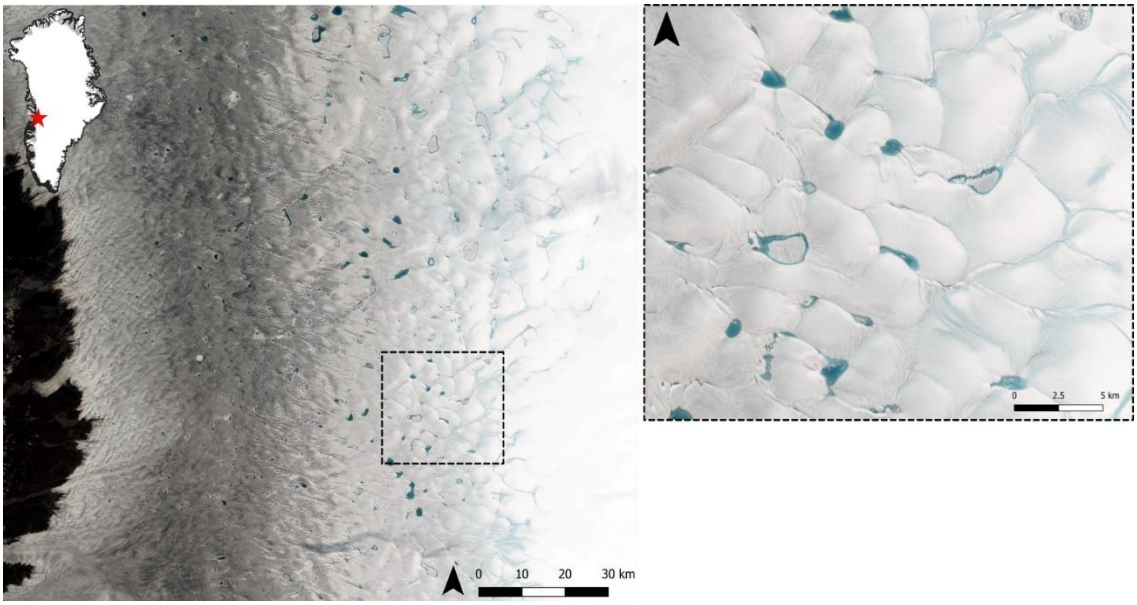

Figure 1.1. The expansive supraglacial hydrologic network, including turquoise-blue supraglacial lakes and channels, on the western GrIS visible in Sentinel-2 satellite imagery.

1.2 Research aim, questions and objectives

The overall purpose of this thesis is to expand supraglacial hydrologic mapping to other understudied regions of the GrIS and to explore the networks evolutionary behaviour at a range of spatial and temporal scales utilising both remotely-sensed and field-acquired imagery. Until now, much of the supraglacial hydrologic research on Greenland has focussed within the southwestern and central western regions of the ice sheet with great hydrologic activity (i.e., an expansive summer meltwater network; Hanna *et al.*, 2008; Lewis and Smith, 2009). However, more recently it has been shown that rapid ablation zone expansion and the amplification of runoff since 1990 has occurred in northern Greenland at almost twice the rate of the south (Noël *et al.,* 2019). This is unprecedented at least over the last millennia (Noël *et al.*, 2019; Hörhold *et al.*, 2023). This has significantly increased the regions relative contribution to total GrIS mass loss through enhanced runoff, with projections of larger runoff volumes expected with further warming (Tedstone and Machguth, 2022). Despite this acknowledgement, little is known about the transportation and storage mechanisms of such meltwater runoff in this region. With this in mind, three key research questions of this thesis and their respective objectives to address them are subsequently outlined below:

RQ1: What does the surface hydrologic system look like at a previously unmapped northern Greenlandic glacier and how does this network evolve over seasonal timescales?

i. To map the supraglacial hydrologic network, including both channels and lakes, using optical imagery to explore, for the first time, its presence and extent at an unmapped northern glacier.
ii. To derive specific supraglacial network metrics to quantify the intra- and inter-seasonal evolution of the supraglacial hydrologic network over consecutive melt seasons.

iii. To explore the relationship between network-derived metrics and modelled runoff from the regional climate model MAR (Modèle Atmosphérique Régional).

RQ2: How has the supraglacial hydrologic network at this prominent northern Greenlandic glacier evolved over the last 30+ years?

i. To use optical imagery via the cloud computing platform Google Earth Engine (GEE) to generate annual supraglacial hydrologic maps and assess the retreat history across the collective melt season months of June, July and August (JJA).

ii. To derive specific supraglacial hydrologic network metrics, including collective network and independent channel and lake metrics, for assessing annual hydrologic network evolution overtime.

iii. To use the regional climate model MAR to explore the regional changes in melt season temperature and runoff and the implications for observed supraglacial network development.

RQ3: What does the minutiae of the supraglacial hydrologic network consist of in the (i) spectrally-complex ice marginal regions and (ii) the bare ice zone of the GrIS beyond freely-available satellite imagery?

i. To use an uncrewed aerial vehicle (UAV) to survey a small area of the southwestern ice marginal region to derive Structure-from-Motion (SfM) models for the mapping of microchannel networks (centimetre-to-metre scale).

ii. To use the UAV-derived orthomosaic model to characterise surface facies of the ice surface to further explore the complex morphology of the ice marginal region.

iii. Use commercial-based WorldView-2 (WV-2) imagery to map and explore the potential for inter-stream tributary networks (>1 m scale) in a section of the bare ice zone.

1.3 Thesis structure

This thesis comprises eight chapters including this Introduction (Chapter 1). The results presented in Chapters 4-6 of this thesis are stand alone. The remaining chapters of this thesis are designed to provide an overview of the current knowledge of supraglacial hydrologic research, introduce the study areas and key methodologies which underpin mapping throughout this thesis and provide a unifying synthesis of this research with a focus on its wider implications and future recommendations for research.

1.3.1 Chapter 2 - Background

Chapter 2 provides a background and summarises the current knowledge of GrIS change, with an emphasis on SMB and hydrologic processes which are dominating GrIS ice mass loss, surface melt and runoff. The selected study sites for Chapters 4-6 are also introduced, including Humboldt (Sermersuaq) Glacier in northern Greenland (Chapter 4-6) and Russell Glacier in southwestern Greenland (Chapter 6).

1.3.2 Chapter 3 - Methodological overview

Chapter 3 provides an introduction to remote sensing and UAVs with an overview of the key methodologies that underpin supraglacial hydrologic mapping used in individual results Chapters 4-6.

1.3.3 Chapter 4-6 - Results

Chapters 4,5 and 6 are standalone results chapters that respond to the three key questions of the thesis outlined above. Chapter 4 is written as a paper and is published in the journal

The Cryosphere. The manuscript is available to view in Appendix A or via https://doi.org/10.5194/tc-17-4729-2023. Chapters 5 and 6 are in a traditional thesis format with additional tables and figures supplied in Appendices B and C. The methodological overview presented in Chapter 3 underpins methods used in Chapters 4-6, with each chapter having their additional own method section presented due to specific approaches and parameters optimised for the data used.

1.3.4 Chapter 7 - Discussion

Chapter 7 provides a thesis synthesis and summary of key findings from Chapters 4-6. Wider implications of these results are considered in relation to the future of GrIS SMB and mass loss, with the identification of future research opportunities and priorities. Limitations of this research are also considered.

1.3.5 Chapter 8 – Conclusion

Chapter 8 provides a succinct thesis overview and concluding remarks.

1.4 Contributions to data chapters

I am the primary author of data Chapter 4, which is published as Rawlins *et al.* (2023) in *The Cryosphere*. For this Chapter/paper, I use satellite-acquired imagery from Sentinel-2 between 2016 and 2020 over the melt season months of May to September to map and quantify the supraglacial hydrologic network at Humboldt Glacier, northern Greenland, for the first time. Kang Yang provided source code for use in Matlab, which is introduced in Chapter 3 of this thesis, to perform the automatic detection and extraction of supraglacial rivers and lakes. Andrew Sole provided assistance with the extraction of regional climate model MAR (Modèle Atmosphérique Regionale) data, freely provided by Xavier Fettweis. All authors provided comments on the draft manuscript.

I am the sole author of Chapter 5, which explores the long-term evolution of the supraglacial hydrologic network at Humboldt Glacier between 1985 and 2021. This chapter utilises the longest running Earth observation satellite programme, Landsat, via the cloud computing platform GEE alongside the automatic river detection algorithm (Yang *et al.*, 2015a; Yang *et al.*, 2017) to create an annual supraglacial hydrology meltwater map used to assess and quantify the long-term inland evolution of the generalised network. The opportunity is also undertaken to additionally quantify terminus retreat from the dataset. This is the first time the supraglacial hydrologic network has been mapped and quantified over a long time period utilising Landsat imagery.

I am also the sole author of Chapter 6 which takes the opportunity to utilise ultra-high-resolution imagery from both (i) a UAV via fieldwork in August 2019 and (ii) commercial-based WV-2 satellite imagery (via an ESA Third Party Imagery Grant) to explore the minutiae of the supraglacial hydrologic network beyond conventional, freely available satellite imagery. This includes the mapping and examination of microchannels, surface facies and inter-stream networks. Andrew Sole and Stephen Livingstone provided logistical support for UAV-based fieldwork in southwest Greenland.

Chapter 2

Background

This chapter aims to review the current understanding of processes governing mass loss of the Greenland Ice Sheet (GrIS). Particular focus is given to reviewing changes in surface mass balance (SMB) contributions to GrIS mass loss and the processes which influence surface melt and runoff. This leads to examining the current knowledge of the supraglacial hydrologic network in existence across Greenland's ablating margins during the melt season, as well as defining independent supraglacial features which comprise this network. Further interactions with the subglacial network and its influence on ice velocity is also considered.

Finally, an introduction to the specific study areas examined in Chapters 4, 5 and 6 of this thesis is provided.

2.1 Introduction to the Greenland Ice Sheet

The Greenland Ice Sheet (GrIS) is the largest reservoir of snow and ice in the northern hemisphere, containing ~2.9 million gigatons (Gt) of ice, equivalent to 10% of all Earths freshwater (Chen *et al.*, 2011; Bamber *et al.*, 2013). If totally melted this would raise global sea level by ~7.4 m, making Greenland a significant concern for current and future global sea level rise (SLR) and to the global climate system (Bamber *et al.*, 2013; Goelzer *et al.*, 2020). Contributions from glaciers and ice caps dominated global SLR during the 20th century excluding peripheral glaciers of the Greenland and Antarctic ice sheets (0.54 mm yr^{-1}; Vaughan *et al.,* 2013). However, this has since changed in the 21st Century. Contributions from both the Greenland and Antarctic ice sheets was four times larger during the period 2010–2019 than during 1992–1999, with Greenland contributing 13.7 mm to SLR over the last ~50 years, with over half occurring since 2010 (Mouginot *et al.*, 2019); making it the current single largest cryospheric contributor to SLR (Chen *et al.*, 2017; Box *et al.*, 2022a).

Since the early 1990's the GrIS has been experiencing accelerating mass loss through increased ice discharge and enhanced meltwater runoff (van den Broeke *et al.*, 2009; Vaughan *et al.*, 2013). These losses are primarily driven by increasing air and ocean temperatures attributed to anthropogenic-induced warming and Arctic amplification: the exacerbation of warming in Arctic regions from regional climate feedbacks (mainly reduced sea ice extent and surface-albedo feedbacks; Serreze and Francis, 2006; Screen and Simmonds, 2010; Masson-Delmotte *et al.*, 2018; Pattyn *et al.*, 2018). Between 1991 and 2019, temperatures across Greenland have significantly warmed by ~4.4°C in winter, 2.7°C in spring and ~1.7°C in summer (Hanna *et al.*, 2021), which is more than double that of the global mean (Pattyn *et al.*, 2018). The most significant warming has been observed along the west and northwest coast of Greenland (~6°C in winter and ~2°C in summer; (Hanna *et al.*, 2021) with sustained mass loss in this region, noted in numerous studies, to be associated

with persistent negative phases of the North Atlantic Oscillation (NAO; (Hanna *et al.*, 2008; Hanna *et al.*, 2016; Hanna *et al.*, 2018; Bevis *et al.*, 2019).

Not only are there concerns about the future contribution of Greenland to SLR and its impacts worldwide to coastal and low-lying communities, but also what implications this will have on the global climate system (Jevrejeva *et al.*, 2016). The Arctic is intrinsically linked to atmospheric and oceanic systems, representing a critical component for the poleward transfer of heat and water exchange, influencing the climate we know today (Delworth *et al.*, 2008; Delworth and Zeng, 2016). Of particular importance is the Atlantic Meridional Overturning Circulation (AMOC), characterised by the northward flow of warm, saline water and the cooling and southward flow of deep water in the Nordic and Labrador Seas: an important component for maintaining the thermohaline circulation (Delworth *et al.*, 2008; Sévellec *et al.*, 2017. There are concerns as to the possibility of major weakening of the AMOC due to perturbation of the freshwater balance, in response to ongoing Arctic Sea ice loss and rapid mass loss observed across the GrIS (van Angelen *et al.*, 2014; van den Broeke *et al.*, 2017; Sévellec *et al.*, 2017). However, large uncertainties remain in regards to the degree in which current levels of freshwater may impact the AMOC (Callaghan *et al.*, 2011). This influence of the GrIS on the climate system, as well its contribution to SLR, therefore highlights the challenges faced today in understanding and predicting ice sheet behaviour and its future impacts (Crozier *et al.*, 2018; Koziol and Arnold, 2018).

2.2 Ice sheet mass balance

2.2.1 Overview of mass balance

Mass balance is an indicator used within cryospheric science to measure the health of a glacier or ice sheet via the difference between its net mass gains (accumulation) and mass losses (ablation) over an annual timeframe (Hock, 2010) and can be defined by the following equation (2.1; Lenaerts *et al.*, 2019).

$$MB\ (Gt\ ^{yr-1}) = SMB - D$$

(MB = Mass Balance; SMB = Surface Mass Balance; D = Ice Discharge)

Equation 2.1

Ice sheets primarily gain mass though snowfall and deposition, typically during the winter months, and lose mass during the summer months through a number of processes, including sublimation, iceberg calving, basal melt from geothermal heating and surface melt and subsequent runoff (

Figure 2.1; Cuffey and Paterson, 2010; Vizcaino, 2014). The quantification of mass loss via ablating processes can be partitioned into two main components; (1) losses by ice discharge made up of calving events and bottom melting at the grounding line of marine-terminating glaciers (Rignot *et al.*, 2010) and; (2) surface mass balance (SMB) which encompasses mass exchanges at the surface, such as snowfall and ablation processes, primarily surface melt (van den Broeke *et al.*, 2009; Khan *et al.*, 2015).

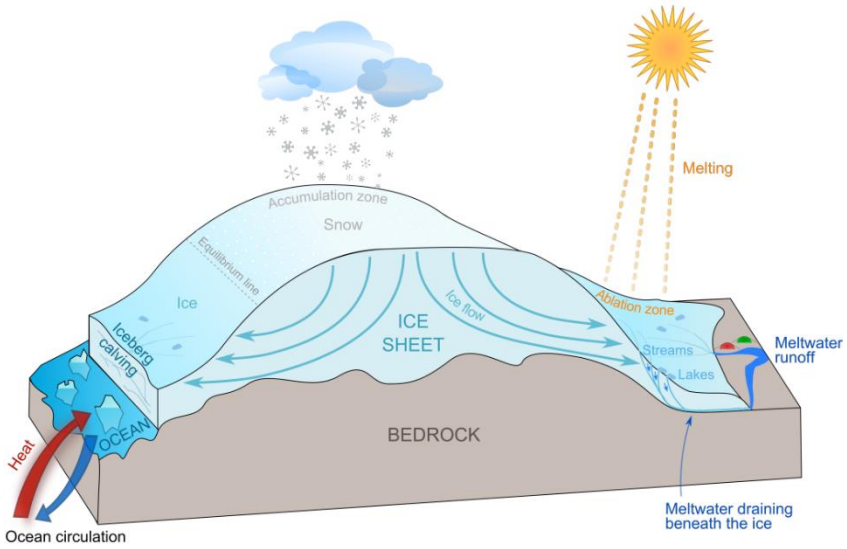

Figure 2.1. Schematic overview of the components comprising the mass balance of the Greenland Ice Sheet. Figure from Tedstone (2015; their Figure 1.1).

Ice flow provides a transport mechanism for the movement of ice from the accumulation zone down to lower, warmer elevations of the ablation zone, whereby subsequent ablation processes occur. The equilibrium line altitude (ELA) is the altitude at which the higher elevation accumulation area is separated from the lower elevation ablation area. Over the course of a full melt-year, if the mass gained is greater than that lost, the ice sheet is in a positive mass balance. If the mass gained is equal to that of mass loss, the ice sheet is said to be 'in balance'. If, however, more mass is lost than gained each year, the ice sheet will be in a negative mass balance (Cuffey and Paterson, 2010).

2.2.2 Mass balance of the Greenland Ice Sheet

The mass balance of the GrIS began to deviate from its natural range of variability during the 1980's and has remained persistently negative since the early 1990's (Rignot *et al.*, 2008; Mouginot *et al.*, 2019; The IMBIE Team, 2020). Recent mass balance reconstructions over a forty-six-year period (1972-2018) by Mouginot *et al.* (2019) reported initial modest losses of 51 ± 17 Gt yr^{-1} during the 1980's, with a six-fold increase to 286 ± 20 Gt yr^{-1} for the period 2010-2018. Bevis *et al.* (2019) similarly reported substantial increases in mass loss, with a four-fold increase in GrIS mass loss between 2003 and 2013 from 102 Gt yr^{-1} to 393 Gt yr^{-1}. This study (Bevis *et al.*, 2019), like many others (Velicogna *et al.*, 2005; Luthcke *et al.*, 2006; Wouters *et al.*, 2008; Chen *et al.*, 2011), used satellite gravitational measurements from the Gravity Recovery and Climate Experiment (GRACE) satellite mission launched in 2002, to directly measure mass change and redistribution across Greenland. Observations early-on from GRACE confirmed the increasing negative mass balance of the GrIS (Velicogna *et al.*, 2005) and these have been used in combination with other methods since (radar and laser altimetry and mass budget method; Sasgen *et al.*, 2012; Shepherd *et al.*, 2012). This has provided additional insights into the physical processes of mass loss and helped reduce modelling uncertainties (Albert *et al.*, 2016). Cumulative ice losses from Greenland as a

whole have been close to the rates predicted by the Intergovernmental Panel on Climate Change (IPCC) for their high-end climate warming scenario. In the most recent IPCC report (Fox-Kemper *et al.*, 2021) the GrIS is estimated to have lost 4890 Gt (4140–5640 Gt) of mass between the period 1992 – 2020 (Figure 2.2). Accelerating trends in mass loss experienced across Greenland is increasing at a rate 1½ times greater than that observed in Antarctica (14.5 ± 2 Gt yr^{-2}) and three times greater than that of glaciers and ice caps (Rignot *et al.*, 2011; Albert *et al.*, 2016).

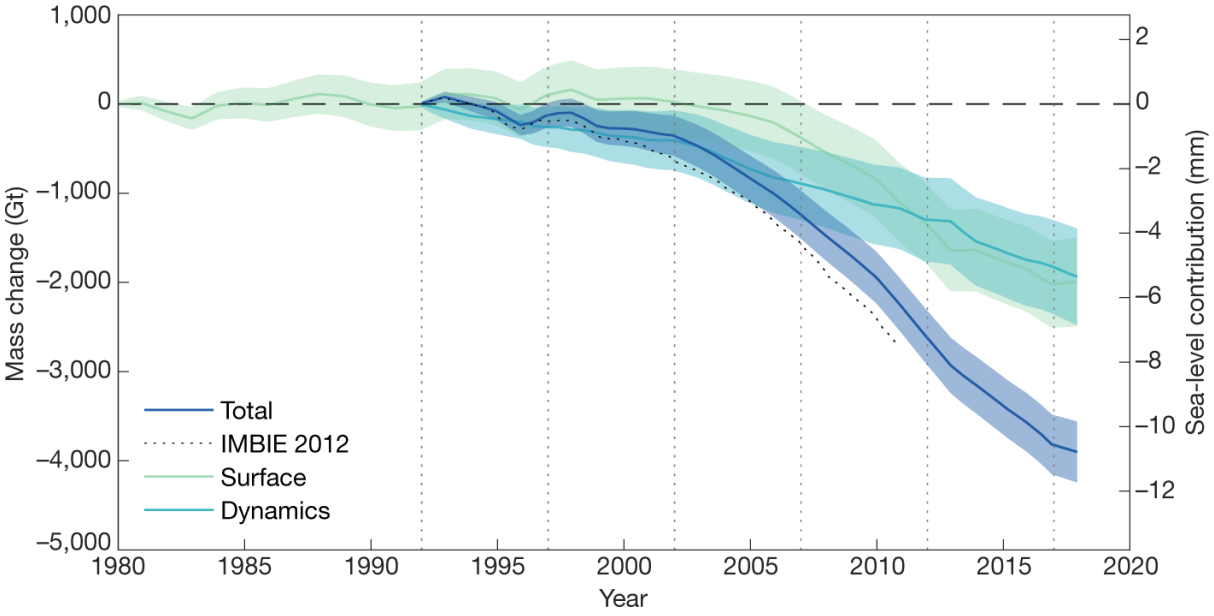

Figure 2.2. Greenland Ice Sheet mass balance (Gt) and sea level contribution (mm) between 1980 to 2018. Mass balance is divided into surface (surface mass balance) and dynamics (ice discharge from marine-terminating glaciers) components. Figure from The IMBIE Team (2020); their Figure 3.

When exploring the two key components of mass loss across the GrIS, SMB and dynamical contributions have varied overtime (van den Broeke *et al.*, 2009; Mouginot *et al.*, 2019; The IMBIE Team, 2020). Between 1996 and 2008, mass loss was equally partitioned between both ice discharge and SMB (van den Broeke *et al.*, 2009). In particular, ice loss was largely

concentrated in the southeast and northwest regions of the GrIS, due to increasing ice discharge from marine-terminating glaciers as a result of 'dynamic thinning'; a combined process of surface thinning, accelerated ice velocity and margin retreat (Nick *et al.*, 2009; Pritchard *et al.*, 2009). However, as discussed by Enderlin *et al.* (2014), this acceleration of outlet glaciers was short lived and non-uniform. Since 2009, Greenland-wide mass loss has become dominated by SMB, primarily via enhanced surface meltwater runoff which accounts for up to 68% of mass loss and is spatially constrained to a narrow zone along the ablating margins of the ice sheet (van den Broeke *et al.*, 2017). This SMB component, however, has high temporal variability. For example, between 2007 and 2012, 70% of total GrIS mass loss (193 ± 37 Gt yr^{-1}) was due to SMB, compared to 27% (22 ± 20 Gt yr^{-1}) over the preceding 15 years and 57% (139 ± 38 Gt yr^{-1}) between 2012 and 2017 (The IMBIE Team, 2020). This variable contribution is attributed to variations in atmospheric forcing, in particular the North Atlantic Oscillation (NAO) with negative phases promoting extreme melt events which can extend to the highest of elevations (>3000 m a.s.l; Nghiem *et al.*, 2012; Lenaerts *et al.*, 2019) and positive phases promoting cooler atmospheric conditions, summertime precipitation and reduced SMB contributions (Bevis *et al.*, 2019). As discussed by Slater *et al.* (2021), runoff is 60% more variable year-to-year due to such large-scale fluctuations of atmospheric circulation over the ice sheet.

2.3 Surface melt and runoff

Surface melt, via the melting of snow and ice, is generated by the net influx of energy from the atmosphere to the ice surface, driving ablation in the form of either sublimation or melting with the melt energy flux (M, W m^{-2}) becoming positive when the ice/snow surface reaches melting point (i.e., if the surface temperatures reach 0°C; Mantelli *et al.*, 2015). The melt rate of an ice surface is determined by the surface energy balance (SEB), which is the sum of all energy fluxes occurring towards and away from the surface, controlled by

meteorological conditions and the physical properties of ice (Hock, 2005). The SEB equation (equation 2.2) is as follows:

$$Q_M = Q_N + Q_H + Q_L + Q_G + Q_R$$

(Q_M = energy available for melting; Q_N = net radiation; Q_H = sensible heat flux; Q_L = latent heat flux; Q_G = ground heat flux (temperature change); QR = sensible heat flux of rain)

Equation 2.2

The most important energy source for surface runoff is the absorption of solar radiation, largely determined by the time of year, time of day, amount of cloud cover and surface albedo (Cuffey and Paterson, 2010; van Angelen *et al.*, 2014; Mantelli *et al.*, 2015).

2.3.1 Atmospheric and meteorological influences

Net incoming solar radiation is, of course, at its greatest during summer, with the melt season extending between May and September for the GrIS, typically peaking in July (Howat *et al.*, 2010). Net radiation exhibits large diurnal fluctuations, with higher values during the day and lower values during the night (Hock, 2005). Such diurnal fluctuations in the rise and fall in daily surface temperatures, wind and humidity gradients between the air and ice surface also affect turbulent heat fluxes (sensible and latent heat fluxes), influencing subsequent melt rates (Hock, 2005). At high latitudes and on ice however, such components are further complicated by solar zenith angles, with a minimum angle of 37° and 60° in southernmost and northernmost Greenland, respectively (Wang and Zender, 2010), which prolong the daily exposure to solar radiation.

Regulation of shortwave radiation by cloud cover also has implications on the SEB and subsequent melt extent (Bennartz *et al.*, 2013) and meltwater runoff (Van Tricht *et al.*, 2016)

via the competing effects of shortwave radiation shading (i.e., cooling) from cloudy conditions and longwave radiation trapping (i.e., warming; Ryan *et al.*, 2022). Clouds can increase the long-wave radiation emitted to the surface due to having a higher emissivity than a clear-sky, increasing the proportion of diffuse radiation and altering the spectral distribution towards shorter wavelengths (Van Tricht *et al.*, 2016; Wang *et al.*, 2018; Djoumna *et al.*, 2021). The strongest of these radiative effects have been found near the summit of Greenland, enhancing melt by up to one-third relative to clear skies (Van Tricht *et al.*, 2016). In a warmer climate, it is expected that shortwave shading will strengthen in the ablation zone due to decreased surface albedo (Ryan *et al.*, 2022).

2.3.2 Albedo

Through increased sunlight and absorbed solar radiation through the melt season, surface conditions shift from a high reflective, dry snow cover to lower albedo wet snow with larger grains and even lower albedo across the bare ice ablation zone (Wiscombe and Warren, 1980; Wehrlé *et al.*, 2021). Albedo is an important modifier of the energy budget that varies greatly spatially and temporally over the ice surface. Albedo ranges from 0.1 for dirty ice to 0.9 for fresh snow (Cuffey and Paterson, 2010). Many factors can affect the albedo of an ice surface, including (i) melting of the snowpack which increases snow grain size (Brun, 1989), (ii) the feedback between meltwater accumulation and runoff through supraglacial lakes and channels (Ryan *et al.*, 2018; Pitcher and Smith, 2019; Leidman *et al.*, 2023), (iii) the presence of dust, sediment and wind-blown deposits on bare ice, including their aggregation to create cryoconite holes (Cook *et al.*, 2018; Ryan *et al.*, 2018; 2019), and (iv) the presence of microorganisms and organic matter such as pigmented algae (Stibal *et al.*, 2017; Cook *et al.*, 2020), which can further decrease surface albedo. Such impurities in ice have been shown to have a drastic effect on the albedo of the GrIS surface. For example, the 'dark zone' in southwest Greenland, which is a conspicuous bare ice feature extending 20–75 km from the ice margin and clearly visible from space during the summer melt season, has albedo

values which reach as low as 0.27 due to the expanse of surface water and distributed abiotic sediment (i.e., dust, melt-out black carbon) and microbial communities (pigmented algae; Ryan *et al.*, 2018; 2019). In particular, microbial processes have been shown to play a key role in driving the darkening of this region, with longer periods of snow-free ice and warmer air temperatures driving algal blooms and subsequent melt and runoff amplification across this area of the ice sheet (Wientjes and Oerlemans, 2010; Wientjes *et al.*, 2011; Ryan *et al.*, 2018). As darker surfaces absorb more radiation than brighter, more reflective surfaces, more melt is produced creating a positive feedback loop (Stroeve, 2001; Box *et al.*, 2012; Tedesco *et al.*, 2016).

2.3.3 Firn and the percolation zone

In the high-elevation accumulation zone, surface melting may still occur in an area known as the percolation zone. However, rather than meltwater running directly across the ice surface, complex firn processes of melting and refreezing govern the proportion of meltwater that is instead stored and refrozen locally (Machguth *et al.*, 2016; Ashmore *et al.*, 2020; Culberg *et al.*, 2021). Firn is the transitional material between seasonal snow and ice, with ample pore space between snow grains enabling the percolation of meltwater into firn layers to locally refreeze – if firn temperatures are below freezing. Currently, the percolation zone, may have the potential to buffer a considerable amount of meltwater and, as such, reduce over-ice runoff (Harper *et al.*, 2012). Unlike meltwater below the ELA, which may percolate into the snow pack accumulated from the previous winter, refreeze, and delay exposure of bare ice until saturation is reached, surface meltwater at higher elevations (percolation zone) can penetrate the snowpack into cold, deep firn (up to 10 m) and persist for many months to either refreeze or migrate downglacier to become runoff in the future (Humphrey *et al.*, 2012; Steger *et al.*, 2017a). If not accounted for in SEB and runoff models, such model estimates will show more water exiting the system than actually observed (Cuffey and Paterson, 2010). However, the formation of thick, low-permeability, near-surface ice layers

known as ice slabs may prevent such infiltration, with widespread layers up to 5.5 m in depth recorded in the lower percolation zone in spring 2013 by Machguth *et al.* (2016) after the extreme melt season of 2012 (Nghiem *et al.*, 2012). Such ice slabs can prevent meltwater reaching the pore space below with such low-permeability horizons developing rapidly during extreme melt seasons and promoting runoff, which can expand and thicken overtime. Jullien *et al.* (2023) found ice slabs expanded by 44% between 2012 and 2018 and will be an important ongoing control of runoff into the future.

2.3.4 Change in meltwater runoff

Over the last two decades, the lengthening and intensification of Greenland's melt seasons, observed through both automatic weather stations and remote sensing applications (Fettweis *et al.*, 2011; Chu, 2014), has driven enhanced ablation in the form of melt and runoff across various GrIS regions. Much of this has occurred along western and southwestern regions of the GrIS: a region dominated by strong warming. This is attributed to fluctuations in climate-driven temperature and insolation at its wide, flat ablation zone surface alongside impacts from positive feedback mechanisms driven by absorbed solar radiation across its dark bare ice surface (Fettweis *et al.*, 2013; van Angelen *et al.*, 2014; Lenaerts *et al.*, 2015; van den Broeke *et al.*, 2017; Bevis *et al.*, 2019). Southwestern Greenland in particular has contributed the most to total ice sheet runoff, accounting for 32% between 1958 and 1990 and 30% between 1991 and 2017 (Figure 2.3; Noël *et al.*, 2019). Pronounced latitudinal differences however exist in the response of the GrIS to recent warming, as shown by Noël *et al.* (2019), whereby the ablation area in northern Greenland has expanded by 46% (twice as much as the south) since 1990. Additionally, snowline retreat has moved the ELA upward by 200 m in northern Greenland (900–1100 m a.s.l) and 100 m in southern Greenland (1350–1450 m a.s.l) leading to an increase in runoff by 12 Gt yr^{-1} and 17 Gt y^{-1}, respectively. North Greenland has therefore significantly increased its relative

contribution to total GrIS mass loss through enhanced runoff, in particular an increase in the saturation of the percolation zone since the mid-1990s (Noël *et al.*, 2019).

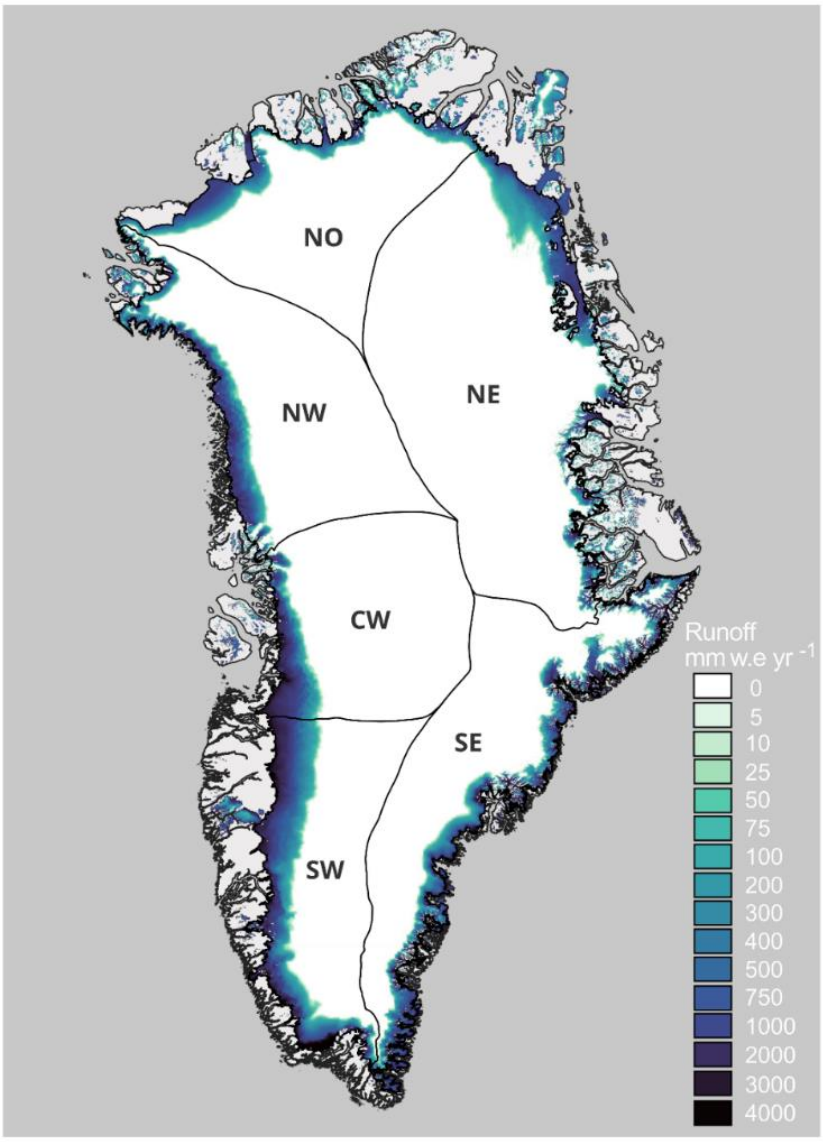

Figure 2.3. Runoff patterns (mm w.e. yr^{-1}) across different sectors of the GrIS between 1958 and 2017 modelled by RACMO2.3p2 at 1 km horizontal resolution. Map reproduced using data from Noël *et al.* (2019).

Additionally, a string of record-setting melt years, including the melt anomalies of 2010, the extreme melt event of 2012 and, most recently 2019, has shown the susceptibility of the GrIS to rapid mass loss via SMB processes (Mernild and Liston, 2012; Nghiem *et al.*, 2012; Tedesco *et al.*, 2013; Tedesco and Fettweis, 2020; Elmes *et al.*, 2021). The 2012 extreme melt event was the largest and most expansive to have occurred in Greenland since the beginning of the satellite era (Tedesco *et al.*, 2013), with 98% of the GrIS experiencing surface melt, reaching elevations of up to 3200 m a.s.l (Nghiem *et al.*, 2012; Bennartz *et al.*, 2013; Tedesco *et al.*, 2013). Further observations by Trusel *et al.* (2018) found this magnitude of melting was exceptional over at least the last 350 years. Surface melting in 2019 also reached record levels, with melt observed over 90% of the ice sheet on at least one-day, reaching Summit (3200 m a.s.l) and much of the high-altitude areas, with melting occurring for an additional 35 days compared to the 1981–2010 average (Tedesco *et al.*, 2019). Today, the increasing duration and extent of surface melting and runoff across the GrIS is occurring at magnitudes unseen for several centuries, with up to a 575% increase in melt intensity of the last 20 years relative to the pre-industrial era (Trusel *et al.*, 2018).

2.4 Greenland Ice Sheet Hydrology

Ice sheet hydrology is the scientific study concerning the storage and movement of surface meltwater in the cryospheric environment and consists of three main components: (i) the supraglacial routing of meltwater across the ice surface; (ii) the englacial movement of meltwater internally through ice and; (iii) the subglacial transport of meltwater at the ice-bed interface, with potential implications for localised ice flow (Figure 2.4; Cuffey and Paterson, 2010; Colgan *et al.*, 2011; Irvine-Fynn *et al.*, 2011; Chu, 2014; Nienow *et al.*, 2017; Pitcher and Smith, 2019).

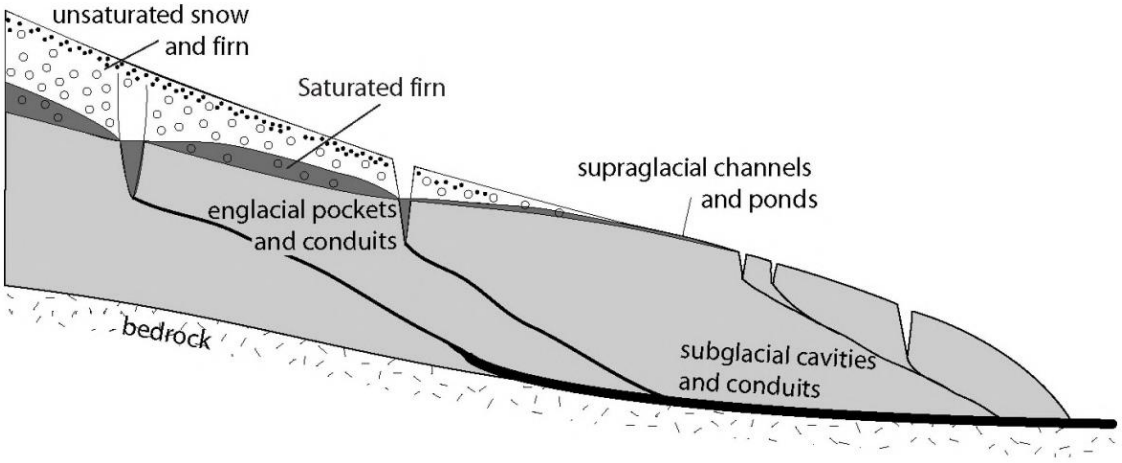

Figure 2.4. Simple schematic of the hydrologic system of a glacier and/or ice sheet consisting of the supra-, en- and subglacial hydrologic systems. Figure taken from Jansson (2007; their Figure 2.1) which was based on Rothlisberger and Lang (1987).

The supraglacial hydrologic system on the GrIS is extremely complex, consisting of a network of supraglacial channels (e.g., rivers and streams), supraglacial lakes (SGLs), crevasses and moulins, which comprise one of the least studied hydrologic systems on Earth (Figure 2.5; Yang and Li, 2014; Smith *et al.*, 2015). As such, supraglacial hydrology plays a key role in the production, transportation, storage and release of seasonal meltwater at the surface, and establishes a direct connection between the supraglacial, englacial and subglacial systems (Yang and Li, 2014; Mantelli *et al.*, 2015).

Despite functioning as a highly complex interconnected hydrologic network, supraglacial channels and lakes have been commonly studied as independent features due to differences in their characteristics (i.e., size and shape) and their varying ability to be observed, extracted and mapped from remotely-sensed imagery (Yang *et al.*, 2021). This has resulted in a variable and incomplete picture and understanding of their collective impact on meltwater routing and storage on the GrIS. In Sections 2.5 and 2.6, supraglacial channels

and lakes (SGLs) are further defined individually. However, in this thesis, they are both encapsulated within the term; the supraglacial hydrologic network.

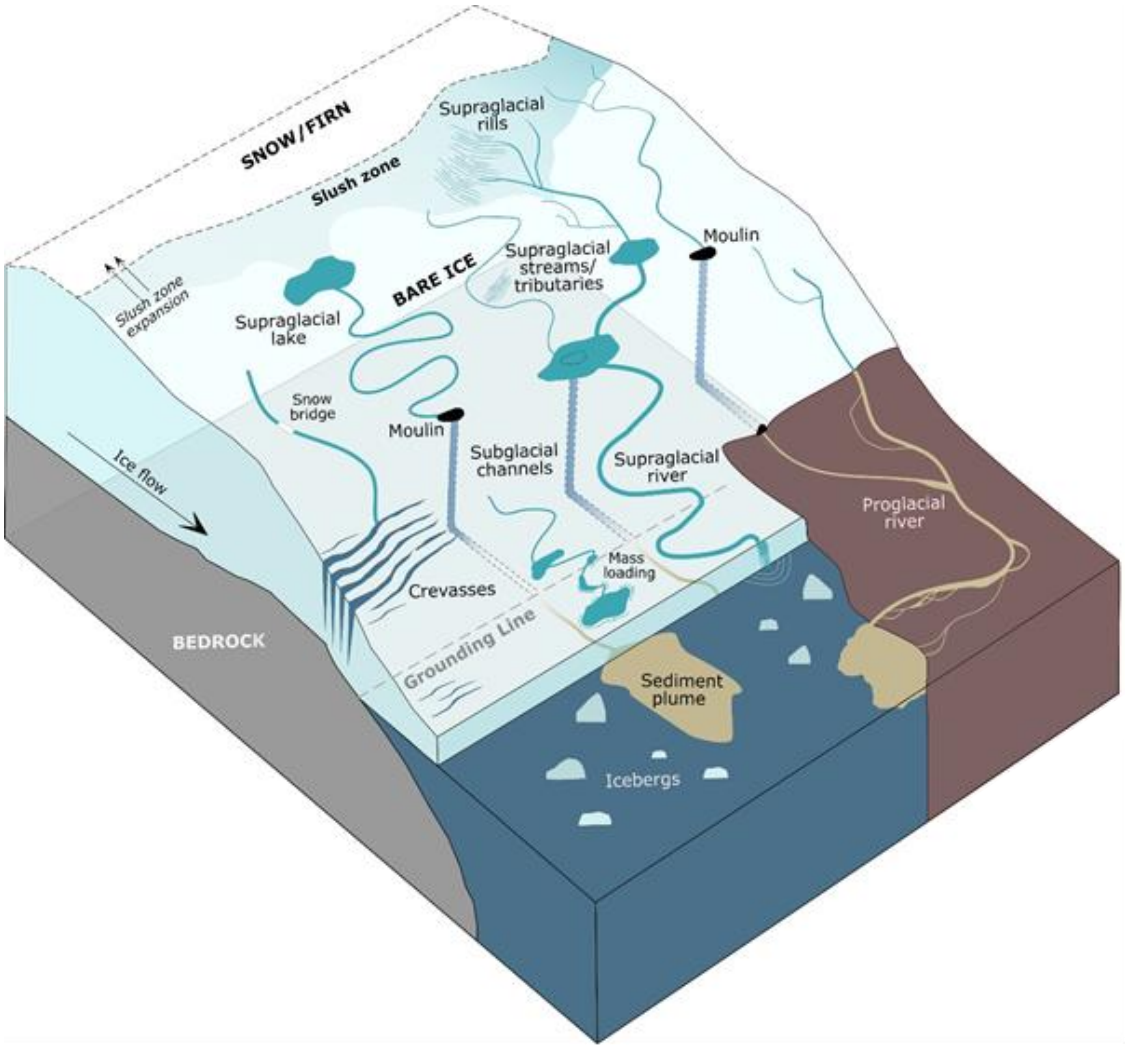

Figure 2.5. Schematic of the components of the supraglacial hydrologic network on the GrIS. Figure adapted from Pitcher and Smith (2019) with permission.

Much of the glaciological research into ice sheet hydrology has been based upon initial work that explored the movement of water and related processes at temperate-alpine glaciers, with the conditioned assumption that these processes can be scaled up effectively for large ice sheets (Bartholomew *et al.*, 2010; Chu, 2014; Lindbäck *et al.*, 2015). Several reviews have

focussed on a wealth of theoretical and field-based research in these alpine environments during the 20th Century. Fountain and Walder (1998) proposed one of the first conceptual frameworks for the interactions of meltwater flow on, in, under and from glaciers based within temperate regions, extending the scope of previous work by Rothlisberger and Lang (1987). Jansson *et al.* (2007) provided a review on the theoretical knowledge of such water flow and its applicability on larger ice sheet scales with Irvine-Fynn *et al.* (2011) providing a further, detailed overview of the hydrological processes on polythermal glaciers, including polar ice masses. At these locations, distinct analogies of the supraglacial, englacial and subglacial hydrologic networks were found between nontemperate valley glaciers and ice sheets,but with recognition that these high-latitude ice masses tend to have reduced surface slopes (with enhanced emphasis on supraglacial processes) and that thick ice (>1 km) and high overburden pressure of ice interiors promote fast creep closure of unpressurised subglacial conduits (Greenwood *et al.*, 2016). Nienow *et al.* (2017) reviewed understanding of ice sheet hydrology on the GrIS, which has undergone considerable advances throughout the 21st Century due to increasing melt rates. Here, examination of the supraglacial, englacial and subglacial processes and hydro-dynamic coupling were made, with recognition of ground-breaking work that found meltwater penetrating thick (>1 km) cold ice with implications for ice motion depending on the ability of the subglacial drainage system to accommodate melt inputs. Finally, a recent review by Pitcher and Smith (2019) provided the first synthesis and review of supraglacial channels only, reviewing their geographical location, formation and morphometrics utilising the wealth of hydrological research knowledge that continues to progress today.

2.4.1 Development and current interest in supraglacial hydrology

The history of supraglacial hydrologic research spans several decades, and first evolved from early observations of channel morphology and formation mechanisms derived from alpine-

based studies, to detailed studies of their hydrological dynamics to more recent broad-scale network quantification and morphometric analysis from satellite-acquired imagery.

Historical records of meltwater transport on the surface of ice sheets can be dated back more than 100 years via observational records. As identified and reviewed by Pitcher and Smith (2019), the presence of channelised water on Greenland was recounted by numerous early polar explorers during traverses across the ice sheet. Reports by Fridtjof Nansen (1906) and a Swiss team led by Alfred de Quervain (1909; Barr, 2015), reported crossing such channels with 'depths submerging explorers' ankles and the loss of equipment in such meltwater rivers when performing an eastward traverse (Pitcher and Smith, 2019). With developments in aerial surveying and photography into the mid-20th Century, it is reported that the presence of such meltwater channels was commonly used for navigational purposes by the Arctic Air-Route Expedition and the US military in southwest Greenland (Chapman, 1932). Military-based research also extended into glaciological studies within the vicinity of the Thule Air Base, north Greenland (

Figure 2.6), including the collection of accumulation and ablation data (including mention of meltwater channels) in 1954 (Schytt, 1955) and 1956 (Griffiths, 1960), including the characterisation of supraglacial channels (including details regarding channel width, spacing, morphometry and lateral spacing) by Nobles (1960).

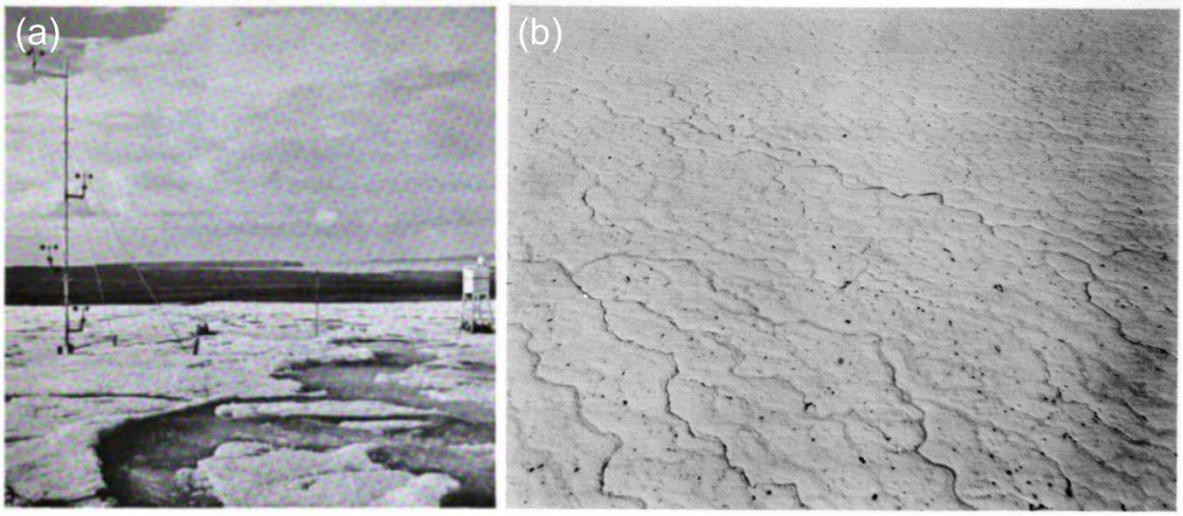

Figure 2.6. Examples of early supraglacial hydrologic research on the GrIS. (a) Image from Schytt (1955) showing a weather station and ablation stake at Thule Ramp (569 m a.s.l), north-western Greenland for monitoring accumulation and ablation. A supraglacial stream is visible with Schytt (1955) noting *'unusually heavy runoff'* during the summer melt season of 1954. (b) Image from Nobles (1960) showing supraglacial streams and small meltwater ponds on Nunatarssuaq ice ramp, near Thule, northwestern Greenland, during the ablation season of 1955.

Such observations led to more targeted and detailed field investigations of supraglacial hydrology, predominately that of supraglacial channels, in the more accessible regions of alpine glaciers. This included the discovery of the perennial nature of ice marginal stream channels by Ferguson (1973) and studies specifically characterising hydraulic channel geometry, meandering behaviour, longitudinal profile and comparisons with their terrestrial-based counterparts (Knighton, 1972; Parker, 1975; Knighton, 1981a; Knighton, 1981b; Marston, 1983; Knighton, 1985; Dozier, 1989).

With an increasing awareness of accelerating mass loss and an expanding melt extent across the GrIS, there has been a growing body of literature into ice sheet hydrology over the last two decades (Figure 2.7). This has included across both independent supraglacial features and the overall nature of the supraglacial hydrologic network, due to its governance of ice sheet SMB and potential for driving significant dynamical change (Chu, 2014; Koziol, 2018). Such research has largely been facilitated by the advancements, acquisition and availability of geospatial datasets, predominately remotely-sensed data (i.e., satellite-acquired imagery), which continues to increase in coverage, temporal and spatial resolution (further introduced in Chapter 3).

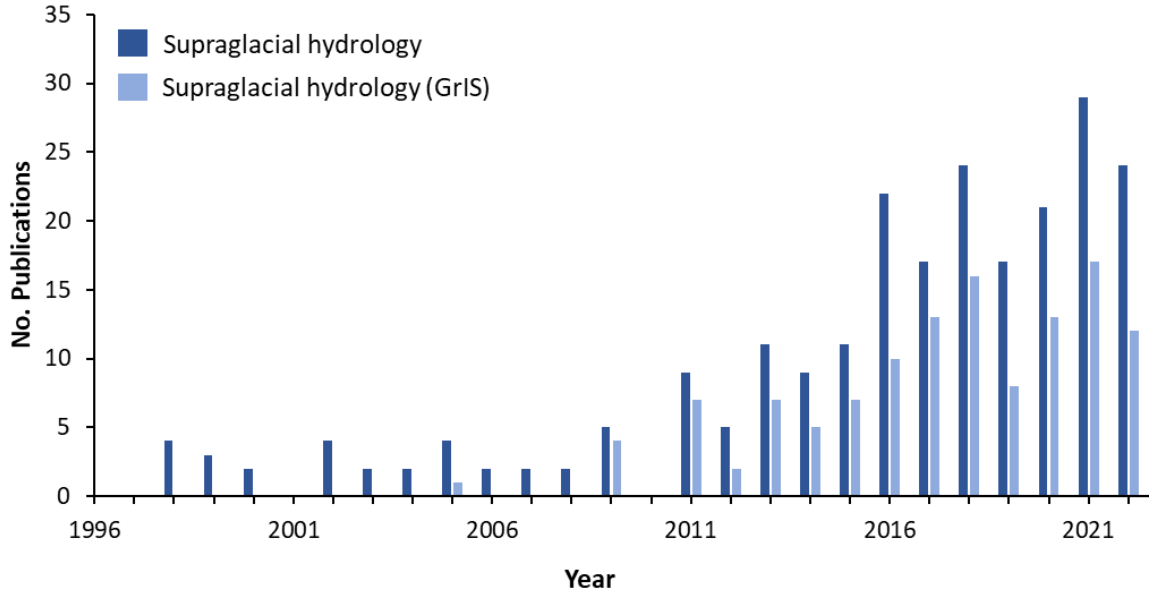

Figure 2.7. The number of scientific-focussed studies on supraglacial hydrology (worldwide) and supraglacial hydrology focussed on the GrIS containing the words 'supraglacial hydrology', 'supraglacial lakes' and 'supraglacial channels' from a search of Web of Science (search date: 20th December 2022, glaciological studies only).

Ice sheets are cold, harsh, remote and logistically difficult-to-study environments. The supraglacial hydrologic network can expand tens of kilometres from the ice margin, hence why long-term field-based scientific observations are somewhat limited and understanding is largely built upon more accessible, alpine-focussed investigations. The use and advancements of remotely-sensed data and automated detection approaches (further discussed in Chapter 3), however, has expanded the possibility of examining such surface systems from a distance and, over time at varying resolutions, enabling more broad-scale morphometric characterisations of supraglacial hydrology to be made, including that of supraglacial channels, which are narrow and hard-to-map features (Yang and Smith, 2013).

Much of the hydrologic interest to-date on the GrIS has focussed on western and south-western regions of the GrIS, both in terms of satellite- and field-based studies, due to the extensiveness of the supraglacial hydrologic network across this wide and (somewhat)

accessible ablation zone. These turquoise-coloured supraglacial lakes and dense interconnected networks of rivers and stream channels have been shown to progressively develop inland with snowline migration throughout the melt season (Sundal *et al.*, 2009; Sundal *et al.*, 2011). Understanding the spatial distribution of these networks, the inter and intra-annual behaviours of these features and building a holistic, Greenland-wide map is an ongoing process involving both mapping and modelling at increasingly higher spatial and temporal resolution imagery to generate more in-depth ice-sheet understanding into the effects of increasing melt and runoff.

2.4.2 Spatial distribution and network configuration

2.4.2.1 Western and southwestern GrIS

As already mentioned, within Greenland, a large fraction of supraglacial hydrologic research, including as independent supraglacial features (i.e., channels and lakes) and as a collective network, has been conducted in the largest melt producing sectors of western and south-western regions of the ice sheet. Here, the ablation zone during the summer melt season is dominated by an extensive hydrologic network of both channels and lakes that control surface meltwater routing and storage (Smith *et al.*, 2017). Thomsen (1986) was the first to delineate a series of perennial supraglacial channel networks distributed in the Jakobshavn Isbrae region of western Greenland from high-resolution aerial photographs, revealing supraglacial drainage patterns on the GrIS for the first time, with recognition that the drainage pattern was influenced by local and general surface topography. Since then, broad-scale morphometric studies of the supraglacial hydrologic network on the GrIS has been greatly facilitated through the acquisition and availability of remotely-sensed imagery. Joughin *et al.* (2013) used high-resolution commercial-based satellite imagery (0.6 m; Worldview (WV)) to manually delineate supraglacial channels in a small area (33 x 57 km) south of Jakobshavn Isbrae, western Greenland, between 2009 and 2011, revealing a trellis-

like drainage pattern where channels flow roughly transverse to the direction of ice flow. Lampkin and VanderBerg (2014) tracked large supraglacial channels using Landsat-7 imagery (30 m) throughout the 2007 melt season, again from the Jakobshavn outlet region. This study found supraglacial channels increased in total number and mean length during the melt season, co-evolving with surface melt. Major, or 'high order' supraglacial channels dominated elevations >800 m a.s.l and extended to a maximum elevation of 1647 m a.s.l. The lengthening of supraglacial channels at higher elevations was further reported by Poinar *et al.* (2015), who found channels of up to ~55 km in length reached elevations of 1700 m a.s.l, whereas shorter streams measuring ~6 km were common at lower elevations (1200 m a.s.l). Lampkin and VanderBerg (2014) were also the first to develop a qualitative classification system on which to base their findings, dividing the satellite-mapped supraglacial hydrologic network into three key-classes based on their morphological characteristics and topological relationships: (1) tributary channels defined as those flowing into another channel or SGL; (2) connector channels representing flow between two SGLs and; (3) terminal channels that cease into SGLs, open moulins or crevasses (Figure 2.8). It was found that tributary channels dominated earlier in the melt season, with connector configurations most prevalent during the melt season peak, with the connection to lake basins promoting shorter channel lengths, and terminal configurations dominating later into the melt season.

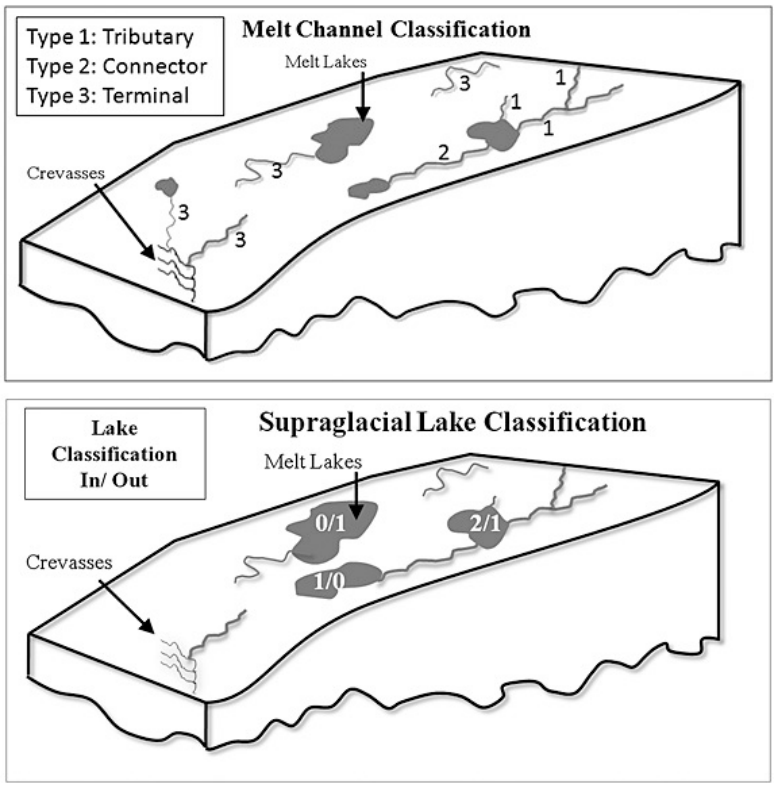

Figure 2.8. Schematic of the supraglacial hydrologic classification system used by Lampkin and Vanderberg (2014; their Figure 3). (a) Classification of supraglacial channels depending on their connection with SGLs, from type 1 (tributary), type 2 (connector) and type 3 (terminal); (b) classification of SGLs based on in and output connections with supraglacial channels.

As hydrologic research progressed, Yang and Smith (2013) emphasised the need to gain a better understanding of the supraglacial hydrologic network on the GrIS, in particular (i) via higher resolution imagery (e.g.,WV) to examine narrow channels that are difficult to resolve in coarse resolution imagery and (ii) via new automated computational methods to examine them over multiple images across large areas of the ablation zone without the requirement of manual digitisation. Termed the 'automatic river detection algorithm' (further examined in Chapter 3), supraglacial channels, including narrow stream channels, were used to test the effectiveness of the algorithm and were subsequently mapped from WV-2 imagery across an area of the southwestern ablation zone of the GrIS near Kangerlussuaq. This test resulted

in the identification of 62,682 actively flowing supraglacial streams and 92 SGLs, with further refinements suggested for dealing with slushy (highly water saturated) regions. This automated method (Yang and Smith, 2013) has continued to be utilised for a wealth of other broad-scale, remotely-sensed GrIS hydrologic studies. This includes Smith *et al*. (2015), who used the method to extract 523 supraglacial channels classed as 'high order' primary channels across a 6812 km^2 area of western Greenland to characterise supraglacial transport, storage and drainage pattern. Efficient supraglacial drainage was found throughout these 523 channels, all of which terminated in moulins before reaching the ice edge. Similarly, Yang *et al*. (2021) used the automatic river detection algorithm (and developments therein of this method; Yang *et al.*, 2015a; Yang *et al.*, 2017) on seven Landsat 8 (30 m) images between June and August 2015 to assess the seasonal evolution of the supraglacial network that feed two major drainage basins in southwestern Greenland, Isortoq and Watson (Qinnguata Kuussua), collectively covering ~11,000 km^2. This study found the progression of the supraglacial network from low (<1500 m a.s.l) to high (>1600 m a.s.l) elevations as the melt season progressed, with supraglacial river channel area peaking 7-10 days earlier than SGLs. Overall total surface meltwater area and discharge were dominated by supraglacial river channels and meltwater volume dominated by SGLs.

The collection, routing, storage and evacuation of melt through the supraglacial hydrologic network was acknowledged by Yang and Smith (2016) to occur through supraglacial internally drained catchments (IDCs) on the GrIS. These are defined as hydrologic units which control the volume and locations of meltwater moving across and penetrating the ice surface, and provided a new scale (elevation-area relationship) for studying surface hydrologic processes on the GrIS. Yang and Smith (2016) examined 919 IDCs covering 22,788 km^2 in south-western Greenland and found IDC areas increased with elevation and

the presence of high-elevation moulins indicated the penetration of surface melt at surprisingly high elevations

2.4.2.2 Other ice sheet sectors

In more recent years, studies have begun to explore the supraglacial hydrology of other GrIS regions and surrounding glaciers and ice caps due to a need to holistically understand the existence and behaviour of networks in other ice sheet regions; a key aim of this thesis. Yang *et al.* (2019) utilised the automatic river detection algorithm (Yang *et al.*, 2015a; Yang *et al.*, 2017) to map the supraglacial hydrologic network near Inglefield Land, northwestern Greenland, as well as the Devon and Barnes Ice Caps, using both Sentinel-2 (10 m) and Landsat 8 (30 m) imagery covering a total area of 10,000 km^2. In particular, in northwest Greenland, supraglacial channels were found to be densely-packed and sub-parallel in nature, reaching lengths of 65 km originating from high-elevation slush fields (1500 m a.s.l). This was found to be very different to the dendritic-style of drainage in the western and southwestern regions of the ice sheet, with meltwater transported directly to the ice margin without interruption from moulins or crevasses, as well as a lack of interconnectivity with SGLs, indicating limited variations in surface relief. This study was also the first to map the supraglacial hydrologic network from Sentinel-2 imagery and highlighted the superiority of Sentinel-2 imagery compared to Landsat for better extracting the narrow and continuous forms of supraglacial channels, building a more complete picture of the network. Seasonal evolution of the supraglacial hydrologic network over seven days in 2015 was also conducted in northeast Greenland by Lu *et al.* (2021) encompassing Zachariæ Isstrøm and Nioghalvfjerdsfjorden (79°N) glaciers. The network here was found to extend up to 1400 m a.s.l, with network characteristics influenced by differing flow regimes, as further discussed in Section 2.4.2.4.

2.4.2.3 DEM modelling for supraglacial network mapping

Digital elevation model (DEM)-based extraction of Greenland's supraglacial hydrologic network has also been explored as a technique for mapping glacier-wide networks, with varying degrees of success. Predominately, DEM-based flow routing, which is a widely accepted, simplistic method for delineating channels from DEMs in a terrestrial setting, can be performed using built-in GIS-based tools (QGIS.org, 2023; ESRI, 2023). Such flow routing is typically performed using a standard D8 (deterministic eight-direction) flow routing algorithm (O'Callaghan and Mark, 1984) and assumes an impermeable surface with no surface storage, whereby sinks (low elevation pixels surrounded by high elevation pixels) are levelled and water flow routed directly to a catchment outlet (Tarboton *et al.*, 1991; King *et al.*, 2016). This is problematic on icy surfaces as, in reality, the presence of meltwater sinks, such as moulins, can fragment the network and capture runoff before it has time to reach the ice edge (Yang and Smith, 2016; Crozier *et al.*, 2018). Yang *et al.* (2015b) mapped a 24,000 km^2 area of south-western Greenland and found DEM-derived supraglacial networks were significantly overestimated (with 100% DEM filling) when compared to satellite-derived networks, with suggestions of retaining meltwater sinks (i.e., SGLs and moulins) to produce more realistic networks whilst issuing a caution of using coarse resolution DEMs (30-40 m) to perform such work. To overcome such limitations, Karlstrom and Yang (2016) manually identified moulin locations from WV-1 imagery and preserved sinks across resampled, higher resolution DEMs (2 m) to map four regions in southwestern Greenland with increasing elevation (1000–1600 m) over the 2011 melt season. King *et al.* (2016) furthered such work and assessed the performance of D8 flow routing on newly available 2 m DEMs (WV-1) via the manual identification and retention of sinks (i.e., moulins) across the western margin of Greenland and compared outputs to manually digitised channels from multi-spectral imagery. This study found flow routing was capable of replicating 99% of the satellite-derived network when moulin locations were properly determined, however channel initiation

thresholds required location-specific values. Overtime, the viability of using DEMs to produce realistic supraglacial hydrologic network has improved greatly when terminal points are considered.

2.4.2.4 Controls on supraglacial drainage configuration

Collectively, supraglacial hydrologic studies have shown the variability of supraglacial hydrologic or drainage patterns in different regions of the GrIS. From a dendritic and centripetal pattern of drainage recognised in western and southwestern Greenland, which displays a branching network of channels and lakes that converges at terminal points (i.e., moulins; Smith *et al.*, 2015; Yang *et al.*, 2021; Figure 2.9b) to sub-parallel styles of drainage with elongated channels that transport melt directly to the ice edge in northern regions of the ice sheet (Figure 2.9a, 2.9c; Yang *et al.*, 2019). This structure controls the location and characteristics of surface-to-bed connections (Smith *et al.*, 2017; Crozier *et al.*, 2018; Mejia *et al.*, 2022) as well as the timing and magnitude of meltwater evacuation from the surface through IDCs (Selmes *et al.*, 2011; Smith *et al.*, 2015; Igneczi *et al.*, 2016; Yang and Smith, 2016).

Such differences in large-scale surface drainage patterns and the spatial distribution of the network are primarily determined by ice surface topography (Luthcke *et al.*, 2006; Banwell *et al.*, 2012; Leeson *et al.*, 2012; Igneczi *et al.*, 2016; Karlstrom and Yang, 2016), influenced by variations in bed roughness and slipperiness and its subsequent transmission through ice to the surface (Crozier *et al.*, 2018; Ignéczi *et al.*, 2018). At wavelengths greater than ice thickness, bedrock dominates surface topography and preconditions the large-scale

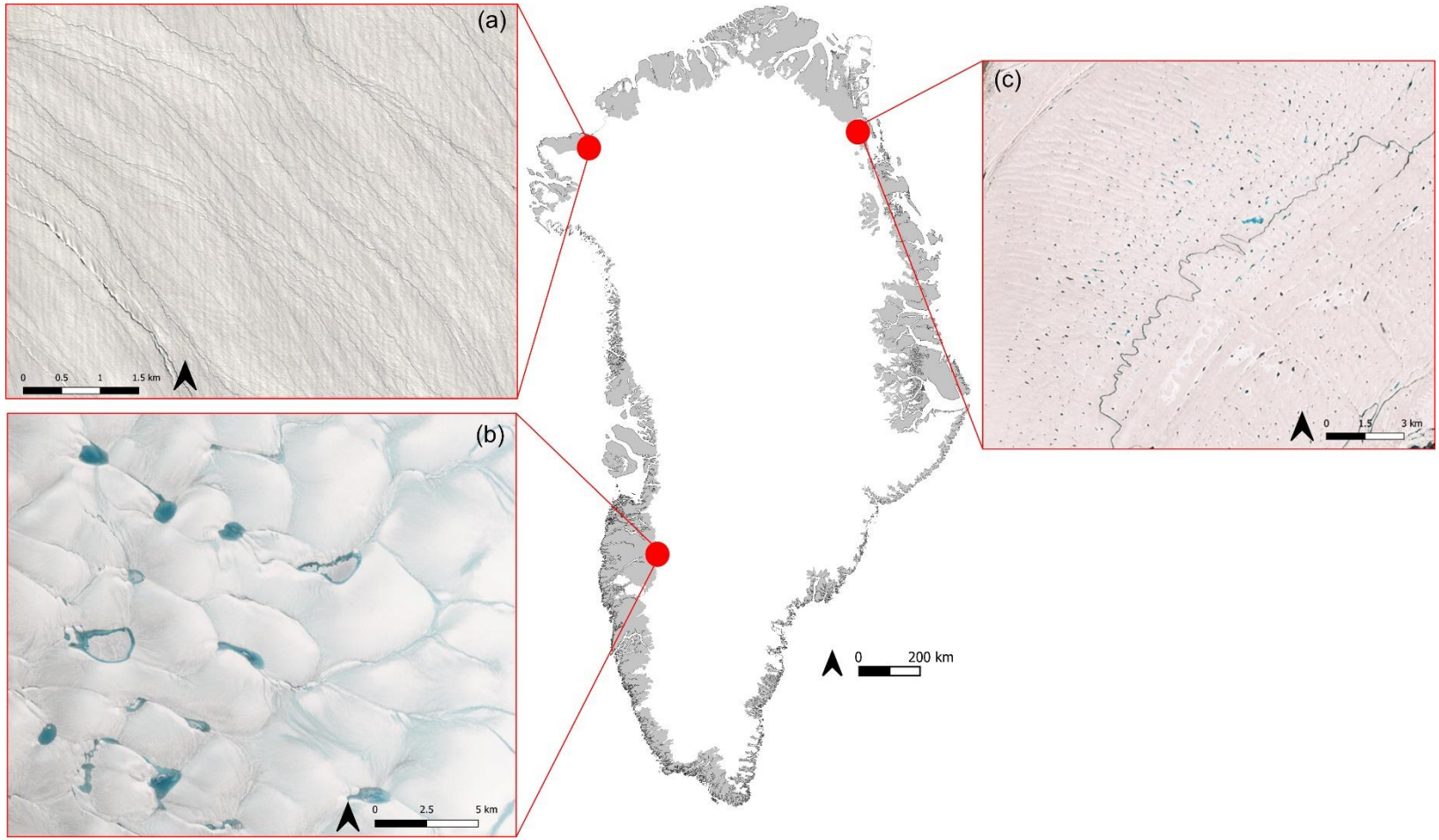

Figure 2.9. Examples of the differing drainage styles of the supraglacial hydrologic network in three regions of the GrIS, as identified in relevant literature. (a) Sub-parallel, densely packed supraglacial channels up to 65 km in length near Inglefield Land, identified by Yang *et al.* (2019). Sentinel-2 image from 23rd July 2016; (b) dendritic, 'trellis' style of drainage in western Greenland with interconnected supraglacial channels and SGLs. Sentinel-2 image from 7th July 2016; (c) the supraglacial network on the floating tongue of Nioghalvfjerdsfjorden (79°N glacier), with ice flow regimes influencing hydromorphology, as identified by Lu *et al.* (2021). Image from ESRI satellite, ArcGIS Pro.

structure of the surface hydrologic network, with surface drainage basins fixed in space (Karlstrom and Yang, 2016). The basal transfer of bed topography to the surface has been shown to occur at wavelengths between three to eight times that of ice thickness (Figure 2.10; Raymond and Gudmundsson, 2005; Lampkin and VanderBerg, 2011), with deviations in surface geometry at smaller wavelengths reflecting physical-based processes, including the SEB and fluvial erosion via thermal energy (Cuffey and Paterson, 2010; Crozier *et al.*, 2018).

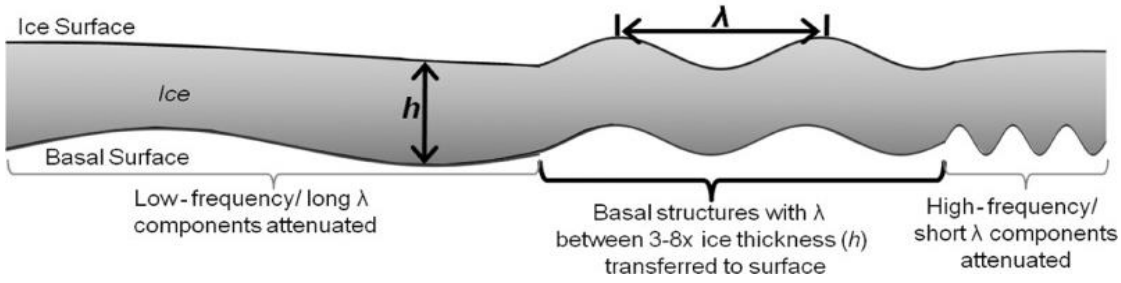

Figure 2.10. Schematic taken from Lampkin and Vanderberg (2011) showing the basal-to-surface topography transfer as a function of ice thickness. (*h*) Denotes ice thickness, (λ) indicates surface and basal wavelength, with three to eight times the ice thickness readily transferable to the ice surface. High frequency wavelengths are unable to be expressed on the ice surface.

Additionally, underlying ice flow processes and flow regimes also control how effectively such topography is transmitted to the ice surface. As discussed by Ignéczi *et al.* (2018), faster basal sliding promotes the more efficient transfer of basal topography to expressions on the ice surface, forming a greater number of topographical depressions and controls on the location, size and shape of the supraglacial network. Work conducted by Lu *et al.* (2021) at Nioghalvfjerdsfjorden (79°N) glacier found such differences in the hydromorphology of the supraglacial network due to ice flow regime differences. In areas of fast flow (186–486 m yr^{-1}) at Nioghalvfjerdsfjorden (79°N) glacier), shorter channels and smaller SGLs were present

with more instances of rivers terminating in moulins. In contrast, in the slow regime (32 m yr^{-1}) which is mainly controlled by ice deformation, supraglacial rivers were long and continuously flowed off the ice sheet edge or towards other flow regimes, with limited opportunity to penetrate to the ice sheet bed. This is similar to the supraglacial hydrologic network mapped at slow moving ice near Inglefield Land (northwest Greenland) by Yang *et al.* (2019) and again by Li *et al.* (2022), with drainage dominated by sub-parallel, lengthy channels up to 65 km in length. Additionally, changes in surface-to-bed meltwater connections on the surface (i.e., new connections) can impact ice dynamics and potentially accelerate (Selmes *et al.*, 2011) or decelerate (Tedstone *et al.*, 2015) ice sheet motion.

2.5 Supraglacial channels

2.5.1 Definition

Supraglacial channels are ubiquitous meltwater features found across melt-prone ablation zones of ice sheets and glaciers during the summer melt season (Smith *et al.*, 2015; King *et al.*, 2016). They play an important role in the spatial and temporal distribution of meltwater in glacial environments, serving as an initial step for conveying surface meltwater to SGLs, crevasses and moulins and subsequently to ice margin (Smith *et al.*, 2015). Supraglacial channels also play a key role in moderating the flux and timing of meltwater to en- and sub-glacial hydrologic systems, where its input has been observed to influence localised ice velocity on diurnal to seasonal scales (Bartholomew *et al.*, 2010; Sundal *et al.*, 2011).

A supraglacial channel transporting meltwater on the surface of an ice mass can be largely categorised into two primary terms: (1) supraglacial rivers and (2) supraglacial streams (Smith et al., 2015; Pitcher and Smith, 2019). Channels is often a generic term used to encompass both rivers and streams collectively. Separately, these two terms represent two key types of channels (Table 2.1). Supraglacial rivers are primarily main-stem channels, equivalent to the

highest level of stream order representing the hydrographical structure of a catchment, and, typically, perennially reoccupy the same location each year, even as abandoned channels are advected downglacier (Figure 2.11a-b; Karlstrom and Yang, 2016). These rivers are typically regularly spaced, have elongated patterns, can form canyonised features (Germain and Moorman, 2019) and abruptly terminate in moulins (King *et al.*, 2016; Yang *et al.*, 2019b). In contrast, supraglacial streams are of lower-order, tributary-type, narrower channels that feed meltwater to the larger primary rivers downstream (Figure 2.11c-d). These streams are described as transient as they have shallower depths, can change planform rapidly and typically emanate from slush fields at high elevations (Pitcher and Smith, 2019). Further, smaller stream-type channels also exist, such as microchannels, which are a subsidiary network of branching channels measuring millimetres-to-tens of centimetres wide and occur within the porous upper layer of the weathering crust (Table 2.1; Figure 2.11e-f; Rippin *et al.*, 2015).

Table 2.1. List of the variety of channels and their characteristics which are encompassed under the umbrella term supraglacial channels. The sensor with which they can be observed is also given in relation to those used in this thesis (and introduced in Chapter 3).

Channel Type	Characteristics	Sensor
Supraglacial Rivers	• Primary, main stem channel • High stream order • Wide channel width (10 – 50 m) and depth sometimes with canyonised features • Multi-year stability • Elongated patterns • Can exhibit braided characteristics • Often connect with and/or terminate in supraglacial lakes or moulins	Observable in a range of optical remotely sensed imagery, including: • Landsat-5 ,-7, -8, -9 • Sentinel-2 • Worldview -2 • UAV imagery (Figure 2.11a-b)

Supraglacial Streams	• Secondary, tributary-style channels • Feed primary channels (rivers) • Low stream order • Narrow width (1 - >10m), shallow depth • Likely transient on yearly-to-multiyear timescales • Can emanate from slush zones at high elevations • Can form inter-stream networks when occurring between and with primary channel networks • Can also exhibit braided characteristics and anastomose	Observable in a range of optical remotely sensed imagery, including: • Sentinel-2 • Worldview-2 • UAV imagery (Figure 2.11c-d)
Microchannels	• Shallow, slush-like flows (e.g., shallow rills) in a weathering crust • Widths of millimetres to few centimetres wide (<0.5 m) • Only visible in ultra-high-resolution imagery and field-based studies	Observable in ultra-high-resolution remotely sensed imagery and field-based studies, including: • Worldview-2 • UAV imagery (Figure 2.11e-f)
Slush	• Transitionary substrate • Can include rill-type structures (i.e., microchannels) and supraglacial streams	Observable in a range of optical remotely-sensed imagery, including: • Landsat • Sentinel-2 • Worldview-2 • UAV imagery (Figure 2.11g-h)

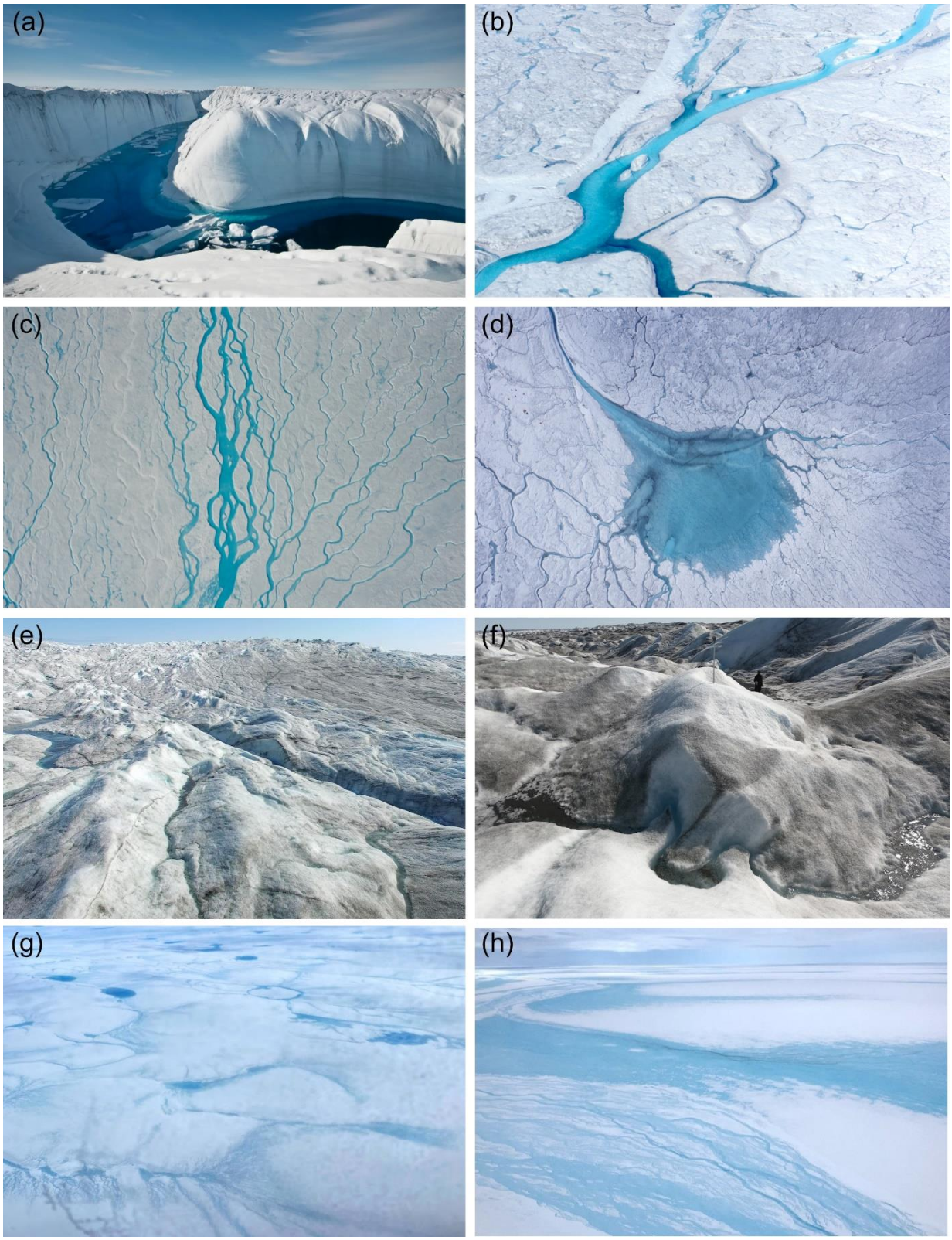
(a)
(b)
(c)
(d)
(e)
(f)
(g)
(h)

Figure 2.11. Examples of different supraglacial channels which vary in size, as described in Table 2.1. (a) Supraglacial river with canyonised feature in southwest Greenland. Image credit: I. Joughin; (b) supraglacial river channel with braided characteristics. Image credit: M. Tedesco; (c) supraglacial streams which interconnect and anastomose. Image credit: Alfred Wegener Institute; (d) supraglacial streams feeding into a supraglacial lake; Image credit: Brown University; (e-f) microchannel networks in the ice marginal region of Russell Glacier, southwest Greenland. Image credit: L. Rawlins; (g) slush zones with some distinguishable rill-type channels. Image credit: L. Rawlins; (h) dense slush zone at 1700 m a.s.l in southwest Greenland with some rill-type channelisation. Image credit: Greenlandguidance.com

2.5.2 Formation, evolution and morphology

Unlike their terrestrial counterparts (alluvial and bedrock river systems) which evolve through mechanical erosion, supraglacial channels are mechanistically different in that they lack sufficient sediment load, adjust channel form rapidly and evolve through the temperature-driven action of moving water, known as thermal erosion (Karlstrom *et al.*, 2013; Yang *et al.*, 2016). Thermal erosion occurs when meltwater draining downhill, dictated by surface topography, allows for rates of thermal incision to exceed that of ice surface ablation (Marston, 1983). Thermal incision primarily occurs due to the frictional heat from flow energy, accounting for 50-75% of incision rates occurring at the surface, as well as negligible heat supplied from shortwave solar radiation and sensible heat flux from the air to the channel (Marston, 1983). Thermal incision rates have been known to exceed several centimetres per day in warm temperate ice (Isenko and Mavlydov, 2002), with meltwater temperatures of 0.005-0.01◦C accounting for observed incision rates of up to 5 cm per day (Marston, 1983).

A study by Kostrzewski and Zwolinski (1995) conceptualised the process of channel development into three key stages, reflecting the seasonal variations of ablation at Ragnarbreen Glacier, Svalbard (Kamintzis, 2015) and is shown in Figure 2.12. The initial stage of channel formation begins when meltwater generated at the snow surface forms a primary

incision as infiltration occurs through the snowpack, forming rills that coalesce into channels (Knighton, 1985). Once snow cover has melted (mid-ablation season) and solar radiation reaches the bare ice surface, direct thawing and melt of the ice surface is initiated. This creates a superficial layer with increased permeability and thermal conductivity, allowing channel banks to expand laterally (Kostrzewski and Zwolinski, 1995; Kamintzis, 2015). At this point, there is a faster rate of change in the width of channels than in depth, due to 'warmer' bank expansion compared to the 'cooler' channel base. As the melt season progresses, the process of planform adjustment occurs, through the formation of meanders from the increased resistance from flowing water on channel banks (Kostrzewski and Zwolinski, 1995).

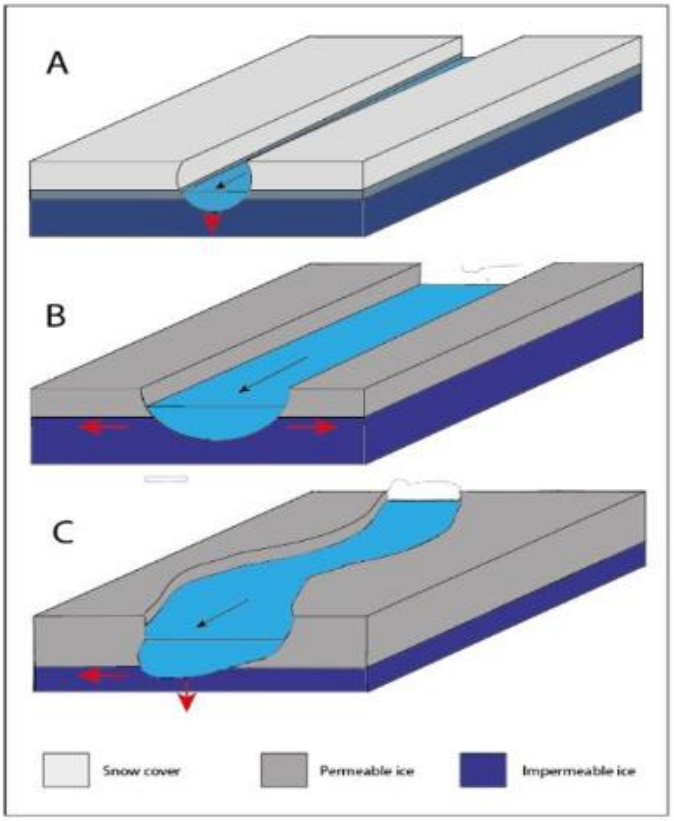

Figure 2.12. Three stage development of a supraglacial channel; (A) initial incision into snow cover; (B) Sideways melt when snowpack is removed; (C) Downward and lateral melt forming a thalweg and meandering planform. Taken from Kamintzis, 2015 (modified from Kostrzewski and Zwoliñski, 1995).

Despite the fundamental differences in mechanisms and incision rates, many studies have observed the similarities of supraglacial channel planform morphology to those found within terrestrial river systems (Karlstrom *et al.*, 2013; Chu, 2014). Meandering is one of the most commonly observed channel forms in supraglacial environments with much of their understanding built on field-based literature on alpine glaciers from before the late 1980's (Leopold and Wolman, 1960; Parker, 1975; Hambrey, 1977; Knighton, 1981b; Marston, 1983; Knighton, 1985). In alluvial rivers, sediment load is a key driver for the erosional and depositional processes promoting meander development (Ahmed et al., 2019). However, as discussed previously, this is largely deficient in supraglacial channels, inferring a greater importance of hydrodynamics in channel behaviour on ice (Knighton, 1985). The main mechanism cited for promoting the formation and sinuosity of meandering supraglacial channels is asymmetrical helical flow, driving differential melting at bend apexes (Marston, 1983). Karlstrom *et al.* (2013) furthered the understanding of this mechanism through the development of a flow model in curved channels. Channel sinuosity ultimately provides a natural vehicle for streamwise variation in heat transfer as channel bends locally decrease the thickness of the boundary layers separating flowing meltwater and glacial ice, increasing lateral temperature and velocity gradients (Parker, 1975; Karlstrom *et al.*, 2013). This mechanism provides positive feedbacks, that increases frictional dissipation and heat transfer in regions of high channel curvature, leading to increased thermal erosion (Karlstrom *et al.*, 2013).

These supraglacial planform features have also been observed on polythermal glaciers and across the marginal extent of the GrIS (Karlstrom *et al.*, 2014; Rippin *et al.*, 2015; Bash and Moorman, 2020). For example, Rippin *et al.* (2015) found significant meandering of surface meltwater channels on the polythermal glacier of Midtre Lovénbreen in Svalbard, via high-resolution imagery taken from an uncrewed aerial vehicle (UAV). Alongside this, the

presence of 'pinched off' meander loops were also observed, indicative of the dynamic and rapid erosional behaviour of such channels. So much so, that the continuous erosion and pronounced meander loops breach, reforming into a newly efficient channel for meltwater flow 'eliminating the need for water to follow the more torturous meander' (Rippin *et al.*, 2015 - p1285). This process mimics the behaviour seen in lowland terrestrial systems (Yang *et al.*, 2016). Similar meander loops were also reported by Marston (1983), but these were completely detached from the main channel: a product of vertical abandonment from rapid down cutting, which has been recognised as a process of englacial 'cut and closure' (Gulley *et al.*, 2009).

2.6 Supraglacial lakes

A significant feature observed within the supraglacial environment of the GrIS is the widespread occurrence of SGLs. SGLs are areas of ponded meltwater that reside in topographical depressions (Leeson *et al.*, 2012), primarily controlled by bedrock topography which is expressed on the ice surface (Lampkin and VanderBerg, 2011). This results in SGL locations being static, remaining in similar locations year-on-year (Selmes *et al.*, 2011; Selmes *et al.*, 2013). They are primarily fed by surface meltwater transported via supraglacial channels, providing a significant temporary meltwater store in lakes of metre-to-kilometre-scale size (Fitzpatrick *et al.*, 2014).

These surface meltwater features develop seasonally across the GrIS ablation zone, first forming within the lower expanse of the melt-prone zone in late May and expanding in size and elevation as seasonal air temperatures rise and the melt season progresses (Sundal *et al.*, 2009; Leeson *et al.*, 2012). Numerous studies have mapped the occurrence and seasonal evolution of lakes in various regions of the GrIS (Box and Ski, 2007; Sundal *et al.*, 2009; Lampkin, 2011; Lampkin and VanderBerg, 2011; Selmes *et al.*, 2011; Banwell *et al.*, 2012; Leeson *et al.*, 2012; Liang *et al.*, 2012; Selmes *et al.*, 2013; Fitzpatrick *et al.*, 2014; Gledhill

and Williamson, 2018; Otto *et al.*, 2022), which has played a pivotal role in the examination of SGL dynamics. These studies provided observations of SGLs using satellite-acquired imagery and found season, elevation and topography to be major controlling factors on SGL location and area (Luthcke *et al.*, 2006; Box and Ski, 2007; Sundal *et al.*, 2009; Selmes *et al.*, 2011; Leeson *et al.*, 2012; Liang *et al.*, 2012; Chu, 2014; Fitzpatrick *et al.*, 2014). In particular, Lampkin (2011) found small lakes clustered in lower elevation regions (500–900 m) whilst larger, sparse and shallower lakes formed over multiple years at higher elevations (>1200 m); a result of ice thickness and reduced transmission of bedrock topography to the surface at higher elevations.

Additionally, SGLs have received widespread scientific interest since 2006 after the identification that SGLs can drain rapidly via moulins at discharge rates of 8700 and 2200 ms^{-1} through thick (>1 km), cold ice over a matter of hours (24 hours; Das *et al.*, 2008; Doyle *et al.*, 2013). Up to 55% of lakes on the GrIS drain rapidly (<1 day) via hydrofracture, with this behaviour shown to have a short-lived influence on ice dynamics (Hoffman *et al.*, 2011; Joughin *et al.*, 2013; Koziol and Arnold, 2018; Davison *et al.*, 2019), which is further explored in Section 2.7. Their rapid disappearance can also cause cascading SGL drainage, whereby the drainage of one cluster of SGLs results in the drainage of others upstream, due to the transient induction of tensile stresses and extensional flow (termed 'tensile shock') which establishes new surface-to-bed connections and lake drainages up to 135 km inland from the ice margin (Christoffersen *et al.*, 2018). The remainder of SGL drainages either drain slowly overland (via supraglacial channel outflow) or freeze over during winter (Figure 2.13; Selmes *et al.*, 2013; Kingslake *et al.*, 2015; Koziol *et al.*, 2017; Davison *et al.*, 2019).

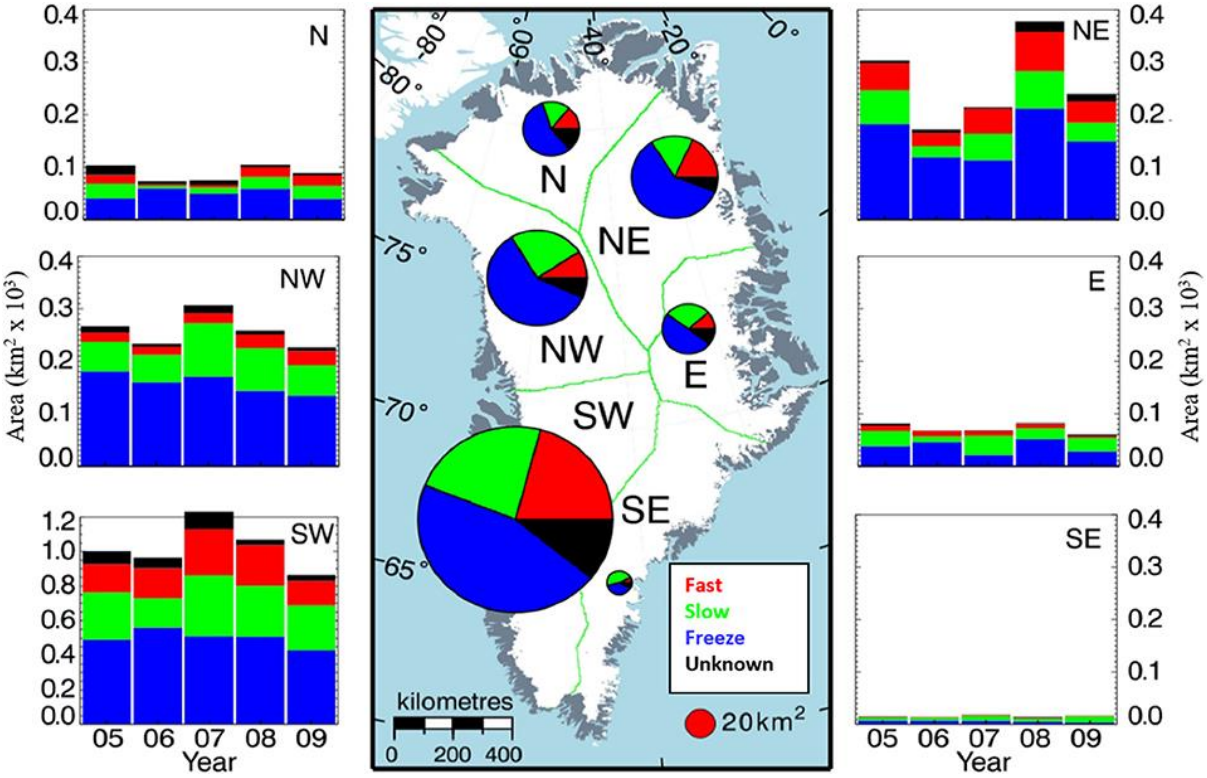

Figure 2.13. The distribution of SGL area and drainage type on the GrIS between 2005 and 2009, split between fast (or rapid) draining SGLs, slow draining SGLs and those that freeze over during winter and unknown drainage types. Bar charts show area and proportion of SGL drainage types per year. Figure taken from Davidson *et al.* (2019) which was adapted from Selmes *et al.* (2013).

The presence of ice lids, which are a 1-3 m ice cover formed on the surface on the SGLs (Figure 2.14), are also SGL characteristics and are typically removed or partially removed during the summer melt season, and can reform at the end of the melt season if the lake has not drained (Schröder *et al.*, 2020). Such ice lids have been shown to preserve SGLs with liquid water over winter as buried lakes (Law *et al.*, 2020), as well as in years where surface melt may not reveal such features observable by optical remote sensors.

Figure 2.14. Image of a supraglacial lake with partial ice lid coverage. Image credit: Lawrence Smith.

2.7 Subglacial connectivity and ice dynamics

Surface melt, discharge and its spatial complexity is of primary importance for assessing the dynamical changes occurring across the GrIS, due to its major interaction with ice sheet dynamics (Bartholomew *et al.*, 2011; Palmer *et al.*, 2011; Van den Broeke *et al.*, 2011). Prior to the 21st century, it was believed ice sheets were stable over millennial timescales with meltwater incapable of penetrating the cold, impermeable ice surface layer and/or reach the bed due to considerable ice thickness (Nienow *et al.*, 2017). One of the first studies to indicate a link between seasonal meltwater production and GrIS dynamics was Joughin *et al.* (1996). This study observed a threefold increase in flow at Ryder Glacier (Greenland), inferred from SGL drainages. However, it was unknown whether this was a widespread phenomenon occurring at outlet glaciers throughout Greenland (Joughin *et al.*, 1996b; Nienow *et al.*, 2017). Other studies since have observed seasonal speedups at numerous outlet glaciers, particularly along the western flanks of the GrIS. Zwally *et al.* (2002) used a

GPS time series from Swiss Camp, central-west Greenland, which displayed seasonal speedups of 5-28% at ice over 1 km thick, correlating with summer melt rates and the rapid migration of surface water to the ice-bed interface. Joughin *et al.* (2008) similarly found melt-induced speedups of 50-100% along western regions, with results suggesting meltwater-induced acceleration may occur across large regions of the GrIS and have a considerable effect on the ice sheets future evolution. Confirmation of this link between meltwater drainage and influence on ice dynamics was later provided by Das *et al*. (2008), with evidence of meltwater fracture propagation (or hydrofracture) evolving into moulin flow in thick, cold ice, acting as the direct conduit for surface-bed connections.

With enhanced surface meltwater production, transportation and delivery from the GrIS surface to the ice-bed interface, it was hypothesised that this could induce a stronger ice velocity response; particularly under the current warming scenario (Zwally *et al.*, 2002; Parizek and Alley, 2004; Chu, 2014). However, further work (Hoffman *et al.*, 2011; Sole *et al.*, 2011; Chandler *et al.*, 2013; Cowton *et al.*, 2013) has given a more nuanced view of this mechanism, highlighting the importance of a channelised subglacial system for stabilising ice velocity (Schoof, 2010). The periods of increased ice velocity frequently occurs at the onset of the melt season, at which time the subglacial drainage system is described as 'inefficient', being highly sensitive to initial influxes of water from the surface (Figure 2.15a; Kamb, 1987; Zwally *et al.*, 2002; Bartholomew *et al.*, 2010; Sole *et al.*, 2011; Chandler *et al.*, 2013; Cowton *et al.*, 2013; Chu, 2014). This highly pressurised system was observed by Das *et al.* (2008) to drive short-lived uplift, horizontal velocity acceleration and an increase in localised seismicity. As the melt season progresses with sustained inputs of meltwater to the ice-bed interface, the subglacial hydrologic system evolves into an efficient network of subglacial channels (Figure 2.15b; Rennermalm *et al.*, 2013). This efficient system is able to evacuate large volumes of water quickly and effectively, reducing basal water pressure and

moderating ice velocity within ablating regions (Bartholomew *et al.*, 2010; Sundal *et al.*, 2011). Observations by van de Wal *et al.* (2008) found that even though ice velocities in west GrIS responded more quickly and strongly to meltwater input at the start of the melt season than previously expected, annual velocities within this region over a 17-year study period were actually decreasing (-10%), attributed to seasonal subglacial efficiencies. This coupling between an efficient subglacial system and ice deceleration has also been noted by Davison *et al.* (2020), who found a net-slow down of land-terminating Greenlandic glaciers on annual to decadal time-scales, despite increases in surface melt and runoff. This study suggests that even with increased runoff supply, ice flow within marginal regions is likely to continue on a decelerating trend, driven by cavity expansion and drainage efficiency.

It is worth noting that these efficient systems can still become overwhelmed with short-term accelerations superimposed upon this seasonal cycle lasting several hours to days attributed to variations in surface meltwater input (Figure 2.15c; Schoof, 2010; Andrews *et al.*, 2014). Hoffman *et al.* (2011) observed short-lived (~1 day) and localised (<10 km) velocity events in western Greenland over the summer season of 2007, attributed to sudden meltwater pulses from rapid SGL drainage events. Similar observations were also made by Andrews *et al.* (2018) who found the occurrence of SGL drainages not only influenced maximum velocity, but induced widespread strain perturbations for the initiation and cascading drainage of nearby fractures and SGLs.

Additionally, meltwater inputs into moulins via supraglacial river channels has also been shown to have a first-order control on the diurnal variability of subglacial water pressure fluctuations and subsequent ice velocity, even in relatively thick ice (1 km) and >40 km inland from the ice terminus in southwestern Greenland (Smith *et al.*, 2021; Mejia *et al.*, 2022). Extreme rainfall events during the late-melt-season of 2011 have also been linked to enhanced sliding observed further inland by Doyle *et al.* (2015). This is an interesting yet

concerning insight into further impacts of increasing precipitation alongside melt production in a warming climate.

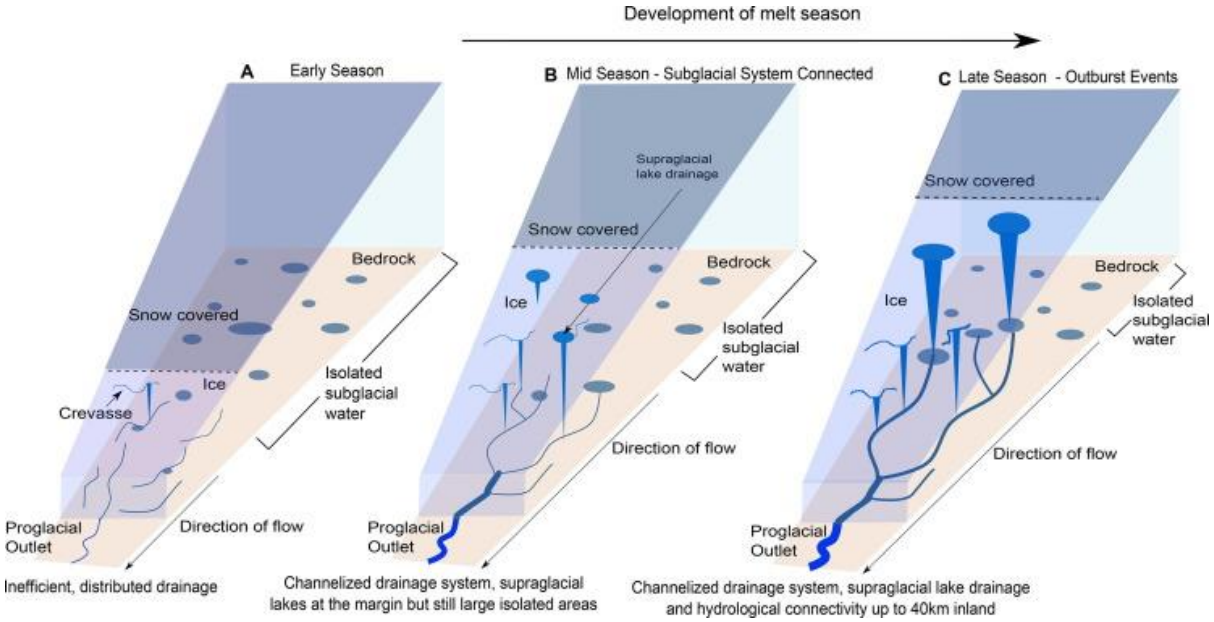

Figure 2.15. Diagram to illustrate conceptual model of subglacial hydrology development taken from Hatton *et al.* (2019; their Figure 6). Panel A represents the subglacial network early in the melt season with inefficient, distributed drainage and areas of isolated subglacial water further inland; B represents the subglacial network once surface meltwater enters the system, with drainage becoming more efficient with melt inputs from crevasses, supraglacial lake drainages and moulins; C represents the channelised subglacial network late into the melt season once the snow line has retreated to maximum extent and melt inputs occur at more isolated regions of the bed further inland. Outburst events from supraglacial lake drainages can also overwhelm the system.

2.7.1 Interior ice dynamics

At present, there are many questions as to whether or not surface meltwater produced at higher elevations may be able to penetrate the thick ice interior as warming continues, influencing larger ice velocity fluctuations further inland (Doyle *et al.*, 2014). A key feature in the delivery of surface meltwater to the bed is drainage via SGLs, which concurrent with the

expansion of surface melt and the inland movement of the equilibrium line, are now forming at higher elevations (Howat *et al.*, 2013; Leeson *et al.*, 2015; Poinar *et al.*, 2015; Gledhill and Williamson, 2018; Otto *et al.*, 2022). Based on observations of surface strain rates, Poinar *et al.* (2015) suggested that increased surface melt and SGLs occurring above ~1600 m are likely to drain via supraglacial outlet channels. This is due to longer-wavelength surface topography at the ice interior, leading to shallower and broader SGLs, with meltwater conveyed via outflow channels into moulins downstream. Poinar *et al.* (2015) also suggested that crevassing and moulin initiation inland is unlikely to occur, despite the migration of the ELA. Similar findings were also made by Stevens *et al.* (2015). This study concluded that reduced strain rates at the ice interior resulted in the unlikely progression of rapid drainage events and hydrofracturing inland, reducing the likelihood of inland expansion of ice flow (Stevens *et al.*, 2015).

In contrast to this, more recent studies from Hoffman *et al.* (2018) and Christoffersen *et al.* (2018) suggest that fracturing of ice is possible at higher elevations, which may permit meltwater access to the frozen basal zone, promoting faster sliding. Hoffman *et al.* (2018) suggests stresses built from SGL drainages downstream of low-risk inland regions may trigger stress perturbations and surface-to-bed connections kilometres away from such drainage events, making inland areas more vulnerable than previously thought. Similarly, conclusions from a modelling study by Christoffersen *et al.* (2018) also suggests increased tensile stress perturbations that expand inland and across larger distances as lakes become more numerous and migrate inland. This study also provided further evidence of fracturing inland via WV imagery, which revealed water-filled crevasses at elevations of 1800 m during June 2010 (Christoffersen *et al.*, 2018). These modelling and observational studies together build on previous findings by Yang and Smith (2016), who observed almost all runoff

produced above 1600 m entered moulins at the same elevation, indicating modest but the significant penetration of meltwater at high elevations.

As such, with the observed penetration of meltwater at these higher elevations (>1600 m), it is expected meltwater will reach new areas of the frozen basal zone. This is further complicated by the potential inability for hydraulically-efficient subglacial channels that form in the ablation zone to form further inland. Due to interior regions having shallow surface slopes, a low-hydraulic gradient and high creep-closure rates due to ice thickness, the development of efficient systems are hindered (Bartholomew *et al.*, 2011; Chandler *et al.*, 2013; Meierbachtol *et al.*, 2013; Dow *et al.*, 2014; Doyle *et al.*, 2014; Moon *et al.*, 2014). This in turn may drive interior-accelerations, exceeding observed net deceleration in ice-marginal areas (Doyle *et al.*, 2014).

2.8 Study areas

The GrIS is typically split into 7 main ice sheet regions separated along major ice divides as follows; (i) southwest (SW), (ii) central west (CW), (iii) northwest (NW), (iv) north (No), (v) northeast (NE), (vi) central east (CE) and (vii) southeast (SE), as shown in Figure 2.16, which aids in the partitioning of mass change and loss estimates from separate sectors (Mouginot and Rignot, 2019). Within each of these sectors, land- and marine-terminating outlet glaciers are present, with different sectors of the ice sheet experiencing different climate sensitivities and, in turn, outlet glacier-related responses (Box *et al.*, 2022a).

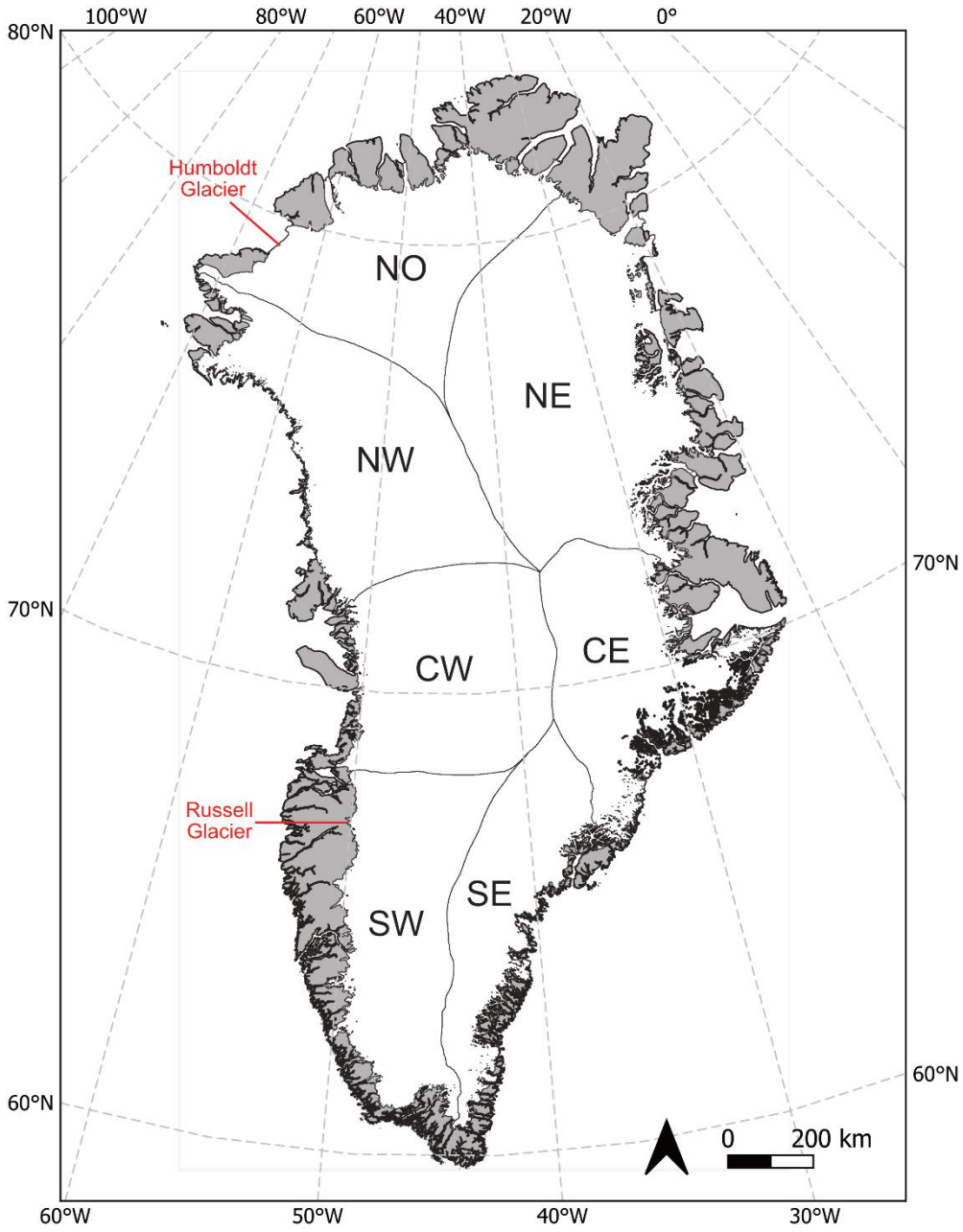

Figure 2.16. The seven main regions of the GrIS which are partitioned along major ice divides, as per Mouginot and Rignot (2019). The two key study sites of this thesis are also denoted; (i) Humboldt (Sermersuaq) Glacier in northern Greenland and (ii) Russell Glacier in southwestern Greenland.

2.8.1 Humboldt Glacier

The outlet glaciers in the northern sector of the GrIS comprise ~14% of the total ice sheet area, with 82% of the northern sector predominately drained by 12 marine-terminating

glaciers which together hold a SLE of 93 cm (Mouginot *et al.*, 2019). Since 1990, this sector has experienced some of the most pronounced changes in surface melt and runoff, attributed to the rapid expansion of the ablation (46%) and bare ice (33%) zone at rates twice as fast than in southern Greenland, with this trend expected to continue with ongoing climatic warming (Noël *et al.*, 2019).

Of the northern outlet glaciers that drain the GrIS, Humboldt Glacier, known as Sermersuaq Glacier in Greenlandic (79.48 °N, 63.11 °W), is the widest marine-terminating outlet glacier in Greenland, spanning ~91 km across the Kane Basin and is responsible for draining ~5% of the ice sheet alone (Rignot and Kanagaratnam, 2006; Hill *et al.*, 2017; Rignot *et al.*, 2021). Calving from its wide terminus is predominately via large, tabular icebergs of <1 km diameter into the Kane Basin (Figure 2.17), which are especially concentrated to the north of the terminus and are typical of cold regions such as those observed in Antarctica (Rignot *et al.*, 2021).

Since the late 1990s, Humboldt Glacier has experienced rapid rates of retreat (~162 m a^{-1}) attributed to increases in mean summer air temperatures and sea-ice decline (Carr *et al.*, 2015). Holding an ice volume equivalent of 19 cm of SLR, Humboldt Glacier is the fourth largest Greenland glacial contributor to SLR (Rignot *et al.*, 2021) having lost 161 gigatonnes (Gt) since 1972 and 311 km^2 of its area between 2000 and 2010; the largest outlet glacier area change of a Greenland-wide study (Box and Decker, 2011).

Until recently, few glaciological studies had focussed on Humboldt Glacier (Joughin *et al.*, 1996a; Rignot *et al.*, 2001; Carr *et al.*, 2015; Hill *et al.*, 2017; Livingstone *et al.*, 2017; Hill *et al.*, 2018; Mouginot *et al.*, 2019; Gray, 2021; Rignot *et al.*, 2021; Hillebrand *et al.*, 2022). Studies that have examined Humboldt Glacier identified a distinctive ice velocity divide between the northern and southern sectors (Rignot *et al.*, 2001, 2021; Carr *et al.*, 2015); the

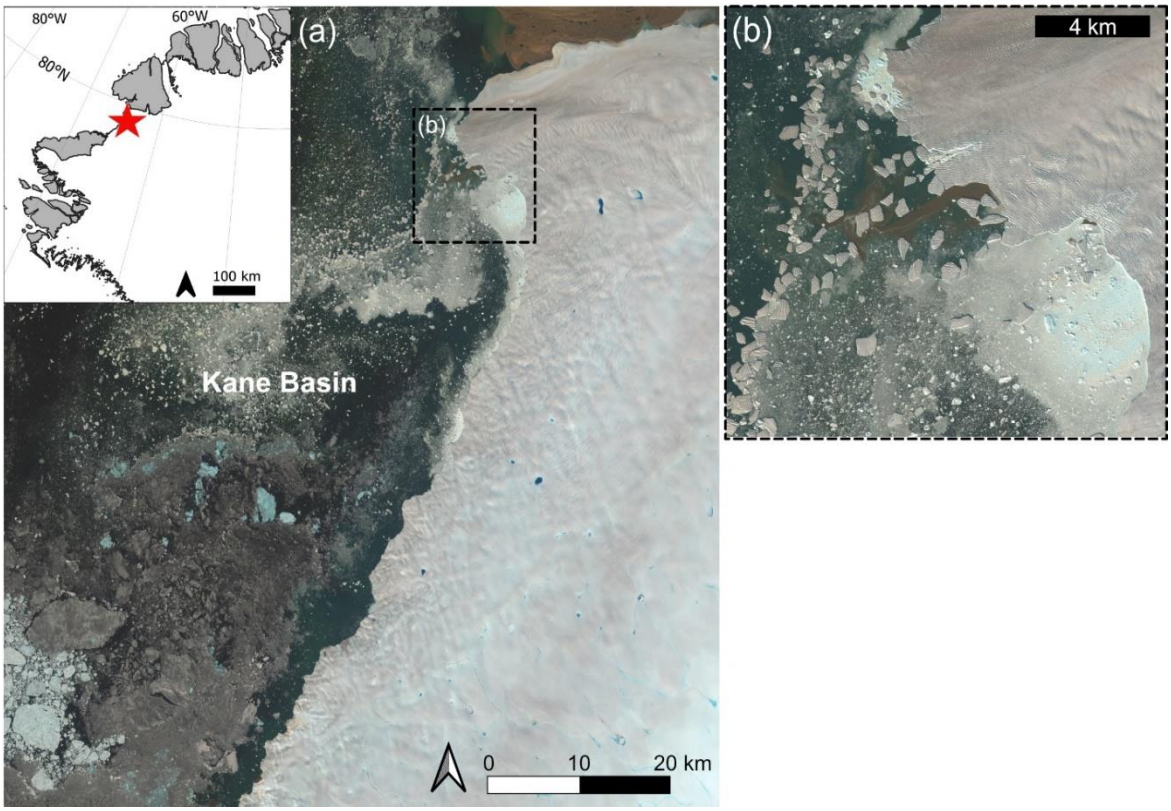

Figure 2.17. Humboldt (Sermersuaq) Glacier in northern Greenland with its wide (~91 km) terminus draining into the Kane Basin. Large, tabular icebergs are observed calving from its northern edge of the terminus into the Kane Basin. Sentinel-2 image from 27th July 2019.

northern sector has up to four times faster ice flow than the south. In terms of surface hydrology, several studies have noted the presence of SGLs (Joughin *et al.*, 1996a; Selmes *et al.*, 2011; Carr *et al.*, 2015), however none to-date have examined the overall drainage system, including both channels and lakes. . Humboldt Glacier is the primary study location of Chapters 4 and 5, due to (i) its importance as a large, outlet draining glacier, not only for northern Greenland but for the whole of the ice sheet and (ii) the potential impact increasing surface meltwater runoff may have on dynamical processes (e.g., runaway retreat) and subsequent ice loss. In Chapter 4, the seasonal evolution of the supraglacial hydrologic network across consecutive melt seasons (2016-2020) is examined and in Chapter 5,the long term, multi-annual evolution of the supraglacial network is conducted over 37 years (1985-

2021). A small section (20.3 km^2) of the bare ice zone of Humboldt Glacier also features in mapping small-scale features from commercial-based imagery (WV-2) in Chapter 6.

2.8.2 Russell Glacier

Southwestern Greenland is predominately drained by land-terminating glaciers (72%) and holds a SLE of 74 cm. This region is primarily controlled by SMB processes and is particularly susceptible to the melt-elevation feedback whereby the flatter elevation profile, thinner seasonal snow cover and darker ablation area yields larger melt volumes (Mikkelsen *et al.*, 2016; van As *et al.*, 2017).

Russell Glacier is a land-terminating outlet glacier located on the southwestern coast of the GrIS, ~35 km east of the settlement of Kangerlussuaq (67.15 °N, 50.03 °W; Figure 2.18). Russell Glacier is sandwiched between two larger, neighbouring glaciers; Isunnguata Sermia Glacier to the north and Leverett Glacier to the south. Russell Glacier has the smallest of the three catchments in this area, totalling ~70.2 km^2 (Mankoff *et al.*, 2020), with Isunnguata Sermia draining ~7146 km^2 and its distributary glacier to the south, Leverett Glacier, draining ~837 km^2. This region of the GrIS, in particular Russell Glacier, has received considerable scientific attention due to its ease-of-access for field-based studies and various scientifically intriguing features (i.e., rapidly draining supraglacial lakes, dense supraglacial river networks), hence the location for field-based work in this thesis (Chapter 6). This marginal part of the GrIS is characteristically dark, influenced by a host of light-absorbing impurities including inorganic pollutants, cryoconite material and glacial algae (Tedstone *et al.*, 2017; Ryan *et al.*, 2018) that impact albedo across this region.

Russell Glacier is isolated from marine influences; therefore, its dynamics are directly attributable to surface melt forcing. It does, however, have a number of ice-dammed lakes across its northern-flank, with one in-particular (~1 km^2) known to drain repeatedly, with consistent yearly jökulhlaup-style cycles between 1940 and 1987 (Sugden *et al.*, 1985; Russell, 1989) and again since 2007 (Mernild and Hasholt, 2009; Carrivick, 2011; Russell *et al.*, 2011; Carrivick *et al.*, 2013; Carrivick and Quincey, 2014; Carrivick *et al.*, 2017).

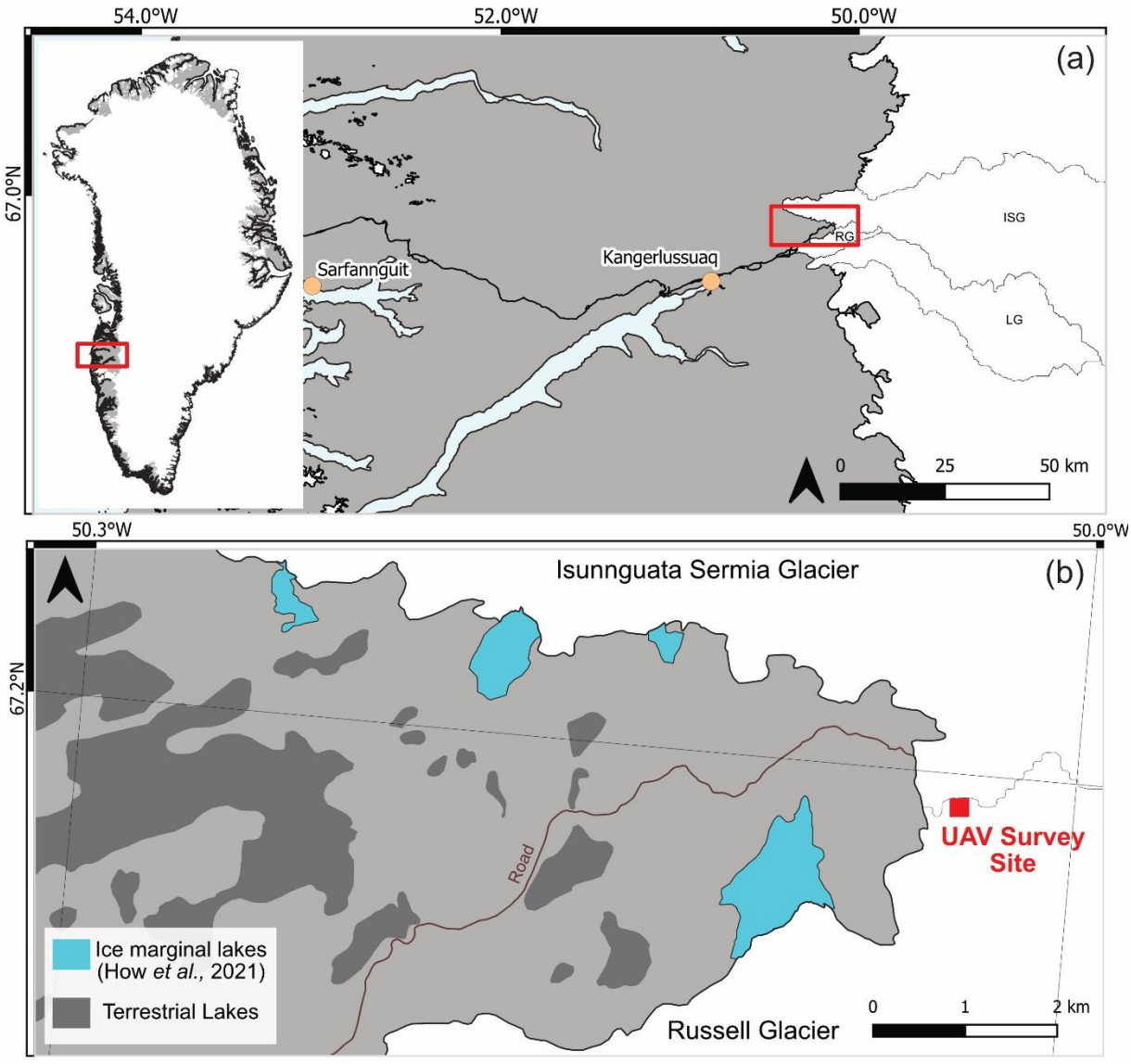

Figure 2.18. (a) Location of Russell Glacier, south-western Greenland, ~35 km from the nearest town of Kangerlussuaq; (b) Close up of Russell Glacier and the northern, neighbouring Isunnguata Sermia Glacier, with the field-based survey site identified for Chapter 6. Ice marginal lakes are sourced from How *et al.* (2021).

Chapter 3

Methodological Overview

This chapter provides an introduction to remote sensing and its application within the field of glaciology, in particular the acquisition and use of imagery from both satellite and uncrewed aerial vehicles (UAV) for the mapping and quantification of supraglacial features.

A detailed overview of the key method used for the delineation of the supraglacial hydrologic system used throughout this thesis is provided, including each image processing step which underpins network delineation and mapping in Chapters 4, 5 and 6. Associated parameters that are altered within this method, dependent upon the type and resolution of imagery used, are further described in the relevant data Chapter (4-6).

An overview of UAVs and the photogrammetric method of Structure-from-Motion (SfM) is also described, which underpins field-based work conducted in Chapter 6. Again, specific methodological parameters used are described in-detail within the data chapter (6).

3.1 Remote sensing

Remote sensing is defined as the acquisition of information about an object or phenomenon via the measurement of reflected and/or emitted radiation at distance, typically from a satellite or aircraft (Elachi and Van Zyl, 2021). As a core technology for Earth observation, remote sensing via satellite-applications provides critical information for the observation, interpretation, analysis and monitoring of Earth's physical, chemical and biological systems over large spatial and temporal scales (Li *et al.*, 2009). Within the field of glaciology, remote sensing has become a powerful tool in the study of these isolated, often inaccessible and inhospitable environments, with development in remote sensing over the last ~50 years revolutionising the ability to map, monitor and quantify changes occurring across the cryosphere on a world-wide scale (Gao and Liu, 2001; Tedesco, 2015).

Remote sensing imaging instruments can primarily be divided into two subclasses that allow imaging from two different approaches: (i) active and (ii) passive remote sensing (Tedesco, 2015). Active remote sensing platforms produce and emit their own energy to illuminate the target with the strength of the returned signal measured. Typically, active sensing includes the use of Light Detection and Ranging (LIDAR) and Synthetic-aperture radar (SAR) systems, which are not sensitive to daylight or weather conditions (i.e. cloud; Gao and Liu, 2001). Such active sensing has supported a wealth of glaciological operations, with examples including the use of LIDAR for monitoring elevation (Krabill *et al.*, 1995) and dynamics (Abdalati and Krabill, 1999) of both ice sheets and glaciers and the production of high-resolution digital elevation models (DEMs; Abermann *et al.*, 2010). SAR has also provided an invaluable resource in imaging ice surface deformation and relief (Joughin *et al.*, 2010; Jawak *et al.*, 2015), crevasse mapping (Bindschadler *et al.*, 1987; Rignot and MacAyeal, 1998; Jezek, 2003; Glasser *et al.*, 2009), monitoring calving and surge activity (Wesche *et al.*, 2013; Krieger and Floricioiu, 2017; Baumhoer *et al.*, 2018; Leclercq *et al.*, 2021; Zhang *et al.*, 2021)

and ice velocity field mapping (Goldstein *et al.*, 1993; Joughin *et al.*, 1996a; Rignot *et al.*, 1997; Luckman *et al.*, 2003).

In terms of passive remote sensing (also referred to as optical or multispectral remote sensing), this refers to the interaction between the originating light source (i.e., the sun) and the Earth surface. Sensors detect solar radiation reflected from the Earth's surface across a range of wavelengths or 'bands' of the electromagnetic (EM) spectrum, ranging from the visible and near infrared (VNIR) portions of EM (0.35 – 2.5 μm) to emitted radiation in thermal infra-red (TIR; 8 – 14 μm), recorded as brightness temperature by the sensor (Shaw and Burke, 2003; Rees, 2005) . Each surface type has a unique spectral signature meaning it can be differentiated and identified, for example rock versus soil (Price, 1994). In glaciology, glacial zones, such as the accumulation and ablation zones, have their own specific reflectance characteristics within the VNIR region, with these facies able to be mapped automatically (Racoviteanu *et al.*, 2008). Snow has a very high reflectance in the visible wavelength region (0.4–0.7 μm) and a low reflectance in the NIR (0.8-2.5 μm) regions, whereas ice is almost transparent in visible wavelengths (0.4–0.7 μm) but moderately absorptive in NIR (0.8–2.5 μm; Racoviteanu, Williams and Barry, 2008). For other features, such as debris cover and surface meltwater features (i.e., supraglacial lakes (SGLs)), the use of spectral indices, which is a combination of spectral reflectance from two or more bands that highlight a particular feature, has become a practical solution for extracting pixel information and specific glaciological features, utilising the strength of each index which often ranges between −1 and +1 (Kääb *et al.*, 2014).

A number of well-established indices for glaciological applications have been widely applied and are described in Table 3.1. Briefly, examples include the Normalised Difference Snow Index (NDSI) for the large-scale mapping of snow cover (König *et al.*, 2001; Gupta *et al.*, 2005; Kour *et al.*, 2015; Sood *et al.*, 2020) and the Normalised Difference Water Index

(NDWI), plus modifications ($NDWI_{ice}$), for widespread supraglacial and proglacial lake mapping (Yang and Smith, 2013; Moussavi *et al.*, 2016; Watson *et al.*, 2018; Williamson *et al.*, 2018; Stokes *et al.*, 2019; Arthur *et al.*, 2020a; How *et al.*, 2021; Dell *et al.*, 2022). The success of these spectral indices is, however, highly dependent on a number of factors, including differential solar illumination of the Earth's surface during different times of year, complex terrain with shadowing, rocky outcrops and fresh snow and cloud cover, which can all impede effective and accurate extraction, particularly for water bodies (Gao *et al.*, 2016; Khalid *et al.*, 2021). This means time- and location- dependent adaptive thresholding of spectral indices may be required to reduce uncertainties in extraction results (Härer *et al.*, 2018).

Table 3.1. Examples of common spectral indices used within the field of glaciology to perform specific spectral enhancement tasks for surface feature extraction and delineation. The spectral indices (index), equation (expression), what is typically mapped via this index (target) and original scientific sources (references) are provided where applicable.

Index	Expression	Target	References
NDSI *(Normalised difference snow index)*	$\frac{(Green - SWIR)}{(Green + SWIR)}$	Mapping and differentiating between snow-ice and non-snow-and-ice areas	(Dozier, 1989)
NDGI *(Normalised difference glacier index)*	$\frac{(Green - Red)}{(Green + Red)}$	Glacier detection and monitoring	(Keshri *et al.*, 2009)
NDDI *(Normalised*	$\frac{(SWIR - TIR)}{(SWIR + TIR)}$	Mapping and differentiating	(Shukla and Ali, 2016)

difference debris index)		between supraglacial debris and terrain	
NDWI *(Normalised difference water index)*	$\frac{(Green - NIR)}{(Green + NIR\ )}$	Mapping surface water	(McFeeters, 1996)
MNDWI *(Modified normalised different water index)*	$\frac{(Green - SWIR)}{(Green + SWIR\ )}$	Modified mapping surface water index	(Xu, 2005)
NDW_{Iice} *(Normalised difference water index ice)*	$\frac{(Blue - Red)}{(Blue + Red\ )}$	Adapted mapping surface water index for ice surfaces	(Yang and Smith, 2013)
Brightness	$\frac{(Red + Green + Blue)}{(3)}$	Mapping snow covered areas	

3.1.1 Satellite platforms for remote sensing

One of the most successful, longest, and continuous Earth observation and VNIR programmes is the open access Landsat programme operated by NASA and the U.S. Geological Survey (USGS), which has been continuously acquiring observational data since 1972 across a range of wavelengths along the EM spectrum (Wulder *et al.*, 2019). The development of the program overtime has seen the addition of a number of unique satellites and sensors for Earth observation (Figure 3.1), as follows:

- Landsat 1-5 Multispectral Scanner (MSS) images consisting of four bands at 60 m resolution;

- Landsat 4-5 Thematic Mapper (TM) consisting of seven bands (including thermal infrared) at 30 m resolution;
- Landsat 7 Enhanced Thematic Mapper Plus (ETM+) images consisting of eight spectral bands, with seven at 30 m resolution and the panchromatic band at 15 m;
- Landsat 8-9 Operational Land Imager (OLI) and Thermal Infrared Sensor (TIRS) with images consisting of eleven spectral bands, with eight at a resolution of 30 m, a panchromatic band at 15 m and two thermal infrared bands at 100 m (Wulder *et al.*, 2019)

This satellite series has provided the single-best, long-term, continual record of the cryosphere and has allowed for glacial and geomorphologic mapping and monitoring over local, regional and global scales, including glacier inventories from the Canadian Cordillera (Sidjak, 1999; Bolch *et al.*, 2010), high mountain Asia (Kamp and Pan, 2015; Mölg *et al.*, 2018), New Zealand (Paul *et al.*, 2023), European mountain ranges (Paul *et al.*, 2008; Kellerer-Pirklbauer *et al.*, 2012), Scandinavia (Andreassen *et al.*, 2008; Paul *et al.*, 2008; Andreassen *et al.*, 2012) and the development of the global-wide Randolph Glacier Inventory (excluding Greenland and Antarctica; Pfeffer *et al.*, 2014).

Another Earth observation satellite platform that also provides freely available imagery and shares many of the technical characteristics of the Landsat programme, but at higher resolution, is the more recently introduced Sentinel-2 satellites as part of the European Space Agencies (ESA) Copernicus programme (Wulder *et al.*, 2019). Sentinel-2 has systematically acquired high-resolution (10 m) imagery of the Earth's surface via Sentinel-2A and Sentinel-2B systems since launching in 2015 and 2017, respectively (Figure 3.1). Equipped with a wide swath (290 km), high-resolution Multispectral instrument (MSI), Sentinel-2 data contains thirteen spectral bands spanning the visible to near and shortwave infrared (SWIR) spectrum at varying spatial resolutions across pre-defined grids or 'tiles' of

100 km x 100 km. These spectral bands include four visible bands at 10 m spatial resolution, six bands at 20 m and three bands at 60 m. Key advancements of the Sentinel-2 programme over the Landsat programme is its higher spatial resolution and shorter revisit times, achieving 5-day repeat visits at the equator and up to one image per day at higher latitudes up to 83° N, thanks to its overlapping swaths. Sentinel-2 data has also been shown to compliment ongoing Landsat-products due to their similarities in spectral bands, providing greater repeat coverage capabilities improving the observational frequency over an area as well as its higher spatial resolution aiding in the further identification and verification of glaciological features (Pope *et al.*, 2016; Williamson *et al.*, 2018). Many other satellite platforms for both optical (passive) and active imaging are also operational, with freely available data obtainable from the (i) TERRA satellite launched in 1999, which provides optical imagery via its ASTER (Advanced Spaceborne Thermal Emission and Reflection Radiometer; 15 – 90 m spatial resolution) and MODIS (Moderate-Resolution Imaging Spectroradiometer; 250 m spatial resolution) sensors and ICESat (2003-2010) and its successor ICESat-2 (2018-present) satellites, which provide elevation data, to name only a few.

Commercial imagery, which often comprises ultra-high-resolution imagery at cost, is also available from platforms such as SPOT (1.5 m panchromatic and 6 m multispectral), Quickbird (0.61 m panchromatic, 2.4 m multispectral), the Worldview (WV) series (0.31 – 0.46 m panchromatic, 1.23 - 1.84 m multispectral) and, more recently, Planet Labs (0.50 – 5 m). The first commercial satellite to be launched in 1986, SPOT-1, paved the way for the commercial satellite Earth observational market, with the demand for increased performance and ever-increasing resolutions overtime driving the industry's growth (Denis *et al.*, 2017). Until recently, much of these commercial-based Earth observational services were aimed towards private customers, predominately governmental and major economical firms who could afford such imaging products, with some freely available imagery provided

to specific sub-sections of industry; an example being Worldview (WV), with free access to this imagery only available to federally-funded researchers (Pope *et al.*, 2014; Denis *et al.*, 2017). In the last two decades, however, commercial-based imagery has gradually become more available to researchers through supportive grants (e.g., Third Party Missions scheme via ESA) and the advent of several low-cost satellite constellations via Planet Labs (2010), such as their RapidEye and PlanetScope constellations. Whilst this can make such imagery more affordable and somewhat available due to short build and launch cycles with a 2–4 year operational lifetime, often there are still limitations to commercially acquired imagery including orbital constraints (i.e., orbits may not be maintained and limited high-latitude coverage (Roy *et al.*, 2021).

Nonetheless, in the field of cryospheric science, commercial-based imaging is proven to be incredibly beneficial. Jawak *et al.* (2019) utilised WV-2 imagery to accurately classify the surface glacier facies of five Himalayan glaciers using object-based image analysis and, in particular, to separately isolate crevasse zones. Datta and Wouters (2021) used the Planet Labs PlanetScope and SkySat imagery alongside freely-available Landsat and Sentinel-2 imagery to derive 46 supraglacial lake depth estimates on the western GrIS and highly accurate identification of small-scale supraglacial features to help interpret the temporal evolution of SGL characteristics over time, providing for the first time, the successful use of multiple imagery sources (both public and commercial) to derive such estimates. Yang and Smith (2013) also utilised WV-2 multispectral imagery to develop a new automatic river detection algorithm to extract linear features from satellite imagery that could be applied to the GrIS and glaciated regions as well other remote sensing datasets (Yang *et al.*, 2019b; Lu *et al.*, 2021), including within this thesis which is further explored in Section 3.2.

The ever-increasing acquisition of newly available and higher-resolution datasets alongside computational enhancements and complementary multi-imaging uses continues to provide

advancements in the scientific understanding of the cryosphere and verification of the processes encompassed within it, particularly within an unprecedented warming world.

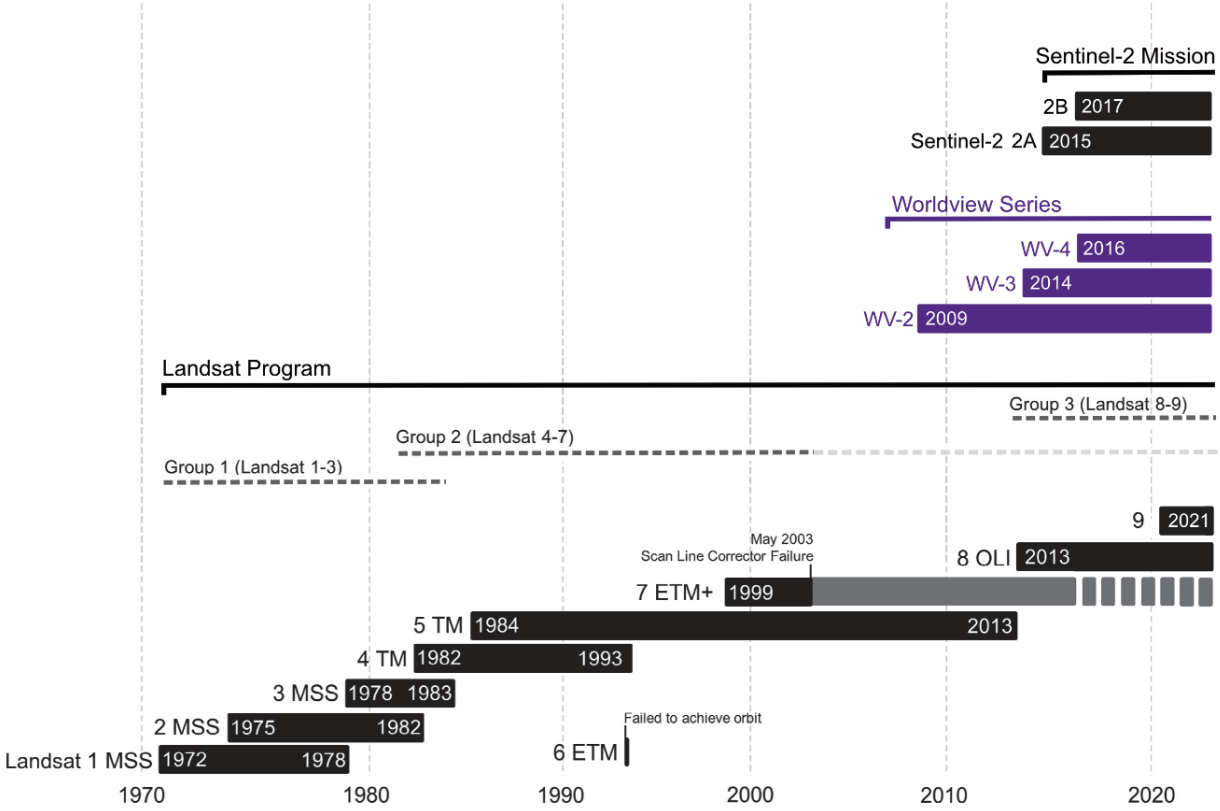

Figure 3.1. Timeline of satellite sensors for Landsat, Sentinel-2 and Worldview; the predominant satellites used in this thesis, with figure adapted from Young *et al.* (2017). Sensors include the Landsat Programme which extends from 1972 to present with data freely available for public download (black) and the further addition of two optical satellites (i) the Sentinel-2 mission led by ESA with data freely available (black) and (ii) the Worldview Series via MAXAR which is commercial imagery and represented here in purple.

3.1.2 UAV platforms for field-based remote sensing

Not only does remote sensing apply to satellite-derived platforms, but to a variety of terrestrial- and aerial-based platforms including balloons, kites, and uncrewed aerial vehicles (UAVs). These platforms are capable of carrying a wide range of sensors to perform both

passive (optical) and active sensing, including optical and thermal cameras and LIDAR. In this thesis, focus is drawn to the use of optical imaging via UAVs carrying optical cameras and thus their ability to produce high spatio-temporal imaging resolution surveys of the ice surface.

UAVs encompass various forms, including multi-rotors, helicopters, fixed-wings and combined vertical take-off and landing (VTOL) systems, each of which have their own associated advantages and disadvantages (Bhardwaj *et al.*, 2016). In recent years, UAVs have emerged as an on-demand, cost-effective method of acquiring geospatial data at high spatial and temporal resolutions that is not feasible with crewed or satellite-acquired operations (Nex *et al.*, 2022). In the context of the work carried out here, this enables the examination of small-scale, microchannel networks (mm to cm scale) that would not otherwise be mapped or investigated due to the resolution of satellite imagery (in particular, freely available imagery) making them imperceptible.

The use and advancements of UAVs and associated technology (e.g., photogrammetry) within the field of glaciology has expanded dramatically in recent years (Figure 3.2). The advent of lightweight, cost-friendly and adaptable platforms coupled with the attainment of high spatial and temporal surveys means it is now possible to flexibly acquire data and imagery at sub-centimetre resolution and with high positional accuracy that other remote sensing products cannot achieve (Alvarez-Vanhard *et al.*, 2021). Also, such data/imagery and outputs, such as photogrammetric models (introduced in Section 3.4) are able to bridge the gap and provide 'ground-truthing' of satellite-derived data, as well as fill gaps between sparse or discontinuous observations (Bhardwaj *et al.*, 2016; Alvarez-Vanhard *et al.*, 2021).

The first UAV paper to be published within cryospheric science was by Hodson *et al.* (2007) who used a camera mounted on a 323 Heliball UAV to quantify cryoconite at high spatial resolution at Midtre Lovénbreen, Svalbard; paving the way for initiating this approach in exploring various glaciological phenomena beyond typical measurements (e.g., mass balance, glacier geometry, and dynamics; Bhardwaj *et al.*, 2016). Since then, UAVs have been used for a wealth of worldwide glaciological research, from exploring surface meltwater features and roughness (Rippin *et al.*, 2015; Leidman *et al.*, 2021b; Bash *et al.*, 2022; Leidman *et al.*, 2023) to the production of high resolution orthomosaics, DEMs and ice velocity surveys (Kraaijenbrink *et al.*, 2016; Jouvet *et al.*, 2019). The development of UAV workflows and automated approaches to feature mapping, including from Bash *et al.* (2022) who developed a semi-automatic framework for the identification and mapping of supraglacial features from UAV imagery, is aiding in the efficiency of collection and analysis of rich field-data for cryospheric advancements.

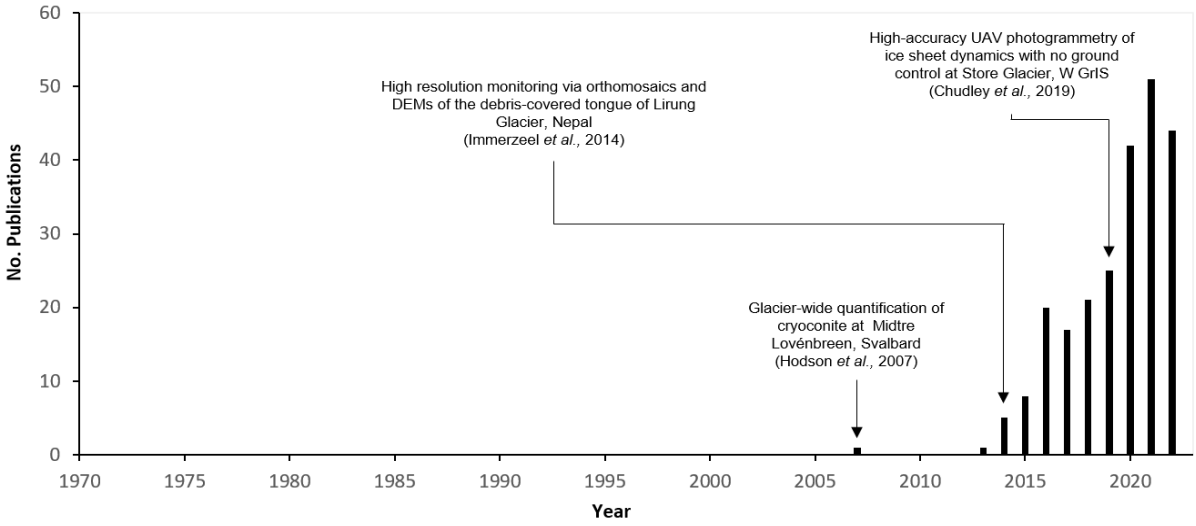

Figure 3.2. Web of Science publication results for search terms including 'UAV cryosphere' or 'UAV glacier' (search date: 17th February 2023, cryospheric studies only).

Their use, however, has not come without its range of technical and practical challenges, particularly within the harsh environments of glaciated regions. Weather conditions,

including wind gusts, precipitation and cold temperatures, can impact UAV stability and compound drainage to batteries (Gaffey and Bhardwaj, 2020). The choice of sensor can also be impacted by such conditions and, depending on the payload, can further drive energy consumption and decrease flight time. At high latitudes, extreme magnetic declination can cause on-board compass readings and automated flight paths to fail (Gaffey and Bhardwaj, 2020). In high mountainous regions, such as the Himalayas, flight elevation, low air pressure conditions and poor reception for automatic navigation GPS satellite signals can make logistics difficult, which also put constraint on automated flight plans with the possibility of losing a UAV to collision (Bhardwaj *et al.*, 2016). Many considerations and in-depth pre-planning are required for the use of UAVs for implementing its use for such research.

Over time, technological advancements in both off-the-shelf and DIY UAVs have begun to extend UAV capabilities which can be utilised for glaciological purposes. This includes the use of onboard Real-Time Kinematic (RTK) technology that can accurately correct image location in real time without ground control points (GCPs) or GNSS post-processing (Chudley *et al.*, 2019) and extended battery life for extended performance in low temperatures. For example, Jouvet *et al.*, (2019) developed an open-source, low-cost, high endurance UAV able to fly for up to 3 h (or 180 km) to monitor calving activity.

3.1.3 Remote sensing platforms used in this thesis

For the work conducted in this thesis, differing satellite platforms are used to map and quantify the supraglacial hydrologic network of the GrIS across a multitude of spatial and temporal scales and are summarised in Table 3.2.

Sentinel-2 imagery (10 m) is utilised in Chapter 4 to explore the high spatio-temporal evolution of the supraglacial drainage system over multiple melt seasons (2016-2020) at Humboldt (Sermersuaq) Glacier between May and September. A total of 176 Sentinel-2 Level-1C (orthorectified top-of-atmosphere reflectance) images across four Sentinel-2 tiles

(100 km^2) with sub-pixel multispectral registration (Baillarin *et al.*, 2012) are acquired from the European Space Agency (ESA) Copernicus Open Access Hub (https://scihub.copernicus.eu/).

Landsat-derived imagery (30 m) from Landsat platforms 5-8 are used in Chapter 5 to explore the evolution of the generalised drainage structure of Humboldt Glacier over a much larger time period (1985–2021). This Chapter utilises, for the first time, Landsat's long-term record for combined supraglacial river channel and lake mapping, with imagery acquired via Google Earth Engine (GEE) courtesy of the USGS. A total of 1429 images from 102 individual image tiles (~170 x 183 km) are used across a 37-year period spanning the main melt season months of June, July and August.

In Chapter 6, specific interest is given to the mapping and classification of small-scale features that can only be mapped using ultra-high-resolution imagery from field- and commercial-based imagery. A single UAV flight and UAV-derived photogrammetric models from a field study conducted in August 2019 is used to map small ice-marginal supraglacial streams and microchannels (<0.5 m wide) and perform surface facies classification at a southwestern outlet glacier of the GrIS, Russell glacier; a spectrally-complex, debris-rich ice margin. A subset of WV-2 imagery, supplied by an ESA third-party imagery grant, is utilised to explore commercially-available ultra-high-resolution panchromatic imagery (0.5 m) for mapping narrow, inter-stream networks within a 20.3 km^2 section of the bare ice zone (~790 m a.s.l) of Humboldt Glacier; features which are typically missed and unmapped from freely-available imagery.

Table 3.2. Details of the image types used within Chapters 4-6 of this thesis including spatial resolutions, details of spectral bands used and the research purpose of each image type used throughout this thesis.

Platform	Spatial Resolution (m)	Spectral Bands used	Source	Use
Sentinel-2A	10	Band 3 (Green) Band 8 (NIR)	Copernicus Open Access Hub (https://scihub.copernicus.eu/)	Supraglacial hydrologic mapping *(Chapter 4)*
Landsat-5 (TM)	30	Band 2 (Green) Band 4 (NIR)	Google Earth Engine courtesy of USGS	Supraglacial hydrologic mapping Terminus Change *(Chapter 5)*
Landsat-7 (ETM+)	30	Band 2 (Green) Band 4 (NIR)	Google Earth Engine courtesy of USGS	Supraglacial hydrologic mapping Terminus Change *(Chapter 5)*
Landsat-8 (OLI/TIRS)	30	Band 3 (Green) Band 5 (NIR)	Google Earth Engine courtesy of USGS	Supraglacial hydrologic mapping Terminus Change *(Chapter 5)*
WorldView-2 (Panchromatic)	0.5	Panchromatic	European Space Agency (Third Party Imagery)	Inter-stream mapping *(Chapter 6)*
UAV	0.09 – 1.8	Red Green Blue	Fieldwork (August 2019)	Microchannel and surface facies mapping *(Chapter 6)*

3.2 Supraglacial hydrologic network mapping methodology

The recent availability of moderate-to-ultra high-resolution imagery ranging from free-to-commercially available products, alongside increasing volumes of data from higher spatio-temporal coverages, has required the need for the implementation of automated methods

for efficient and rapid mapping applications. Manual delineation or the 'digitisation' of features, such as for both supraglacial channels and lakes (mapped as a collective network for this thesis), has been widely implemented within the cryospheric field previously. For example, Colgan *et al.* (2011) and McGrath *et al.* (2011) manually digitised supraglacial rivers for a small area of the Sermeq Avannarleq ablation zone in western Greenland from WV-1 images. McMillan *et al.* (2007) manually identified 292 SGLs using ASTER images and, similarly, Lampkin and VanderBerg (2011) manually digitised 1190 SGLs from Landsat-7 images. Whilst manual digitisation can make full use of the user's prior knowledge and may have higher detection accuracies, it can be incredibly time intensive, subject to user bias and limited to smaller study areas (Hochreuther *et al.*, 2021).

The development of automated techniques, such as applications of prescribed thresholds introduced by Box and Ski (2007), who automatically detected SGLs on the western GrIS in individual images based on a specific pixel threshold in MODIS imagery, further led to the development of semi- and fully-automated techniques over larger glacier-wide areas (Liang *et al.*, 2012). The automation of SGL extraction using thresholding techniques from spectral indices, predominately the well-established NDWI (Huggel *et al.*, 2002; Xu, 2005; Morriss *et al.*, 2013; Williamson *et al.*, 2017; Williamson *et al.*, 2018; Stokes *et al.*, 2019) and subsequent modifications, as discussed further in Section 3.2.1, have been applied successfully to extract spectral information of individual water pixels. More recently, pixel- and object-based classifications (Johansson and Brown, 2013; Halberstadt *et al.*, 2020; Hu *et al.*, 2022), are now widely applied due to the large and often uniform size and shape of SGLs, which are distinguishable in high-resolution optical imagery. Instead of the classification of individual pixels, pixel- and object-based classifications focus on differences between groups of pixels or objects which exhibit similar textures, tones and shapes (Johansson and Brown, 2013). For supraglacial channels (i.e., rivers and streams), however, their narrower widths (1–30 m)

and complex interconnected networks required new computational methods able to take into account these challenging features.

The development of an automatic river detection method by Yang and Smith (2013) and further developments by Yang *et al.* (2015a; 2017) provided the first automated procedure for effectively and efficiently extracting supraglacial channels (i.e., rivers and streams) from satellite-acquired imagery, which is difficult to achieve without manual intervention. Originally developed for WV-acquired imagery (Yang and Smith, 2013), this algorithm has been applied to a suite of different satellite imaging sensors at varying resolutions, including Sentinel-2 (10 m; Yang *et al.*, 2019b; Lu *et al.*, 2021) and Landsat (30 m; Yang *et al.*, 2019b; Yang *et al.*, 2021) imagery, with its uses able to map the supraglacial hydrologic network and its varying sized channels, from large-scale main-stem river and generalised network mapping from Landsat imagery, to narrower inter-stream tributary networks from Sentinel-2 and ultra-high resolution WV imagery.

This automatic river detection algorithm is a key method used throughout this thesis for the subsequent mapping and exploration of the evolution of the supraglacial hydrologic network on the GrIS (Chapters 4-6). This method consists of four key stages which are represented in Figure 3.3: (i) use of an NDWI for the spectral enhancement of water; (ii) application of a band-pass filter to remove low- and high-frequency noise; (iii) application of a Gabor filter to enhance curvilinear channel features; (iii) application of a parsimonious path-opening algorithm to retain network connectivity, and; (iv) employment of thresholds to classify the enhanced image and obtain a hydrologic map, including both channels and lakes separately. These individual stages are further described below, with individual parameters used for the different imaging platforms given in the respective data chapters; Chapters 4, 5 and 6.

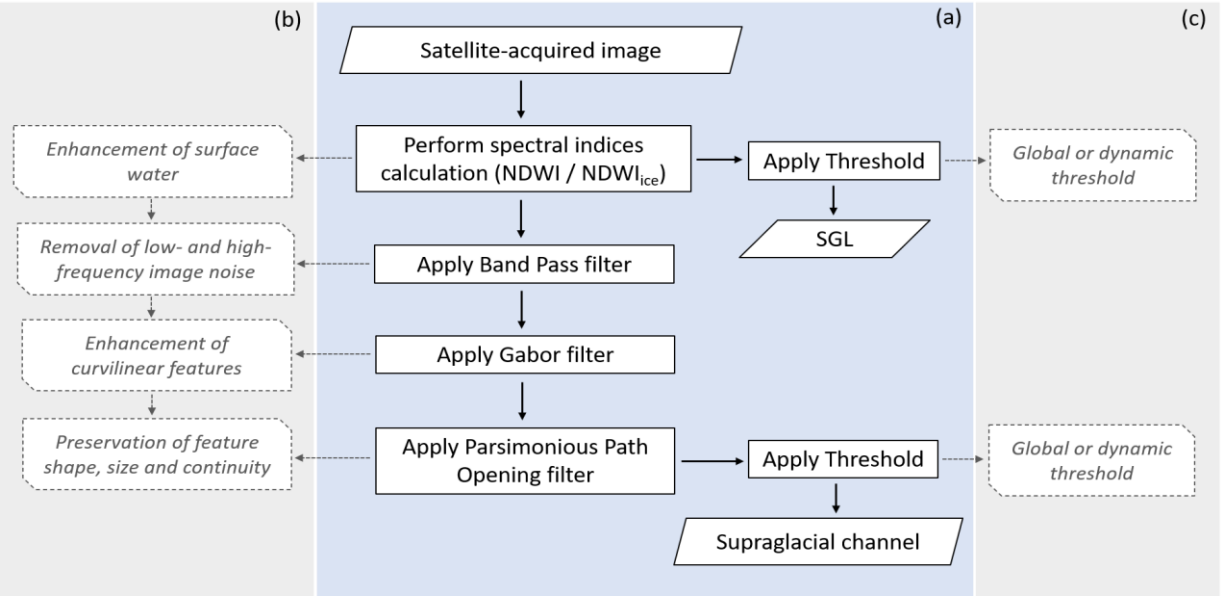

Figure 3.3. Schematic showing the general workflow of the automatic linear detection algorithm developed by Yang *et al.* (2015a; 2017). (a) Main workflow begins with the satellite-acquired image, followed by subsequent image filtering steps and the final application of thresholding for the delineation of network features, which are ultimately combined post-processing. (b) Brief descriptors of the four key processing steps; (c) denoting whether the application of a threshold can be via global or dynamic thresholding

3.2.1 Normalised Difference Water Index

The first step in the automatic river detection algorithm is the identification of surface meltwater features in satellite-derived imagery via the calculation of an NDWI (Figure 3.4c), which is a satellite-derived spectral index for the enhancement of liquid water on the ice surface (Yang *et al.*, 2015a). This index is commonly used for the extraction of water bodies within terrestrial environments and for monitoring moisture changes related to vegetation and soil features (McFeeters, 1996). This spectral index commonly utilises the green and near-infrared channels from remotely-sensed optical imagery and is calculated via the following Equation (3.1; McFeeters, 1996)

$$NDWI = \frac{(Green - NIR)}{(Green + NIR)}$$

Equation 3.1

In recent years, various modifications to this equation have taken place to further its applied use in cryospheric studies, in particular for the spectral enhancement of 'liquid' water features for extraction on ice surfaces. Normalisation ratios from the traditional green, NIR and shortwave infrared (SWIR) channels have been used for discerning 'water' and 'non-water' pixels for lake identifications across various glacial locations, including debris-covered glaciers in the Himalayas to the ablating margins of the Greenland and Antarctic Ice Sheets (Watson *et al.*, 2018; Stokes *et al.*, 2019; Dirscherl *et al.*, 2020; Lu *et al.*, 2020; How *et al.*, 2021; Lu *et al.*, 2021; Yang *et al.*, 2021; Corr *et al.*, 2022).

Some of the key challenges when extracting meltwater features from the surfaces of glaciers and ice sheets, however, is distinguishing between various glaciological features which possess similar spectral signatures, for example SGLs, rivers and streams with blue ice and slush zones. The use of the blue and red channels from optical imagery, commonly referred to as $NDWI_{ice}$ (Equation 3.2), was tested by Yang and Smith (2013) for a more tailored approach to delineating actively flowing supraglacial rivers and streams from other features such as slush, blue ice, dry channels and crevasses on the Greenland Ice Sheet.

$$NDWI_{ice} = \frac{(Blue - Red)}{(Blue + Red)}$$

Equation 3.2

$NDWI_{ice}$ has been successfully tested and used on WV-2 imagery (Yang and Smith, 2013; Smith *et al.*, 2015; Yang *et al.*, 2016), and has also been applied to other optical imaging

sensors including Sentinel-2 and Landsat 8 imagery (Benedek and Willis, 2021). Similar successes in SGL and channel delineations have been shown with fewer false classifications over blue ice and slush areas across different cryospheric locations, including Antarctica where blue ice can be particularly challenging (Arthur *et al.*, 2020a; Dell *et al.*, 2020; Tuckett *et al.*, 2021; Corr *et al.*, 2022). Both spectral indices, NDWI and $NDWI_{ice}$, are widely utilised, dependent upon the nature of mapping requirements. For mapping conducted in Chapters 4 and 5 of this thesis, the original NDWI (McFeeters, 1996) is used, with further reasonings explored in Chapter 4.

As SGLs appear as relatively uniform shapes in imagery, computed NDWI images can be used directly for SGL extraction via the application of an image threshold. Thresholding is a relatively simple yet effective method of segmenting an image based on pixel intensity to create one that is of binary form (0, 1). Threshold values for SGL extraction can typically range anywhere between >0.1 and >0.5 (Lu *et al.*, 2021), with lower thresholds identifying large numbers of lakes (and larger lake areas) including those with shallower characteristics, large (wide) supraglacial rivers and areas of slush, whilst higher thresholds lead to the identification of smaller numbers of lakes (and therefore smaller individual lake areas; Stokes *et al.*, 2019). For research conducted within this thesis, both global (i.e., one threshold across multiple images) and dynamic (i.e., independent thresholds for individual images) thresholds for SGL extraction are used based upon the empirical determination of a threshold from the image histogram and comparison with SGL presence in RGB images. Further details on specific parameters used are defined in the relevant data chapter.

As supraglacial networks (i.e., river and stream channels) are challenging to extract from satellite-acquired imagery, even after the performance of an NDWI, further filtering steps are required to enhance and retain their narrow, curvilinear forms (Yang *et al.*, 2015a; Yang *et al.*, 2017) and are described below.

3.2.2 Band pass filtering

A primary difficulty in the successful detection and delineation of supraglacial channels is that these thin and often un-uniform features, especially in regard to narrow and tributary-type channels in high-resolution imagery, can exhibit low spectral contrast against the icy background, therefore requiring a level of enhancement prior to extraction.

The first filter to be applied to the output NDWI image in the automatic river detection algorithm for supraglacial channel extraction is a band-pass Discrete Fourier Transform (DFT), used to remove low- and high-frequency image noise (Figure 3.4d; Yang *et al.*, 2015). On the ice surface, locally different ice surface facies (e.g., bright snow and darker dust patches/zones) belong to low-frequency information in the image, which can induce noise and reduce supraglacial channel delineation accuracy (Yang and Smith, 2013). The application of a DFT therefore allows frequencies in a specified range to pass through, while attenuating or removing other, undesirable image components. For the range of imagery used in this thesis, high-pass filters with frequencies based upon prior work, range between 1/500 – 1/50 m^{-1} for Landsat imagery, 1/200 – 1/40 m^{-1} for Sentinel-2 imagery (Karlstrom and Yang, 2016; Yang *et al.*, 2017) and 1/200 – 1/10 m^{-1} for WV-2 imagery (Yang *et al.*, 2016; Yang *et al.*, 2022) are utilised. Such filtering enables the supraglacial network comprised of a variety of channels to become the dominant topographic feature.

3.2.3 Gabor filtering

The second filter applied to the image in this method is a Gabor filter, frequently used in image processing and computer vision for detecting local structural patterns via edge and texture analysis and are based on a sinusoidal plane wave with a particular frequency and orientation (Turner, 1986). This simply means that the highest response of the filter is seen at edges and at points where the texture changes; in this case supraglacial channels where

their cross sections exhibit Gaussian-shapes in pre-processed images (Yang *et al.*, 2015a). The requirement for this filter is to further enhance supraglacial channels against the surrounding snow/firn/ice surface background (Figure 3.4d). As mentioned by Yang *et al.* (2015a), the use of a Gabor filter performs better than the other enhancement filters, such as a flexible linear matched filter, helping to enhance curvilinear features whilst simultaneously suppressing noise and background. The application of Gabor filters has been widely applied to a number of different studies, both within glaciology and across numerous scientific fields. For example, in biomedical images, Gabor filters aid in the enhancement of retinal blood vessels (Al Zaid *et al.*, 2018; Ali *et al.*, 2018), the detection of lung cancer (Avinash *et al.*, 2016) and brain abnormalities (Singh and Singla, 2020). Within urban planning, Gabor filters have been used for road lane and building detection (Li *et al.*, 2016; Munawar *et al.*, 2021), mapping overhead cables (Xin *et al.*, 2019) and aiding in tunnel inspections for the detection of cracks (Medina *et al.*, 2017). Within the Geosciences, Gabor filters have also been widely applied for the visualisation of seismic fault and fracture patterns and flow structures of rock glaciers (Brenning *et al.*, 2012).

Its uses across this vast array of disciplines shows its versatility, and the prior application of this filter for the pre-processing of satellite images for supraglacial river extraction (Yang and Smith, 2013; Yang *et al.*, 2015a; 2017) demonstrates its success in the ability to aid in mapping continuous river networks.

3.2.4 Parsimonious path opening filtering

The final filter to be applied to the images is a parsimonious path opening filter (PPO), a flexible mathematical morphological operator used to homogenise the brightness of pixels along linear features whilst preserving their shape and size (Figure 3.4e; Yang *et al.*, 2015). Long, thin structures and their successful extraction is a non-trivial task in image processing. As both terrestrial and supraglacial rivers do not typically follow a straight course, and with

pixel intensity varying greatly along such channel courses (even after Gabor filtering) further image processing is often required. In general, path opening and closing in mathematical morphology are tools used to preserve long, thin structures in grey-scale images based on a defined class and length criterion (Morard *et al.*, 2014). In its most basic form, these operations perform dilation or erosion to an image; dilation being the process of adding pixels to the boundary of objects in an image, and erosion being their removal. However, the use of such tools produces many paths which are redundant, causing processing to be slow and computationally intensive, especially across large study areas (Yang *et al.*, 2015a). PPO was therefore proposed as an alternative operator. This algorithm only identifies a subset of potential pathways in an image compared to conventional path opening based on pixel intensity, which is then subsequently opened to retrieve information, which can be achieved much faster and still obtain comparable results (Morard *et al.*, 2014; Yang *et al.*, 2015a). As a result, this operator is successfully used in images, aiding in the increased stabilisation of pixels across subsequent river courses before final extraction via thresholding. PPO parameters are defined in the relevant data chapter,

3.2.5 Thresholding

Thresholding can be an incredibly difficult task for the extraction of features from images and can be based upon several methods. Within the field of glaciology for the extraction of supraglacial features, thresholding methods have included (i) the manual selection of a threshold value from empirical, iterative values; (ii) via image histograms whereby the slope of the image histogram can dynamically determine the reflectance difference between surfaces, in this case ice and water (Liang *et al.*, 2012); (iii) via bimodal histograms whereby automatic thresholding methods such as OTSU can segment images via the minimisation in variance of classes based on different intensity values in bimodal images (Yang *et al.*, 2015a; Yang and Smith, 2016); (iv) via object orientation classification method that groups pixels or

objects depending on size, shape and contextual information for the segmentation process (Johansson and Brown, 2013) and (v) via textural analysis in images that identifies features based on a maximum-likelihood algorithm, which is a supervised classification algorithm (Lettang *et al.*, 2013; Dirscherl *et al.*, 2020). Threshold values can also be classed as *global* or *dynamic*, with *global thresholding* relating to the use of a single threshold value used across a number of images and *dynamic thresholding* relating to the use of different thresholds computed from particular images. Both *global* and *dynamic* thresholding are used within this thesis and are described further in the relevant data chapter.

Thresholding of Gabor-PPO filtered images for the extraction of supraglacial channels is a particularly difficult task. Set the threshold too high and supraglacial rivers and streams may be eliminated or become highly fragmented, rendering the pre-processing phases, which have aided in their preservation (i.e., Gabor-PPO filtering), ineffective. Set the threshold too low and background noise may hinder subsequent outputs. In studies by Yang *et al.* (2019) and Yang *et al.* (2021), thresholds set between 20 and 25 (out of 255) extracted mainly main-stem supraglacial rivers and some well-established tributary channels. In Lu *et al.* (2021), a lower threshold of 5 (out of 255) allowed the extraction of both main-stem supraglacial river channels and narrower-tributary channels (within the associated image resolution) alongside the retention of slush zones; an important transitionary material for melt mobilisation in the early melt season. In the original linear enhancement method study by Yang *et al.* (2015a), it was empirically found that deriving a threshold based on the mean + 0.5 standard deviation of the image histogram achieved a good balance between channel extraction and the suppression of non-river or noisy-retained regions. For attaining global and dynamic thresholds from Gabor-PPO filtered images in this thesis, the mean + 0.5 standard deviation approach plus manual verification (from the manual delineation of test areas) was

successfully applied (Figure 3.4f). Further details on specific parameters used are defined in the relevant data chapter.

Finally, combining both the NDWI-thresholded SGLs (and potential large river channels) and Gabor-PPO-thresholded channels extractions yield a final meltwater mask raster, with river and SGL pixels assigned a value of 1 and background ice 0. This is then used to calculate meltwater metrics covered by the extracted supraglacial hydrologic network. Final meltwater raster masks are also further vectorised using ArcScan for ArcGIS to better generate individual channel and SGL polylines and polygons for further analysis; analysis of which is described accordingly in each data Chapter (Chapters 4, 5 and 6).

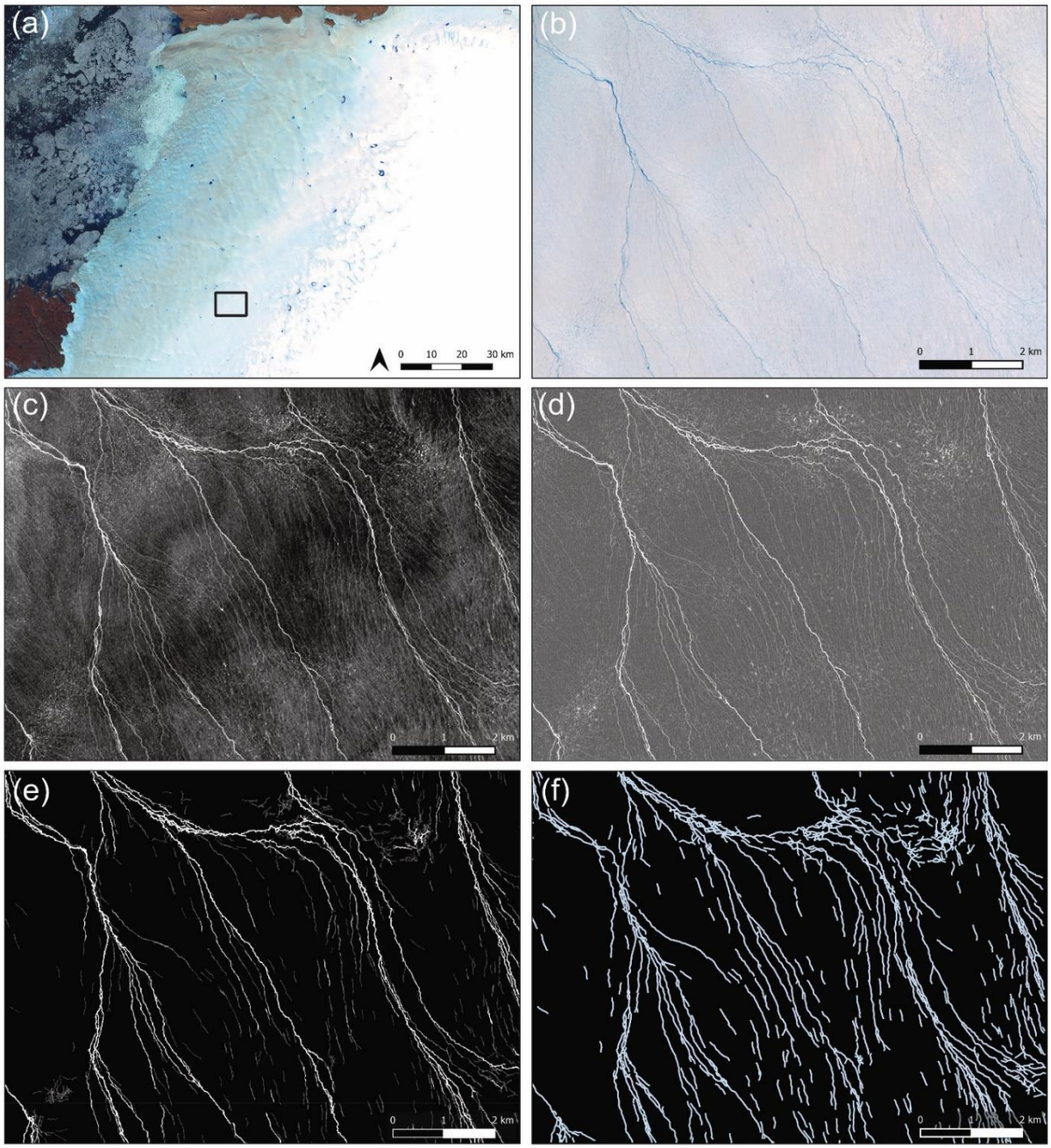

Figure 3.4. (a) RGB image of Humboldt Glacier and identification box for (b) – (g); (b) RGB image of supraglacial channels; (c) NDWI image; (d) image after band pass and Gabor filtering; (e) image after parsimonious path-opening; (g) output image after application of a threshold and vectorisation of channels.

3.3 Humboldt drainage catchment delineation

Whilst several GrIS drainage catchments are already available for the GrIS, a new, supraglacial hydrologic basin for mapping at Humboldt (Sermersuaq) Glacier was created for the purpose of this thesis (Chapters 4-5). Already available GrIS catchments include Mouginot and Rignot (2019), who divided the GrIS into glacier catchments (including peripheral glaciers and icecaps) based upon ice flow direction and surface slope, and Mankoff *et al.* (2020), who divided glacier catchments based upon subglacial water routing via Shreve's equation (1972) and a single flow, D8 algorithm (O'Callaghan and Mark, 1984) to calculate basins (with those <1 km^2 absorbed by their neighbours). To best estimate supraglacial hydrologic catchments for Humboldt Glacier, a new catchment was devised, taking into account surface flow routing and manually-identified outlet or 'terminal' points following the methodology of Karlstrom and Yang (2016; Figure 3.5). In hydrologic mapping of glaciated environments, it is incredibly important to include the effects of such terminal points (i.e., SGLs that drain and moulins where meltwater can leave the supraglacial environment) in mapping to enable a more realistic model into the components and behaviour of such systems.

Typically, in conventional DEM-based hydrologic modelling, sinks which have undefined flow directions and considered erroneous in pre-processing stages, are removed to create a depressionless-DEM in a process known as sink filling, with flow direction and subsequent basins (or catchments) derived from this. In landscapes such as karst and glacial environments, however, such sinks can often be representative of terminal lakes (i.e., SGLs that drain) or conduits such as moulins, which are important entry points for meltwater into the en- and sub-glacial hydrologic systems (Nienow *et al.*, 2017). Therefore, inclusion of these realistic points-of-entry or terminal points and their effects are an important component when deriving DEM-hydrologic modelling in such environments (Karlstrom and

Yang, 2016). In order to include their effects and produce a more realistic supraglacial drainage catchment, the preservation of such sinks, i.e., moulins and the identification of terminal supraglacial lakes, is required.

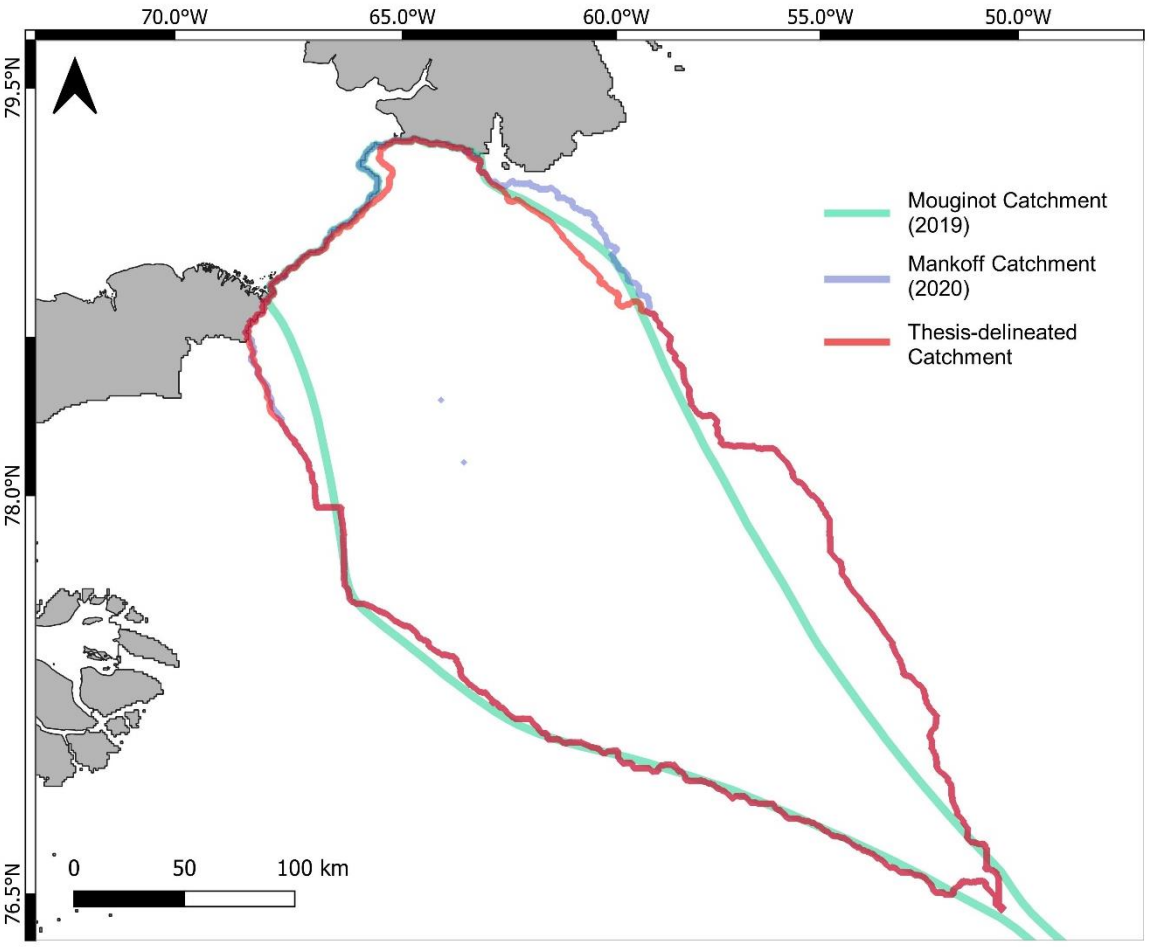

Figure 3.5. The different drainage catchments or basins used for Humboldt Glacier, North Greenland, including Mouginot *et al.* (2019) and Mankoff *et al.* (2020). The DEM flow routing derived catchment for use in this thesis is also shown as a comparison, and maps closely to Mankoff *et al.* (2020).

For the identification of moulins as terminal points for the catchment, Sentinel-2 imagery courtesy of the Copernicus Open Access Hub (https://scihub.copernicus.eu) and the 10 m mosaic ArcticDEM obtained from the Polar Geospatial Centre (https://www.pgc.umn.edu/data/arcticdem/) was used. Moulins characteristically look like pinhole features in ice, both within satellite images and DEMs (Figure 3.6a) and so can be manually identified with a high degree of confidence. Also, the abrupt termination of a primary river channel can often infer such presence (Figure 3.6a; Smith *et al.*, 2015; Wyatt and Sharp, 2015; Yang and Smith, 2016). Care is, however, taken as sometimes rivers can abruptly end, but reappear a short distance downstream due to the presence of a snow bridge (Figure 3.6b) or the development of an englacial conduit along its course, with development of a deep incision which has become cut-off from the surface, known as cut-and-closure (Gulley *et al.*, 2009). Also, active moulins reform in the same location each year, even with ice advection, due to the controls of basal topography on surface features (Irvine-Fynn *et al.*, 2011) . However, on occasion, moulins may advect with ice flow and subsequently close, forming a chain of old-to-new moulins (Figure 3.6a; McGrath *et al.*, 2011).

To identify terminal SGLs, defined here as an SGL that does not have an outflow channel or is further connected to other SGLs downstream, known as connector-lakes (Figure 3.6c; (Lampkin and VanderBerg, 2014), this was performed using the ArcticDEM and hydrology toolset in ArcGIS Pro (v.2.4). The tool *Sink Evaluation* ascertained the locations of sinks, which alongside a depression area threshold (Adep = 0.01 km^2) subsequently identified potential SGL locations, which were then compared to with overlain contemporaneous Sentinel-2 imagery for assessment: if a depression contained an SGL from compared imagery and the SGL was terminal, it was determined as a basin outlet. These results were combined with moulin locations to create a full basin outlet dataset of where water has the potential to be removed from the ice surface.

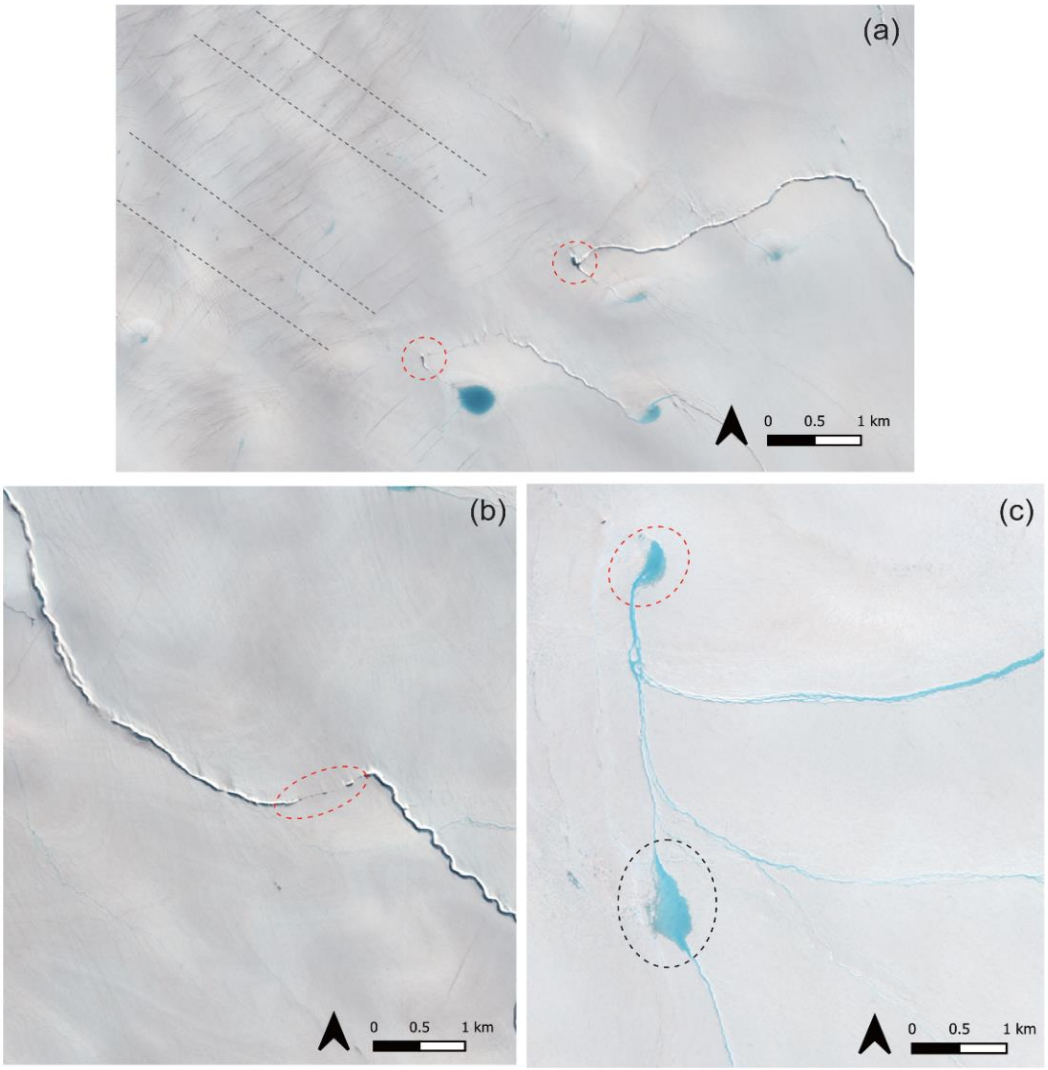

Figure 3.6. Sentinel-2 image (RGB) from 25th July 2020 depicting various terminal and non-terminal points for representing basin outles across Humboldt Glacier for catchment delineation; (a) Red circles denote two supraglacial rivers terminating into moulins. Two parallel lines depict the advection of each moulin with ice flow showing the chain-like characteristics of old-to-new and the care needed in identifying active moulins; (b) a main-stem supraglacial river with canyonised features. Red circle shows the abrupt end and reappearance of the channel due to a snow bridge, which covers ~760 m of the channel, meaning no terminal point is present; (c) two supraglacial lakes, with the black circle denoting a 'connector lake' meaning there is an inflow an outflow channel and the red circle denoting a 'terminal lake' where there is no further outflow channel or connected lake, hence terminal point

All subsequent basin outlets from this dataset are retained, with other sinks which not meet the criteria (<0.1 km^2 or pathway lakes which are not truly terminal points) filled, creating a partially-filled DEM raster. Flow direction was then identified using this partially-filled DEM using a D8 (deterministic eight-direction), flow routing algorithm to approximate water flow direction across the ice surface This grid-based D8 algorithm computes flow direction from each cell to one of eight nearest neighbours along the steepest downslope gradient (Figure 3.7; O'Callaghan and Mark, 1984) and is one of the most commonly used methods for approximating flow direction across topographical surfaces. An accumulation threshold (A_{acc}) of 2000, which identifies the general drainage network pattern including tributaries, was applied which creates a DEM-modelled supraglacial drainage network.

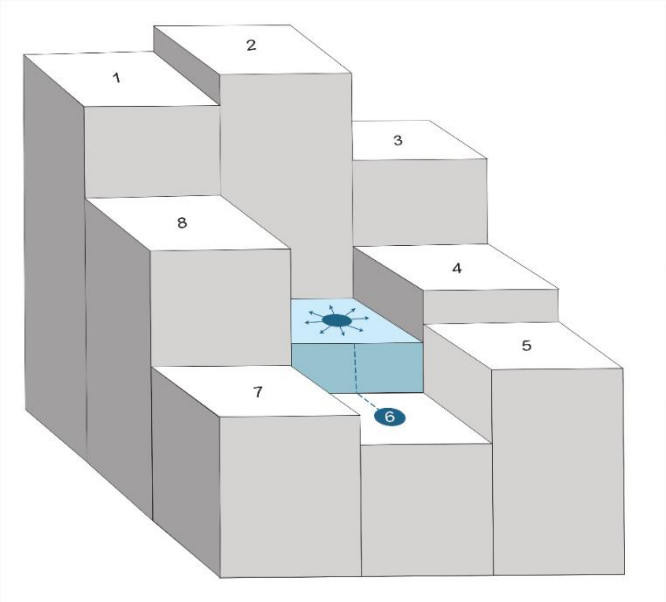

Figure 3.7. Simple schematic representing the implementation of the D8 flow routing algorithm (O'Callaghan and Mark, 1984), whereby the determination of flow direction is computed based on the surrounding eight nearest neighbour cells, with preferential flow being in the direction of steepest descent.

This DEM-modelled hydrologic catchment (Figure 3.8) was used throughout this thesis to define the boundary of the Humboldt Glacier hydrologic catchment, in particular for mapping conducted in Chapters 4 and 5. The DEM-modelled depressions and supraglacial drainage network also created during this process are further utilised within the discussion

(Chapter 7) of this thesis to examine potential future expansion of this system with ongoing climatic warming.

Figure 3.8. The DEM-derived drainage basin for Humboldt Glacier spanning an area of 53,427 km^2 and used throughout Chapters 4 and 5.

3.4 UAV Structure-from-Motion methodology

In Chapter 6, UAV-derived imagery via a quadcopter from fieldwork conducted in the on-ice, ice marginal region of Russell Glacier, southwestern Greenland in August 2019 is used to explore the spectrally-complex and, subsequent, hard-to-map minutiae of the supraglacial network (i.e., streams and microchannels) and characterisation of surface facies. For this, photogrammetric models via Structure-from-Motion (SfM) are built from such UAV-derived imagery. In this section, the SfM workflow is described along with consideration and accuracies for photogrammetric models. Further details regarding UAV surveying, photogrammetric parameters used and model outputs are provided in Chapter 6.

3.4.1 SfM overview

Structure-from-Motion (SfM) is a computer vision and photogrammetric imaging technique that involves the reconstruction of a three-dimensional structure or scene from a sequence of overlapping two-dimensional images (Smith *et al.*, 2016). Such images can be taken from a number of platforms, including those that are ground-based platforms (e.g., time lapse cameras crewed and uncrewed aerial (UAV) platforms.

Unlike traditional photogrammetry, where precise knowledge of the 3D scene, camera pose and orientation are required for the triangulation and reconstruction of scene geometry (Hartley and Sturm, 1997), the SfM approach requires none of these to be known prior to scene reconstruction (Westoby *et al.*, 2012). Instead, such parameters are automatically solved and a network of targets, known as ground control points (GCPs) with known 3D positions are utilised instead (Smith *et al.*, 2016). This workflow is expedited into the automatic generation of high spatio-temporal resolution products that are inherently multidimensional, with associated x, y, z, point orientation, colour and texture readily available and easily transformable into further products, such as orthomosaics and DEMs (Bemis *et al.*, 2014); two key products that are produced and analysed in Chapter 6. The

process of SfM can be divided into four key processes: (i) extraction and matching of key features from images; (ii) bundle adjustment (iii) georeferencing using GCPS and; (iv) dense point cloud generation, which is further explained in Section 3.4 and underpin work conducted in Chapter 6.

3.4.2 SfM workflow

The standard SfM workflow for optical-based imagery adopted by many commercial (Agisoft Metashape (2021); Pix4D (2016)) and open-source (MicMac; Rupnik *et al.*, 2017)) software packages offer automated routines for the generation of high spatio-temporal products driven through advances in 3D computer vision algorithms. These software packages offer low-cost workflows with ease of data processing for both expert and non-expert users (Berra and Peppa, 2020). Although the exact specifics of the SfM workflow will vary between different software packages, a distinct commonality exists in their overall procedures (Smith *et al.*, 2016), which is summarised into four key phases below. For SfM processing in Chapter 6 of this thesis, Agisoft Metashape Pro (v.1.6.0 and v1.6.3) software is used, with specific parameters further discussed in the chapter 6.

3.4.2.1 Key point feature detection

The first stage in the SfM process is the identification of key features, known as 'key points', in each image which may be used for image correspondence (Smith *et al.*, 2016). SIFT, or Scale Invariant Feature Transform, is the most common key feature detection algorithm used in SfM (Lowe, 2004).

SIFT involves the automatic identification and extraction of key points in all input images for storage in a database, invariant of image scaling, rotation, changes in illumination and camera viewpoint (Westoby *et al.*, 2012). Following this, image matching is completed by individually comparing each feature from an image to the prior database and finding candidate matching features based on Euclidean distance (i.e., distance between two

points; Smith *et al.*, 2016). Finally key point descriptors are created which describes each key point as a high-dimensional vector, computed through the transformation of local image gradients into a 3D visual representation that is largely insensitive to changeable illumination conditions and orientation.

It is important that such images have sufficient front (horizontal) and side (vertical) overlap, typically 60-80% (Figure 3.9; Westoby *et al.*, 2012) to ensure the entirety of the survey scene is covered and to offer enough corresponding key points in the sequence of images to subsequently match and align them. This also increases the accuracy and efficiency of image alignment for reconstruction during the 'SIFT' process. For UAV surveying conducted in Chapter 6, a horizontal and vertical overlap of 80% and 75% respectively is applied.

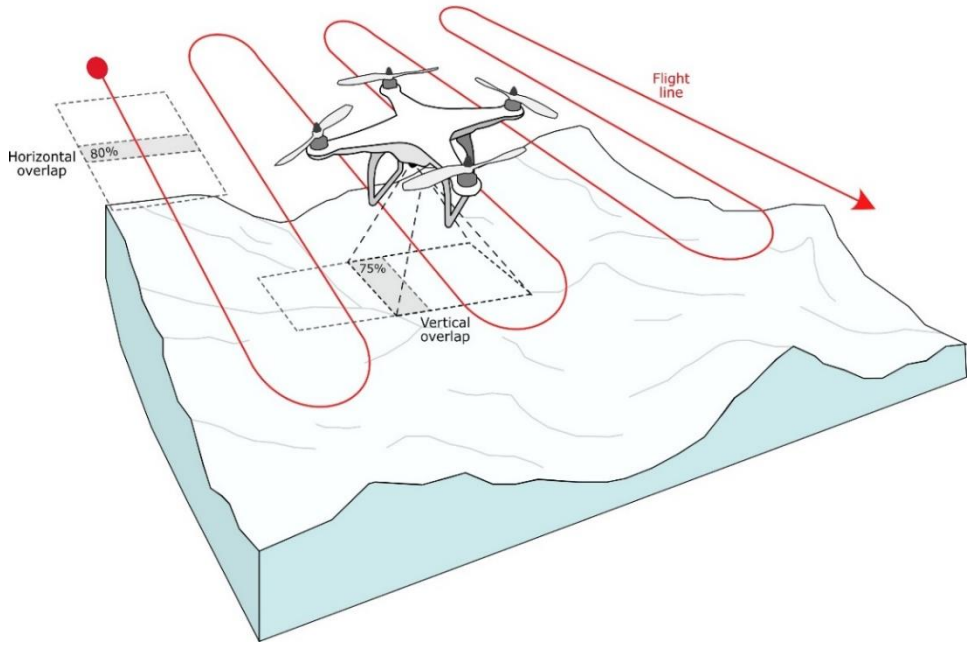

Figure 3.9. Schematic of image acquisition of a the scene with a UAV quadcopter and the bottom-mounted optical camera with field-of-view. Both horizontal and vertical overlapping of image footprints are displayed via the grey shaded areas. A greater number of overlapping images will increase flight time however is likely to produce a denser point cloud because more features should be resolvable for key point matching, leading to a higher resolution model.

3.4.2.2 Bundle adjustment

Following key point matching, SfM utilises and applies a bundle adjustment procedure; an important step within the SfM process. Bundle adjustment is the refinement of a visual reconstruction to produce an optimal 3D structure and camera parameters whilst minimising reprojection errors, typically solved using a non-linear refinement approach (Triggs *et al.*, 2000). Put simply, this refers to a 'bundle' of light rays leaving each 3D feature and converging on each camera centre, which are then 'adjusted' optimally with respect to both feature and camera positions (Triggs *et al.*, 2000). Bundle adjustment is typically solved using (i) initialisation values obtained from sequences of randomly selected matched key points and, complementarily, parameters from the cameras and poses and (ii) a non-linear refinement approach which involves iteratively adjusting camera parameters and 3D point locations until the sum of squared reprojection error is minimised (Shum *et al.*, 1999; Mouragnon *et al.*, 2006). This will ultimately produce a 3D representation of the scene as a sparse point cloud made of a sufficient number of matched key points which can then be georeferenced in space.

3.4.2.3 Georeferencing using GCPs

The resulting sparse point cloud produced from the prior steps is subsequently presented, but in an unscaled, arbitrary coordinate system. To align this output to absolute real-world coordinates, a 3D seven parameter linear similarity transformation (3 parameters for translation, 3 for rotation and 1 for scaling) is applied (Smith *et al.*, 2016). This transformation is based on a number of GCPs with known coordinates (x, y, z) taken from the surveyed scene. GCPs are fixed markers or points on the ground with a known geographic location that can be used to accurately georeference SfM models. GCPs can range from a number of photo-identifiable objects already statically present in the survey scene (e.g., a large boulder), or markers of high contrast with a centroid physically introduced and placed homogenously within the survey area (prior to flying), which are subsequently surveyed with

precise GPS systems, such as a differential GPS (dGPS) to employ accurate geodetic positioning. Typically, at least three GCPs are required within a survey area (Oniga *et al.*, 2020). However, the more GCPs used and the more uniform their distribution within the survey scene, both around the edge and within the interior, the better the resulting accuracy of the model, as well as aiding in reducing planimetric and altimetric errors (Wolf *et al.*, 2014; Gindraux *et al.*, 2017; Martínez-Carricondo *et al.*, 2018; Oniga *et al.*, 2020). For the survey conducted in Chapter 6, five black-and-white, highly identifiable GCP markers (Figure 3.10) were placed homogenously throughout the scene. The identification of GCPs and the assignment of their specific coordinates is key in providing essential information to refine estimates of SfM camera parameters as well as the reconstructed geometry of the 3D scene as a sparse point cloud. With this new GCP information included in the model, the bundle adjustment procedure can be rerun to further optimise image alignment and the sparse point cloud based upon the associated GCP coordinates (Javernick *et al.*, 2014). A total of 137,796 key points comprised the sparse point cloud in Chapter 6.

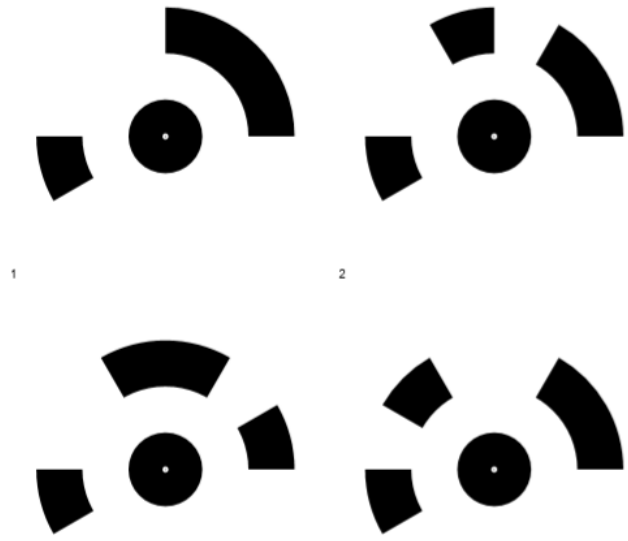

Figure 3.10. Example of coded GCPs, which are highly identifiable markers which can be implemented into the survey scene and used to georeference SfM models post-survey

3.4.2.4 Dense point cloud generation

The camera poses and parameters obtained from the final bundle adjustment of the sparse point cloud are then applied to generate a densified point cloud using Multi View Stereo algorithms (Smith *et al.*, 2016). A dense point cloud is still a collection of points positioned accurately via GPS coordinates, but it contains exponentially more information and better represents the form and appearance of the surface in 3D. The dense point cloud can be generated using depth maps, performed by dense stereo matching (Bemis *et al.*, 2014; Smith *et al.*, 2016). This is the process of calculating corresponding points for each pixel from two or more overlapping image pairs, taking into account their interior and exterior parameters estimated during bundle adjustment, with pairwise depth maps for each camera merged and combined alongside noise filtering to create a dense point cloud (Wu *et al.*, 2021). Differing depth filtering algorithms ranging between mild and aggressive are available in Agisoft Metashape Pro for best removing noise artefacts and spurious points. Once complete, the dense point cloud can be used as a reconstruction base for building mesh surfaces, orthomosaics and DEMs, which are often desired output products yielding vast amounts of information for geoscientists (Smith *et al.*, 2016).

The final dense point cloud was comprised of 29,435,694 points with a further orthomosaic (realistic-based model) and DEM generated with resolutions of 0.009 m pix^{-1} and 0.18 m pix^{-1}. Both models also have an overall projection error of 0.09 m (easting = 0.01 m; northing = 0.05 m; elevation = 0.08 m) and are further described in Chapter 6.

3.4.3 Considerations and accuracy of SfM modelling

Despite the clear advantage of using SfM in glaciological applications, the quality of the final reconstructed output, whether that be a dense point cloud, orthomosaic or DEM, is highly dependent upon a variety of diverse factors present at the time of image acquisition and

during stages of the SfM process. The environment itself, flight design, camera quality, camera calibration, SfM algorithms and georeferencing strategy can all affect the accuracy and resolution of the finalised SfM model (James and Robson, 2012; Bemis *et al.*, 2014), with such factors requiring considerable pre-planning and forward-thinking prior to completing UAV surveys and SfM-modelling.

In SfM photogrammetry, the quality of the generated point cloud is primarily controlled by the texture, sharpness and resolution of the input images (Dall'Asta *et al.*, 2015; Fugazza *et al.*, 2018; Nielsen *et al.*, 2023), which influence the performance of dense matching algorithms. Image texture, in particular, is an important control on the density and quality of point clouds due to the derivation of 3D information from acquired imagery and the ability of SfM to identify common features across multiple images of the same scene. Image texture can originate from local variations in surface colouring or local height variations of the surface topography, (i.e., roughness; Nielsen *et al.*, 2023). If too few texture variations are found, for example on fresh snow surfaces or surfaces with irregular lighting conditions (i.e., shadows cast from terrain), this can result in false key point matching and data holes within point clouds (Westoby *et al.*, 2012; Fonstad *et al.*, 2013). It is therefore important to ensure the survey scene has sufficient texture for production of the highest quality of model output. Also prior to conducting the SfM workflow, any blurred images that may obscure key point matching between photographs are removed to, again, ensure high quality model outputs (Sieberth *et al.*, 2016).

A further control on point cloud and subsequent model quality is the resolution of captured imagery, controlled by ground sampling distance (GSD). GSD is the amount of ground / surface area covered by a single image in a flight and is controlled by the distance between the camera and the feature of interest. A low flight altitude will lead to a reduced GSD, resulting in the increased spatial resolution of the acquired imagery and, subsequently,

reduction of errors for key point locations and GCP target centres for georeferencing. Flying at a low altitude, however, can limit spatial coverage. Fly at a high altitude and GSD increases, resulting in lower resolution images but greater spatial coverage (Bash *et al.*, 2018). Depending upon the requirement of the subsequent SfM models, high-resolution 3D models can still be obtained with a high altitude, lower GSD.

In addition to flight height and GSD, adequate forward and side overlap of image swaths is required to ensure full capture of the survey scene and for best possible extraction of key points for building 3D point clouds (Figure 3.9). A forward (horizontal) overlap of 60% is typically recommended and 60-80% for side (vertical) overlap (Dandois *et al.*, 2015; Sadeq, 2019). High percentages of forward and side overlap increase the number of swaths/images needed to image the study area, thereby increasing flight duration, which can have implications for power supply and data storage. Therefore, operators may choose to reduce the amount of overlap to help lengthen flight times and data volumes, or vice versa, in planning phases (Bash *et al.*, 2018; Singh and Frazier, 2018).

In terms of the accuracy of 3D models in space, the SfM workflow is strongly controlled by the number and distribution of GCPs in a surveyed scene and their subsequent appearance (because of GSD) in acquired imagery. As mentioned in Section 3.4.2.3, the number and distribution of GCPs is important to produce accurate reconstructions of the survey area (Oniga *et al.*, 2020). It has been shown that installing many GCPs that are well-distributed across the survey scene, including around the edges and within the interior of the survey scene, helps to reduce bundle adjustment errors and control doming effects of high-resolution SfM models (James *et al.*, 2020). If not placed evenly, geolocation errors within SfM models can be upwards of metres, with Javernick *et al.* (2014) and Smith *et al.*, (2014) reporting an increase of 0.27 m and 0.47 m in RMSE of their SfM models due to GCP distribution. James and Robson (2012) also reported an RMSE of 2.09 m when

georeferencing with certain groups of GCPs. Of course, in glaciated environments, well-distributed GCPs may not always be possible due to terrain or inaccessibility (e.g., crevasse fields or ice marginal zones). Therefore, care must be taken in designing and implementing GCP placement. It is worth noting that increasing the number and density of GCPs will only increase model accuracy up to a certain point, after which no further increase in accuracy is observed (Figure 3.11; Gindraux *et al.*, 2017; Baurley, 2022; Liu *et al.*, 2022).

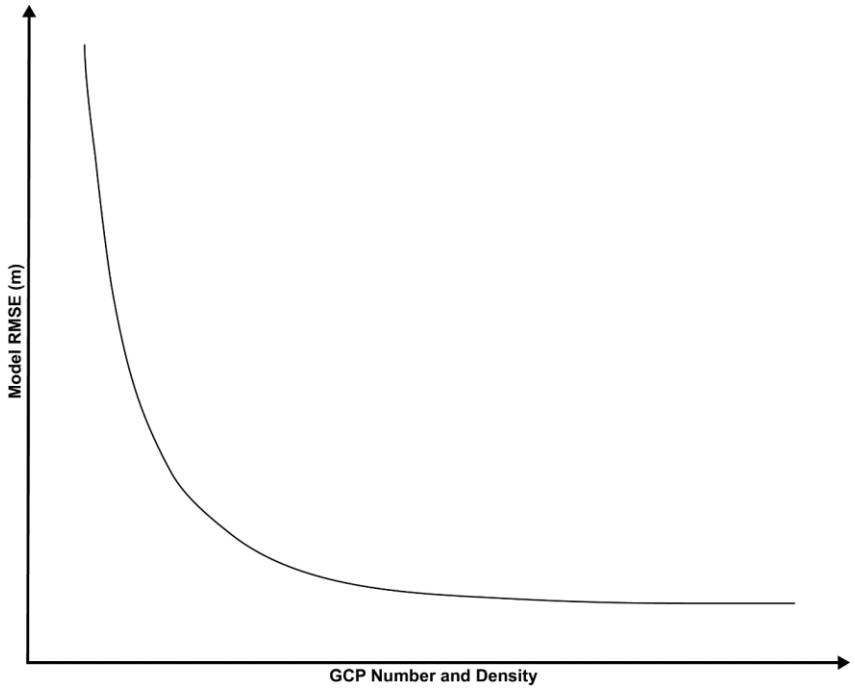

Figure 3.11. Simple schematic illustrating the relationship between GCP number and density vs the RMSE of the final photogrammetric model. It represents increases in the number and density of GCPs will only improve the RMSE of a model up until a certain point, at which no further impact will occur on the model. This schematic was produced by Baurley *et al.* (2022; their Figure 31) based on data from Tahar *et al.* (2012), Gindraux *et al.* (2017) and Sanz-Ablanedo *et al.* (2018).

The effectiveness of the re-alignment process during georeferencing process in the SfM workflow is highly dependent upon the original GCP set-up and associated errors with GCP coordinates (estimates of their point error). Vertical and horizontal errors will be present with

the deployment of the dGPS, which can be somewhat reduced by statically sampling a GCPs position over a period of time. With developing UAV technology, the use of GNSS real-time kinematic (RTK) and a post-processing kinematic (PPK) on-board methods can be implemented, eliminating the need for on-the-ground GCPs (Chudley *et al.*, 2019); particularly useful for inaccessible regions where GCP placement is impeded. Errors may also arise when distinguishing GCP markers in imagery during georeferencing, as a result of GSD limitations making the centroid of the GCP difficult to pinpoint (pixelated), limiting the achievable accuracy of the reconstruction as these positional errors propagate directly into the reconstructed points; again, a consideration in model production.

A full, detailed methodology regarding the use of a UAV, flight design details and production of UAV-derived SfM models used in this thesis for exploring fine-scale supraglacial features are further presented in Chapter 6.

Chapter 4

Seasonal evolution of the supraglacial hydrologic network at Humboldt (Sermersuaq) Glacier, northern Greenland, between 2016 and 2020.

This Chapter is published (November 2023) in the journal *The Cryosphere* (see Rawlins *et al.* (2023). The published manuscript can be viewed in Appendix A or via the link below.

For consistency of the thesis, the reference style has been altered from the manuscript version to match the format of the rest of the thesis, including table and figure numbers. Tables and figures that were also included in Supplementary Information are either included in the main-text or added into Thesis Appendix A.

I declare that this work submitted is my own, with my contribution including conceiving the idea for this paper (and Chapter), data collection, processing and analysis, figure creation and manuscript writing. The contribution of the co-authors was as follows: Kang Yang provided the automatic river detection algorithm code for use in Matlab; Andrew Sole aided with regional climate model MAR (Modèle Atmosphérique Régional) extraction for Humboldt Glacier via Matlab; David Rippin, Andrew Sole, Stephen Livingstone and Kang Yang all provided comments on draft versions of the manuscript produced by myself (Lauren Rawlins). Acknowledgement is also given to Xavier Fettweis for the availability of MAR data.

Citation: Rawlins, L. D., Rippin, D. M., Sole, A. J., Livingstone, S. J., and Yang, K. (2023). Seasonal evolution of the supraglacial drainage network at Humboldt Glacier, northern Greenland, between 2016 and 2020 , The Cryosphere, 17, 4729-4750, https://doi.org/10.5194/tc-17-4729-2023

4.1 Introduction

The Greenland Ice Sheet (GrIS) has experienced significant mass loss throughout the 21st Century and currently represents the largest single cryospheric component of global sea level rise, contributing an estimated 10.6 ± 0.9 mm since 1992 (The IMBIE Team, 2020). Over the last two decades, GrIS mass loss has become increasingly dominated by surface mass balance (SMB) processes, accounting for 60% of ice loss annually since 1991, with the remainder attributed to dynamical mass losses from marine-terminating glaciers along the ice sheet periphery (Van den Broeke *et al.*, 2016). Such SMB losses are being increasingly revealed by the magnitude and spatial extent of seasonal surface melting and runoff (Trusel *et al.*, 2018), attributed to climate-driven atmospheric warming (Hanna *et al.*, 2012; Hanna *et al.*, 2021), summertime atmospheric circulatory behaviour (i.e. Greenland Blocking Index; Hanna *et al.*, 2012, 2021; McLeod and Mote, 2016; van den Broeke *et al.*, 2017) and the ongoing expansion (Noël *et al.*, 2019) and darkening (Tedesco *et al.*, 2016; Ryan *et al.*, 2018; 2019; Riihelä *et al.*, 2019) of the bare ice zone. Between 2011 and 2020, runoff was 21% higher than any of the preceding three decades (Slater *et al.*, 2021).

Surface runoff is transported by an expansive and complex supraglacial hydrologic network (also termed supraglacial drainage system) which is activated during the summer season (Pitcher and Smith, 2019). This hydrologic network, made up of an ephemeral network of interconnected supraglacial rivers and lakes, transports and stores large volumes of surface meltwater on the ablating ice surface (Rippin and Rawlins, 2021). Such runoff can become intercepted by crevasses and moulins, that provide connections to the ice sheet bed where the timing and delivery of such water has been shown to affect ice velocity (Zwally *et al.*, 2002; Bartholomew *et al.*, 2010; Hoffman *et al.*, 2011; Sole *et al.*, 2011; Andrews *et al.*, 2014; Nienow *et al.*, 2017). In particular, meltwater delivery into an inefficient subglacial configuration, such as linked cavities (Kamb, 1987) which typically occurs during the early

period of the melt season, can temporarily overwhelm the subglacial hydrologic system, increasing water pressure and enhancing subsequent sliding (Andrews *et al.*, 2014; Davison *et al.*, 2019). In some regions where moulins and crevasses are absent, supraglacial rivers can extend undisturbed for tens of kilometres across the bare ice surface, flowing directly into the proglacial zone (Yang *et al.*, 2019b; Li *et al.*, 2022). Ultimately, much of this meltwater will end up in the ocean, contributing directly to global sea level rise (Pitcher and Smith, 2019).

Whilst many remote sensing studies have examined components of the supraglacial hydrologic network in-depth across the largest melt producing western and southwestern sectors of the GrIS (Smith *et al.*, 2015; Gleason *et al.*, 2016; Gleason *et al.*, 2021; Yang *et al.*, 2021), it is only recently that other significant ice sheet sectors have begun to be mapped (Gledhill and Williamson, 2018; Macdonald *et al.*, 2018; Yang *et al.*, 2019b; Schröder *et al.*, 2020; Boghosian *et al.*, 2021; Lu *et al.*, 2021; Turton *et al.*, 2021; Li *et al.*, 2022). Focus has only recently shifted to the rapidly changing northern regions of the GrIS, with evidence of inland expansion of supraglacial lakes observed in north east Greenland (Turton *et al.*, 2021) which align with climate model projections (Leeson *et al.*, 2015) and the existence of a widespread supraglacial network (Lu *et al.*, 2021). This study utilises Sentinel-2 satellite imagery to map the supraglacial drainage network, including both rivers and lakes, on a major northern outlet glacier of the GrIS - Humboldt (Sermersuaq) Glacier, to examine its seasonal behaviour at high spatial (10 m) and temporal resolution over five consecutive melt years (2016–2020; Figure 4.1).

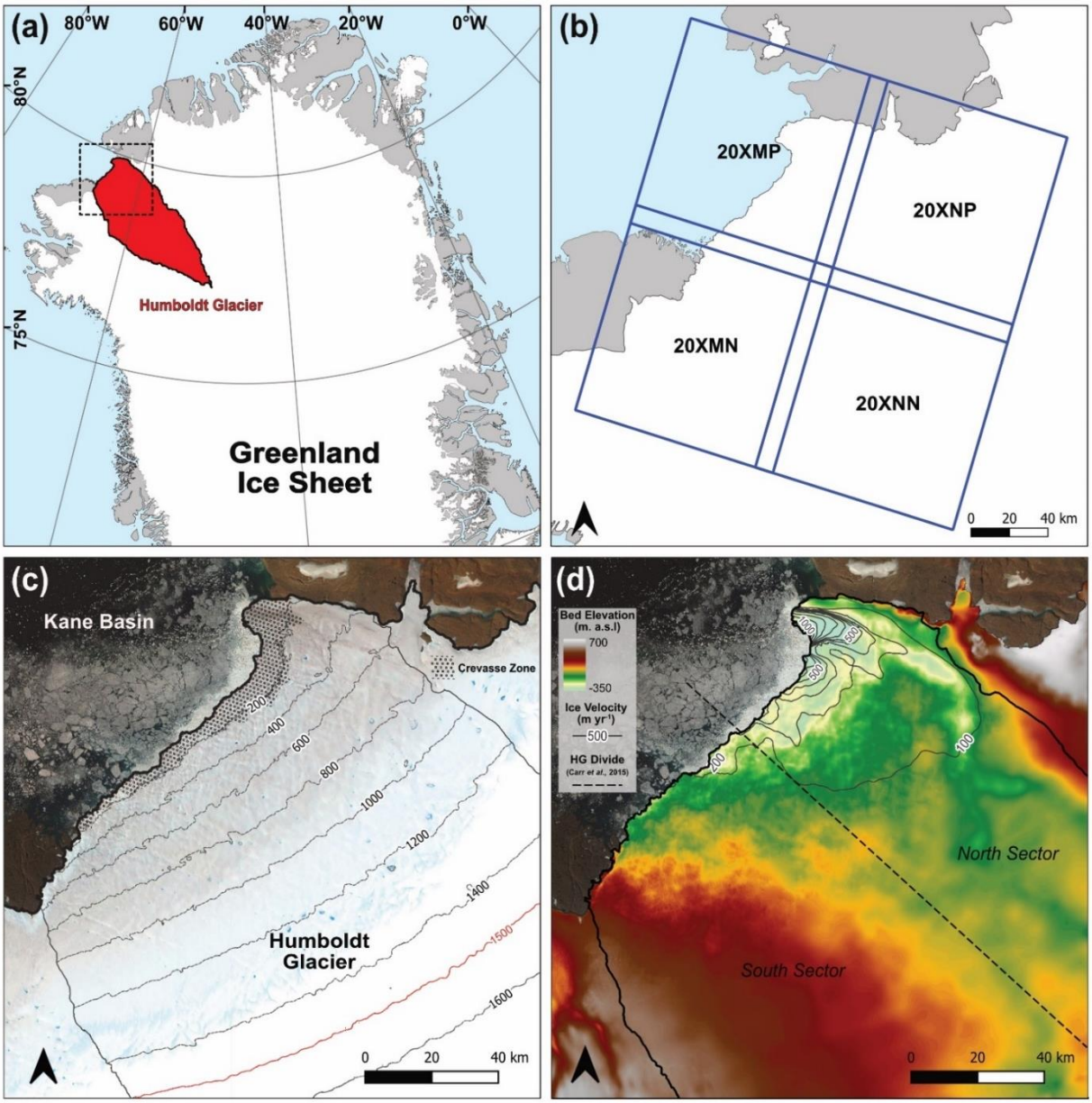

Figure 4.1. (a) Study location of Humboldt (Sermersuaq) Glacier, north Greenland, and its highlighted drainage basin (shaded red). The dashed box shows the inset for other figure boxes (b-d); (b) The four Sentinel-2 tiles used for extraction of the supraglacial drainage network across the study region; (c) True colour (R: band 4; G: band 3; B: band 2) Sentinel-2 image of Humboldt Glacier acquired from 25th July 2020 courtesy of the Copernicus Open Access Hub (https://scihub.copernicus.eu: last access December 2022). Humboldt Glacier denoted drainage basin and 200 m contour lines derived from ArcticDEM (10 m) are shown. The 1500 m a.s.l contour denotes the maximum melt extent. The shaded section up to 200 m a.s.l also shows the heavily crevassed zone that exists within the northern sector of the terminus; (d) Bed topography of Humboldt Glacier and the surrounding area from BedMachine version 4 (Morlighem *et al.*, 2021), ice velocity contours via NASAs MEaSUREs ITS_LIVE project (Gardener *et al.*, 2019) and the division of Humboldt's north and south sectors (dashed line) as per Carr *et al.* (2015).

4.2 Methodology

4.2.1 Data sources

Earth-observing satellites enable the study of supraglacial drainage features with broad spatial and temporal coverages (Rennermalm *et al.*, 2013; Yang and Smith, 2013; Chu, 2014). Over the last four decades, the Landsat program has provided a wealth of remotely-sensed data for the mapping and quantification of a number of supraglacial features such as SGLs (Lampkin and VanderBerg, 2011; Pope *et al.*, 2016; Gledhill and Williamson, 2018; Yang *et al.*, 2019a; Otto *et al.*, 2022), as well as for exploring the generalised configuration (i.e., main river stems) of the supraglacial hydrologic network (Lampkin and VanderBerg, 2014; Yang *et al.*, 2021). But, its spatial resolution in the visible spectrum (30 m) precludes the reliable delineation of numerous smaller supraglacial rivers (Yang *et al.*, 2019b). This has resulted in these complex networks being unmapped and underrepresented (Chu, 2014). The application of the Multispectral Instrument (MSI) on Sentinel-2 satellites (Sentinel-2A and -2B), which launched in 2015 and 2017 respectively, offers a higher-resolution (10 m) perspective of such systems (Yang *et al.*, 2019b; Lu *et al.*, 2020; Lu *et al.*, 2021). Sentinel-2 imagery enables the detection and delineation of both wide, main-stem river channels, which have high stream orders and are perennially reoccupied (Pitcher and Smith, 2019) as well as narrower (one pixel, or 10 m), tributary-style channels that are lower-order and shallower in depth (Smith *et al.*, 2015; Figure 4.2). Sentinel-2 imagery has also been shown to better-resolve supraglacial networks in general for mapping purposes at a glacier-wide scale, particularly in terms of river continuity (Yang *et al.*, 2019b), which contributes to its preferred use in this study.

For the years 2016 to 2020, a total of 176 Sentinel-2 Level-1C (orthorectified top-of-atmosphere reflectance) images with sub-pixel multispectral registration (Baillarin *et al.*, 2012) were acquired over Humboldt Glacier (Figure 4.2b; Appendix A, Table A.1) obtained

from ESA's Scientific Data Hub (https://scihub.copernicus.eu/dhus/#/home: last access 15 December 2022). These images covered the entirety of the study area on forty-four days between the months of May and September across the study period, equating to 1-2 images per month, allowing us to gain a full melt season perspective of supraglacial hydrologic network evolution for the Humboldt Glacier drainage catchment. For scenes with cloud cover below a 20% threshold, cloud coverage was typically restricted to the Kane Basin waterway (Figure 4.1c) or ice interior locations beyond the melt extent, and thus did not pose any significant problems for river and lake mapping.

The Humboldt Glacier drainage catchment was generated using the ArcticDEM 10 m mosaic product obtained from the Polar Geospatial Centre (https://www.pgc.umn.edu/data/arcticdem/: last access 15 December 2022) and delineated following the method of Karlstrom and Yang (2016). Elevation contours at 100 m intervals were defined across the Humboldt Glacier basin up to 1500 m a.s.l (maximum limit of the melt-prone zone), equating to a size of 13,488 km^2. Daily surface meltwater production and runoff for the study area were extracted from the Modèle Atmosphérique Régional (MAR) regional climate model (RCM) v3.11 at 6 km resolution (available at ftp://ftp.climato.be/: last access 15 December 2022, Fettweis et al., 2017; 2020; 2021). MAR is among the best RCM to cover the GrIS as it explicitly models important polar processes (i.e. SMB) forced with ERA5 reanalysis data and has been extensively evaluated against in situ automatic weather station and satellite data (for a detailed description of MAR v3.11, see Amory *et al.,* 2021; Fettweis *et al.,* 2020, 2021). MAR has now been widely used in other GrIS-based supraglacial hydrologic studies (Smith *et al.,* 2017; Yang *et al.,* 2019b; Lu *et al.,* 2020) for quantifying the relationship between modelled runoff and satellite-derived meltwater metrics for RCM accuracy validation. The version MAR 3.11 used in this study was run at high spatial (6 km) and temporal (daily) resolution to generate estimates of daily meltwater production and runoff (R) in millimetres of water equivalent per day (mm w.e. d^{-1}) within each grid cell to

assess the spatial and temporal distribution of meltwater against mapped supraglacial rivers and lakes, similar to other studies (Yang *et al.,* 2019b; Lu *et al.,* 2020, 2021; Yang *et al.,* 2021). MAR grid cells were also sampled at each 100 m interval to assess elevational gradients in both mapped drainage and runoff. A MAR uncertainty value of ±15 % was also calculated (Fettweis *et al.,* 2020).

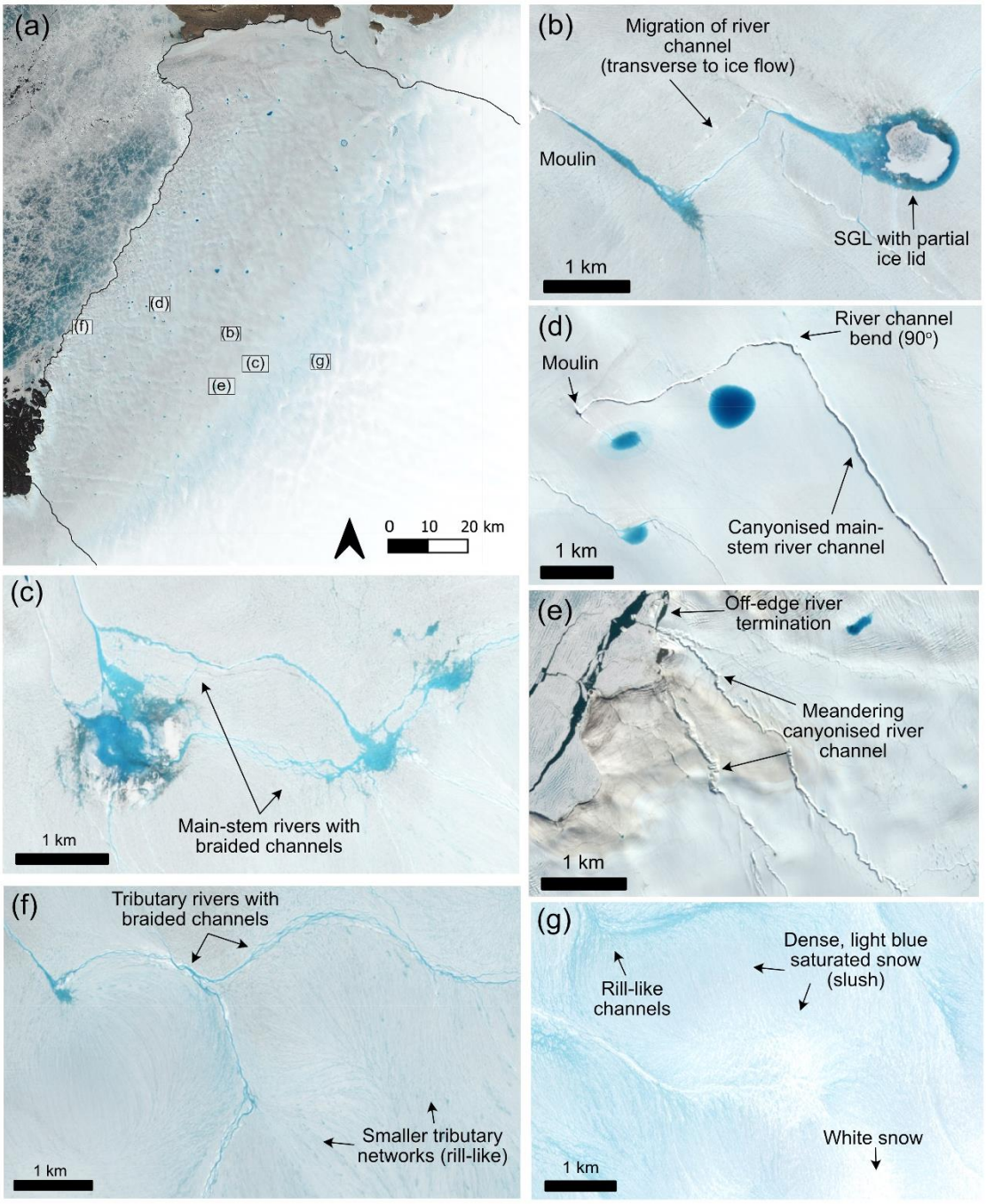

Figure 4.2. Example of the supraglacial drainage features found across the study region of Humboldt Glacier from a Sentinel-2 image taken on 23rd June 2020 (RGB). (a) A supraglacial lake with a central ice-lid feeding an outlet supraglacial river, with evidence of river advection transverse to ice flow; (b) a large canyonised supraglacial river with a 90-degree bend terminating abruptly in a moulin; (c) Deep, canyonised supraglacial rivers flowing off the ice edge; (d) Braided supraglacial rivers flowing between supraglacial lakes, known as 'connector' lakes; (e) Narrow supraglacial rivers with rill-features seen in the higher elevation regions of Humboldt Glacier, flowing and coalescing into braided tributary rivers. The Sentinel-2 image is courtesy of the Copernicus Open Access Hub (https://scihub.copernicus.eu).

4.2.2 Supraglacial river and lake extraction

To effectively delineate supraglacial rivers from remotely sensed imagery, an automatic linear enhancement method developed by Yang *et al.* (2015a) was used, which characterises supraglacial rivers according to their Gaussian-like brightness cross sections and longitudinal open channel morphology. Firstly, a Normalised Difference Water Index (NDWI) was performed following McFeeters (1996) to differentiate active surface meltwater from the background ice and snow (Lu *et al.*, 2020; Li *et al.*, 2022). This equation (4.1) utilises Band 3 ('Green') and Band 8 ('NIR') from Sentinel-2 imagery, as follows:

$$NDWI = \frac{(Green - NIR)}{(Green + NIR)}$$

Equation 4.1

An ice-derived spectral index, $NDWI_{ice}$, has been widely applied to supraglacial mapping studies in recent years (Yang and Smith, 2013; Moussavi et al., 2016; Williamson et al., 2018; Yang et al., 2021), as it produces fewer false classifications of blue ice and slush areas. We use NDWI (Mcfeeters, 1996) here because of its successful implementation in other studies (Stokes et al., 2019; Lu et al., 2020; 2021; Corr et al., 2022) and its ability to map all active surface melt of interest, including slush zones. Additionally, preliminary testing of a small sample area found NDWI (McFeeters, 1996) to produce more regularly connected river channels by 16.3% compared to $NDWI_{ice}$ (Figure 4.3).

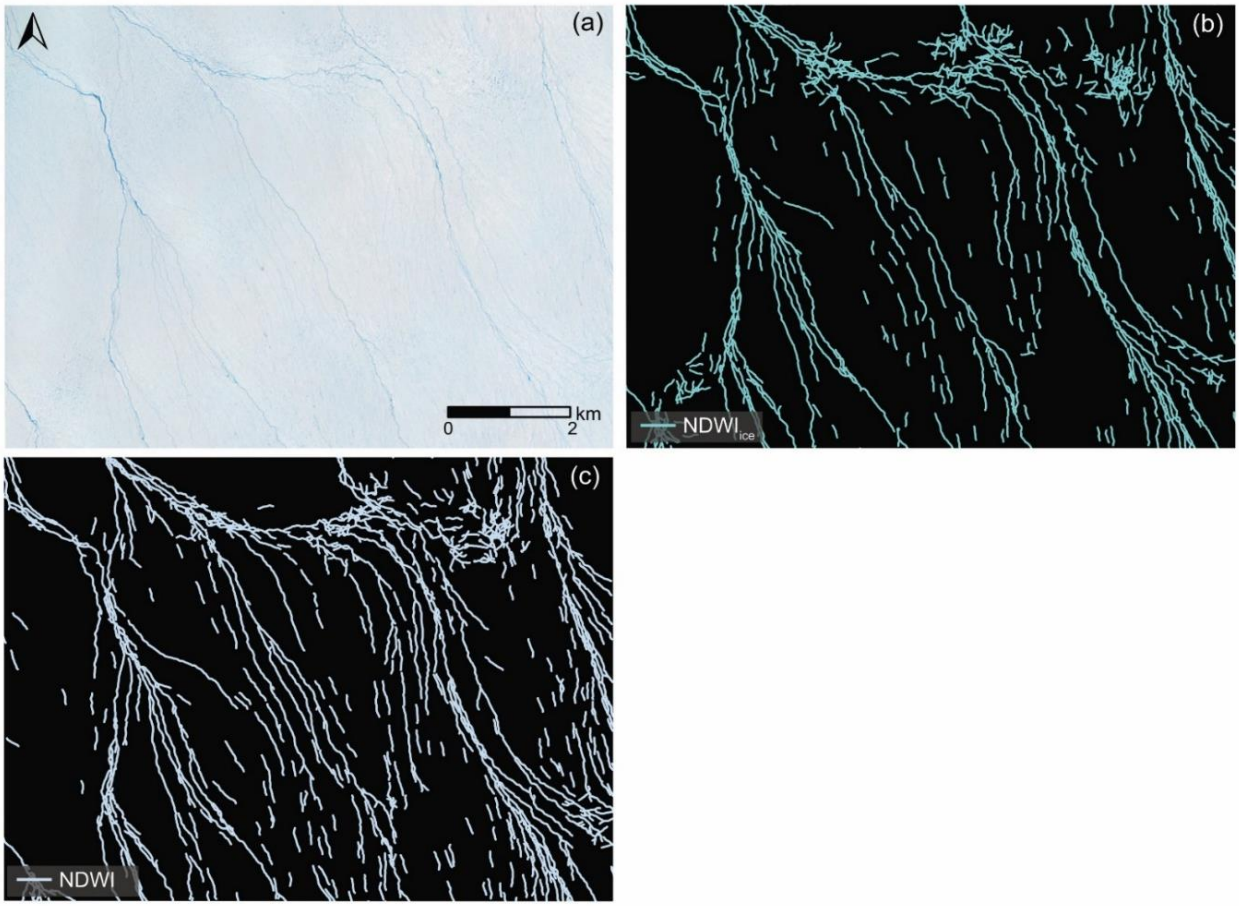

Figure 4.3. Comparative assessment between NDWIice (Yang *et al.*, 2013) and NDWI (McFeeters, 1996). (a) RGB imagine of the sample area used on Humboldt Glacier for supraglacial river extraction and comparison. This area included both primary, main stem and tributary-river type channels; (b) delineation of supraglacial river channels using the NDWIice spectral index, showing instances of channel breaks and less continual forms; (c) delineation of supraglacial river channels using NDWI (McFeeters, 1996) showing the extraction of more continual river channels whichw ere 16.8% longer than those derived from NDWIice, hence its preferred use.

Next, an ice mask was applied, created from manually digitising the Humboldt Glacier terminus from the latest, end-of-season image (late-August/early-September) in each of the study years, to extract ice-only regions and remove surrounding land, rocky outcrops and the ocean of the Kane Basin. A separate crevasse mask was delineated from manually identifying the heavily crevassed zone known to extend up to 25 km from the northern sector of the terminus, with particular prevalence across the 7 km floating section (Carr *et al.*, 2015).

This mask was applied and this section of the terminus removed to avoid the erroneous delineation of crevasses and crevasse shadows in this area during image processing, as well as to reduce the effects of drainage overestimation in these ice marginal regions in further calculations (Ignéczi *et al.*, 2018). A global NDWI threshold (t_{ndwi} = 0.4) was then applied to the masked NDWI image to extract SGLs and bright, wide, main-stem river segments. To aid in delineating narrower river segments and obtain a complete and continual supraglacial network, the automatic river detection algorithm for linear enhancement (Yang *et al.*, 2015a) was then applied. This involved the removal of the low-frequency image background and high-frequency image noise using a band-pass filter ramped between 1/200 m^{-1} and 1/40 m^{-1} (Yang *et al.*, 2019b), before the application of a Gabor filter to enhance the cross sections of smaller rivers (<2-pixel width). This was followed by a parsimonious path opening (PPO) operator, which is a flexible mathematical morphological operator, to stabilise linear brightness across river lengths and preserve connectivity, with a minimum path length of 20 pixels.

After Gabor-PPO filtering, the supraglacial river network becomes easier to differentiate and delineate from the surrounding icy background. A global pixel brightness threshold of 5 (out of 255) denoted t^5, was used to extract supraglacial rivers of varying widths from Gabor-PPO opened filtered images (Lu *et al.*, 2020), i.e., from tributary-style rivers to main-stem, large river channels. Hydrologically connected slush zones, which is where the pore space of snow becomes entirely water saturated when temperatures permit melting (above freezing, 0 ◦C) and forms expansive fields of ponded surface water, were retained as they play an important role in the initial mobilisation of melt as slush flows or within rill-type channels and the inland expansion of the melt-prone zone as summer progresses (Holmes, 1955; Marston, 1983; Cuffey and Paterson, 2010; Chu, 2014; Rippin and Rawlins, 2021). Slush zones can be spectrally distinguished in true-colour satellite images as dense, light blue patches on the surface as snow becomes water saturated (Fig. 2g), and they can be partially distinguished

in NDWI images as bright, dense features similar to that of individual linear river channels (Lu et al., 2021). For mapping conducted in this study, slush zones are mapped inclusively within the drainage network and not treated independently due to their overall hydrologic importance and spectral similarity to other hydrological components. Whilst dynamic thresholding techniques have been used in other studies, particularly in the identification and mapping SGLs across independent dates and/or years (Selmes *et al.*, 2011; Williamson *et al.*, 2017), applying these two separate thresholds (t_{ndwi} and t^5) to all images across this study period is reasonable for exploring the seasonal behaviour over the available dates used. Finally, these masks were vectorised into separate river channel polylines and lake polygons for analysis, with a size threshold of 0.1 km^2 applied to SGLs.

To assess the ability of the automated mapping technique in the capture of supraglacial rivers at Humboldt Glacier, a small area was manually digitised and shown in Figure 4.4. The overall spatial pattern extracted was similar and the difference between manual vs automated river area was 5.4%, with automated rivers tending to have several gaps in the network compared to manual results. A similar finding was also noted by Lu *et al.* (2020) who found a difference of 13.6% between manual vs automated supraglacial rivers also using Sentinel-2 imagery.

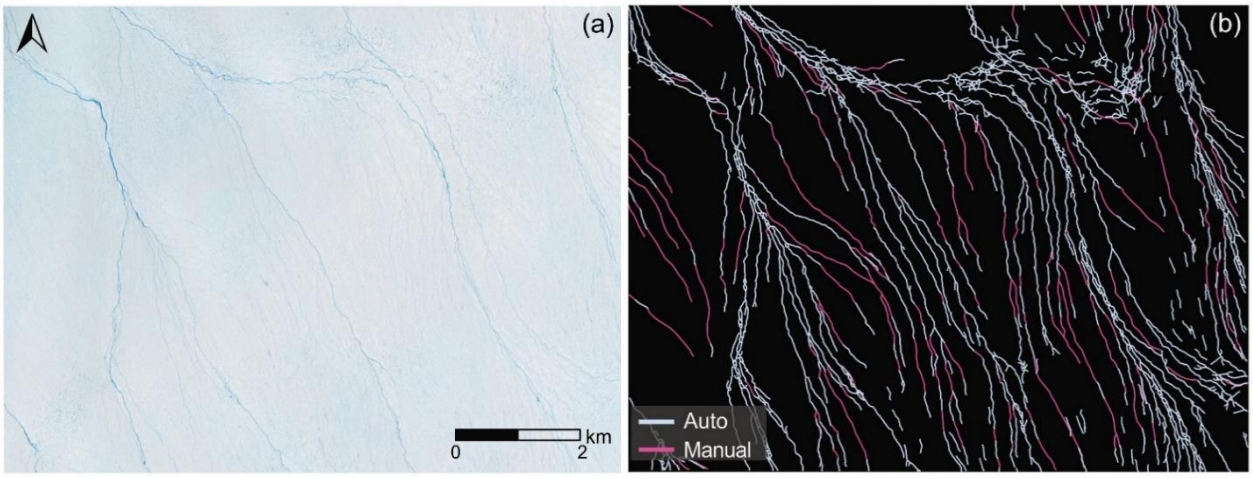

Figure 4.4. (a) RGB image of a sample area of Humboldt Glacier with both main-stem and tributary supraglacial river channels present; (b) a performance accuracy assessment comparing the automatically delineated supraglacial hydrologic system from NDWI (McFeeters, 1996) and the automatic river detection algorithm versus manually digitised networks to assess their differences, with automated rivers being 5.4% shorter than those manually derived.

4.2.3 Supraglacial river and lake quantification

To characterise the extracted supraglacial hydrologic network, metrics were calculated for both rivers and lakes. These metrics are summarised in Appendix A, Table A2 and include meltwater area (km^2), meltwater area fraction (MF, %), the number of supraglacial lakes (L_n) and supraglacial lake area (L_a). MF is defined as the percentage total meltwater area across the drainage catchment below a conservative upper melt limit of 1500 m a.s.l for each date mapped, which is then also further divided into separate feature ratios including river area fraction (RF) and lake area fraction (LF). MF was also calculated across 100 m elevation contours from above the heavily crevassed zone at 200 m a.s.l, to the maximum melt extent at 1500 m a.s.l. To explore the relationship between remotely-mapped drainage and modelled RCM MAR runoff (R), a Spearman's rank correlation (r_s) was performed and linear regression analysis undertaken with subsequent R^2, r_s and *P*-values reported.

4.3 Results

4.3.1 Spatial characteristics of the supraglacial drainage network

Supraglacial rivers and lakes were mapped from a total of forty-four dates across the lower melt-prone 13,488 km^2 Humboldt Glacier drainage basin from the melt seasons of 2016 to 2020. The mapped supraglacial hydrologic network across Humboldt Glacier is shown extend up to 1500 m a.s.l, with well-developed, main-stem river channels occurring up to 1000 m a.s.l, which we characterise as the persistent zone, and an ephemeral network of tributary-style rivers and slush zones extending beyond 1000 m a.s.l in a transient zone up

to maximum extent (Figure 4.5a). Active supraglacial rivers and lakes form progressively up-glacier from low elevations (200 m a.s.l) to a maximum of 1440 m a.s.l as the melt seasons progress across the study period, with interannual variability observed.

Within the lower elevation regions (<400 m a.s.l), collectively the supraglacial hydrologic network is largely fragmented, with many short (<750 m long), supraglacial rivers observed alongside small SGLs with an average size of 0.23 km^2: the smallest observed across all elevation bands. At greater elevations, beyond 400 m a.s.l, we observe large, main-stem supraglacial rivers, some with incised-canyon features (Figure 4.2b), interconnected with increasingly larger SGLs. At elevations >1000 m a.s.l, average SGL size is 0.41 km^2, with a maximum SGL size of 2.08 km^2. SGLs and rivers parallel to ice flow tend to be highly persistent year-on-year across the study period. In Figure 4.5b, we also see some evidence of a potential main-river reconfigurations, with the north-westward advection of a river channel that runs transverse to ice flow. In the upper parts of the catchment, the supraglacial drainage network becomes increasingly dense, especially between 800–1000 m a.s.l, where we see a 120% increase in average meltwater area (94.5 km^2) compared to 200–400 m a.s.l (42.9 km^2), a 79% increase compared to 400–600 m a.s.l (54.2 km^2) and a 10% increase compared to 600–800 m a.s.l. Not only are persistent main-stem rivers still present up to 1000 m a.s.l, but an extensively connected tributary river system is also observed within this persistent zone.

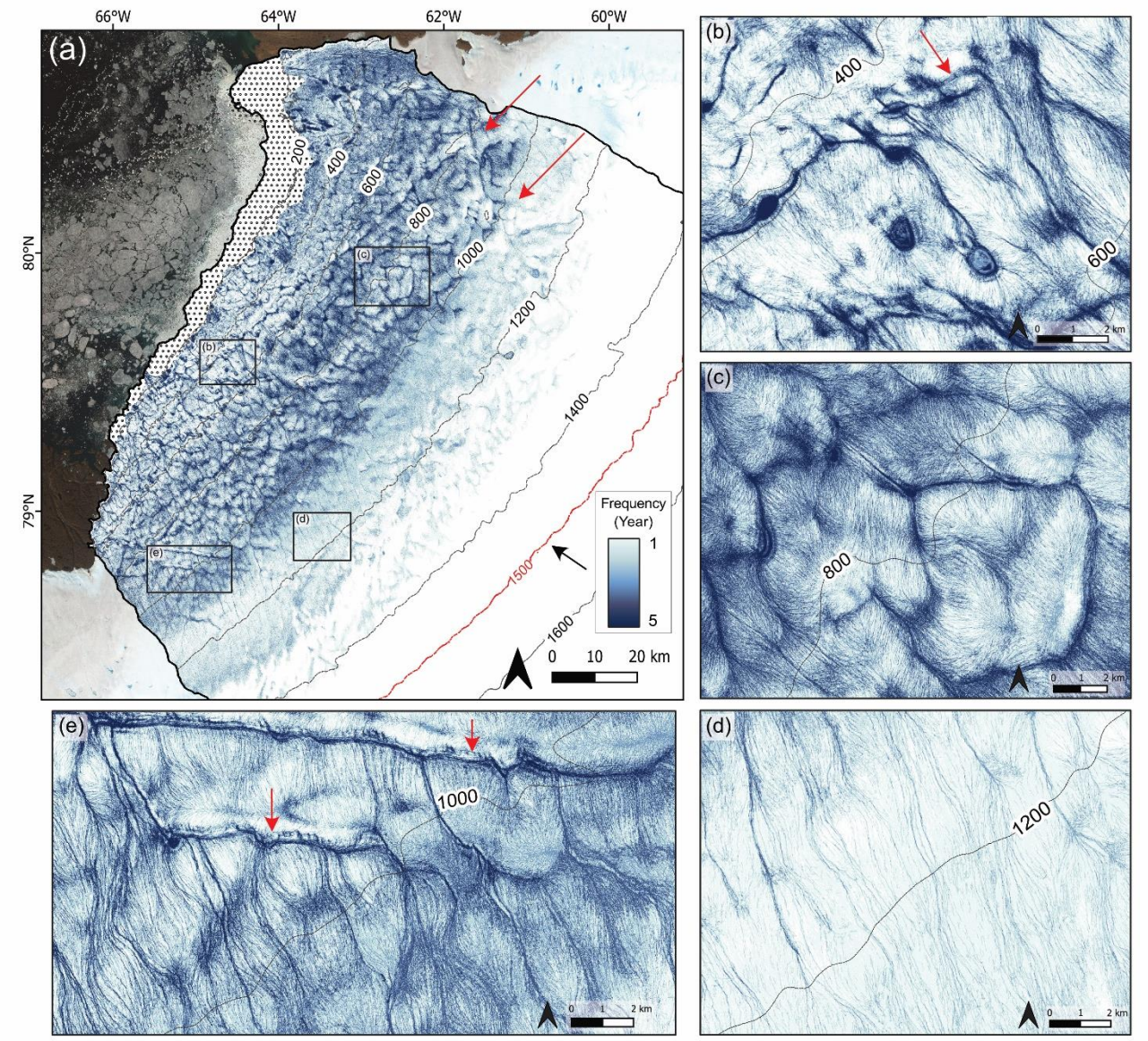

Figure 4.5. (a) Map showing the yearly recurrence of the supraglacial hydrologic network across the study period (2016 to 2020) at Humboldt Glacier. Dark blue shades denote a higher frequency of occurrence, which is highly prominent in the persistent zone below 1000 m a.s.l, with rivers and lakes typically reforming in the same location each year. Red arrows denote the location and direction of two distinct parallel drainage structures. Black arrows represent ice flow direction. The background Sentinel-2 image courtesy of the Copernicus Open Access Hub (https://scihub.copernicus.eu); (b) close-up panel showing highly persistent rivers in the persistent zone with a prominent 90-degree angle in their channel form. Red arrow denotes some channel reconfiguration due to ice advection; (c) close-up panel showing the dendritic supraglacial drainage structure typical in the northern sector; (d) close-up panel of the transient zone (> 1000 m a.s.l) where yearly river persistence is lower and characterised by lengthy tributary river channels; (e) close-up panel showing the more parallel-form of supraglacial drainage structure in the southern sector with red arrows denoting some channel advection with ice motion.

The drainage network up to 1000 m a.s.l, in particular within the central and northern reaches of Humboldt Glacier, is dendritic in nature (Figure 4.5c). This type of drainage, however, is not uniform across Humboldt Glacier, with the supraglacial network to the south exhibiting a more sub-parallel drainage style (Figure 4.5e), with this configuration extending beyond the persistent zone and into the more transient zone with slush zone development and inland evolution a key part of the temporal aspect of the network at higher elevations (Figure 4.5a). Even though density remains high until 1300 m a.s.l, vastly transient tributary rivers and slush zones dominate, feeding meltwater from headwater regions downstream. In terms of SGLs, the maximum recorded elevation was 1346 m a.s.l both in 2019 and 2020. Fewer SGLs are observed in the transient zone, accounting for 16% of total SGL area across the study period. However, average SGL area increases with elevation, with lakes in this zone being 54% larger (0.4 km^2) on average than those found below 1000 m a.s.l (0.26 km^2). The single largest SGL size of 2.08 km^2 was recorded in 2016 at 1150 m a.s.l.

A key feature that is particularly prominent in the supraglacial hydrologic network is the presence of two parallel lines that track across-glacier from a south-west to north-east direction (Figure 4.5a). Many supraglacial rivers and lakes are aligned along these two features which appear as depressions in the ice surface, with the abrupt termination of many rivers indicating the presence of surface fractures (i.e., moulins), demonstrating a strong structural element here which influences drainage configuration.

4.3.2 Temporal evolution of the supraglacial drainage network

Typically, the supraglacial hydrologic network becomes active in early-June with the on-set of melt production and runoff in the region, with only a small number of large-stem supraglacial rivers becoming active and subsequently recorded (MF <3.2%) during this time within the mapped elevation bands of 200 – 950 m a.s.l. By late June a widespread (500 m to 1150 m a.s.l) slush zone develops and advances up-glacier as the melt season progresses

runoff increases, with MF ranging between 11.4 and 19.9%. As bare ice is exposed below this slush zone, the drainage system becomes increasingly channelised (Figure 4.6). The formation of the slush zone at the end of June typically coincides with maximum melt storage in SGLs (both numbers and size of lakes). The network with the largest expanse of slush zone and number of SGLs in this study was observed on 30th June 2019 (Figure 4.6), with 2685 km^2 (19.9%) of the Humboldt Glacier ice surface comprised of a hydrologically-connected, unchannelised system and 111 SGLs recorded (total area 27.4 km^2). As the season progresses, the slush zone shifts upglacier whilst reducing in size, with average June MF decreasing by up to 33% before stagnating at a maximum inland extent, ranging between 1050 m a.s.l (2018) and 1440 m a.s.l (2020) across the study period. At this elevation, the slush zone operates thereafter as headwaters, feeding the complex, transient, tributary systems below and further suppling the larger, well-defined supraglacial rivers at lower elevations (<1000 m a.s.l).

Towards the end of the melt season, despite melt and runoff cessation, the supraglacial drainage network remains (Figure 4.6).

The interannual variability in seasonal behaviour of the supraglacial hydrologic network between 2016 and 2020 (Figure 4.6) corresponds to the length and intensity of the melt season. Drainage within the melt seasons of 2016, 2019 and 2020 follow a similar pattern characterised by a rapid increase and peak in MF in late-June, yielding values of 11.4% (R = 7.1 mm day^{-1}), 19.9% (R = 19.4 mm day^{-1}) and 12.1% (R = 19.6 mm day^{-1}) respectively (Figure 4.7); concurrent with early-season melt production and runoff. These high MF values are largely associated with widespread slush zone initiation, with a subsequent peak in MF increasing the drainage network area by 267% in 2016 (28th June) and 322% in 2019 (30th June), with its spatial extent observed below 1000 m a.s.l at this time (Appendix A, Figure A1). The beginning of the melt season in 2020 is an exception, with an anomalously high MF

(11.6%) recorded on the 15th June reaching 1100 m a.s.l, as well as a high number (57) and cumulative area of SGLs (11.2 km^2; Figure 4.7). This high is followed by a 66% reduction in MF by the 23rd June, after which the networks behaviour is similar to that of other seasons, with a subsequent MF increase of 211% to its peak at the end of June (28th June; Figure 4.7). Despite high rates of melt production and runoff throughout July across these three melt seasons, MF plateaus and reduces, reaching a steady-state of between 7.6% and 13.9%. The number of SGLs also reduces on average between 20% and 27% throughout July, with cumulative SGL area reducing between 9% and 38%.

By the end of July, the supraglacial hydrologic network consistently extends to 75-80 km inland (1440 m a.s.l) at its maximum areal extent. As melt and runoff declines into August, the hydrologic network reduces between 53% (2016) and 9% (2020). In 2019, persistent high rates of melt production and runoff result in persistence of the networks maximum inland extent and even a late-season increase of 54% in MF from the 5th August to 13th August. 2019 is registered as an exceptional year at Humboldt Glacier, with an average meltwater area up to 75% greater in June compared to 2016, between 25% and 92% greater in July compared to 2016 and 2020 and up to three times greater (300%) in August compared to both 2016 and 2020. Additionally, 129% and 86% more lakes are recorded compared to 2016 and 2020 respectively, with SGLs persisting much later into the melt season (mid-August) than the other years.

The supraglacial hydrologic network in 2017 and 2018 behaves quite differently to the other melt years (Appendix A, Figure A2). Until late-July, MF remains low (<7%; Figure 4.7) with runoff predominately occurring within the lower 700 m of the Humboldt Glacier basin (Appendix A, Figure A1). The number and area of SGLs is also low during this period, with an average of 15 lakes observed in June and July across 2017 and 2018 with a cumulative average area of 21.5 km^2 and 31.1 km^2 respectively; 280% lower than average lake counts

and 218% lower than cumulative average area for the same monthly periods across 2016, 2019 and 2020. Unlike the other study years, peak MF does not occur until much later in the melt season, reaching 10.2% on 22nd August 2017 and 7.2% on 20th August 2018 with a 690 km^2 (197%) and 521 km^2 (135%) increase in meltwater area to its prior mapped date respectively; concurrent with peak runoff and the widespread occurrence of a late slush zone. Similarly, SGL numbers and area also peak on these dates, with 54 (15.8 km^2) and 74 (20 km^2) lakes recorded, comprising 32% and 39% of total lakes recorded per year respectively. Examination of the maximum extent of the supraglacial hydrologic network is also revealed to be limited, with a maximum elevation of ~1150 m in 2017 and ~1050 m in 2018, equivalent to between 48 and 51 km inland.

When comparing what could be considered as high vs low melt year seasonal patterns, the supraglacial hydrologic network is twice as large during high melt years (2016, 2019 and 2020) and is seen to form at elevations ~300 m higher than in low melt years (2017, 2018; Appendix A, Figure A2). In terms of the average number of SGLs, there is almost double the number of SGLs observed (92%) in the high melt years compared to low melt years with average SGL area also being 111% higher, showing large year-on-year variability of this system.

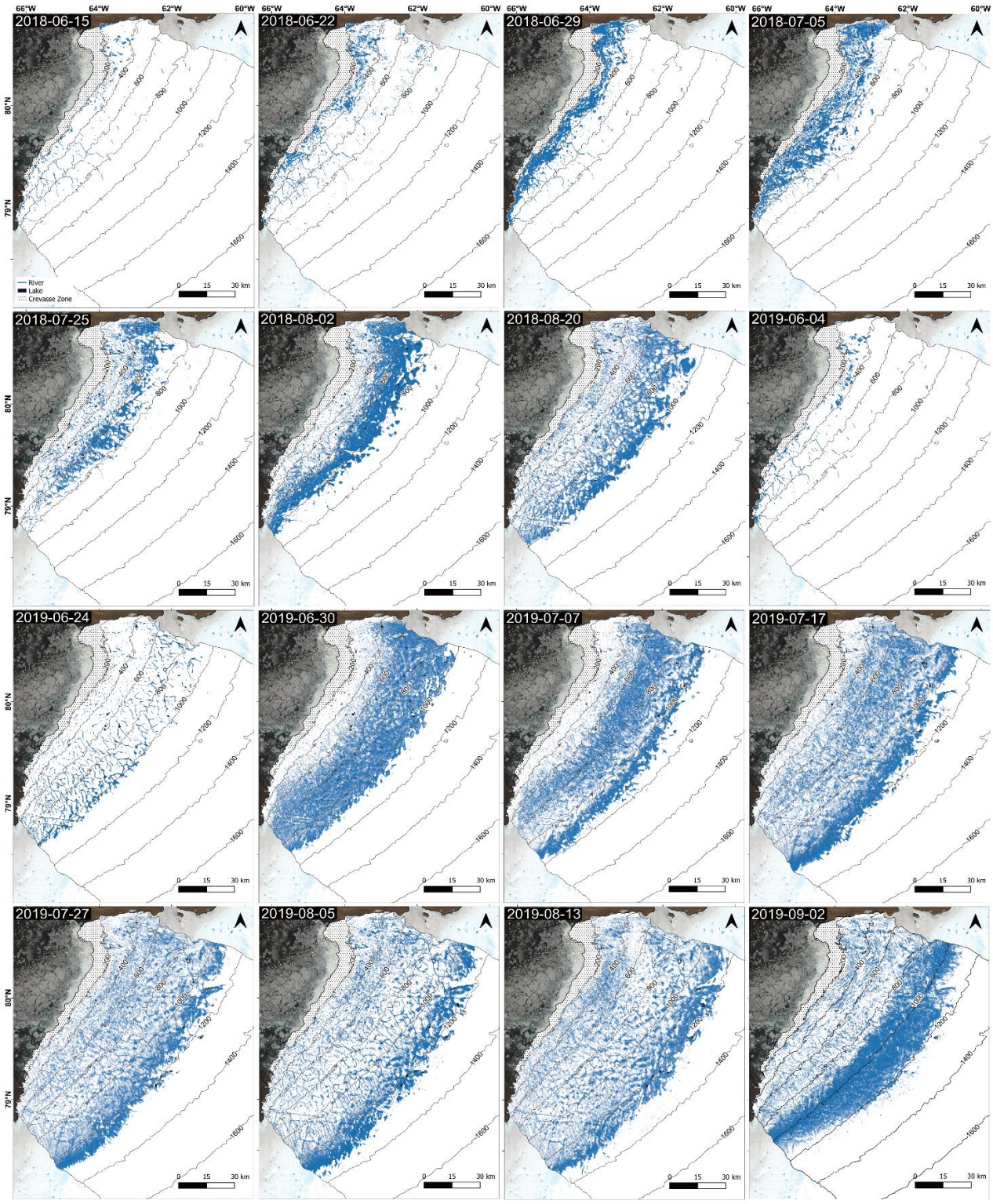

Figure 4.6. Satellite-derived mapping of the temporal evolution of the supraglacial hydrologic network, including rivers and lakes, across the Humboldt Glacier drainage basin from two melt years during the study period; 2018 showing the typical behaviour of a low melt year and 2019 showing the behaviour during a high melt year. The background image is a Sentinel-2 image courtesy of the Copernicus Open Access Hub (https://scihub.copernicus.eu). For all mapped study dates, please refer to Appendix A, Figure A2.

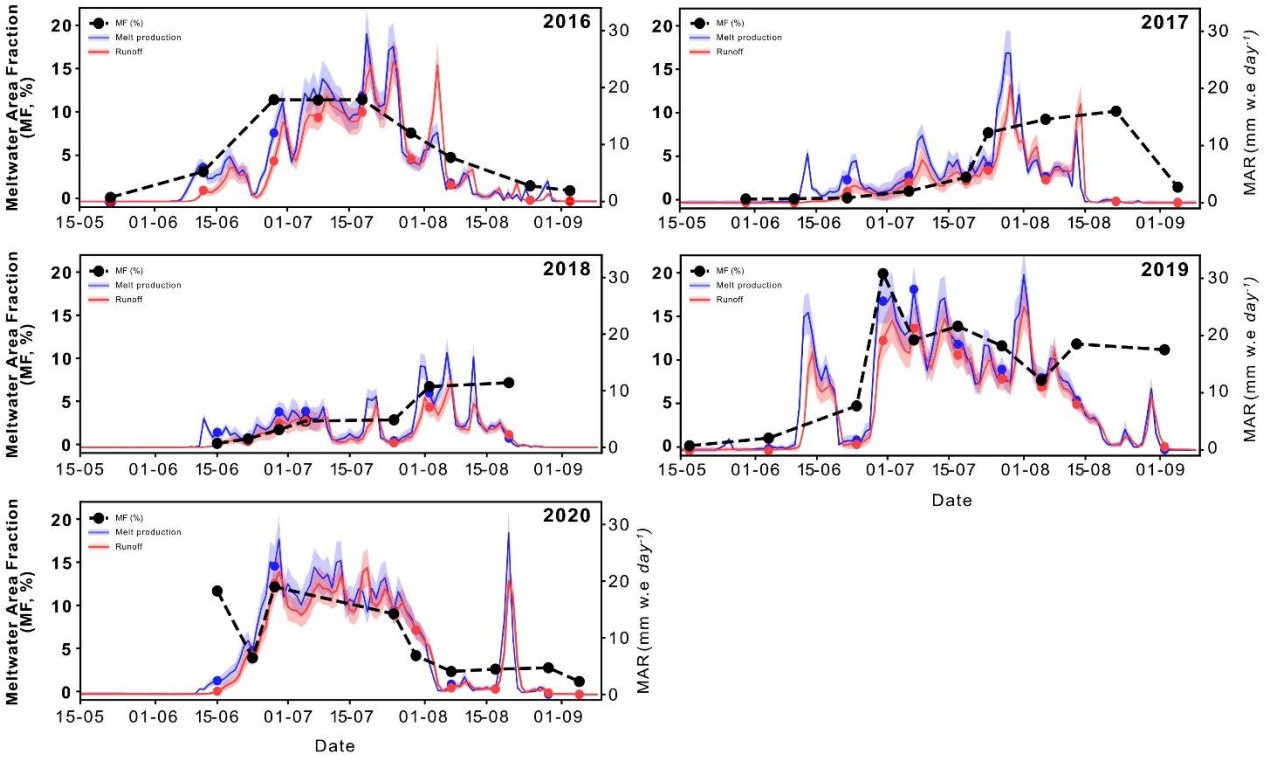

Figure 4.7. The satellite-derived water metric meltwater area fraction (MF, %) for each mapped date across the study period alongside MAR v3.11 derived melt production and runoff values (mm w.e day-1) for the Humboldt Glacier catchment. The ±15 % uncertainty envelopes are provided for MAR-derived values (Fettweis et al., 2020)

The contribution of rivers and SGLs to the supraglacial drainage network follows the same general seasonal trend as MF. RF and LF (%) peak at the end of June in the high-melt years of 2016, 2019 and 2020 and in mid-August for the low-melt years of 2017 and 2018 (Figure 4.8), i.e. when hydrologically connected slush zones are most prominent and SGL numbers are shown to peak. Overall, the network is largely composed of supraglacial rivers, with RF accounting for an average of 6.2 % ± 5.6 % (mean ± SD) of the HG catchment across the study dates and is higher during high-melt years (7.8 % ± 6.0 %) compared to low-melt years (3.5 % ± 3.4 %). The highest RF recorded occurred on the 7 July 2019 and measured 24.5 %; the highest RF measured in a supraglacial hydrologic study. For SGLs, average LF was much lower, accounting for an average of 0.07 % ± 0.06 % of the melt-prone area of the

catchment, with slightly higher LF in high-melt years (0.08 % ± 0.07 %) compared to low-melt years (0.05 % ± 0.04 %). In terms of the overall contribution of supraglacial rivers and SGLs to peak meltwater area fraction, 98 % of the network is dominated by supraglacial rivers across all study years, with SGLs playing a less dominant role in HG's drainage network. In comparison, rivers contribute ~ 62 % to the drainage network in southwestern Greenland, with SGLs contributing ~ 38 % (Yang et al., 2021).

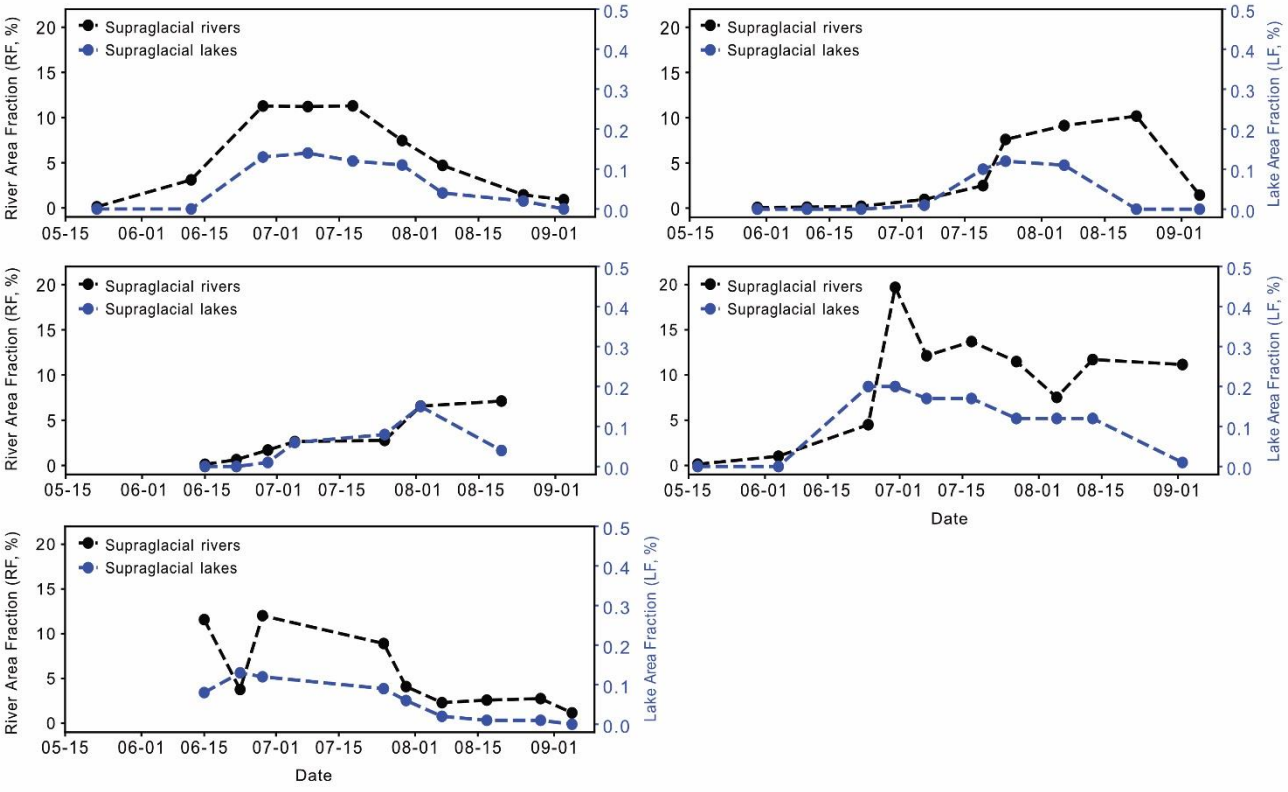

Figure 4.8. River area fraction (RF, %) and lake area fraction (LF, %) across the melt-prone zone of HG for each mapped date across the study period. On average, 98 % of the supraglacial drainage network across the study period at HG is comprised of RF.

4.3.3 Supraglacial hydrology and MAR runoff

A strong positive linear relationship was identified between satellite-derived MF and regional climate model MAR surface R for the Humboldt Glacier catchment across the study period 2016 to 2020 (Figure 4.: $R^2 = 0.77$, Rs = 0.91, $P = <0.001$) up until peak MF values and rapid surface runoff decline at the end of the melt season. Both MF and R increased concurrently each year as the melt season progressed, with peak runoff often coinciding with the existence of expansive slush fields across the upper part of the catchment. Runoff remained high until maximum extent occurred, particularly for high melt years: 2016 (29th July, R = 7.5 mm day^{-1}), 2019 (13th August, R = 8.2 mm day^{-1}) and 2020 (30th July, R = 11.4 mm day^{-1}). For low melt years, runoff remained relatively high until early August (6th August 2017, R = 4.0 mm day^{-1}; 2nd August 2018, R = 7.1 mm day^{-1}), with maximum extent occurring within two-weeks (the next mapped date). This relationship between MF and R shows the reliability of simulated variations in seasonal surface meltwater runoff in capturing the behaviour of the supraglacial hydrologic network via satellite-derived water metrics, particularly during high melt years and until runoff declines each melt season

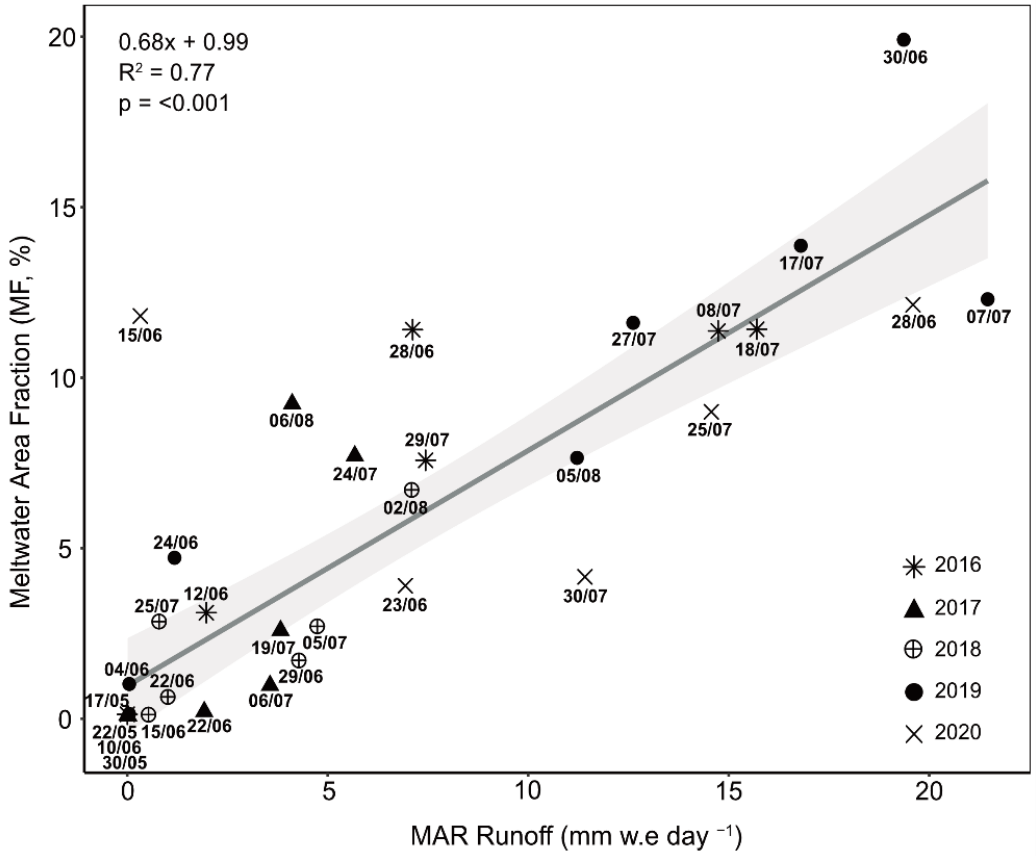

Figure 4.9. Linear relationship between the satellite-derived water metric meltwater area fraction (MF, %) and RCM-derived runoff from MAR v3.11 for each year studied up until runoff declines.

4.4 Discussion

4.4.1 Spatial characteristics of the supraglacial drainage network

Our satellite-derived mapping reveals a complex supraglacial hydrologic network at Humboldt Glacier that reaches a maximum elevation of 1440 m a.s.l, recorded in 2020. This maximum elevation is 400 m lower than supraglacial drainage observations in southwestern Greenland (~1800 m a.s.l; Yang et al., 2021), consistent with observations by Ryan et al. (2019) who found the maximum snowline elevation to be 400 m lower in northern Greenland than southwestern Greenland. Up to elevations of 1000 m a.s.l, the supraglacial drainage network is highly persistent across the study period, with a highly variable system beyond

this elevation observed within the transient zone; defined in this study as a high elevation region whereby drainage is transient in time, but not necessarily space. The yearly recurrence of meltwater pixels in the supraglacial hydrologic network (Figure 4.5) demonstrates the t stability of SGLs in particular, which, re-occupy the same location year-on-year despite ice advection (Smith *et al.*, 2015; Pitcher and Smith, 2019). SGLs increase in size with elevation, with higher elevation lakes persisting for longer (i.e., incapable of draining) and undergoing greater season expansion (Gledhill and Williamson, 2018; Yang et al., 2021). Larger lakes at higher elevations are the result of longer wavelength bed undulations being favourably transferred to the ice surface through thicker ice creating large, shallow surface depressions (Ng et al., 2018). Unlike SGLs found <400 m a.s.l, which are smaller and have likely reached their maximum available melt area, higher-elevation lakes are not yet topographically constrained (Krawczynski et al., 2009). This is similar to observations in southwestern Greenland where SGL size was larger and more variable >1400 m a.s.l, with 21% of these lakes draining via hydrofracture (Yang et al., 2021)

Whilst SGL location is known to be largely controlled by bed topography (Lampkin and VanderBerg, 2011; Ignéczi *et al.*, 2018), this study also notes that many well-established rivers that are longitudinal to ice flow, including many with canyonised features, also reoccupy locations (Macdonald et al., 2018; Boghosian et al., 2021).. Supraglacial rivers that are transverse to ice flow or have a transverse element to their channel, however, may be less stable in some areas by up ~300 m (Figure 4.5a) over the study period, probably due to the impact of ice advection. In the transient zone, the network recurrence is reduced, with tributary rivers and slush zones dominating at higher elevations. Here, their persistence is highly reliant on there being enough melt at higher elevations to initiate and sustain channel formation, which in 2017 and 2018, was limited and therefore drainage occurrence was much reduced in this zone. Also, tributary rivers are typically lower order with narrower channels and shallower depths (Smith *et al.*, 2015; Pitcher and Smith, 2019), meaning their

form has the potential to migrate, close and reform quickly, if melt is available. The transient zone is therefore is not only influenced by melt availability overtime, but the potential for migration in space. In agreement with previous studies (Joughin *et al.*, 2013; Poinar *et al.*, 2015), we also show that rivers tend to be longer at higher elevations (>25 km long), consistent with observations in SW GrIS (>40 km long), likely due to the basal transfer of only long-wavelength basal undulations to the surface due to thicker ice and the reduced presence of surface crevassing (Gudmundsson, 2003; Lampkin and VanderBerg, 2011; Crozier *et al.*, 2018).

Drainage patterns are also shown to vary across Humboldt Glacier, with a dendritic-style of drainage observed in the northern sector and a parallel-style drainage observed in the southern sector. These differing patterns not only highlight variations across different hydrologic catchments of the GrIS, but also intra-catchment variations, which may stem from local variations in surface topography via the transmission of basal topography (Raymond and Gudmundsson, 2005; Ng *et al.*, 2018) controlled by bed roughness/ structure wavelength transfer and differing ice flow regimes (Gudmundsson, 2003; Lampkin and VanderBerg, 2011; Crozier *et al.*, 2018; Ignéczi *et al.*, 2018). This has been shown to play an important role in mapped rivers and lake hydromorphology at both 79°N Glacier (Lu *et al.*, 2021) and across the Devon Ice Cap (Wyatt and Sharp, 2015).

In the northern sector of Humboldt Glacier, we observed short supraglacial rivers and small SGLs at lower elevations (200-400 m a.s.l) and a prominent dendritic-style drainage pattern of interconnected rivers and lakes up to 1000 m a.s.l, with some larger rivers abruptly terminating. Such characteristics suggest the interception of runoff by crevasses and moulins, with such capture directed to the en- and sub-glacial system with the potential for pronounced impacts on localised flow rates (Catania *et al.*, 2008; Schoof, 2010; Mejia *et al.*, 2022).). This drainage style is typical of that observed within the western and southwestern

sectors of GrIS, whereby structurally-controlled drainage of supraglacial rivers flowing between SGLs promote shorter river channels, whilst high rates of crevassing at lower elevations (<1000 m a.s.l) means virtually all surface meltwater is captured and diverted before reaching the ice edge. This more compact style of drainage is likely to create a 'flashier' response in hydrographs, with a greater runoff peak and shorter rising limb (Smith et al., 2017). Additionally, as shown by Carr *et al.* (2015) and Rignot *et al.* (2021), this sector of Humboldt Glacier sits within a 475 m deep basal trough that extends ~45 km wide and >70 km inland and is characterised by fast rates of flow (200–600 m yr^{-1}). Faster basal sliding has the ability to promote the more efficient transfer of basal topography to the surface and can subsequently precondition the large-scale spatial structure of the surface drainage system, including drainage fragmentation due to higher rates of crevassing and moulin formation, which can further supply meltwater to this faster-flowing sector (Crozier *et al.*, 2018; Ignéczi *et al.*, 2018).

In comparison, the sub-parallel drainage structure of the supraglacial network in the southern sector sector differs greatly to that of the northern sector of HG and observed drainage in western and southwestern regions of the GrIS. Drainage largely consists of continuously-flowing rivers that drain surface meltwater from the slush zone at ~1500 m a.s.l to much lower elevations (200 m a.s.l), with some rivers directly terminating off the ice sheet edge. This suggests limited opportunities for meltwater to penetrate to the ice sheet bed with meltwater having longer transport times to travel to the catchment outlet (i.e., proglacial zone/Kane Basin) with the hydrograph expected to have a more subdued and longer rising limb (Karamouz et al., 2013; Yang et al., 2019a). Within this southern sector of HG, ice velocity is significantly slower (<100 m yr^{-1}; Rignot et al., 2021) than its northern counterpart, with relatively thick ice contributing to the absence of crevasses and moulins (Oswald and Gogineni, 2011; Yang et al., 2019a; Andrews et al., 2022), as well as controlling the

hydromorphology of the drainage network found here. Similar drainage hydromorphology was also mapped at the neighbouring glacier at Inglefield Land (Yang *et al.*, 2019b; Li *et al.*, 2022), with supraglacial rivers flowing uninterrupted into the proglacial zone, with discharge into terrestrial rivers directly reflecting the timing and intensity of surface meltwater runoff from the outlet glacier catchment without modification from en- and/or subglacial processes.

The supraglacial drainage configuration is also further influenced by significant structural elements which were identified by Livingstone *et al*. (2017) via the Moderate-Resolution Imaging Spectroradiometer (MODIS) mosaic of Greenland (Haran *et al.*, 2013). Two linear structures expressed as depressions on the ice surface that run in a southwest to northeast direction across Humboldt Glacier are clearly visible on the mapped glacier surface in this study (Figure 4.5a; Figure 4.), with many supraglacial rivers and SGLs aligned-to or terminating at them. Some longitudinal rivers are also shown to suddenly change direction when encountering these structures, with subsequent channels diverting at a 90-degree angle, transverse to ice flow (Figure 4.5a, 4.5b). It is at the intersection of such structures we observe some channel advection with spacing of 300 m (Figure 4.5a), broadly representing the ice displacement over the study period. Other basal structures are also reflected within the supraglacial drainage system, including many V- and X- shaped patterns clearly controlled by depressions in the bed. There is a strong glacier-wide emphasis here of these structures influential control on drainage, which are reproduced here in Figure 4. based on Livingstone *et al*. (2017) from MODIS imagery (MOG2015, Haran *et al.*, 2018) and also within bed topography data from BedMachine (version 4; Morlighem *et al.*, 2017, 2021).

This identification provides independent confirmation of the existence of these depressions in the bed and their subsequent expression on the surface, as well as how they significantly control the multi-year surface drainage configuration within the vicinity of such structures.

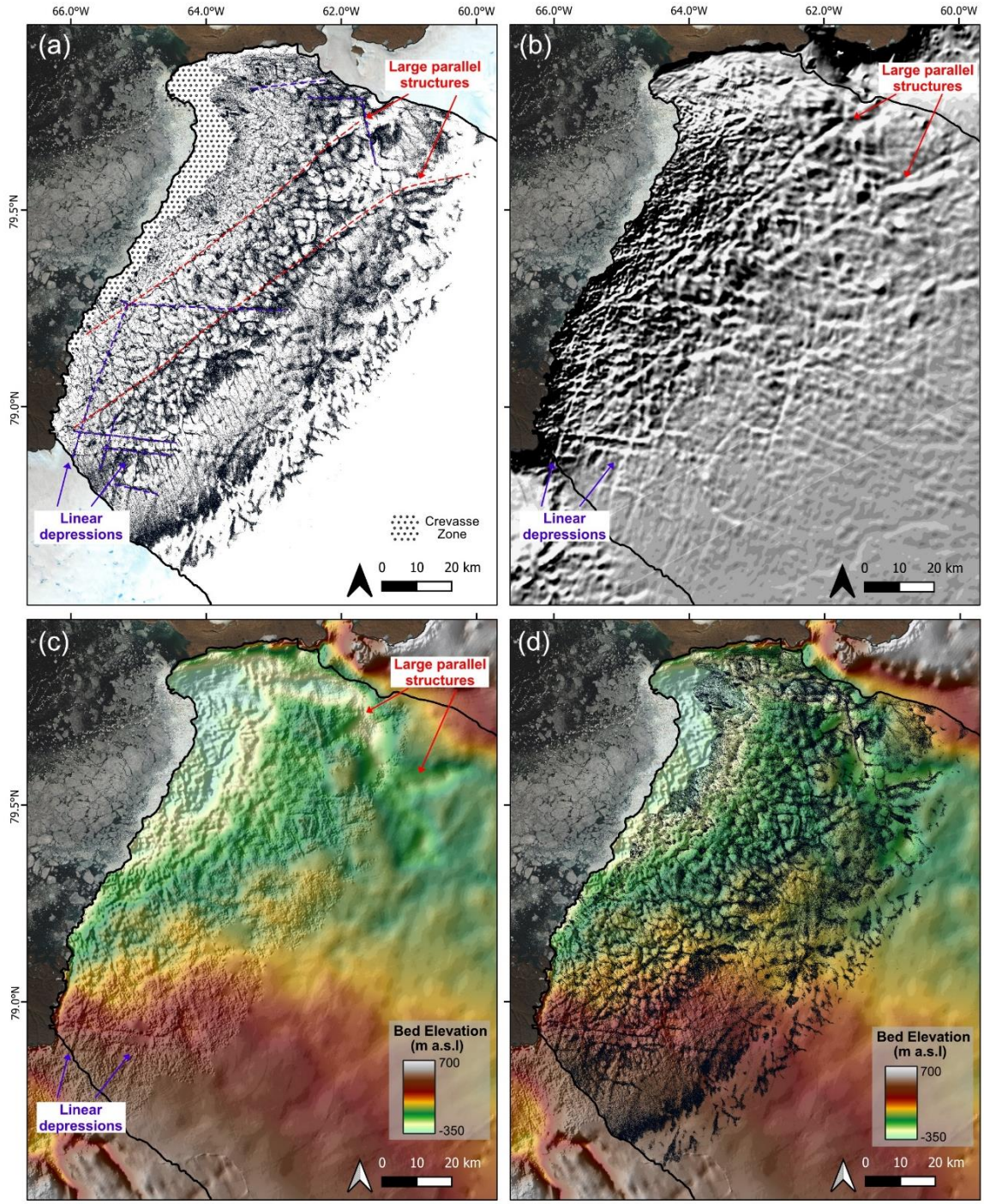

Figure 4.10. The supraglacial drainage network at its maximum extent across 2016 to 2020 showing the two parallel structures orientated southwest to northeast identified by red dashed lines. Other V- and X-shaped structures are also highlighted by purple dashed lines; (b) Moderate-Resolution Imaging Spectroradiometer (MODIS) Mosaic of Greenland (MOG2015, Haran *et al.*, 2018) showing evidence of the these structures on the ice surface; (c) Bed topography via BedMachine (Morlighem *et al.*, 2020) showing the structures as depressions within the bed; (d) the supraglacial drainage network as presented in (a) overlain on top of bed topography presented in (c) showing the overall influence bed topography has on the surface drainage structure at Humboldt Glacier.

The supraglacial drainage network at HG is also shown to be largely dominated by supraglacial rivers (98%), consistent with findings by Lu et al. (2021) in northeast Greenland where supraglacial rivers also dominate the surface drainage network (83.8%). Such river contributions in northern Greenland are significantly higher than southwestern GrIS, whereby supraglacial rivers account for an average of 62% of the network (Yang et al. 2021). The difference in contribution of rivers and SGLs to the drainage network between north and southwest Greenland is likely the result of (i) reduced lake distributions and storage >800 m a.s.l in northern Greenland due to surface topographic constraints (i.e.,reduced number of available depressions due to ice thickness; Ignéczi et al., 2016; Lu et al., 2021), (ii) steeper northern surface slopes promoting meltwater runoff over storage, with gentler elevation gradients in southwest Greenland promoting a wider, more susceptible ablation zone to melt and meltwater ponding (Mikkelsen et al., 2016; van As et al., 2017). At HG, the maximum supraglacial RF recorded for a single date across the melt-prone zone reached 24.5%: the largest RF value recorded to-date from a supraglacial drainage mapping study (e.g., 5.3% in northeast Greenland, 5.5% at the Devon Ice Cap and ~14% for southwest Greenland). A reason for this large value is likely due to the inclusion of expansive hydrologically-connected slush zones within hydrologic mapping, which are prevalent during the early-to-mid melt season when snow becomes water saturated. This slush zone progressively moves upglacier and is removed to reveal the bare ice below. Additionally, a lower river threshold (t^5) was used in this study compared to other studies (e.g., t^{20}, Lu et al., 2021), allowing narrower supraglacial rivers and slush zones to be captured, increasing the overall supraglacial drainage and river components. Whilst supraglacial rivers are likely to dominate the drainage network here, similar to northeast Greenland (Lu et al., 2021) regardless of the threshold used due to reduced lake presence, care should be taken when directly comparing drainage network statistics between mapping studies from differing regions of the GrIS.

4.4.2 Temporal evolution of the supraglacial drainage network

Across the study period (2016–2020), we observe the seasonal development and inland evolution of the supraglacial hydrologic network as the melt season progresses and runoff increases up to the maximum melt extent, which typically occurs at the end-of-July. During the early melt season and at higher elevations as melt progresses, we observe the growth and inland migration of a large, poorly channelised slush zone (Greuell and Knap, 2000). Within this zone, slush flows can occur as surface melt percolates and saturates the snowpack, promoting slush mobilisation into topographical lows and initiating the reopening of perennially-occupied channels (Cuffey and Paterson, 2010; Irvine-Fynn *et al.*, 2011). On higher-draining slopes, such mobilisation can form slush-filled rills, which coalesce into networks of arborescent tributary channels, efficiently transporting melt to larger, primary river channels and, subsequently, the transportation of melt down-glacier (Marston, 1983; Cuffey and Paterson, 2010; Chu, 2014; Rippin and Rawlins, 2021). The seasonal development of the hydrologic network is shown to transform from a system initially dominated by water percolation to one dominated by channelised, efficient flow (Figure 4.6); further confirming behaviour identified across multiple supraglacial drainage mapping studies across the GrIS (Lu *et al.*, 2021; Yang *et al.*, 2021; Li *et al.*, 2022).

The rate and extent of the spatial and temporal evolution of the supraglacial hydrologic network is highly variable between years. Several years within the last decade have been characterised by high air temperatures and extreme melt events, including two years represented within this study; 2016 and 2019. Both years, in particular 2019, experienced a strong negative North Atlantic Oscillation and simultaneously a positive East Atlantic index and Greenland Blocking Index phase, which are associated with persistent, anticyclonic conditions over Greenland driving enhanced surface mass loss (Lim *et al.*, 2016; Cullather *et al.*, 2020; Zhang *et al.*, 2021). Mass loss during summer 2019, in particular, was promoted by

enhanced solar radiation, reduced cloud cover and the north-westward advection of warm, moist air from the western margins as a result of such atmospheric variability (Cullather *et al.*, 2020; Tedesco and Fettweis, 2020; Elmes *et al.*, 2021; Hanna *et al.*, 2021). Combined with low snow accumulation in the 2018/19 winter (Sasgen *et al.*, 2020), extensive melting occurred along much of the Greenland coast, with surface melt experienced in the north being the highest on the record since 1948 (Tedesco and Fettweis, 2020). It was during this exceptional and long melt year that we observed the highest MF values (19.9% or 2685 km^2 recorded on the 30th June 2019) and second highest areal extent of supraglacial drainage network (1375 m a.s.l; Figure 4.6). Ablation continued throughout September (Tedesco *et al.*, 2019; Sasgen *et al.*, 2020; Tedesco and Fettweis, 2020), however this was beyond our mapped timeframe. The year 2019 also recorded the largest number of SGLs (527) and cumulative lake areas (151.8 km^2). The hydrologic expansion of the drainage network was also rapid, in-line with a record early-melt season event, which combined with low snow accumulation (Tedesco and Fettweis, 2020), promoted rapid snowpack warming, disintegration and exposure of the bare ice zone, resulting in an enhanced melt-albedo feedback mechanism (Tedesco and Fettweis, 2020). Similar findings by Turton *et al.* (2021) and (Hochreuther *et al.* (2021) at 79°N Glacier recorded the largest SGL numbers and extents of their study periods in 2019, indicating the widespread impact of this extreme melt event, particularly across the GrIS northern sector.

Similar seasonal and multi-annual behavioural patterns during 2017 and 2018 were, again, also observed by (Turton *et al.*, 2021) and (Lu *et al.*, 2021) on the north-eastern glacier of 79°N and (Otto *et al.*, 2022) on the northern Ryder Glacier. These findings all record a slow rate of SGL increase and late area peak (early-August) in 2017 and 2018, with (Lu *et al.*, 2021) confirming the late area peak in combined supraglacial drainage mapping of both lakes and rivers during August 2017. SGL mapping by (Turton *et al.*, 2021) also identified the delayed development and lower SGL presence during the 2018 melt season, with SGLs largely

limited to <900 m a.s.l. Such findings are consistent with observations in this study, with the onset and inland evolution of the supraglacial network, including both rivers and lakes, delayed by ~1 month compared to other the other study years (2016, 2019, 2020) and the limited areal development of the network (<1150 m a.s.l). Both the melt seasons of 2017 and 2018 recorded below average melt (1981–2010 reference period) and melt extents (32.9% and 44% respectively) across the GrIS (Tedesco *et al.*, 2017, 2018; Sasgen *et al.*, 2020). There was heavy springtime snowfall and late surviving snow in bare ice areas (Tedesco *et al.*, 2017, 2018); consistent with a strongly positive average summer (JJA) North Atlantic Oscillation and a negative Greenland Blocking Index, hypothesised to inhibit surface melt and promote increased summertime snowfall (Ruan *et al.*, 2019; Sasgen *et al.*, 2020), hence these anomalously cold summers.

The anomalously early spike in satellite-derived meltwater area recorded in early-June 2020 raises questions as to how extreme melt years, such as 2019, may precondition the ice surface (Cullather *et al.*, 2020) and affect surface conditions and subsequent surface hydrologic behaviour the following year (Culberg *et al.*, 2021). Some SGLs on the GrIS have been found to persist throughout the winter months, due to insulation from a layer of ice and/or snow (Koenig *et al.*, 2015; Law *et al.*, 2020; Schröder *et al.*, 2020). This lake persistence includes the winter of 2019/2020, when late-summer surface melt and high autumnal temperatures (August – November) are believed to have increased subsurface firn temperatures, delaying and even decreasing the ability for subsurface meltwater freezing in northern Greenland, contributing to higher totals of liquid-buried SGLs (Dunmire *et al.*, 2021). This alongside a drier-than-average (1981–2020) winter and spring (Moon *et al.*, 2020; Tedesco and Fettweis, 2020), has the potential to cause the rapid disintegration of limited snow present and the subsequent swift exposure of the bare ice zone the following summer. This swift exposure would also include that of perennial rivers and lakes, much earlier in the

melt season than expected, hence the increased MF value observed in this study despite low MAR-derived melt production and runoff values.

4.4.3 Satellite-derived MF and runoff simulations

We found a positive linear relationship between satellite-derived MF and MAR simulated R before runoff declined (Figure 4.), showing how the MF-R relationship can be used to reliably simulate seasonal surface meltwater variation and provide further understanding into how runoff is routed and stored, at least up to peak melt events. This finding supports other studies that have used satellite-derived meltwater metrics and RCM-modelled runoff which have focussed on the southwest GrIS (Yang *et al.*, 2021), Northern GrIS (Lu *et al.*, 2021; Li *et al.*, 2022) and the Devon Ice Cap (Lu *et al.*, 2020). In terms of post-peak melt events, surface meltwater can still cover a substantially large area even after surface runoff has reduced and ceased, as seen in this study. This is known as the 'delay' effect (Lu *et al.*, 2021), whereby meltwater may continue to be routed or stored on the ice surface via the slow routing of melt out of snowpack/firn at higher elevations, the stagnation and subsequent preservation of transported meltwater in large supraglacial rivers or the storage of melt in SGLs. Therefore, whilst this MF-R relationship is promising in providing comparative assessments between satellite observations and RCM-modelled runoff at Humboldt Glacier, calculated runoff volume via satellite- (Yang *et al.*, 2021) or field-based measurements (Smith *et al.*, 2017) are required to provide further validation of such relationships, in particular over space and time across a full melt season.

4.4.4 Future implications

Substantial changes have taken place at Humboldt Glacier over the last two decades driven by atmospheric and oceanic change (Carr *et al.*, 2015; Rignot *et al.*, 2021). It is therefore important to consider Humboldt Glacier and the overall northern regions sensitivity to such warming under present climate scenarios. Northern Greenland is expected to undergo the

greatest warming of the 21st Century across the GrIS (Hill *et al.*, 2017), and given its already low rates of winter accumulation compared to other ice sheet sectors (Goelzer *et al.*, 2013), means this region is likely to become ever more sensitive to climatic change in the future. Mapping performed within this study illustrates the multi-annual persistence of the supraglacial drainage network within this high latitudinal region (Figure 4.5a) and the rapid and extensive response of this system to high melt years (Figure 4.6). This response, in particular to the extreme melt year of 2019, can precondition the ice surface for the following melt season, resulting in earlier but widespread hydrologic activity and longer-lasting melt season. This preconditioning and subsequent behaviour is likely to become increasingly normalised as melt events and atmospheric variability, such as persistent blocking events, increase in frequency and intensity (Rahmstorf and Coumou, 2011; McLeod and Mote, 2016).

Inland migration of the supraglacial hydrologic network is also projected with continued warming (Leeson *et al.*, 2015), with recent work already showing ablation area expansion and amplification of melt and runoff post-1990 across Northern Greenland (Noël *et al.*, 2019). Many more surface depressions for future SGL locations are present above the current northern ELA (Igneczi *et al.*, 2016), with the potential to accumulate high volumes of meltwater and feed lengthening overflow supraglacial rivers that extend tens of kilometres downstream to non-local, low elevation moulins (Poinar *et al.*, 2015). For ponded water, if ice becomes thin enough (Poinar *et al.*, 2015), or localised ice columns become vulnerable to fracture from refrozen ice complexities within firn (ice-blobs; (Culberg *et al.*, 2022) new hydrofracture events will bring such meltwater to isolated areas of the ice sheet bed. This could have knock-on impacts to ice flow, with the likely delivery of water and heat to a persistent inefficient subglacial system, where thicker, flatter ice may prohibit the

development of an efficient subglacial system (Dow *et al.*, 2014), enhancing ice flow (Christoffersen *et al.*, 2018).

Persistent low-permeability ice slabs which block vertical percolation have continued to thicken overtime in the lower accumulation zone. Ice slabs are expected to enhance runoff from Greenland's interior, particularly in consecutive warm summers (MacFerrin *et al.*, 2019). Enhanced runoff and inland expansion of the supraglacial hydrologic network will impact meltwater feedback processes, not only in driving overall SMB decline (Noël *et al.*, 2021) but further impacting dynamical behaviour, including hydrofracture potential. At Humboldt Glacier, a particular concern is the vulnerability of its northern terminus to increased hydrofracture events from greater melt runoff (Carr *et al.*, 2015). Such events at Humboldt Glacier have the potential to promote future rapid run-away retreat, especially if the northern sector of the terminus retreats beyond its pinning point into the deepened bed (below sea level) in which is sits (Carr *et al.*, 2015; Hillebrand *et al.*, 2022).

As the northern region mainly consists of fast-flowing, marine-terminating outlet glaciers, like Humboldt Glacier, that drain a large proportion of the GrIS, further understanding of the mechanisms that drive their dynamical behaviour, in particular related to enhanced runoff, are required for predicting their future contribution to GrIS mass loss and subsequent sea level rise.

4.5 Conclusion

In this study, we mapped and quantified for the first time, the spatial and temporal evolution of the supraglacial hydrologic network, including both rivers and lakes, using 10 m Sentinel-2 images from the melt seasons of 2016 to 2020 at Humboldt Glacier, northern Greenland. We identify an extensive supraglacial hydrologic network exists at Humboldt Glacier that is particularly prevalent up to 1000 m a.s.l with a further variable transient zone extending up

to 1500 m a.s.l. The seasonal evolutionary behaviour of this network migrates up-glacier in response to increasing runoff as air temperatures rise throughout the melt season, with the network transforming from an inefficient system dominated by water percolation and slush flows to one dominated by channelised, efficient flow. Interannual variability of the extent and behaviour of the system is associated with high and low melt years across the study period, with the low melt years of 2017 and 2018 having both limited and delayed spatial development. The extreme melt year of 2019 showed the extensive development and persistence of the supraglacial hydrologic network into September, which followed by low snow accumulation during the subsequent winter/spring, preconditioned the ice sheet for earlier hydrologic activity in 2020; behaviour which may become more representative with extreme melt events and longer-lasting melt seasons into the future. This work ultimately contributes to advancing our understanding of supraglacial hydrologic processes across the Greenland Ice Sheet by expanding detailed hydrologic mapping to other understudied regions of the ice sheet, in particular to Greenland's rapidly changing northern region, aiding in projections of future mass loss as enhanced runoff continues with climatic warming.

Chapter 5

Multi-annual evolution of the supraglacial hydrologic network and terminus change at Humboldt (Sermersuaq) Glacier, northern Greenland, between 1985 and 2021

5.1 Introduction

5.1.1 Chapter outline

As outlined previously in Chapter 4, many studies (Smith *et al.*, 2015; King *et al.*, 2016; Yang *et al.*, 2016; Smith *et al.*, 2017; Yang *et al.*, 2019b; Lu *et al.*, 2020; Yang *et al.*, 2021; Li *et al.*, 2022; Yang *et al.*, 2022) have explored the supraglacial hydrologic network that is present on the GrIS, and indeed the components that comprise it (i.e., rivers and/or lakes). However, these are typically confined to within a single melt season, within a small region of the ice sheet and/or focus on individual parts of this interconnected system; a key objective that Chapter 4 addressed by being the first study to map and quantify this integrated network at Humboldt (Sermersuaq) Glacier – a large hydrologic catchment in northern region of the Greenland Ice Sheet (GrIS) - at high spatial (10 m) and temporal resolution across multiple melt seasons (2016 – 2020).

In this Chapter, the wealth of freely available Landsat satellite imagery available via Google Earth Engine is used to explore the evolution of the generalised supraglacial hydrologic network (i.e., primary supraglacial rivers and supraglacial lakes (SGLs)) over a 37-year period (1985-2021) within the Humboldt Glacier catchment, as well as examine its terminus retreat. Understanding the evolution of the supraglacial hydrologic network across the GrIS, in particular the river network, remains spatially uneven. Less studied regions such as northern and eastern Greenland are currently undergoing, and projected to experience, some of the most rapid rates of mass loss (Noël *et al.*, 2019) yet we have an incomplete knowledge of their existing hydrologic network. To-date, no other study has explored how the supraglacial hydrologic network, encompassing both rivers and lakes, has evolved over long periods of time across Greenland, utilising long term satellite-era optical products. Hence, the profound opportunity is undertaken in this Chapter to map and quantify for the first time this

long-term record of supraglacial hydrologic network change, both as a collective network and across individual river and SGL components.

5.1.2 Introduction to Google Earth Engine

Since the birth of Earth-observational satellites in the 1970's, spaceborne data has and continues to provide scientists with an invaluable visual record of Earth and its climate system. For the cryosphere, satellite data has become an integral resource, revolutionising the physical ability to observe, understand and document such remote and fragile landscapes, in particular the changing nature of the cryosphere under climatic warming (Taylor *et al.*, 2021).

One of the most valued and the longest running earth-observational satellite programs to exist is the Landsat series, which has continually acquired space-based optical imagery since its launch (Landsat-1) in 1972. Now, in the year 2023, this Landsat series comprises 9 satellites, the most recent of which launched in 2021, and continues to provide a wealth of freely available moderate-resolution imagery (30 m optical; 15 m panchromatic) repeatedly covering the Earth surface from 81 degrees north to 81 degrees south. This continual coverage, particularly over glaciated regions, has allowed for widespread glacial and geomorphic mapping, including glacier inventories from the Canadian Cordillera (Sidjak, 1999; Bolch *et al.*, 2010; Wheate *et al.*, 2014), high mountain Asia (Kamp and Pan, 2015; Mölg *et al.*, 2018), New Zealand (Baumann *et al.*, 2021; Paul *et al.*, 2023), European mountain ranges (Kääb *et al.*, 2002; Paul *et al.*, 2011), Scandinavia (Andreassen *et al.*, 2008; Andreassen *et al.*, 2012) and the famous global-wide Randolph Glacier Inventory (excluding Greenland and Antarctica ice sheets; Pfeffer *et al.*, 2014).

Over the last 40 years, technological advancements and the rapid increase in the number of remote sensing datasets with a multitude of characteristics (spectral, spatial, temporal and

radiometric resolutions) has led to significant challenges in accessing and working with vast quantities of data, known as *big data* (Chi *et al.*, 2016). In 2010, Google introduced the open-access cloud computing platform Google Earth Engine, or GEE, to address the challenges of *big data* by providing the computational power needed for processing and analysing such datasets (Gorelick *et al.*, 2017). Now containing a petabyte-scale database of satellite imagery and other geospatial datasets, such as digital elevation models (DEMs; e.g., Shuttle Radar Topography Mission data, or SRTM) and climate model data (e.g., ERA-5 reanalysis data; Gorelick *et al.*, 2017) to name a few, GEE is widely utilised across a plethora of different fields, including glaciology, for a multitude of different tasks. These are largely image processing and classification tasks such as supervised machine learning algorithms and spectral indices (Amani *et al.*, 2020). Its usage has also significantly increased in recent years alongside the development of field-specific tools, for example glaciology-based tools such as the Google Earth Engine Digitisation Tool (GEEDIT; Lea, 2018) for the manual digitisation and export of glacial margin information, GERALDINE (Google Earth Engine supRaglAciaL Debris INput dEtector) created for the identification and monitoring of supraglacial landslides (Smith *et al.*, 2020), and iceberg detection tools for the automatic detection and examination of iceberg densities and distributions around Greenland (Shiggins *et al.*, 2023). The remarkable capabilities of GEE have provided unprecedented opportunities to quickly and efficiently access and process satellite imagery to quantify and assess features and/or characteristics across cryospheric landscapes.

Utilising this wealth of optical data available via GEE, the aim of this chapter is to understand the long-term evolution of Humboldt Glacier between the period 1985-2021 by assessing both its terminus change and the development of the supraglacial hydrologic network overtime. The associated objectives include:

i) To delineate the annual end-of-melt season terminus at Humboldt Glacier to assess length changes of this marine-terminating glacier between 1985–2021 and explore driving factors for such observations

ii) To use both GEE and the automatic river detection algorithm (Yang *et al.*, 2015a; Yang *et al.*, 2017) to derive annual supraglacial hydrologic network maps across the melt season months of June, July and August (JJA) between 1985-2021

iii) Derive specific supraglacial hydrologic network metrics, including independent river and lake metrics, for assessing their temporal evolution overtime

iv) To use outputs from the regional climate model MAR to explore the regional changes in JJA temperature and runoff and the implications for observed supraglacial network development.

Whilst Landsat imagery is only able to provide mapping for the generalised supraglacial hydrologic network, in particular larger primary supraglacial rivers, due to its coarse resolution (30 m; Yang *et al.*, 2019), it is able to provide novel insights into how this system has evolved overtime.

5.2 Methodology

The methodology performed in this Chapter consists of three key steps; (a) a GEE workflow for image search and processing; (b) a terminus workflow for the manual digitisation and quantification of the terminus of Humboldt Glacier and (c) a hydrologic workflow for the mapping of the supraglacial hydrologic network post-GEE using the automatic river detection algorithm (Yang *et al.*, 2015a; Yang *et al.*, 2017) and subsequent thresholding techniques. These three workflows are summarised in Figure 5.1 and are further described below.

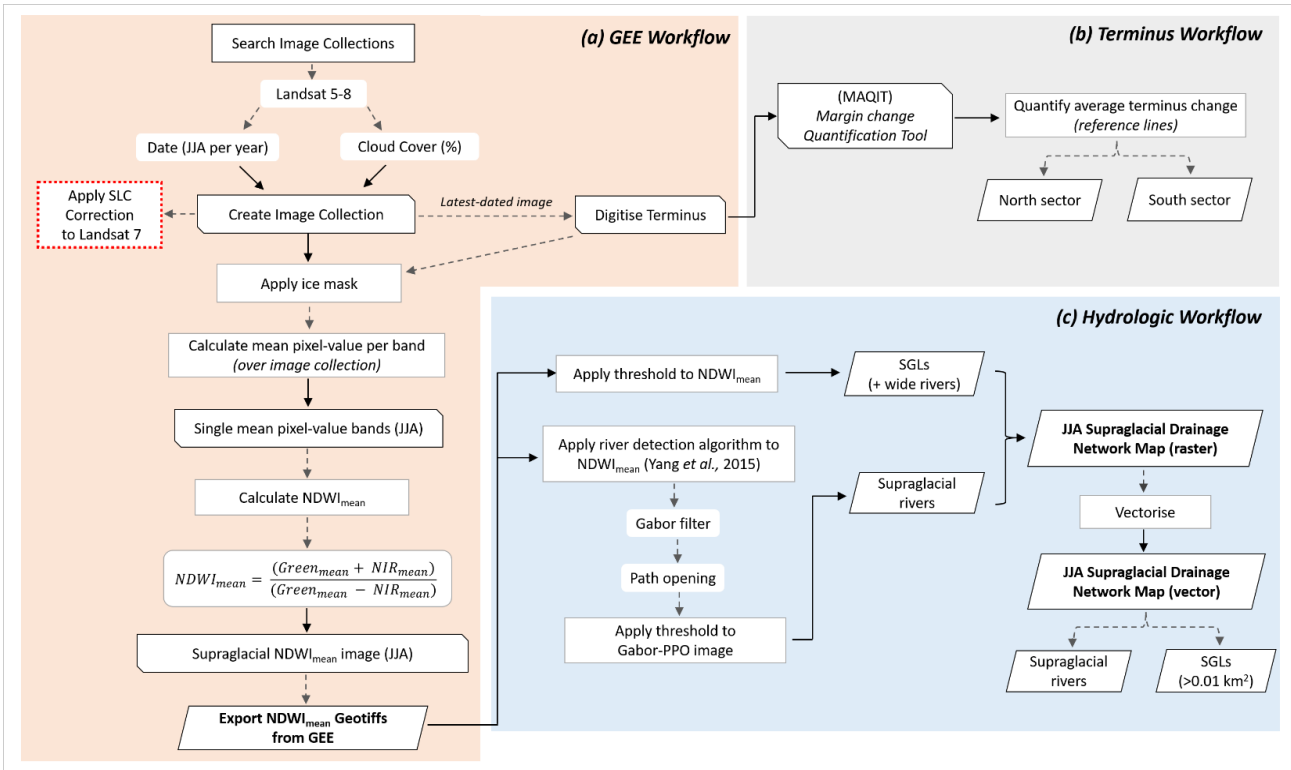

Figure 5.1. Schematic showing the methodological workflow for Chapter 5, which is split into three major themes: (a) GEE workflow, which focusses on image collection, processing of an annual NDWI image (NDWImean) and output of Geotiffs; (b) terminus workflow which uses the digitised termini of Humboldt Glacier from the GEE workflow (a) to additionally assess terminus change overtime via the tool MAQIT; (c) hydrologic workflow which uses the exported NDWImean annual images from GEE as inputs into the automatic river detection algorithm alongside the application of thresholding for deriving annual supraglacial hydrologic networks, including individually mapped and river and SGLs.

5.2.1 Image collection via Google Earth Engine

To explore and download available Landsat imagery for the manual delineation of the Humboldt Glacier terminus and supraglacial hydrologic mapping for the study period 1985–2021, the cloud computing platform GEE was utilised. Primarily, Landsat Collection 1 Tier 1 (top-of-atmosphere and radiometrically corrected) products from Landsat-5, -7 and -8 programs, with the year 1985 being the earliest available imagery for the Humboldt region. Overall, 102 individual Landsat image tiles were examined across the Humboldt region

throughout the study period, culminating in 1429 images used for mapping (Figure 5.2). Whilst panchromatic Landsat imagery was available at a higher resolution (15 m) than standard Landsat optical imagery (30 m), panchromatic imagery was only available post-1999. Therefore, for consistency across the study period, 30 m imagery was utilised.

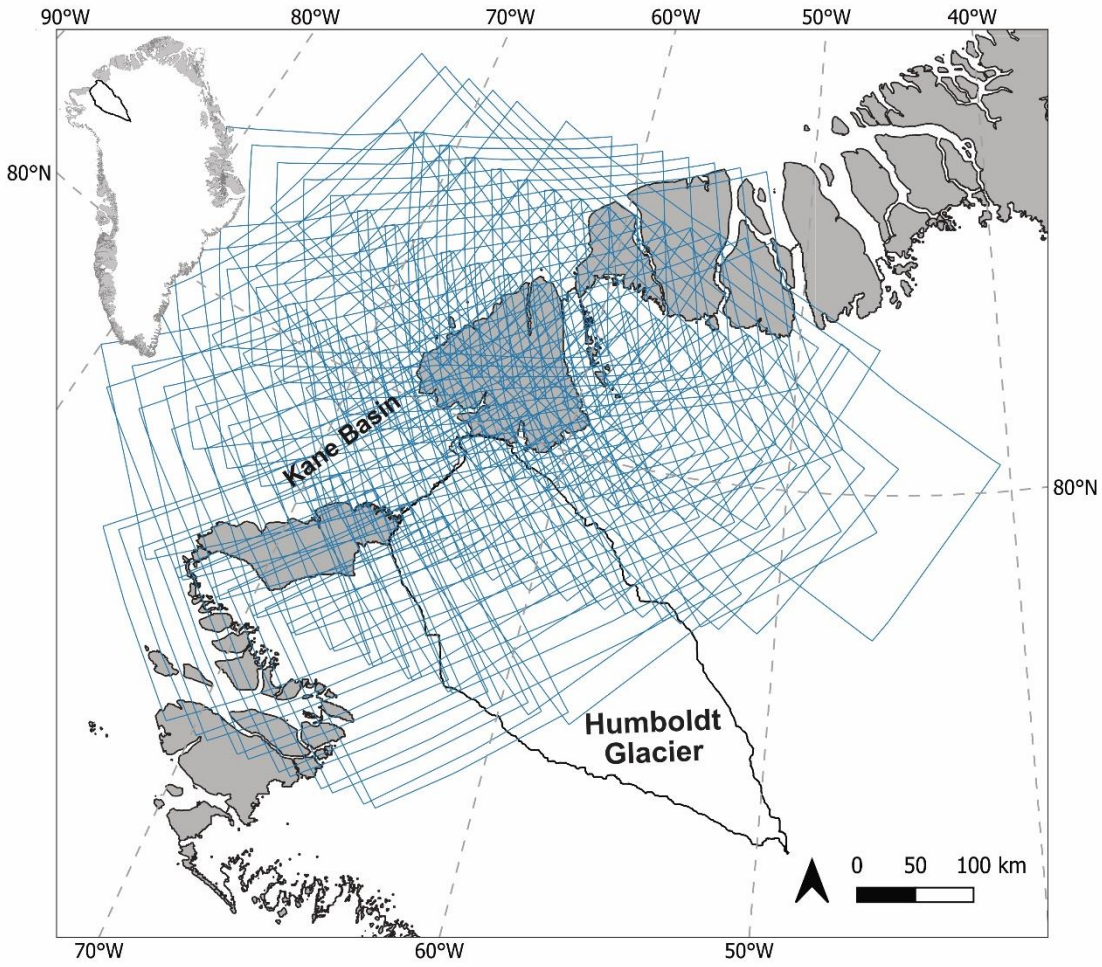

Figure 5.2. The location of Humboldt Glacier and the array of Landsat tiles searched and used across the region for mapping conducted in this Chapter across the 37 year study period (1985-2021). Inset map shows the general location of the Humboldt Glacier hydrologic catchment in northern Greenland.

Images were filtered for cloud cover and date range covering the main summer melt season months of June, July and August (JJA) encompassed over the Humboldt Glacier region (Figure 5.1a). For earlier years (prior to 2014), the number of images available were often

low, and so a higher cloud cover percentage (<40%) was used to exploit as many available images as possible (Figure 5.3). Typically, any encountered cloud cover was confined to the Kane Basin waterway (Figure 5.2) or interior locations, so did not pose significant problems in the image classification or feature delineation steps post-GEE. With the increase in image numbers over time, cloud cover percentage within image searching was subsequently reduced to <10% post-2014 due to the introduction of Landsat-8. Due to heavy cloud cover and no suitable or available imagery for the years 1993, 1996, 1997, 2001 and 2002, these were excluded from the study.

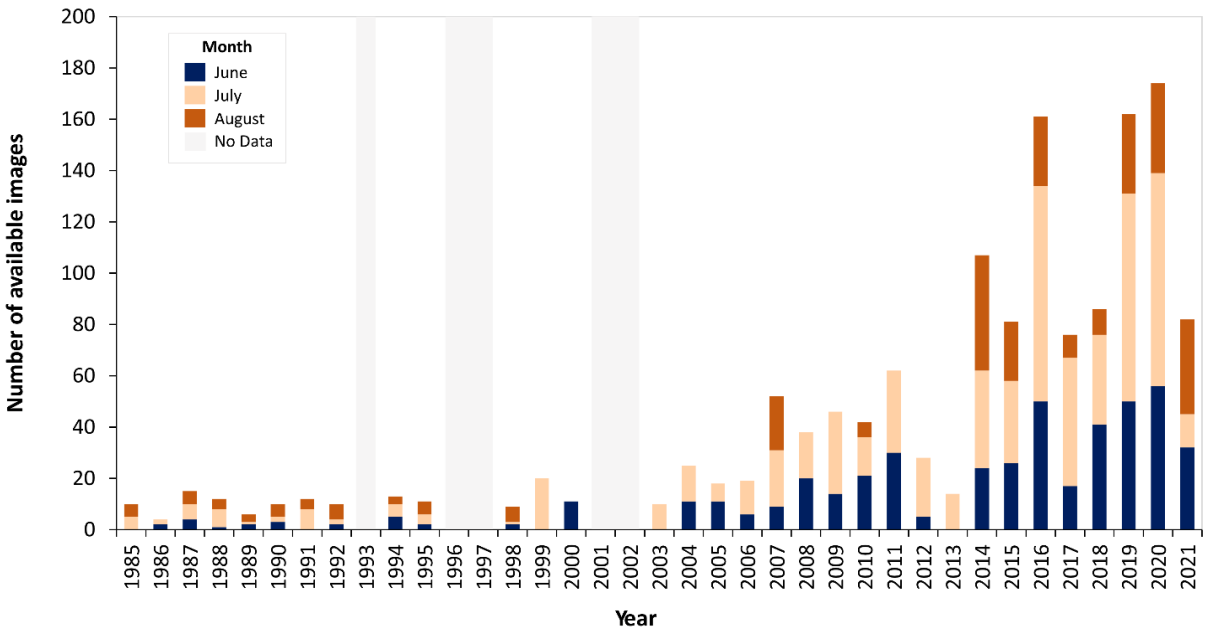

Figure 5.3. The availability of Landsat imagery in Google Earth Engine (GEE) for each year across the study period (1985 – 2021) split between the three key melt season months; June, July and August (JJA). Cloud cover percentage was set to <40% to maximise image availability from the region, however this was reduced to <10% post-2013 as the number of images increased with the successful launch of Landsat 8. The years 1993, 1996, 1997, 2001 and 2002 were not mapped in this study due to either heavy cloud cover or minimal-to-no images available for these time periods.

It is noted that the annual $NDWI_{mean}$ maps derived from the yearly image collections in GEE were variable (i.e., not fully representative of the JJA timeframe) depending upon image availability against the search parameters, as shown Figure 5.2. Therefore, for some years in this study, only mapping occurred in a certain month rather than across the JJA melt season. Consequently, some underrepresentation of the full mapped supraglacial hydrologic system may have occurred in particular years, for example 1999, 2003 and 2013, which only had images available in the month of July. These years were still mapped, however, rather than removed from the study as July is typically when maximum melt and inland extent occurs. Therefore, the network is assumed to be mostly developed at this point (Rawlins *et al.*, *2023*; Yang *et al.*, 2021).

Due to the scanner line corrector (SLC; USGS, 2003) failure across the Landsat-7 collection, which appears as regularly-spaced lines leaving data gaps in images for the years 2003-2013, corrections to these images were applied in GEE to aid in reducing data loss. A focal mean, known as a morphological filter which performs a simple blend operation on a local group of pixels, was applied to each band of an image by inputting the pixels in a custom kernel and applying a blend, successfully filling many of the SLC errors (Figure 5.4). This focal mean is widely used in GEE for correcting SLC errors on Landsat 7 ETM images, with this filter based upon the original *Gap-Fill algorithm* developed to improve Landsat 7 imagery based on the method by the USGS (Storey *et al.*, 2005). Subsequent corrected images were added to yearly image collections for further use (see Section 5.2.2 and 5.2.3).

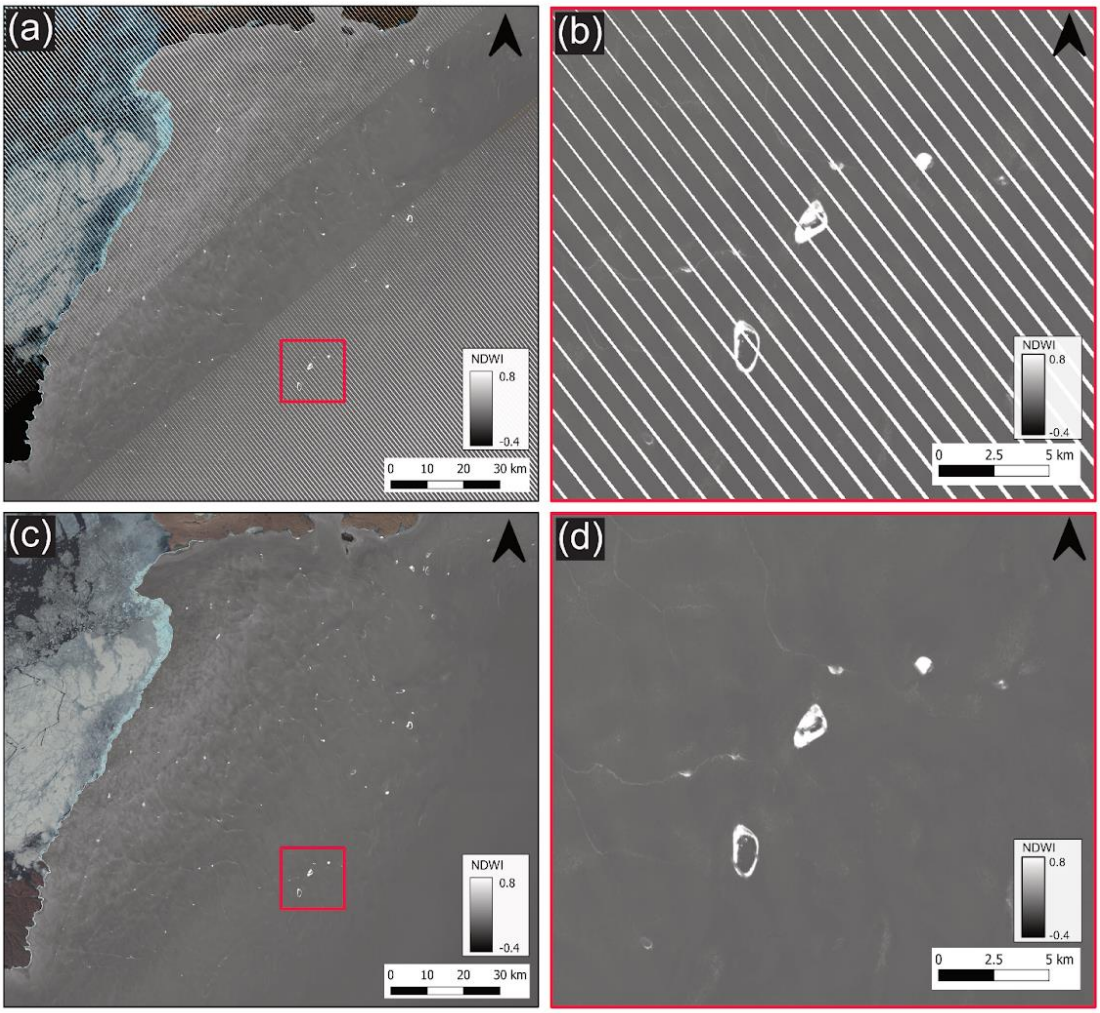

Figure 5.4. Example of the Landsat-7 SLC errors present across Humboldt Glacier with red squares denoting zoom-in locations; (a) Humboldt Glacier with SLC errors; (b) zoom-in of SLC errors present; (c) Humboldt Glacier with subsequent correction of errors using a focal mean; (d) zoom-in of SLC-corrected errors. Background image is an NDWI processed Landsat image from July 2021 with NDWI values ranging between 0.8 (water) and -0.4 (ice).

5.2.2 Terminus delineation and change quantification

For the manual digitisation of the Humboldt Glacier terminus to assess change over the 37-year period, the latest dated image within each yearly image collection created in GEE (as described in Section 5.2.1) was used. The latest available image per year was used because

of (i) the ability to better distinguish the terminus from ice melange due to its removal at this time of year, with its presence often impeding reliable digitisation (Moon and Joughin, 2008) and; (ii) the later date can help represent the most stable phase of a terminus within the JJA period for the selected year as the melt season draws to a close (Fahrner *et al.*, 2021). This also follows similar protocols performed by Fahrner *et al.* (2021) who only digitised the margins of Greenlandic tidewater glaciers from images towards the end of the melt season (September) for their study period when the terminus typically reached annual minimum extent.

Once digitised, the retreat of Humboldt Glacier across the study period (1985–2021) was examined using the Margin change Quantification Tool (MAQIT) v1.03 (Lea, 2018); Figure 5.1b), which quantifies margin distance change via delineated terminus positions and glacier centrelines. For Humboldt Glacier, six separate centrelines or 'reference lines' were produced (Figure 5.5) across the terminus in order to assess mean terminus change across the terminus width and also assess its contrasting retreat behaviours within the north and south sectors as identified by Carr *et al.* (2015). As such, three reference lines were positioned in the northern sector and three reference lines in southern sector based on ice velocity profiles and manual examination to gain a representative sample of each sector and across the full terminus. The north and south sectors follow divisions created by Carr *et al.* (2015) and were applied for consistency between studies of Humboldt Glacier.

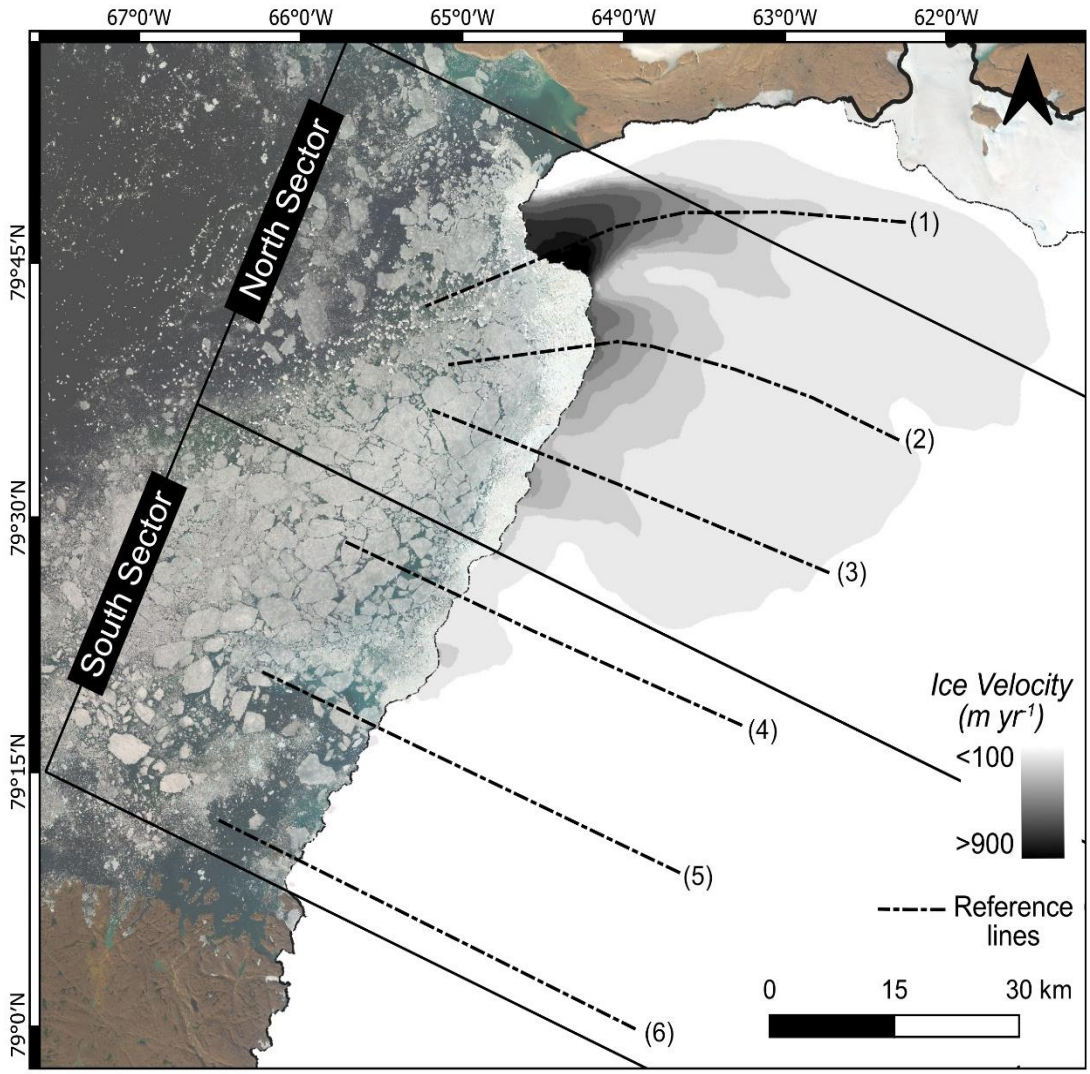

Figure 5.5. Map showing Humboldt Glacier with the north and south sectors of the terminus divided as per Carr *et al.* (2015). Within these sectors, centrelines 1–3 act as reference lines for terminus change quantification for the northern sector and centrelines 4–6 as reference lines for terminus change quantification for the south sector. These reference lines were chosen based on ice velocity profiles of the north and south sectors as well as best capturing varied terminus behaviour (particularly in the north). Ice velocity data sourced from NASAs MEaSUREs ITS_LIVE project (Gardener et al., 2019).

5.2.3 Supraglacial river and lake mapping

To map the supraglacial hydrologic network, an approach was sought to derive annual NDWI maps from Landsat-era products in GEE, to efficiently enhance the existence of liquid

water in the image collection, with the utilisation of the Yang *et al.* (2015, 2017) automatic river detection algorithm to extract an in-tact annual JJA network. As such, mapping was split into two separate workflows; (i) the GEE workflow (Figure 5.1a) and the hydrologic workflow (Figure 5.1c). For images in the image collection, derived in Section 5.2.1, the digitised terminus for each year, as performed in Section 5.2.2, was applied to all images in the annual GEE image collection to clip Landsat images to the subsequent catchment and annual extent of Humboldt Glacier, aiding in the removal of the Kane Basin waterway and surrounding land, producing the ice-only Humboldt region. In order to generate an NDWI image to first enhance liquid water on the ice surface, the mean pixel value of all bands for each image in the image collection for JJA was created and NDWI (using Green and NIR bands; McFeeters, 1996) calculated based on these mean values, producing a single $NDWI_{mean}$ image per year. A built-in per-pixel ordering function, known as *qualityMosaic* in GEE, was originally considered. This is the process of taking the maximum pixel values across all individual bands of images in the collection and calculating a new, composite NDWI from these maximum pixel values to derive a 'maximum meltwater map', referred to $NDWI_{max}$. This method has already been successfully implemented for supraglacial lake mapping in Antarctica (Tuckett *et al.*, 2021). However, due to issues with the promotion and exacerbation of slush zones with $NDWI_{max}$, particularly during the month of June when melting of the snowpack typically occurs, which was undesired for mapping in this work, $NDWI_{mean}$ calculations provided better output images for examining the generalised hydrologic structure, i.e. large, primary supraglacial rivers and SGLs, over the desired timeframe (Figure 5.6). For some years, there were occasional georeferencing problems with some of the filtered images, or images with edge detection problems that caused inconsistencies with NDWI calculations. These problem images were manually identified in image collections and subsequently removed from mean pixel calculations and compositing. Finally, mean pixel NDWI images were then exported as Geotiffs. For the 37-year study period

investigated (1985 - 2021), 32 years were successfully processed into $NDWI_{mean}$ annual (JJA) maps and exported from GEE from a total of 1429 Landsat-era images.

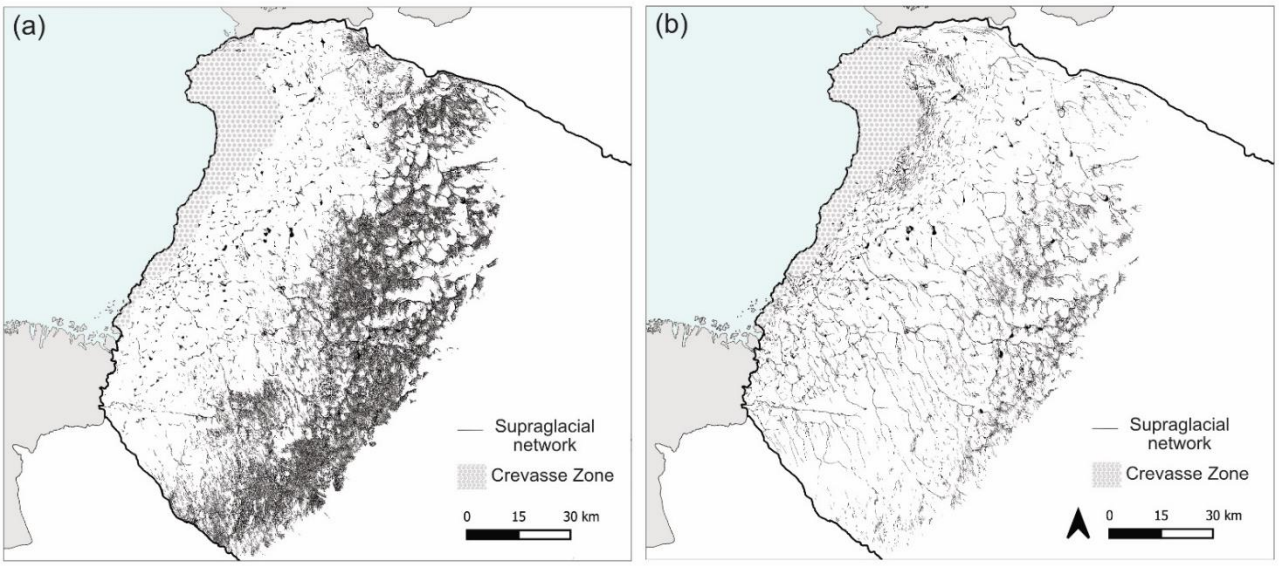

Figure 5.6. (a) Map showing the supraglacial hydrologic network delineated from NDWImax; the method of promoting the maximum pixel value in the annual image collection to gain a maximum meltwater map; (b) Map showing the supraglacial hydrologic network delineated from NDWImean, the preferred method for this Chapter, whereby the mean NDWI pixel value is taken across the annual image collection to extract the generalised supraglacial network only without slush exacerbation.

To delineate and map the supraglacial hydrologic network from exported $NDWI_{mean}$ images, they were then passed through the automatic river detection algorithm in Matlab (v2019a) following Yang *et al.* (2015a) aiding in the characterisation of rivers according to their Gaussian-like brightness cross sections and longitudinal continuity (Figure 5.1c). Parameters within this detection were adapted for the processing of Landsat imagery due to the coarser resolution, with the bandpass filter ramped to between 1/500 m^{-1} and 1/50 m^{-1}. A typical Gabor filter set to 2 and the path opening filter set to 20 was then applied.

A set of variable, image-specific thresholds were then applied to both annual $NDWI_{mean}$ images and Gabor-path opened (Gabor-PPO) images. An $NDWI_{mean}$ threshold was applied

to each single-composited annual $NDWI_{mean}$ image, with this threshold ranging between 0.1 and 0.53, based on thresholds used in comparative studies (Lu *et al.*, 2021; Li *et al.*, 2022), individual image histograms (number of pixels in an image as a function of their intensity), and comparisons with true colour composite images (RGBs) to best capture overall JJA lake presence. These thresholds also often extracted bright, wide supraglacial rivers, which have similar spectral intensities to SGLs (Yang *et al.*, 2021). A separate image-specific threshold of between 8 and 10 (out of 255) was also applied to Gabor-PPO composited yearly images to extract supraglacial rivers, with this variable threshold based on (i) the mean + 0.5 standard deviation of an image used by (Yang *et al.*, 2015a) which produced consistent results in Chapter 4 with Sentinel-2 data and (ii) comparisons with RGB and NDWI images.

Combining both the $NDWI_{mean}$ and Gabor-PPO extraction results yielded a final yearly supraglacial meltwater mask raster consisting of both supraglacial rivers and lakes. Due to the potential of incorrectly classifying crevasses as supraglacial rivers within the heavily crevassed terminal zone of Humboldt Glacier in the northern sector (in the lower 25 km), a universal crevasse mask was applied to river output masks to remove delineated lines within this zone (Figure 5.6). Lakes, however, were retained by applying a size threshold of $>0.01km^2$. Finally, the extension for ArcMap, ArcScan (Bajjali, 2018), was used to generate river polylines and lake polygons from the supraglacial meltwater mask raster in order to better distinguish supraglacial rivers and lakes and to provide further individual quantification. The maximum line width in used in the ArcScan Vectorization Settings was set to 10 pixels, which converted raster segments > 300 m wide into lake polygons and raster segments narrower than 300 m into river polylines; settings similarly used by Lu *et al.* (2021).

To assess the performance of automatic vs manual delineation of the supraglacial hydrologic network from Landsat imagery, a small sample region of the network was manually digitised and compared against the automatically extracted results described in this Section (5.2.3;

Figure 5.7). The overall spatial pattern for both delineations is very similar, but the sum length of the automated extraction results is 9.9% shorter than manual digitisation, due to several gaps in automatically-mapped tributary rivers. This result is similar to performance accuracy reports by Lu *et al.* (2020), who found rivers mapped using automated techniques were 13.6% shorter than manually digitised results for a small section of the Devon Ice Cap.

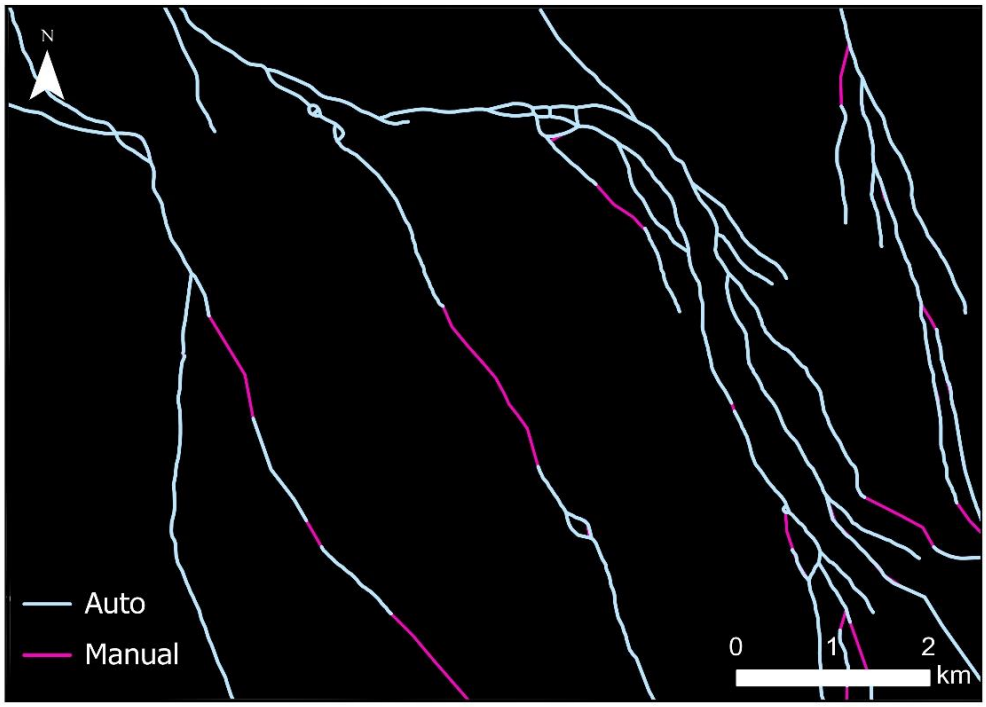

Figure 5.7. Map showing the manual digitisation of a sample area of the Landsat-extracted supraglacial network vs automatic delineation using the method by Yang *et al.* (2015a; 2017) at Humboldt Glacier. The manually-digitised network captures river channels that are delineated automatically, but are more continuous, hence their presence in the breaks of the automated network.

5.2.4 Elevation quantification

To quantify changes in hydrologic network extent in terms of elevation over all the years studied, the Greenland Ice Mapping Project (GIMP) DEM was used (Howat *et al.*, 2014). This DEM uses land elevation data that are horizontally and vertically registered to the average ICESat elevations for the 2003-2009 time period and has a mean associated error bound of

± 17.7 m collectively across the four 30 m resolution tiles across the Humboldt Glacier region (Howat *et al.*, 2014). Even though the data used to build the DEM covered only part of the mapped time period, between 2003-2009, it is one of the earliest widespread DEM datasets available for Greenland. This DEM has been successfully applied in examinations of inland SGL advance for a ~6200 km^2 sector of the north-western GrIS by Gledhill and Williamson (2018). Acknowledgement within this study by Gledhill and Williamson (2018), which is also repeated here, recognises the potential for small insignificant errors (within tens of metres) of using this DEM due to the associated date range (2003-2009) and ice thinning that may have occurred across the full study period. However, as already stated within the Gledhill and Williamson (2018) study, the overall magnitude of errors for reaching sound conclusions were minimal, hence its use.

To explore both drainage area and inland expansion overtime, discrete elevation bands of 200 m intervals spanning the lowest elevation of 7 m a.s.l to 1600 m a.s.l were created. To separately explore the elevations where SGLs occur overtime, SGL centroids (centre points of SGLs) were created for each mapped SGL and subsequent central elevation recorded (a.s.l).

5.2.5 Temperature and runoff

To link observed changes in the supraglacial hydrologic system over the study period to external forcing, mean, minimum and maximum temperature data (between 1985-2021) were derived from the regional climate model Modele Atmospherique Regionale (MAR) v3.12.1 at 6 km resolution. MAR is a widely used and reputable regional climate model (RCM) developed for the polar regions and forced by ERA-interim reanalysis data. MAR data is also used to determine total annual runoff per year (mm w.e. yr^{-1}) across the study period, which has a modelled uncertainty value of 15%, as per Fettweis *et al.* (2020). A 30-year baseline period between 1951-1980 was also created for mean JJA temperatures and total

runoff for the Humboldt catchment, again using MAR (v3.12.1) data at 6 km resolution. This baseline reference period is also used by Box *et al*. (2009) and the NASA Goddard Institute of Space Sciences (NASA GISS), who consider this 30-year period a 'climate norm' sufficient to establish a long-term mean for subsequent comparative assessment.

The RCM MAR was used instead of real time automatic weather station data for two key reasons. Automatic weather station data for use at Humboldt Glacier are available at (i) Qaanaaq (77.5 °N, 69.2 °W) and (ii) Qaanaaq Mittarfik (77.5 °N, 69.4 °W) via the Danish Meteorological Institute (Jensen, 2022); as used by Carr *et al*. (2015), and (iii) Thule (76.4 °N, 68.3 °W) via the Programme for Monitoring of the Greenland Ice Sheet (PROMICE; Fausto *et al.*, 2021). Qaanaaq and Qaanaaq Mittarfik are, however, ~190 km from Humboldt Glacier and contain large data gaps between 1980 and 2001, and Thule is ~290 km from Humboldt Glacier and only started operating in August 2010. As such, RCM MAR was deemed the best approach for providing a long-term, continuous climate dataset at Humboldt Glacier for the purpose of this study.

5.2.6 Quantification and statistical analyses

To quantify the mapped supraglacial hydrologic network at Humboldt Glacier for the composite months per year between 1985 and 2021, supraglacial drainage area was recorded in km^2 based on the total coverage of the network within the Humboldt Glacier hydrologic catchment. This hydrologic catchment was also defined and utilised in Chapter 4. Quantification of the supraglacial hydrologic network area was also undertaken for each 200 m elevation band and the mean and maximum elevation (m a.s.l) of each year determined. Separate quantification of SGLs was also undertaken, with total SGL area per year (km^2) recorded, as well as mean individual SGL size (km^2) and mean and maximum elevation per year (m a.s.l). All results are summarised and provided in Table B1 and B2 in Appendix B.

To quantify supraglacial hydrologic change over the study period as well as the influence of external variables, in this case surface temperature anomalies for JJA and total yearly runoff derived from regional climate model MAR, two statistical techniques were used. These are: (i) the use of the Pearson's product-moment correlation coefficient (*r*) to assess the strength and nature of the correlations between calculated drainage metrics (i.e., drainage area and lake area (km^2), elevational extent of the drainage network, JJA surface-temperature anomalies (°C) and total annual runoff (mm w.e. yr^{-1}) across the study period as well as the influence of the latter external independent factors on the mapped drainage network and; (ii) the coefficient of determination (R^2) which is a statistical measure determined from a linear regression model to quantify how external variables, in this case, variables such as 37-year study period, JJA surface-temperature anomalies and total annual runoff, explained observed drainage metrics.

Prior to statistical analysis, a series of assumption checks were conducted on all datasets to ensure a higher confidence in the results derived from the analysis. These are: (i) the removal of missing data in the drainage metric datasets from the years 1993, 1996, 1997, 2001, 2002 to avoid incorrect data assumptions; (ii) the use of the Shapiro-Wilk test to check data normality and (iii) the assessment of quantile-quantile (QQ) plots to visually assess the distribution of data quantiles against a normal distribution. Any datasets failing these tests were not used in further analysis.

5.3 Results

5.3.1 Terminus change (1985 – 2021)

Figure 5.8 shows the mean terminus change over the 37-year study period at Humboldt Glacier across the ~91 km wide terminus as well as within the divided north and south sectors, which have markedly different retreat behaviours as observed by Carr *et al.* (2015) and Rignot *et al.* (2021). Overall, Humboldt Glacier retreated 4.7 ± 0.09 km on average

across its ~91 km wide terminus during the study period with an average rate of 126 m a^{-1}. A distinct consistent increasing trend in terminus retreat post-1999 is observed, with the average rate of retreat between 2000–2021 (145 m a^{-1}) being 2.8 times greater than between 1985–1999 (51 m a^{-1}).

Exploration of the two distinctive glacier sectors show the northern stretch of terminus (Figure 5.9) retreated an average of 8.1 km ± 0.1 km across 37 years, with a maximum of 13.4 ± 0.03 km of retreat recorded at reference line (1) and a minimum retreat of 2.1 ± 0.03 km at reference line (3). In the south sector (Figure 5.10), average retreat was recorded at 1.2 ± 0.1 km across the study period, with a maximum retreat of 3.4 ± 0.03 km observed at reference line (4) and a minimum retreat 0.1 ± 0.03 km at reference line (5). Examination of the rate of change overtime in these two distinct sectors shows 87% of retreat at Humboldt Glacier occurred within the northern sector post-1999: also identified when examining full terminus retreat. This northern retreat post-1999 cumulatively resulted in the retreat of 7.1 km from 1999 to 2021. During this period, average retreat rates in the northern sector (93 m a^{-1}) were an order of magnitude higher than those in the south (9 m a^{-1}). Conversely, the south sector of the terminus remained relatively stable until 2010, with 80% of its retreat (998.7 m) occurring during the last 11 years, in particular during 2010, 2011, 2012, 2017 and 2021. The year 2016 saw a minor reprieve in retreat in both the north and south sectors with an advance of 100 m and 159 m in terminus position, respectively, during this year, before retreat resumed.

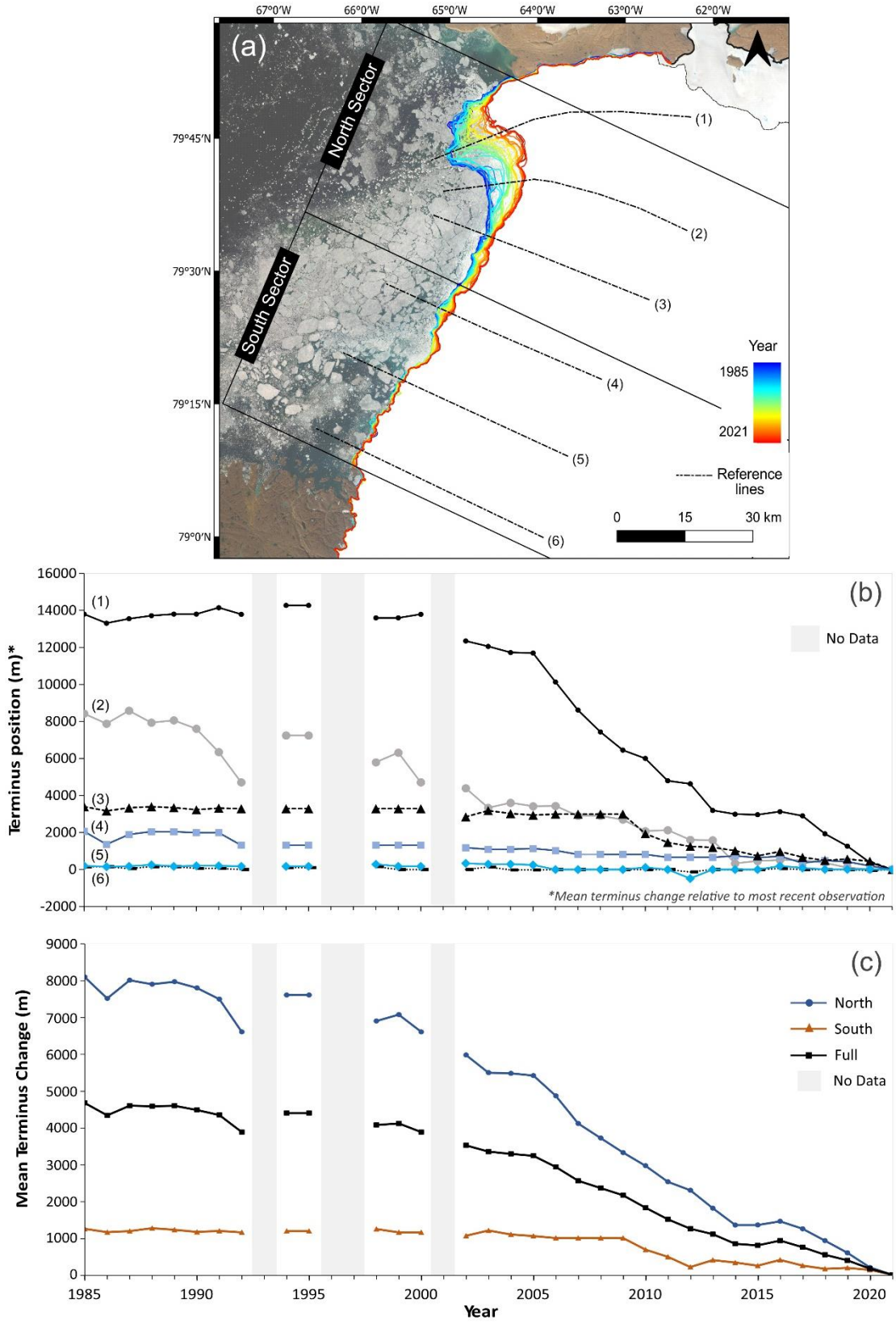

Figure 5.8. (a) Map showing the terminus positions of Humboldt Glacier from 1985 to 2021; (b) Terminus position change (relative to most recent observation) for each reference line (1–6) and; (c) Mean terminus change (m) for the north and south sectors as well as the full terminus across the study period. Grey bars represent years with missing data.

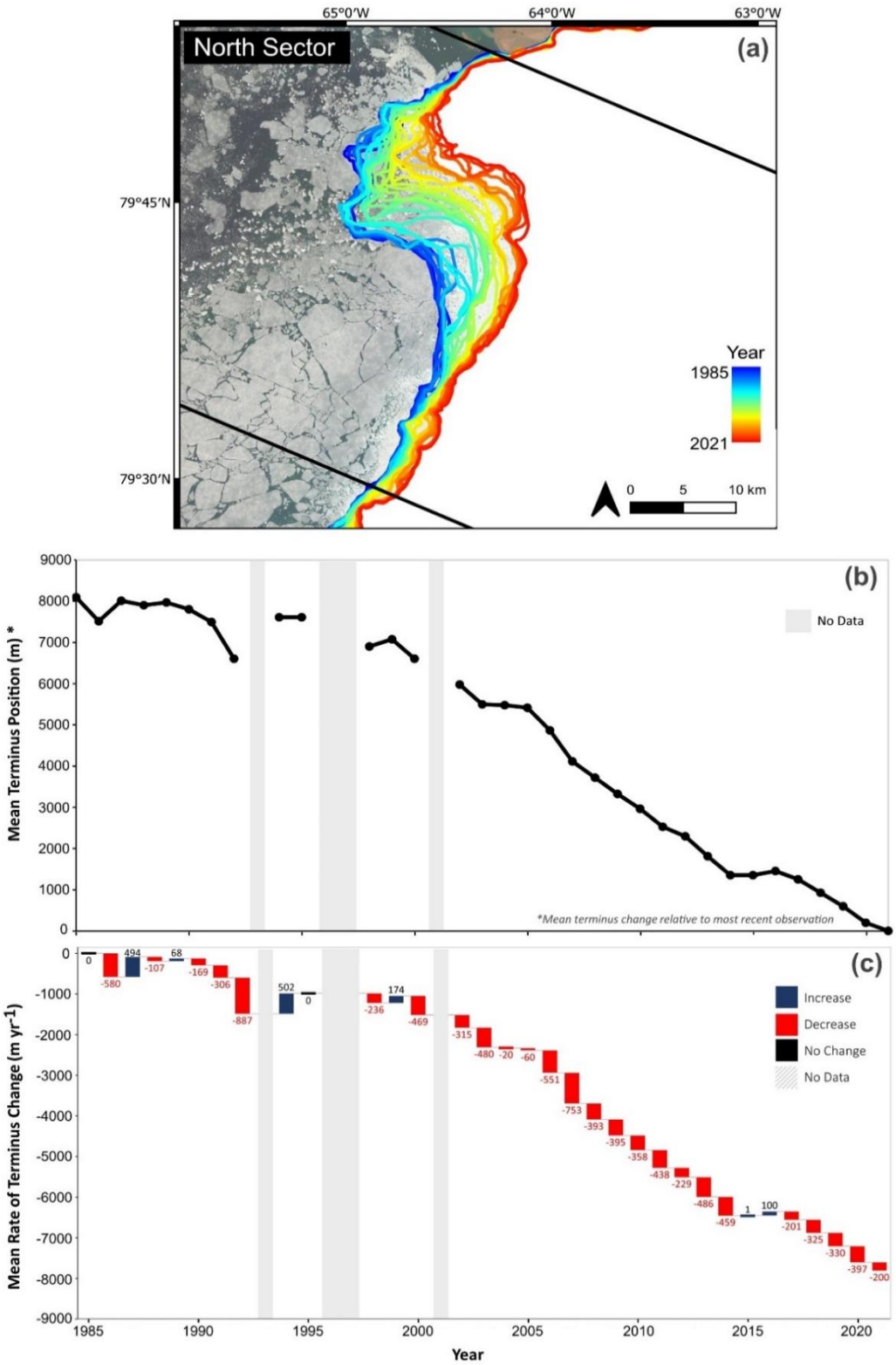

Figure 5.9. (a) Northern sector of the Humboldt Glacier terminus with annual terminus outlines between 1985 and 2021; (b) Mean northern terminus position (m) with each annual position relative to the most recent observation; (c) Mean rate of annual terminus change (m yr^{-1}). Blue bars represent an increase (advance) in terminus position and red bars represent a decrease (retreat) in terminus position. Black bars represent no change. Grey bars in (b) and (c) represent no data.

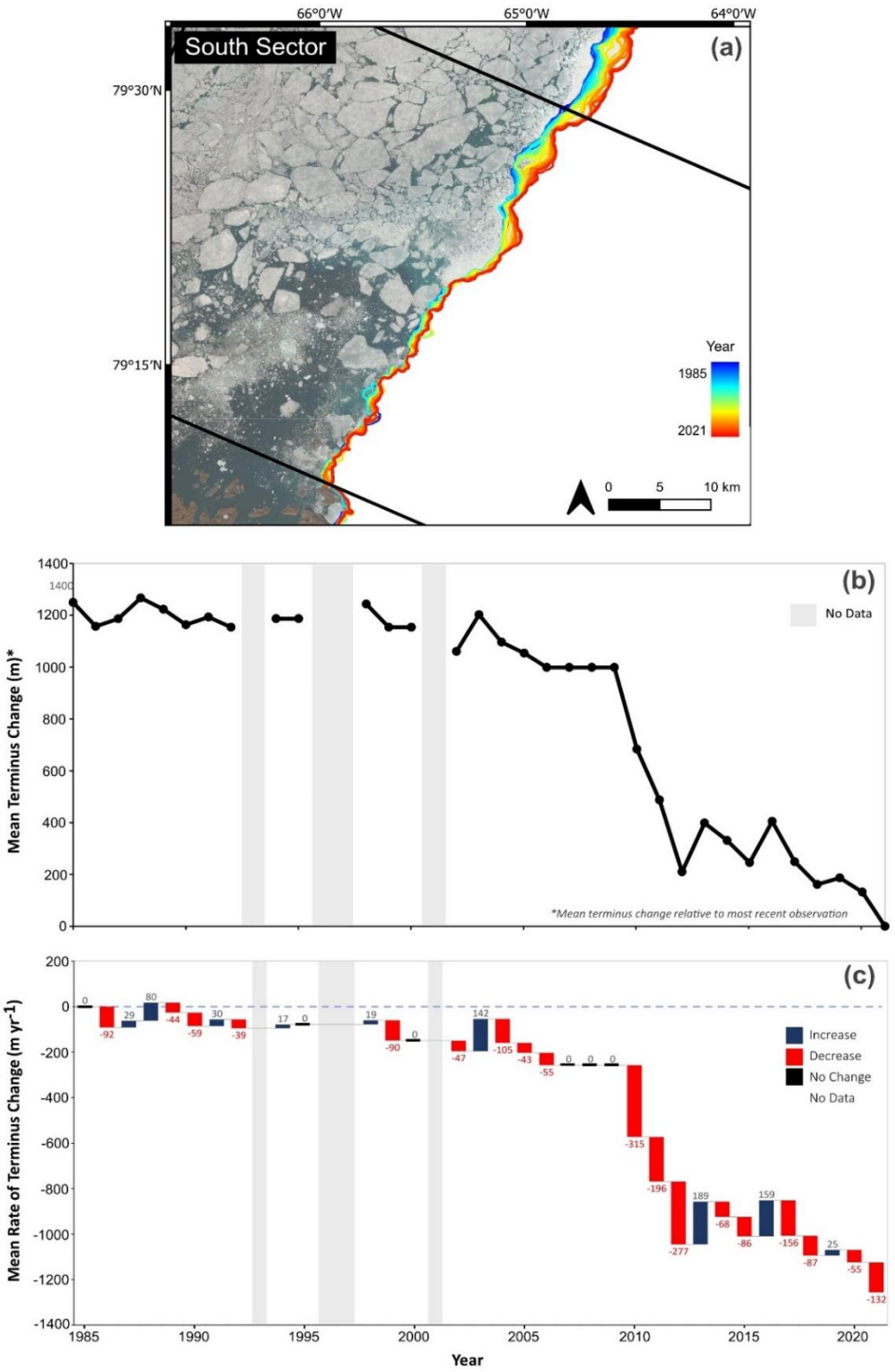

Figure 5.10. (a) Southern sector of the Humboldt Glacier terminus with annual terminus outlines between 1985 and 2021; (b) Mean southern terminus position (m) with each annual position relative to the most recent observation; (c) Mean annual rate of terminus change (m yr^{-1}). Blue bars represent an increase (advance) in terminus position and red bars represent a decrease (retreat) in terminus position. Black bars represent no change. Grey bars in (b) and (c) represent no data.

5.3.2 Supraglacial hydrologic network evolution

Figure 5.11 shows the supraglacial hydrologic network per decade across the 37-year study period, with individually mapped years provided in Appendix B, Figure B1. In the 1985-2021 period, the supraglacial hydrologic network at Humboldt Glacier is shown to have doubled in area (98%; Figure 5.11; Figure 5.12a), with a mean drainage area increase of 9 km^2 a^{-1} and a significant positive correlation confirming this observed trend (r = 0.39, *P* = 0.01; Figure 5.13a). A 5-year rolling mean (Figure 5.12b), taking into account interannual variability, shows a 68% (4.8 km^2 a^{-1}) increase in the overall drainage area observed across the study period. The upglacier limit of the supraglacial hydrologic network has also migrated inland by a maximum elevation of 432 m (11.7 m a^{-1}) and mean elevation of 293.6 m (7.9 m a^{-1}), with the network reaching a maximum recorded elevation of 1464 m a.s.l in 2021 and the highest confirmed lake recorded at 1373 m a.s.l in 2020 (Figure 5.11; Figure 5.12a). This long-term trend in inland expansion is confirmed with a strong correlation (Figure 5.13b; 5.13c), particularly for maximum inland drainage elevation overtime (r = 0.70, *P* = 0.01; Figure 5.13c). A further correlation is also found between the size of the drainage area and maximum elevation, with a greater drainage area positively correlating with a higher elevational extent (R^2 = 0.42, r = 0.65, *P* = <0.001; Figure 5.13d).

Over decadal timescales, 2010–2021 recorded the largest network expansion in both area covered and maximum elevation reached, with an increase of 43% and 12%, respectively, from the preceding decade (2000 – 2009), and a 42% and 56% respectively compared to 1985–1989. Elevation dependent supraglacial drainage area per year varies considerably across the Humboldt Glacier catchment (Figure 5.12c), with both large interannual variability across elevation over time as well as an overall trend towards increasing inland drainage concentration over time. In years which experienced lower drainage areas, for example 1986, 1992, 2000 and 2006, the supraglacial hydrologic network is typically constrained to the lower elevations of the ablation region (<800 m). Similarly, years 2004, 2013, 2017 and

2018 also have lower drainage areas which are also constrained to <1000 m. Years with considerably larger supraglacial drainage areas, including 1998, 2008, 2014, 2019 and 2021 all consistently reach elevations >1200 m, with 2015 marking the first year that drainage reached >1400 m.

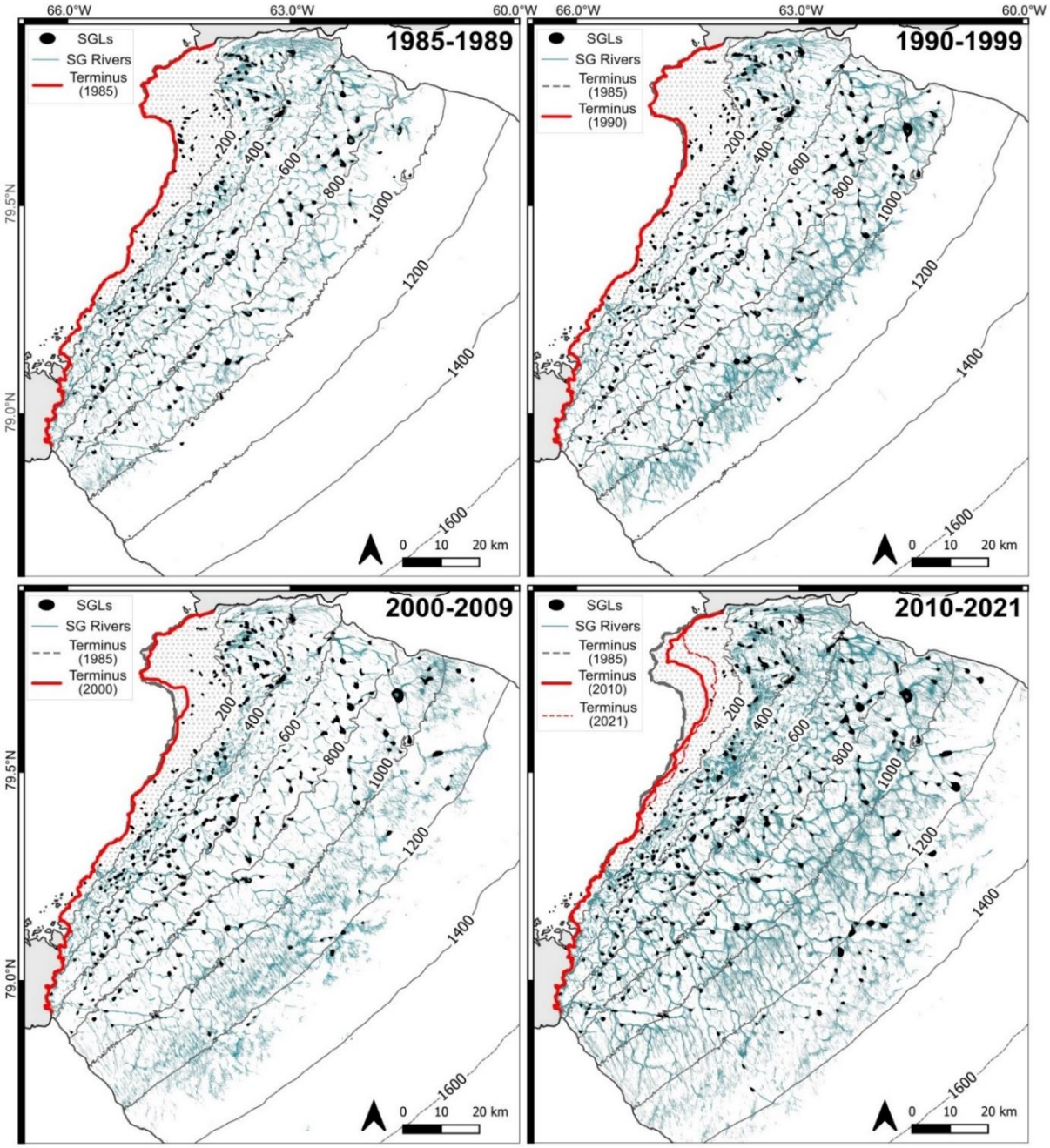

Figure 5.11. Map panels showing the supraglacial hydrologic network per decade at Humboldt Glacier across the study period 1985 – 2021. Inland migration of the network is clearly shown overtime. Terminus positions related to the decade denoted in the associated map panel are also shown, with the 1985 terminus visible throughout for reference.

Examining the individual components that comprise the supraglacial hydrologic network over time (Figure 5.12a), on average 80% of the system at Humboldt Glacier is made up of supraglacial rivers, with the largest cumulative river area (89.8%) observed in 2014 and the least (46.6%) in 2006. The remaining 20% of average annual supraglacial drainage area comprises SGLs, with 33% of these possessing an area of >0.1 km^2, and the remaining an area between >0.01 km^2 and <0.1 km^2. The composition of the network has, however, experienced large Interannual variability overtime (Figure 5.11a). The period 2000–2009 recorded the highest average percentage (25%) of SGLs comprising the hydrologic network, with a number of individual years during this period recording the highest values across the study period; 54% (2006) and 37% (2004). During 2010–2021, the percentage of surface meltwater coverage made up of SGLs reduced by 16% from the prior decade, despite both collective and individual SGL area increasing by 12% (52.9 km^2 to 59.7 km^2) and 38% (0.36 km^2 to 0.49 km^2) respectively, with supraglacial rivers becoming increasingly extensive and dominant throughout this decade, particularly as the extend inland.

Elevation dependent supraglacial drainage area per year varies considerably across the catchment (Figure 5.12c), with both large interannual variability across elevation over time as well as an overall trend towards increasing inland drainage concentration over time. In years which experienced lower drainage areas, for example 1986, 1992, 2000 and 2006, the supraglacial hydrologic network is typically constrained to the lower elevations of the ablation region (<800 m). Similarly, years 2004, 2013, 2017 and 2018 also have lower drainage areas which are also constrained to <1000 m. Years with considerably larger supraglacial drainage areas, including 1998, 2008, 2014, 2019 and 2021 all consistently reach elevations >1200 m, with 2015 marking the first year that drainage reached >1400 m.

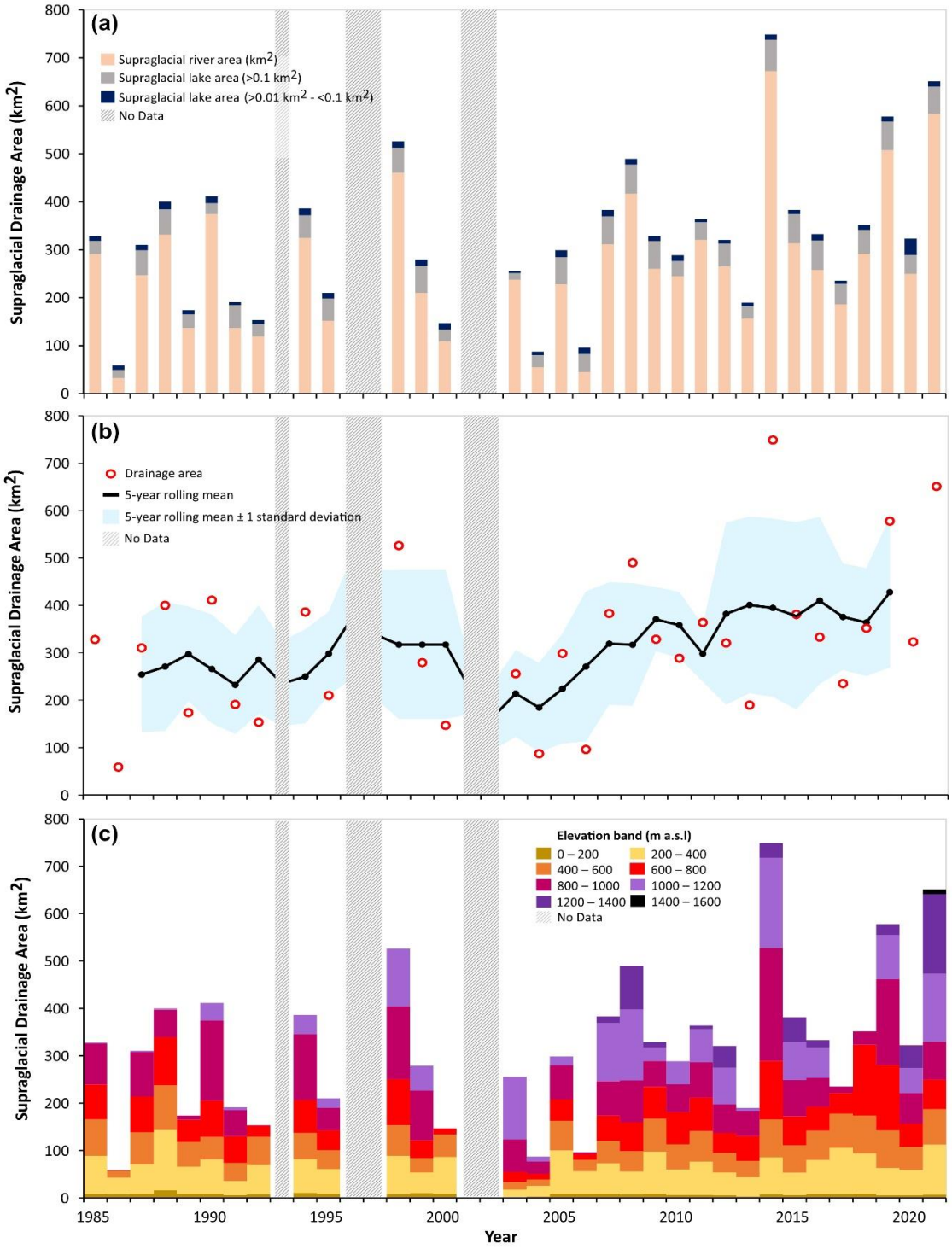

Figure 5.12. (a) Annual supraglacial drainage area (km^2) between 1985 and 2021. Bars are divided into components (rivers and SGLs) of the drainage area, including SGLs based on size (i) >0.1 km^2 and (ii) >0.01 km^2 and <0.1 km^2; (b) 5-year rolling average of total supraglacial drainage area across alongside the 5-year rolling average standard deviation ± 1 to show associated variation. 5-year rolling average points are centred on the 5-year period calculated. Total drainage area is also represented for reference by red dots; (c) Supraglacial drainage area divided into 200 m elevation bands from 0 to 1600 m a.s.l. Grey bands denote missing data.

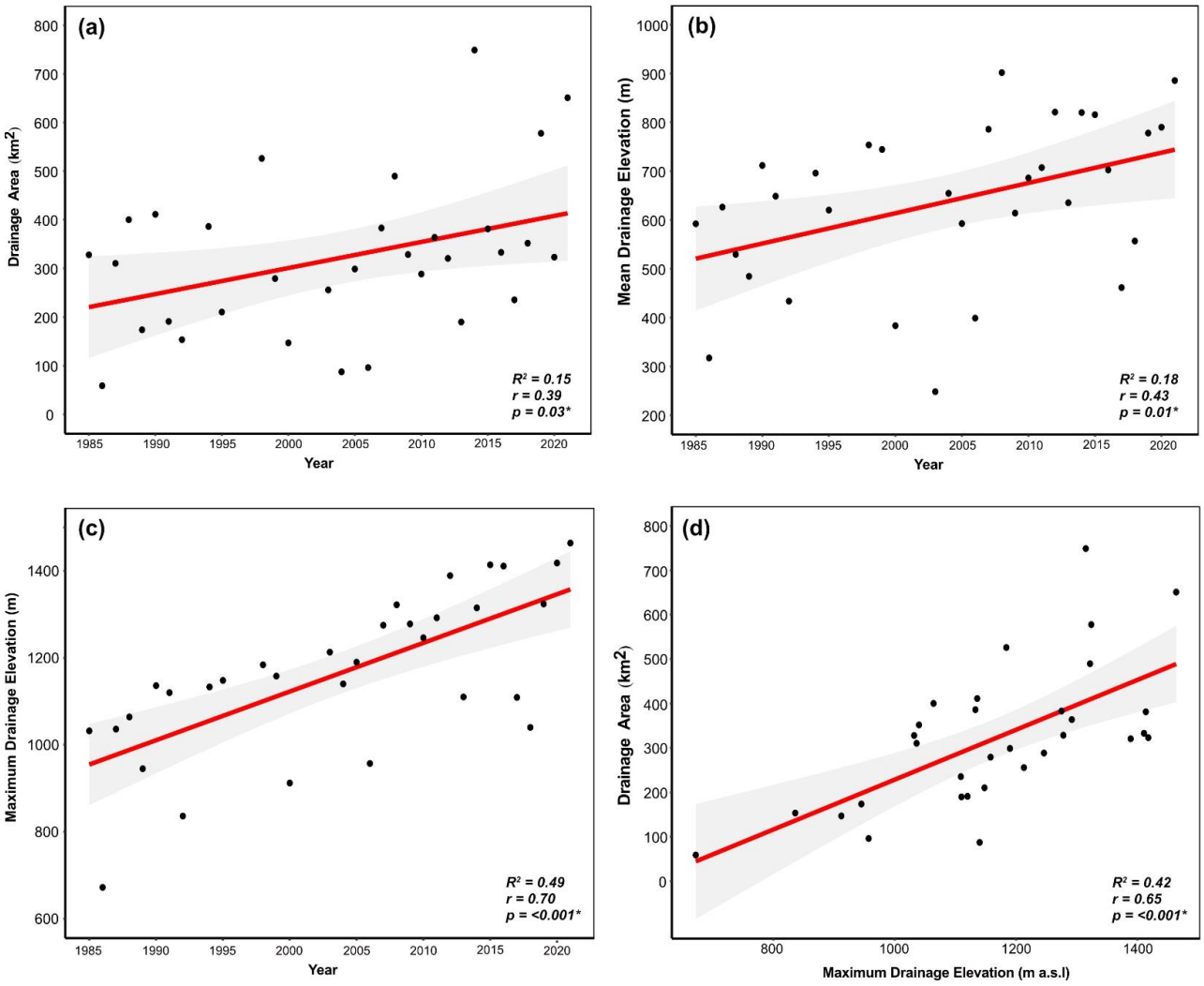

Figure 5.13. Linear regression models showing the relationship between (a) drainage area and time; (b) mean drainage elevation and time; (c) maximum drainage elevation and time, and; (d) drainage area and maximum drainage elevation (m a.s.l). Grey area represents the standard error of the regression line. Associated R^2 values are stated alongside Pearson correlation (r) and *P* values. Significant results are italicised and in bold.

5.3.3 Generalised supraglacial hydrologic structure

The recurrence and structure of the generalised supraglacial hydrologic network at Humboldt Glacier over the 32 mapped years mapped is presented in Figure 5.14. The recurrence refers to the number of years a given pixel is identified as being water (Tuckett *et al.*, 2021) and therefore the annual reuse of the network. In general, the network frequently recurs in the lower ablation zone (<1000 m a.s.l) of Humboldt Glacier and reduces in

frequency with increasing elevation, which is clearly seen; the result of inland expansion of the system, particularly within the last decade.

Examining the network recurrence in-detail, between 200-1000 m a.s.l, the maximum recurrence (both rivers and SGLs) was between 26 and 32 years, with the network recurring in the same, or similar, location each year. For supraglacial river channels, their generalised structure is relatively static, implying a long-term topographic control. There is, however, some observed river channel migration that has occurred across 32 years within these large, primary-style channels, but of no more than 400 m laterally and 900 m longitudinally to ice flow.

Above 1000 m a.s.l, the recurrency frequency for supraglacial rivers decreases, with a maximum of 23 years between 1000-1200 m a.s.l, 11 years between 1200-1400 m a.s.l and 4 years between 1400-1600 m a.s.l (Figure 5.14). This provides evidence of the expanding supraglacial hydrologic network in more recent years, particularly between 1200–1400 m and 1400–1600 m a.s.l where the supraglacial network has been persistently reoccurring since 2011 and 2015, respectively (see Appendix B, Figure B1). In addition, this recurrence map highlights that SGLs have a much higher frequency-of-return and at higher elevations than that of supraglacial rivers, with lake recurrence of up to 13 years reaching elevations of 1200 m a.s.l. Again, this provides further evidence of SGLs reforming in the same location, even at high elevations, when melt is available.

An area of Humboldt Glacier where yearly recurrence is particularly low despite its low elevation is within the highly-crevassed terminus zone. Below 400 m a.s.l, in this zone, much of the network is made up of small, segmented supraglacial rivers (<4 km long) alongside small SGLs (average size of 0.24 km^2). In particular, lakes that are mapped within the lower 25 km of the northern terminus are elongate in shape, likely representing ponded water within crevasses. As a result, their recurrence is much reduced, likely due to a combination

of their short-lived nature and/or terminus retreat, with 60% having a maximum yearly recurrence of <11 years.

In terms of the long-term structure of the generalised hydrologic network, a dendritic-type drainage network dominates the mid- to upper-ablation zone in the northern sector, with supraglacial rivers flowing between, and sometimes terminating in SGLs, inferred from the sudden break of a long, flowing river channel that does not continue further downstream. In the south, the supraglacial network differs, displaying a style of drainage in which channels are (i) more aligned with the direction of ice flow, (ii) less-disrupted and (iii) terminate directly off the glacier terminus. Over the study period, it is clear that the expansion of the network inland has involved the lengthening of already-existing channels into the higher elevation zone (>1000 m a.s.l) with the generalised structure remaining stable (Figure 5.11; Figure 5.14).

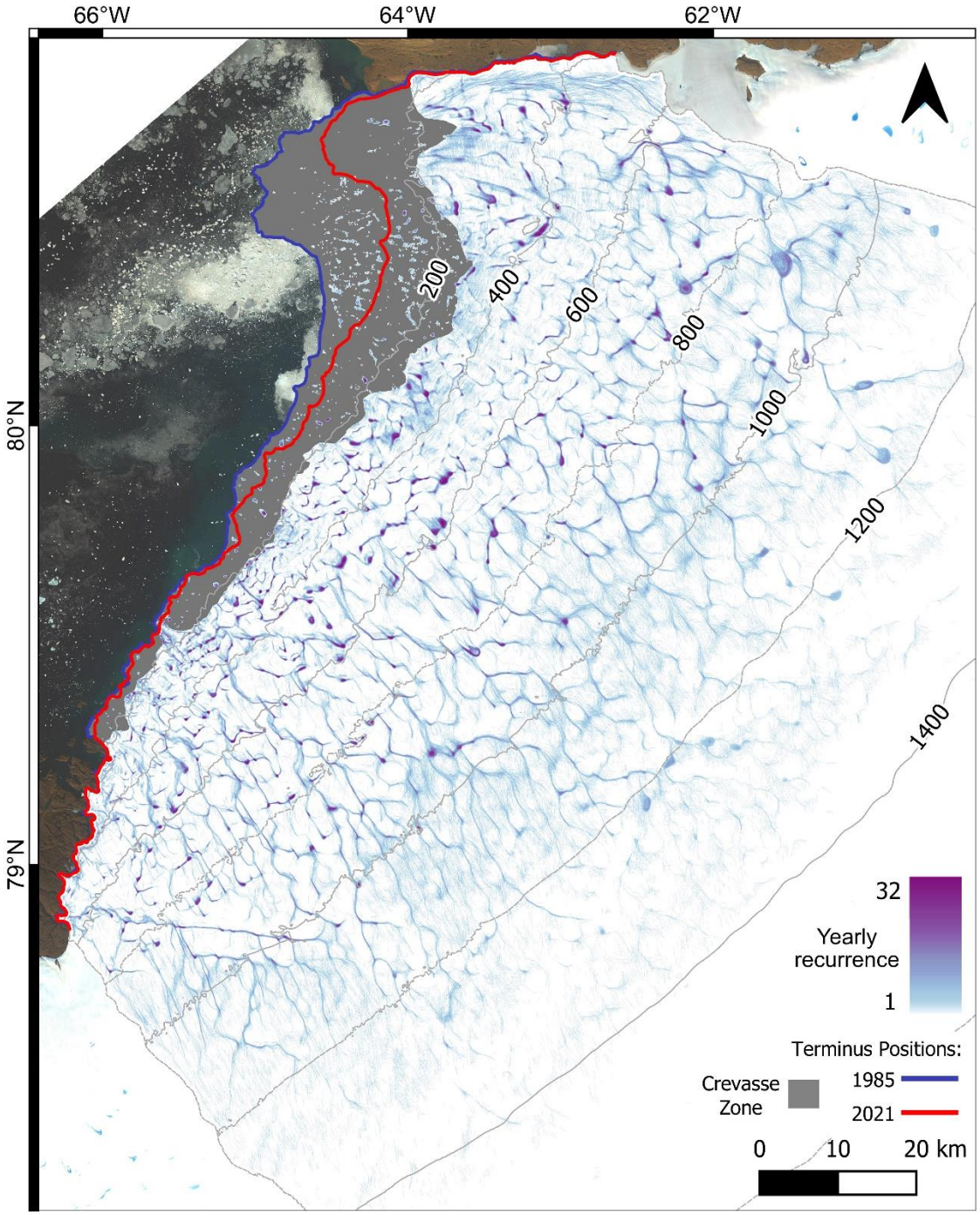

Figure 5.14. Spatial distribution of the supraglacial hydrologic network (rivers and lakes) across Humboldt Glacier and its yearly recurrence between 1985 and 2021. The maximum possible occurrence is 32 as 5 years (1993, 1996, 1997, 2001 and 2002 were excluded due to missing data). Pixels with rivers and lakes (melt) are assigned a value of 1 and background (no melt) assigned a value of 0 per year, with pixels summed to derive the above yearly recurrence map. The darker the colour, the more frequent the revisit.

5.3.4 Supraglacial lakes

A total of 13,572 SGLs >0.01 km^2 were mapped collectively for all years across the study period at Humboldt Glacier (Figure 5.15a) covering a cumulative total area of 1753.1 km^2. The number of SGLs >0.01 km^2 mapped across the period ranged between 177 (2003) and 591 (1988) with total annual SGL area ranging between 18.3 km^2 (2003) and 76.5 km^2 (2014). Of the 13,572 SGLs mapped, 33% had an area >0.1 km^2, which accounted for 79% of total SGL area at Humboldt Glacier, with the number of SGLs >0.1 km^2 ranging between 48 (2003) and 204 (1988). Due to the retreating terminus, particularly within the norther sector, 7% of SGLs (909) were lost between 1985 and 2021, but the overall number of SGLs did not significantly change overtime (r = -0.009, P = 0.96; Figure 5.17a). Total SGL area and mean SGL size, however, did significantly increase overtime (r = 0.40, P = 0.02, Figure 5.17b; r = 0.68, P = <0.001, Figure 5.17c) with an 81% increase in area recorded and a growth in mean SGL size by 173%.

In terms of the elevational range of SGLs at Humboldt Glacier, 75% of SGLs recorded, totalling 1030 km^2, occurred below 600 m a.s.l with an average size of 0.9 km^2. Smaller SGLs, as mentioned previously, were concentrated within the highly crevassed zone of the northern sector (Figure 5.15a), with the exception of a few large SGLs reaching 2.3 km^2 between 400-600 m a.s.l. Even though the number of SGLs across the 37-year period did not significantly change, it can be seen in Figure 5.16a that, in certain elevation bands, this does vary. Between 0-200 a.s.l, where the highly crevassed zone is located, the number of SGLs, and total area, does decease over time, which could be associated with terminus retreat and subsequent lake loss. Regardless, interestingly this loss is balanced by expansion elsewhere as SGL numbers remain stable, which perhaps can be seen with the inland advancement of SGLs from 1991. The first detection of SGLs at higher elevations (1000–1200 m a.s.l) occurred from 1991 in this study, with 43 SGLs recorded here between 1991 and

1999. An increase of 91% was seen in the following decade (2000–2009) at this elevation, subsequently followed by another 90% increase in the most recent decade (2010–2021). A similar trend is also seen between 1200–1400 m a.s.l, with SGLs first recorded at this elevation in 2003 (1). The number of SGLs present here between 2010–2021 being four times greater than between 2003–2009. For SGL area over time (Figure 5.16b), an area reduction of 62% occurred between 0–200 m a.s.l and 0.36% between 200-400 m a.s.l when comparing the decadal periods 1985-1989 to 2010-2021. Increases in total SGL area, however, were observed across all other elevation bands >400 m a.s.l between these same decadal periods, but to varying degrees; 10.7% between 400-600 m a.s.l, 32.3% between 600-800 m a.s.l and 99.6% between 800-1000 m a.s.l. The largest observed increase occurred in elevations >1000 m a.s.l, with a total SGL area increase of 2500% between 1000-1200 m a.s.l when comparing the periods 1985 – 1989 to 2010-2021, and 719% between 1200-1400 m a.s.l between 2000-2009 (when SGLs first encroached this elevation) and 2010-2021. Alongside this, mean SGL size also increased overtime (Figure 5.16c), particularly >600 m a.s.l, with a 78.9%, 90.0% and 1083.2% increase in SGL size across each 200 m elevation band between 600 and 1000 m a.s.l between 1985–1989 and 2010-2021. For the elevation band 1200-1400 m a.s.l, mean SGL size increased by 236.9% between 2000–2009 (when SGLs were first recorded at this elevation) and 2010-2021.

Overall, mean SGL elevation significantly increased by 138.6 m between the period 1985-1989 and 2010-2021 ($r = 0.39$, $P = <0.001$; Figure 5.17d) and maximum SGL elevation significantly increased by 269.4 m a.s.l ($r = 0.44$, $P = <0.001$; Figure 5.17e) for the same decadal periods, confirming inland SGL expansion at Humboldt Glacier. It is shown in Figure 5.15b that the expansion of SGLs to higher elevations largely follows the location of surface depressions.

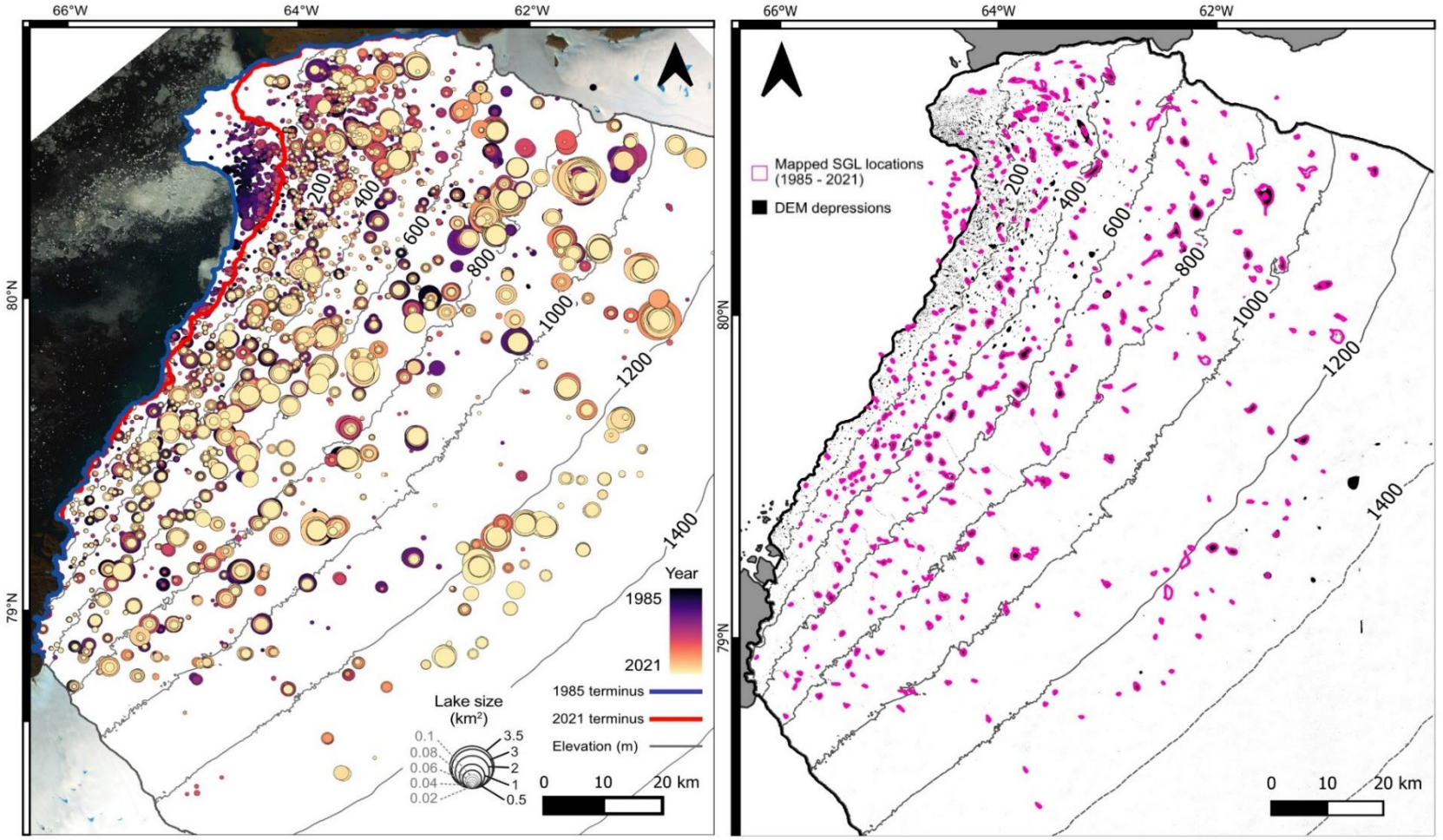

Figure 5.15. (a) SGL numbers and size between 1985 and 2021 at Humboldt Glacier, with colour representing year and the size of each lake point. SGLs have migrated inland overtime, with individual SGL size increasing; (b) The location of DEM-derived surface depressions from the GIMP DEM, with mapped Landsat SGL locations across the study period (1985–2021) overlain. SGLs are shown to form in the locations of surface depressions, and have followed this trend with inland migration.

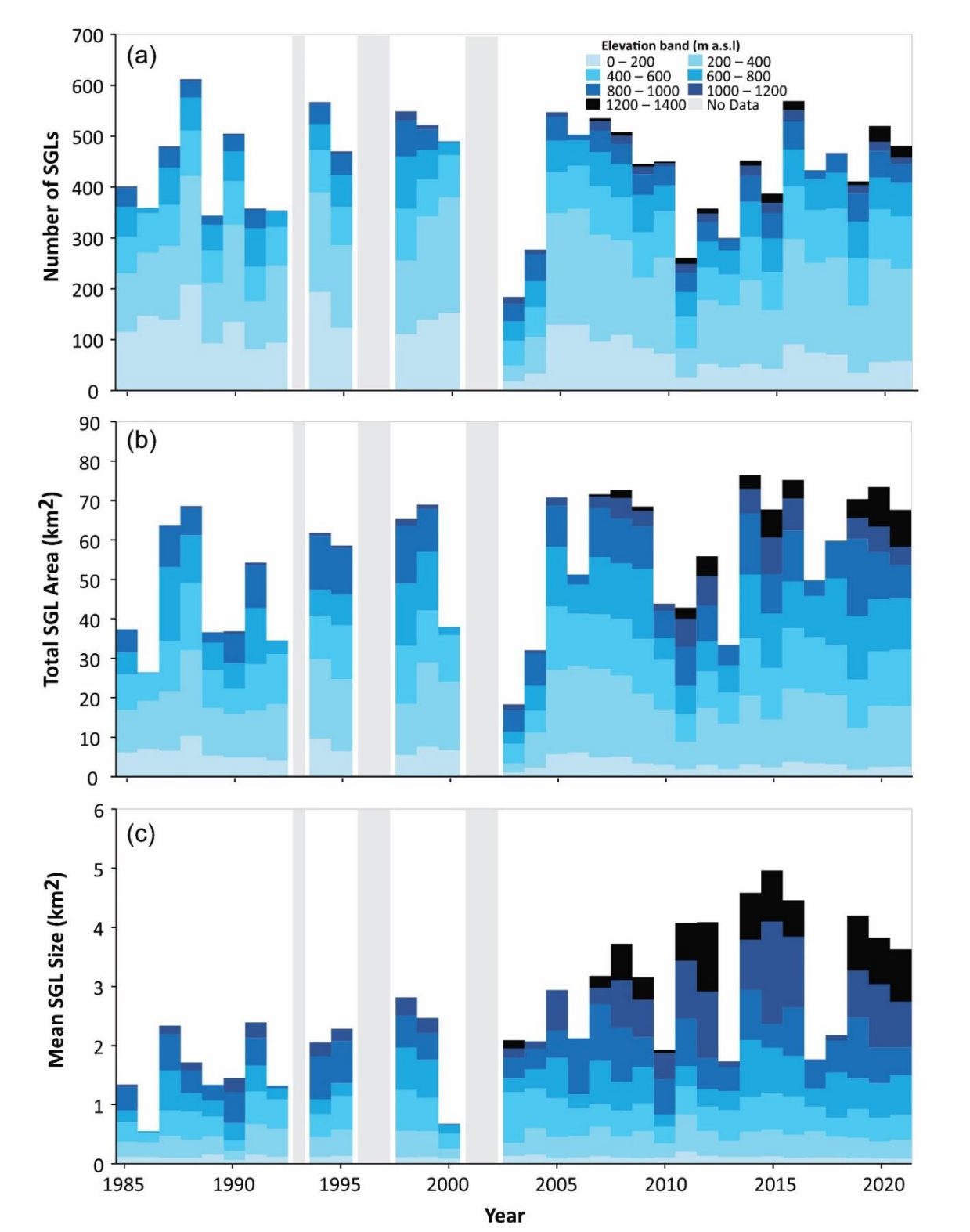

Figure 5.16. Quantification of SGL metrics and map visuals from figure 5.15a as follows: (a) number of SGLs per 200 m elevation band overtime with cumulative bands equalling total number SGLs per year; (b) total SGL area (km^2) per 200m elevation band overtime with cumulative bands per year equalling total SGL area per year, and; (c) mean SGL size (km^2) per 200 m elevation band (note each band represented in graph c is standalone).

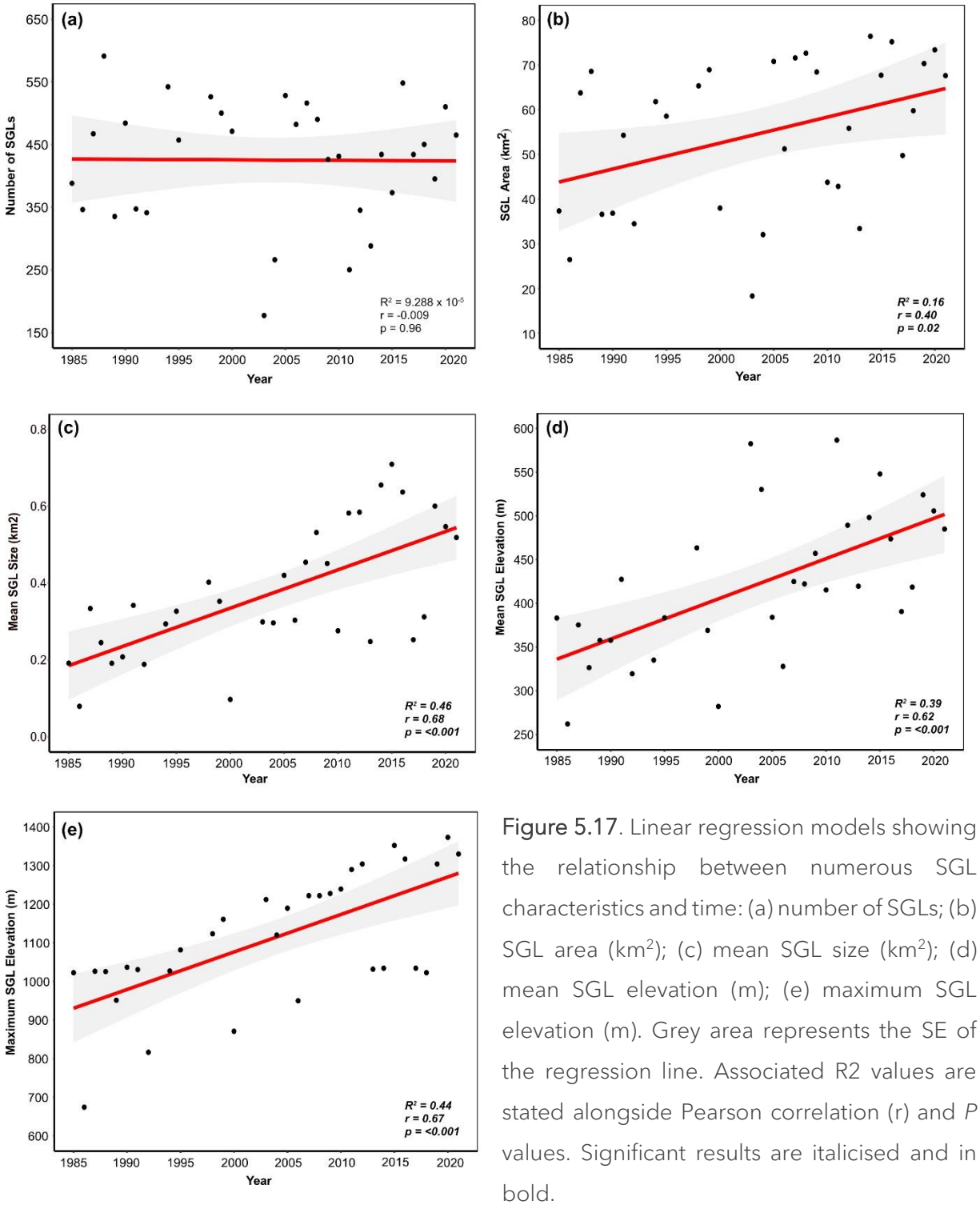

Figure 5.17. Linear regression models showing the relationship between numerous SGL characteristics and time: (a) number of SGLs; (b) SGL area (km^2); (c) mean SGL size (km^2); (d) mean SGL elevation (m); (e) maximum SGL elevation (m). Grey area represents the SE of the regression line. Associated R2 values are stated alongside Pearson correlation (r) and *P* values. Significant results are italicised and in bold.

5.3.5 Impact of surface temperature and runoff on supraglacial hydrologic network evolution

Recent (1985–2021) changes to JJA surface temperature for the Humboldt Glacier catchment were extracted from regional climate model MAR v3.12.1 outputs as anomalies against a baseline created from average JJA surface temperature between the reference period 1951–1980, also derived from MAR. Results in Figure 5.18a show that average JJA surface temperature anomalies increased by +1.3°C across the study period, (from actual temperatures of -3.8°C in 1985 to -2.5°C in 2021) with minimum and maximum JJA surface temperature anomalies also increasing by +1.8°C (-10.1°C in 1985 to -8.3°C in 2021) and +1.2°C (+6°C in 1985 to +7.2°C in 2021), respectively. Between 1985 and 2000, both positive and negative annual temperature anomalies were recorded annually, ranging between -1.6°C (1992) and +1.81°C (1998) with an average anomaly of +0.24°C across this period. Beyond 2001, anomalies were consistently positive, with an average anomaly of +1.34°C between 2001 and 2021 with the years 2008, 2012 and 2019 registering the largest temperature anomalies of 2.51°C, 2.64°C and 2.83°C, respectively. Examining the 5-year moving average of surface temperature anomalies to aid in smoothing out interannual variability also confirmed the presence of persistent anomalies above +1°C post-2000. In the period post-2010, 9 out of 12 of the largest temperature anomalies were recorded.

Exploration of the decadal trends across the study period show the average temperature anomaly recorded between 2010 and 2021 (+1.5°C) was nearly five times larger (451% and 475%, respectively) than that seen between the period 1985 and 1989 (+0.27°C) and 1990 – 1999 (+0.26°C) and 52% higher 2000 and 2009 (+0.99°C). In terms of the maximum temperature anomaly, the period 2010–2021 (+1.47°C) was over ten times higher (1301%) than that seen between 1985-1989 (+0.11°C), 561% higher than 1990-1999 (+0.22°C) and 56% higher than 2000-2009 (+0.95°C). Both long-term warming trends for mean (R^2 = 0.32,

r = 0.57, *P* = <0.001; Figure 5.18b) and maximum (R^2 = 0.28, r = 0.53, *P* = <0.001; Figure 5.18c) JJA surface temperatures were statistically confirmed.

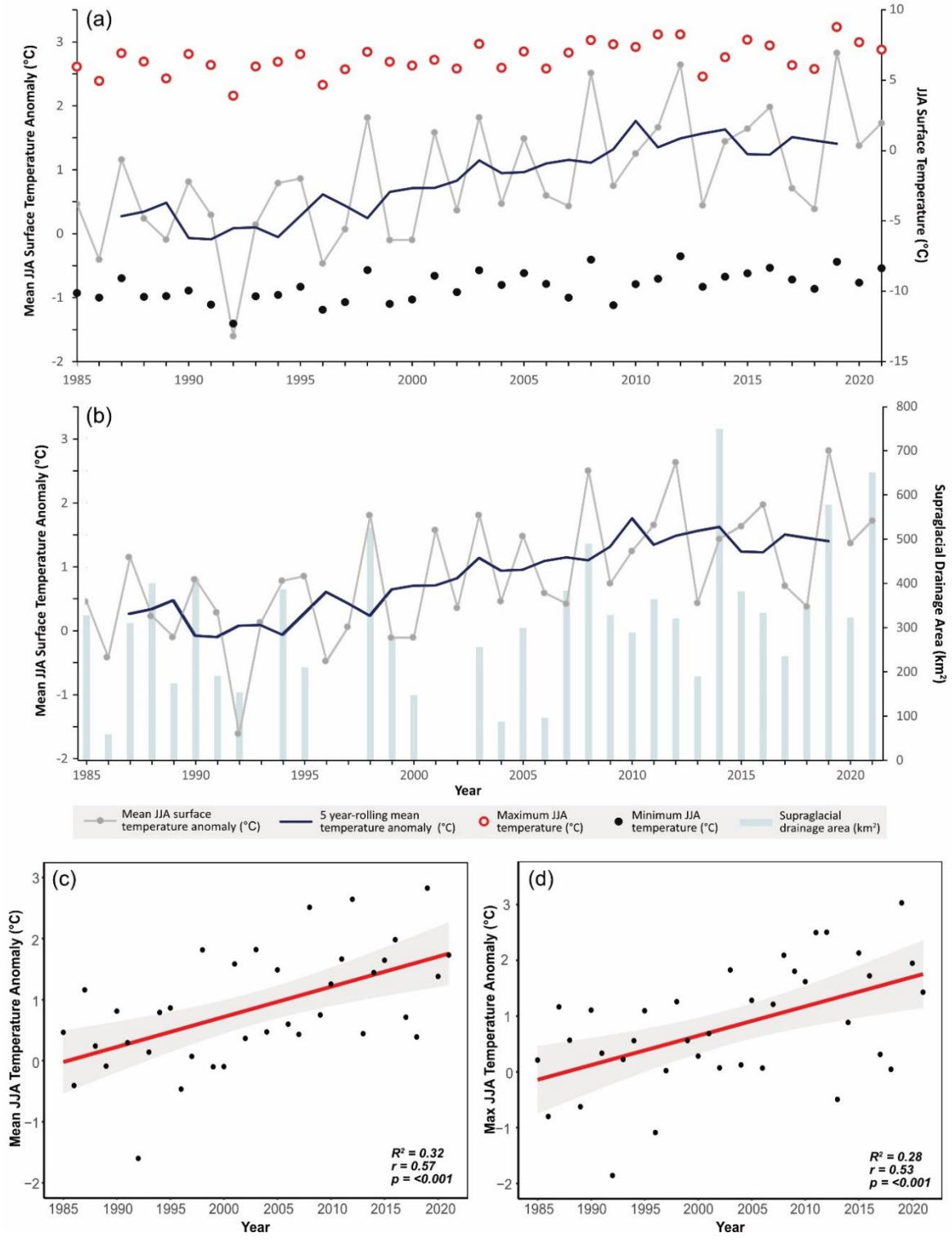

Figure 5.18. (a) MAR-derived JJA surface temperature anomalies (°C), 5-year rolling mean (°C) and minimum and maximum JJA surface temperatures (°C) for the Humboldt drainage catchment (up to a maximum melt extent of 1500 m a.s.l) across the study period 1985–2021; (b) Mean JJA surface temperature anomalies, 5-year rolling mean and supraglacial drainage area (km^2) per year across the study period; (c and d) Linear regression models showing changes to mean and maximum JJA temperature anomalies between 1985–2021. Grey area represents the SE of the regression line. Associated R^2 values are stated alongside Pearson correlation (r) and *P* values. Significant results are italicised and in bold.

Investigating the effect of the JJA regional surface temperature anomalies on observed supraglacial drainage area (km^2) per year across the study period (1985–2021) showed that increased annual drainage area coverage was typically associated with higher JJA temperature anomalies (Figure 5.18b). A key year with an exception to this trend was 2014, which saw the largest recorded drainage area (748.9 km^2) of the study period yet a below-average decadal temperature anomaly of +1.4°C (2010–2021 average was +1.51°C). Lower recorded drainage areas were also associated with lower surface temperature anomalies, particularly pre-2000. Statistically, 36% of the variation in drainage area across the study period was significantly explained by JJA mean surface temperature anomalies with an overall significant moderate positive relationship (R^2 = 0.36, r = 0.60, *P* = <0.001; Figure 5.19a). In terms of the influence of mean JJA surface temperature anomalies on the mean elevation of the supraglacial drainage network over the study period, a moderately positive statistically significant correlation (R^2 = 0.33, r = 0.57, *P* = <0.001; Figure 5.19c) was found, with years of higher recorded anomalies typically associated with a higher mean elevation of the supraglacial network. A stronger, statistically positive correlation (R^2 = 0.62, r = 0.79, *P* = <0.001; Figure 5.19d) was additionally found for mean JJA surface temperature anomalies and the maximum elevation of the supraglacial network. Years with particularly high maximum drainage elevations, particularly beyond the year 2008, such as 1322 m a.s.l in 2008, 1389 m in 2012, 1411 m in 2016, 1324 m in 2019 and 1464 m in 2021 had the

highest accompanying surface temperature anomalies (+2.51°C, +2.64°C, +1.98°C, +2.83°C, +1.71°C respectively).

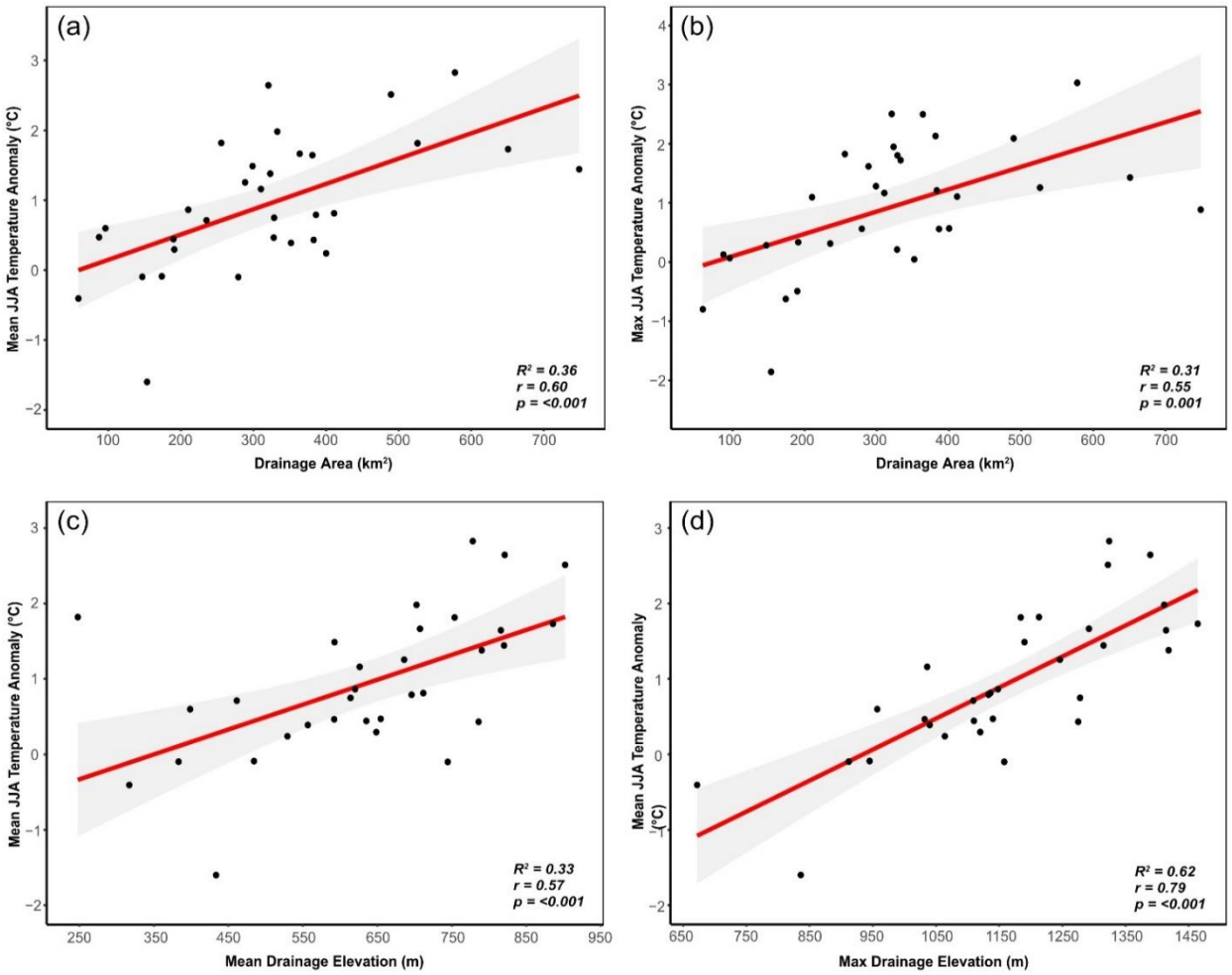

Figure 5.19. Linear regression models showing the relationship mean JJA surface temperature anomalies (°C) and numerous drainage area metrics; (a) mean JJA surface temperature anomalies (°C) and recorded drainage area (km^2); (b) maximum JJA surface temperature anomalies (°C) and recorded drainage area (km^2); (c) mean JJA surface temperature anomalies (°C) and mean drainage elevation (m a.s.l); (d) mean JJA surface temperature anomalies (°C) and maximum drainage elevation (m a.s.l). Grey area represents the standard error of the regression line. Associated R^2 values are stated alongside Pearson correlation (r) and P values. Significant results are italicised and in bold

5.3.6 Changes to regional runoff and its influence on hydrologic network evolution

Total annual runoff derived from MAR (v3.12.1) within the Humboldt Glacier catchment (Figure 5.20a) for 1985–2021 was shown to have large interannual variability, ranging between 60,363 mm w.e. yr^{-1} (1992) and 394,474 mm w.e. yr^{-1} (2012), with an average of 205,612 mm w.e. yr^{-1} across the 37-year period. There are a number of extreme runoff years present across this period, including 1998 (265,567 mm w.e. yr^{-1}), 2008 (343,589 mm w.e. yr^{-1}), 2012 (394,474 mm w.e. yr^{-1}), 2015 (342,717 mm w.e. yr^{-1}) and 2019 (387,430 mm w.e. yr^{-1}). The 5-year rolling mean shows an overall total annual runoff increase of 80% across the study period, with an average runoff increase of 2953 mm w.e. yr^{-1}. Examination of the long-term trend in total annual runoff shows a general positive upward trend across the study period, confirmed statistically in Figure 5.21a (R^2 = 0.36, r = 0.60, P = <0.001). Years post-1998 experienced regularly positive runoff anomalies with an average anomaly of 85,606 mm w.e. yr^{-1} across this period (1998–2021), and post-2008, consistently large anomalies were observed (>191,505 mm w.e. yr^{-1}), with the exception of a few negative years in 2013 and 2018 (Figure 5.20b). Exploration of the decadal trends of runoff, the period 2010–2021 (261,503 mm w.e. yr^{-1}) experienced runoff that was nearly double that (93%) of 1985 – 1989 (136,615 mm w.e. yr^{-1}), 59% higher than runoff between 1990–1999 (164,652 mm w.e. yr^{-1}) and 23% higher than runoff in the preceding decade of 2000–2009 (213,157 mm w.e. yr^{-1}).

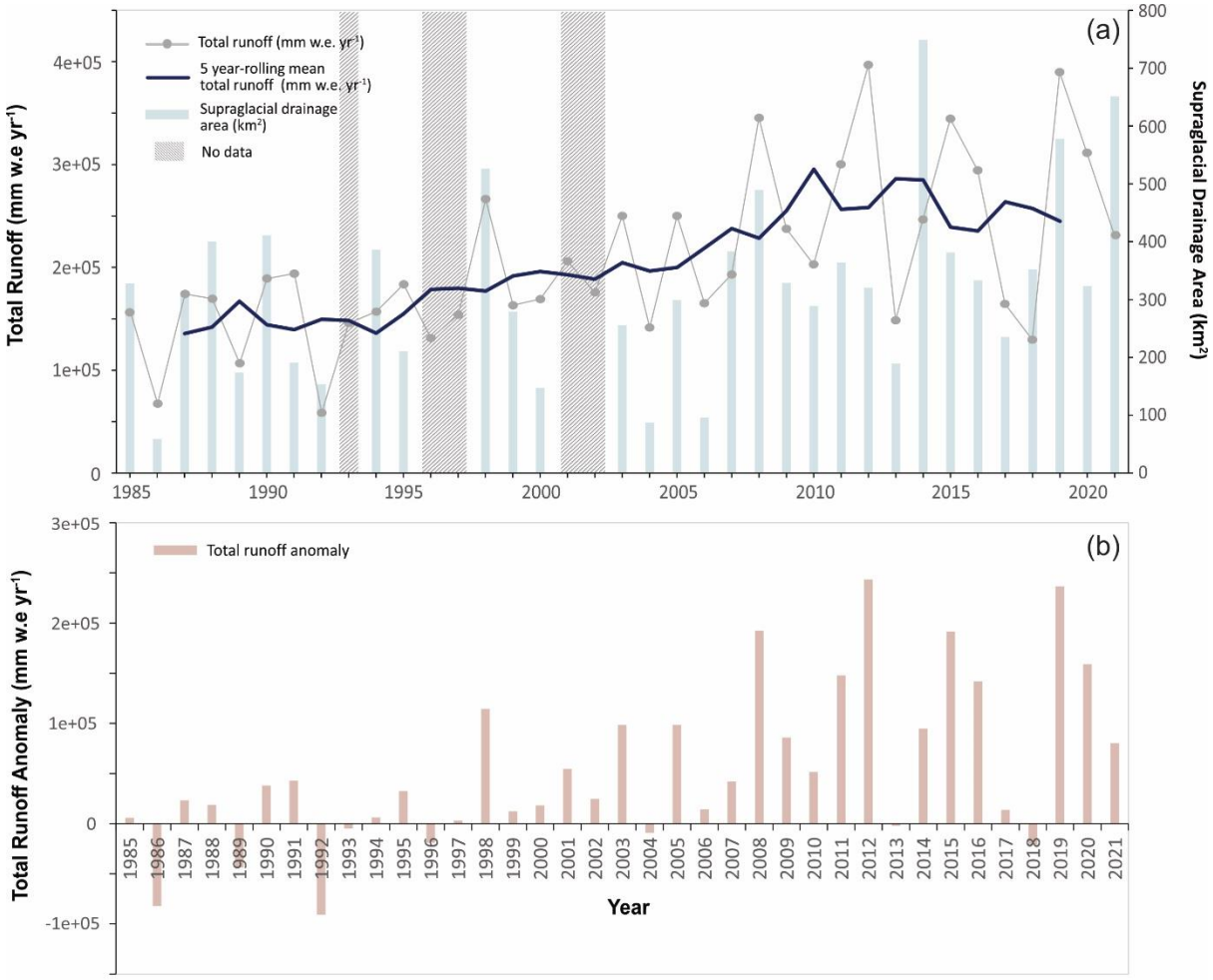

Figure 5.20. (a) MAR-derived total annual runoff (mm w.e. yr^{-1}) across the 37-year study period for Humboldt Glacier alongside a 5-year rolling mean and the quantified supraglacial water metric drainage area (km^2). Grey bars represent no data; (b) MAR-derived total annual runoff anomaly (mm w.e. yr^{-1}) across the 37-year study period calculated based on a runoff baseline for the period 1951–1980.

Total annual runoff displays a moderate, positive significant relationship (R^2 = 0.31, r = 0.55, *P* = <0.001; Figure 5.21b) with mapped supraglacial drainage area at Humboldt Glacier. As presented in Figure 5.20a, typically when low total modelled annual runoff occurs, recorded drainage area is also observed to be low. However, peaks in annual runoff and peaks in drainage area do not always simultaneously coincide. This positive relationship between annual runoff and a high supraglacial drainage area (and low annual runoff and a low

supraglacial drainage area), was seen for particular years, for example in 1998, 2008 and 2019 as high drainage and runoff years. However, for other years, in particular 2014 and 2020, increased drainage area coverage does not necessarily correspond with increased runoff. If, however, we examine the influence of total annual runoff on the mean and maximum drainage elevation of the supraglacial drainage network, a moderately positive significant relationship is observed for the former (R^2 = 0.39, r = 0.62, *P* = <0.001; Figure 5.21c), and a strong positive significant relationship observed for the latter (R^2 = 0.69, r = 0.83, *P* = <0.001; Figure 5.21d), raising an interesting finding of runoff being more closely related to the supraglacial hydrologic networks maximum elevation than the overall drainage area. Finally, total runoff is, unsurprisingly shown to be significantly correlated with mean JJA temperature anomaly (R^2 = 0.38, r = 0.91, *P* = <0.001; Figure 5.21e).

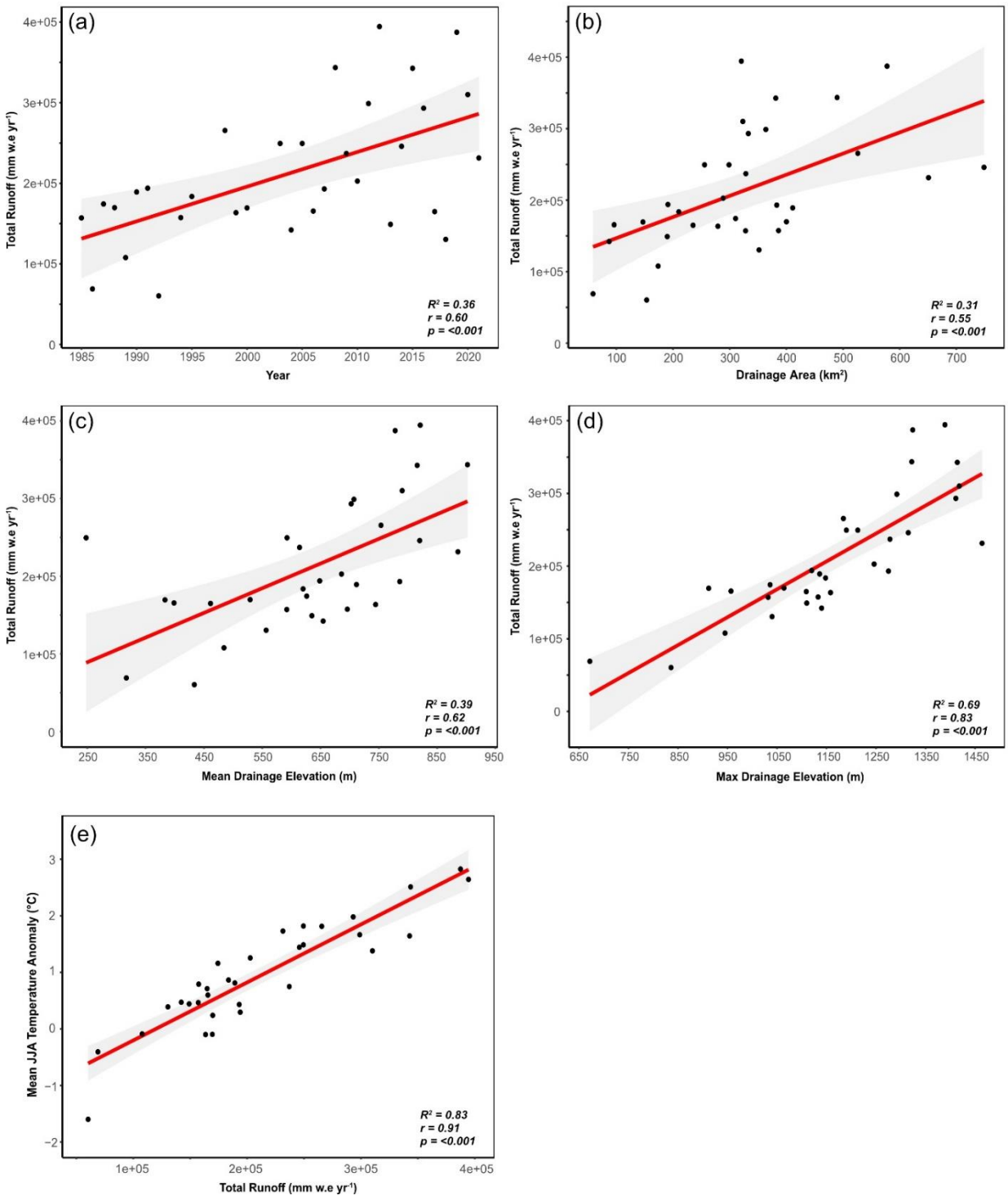

Figure 5.21. Linear regression models showing the relationship between MAR-derived total annual runoff (mm w.e. yr^{-1}) and numerous drainage area metrics; (a) total annual runoff change over the study period; (b) total annual runoff and drainage area (km^2); (c) total annual runoff and mean drainage elevation (m a.s.l); (d) total annual runoff and maximum drainage elevation (m a.s.l); (e) mean JJA temperature anomaly (°C) and total runoff (mm w.e. yr^{-1}). Grey area represents the SE of the regression line. Associated R^2 values are stated alongside Pearson correlation (r) and *P* values. Significant results are italicised and in bold.

5.4 Discussion

5.4.1 Terminus change

The retreat of Humboldt Glacier over the 37-year study period shows two distinct phases with a relatively slow rate between 1985 and 1999 (51 m a^{-1}) and a substantial increase in retreat rate of 2.8 times between 2000 and 2021 (145 m a^{-1}). This enhanced retreat post-2000 is consistent with trends in atmospheric warming, particularly the onset of rapid and consistent warming during the same period (post-2000). Average JJA temperature anomaly (compared to the 1951–1980 baseline) increased by 3.8 times during the period 2000–2021 compared to 1985–1999, from 0.26°C to 1.27°C. This aligns well with the findings of Carr *et al*. (2015), who also observed two distinct phases of Humboldt Glacier retreat between 1975 – 1999 (37 m a^{-1}) and 1999–2012 (162 m a^{-1}) coinciding with warming trends of 0.19°C a^{-1} (1999 – 2010). This synchronous response of glacial retreat and increasing air temperatures was not only observed at Humboldt Glacier, but ice sheet-wide in numerous studies (Howat and Eddy, 2011; King *et al.*, 2020; Moon and Joughin, 2008; Murray *et al.*, 2015). Moon and Joughin (2008) found marked increases in marine-terminating glacial retreat during the period 2000–2006 compared to 1992–2000, coinciding with increases in mean JJA coastal temperatures by 1.1°C. Similarly, Howat and Eddy (2011) found accelerated retreat in 90% of 210 marine-terminating glaciers across the GrIS between 2000-2010 after a period of low-to-moderate retreat between 1972–2000, coincident with the onset of warming temperatures after a period of multi-decadal cooling between 1970-1990.

This response of Greenlandic outlet glaciers, like Humboldt Glacier, to external forcing such as air temperatures, is likely related to the enhanced availability of meltwater at the ice surface. Increased meltwater availability and pooling in SGLs leads to more instances of water-induced fracturing and calving, with the hydrofracturing of crevasses a few kilometres inland of a glacier terminus potentially promoting weakening and subsequent calving once

ice has reached the terminus (Sohn *et al.*, 1998; Carr *et al.*, 2015). Such hydrofracture also increases meltwater supply to the glacier bed, which enhances basal lubrication and leads to short-term ice acceleration (Zwally *et al.*, 2002; Hanna *et al.*, 2008; Sole *et al.*, 2011; Tuckett *et al.*, 2021). The impact of ice velocity on calving, however, is highly dependent on the localised efficiency of the subglacial system, with the potential for adjustments in this system overtime helping to accommodate increased melt without leading to proportionate increases in ice flow (Sundal *et al.*, 2011).

The continued delivery of large quantities of supraglacial meltwater routed along the bed to the terminus can, however, promote submarine melt rates through the entrainment of ambient fjord water via convective-plumes, which have been shown to melt the terminus at rates of up to several metres per day (Jenkins, 2011; Xu *et al.*, 2012; Slater *et al.*, 2016). Controlled by both the turbulent upwelling of plumes from subglacial discharge and the heat content of the ocean near a glacier, including at the ocean surface from localised atmospheric warming (Hanna *et al.*, 2013), such ice-ocean-atmospheric interactions have been found to have a large impact on sustained glacial retreat, acceleration and dynamic thinning of many Greenlandic outlet glaciers over the past two decades (Howat *et al.*, 2005; Rignot and Kanagaratnam, 2006; Holland *et al.*, 2008; Hanna *et al.*, 2013; Slater *et al.*, 2022). For Humboldt Glacier, the Atlantic Intermediate Water (also known as Atlantic Water), is in direct contact with the terminus due to a cyclonic circulation of ocean water in the Kane Basin, bringing Atlantic-derived warmer waters originating from Baffin Bay to the Humboldt Glacier calving front, fuelling its widespread and rapid retreat over the last two decades (Carr *et al.*, 2015; Rignot *et al.*, 2021). Rignot *et al.* (2021) recorded ocean warming at various depths within the Kane Basin and frontal region of Humboldt Glacier, including 0.83°C (50–100 m depth), 1.13°C (150–250 m), 0.86°C (250–350 m) and 0.90°C (350+ m) between 1960 and 2019, providing evidence of oceanic warming overtime through the water column and potential for increased rate of submarine melting and greater calving as a result (Thomas *et*

al., 2003). The presence of buoyant subglacial plumes was also noted by Carr *et al.* (2015) and observed again via imagery in this study (Figure 5.22) showing an active subglacial system whereby heat transfer from a combination of fast-moving and warm plume water may further drive submarine melting at the glacier terminus and, subsequently, be a significant driver of retreat (Slater and Straneo, 2022). Whilst this study does not assess changes in ice velocity across the study period, it is noted by King *et al.* (2018; 2020) that the increasing trend in retreat post-2000 also initiated a step-increase in discharge caused by the perturbation to the glacier stress regime during retreat, further contributing to ice loss.

The asynchronous behaviour of terminus retreat observed between the northern and southern sectors of Humboldt Glacier also provides an interesting look into the long-term spatial complexities of the timing and magnitude of retreat across a single glacier. Retreat post-1999 has been predominately concentrated in the northern sector, with a maximum retreat of 13 km across 37 years and a loss of 7.1 km from 1999 to 2021, with average retreat rates an order of magnitude higher (93 m a^{-1}) than those in the south (9 m a^{-1}). This response can be largely attributed to differences in bed geometry between these two distinctive sectors (Carr *et al.*, 2015; Bunce *et al.*, 2018; Rignot *et al.*, 2021). The northern sector of Humboldt Glacier, as previously stated in Chapter 4 of thesis, is thicker (350–600 m), faster flowing (200–600 m a^{-1}), sits in deep water (300 m) within a trough that is ~475 m deep (reverse sloping in places) and extends ~72 km inland (Carr *et al.*, 2015; Rignot *et al.*, 2021). This promotes many internal and external factors that may not play as important a role in the southern sector, which is thinner (250–300 m), has slower flow (<100 m a^{-1}) and terminates in shallower water (<100 m; Rignot *et al.*, 2021). For example, greater driving stresses and the pronounced exposure of the northern face of the terminus increases the area vulnerable to submarine melting and subglacial plume processes. Also, crevassing within the lower 25 km of the northern calving front, which is heavily prevalent within the lowest 7 km as a result of high longitudinal stresses from its wide width, faster flow and dynamic thinning (van der

Veen, 1998; Carr *et al.*, 2015), can additionally facilitate calving and retreat through increased hydrofracture via the enhanced availability of meltwater from increasing air temperatures (Nick *et al.*, 2013); increased runoff of which has been shown in this work. Enhanced hydrofracture and crevassing has been previously linked to the retreat of Jakobshavn Isbræ Glacier via the impact of terminus crevassing and the weakening of lateral shear margins (Sohn *et al.*, 1998). Satellite imagery supports this mechanism at Humboldt Glacier, as shown by Carr *et al.* (2015) and in this study (Figure 5.22), as numerous water-filled crevasses are present within the highly-crevassed 25 km terminal zone, including the lower 7 km which is near floatation; an area which is more vulnerable to hydrofracture and full-thickness crevassing.

Another factor that also contributed to the break-up and retreat of Jakobshavn Isbræ was the seasonal formation and break-up of ice melange at the glacier front (Amundson *et al.*, 2010; Cassotto *et al.*, 2015). The presence of ice melange, which is a mixture of calved icebergs and sea ice, can form a strong, rigid mass aiding in the application of back-pressure and modulation of calving and ice flow (Amundson *et al.*, 2010; Foga *et al.*, 2014; Cassotto *et al.*, 2015). However, low melange concentrations and/or earlier seasonal break-up can extend the duration of seasonally high calving rates and promote enhanced interannual terminus retreat (Cassotto *et al.*, 2015; Bevan *et al.*, 2019; Cassotto *et al.*, 2021; Brough *et al.*, 2023), as seen in northwest Greenland (Carr *et al.*, 2015; Moon *et al.*, 2015). A reduction in ice melange at the front of Humboldt Glacier also has the potential to expose the wide Humboldt Glacier terminus to further increased internal and external pressures for longer time periods (i.e., rising air and ocean temperatures). In particular, its northern sector, which sits below sea level and in a trough that extends far back into the ice interior (~72 km) could be particularly vulnerable in the future to both reduced ice melange and enhanced exposure to submarine melt, which could be costly with the potential for runaway-type retreat if the

northern sector became detached from its northern pinning point due its deep trough setting (Carr *et al.*, 2015; Rignot *et al.*, 2021).

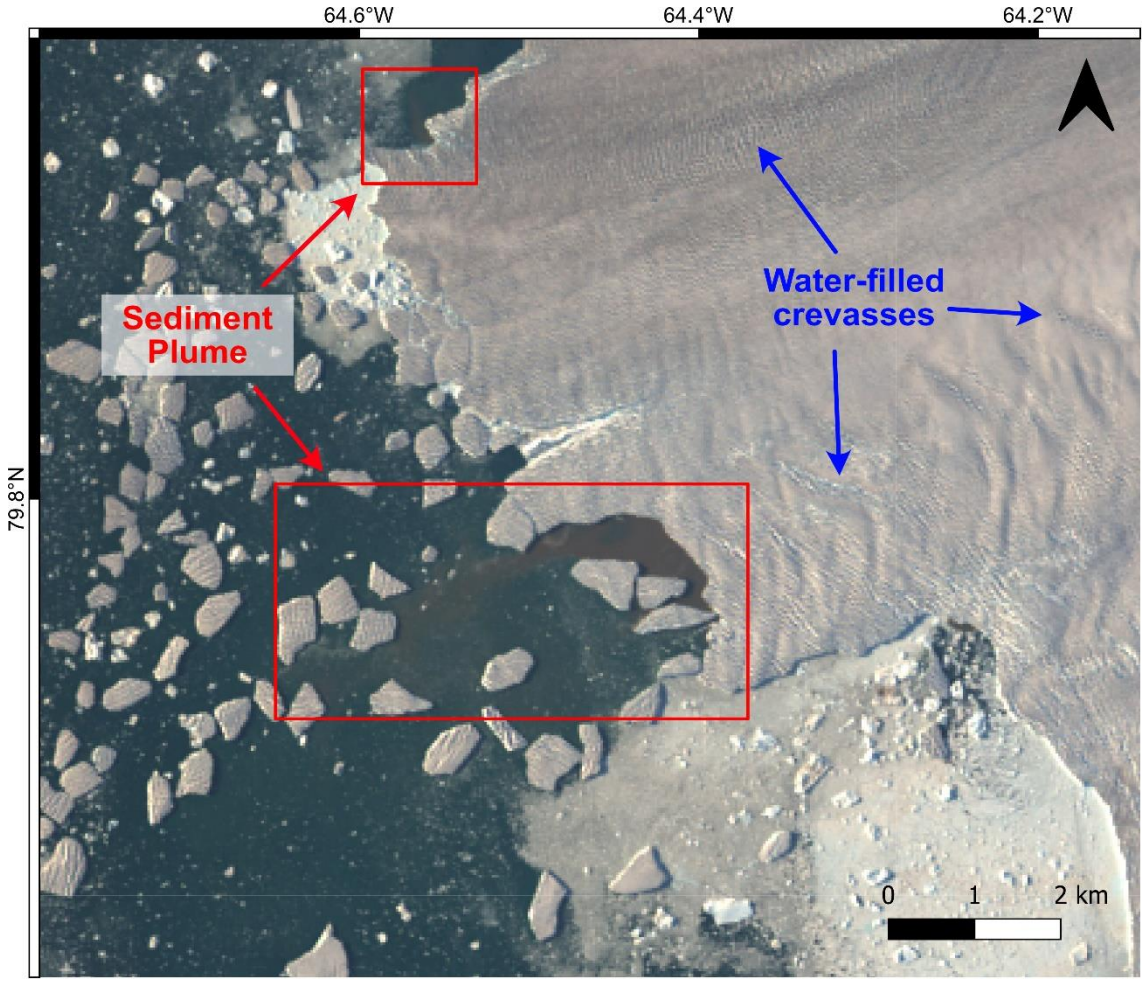

Figure 5.22. Landsat 8 image from 30th July 2019 showing the presence of two subglacial sediment-laden plumes (denoted by the red boxes) at the highly-crevassed northern edge of Humboldt Glacier terminus, providing evidence of an active subglacial hydrologic system with subglacial meltwater output into the Kane Basin.

5.4.2 Long term evolution of the supraglacial hydrologic network

Overall, the results presented in this Chapter provide evidence for an increase in the area of the supraglacial hydrologic network at Humboldt Glacier, as well as the inland expansion of this system over the study period between 1985 and 2021, including both supraglacial rivers and SGLs. Enhanced runoff, driven by increasing air temperatures, particularly post-2000, is

a significant driver of the expansion. Next, the impact of large interannual variability potentially driven by shifts in atmospheric circulation and the stability of the network overtime via bed control, is discussed.

5.4.2.1 Inland migration and area extent

Over the study period, the maximum elevation of the supraglacial hydrologic network increased by 432 m a.s.l (11.7 m a^{-1}), with a mean elevation increase of 293.6 m a.s.l (7.9 m a^{-1}), showing evidence of significant inland expansion across the 37-year period. Whilst, to-date, no other study has explored the long-term inland expansion of the whole supraglacial network (i.e., rivers and lakes), this study is able to confirm its glacier-wide inland migration that are consistent with numerous other observations based on SGLs from across the GrIS (Table 5.1).

Table 5.1. Mean and maximum elevation change of SGL inland expansion across the GrIS from relevant publications, with location of the study and time examined included.

Location	Time Period	Mean elevation change (m a.s.l)	Max elevation change (m a.s.l)	Publication
North-west GrIS *(74.5 °N, 55.9 °'W)*	1985-2016	299	418	(Gledhill and Williamson, 2018)
Sermeq Avannarleq Glacier, West GrIS *(70.1 °N, 50.2 °W)*	2000-2020	300	200	(Zhu *et al.*, 2022)
Ryder Glacier, North GrIS *(81.2 °N, 49.8 °W)*	1985-2020	280	-	(Otto *et al.*, 2022)

The supraglacial hydrologic network across the study period peaked at 1464 m a.s.l in 2021, which is 400 m lower than surface hydrologic observations on southwestern GrIS (~1800 m a.s.l; Yang *et al.* (2021)), which also agrees with observations by Ryan *et al.* (2019) who found maximum snowline elevation to be 400 m lower on northern GrIS than that of southwest GrIS. Alongside the expansion of the supraglacial hydrologic network to higher elevations, the network has also doubled in area (98.5%), with the supraglacial river network area alone increasing by 100.7% and SGL area increasing by 80.5%, with notable accelerations during the 21st Century.

The migration and expansion of the supraglacial hydrologic network appears to have been driven by increases in summer (JJA) surface temperatures which promotes surface melting and runoff across greater portions of the GrIS (Howat *et al.*, 2013), as modelled by the regional climate model MAR in this study. As already mentioned in Section 5.4.1, air temperatures have significantly increased since the 1990s extending from the coastline across the ice sheet, with areas of strongest warming experienced in northern Greenland (Orsi *et al.*, 2017; Hanna *et al.*, 2021) and a corresponding increase in melt extent, intensity and duration particularly concentrated in the last two decades (Steffen *et al.*, 2004; Fettweis *et al.*, 2011; Tedesco *et al.*, 2011; Nghiem *et al.*, 2012; Tedesco *et al.*, 2016; Cullather *et al.*, 2020; Tedesco and Fettweis, 2020). As a result, north Greenland's contribution to total GrIS mass loss through enhanced runoff has significantly increased. Its ablation area has expanded by 46% since 1990 (compared to 25% expansion in southwestern Greenland), with runoff acceleration overtime triggered by rapid snow line retreat, earlier seasonal bare ice exposure and the amplification of subsequent runoff (Noël *et al.*, 2019).

The relationship between maximum drainage elevation and runoff is shown to significantly correlate in this study, more so than increase in drainage area over time, which may be linked to the state of the percolation zone in the lower accumulation area and network efficiency.

At higher elevations, meltwater is able to percolate into porous snow and firn, where it may either fill pore space and subsequently be released as liquid water once saturation is reached or refrozen into distinctive high-density, impermeable ice lenses, with this zone ultimately controlling whether melt runs off or is retained (Steger *et al.*, 2017a; Culberg *et al.*, 2021). As shown by MacFerrin *et al.* (2019), ice slabs began forming during 1990–2000 and have thickened and become widespread along western and northern margins of the ice sheet, leaving these areas highly vulnerable to enhanced runoff. The observation of increased runoff being closely related to higher elevation drainage networks therefore could relate to how much of the percolation zone is already saturated in a given year, particularly if following a successive number of high temperature years, which may drive the quicker, more efficient transition and emanation of melt as runoff from such regions into the well-established surface hydrologic systemat lower elevations (Yang *et al.*, 2021). This is instead of melt saturating and pooling in the leftover snowpack within the ablation zone or saturated firn before the creation of slush-filled rills, which can increase drainage area but not necessarily increase transportable runoff.

Across the whole study period, MAR-modelled runoff increased by 80% at Humboldt Glacier between 2010 and 2021 and annual runoff was 23% higher than the preceding decade (2000–2009); findings that are consistent with those by Slater *et al.* (2020) who found Greenland-wide runoff was 21% higher between 2011 and 2020 than the preceding three decades. During this period, a number of large runoff anomalies were recorded. These anomalies coincided with increased maximum elevations of the supraglacial network which also corresponds to higher supraglacial network elevations (11% greater than the previous decade) and larger mapped drainage areas (52% greater). In particular, a number of notable Greenland-wide extreme melt events occurred during this decade, including 2012 and 2019 (Nghiem *et al.*, 2012; Tedesco and Fettweis, 2020), which recorded 1.5 standard deviations above the decadal mean in this study. Such extreme events, particularly the summers of

2012 and 2019, saw Greenland-wide record-breaking mass losses as a result of higher air temperatures and strong runoff promoted by atmospheric conditions of the North Atlantic Oscillation (NAO) and Greenland Blocking index (GBI; (Bevis *et al.*, 2019). An intensely negative NAO alongside a strong GBI can promote the prevalence of high pressure, clear skies, the enhancement of surface absorption of solar radiation and the northward advection of warm air from southern latitudes (Fettweis *et al.*, 2013; Bevis *et al.*, 2019; Tedesco and Fettweis, 2020), driving increased melt and an enhanced response from the surface hydrologic network to transport and evacuate such melt. Whilst this study has seen a long-term upward trend in drainage area and elevation over 37 years, and thus inland expansion of the hydrologic network, large interannual variability in atmospheric circulation is highly likely to play a role in the response and behaviour of this surface network in certain years.

In contrast to extreme melt events, a number of years with low JJA temperature anomalies and low runoff are also observed, resulting in the supraglacial network area being smaller and constrained to lower elevations (<800 m a.s.l). Such low melt years include 2000, 2004 and 2006. The limited areal coverage (96 km^2) and elevational extent (957 m a.s.l) of the drainage network in 2006, for example, corresponds to similarly mapped low snowline elevations by (Ryan *et al.*, 2019), with the smallest mapped extent of bare ice between 2001 – 2017 occurring during this year, which only saw bare ice exposed across 10% of the GrIS. A lack of SGLs mapped >800 m a.s.l in this northern region of Humboldt Glacier during 2006 was also observed by Sundal *et al.* (2009). Similarly, in low melt years of 2017 and 2018 (1.1 to 1.5 standard deviations below the decadal mean, respectively), the elevational extent of the hydrologic network was limited to <1100 m a.s.l which was substantially lower (14% and 20% respectively) than the average maximum decadal elevation and opposite to the extensive neighbouring melt seasons of 2016 and 2019 (1411 m a.s.l and 1324 m a.s.l respectively). Behaviour of the NAO and GBI can significantly modulate the mass loss of the GrIS, with positive phases of the atmospheric circulatory systems promoting cooler

temperatures and heavier snowfall, dampening the effects on runoff during summer, as seen in 2017 and 2018. This study has shown how sensitive the supraglacial drainage network can be to such changeable external, atmospheric variables.

5.4.2.2 Evolution of network characteristics

The expansion of the supraglacial hydrologic network over time has been largely driven by changes at the highest elevations (Figure 5.11 and Figure 5.14), predominantly through the lengthening of supraglacial river channels, building upon the already-stable generalised structure of primary river channels that persist year-on-year across the study period <1000 m a.s.l. As shown by Poinar *et al.* (2015), supraglacial river channels, in general, tend to lengthen at higher elevations, with channels as long as 40 km reported above 1700 m a.s.l in West Greenland and, in this Chapter, channels extending up to 30 km in length. Compared to the supraglacial network in the earlier years of this study (pre-2000), it was more compact with shorter river lengths meaning runoff may have had a 'flashier' response, with less transport time to reach storage or terminal points (i.e., moulins, terminal lakes or the ice edge). With the observed extension of the network overtime and absence of terminal points (i.e. moulins and lakes) at elevations > 1000 m a.s.l, inferred from undisturbed river channels, meltwater now has a greater distance to travel, presenting potential delays to meltwater reaching non-local moulins further downstream, which may impact the timing and magnitude of melt on the subglacial system, particularly diurnal cycles (Smith *et al.*, 2021). There is the possibility, however, that high-elevation surface-to-bed meltwater connections (>1600 m a.s.l), even during a colder-than-average melt season, may occur in the near future if ice thickness permits, as observed by Yang *et al.* (2021) in Western Greenland. As SGLs are already forming at progressively higher elevations and covering greater extents, particularly increasingly larger SGLs within the mid-to-upper ablation zone, the likelihood of SGLs that have not drained before becoming drain-active in the near future will undoubtedly

supply meltwater to new areas of the ice-bed interface with potential ice dynamic implications (Howat *et al.*, 2013).

The yearly recurrence of rivers at higher elevations (>1200 m a.s.l) shown in this study is also highly variable, with a maximum recurrence interval of 11 years (Figure 5.14). This is likely down to two reasons. Firstly, these high elevation channels have only started to consistently encroach above 1200 m a.s.l since 2008 at Humboldt Glacier, which has coincided with ablation area expansion and increased melt and runoff in the northern regions (Noel *et al.,* 2019). Secondly, the network now occurs here consists of tributary channels that are typically narrower and shallower in profile and more transient in nature (Pitcher and Smith, 2019; Rawlins *et al.*, 2023). This means that they have the ability to frequently change location, unlike their well-established deeply incised counterparts downstream. In the lower elevation regions of Humboldt Glacier, the supraglacial river network has largely remained shorter and fragmented, with smaller SGL sizes that are largely persist throughout the 37-years, except within the lower terminus reaches (<25 km) where the highly crevassed zone and small ponded lakes can drain or advect.

Throughout the study period, the generalised supraglacial drainage structure at Humboldt Glacier has retained high re-occupancy rates below 800 m a.s.l, with much of the network reforming in the same location each year despite ice advection; an acknowledged bed-to-surface topographic control for hydrologic components such as SGLs (Ignéczi *et al.*, 2018). Their long-term configuration, however, is interestingly aligned to topographical controls identified in Chapter 4 of this thesis (cf. Rawlins *et al.*, 2023). Two parallel basal structures, that are shown as depressions in the DEM and are expressed as such on the ice surface, are also evident in mapping of the long-term evolution of the generalised supraglacial hydrologic network of Humboldt Glacier conducted in this study (Appendix B, Figure B1). Many supraglacial rivers and lakes are aligned to such structures from the beginning of the

study in 1985, as shown further in Figure 5.23. Running from a northwest to southeast direction, these topographical influences are visible in the generalised drainage structure of the supraglacial network therefore signifying they play a long-term significant role in the configuration of the network.

5.4.2.3 Components of the supraglacial hydrologic system

This study found that the area of the supraglacial hydrologic network on Humboldt Glacier predominately consists of supraglacial rivers (80%), with the remainder comprised of supraglacial lakes, largely those that are greater than 0.1 km^2 in size. There is large interannual variability in the contribution of rivers versus SGLs to the total area of the hydrologic system, which may be a result of (i) the networks efficiency at transporting and/or storing increasing amounts of runoff; (ii) the interannual variability of runoff; (iii) the relative location of where maximum melt occurs and where there are surface depressions to harbour SGLs, and; (iv) how quickly into the melt season SGLs drain, whereby in higher melt years, SGLs may fill and drain early and not refill due to moulins remaining open as a hydrologic conduit if constant meltwater is supplied (Das *et al.*, 2008; Liang *et al.*, 2012; Stevens *et al.*, 2015; Hoffman *et al.*, 2018). SGL area played a more important role in the supraglacial network between 2000 and 2009 than the other three decades covered across the study period, with the years 2004 and 2006 accounting for the highest SGL percentage of network composition (37% and 53% respectively) whilst also being years with the overall lowest drainage areas.

During 2010–2021, however, a further runoff increase occurred concurrent with an increase in the supraglacial network of 62% (11.8 m a^{-1}) and a decrease in average SGL area by 35%. This increase in the supraglacial river component of the network and subsequent reduction in SGL suggests that over time, rivers continue to become the prominent hydrologic component as they stretch inland to higher elevations, with the potential for less availability

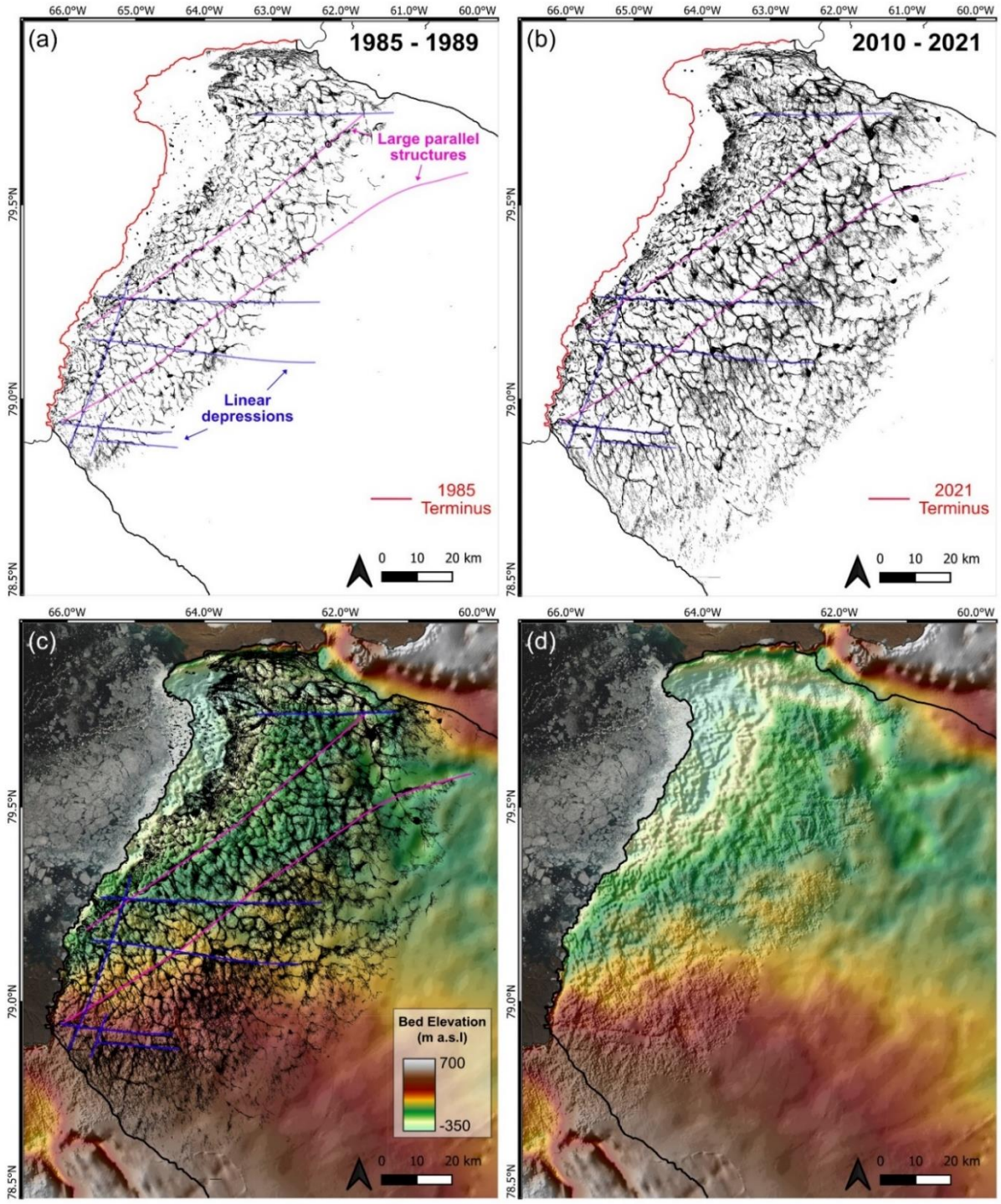

Figure 5.23. Bed topography via BedMachine (Morlighem *et al.*, 2020) showing linear structures as bed depressions and their influence on the long-term (1985–2021) configuration of the supraglacial hydrologic network. (a) The mosaicked supraglacial hydrologic network between 1985–1989 aligned along bed impressions denoted by the pink and blue lines; (b) the collective supraglacial hydrologic network between 2010–2021 showing network configuration and bed influence as the network has lengthened and migrated inland overtime; (c) the fully mapped 1985 – 2021 generalised supraglacial hydrologic network with the bed-to-surface impressions shown like (a-b); (d) BedMachine allowing such depressions to be visualised.

of surface depressions at these higher elevations for meltwater ponding and SGL development. As shown by Lu *et al.* (2021) in northeast Greenland, the contribution of supraglacial rivers to meltwater area also similarly accounts for a larger percentage (83.8%) of the network, with SGLs playing a less dominant role due to few lakes >800 m a.s.l, due to surface topography constraints (Igneczi *et al.*, 2016); similar to observations at Humboldt Glacier whereby 75% of SGLs were found <600 m a.s.l. In contrast, in other ice sheet regions, for example in western and southwestern Greenland, supraglacial rivers are shown to contribute less to the overall supraglacial network (62.3%), whereas there are more SGLs which thus make a more substantial contribution.

5.4.2.4 Supraglacial lakes

Focussing upon SGL characteristics alone over the time period, the number of SGLs did not significantly change despite observed inland progression. The loss of 7% of total SGLs from terminus retreat of Humboldt Glacier is ultimately accounted for in the formation and increased encroachment of new SGLs further inland >1000 m a.s.l from 1998 and >1200 m a.s.l from 2003. The maximum elevation of SGLs over time showed a clear and significant upward trend increasing by 296.4 m a.s.l over 37 years, with an average elevation increase of 138.6 m a.s.l. This rate of inland expansion of SGLs-only at Humboldt Glacier is in-line with a similar study by Otto *et al.* (2022) who found an average elevation increase of between 90 and 280 m a.s.l at Ryder Glacier, north Greenland. However, comparing this to the inland rate by Gledhill and Williamson (2018) from northwest Greenland between 1985-2016, the rate at Humboldt Glacier is lower, which may be due to the reduced availability of surface depressions above the ELA (Igneczi *et al.*, 2016).

This expansion of SGLs inland at Humboldt Glacier over the study period has also largely followed the pattern of surface depressions, as seen in Figure 5.15b, as these provide favourable conditions for SGL formation (Lüthje *et al.*2006; Ignéczi *et al.*, 2018; Otto *et al.*,

2022). SGL size has remained almost constant between 200–400 m (0.31 km^2), likely due to lakes reaching their maximum available area, with regional topographical controls playing an important controlling factor here, including (i) the high occurrence of crevassing preventing lake growth, (ii) the steeper ice sheet surface at lower elevations and (iii) the potential for frequent lake drainages as they reach sufficient melt volume for hydrofracture potential (Krawczynski *et al.*, 2009). In contrast, at higher elevations, SGLs are also shown to have larger individual mean sizes and occur at such elevations during progressively warmer years, likely due to the potential for such lakes to accommodate additional melt due to their shallow yet expansive size, which is in agreement with other work (Sundal *et al.*, 2009; Liang *et al.*, 2012; Fitzpatrick *et al.*, 2014; Gledhill and Williamson, 2018). Surface depressions beyond current locations also provide potential preferable future locations of SGLs with continued inland migration, as depressions are primarily controlled by bed topography and therefore their location is unlikely to significantly change (Lampkin and VanderBerg, 2011; Igneczi *et al.*, 2016). How many further inland depressions within the Humboldt Glacier catchment that have the ability to pond and form SGLs is, however, difficult to distinguish due to the bed-to-surface topographical transfer from changing ice thickness, further explored in the future of Humboldt Glacier in Chapter 7.

5.5 Conclusion

In this Chapter, the long term, multi-annual evolution of the supraglacial hydrologic network is mapped and quantified for the first time at Humboldt Glacier, north Greenland, between 1985 and 2021. Landsat archival imagery via Google Engine Earth (GEE) and an automatic river detection algorithm are used to create annual meltwater maps of the hydrologic network during the key melt season months of June, July and August (JJA), with GEE images additionally utilised to assess terminus change over the same period. Across 37 years, Humboldt Glacier retreated an average of 4.7 ± 0.09 km and a maximum of 13.4 ± 0.03 km,

with 87% of this retreat occurring in the faster flowing northern sector post-1999 at rates an order of magnitude higher than the southern sector. This is attributed to greater terminus exposure of the northern sector to internal and external factors, such as (i) inputs of surface meltwater and hydrofracture potential promoting faster flow in its deep subglacial trough and calving, (ii) increased submarine melt rates from oceanic warming and subglacial plume activity and (iii) earlier seasonal break up and long-term reduction in ice melange. The supraglacial hydrologic network has increased in areal coverage by 98% over 37 years, with a mean and maximum expansion inland of 293 m (7.9 m a^{-1}) and 432 m (11.7 m a^{-1}), respectively; in-line with an 80% increase in meltwater runoff overtime. The largest network expansion occurred between 2010 and 2021, however large interannual variability related to the North Atlantic Oscillation and Greenland Blocking Index (GBI) plays a key role in the response and behaviour of the network to meltwater availability. Of this expansion, supraglacial channels account for 80% of the network, with already-existing channels that are structurally-stable <1000 m a.s.l increasing in length overtime to higher-elevation regions, up to a maximum of 1464 m a.s.l recorded in 2021. The total area of SGLs and their individual size increased by 81% and 174%, respectively, following the pattern of surface depressions inland, with longer wavelength bed undulations at higher elevations promoting their increased size. Such bed-to-surface topographic influences, including two parallel geological-basal structures identified in Chapter 4, are reidentified in this work and shown to control the long-term generalised configuration of the network over 37 years.

This work shows the value of using Landsat imagery and GEE in furthering understanding of the supraglacial hydrologic network's evolution over long timescales, despite image resolution (30 m) and the ability to extract the generalised-structure only. Further long-term mapping from other GrIS regions and beyond are advised to aid in understanding of network evolution over time and the hydro-dynamical responses to runoff in different ice sheet sectors in the past and present in order to better predict behaviours into the future.

Chapter 6

Investigation into supraglacial microchannels, surface facies and inter-stream networks using ultra-high-resolution imagery from UAVs and WorldView-2

For fieldwork and data obtained for this chapter, which was conducted at Russell Glacier, southwest Greenland in 2019, I would like to acknowledge its collection within the territories of the Greenlandic people and thank them and their Elders both past, present and future, for allowing access to their precious land.

6.1 Introduction

The use of satellite imagery has revolutionised our ability to detect and quantify geographical features, and in turn, continues to drive our understanding of the physical landscape. The use of freely available imagery, such as Landsat-era and Sentinel-2 imagery, allows for the extraction and quantification of surface features essentially equivalent to the pixel size, in this case the generalised supraglacial drainage structure of the GrIS surface (Landsat) down to tributary type river channels (Sentinel-2) as studied in Chapter 4 and 5. However, our ability to confidently observe the existence of surface features which are smaller than this poses significant challenges due to resolution restrictions, with implications for fine-scale feature extraction. Many fine-scale supraglacial features have low spatial coverage and occur at spatial scales below such freely available imagery, including narrow stream channels (<10 m) which have been observed to exist as inter-stream tributary-style networks (Smith *et al.*, 2015; Yang *et al.*, 2022), microchannels (<0.5 m; Rippin *et al.*, 2015) and surface fractures such as crevasses (Chudley *et al.*, 2021).

The last decade has seen a rise in the use of uncrewed aerial vehicles (UAVs) and optical sensors for the production of ultra-high-resolution data from field-based studies, with the production of orthomosaics and digital elevation models (DEMs) from Structure-from-Motion stereo-multi vision (SfM-MVS, herein referred to as SfM) providing new opportunities for observational, field-based studies within the field of glaciology (Bhardwaj *et al.*, 2016). For example, Rippin *et al.* (2015) mapped supraglacial drainage pathways over the lower reaches of Midtre Lovénbreen, Svalbard, with high resolution (0.05-0.1 m) UAV imagery revealing an extensive network of small meltwater channels, termed microchannels, ranging between a few centimetres to tens of centimetres wide. Chudley *et al.* (2021) have since been able to detect and classify the presence of surface meltwater and crevasses over a small region (~2,700 km^2) of western Greenland, with the authors suggesting that the observed

ponding and rapid drainage of melt likely occurred via hydrofracture. In contrast to the relatively coarse resolution of remotely sensed images, UAV-derived imagery is better equipped to aid in the extraction of such features with similar spectral signatures, both with each other and with the ice surface (Yang and Smith, 2013).

Debris and microbe-rich ice surfaces composed of fine, dark material called cryoconite, made up of emergent dust deposits, black carbon, and organic matter such as pigmented algal blooms, dominate the upper ~0.3 m of the ablating ice surface within a porous weathering crust, particularly on the western and southwestern GrIS lower ablating margins (Moustafa *et al.*, 2015; Cooper *et al.*, 2018). Cryoconite presence, whether within holes that are melted downwards into the ice (cryoconite holes) or distributed as sediment-type deposits across the surface, can become hydrologically connected via melt transport and consolidated into supraglacial stream beds creating a complex environment. This can create similar spectral properties between different surface facies (I,e., water, cryoconite and the ice surface) causing difficulties in independent feature extraction (Gleason *et al.*, 2016; Leidman *et al.*, 2021b). In particular, the use of automated approaches, such as the automatic river detection algorithm developed by Yang *et al.* (2013; 2015a; 2017) and used throughout this thesis (Chapter 4 and 5), is challenging to implement as it relies on a strong contrast between supraglacial river and/or stream channels and background ice (Yang *et al.*, 2019b). Instead, supervised classification techniques, such as those implemented by Ryan *et al.* (2018) and Leidman *et al.* (2021a) have been successfully used to explore the surface characteristics of the near-margin ablation zones of SW GrIS from UAV imagery, with the former investigating a 25 km east-west transect starting ~10 km from the ice edge and dissecting into the dark zone, and the latter exploring a 1.3 km^2 area and the impact of terrain shadowing on surface facies classification.

Whilst field-based studies are incredibly valuable, for example in the lower reaches of a glacier or ice sheet, they can be challenging to conduct in isolated regions, particularly at higher elevations on the GrIS, where little is known about the finer-scale hydrologic networks at scales beyond freely available imagery (<10 m). Such shortcomings can be somewhat addressed through the advent and use of commercially-available satellite imagery, such as the WorldView (WV) series, which allows fine-scale mapping of features with widths varying between a metre to tens of metres with wide spatial coverage (Yang and Smith, 2013). WV imagery is a commercial-based Earth imaging series of satellites owned by Maxar which have been supplying imagery since its first launch of WV-1 in 2007. To date, four Worldview-satellites have operated, with the latest satellite, WV-4, launched in 2016 and decommissioned in 2020. Of particular interest in this series is the WV-2 satellite launched in 2009, which was the first high resolution, 8-band multispectral commercial satellite in operation, providing both panchromatic imagery at 0.4 m resolution and eight band multispectral imagery at 1.85 m with a capacity to cover 1 million km^2 day^{-1} (Maxar, n.d). Unsurprisingly, such imagery has been increasingly used within the glaciological community over recent years, particularly within the study of glacio- and ice sheet hydrology, due to its ability to accurately map narrow supraglacial features (1-10 m wide), such as supraglacial streams (Yang and Smith, 2013; Chu, 2014), over areas-of-interest that would otherwise be indiscernible in freely available imagery due to resolution impacts or impractical to survey via field-based approaches. For example, studies by Smith *et al*. (2015) and Yang *et al*. (2016) used WV-1 and WV-2 imagery to map the existence of an extensive inter-stream network of thin tributary channels across small regions of the bare ice zone in the southwestern region of the GrIS in addition to larger, main-stem river and tributary networks, which are typically delineated from Landsat and Sentinel-2 imagery, respectively. However, due to the cost for this sub-metre high resolution imagery, the ability to produce large scale mapping and monitoring of such features can be limited. That said, WV-2 imagery with a resolution of ~0.4

m for panchromatic imagery and 1.85 m for optical imagery, provides unique opportunities for confidently mapping features such as narrow inter-stream tributary networks in areas yet to be mapped.

With these studies in mind, the aim of this chapter is to utilise both UAV-derived and WV-2 imagery to explore the minute (cm-m scale) characteristics of two very different ablating zones of the GrIS to further investigate the meltwater characteristics that comprise (i) the spectrally-complex ice marginal zone (<1 km) and (ii) the bare ice zone (25 km). The objectives for this Chapter are to:

(i) Use UAV imagery to survey a small area of the ice marginal region of Russell Glacier, southwest Greenland, to derive SfM orthomosaics for the mapping of supraglacial streams and microchannels (cm-m scale)

(ii) Use the UAV-derived orthomosaic model to characterise surface facies of the ice surface to further explore the complex morphology of this ice marginal region.

(iii) Use commercial-based WV-2 imagery to map and explore the potential for inter-stream tributary networks (>1 m scale) in a section of the bare ice zone at Humboldt (Sermersuaq) Glacier, northern Greenland.

6.2 UAV methodology

6.2.1 UAV platform, mission planning and survey operation

The UAV survey was conducted on-ice ~300 m east from the north-western ice margin (~556 m a.s.l) at Russell Glacier; a land-terminating glacier on the southwest coast of Greenland, ~35 km from the nearest town of Kangerlussuaq Figure 6.16.1a-b). The ice surface in this region is rugged, with highly undulating terrain (Figure 6.1c) is intersected with meltwater streams littering the surface and the existence of a widespread weathering crust; a porous surface layer of ice ~0.3 m thick (Moustafa *et al.*, 2015) underlain by impermeable ice formed

by shortwave radiation penetrating below the surface, causing 'internal' melting (Cooper *et al.*, 2018; Woods and Hewitt, 2022).

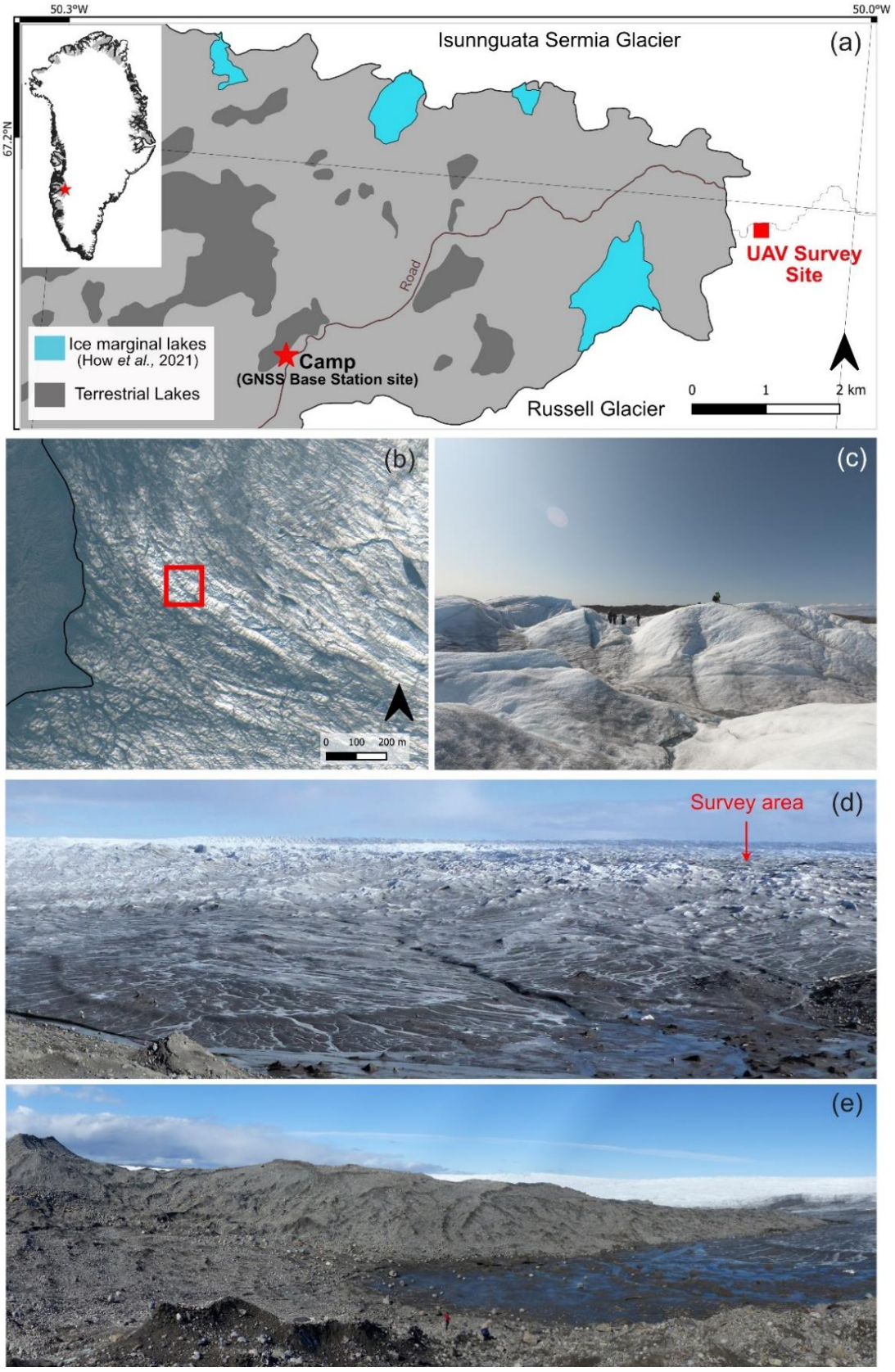

Figure 6.1. (a) UAV survey site in the ice marginal region of Russell Glacier, southwest Greenland. Ice marginal lakes are sourced from How *et al*. (2021) and Two Boat Lake Camp is denoted by the star; (b) WV-2 RGB image of the field location with red box highlighting UAV survey area; (c) image of field location showing the undulating terrain (people for scale); (d) View of the ice marginal region of Russell Glacier from the Little Ice Age moraine showing the widespread undulating ice surface topography and expanse of meltwater streams. Approximate survey location labelled; (e) Image showing the Little Ice Age moraine in close proximity to the survey site (~800 m north; person for scale)

To the west (~300 m) and north-west (~800 m; Figure 6.1) of the surveyed area is a ~50 m high ice-cored Little Ice Age moraine (Figure 6.1e). The UAV survey covered a total area of 7417 m^2 and was conducted at 13:36 local time (West Greenland Summer Time; GMT-2) on the 9th August 2019 on a clear, sunny day, with the calculated sun azimuth angle at ~213° (southwest) and sun elevation angle at ~35°. Solar noon occurred at ~13:25, so melt was relatively high across the surface during the surveyed flight. However, this was not at peak flow as this does not typically occur until ~16:00 during August (Muthyala *et al.*, 2022).

The UAV used for surveying was a DJI Phantom 3 Pro quadcopter (Figure 6.2a) with a built-in bottom-mounted 12-megapixel camera with 94° field of view, built-in GPS and GLONASS. To optimise the number of images taken and to ensure that sufficient overlap was attained across images (a frontal overlap of 80% and a side overlap of 75%), flight paths were pre-programmed in Pix4DCapture software (*PIX4Dcapture*, 2019) and adjusted accordingly at the survey location. Other prior planning and checks with the UAV are summarised in Figure 6.2, alongside field-planning and post-processing steps. The survey was flown at a height of 30 m above the take-off location in a 58 m x 56 m grid with the camera in nadir angle and took ~7 minutes to complete. With the front and side overlap included, this resulted in a UAV-footprint of ~7417 m^2. This scene was largely representative of the ice marginal zone within 1 km of the ice edge.

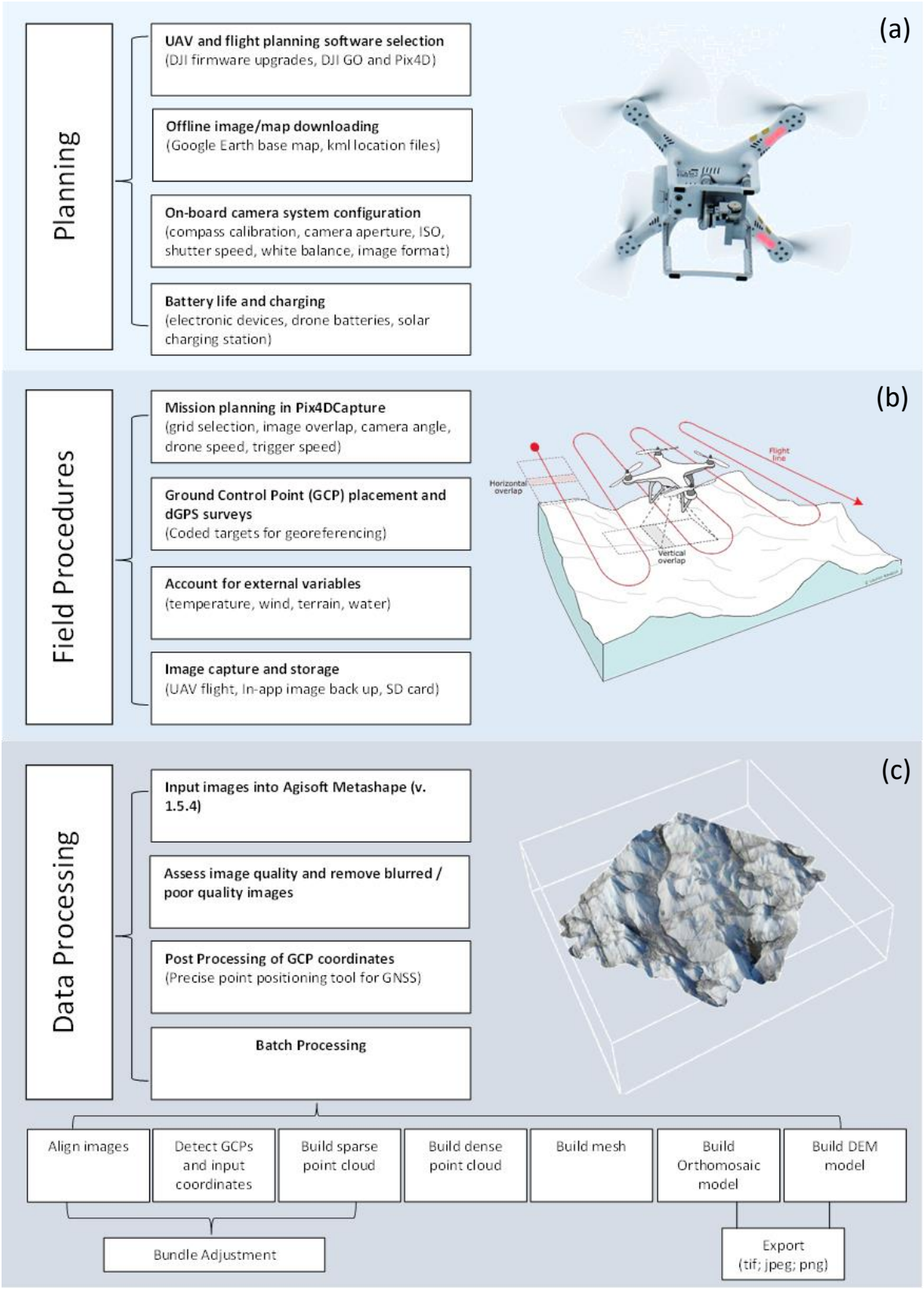

Figure 6.2. Schematic showing the workflow for (a) UAV planning, (b) field procedures and (c) data processing to produce SfM models.

To aid in the accurate georeferencing of photogrammetric models during the post-processing phase, five coded GCPs (white rectangles with black circular patterns downloaded from Agisoft Metashape Pro for clear identification in post-processing) for accurately geo-referencing photogrammetric models in post-processing, were placed homogenously throughout the survey scene (Figure 6.3a, 6.3b). A Trimble R8 GNSS Rover was used to record GCP coordinates (Figure 6.3c). The Trimble R8s GNSS Rover recorded the central coordinates (x, y, z) of five individual GCPs, with the rover stationary and recording its static location every second over the central GCP point for ~20 minutes.

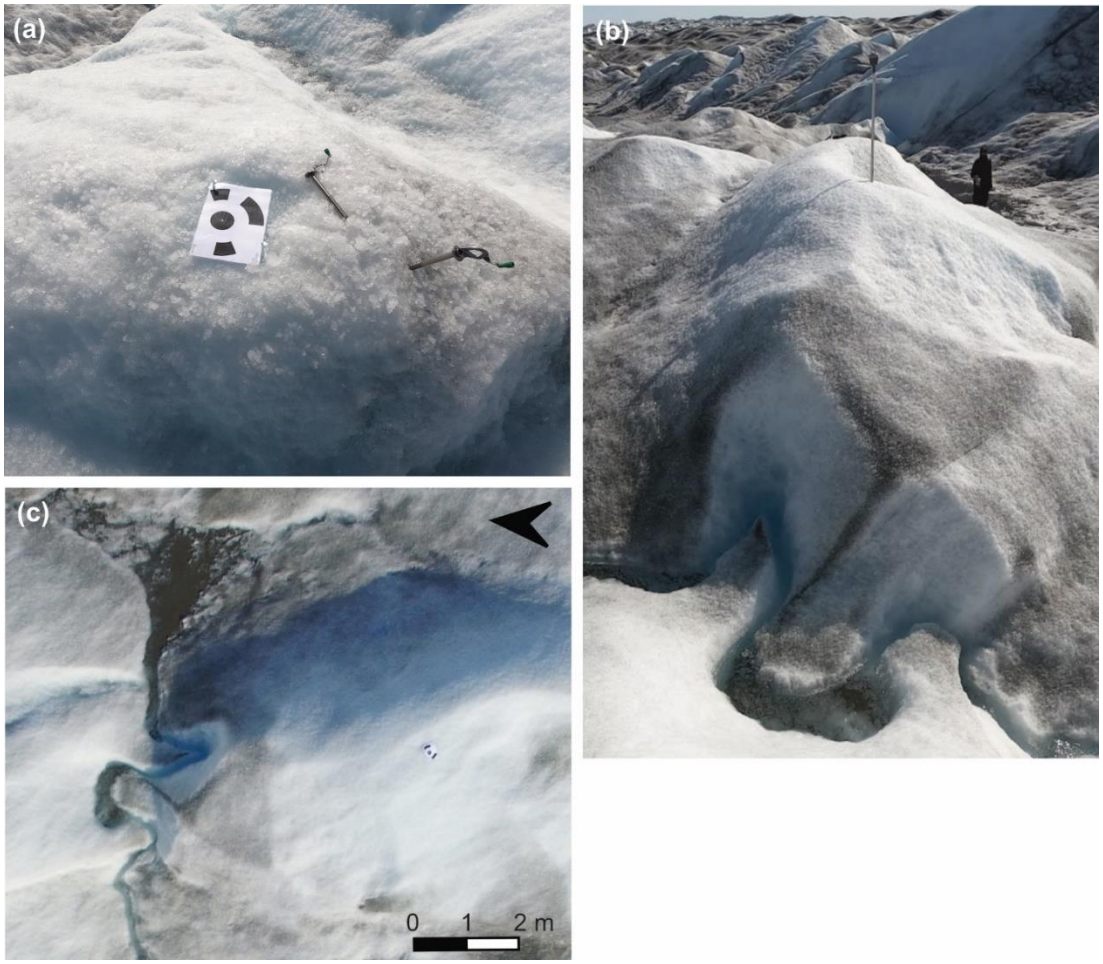

Figure 6.3. (a) Example of a coded GCP installed in the survey location; (b) image showing the Trimble R8 rover sampling the GCP (person for scale) with a microchannel in the foreground; (c) the same GCP from (b) observed from the UAV along with the identifiable microchannel.

Recorded GCP coordinates post-survey were subsequently post-processed using the Canadian online Precise Point Positioning (PPP) tool via Natural Resources Canada (https://webapp.csrs-scrs.nrcan-rncan.gc.ca/geod/tools-outils/ppp.php) to calculate their positions and a mean coordinate value generated from individual surveyed readings for each GCP. Mean latitudinal accuracy of GCPs was 0.008 m, longitudinal accuracy was 0.009 m and vertical (elevational) accuracy was 0.01 m.

6.2.2 SfM model generation

To process the UAV-derived imagery into a high resolution orthomosaic and DEM of the study region (~7417 m^2), the photogrammetric software package Agisoft Metashape Pro (v1.6.3; 2020) was used. Following an initial quality assessment (i.e., identification and removal of any blurred images), a total of seventy-five images were imported into the SfM workflow model and camera positions aligned using high accuracy settings (

Table **6.1**), with common points matched across images and a sparse point cloud displayed. The five PPP-processed GCPs from the survey were added to the workflow and manually identified in individual images for enhanced accuracy: GCP-1 was identified in twelve images; GCP-2 was identified in ten images; GCP-3 was identified in three images; GCP-4 was identified in eight images and; GCP-5 was identified in fifteen images. As GCP-3 was only identified in three images and had a higher overall pixel error due to this (0.9 m), which further increased the model error by 0.32 m, this GCP was removed for further processing (Figure 6.4).

Table 6.1. Agisoft Metashape Pro (v1.6.3) settings for SfM sparse and dense point generation and subsequent GCP errors for SfM processing. GCP-3 was removed from SfM processing due to its high error (m) in relation to other GCPs used throughout the survey scene.

Alignment	
Accuracy	High
Pair Preselection	Generic
Key Point Limit	500,000
Tie Point Limit	10,000
Ground Control Points (GCPs)	
GCP Number	**Error (m)**
GCP-1	0.15
GCP-2	0.07
GCP-3	0.9
GCP-4	0.08
GCP-5	0.05
Dense Cloud Construction	
Quality	High
Depth Filtering	Aggressive

Once the GCPs were added, camera positions were then optimised using the now-known GCP coordinates via bundle adjustment, reducing georeferencing errors from the sparse point cloud (Agisoft Metashape Professional Edition, V1.6, 2020). The final sparse point cloud contained a total of 137,796 tie points. A final dense point cloud, made of 29,435,694 points was then produced using high quality and aggressive depth filtering parameters (

Table **6.1**). A DEM with a resolution of 0.018 m pix^{-1} and an orthomosaic with a resolution of 0.009 m pix^{-1} were created. Both the orthomosaic and DEM models have an overall projection error of 0.09 m (easting = 0.01 m; northing = 0.05 m; elevation = 0.08 m). Both the orthomosaic and DEM were the exported from Agisoft Metashape Pro using the UTM 22 N projection for further analysis.

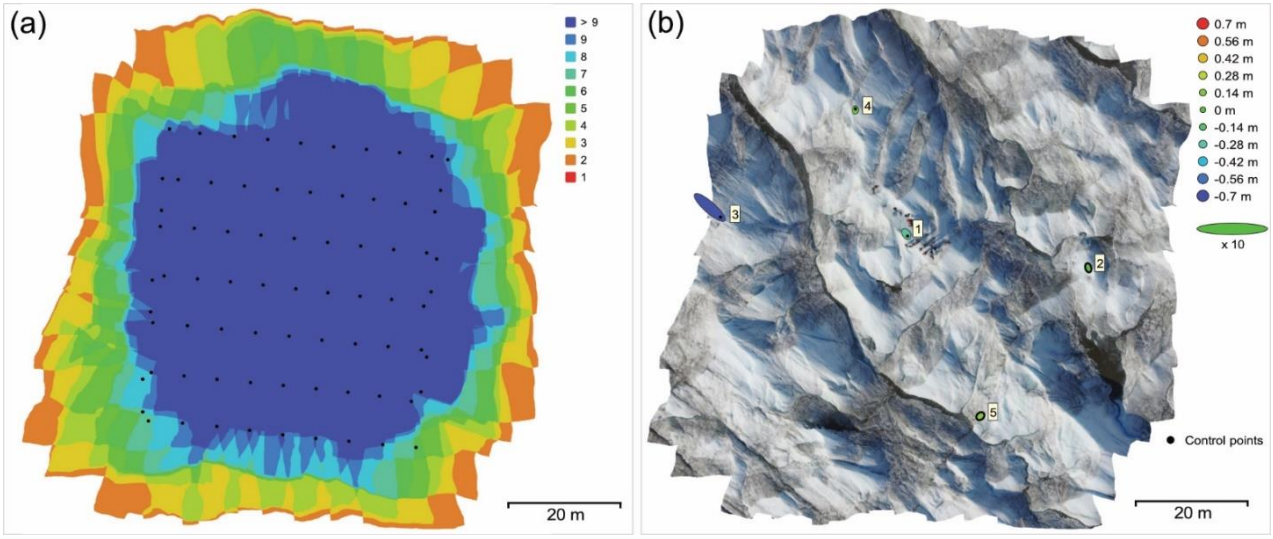

Figure 6.4. (a) Figure showing the number of UAV images that covered the survey area, ranging between 1 and >9 images. Black dots represent the actual flight grid flown by the UAV for image capture; (b) output orthomosaic with GCP positions pinpointed. GCP points have a size and colour associated with them; the larger the circle, the larger the associated positional error of the GCP, with colour representing a positive (red) or negative (blue) error. Note GCP-3 has a large negative error associated with it, hence its removal from the final models.

6.2.3 Shadow correction of the orthomosaic model

The identification of surface features (i.e., meltwater channels) and their classification is an important aspect of understanding the composition of ice surfaces and the effect of surface melt. However, an issue that often complicates such identification and classification is the impact of shadowing. Shadowing from topography and high relief objects can obscure the true terrain and reduce classification accuracy (Leidman *et al.*, 2021a). This is particularly prevalent in polar regions where low sun angles cause long and dark shadowing, with the spectral makeup of such shadows similar to that of dark sediment, which can lead to facies overclassification (Ryan *et al.*, 2018).

For the 7417 m^2 survey performed at Russell Glacier, its hummocky terrain and time of flight (13:36) meant shadowing was a problem within orthomosaic imagery, shadowing at least

21% of the total surveyed area. As such, a shadow correction procedure for UAV imagery developed by Leidman *et al.* (2021a) was followed to help correct this shadowing for improved classification results, which is summarised in Figure 6.5.

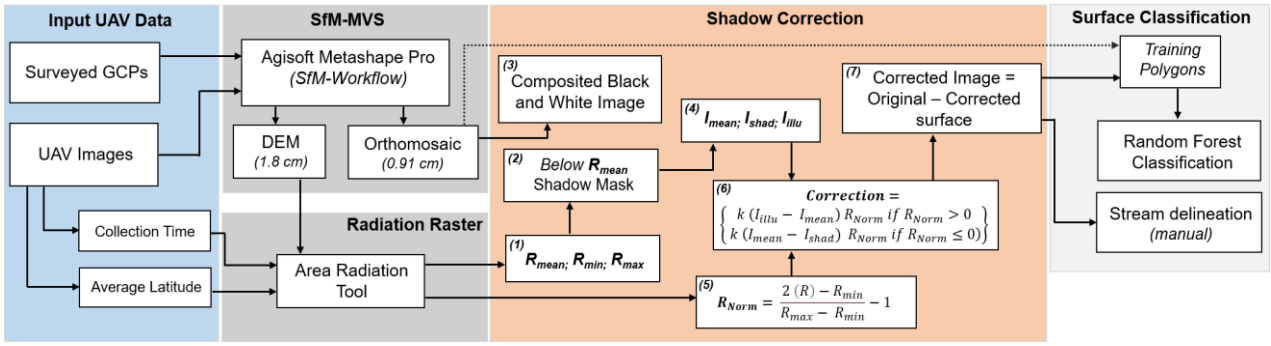

Figure 6.5. The shadow correction workflow for the UAV-derived orthomosaic following the method developed by Leidman *et al.* (2021a). Workflow diagram adapted from Leidman *et al.* (2021a). In the shadow correction section, the radiation raster is denoted to R and the illumination raster denoted to I.

Firstly, the DEM derived from Section 6.2.2 was used within the Area Solar Radiation tool in ArcGIS Pro (v3.0), which calculates the insolation at a given time across the input landscape to create a radiation raster (R) image. For the Area Solar radiation tool, a transmissivity value of 0.545, which is representative for the atmospheric conditions in this area (van den Broeke *et al.*, 2008) was used and solar radiation was calculated for a standard 30 minutes between 13:30 and 14:00 local time (UTC - 2h) for the survey date (9th August, 2019). Whilst this tool is incredibly computationally-intensive, particularly for large areas, as the surveyed area was relatively small (7417 m^2), running time for this tool was relatively short at ~12 hours. This output raster, known as the radiation raster (R), was then examined for shadowed areas, with pixels below the arithmetic mean considered to be 'in shadow' and used to create a shadow mask (R_{mean}). The radiation raster (R) was then normalised to values between -1 and 1 via the following equation:

$$R_{Norm} = \frac{2\,(R) - R_{min}}{R_{max} - R_{min}} - 1$$

Equation 6.1

Following this, an illumination raster (I) is created using the individual red, green and blue channels of the UAV-derived orthomosaic image, with these bands averaged together to create a composite black and white image (I_{sur}). The average value of the illumination surface (I) within shadowed regions (R < Rmean) and unshadowed regions (R ≥ R_{mean}) were calculated using a zonal statistic (I_{shad} and I_{illu} respectively). Using these values (I_{illu} and I_{shad}) and the mean value of the illumination surface (I_{mean}), a correction surface was made following equation:

$$Correction = \begin{Bmatrix} k\,(I_{illu} - I_{mean})\,R_{Norm}\ if\ R_{Norm} > 0 \\ k\,(I_{mean} - I_{shad})\ R_{Norm}\ if\ R_{Norm} \leq 0) \end{Bmatrix}$$

Equation 6.2

Where k is an arbitrary shadowing coefficient greater than 0, in this case, the value 2.5 was used (Leidman *et al.*, (2021a); Leidman, "personal communication", (2023)). Pixels with R > R_{Norm} are given a correction factor scaled to the difference between I_{illu} (illumination of unshadowed regions) and I_{mean} (average value of the illumination surface). Pixels with R ≤ R_{Norm} are given a correction factor scaled to the difference between I_{mean} and I_{shad} (average illumination of shadowed regions). This output correction surface was then subtracted from each band of the orthomosaic (red, green and blue) to create the finalised corrected image (Corrected image = Original – Corrected Surface; Figure 6.6). This process causes areas with below average radiation to be brightened and areas above average radiation to be dimmed, revealing a more homogenously-lit surface (Figure 6.6b).

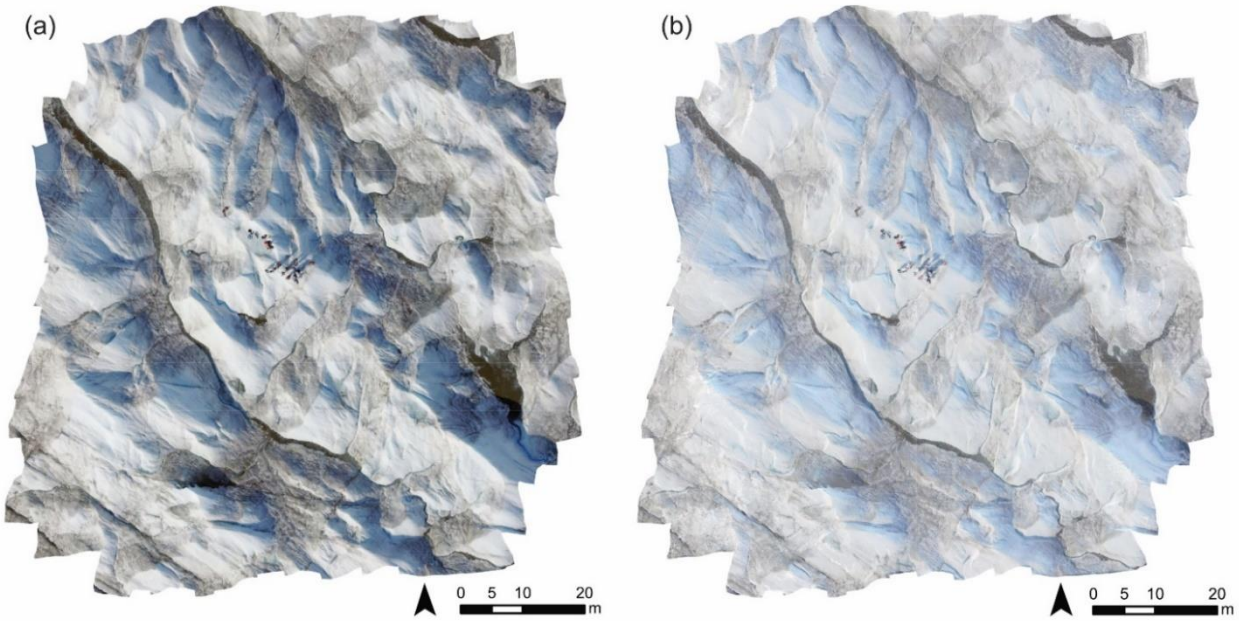

Figure 6.6. (a) The original UAV-derived orthomosaic image with the presence of topographical shadowing; (b) the shadow-corrected orthomosaic image after following the procedure by Leidman *et al*. (2021), whereby topographic shadowing is significantly reduced.

6.2.4 Stream and microchannel mapping

Surface streams and microchannels over the study area were mapped by manually digitising their centrelines using the shadow-corrected orthomosaic. Whilst attempts were made to use the red and blue channels from the orthomosaic image to perform the spectral an $NDWI_{ice}$ classification (Yang and Smith, 2013), which is an NDWI modified index commonly used to enhance surface rivers and streams on icy surfaces, due to the spectral characteristics of small streams within this area (i.e., cryoconite presence in stream beds), automatic delineation was not possible. To extract mean stream width from the three key channels in the survey scene, width measurements at every 1 m interval down the centreline of each channel were undertaken in ArcGIS Pro (v 3.0). Length (m) and area (m^2) measurements are also derived from manual digitisation.

6.2.5 Surface facies characterisation

For the characterisation of different surface facies, a supervised classification algorithm known as Random Forest pixel classification was utilised in ArcGIS Pro (v.3.0). Random forest classification is a machine learning algorithm that builds an ensemble of decision trees based on a training dataset for the classification of pixels and, in turn, land cover (Breiman, 2001). By utilising an ensemble of independent decision trees, random forest classification avoids overfitting that may occur when using a single decision tree. Each tree uses a randomised subset of training data with the final result gathered from a majority. For ice surface facies characterisation, a training dataset consisting of 60 polygon samples was compiled of main features observed within the UAV shadow-corrected orthomosaic image as follows: (i) water (+ cryoconite); (ii) slush; (iii) algae and/or surface cryoconite and; (iv) bare ice (

Figure 6.7).

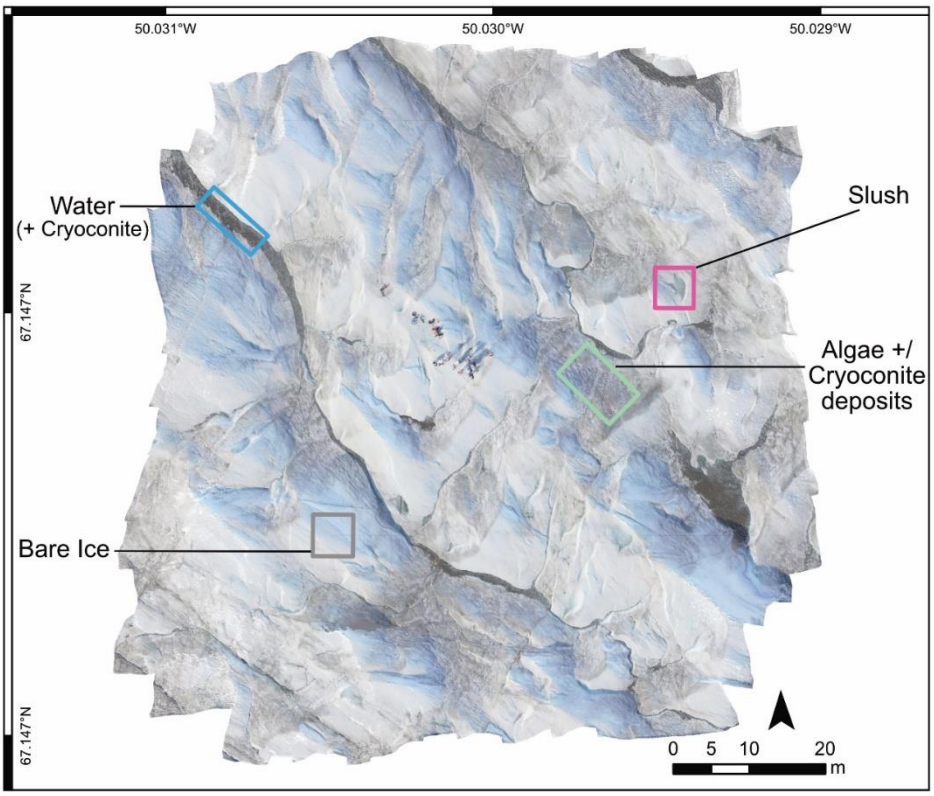

Figure 6.7. Example of surface facies classifications on the UAV-derived, shadow-rectified orthomosaic model; (i) water (+ cryoconite); (ii) slush; (iii) algae +/ surface cryoconite and; (iv) bare ice. People were present in the study area during the flight and can be seen in the centre of the model. They were not classified.

6.2.6 Proxy albedo

A proxy for the albedo of the study area was also determined by exploring the reflectivity of the orthomosaic and, subsequently, meltwater and surface facies. Following the method employed by Rippin *et al.* (2015), emissivity values for individual red, green and blue channels of the orthomosaic image were extracted, with each of these channels digital numbers summed together and averaged to give a proxy for surface reflectance. Whilst a digital photographic image cannot provide an accurate measure of albedo, it is assumed that a direct correlation exists between the signal captured by a camera and the surface albedo or reflectance of a surface (Corripio, 2004). This assumption is further supported by

the fact that much of the energy reflected by various materials, such as snow, is concentrated in the visible range of the electromagnetic spectrum (Corripio, 2004). This simple proxy technique has also been applied to other such studies, including Bash *et al*. (2018), who summed and averaged such digital numbers and scaled this range to automatic weather station albedo values for an enhanced output.

6.3 Worldview-2 methodology

6.3.1 Worldview-2 image acquisition

Access to WV-2 imagery was obtained via a European Space Agency Third Party Imagery Grant (ID: 60295) for a 20.3 km^2 section of the bare ice zone within the Humboldt Glacier catchment at an elevation of ~790 m a.s.l from 30th June 2020 (Figure 6.8). This predefined area was chosen based upon (i) the availability of WV-2 imagery in this region of the ice sheet during the maximum melt month of July and (ii) a particular interest in this area with the potential for certain characteristics to be extracted that pose difficulties for delineation in coarser-resolution imagery (i.e. narrower supraglacial streams).

Even though WV-2 images only provide a snapshot of what is occurring at the surface at a given time due to limited tile coverage, it provides opportunities to not only explore the supraglacial network that exists beyond the resolution capabilities of freely-available satellite imagery, but also provides a source of ground-truthing data that can be used to inform coarser-resolution studies; this is beyond the scope of this Chapter (6) but will be discussed in Chapter 7.

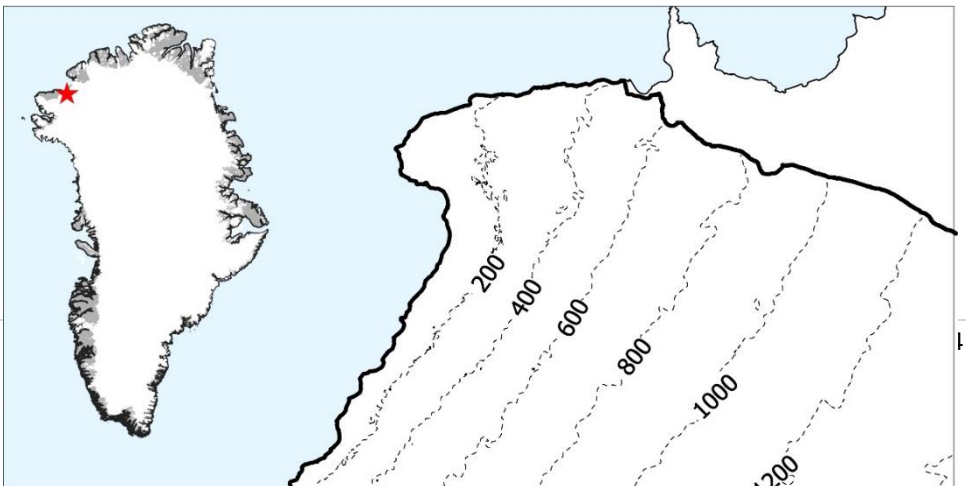

Figure 6.8. Location of the WV-2 tile used for inter-stream mapping at Humboldt Glacier at ~790 m a.s.l (or 25 km inland from the ice margin). Elevation contours are derived from the 10 m ArcticDEM mosaic product (https://www.pgc.umn.edu/data/arcticdem/).

6.3.2 Supraglacial inter-stream delineation

Following the method used throughout the thesis, the automatic river detection algorithm (Yang *et al.*, 2015a; Yang *et al.*, 2017) was performed on the WV-2 tile at Humboldt Glacier. As the WV-2 image contained panchromatic imagery, which is a single band grayscale image at high resolution (0.4 m), liquid water automatically appears darker than the surrounding white ice surface or snow background in these images (Figure 6.9), allowing direct use within the enhancement algorithm (Yang and Smith, 2013).

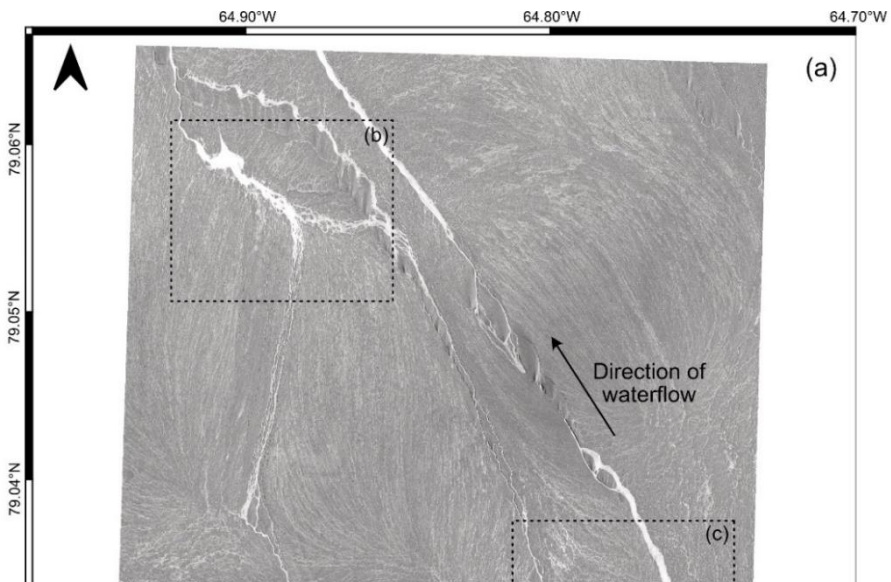

Figure 6.9. (a) Panchromatic image of the 20.3 km^2 area covered by the WV-2 tile (10th July 2019). Areas of white are liquid water and the darker grey background is the ice surface; (b-c) close up areas of the hydrologic network, as identified in (a), to show the ability of WV-2 to observe small-scale features.

This means that the calculation of NDWI from lower resolution (0.18 m) multispectral bands was not required (as per Chapter 4 and 5), allowing the highest resolution possible to be analysed. Alterations to the band pass and path opening filters were conducted to ensure the best extraction results. The band pass filter was ramped to between 1/200 and 1/10 m^{-1} to remove low frequency image background and high frequency image noise (Yang *et al.*, 2016; Yang *et al.*, 2022) and a parsimonious path opening (PPO) filter was set to 10 connected pixels to help preserve longitudinal connectivity. PPO was reduced to 10 for WV-

2 imagery (unlike a value of 20 in Chapter 4 and 5) as due to the image resolution being higher, river and stream segments are less likely to be broken up, missed, or erroneously delineated during extraction. Also, with a higher path opening value, there is the potential for rivers to become over-exaggerated leading to false extractions and overestimation of the network. After Gabor-PPO filtering, a threshold of 40 (grey value range was [0, 255]) was applied to extract such supraglacial river and stream channels.

6.4 UAV-derived results

6.4.1 SfM models and microchannel results

UAV-derived surface models covering a 7417 m^2 area of the Russell Glacier surface were generated. These include an orthomosaic model at 0.009 m pix^{-1} resolution and a DEM at 0.018 m pix^{-1} resolution, as well as secondary SfM-outputs including surface slope, aspect and incoming solar radiation (Wm^{-2}), which are collectively shown in Figure 6.10.

The UAV-derived models, particularly when displayed in 3D (Figure 6.11), capture the highly undulating topography of the on-ice ice marginal region with an approximate wavelength of 10-20 m and an amplitude of ~2-6 m (Appendix C, Figure C2). The elevation ranges between 550.7 m and 561.3 m in elevation with an average slope of 21.7° ± 7.8°. A mean incoming solar radiation value of 328 ± 20.4 Wm^{-2} was derived from modelled ArcGIS Pro estimates with topographical shadows, which were removed during the post-processing stages of SfM-model development, predominately shading north-eastern slopes at the time of surveying. South and west facing slopes encountered the most incoming solar radiation at 452. 8 ± 50.6 Wm^{-2} and 337.6 ± 76.9 Wm^{-2}, respectively, whilst eastern and northern facing slopes encountered the least at 264.5 ± 81.3 Wm^{-2} and 213 ± 76 Wm^{-2}, respectively.

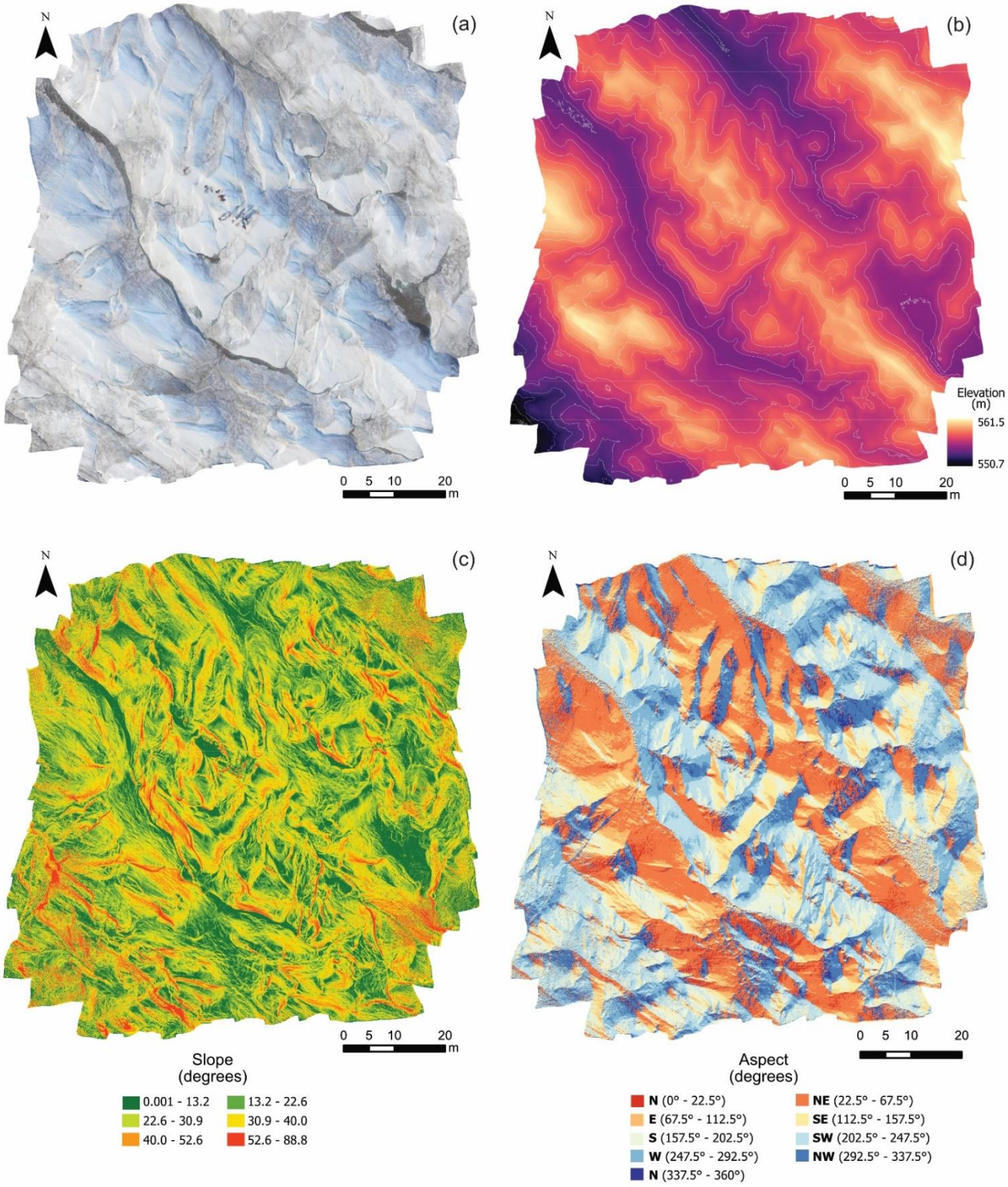
N
(a)
0 5 10 20
m
N
(b)
Elevation
(m)
561.5
550.7
0 5 10 20
m
N
(c)
0 5 10 20
m
Slope
(degrees)
0.001 - 13.2
13.2 - 22.6
22.6 - 30.9
30.9 - 40.0
40.0 - 52.6
52.6 - 88.8
N
(d)
0 5 10 20
Aspect
(degrees)
N (0° - 22.5°)
NE (22.5° - 67.5°)
E (67.5° - 112.5°)
SE (112.5° - 157.5°)
S (157.5° - 202.5°)
SW (202.5° - 247.5°)
W (247.5° - 292.5°)
NW (292.5° - 337.5°)
N (337.5° - 360°)

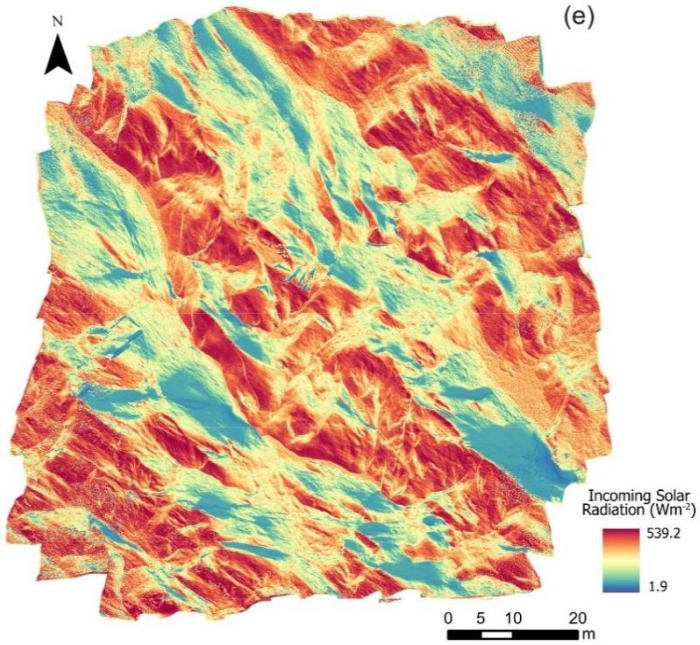

Figure 6.10. Various UAV-produced SfM outputs; (a) Orthomosaic (RGB) and (b) DEM of the survey area; (c) Slope and (d) Aspect, both derived from the DEM of the survey area; (e) Incoming solar radiation (Wm^{-2}) derived from the Area Solar Radiation tool in ArcGIS Pro.

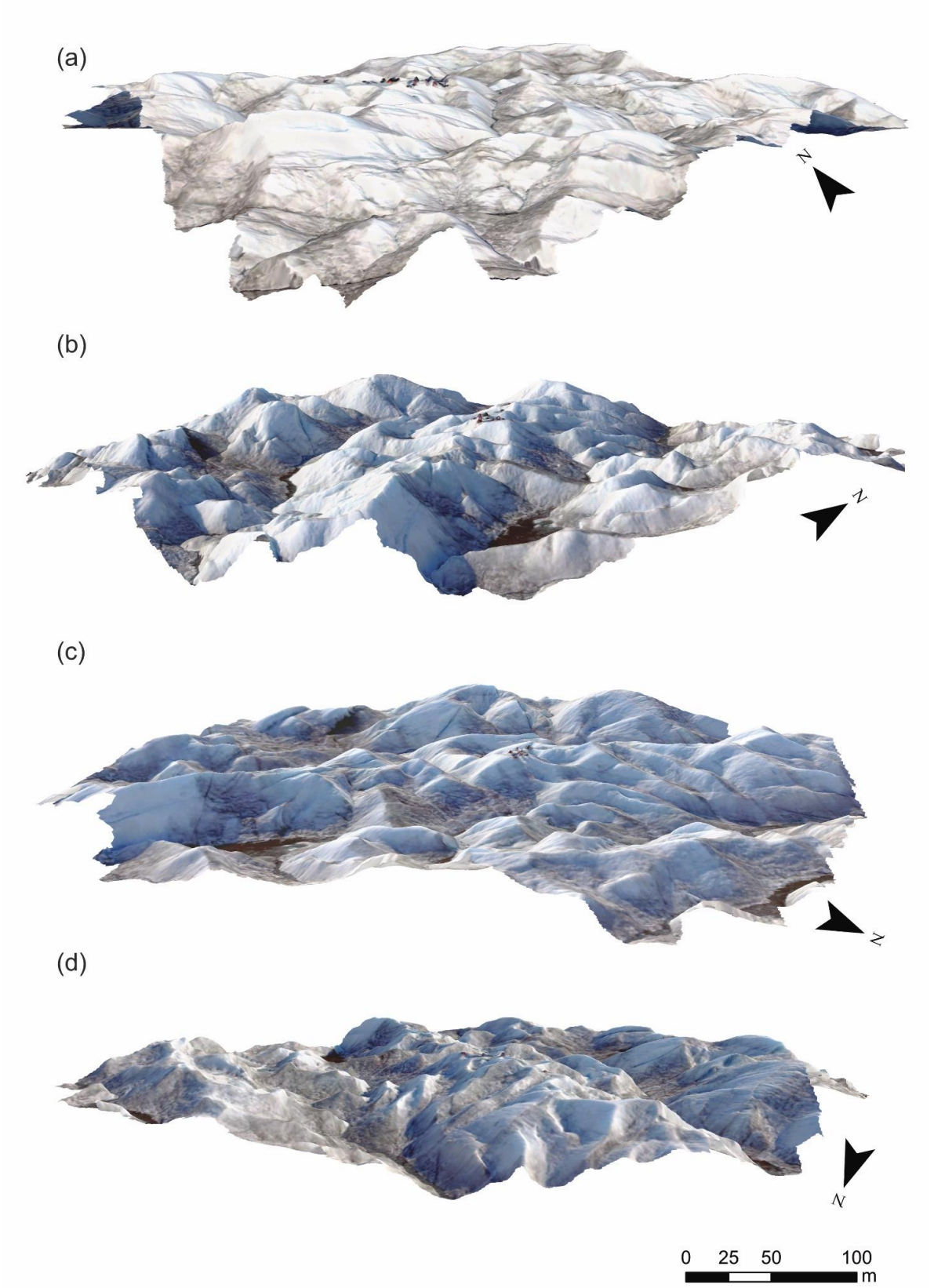

Figure 6.11. 3D visualisation of the orthomosaic model of Russell Glacier from different angles (denoted by the north arrow direction). The orthomosaic is draped over the DEM to form the 3D structure of the surveyed scene.

Three prominent streams flow through the survey area, with an average width of 0.59 ± 0.44 m (mean ± standard deviation) and a maximum recorded width of 2.1 m (Figure 6.13). The length of these three streams within the survey area measure 127.9 m, 89.7 m and 31.6 m, respectively, and cover areas of 87.6 m^2, 46.5 m^2 and 31.2 m^2, with their channels continuing undisturbed beyond the surveyed scene. These streams are orientated and flow in a southeast to northwest direction and are also clearly visible in the UAV-derived DEM in the topographical lows between hummocky terrain (Appendix C, Figure C2). A single meltwater pond is also captured, measuring 56.3 m^2.

A number of finer-scale, microchannels measuring between 0.06 m and 0.5 m wide are also present across the scene (Figure 6.13), largely characteristic of shallow, slush-like flows comprising ice-particles and waterflow through the porous weathering crust flowing downhill on the sides of topographic hummocks. Frozen slush depressions on topographical hummocks (Figure 6.13) and the shallow weathering crust were observed to progressively melt throughout the survey day, forming these shallow microchannels on hummock sides and supplying meltwater to the more established channels at their base. Together, 60 microchannels are mapped across the scene with a mean length of 13.8 m ± 19.5 m and widths down to ~4 cm. A range of channel characteristics are also observed, including the presence of sharp meandering bends in channels at the base of topographical slopes and the field-observation of a meander cut-off occurring within the survey scene area across a 3-day period (Figure 6.12), showing the rapid and dynamical behaviour of these small systems over short timescales. Within both stream and microchannel beds, cryoconite deposits are expansive, ranging from small, independent pitted-type deposits to mats that covered the entirety of stream and pond beds.

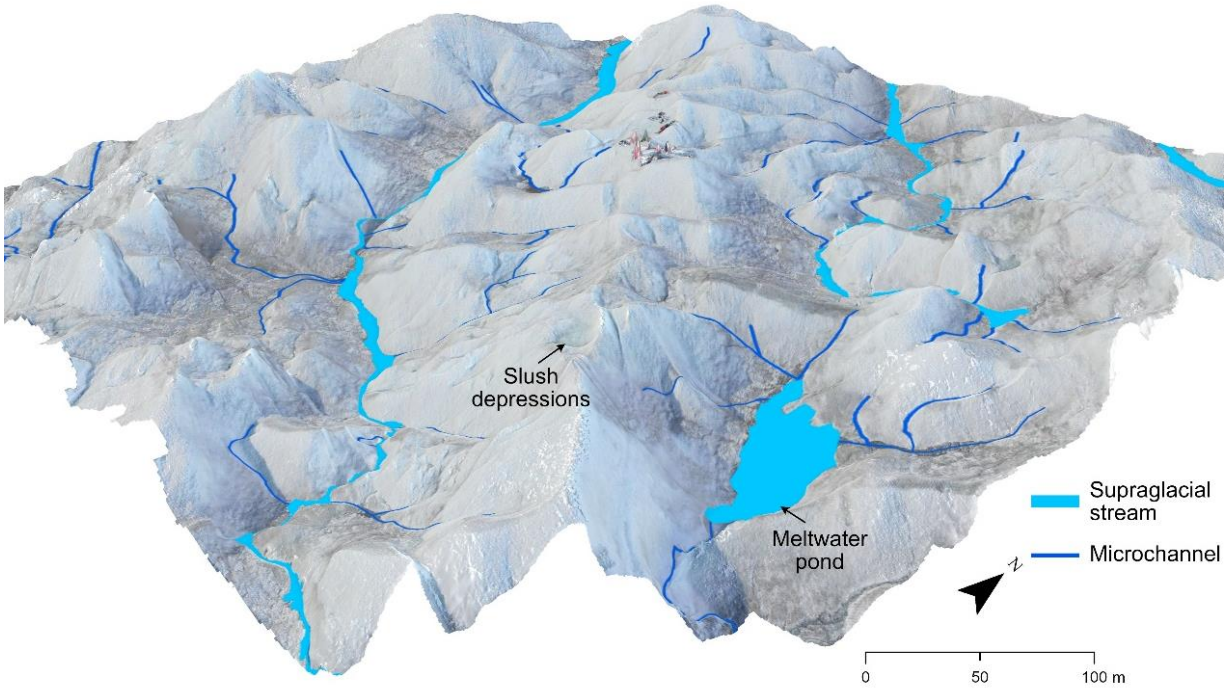

Figure 6.12. 3D overview of the supraglacial 'micro' network derived from the UAV orthomosaic, consisting of three main streams and a meltwater pond sitting between topographic undulations (light blue), and a series of shallow, slush-like microchannels (dark blue) feeding melt from topographic highs to lows. Slush depressions are also present on topographic highs.

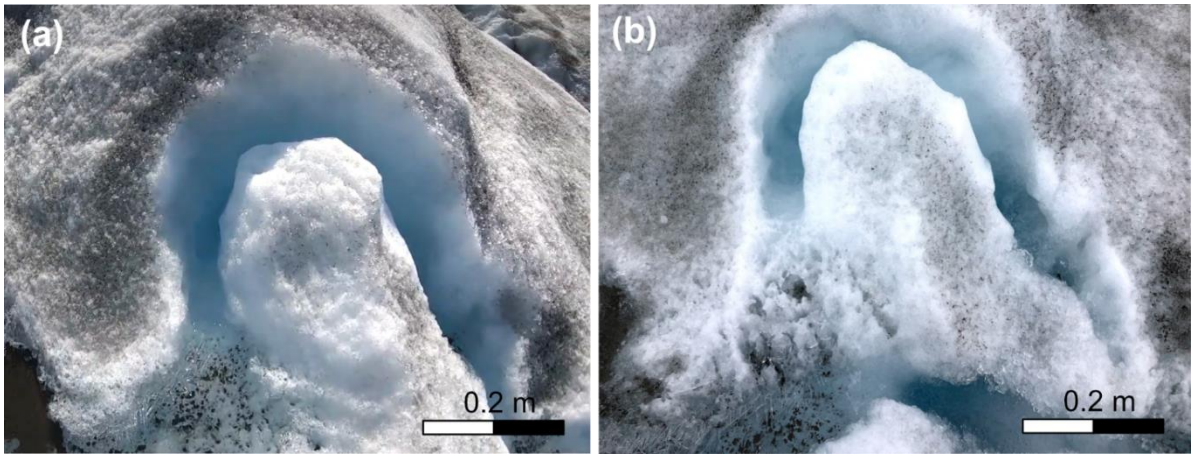

Figure 6.13. The development of a meander cut-off in a supraglacial microchannel observed across a three-day period in the UAV survey location. (a) The microchannel meander which undercuts into the base of a topographic undulation. Pitted cryoconite can be seen in the microchannel bed; (b) the meander now cut-off with crystalised ice blocking meltwater from the loop and a new, straighter channel developed in the forefront.

6.4.2 Surface facies classification

Surface facies classification of the survey scene found 49% of the ice surface was covered by algae and surface cryoconite deposits, with a large remainder (44%) comprising bare ice. Water (including with cryoconite) made up 4.5% of the survey scene and areas of slush comprised the remaining 3.2% (Figure 6.14).

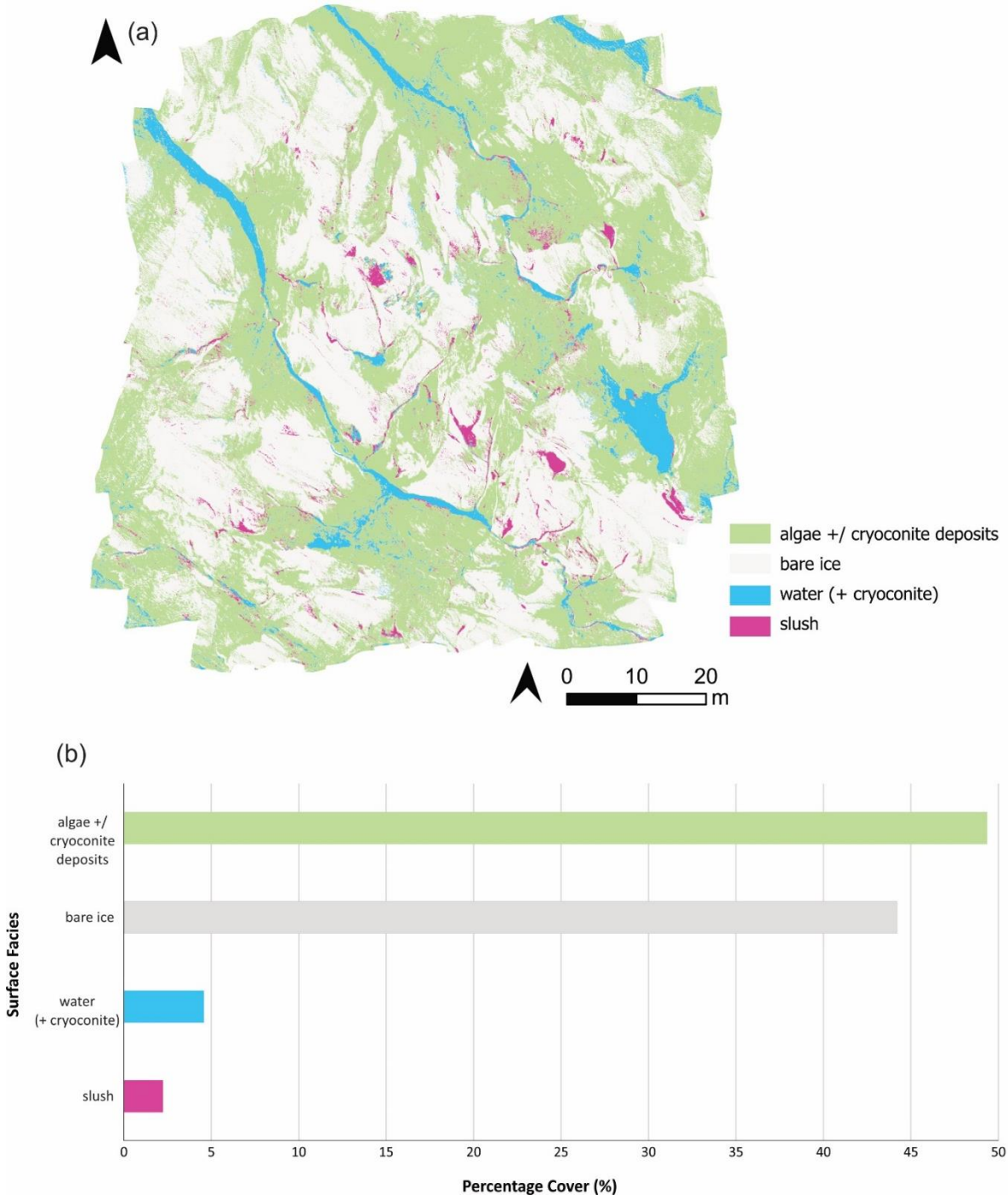

Figure 6.14. (a) Surface facies classification of the UAV survey scene via the supervised classification algorithm, the random forest classifier; (b) associated percentage cover of mapped surface facies classification (i) algae +/ cryoconite deposits, (ii) bare ice, (iii) water (+ cryoconite) and (iv) slush.

In terms of the surface classification distribution across the survey scene, algae and cryoconite deposits are found on slopes with a mean gradient of 23.5° ± 10.9° and predominately occur on the western (32%) and northern (28%) facing slopes of topographical hummocks and the edge of microchannel banks (Figure 6.15). Algae and cryoconite deposits comprise as much as 60% of the surface composition on such slopes. Bare ice is shown to occur on a mean slope of 31.6° ± 12.8 ° and dominates southern (29%) and eastern facing slopes (29%), accounting for up to 51% of surface cover. The surface facies water (with cryoconite) has the lowest mean slope (13.2° ± 10.6°), whilst slush occurs at 18.5° ± 10.4° and is predominately found on northern and eastern (30%) facing slopes.

Incoming solar radiation is highly variable across surface facies (Figure 6.16), with water (+ cryoconite) recording the highest mean solar radiation value of 357 ± 75 Wh^{-2}. Algae and cryoconite deposits record the second highest mean value, with 327 ± 119 Wh^{-2}, which is 8.5% lower than water (+ cryoconite) but 4.6% higher than the mean bare ice value (312 ± 156 Wh^{-2}), even though bare ice values vary considerably.

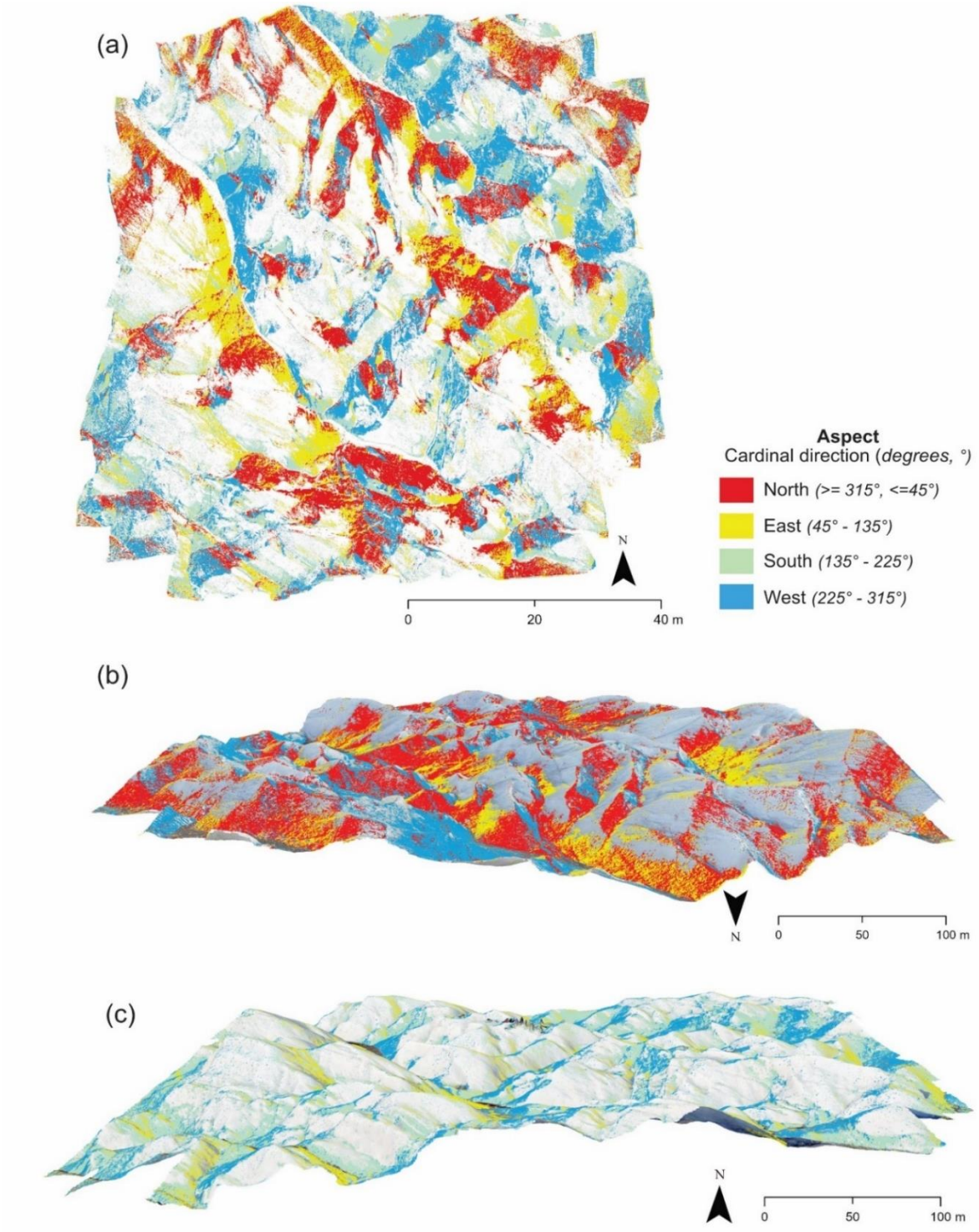

Figure 6.15. (a) Distribution of the prominent surface facies, algae and cryoconite deposits, across the survey scene divided into the four prominent cardinal directions (represented by colouration); (i) north (red), (ii) east (yellow), (iii) south (green) and (iv) west (blue); (b) 3D view looking northwards, visually showing northern and western facing slopes comprise the largest algae +/ cryoconite deposits; (c) 3D view looking south showing predominately southern facing slopes had reduced algae +/ cryoconite deposit coverage.

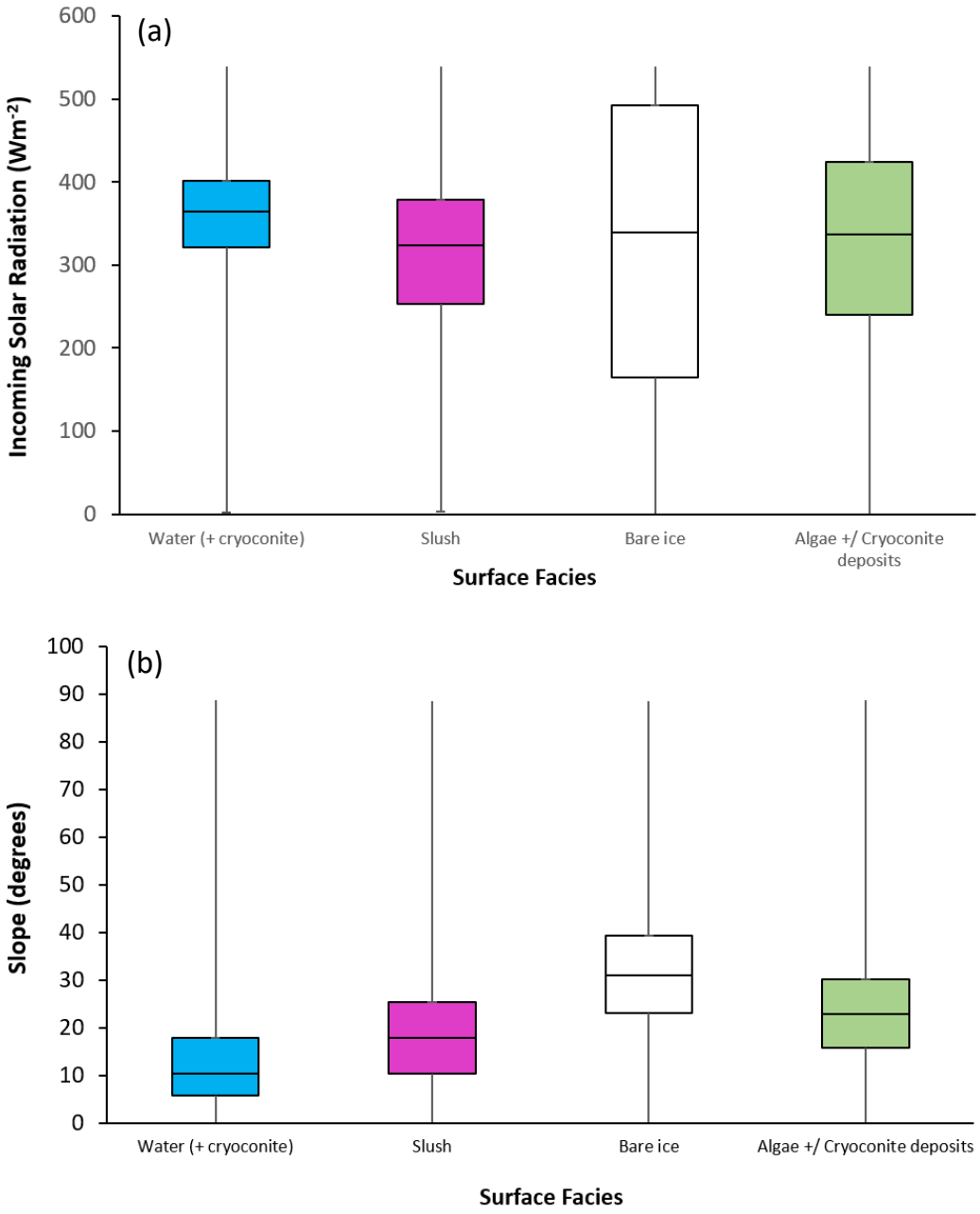

Figure 6.16. (a) Incoming solar radiation (Wm-2) for the different surface facies; (b) the slope (degrees, °) for each surface facies.

6.4.3 Proxy albedo (surface reflectance)

Although measuring albedo is beyond the scope of this work, it is possible to identify and explore differences in surface reflectivity for the characterised surface facies via proxy albedo calculations (cumulative pixel reflectance; see Figure 6.17). There are distinct variations in this proxy albedo, with the lowest values of surface reflectance occurring in areas of surface meltwater (e.g., the three streams located between topographic undulations) and the highest reflectance values, unsurprisingly, observed on bare ice. Mean surface reflectivity of water (with cryoconite) is shown to be 67% darker than bare ice, with some variations in reflectivity in the channel bed due to cryoconite pitting. Swaths of algae and cryoconite deposits across the ice surface are also representative of having a low reflectance, with a mean reflectance value 21% lower than bare ice.

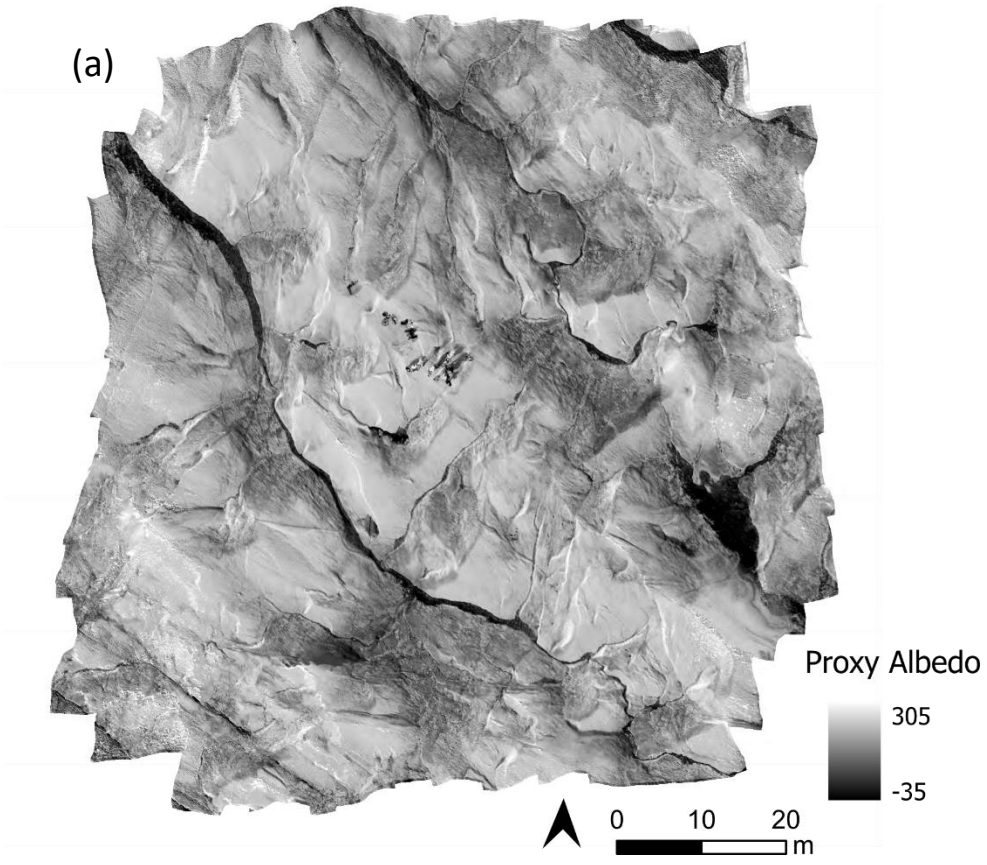

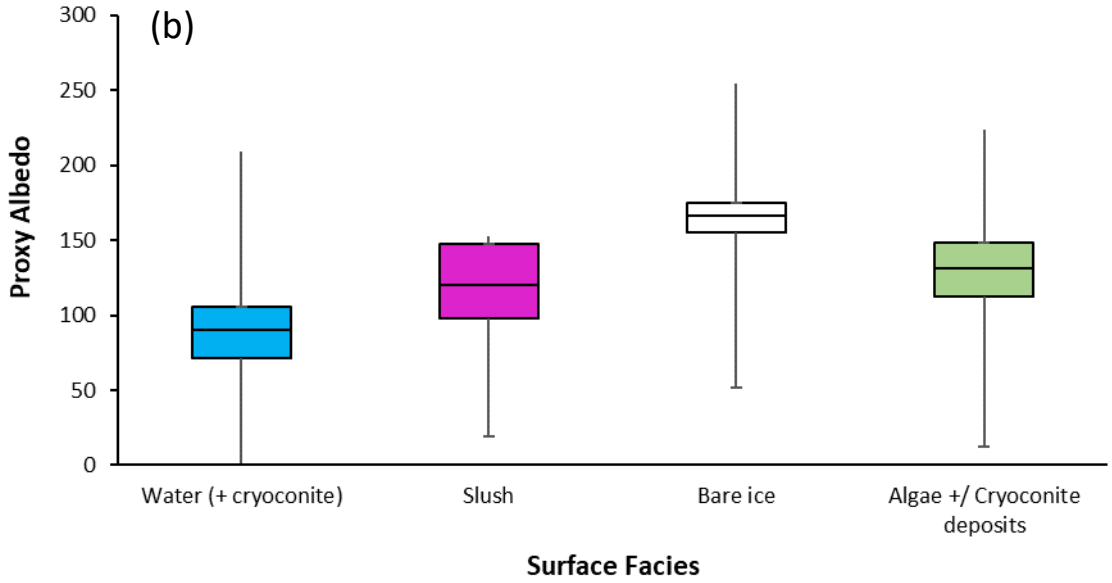

Figure 6.17. (a) Proxy albedo of the shadow-corrected orthomosaic. Darker areas (low values) represent a lower proxy albedo or reflective surface, predominately occurring in areas of water (streams, microchannels and slush) and areas of algae and cryoconite deposits. Lighter areas (high values) represent a higher proxy albedo or reflective surface which is largely seen where bare ice occurs; (b) boxplot showing the range of proxy albedo values for each surface facies classification.

6.5 Discussion of UAV-derived results

6.5.1 Supraglacial microchannel network

Supraglacial stream and microchannel networks derived from the UAV-surveys at Russell Glacier show the overall hydrologic complexity of icy surfaces when viewed in-detail, in particular the spectrally-complex, ice marginal regions which can consist of sediment laden dirty-ice and pigmented algal communities, as prevalent in the western and southwestern regions of the GrIS. The surface hydrology shown in this location is complex, with networks of shallow microchannels reminiscent of slush flows measuring only a few centimetres wide feeding wider streams from topographic highs to lows. The porosity of the weathering crust provides a substrate vulnerable to the initiation supraglacial rill-type initiation for microchannel flow (Schuster, 2001), in line with observations made here.

A study by Leidman *et al.* (2023) similarly used a UAV to examine surface characteristics 2 km east of the ice edge at Russell Glacier, with supraglacial stream widths ranging between 0.8 m and 17 m, with the larger streams occurring within deep canyons perpendicular to ice flow and parallel to stress fractures. The narrow channels found in this work (conducted in this Chapter) within ~300 m of the ice margin were shallower in nature with no canyonised features and occurred within the 'valleys' between topographical hummocks in the direction of ice flow, showing potential differences in their preferential development and evolution mechanisms despite these studies' proximity. A greater coverage of supraglacial stream area was also observed by Leidman *et al.* (2023) of 8%, with 4.5% observed in this study near the ice margin, likely due to the difference in channel size. Higher runoff production rates are known to occur closer to the margin due to lower elevations, marginally steeper slopes (hypsometry) and greater melt rates driven by a darker surface (Mankoff *et al.*, 2020), therefore influencing greater hydrologic mobilisation within a variety of sized channels.

The occurrence of narrow streams (<2 m wide) and microchannel networks (0.04 – 0.5 m wide) is not well-studied on the GrIS due to the requirement for field-based studies and difficulties with accessibility. The presence of such micro-scale networks have been explored on small polythermal glaciers such as Midtre Lovénbreen in Svalbard (Rippin *et al.*, 2015), whereby they can exist as anastomosing networks (branch-off and re-join main channels) that exhibit some meandering features or those that are primarily controlled by glaciological structures (e.g., debris bands, fractures, crevasse scars) and can be straight. The microchannels observed in this ice marginal region of Russell Glacier fit neither of these observations, and instead act as a smaller, subsidiary tributary network, feeding melt from topographical highs to lows into channels below between undulations; a type of miniature watershed. Some microchannels do, however, exhibit some channel meandering, similar to that seen in larger supraglacial streams in Greenland (Karlstrom *et al.*, 2013; Gleason *et al.*,

2016), elsewhere in the Arctic (Hambrey, 1977; Knighton, 1981; Marston, 1983; Rippin *et al.*, 2015) and Canadian glaciers (Figure 6.18; Germain and Moorman, 2019; Bash *et al.*, 2022).

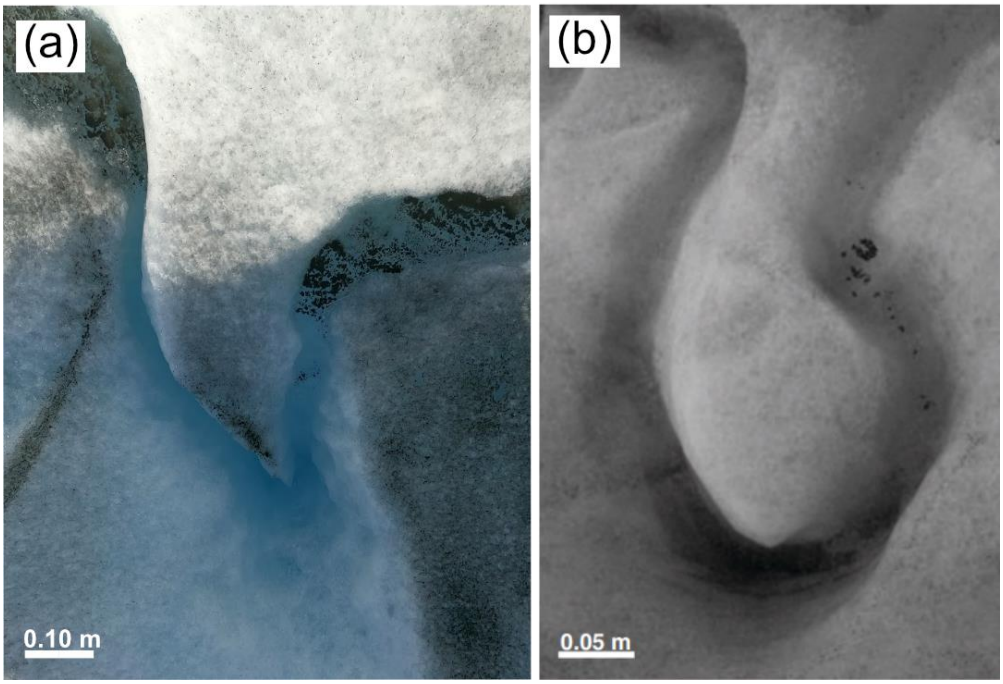

Figure 6.18. Similarities between channel meandering at two different sites; (a) A meander bend in a microchannel within the UAV-surveyed study area of the Russell Glacier margin; (b) A meander bend at Mendenhall Glacier, Alaska (taken from Karlstrom *et al.*, 2013).

The observation of a cut-off loop observed to form across a three-day period via field observations shows clear channel dynamism, with less incised channels likely to change channel path rapidly due to water flow overwhelming channel banks (Germain and Moorman, 2019). As this study was conducted in August (post peak-melt), there is the potential for these shallow channel bend passages to freeze-up with reduced water flow (Figure 6.19), with overnight refreezing during August within stream beds and the weathering crust, as noted by Muthyala *et al.* (2022), causing increased interstitial freezing and a decrease in hydraulic conductivity of waterflow.

.

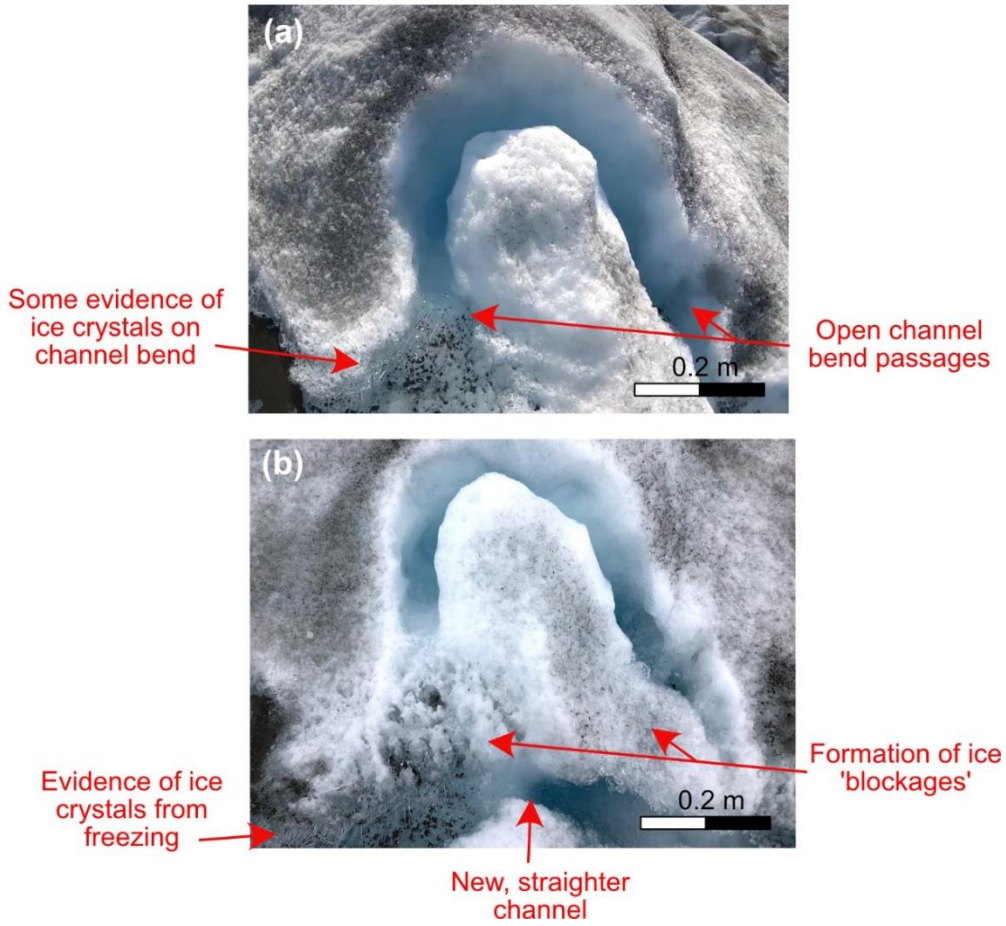

Figure 6.19. (a) Field-observed microchannel meander bend with open channel bend passages; (b) same microchannel meander bend observed 3-days later, whereby channel bends become 'blocked' by the formation of ice with evidence of ice crystals from freezing. Bend closure is potentially driven by overnight refreezing of channel melt and the weathering crust, causing a decrease in hydraulic connectivity of water flow which is preferentially diverted in a newer, straighter channel

6.5.2 Surface facies and topographical influences

Over half of the small area surveyed via the UAV is dominated by the presence of algae and surface cryoconite deposits, which are not only present across the weathering crust of the ice surface but within microchannel beds and topographical lows. Many studies assume that cryoconite deposits are largely located within cryoconite holes and therefore predominantly shaded or ice covered throughout the melt season (MacDonell and Fitzsimons, 2008). This

assumption, however, underplays the importance of cryoconite sediments in altering ablation zone albedo as these deposits are widespread across the ice surface, as revealed in this study, and have been shown by Ryan *et al.* (2018) to account for 73% of the spatial variability of albedo. Cryoconite deposits can occur on the ice surface via the melt-out of particulates from the porous weathering crust, aeolian-deposition and the wash-out of cryoconite from cryoconite holes via meltwater or rainy conditions, accumulating not only on the ice surface but within the hydrologic network (Ryan *et al.*, 2018; Leidman *et al.*, 2021b; Leidman *et al.*, 2023). These widespread deposits have further been shown to provide nutrients for the growth and sustainment of surface ice algae communities, with the availability of meltwater and increases in temperature further promoting their colonisation (Yallop *et al.*, 2012; Lutz *et al.*, 2016).

In this study, algae and cryoconite deposits were dominant on northern and western facing slopes of topographical undulations, which could be due to several favourable conditions. Even though north sloping ice overall receives less sunlight than south-sloping or flat ice in the northern hemisphere (Cook *et al.*, 2018), the range of solar angles leads to uneven melting on such slopes. This promotes shallower slope angles and the potential for cryoconite-based sediments (via melt-out of aeolian-deposited sediment) to thicken and remain on such slopes for longer periods of time. This is unlike southern slopes which receive higher and longer-lasting daily incoming solar radiation and subsequent melt, which can promote higher slope angles and the flushing of sediment into the hydrologic system below. As such, cryoconite dominance on these north and western slopes enhances the likelihood of microbial productivity and accumulation of pigmented photoautotrophs of glacier algae, hence their associated abundance here (Figure 6.20). On these slopes, algae and cryoconite deposits accounts for 60% of the slope area and occur where solar radiation is highest; 52% higher than for bare ice on the same slope.

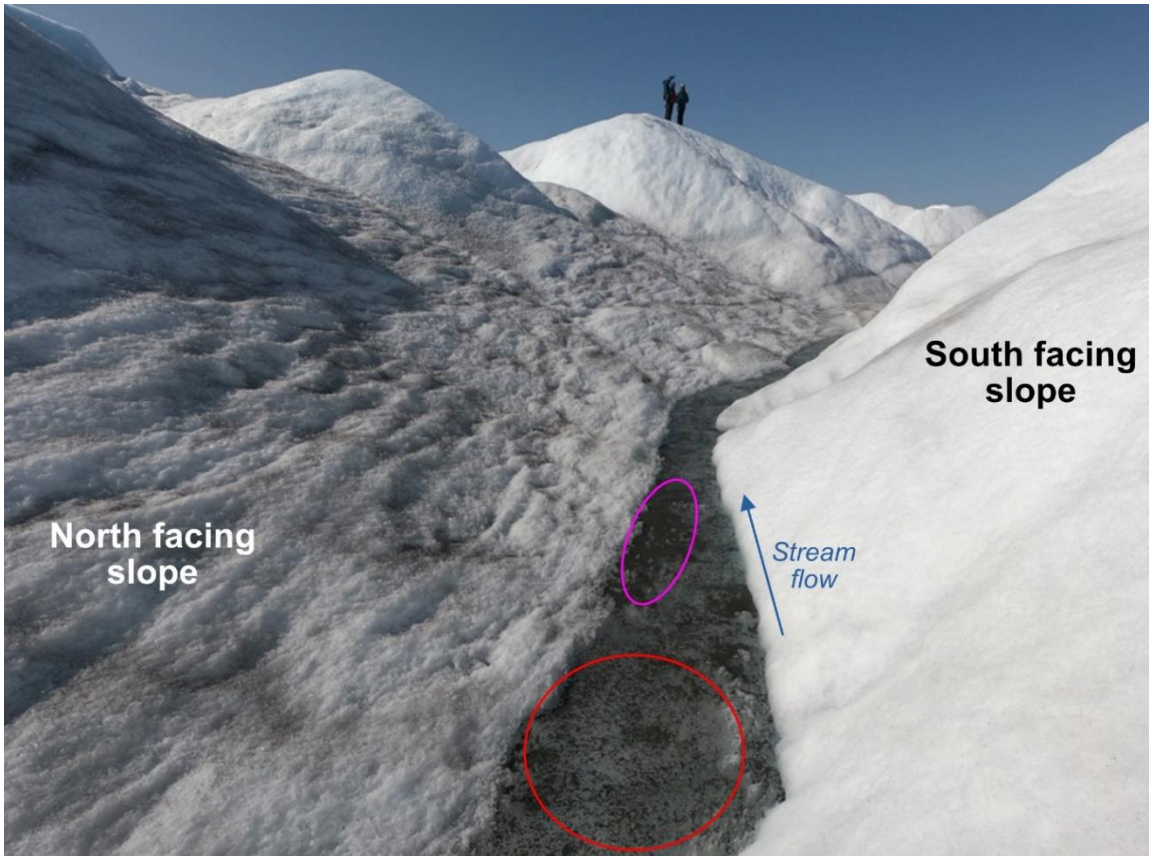

Figure 6.20. Example of the surface facies difference between north vs south facing slopes on topographic undulations of the ice margin of Russell Glacier. The north facing slope has more algae and cryoconite deposits, with the south facing slope composed of highly reflective bare ice. The supraglacial stream in-between these undulations consist of both pitted (red circle) and mats (pink circle) of cryoconite. People are for scale.

From the UAV-derived orthomosaic, it is also observed that algae and cryoconite deposit abundance occurs predominately towards the base of northern and western slopes, which may further be due to the seasonal migration of cryoconite and subsequent algal communities downslope under such uneven melt conditions. This causes an eventual build-up of cryoconite-deposits towards the base, ultimately feeding into the hydrological channels present between the topographical hummocks. This hypothesis is based upon the observations and knowledge of cryoconite hole evolution by Cook *et al.* (2018), whereby cryoconite holes positioned on northern facing slopes form irregular-type holes due to sediment build-up and lateral movement downslope with uneven melting, causing holes to

elongate, migrate and/or coalesce into cryopools at lower gradients. Whilst cryoconite-deposits and algae are still present on southern facing slopes (<40%), melt rates from longer daily solar exposure likely means cryoconite-based sediments via surface melt-out are removed swiftly from their steeper slopes and redistributed in the surface hydrologic system below.

Slope gradient differences of topographic undulations are widespread across this ice marginal region and have been referred to as 'wind sail' features by Cook *et al*. (2018), with cryoconite deposits and algae shown to blanket the shallower surface slopes and base of topographical undulations and bare ice exposed on the steeper slopes and tips of such undulations (Figure 6.21). Not only does uneven solar melting and the migration of melt-out cryoconite deposits influence such characteristics and the distribution of such facies, but katabatic winds may also play a role. The strong movement of high-density air from a higher elevations downslope, which is predominately east-to-west at the survey location, may also influence the topographic-nature of the ice surface (i.e., down-wind slopes being shallower) by enhancing sensible and solar heating (Wang *et al.*, 2021) as well as the deposition of aeolian-transported sediment which preferentially settles in sheltered topographic lows and stream beds, with algal distributions accompanying these refuged areas. Strong katabatic winds cause local erosion on exposed slopes (Anderson *et al.*, 2017), with LIA moraines to the east and north of the study site in close-proximity, with the potential of reworking and translocation of proglacial material onto local ice via aeolian processes.

Figure 6.21. Wind sail' type topographical features across the ice marginal region of Russell Glacier, southwest Greenland. North facing slopes have a shallower slope angle than southern facing slopes, with cryoconite deposits and algal communities blanketed on shallower slopes and between topographic undulations.

Cryoconite deposits are also found in abundance on supraglacial stream banks as well as within channel and meltwater pond beds. Cryoconite was also observed in supraglacial stream channels in recent studies by Leidman *et al.* (2021; 2023), 1-2 km upglacier from our study site at Russell Glacier. These studies found cryoconite made of millimetre-scale consolidated granules typically accumulated in shallow 'floodplain' regions of meltwater streams (average width 4.6 m) and covered up to 91% of the stream bed, with a lack thereof in the channel thalweg where faster flow inhibits deposition (Gleason *et al.*, 2016). These floodplain areas of a stream can be exposed to the atmosphere during low or no flow for

between 9 and 15 hours per day (Leidman *et al.*, 2021b). The microchannels imaged in this UAV study were small (~4–50 cm wide) and not large enough to differentiate a stream thalweg from a floodplain. However, the uniform nature of the cryoconite deposits within both stream and pond bottoms suggests meltwater flow during this time period is relatively low and slow, allowing cryoconite deposits in these shallow waters to be deposited and remain in-situ, with likely exposure during low-flow. Our survey was also conducted in early August, post-peak melt, whereby sediment cover has been shown to increase by up to 0.75% a day despite a reduction in overall melt due to diminished daily stream power, facilitating cryoconite-deposition in stream beds (Leidman *et al.*, 2023). This increase in cover can, however, simultaneously drive a more negative surface mass balance through albedo reduction (Cook *et al.*, 2016; Stibal *et al.*, 2017; Takeuchi *et al.*, 2018; Williamson *et al.*, 2020), particularly late into the melt season, with the potential to extend the number of melt days applicable to large swaths of Greenland's ablating margins (Tedstone *et al.*, 2017; Leidman *et al.*, 2023).

6.5.3 Impact of surface hydrology and facies on ice surface reflectivity and roughness

The widespread occurrence of micro-scale features (i.e., narrow streams, microchannels and cryoconite) at the ice margins can have wider implications on surface reflectance and roughness and, in turn, control melt production rates. The existence of streams, microchannels (<0.5 m wide) and cryoconite deposits, which also sustain algal communities, are widespread and dark, and have been found to have albedo values as low as 0.27 (for comparison, clean ice typically has an albedo of between 0.45 and 0.55; Ryan *et al.*, 2019). Darker ice surfaces absorb more radiation, driving further melt, known as a positive feedback loop (Stroeve, 2001), which can further sustain algal blooms, which continue darkening the ice surface and release more ice-bound sediment deposits; a self-sustaining mechanism in driving secondary surface melt (Di Mauro *et al.*, 2020; McCutcheon *et al.*, 2021). Also not

only is the presence of surface water darker than its surroundings, with 38% of incoming solar radiation modelled to be absorbed by the bed and 51% by the water column (Bray *et al.*, 2017), but cryoconite-based deposits within channel beds can also disproportionately lowers albedo. Such wetted cryoconite can absorb 23% more incoming solar radiation (Boggild *et al.*, 2010) which can increase water temperatures by up to 0.4°C (Isenko *et al.*, 2005). This generates more internal thermal energy that preferentially expands the channel laterally rather than vertically, continuing the exposure of the channel bed to direct solar radiation (Karlstrom *et al.*, 2013; Leidman *et al.*, 2023).

These surface features, also termed 'microscale' features (i.e., cryoconite holes and cryoconite deposits, a weathering crust and meltwater streams) can further affect the surface energy balance by increasing ice surface roughness, beyond that of mesoscale (metre-scale) undulations which are important for setting regional ice slopes and large-scale roughness (Arnold *et al.*, 2006; Ng *et al.*, 2018). Turbulent heat fluxes, relating to both sensible and latent heat fluxes, are important sources and sinks of energy for ice. Turbulent fluxes can account for up to 80% of the energy available for ablation (Willis *et al.*, 2002) and have been shown to be strongly influenced by roughness, including from that of microscale features. In general, a rougher surface generates more turbulence within the ice/atmosphere boundary layer affecting heat fluxes and enhancing melt rates; all affecting the overall surface mass balance of a glacier or ice sheet (Cathles *et al.*, 2011). As shown by Rippin *et al.* (2015), high supraglacial drainage density results in low surface reflectance and the association of high surface roughness, with the hydrologic network not only controlling surface roughness via vertical and lateral incision, but surface roughness also controlling the spatial pattern of the network. Muthyala *et al.* (2022) also found that large turbulent energy fluxes significantly occurred during peak melting; in agreement with Fausto *et al.* (2016) who similarly found nonradiative energy fluxes contributed up to 76% of daily melt energy during the 2012 melt season. Finally, Irvine-Fynn *et al.* (2022) recently found that roughness variations on a high-

Arctic glacier were related to the vertical movement of impurities and hydrological activation of the ice surface, with supraglacial hydrology modulating such roughness. With forecasts of rising air temperatures, cloudiness and rainfall at higher latitudes, enhancement of the turbulent energy fluxes at the ice surface may result in rising ablation and the increased prevalence of rill-dominated hydrology (Irvine-Fynn *et al.*, 2022). The presence of cryoconite deposits also contributes to the development of a rougher surface via surface irregularities at metre to sub-metre scales with subsequent heat flux implications, showing the complex relationships that exist between cryoconite morphodynamics and ice surface melt rate (Cook *et al.*, 2016). Therefore, not only are these microscale features collectively impacting surface albedo through the darkening of the surface driving a positive melt feedback loop, but their influence also impacts surface roughness (Irvine-Fynn *et al.*, 2022).

6.6 WV-2 results

6.6.1 Inter-stream networks

From the 20.3 km^2 mapped ice surface of Humboldt Glacier from WV-2 imagery, a range of supraglacial channels, including both main-stem river and inter-stream tributary networks are present ranging in size and width (Figure 6.22). The main-stem supraglacial river and tributary channels extracted from the imagery range in width of between 10–49 m and include highly braided channel segments ranging between 3–5 m wide. It should be noted that supraglacial rivers do not truly 'braid' like terrestrial river channels due to their limited sediment supply for the creation of channel bars. However, they anastomose, separated by small ice islands which reconnect into a main channel (Figure 6.23; Yang *et al.*, 2016). These main-stem river channels are continuous throughout the image with lengths between 2.37 km and 6.95 km, which continue beyond the WV-2 scene. One river channel, however, is less continuous and is interrupted by a 420 m long snow bridge (Figure 6.23c). For the inter-stream tributary networks, smaller transient channels range between 1–2 m wide and exhibit

sinuous characteristics as well as being highly anastomosing, with stream channels highly intersected with each other before connecting with the main river channel (Figure 6.23). When comparing such WV-2 mapping with the same area mapped from Chapter 4 (Sentinel-2) and Chapter 5 (Landsat; Appendix C, Figure C3), such inter-stream networks are not well resolved or distinguished. This highlights how such ultra-high-resolution imagery can reveal aspects of the network unable to be seen by coarser resolution data or, unless field-based data is obtained (further discussed in Chapter 7, Section 7.3).

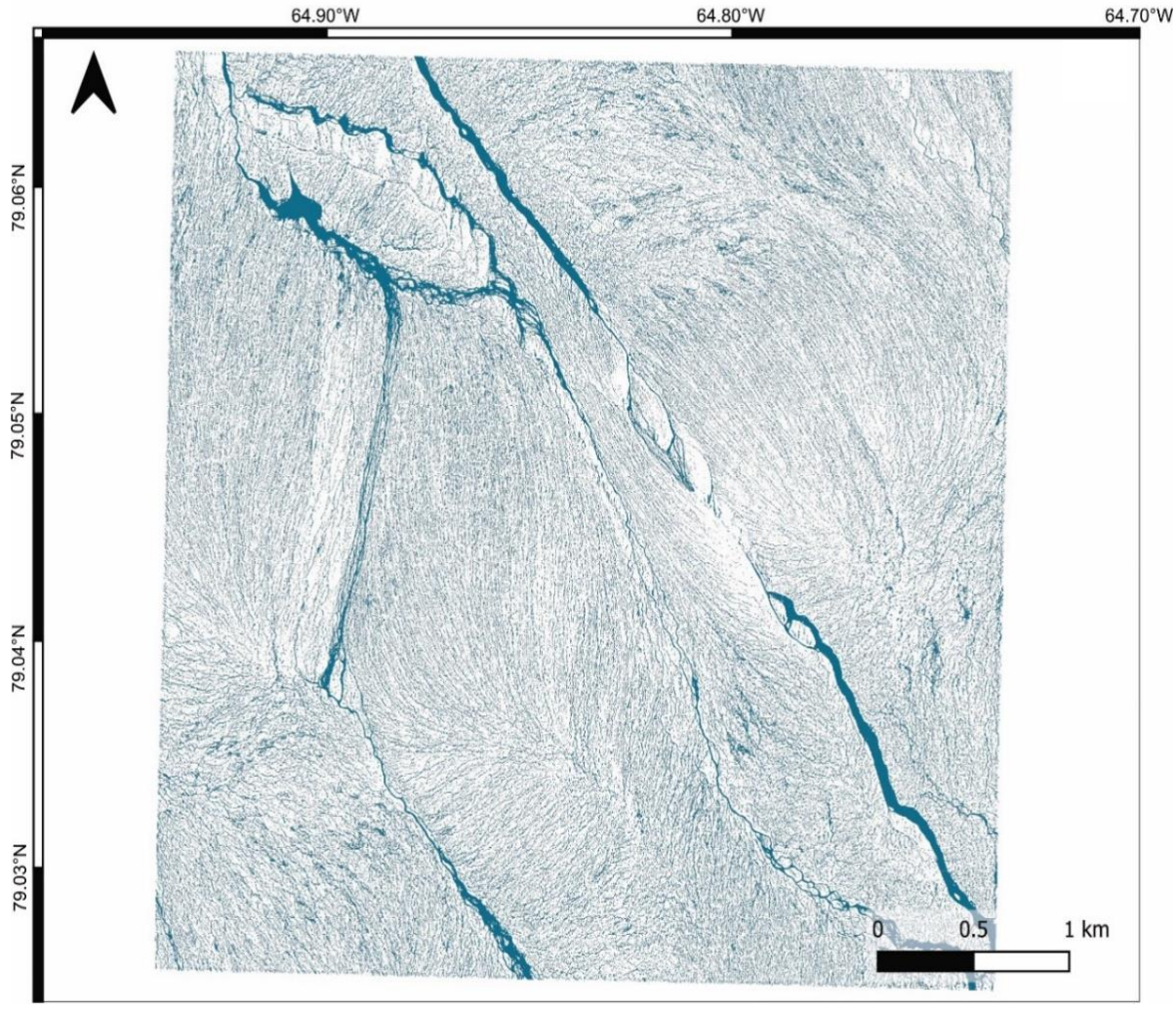

Figure 6.22. Extracted supraglacial hydrologic network (rivers and inter-stream network) from WV-2 imagery covering a 20.3 km^2 section of the bare ice zone at Humboldt Glacier, north Greenland.

The total mapped area of both supraglacial rivers and inter-stream networks is 3.8 km^2, which equates to 18.7% of the total WV-2 tile area (20.3 km^2). In terms of the area ratios between the main-stem river channels present within this image and the inter-stream networks, main-stem rivers comprise 0.52 km^2, or 14%, of the mapped supraglacial network, with the inter-stream network accounting for the remainder of the supraglacial network (3.21 km^2, or 86% respectively). Drainage density, or D_d of the network, equates to 4.85 km^{-1}, with large rivers equating to 1.20 km^{-1} or 25% of the total D_d.

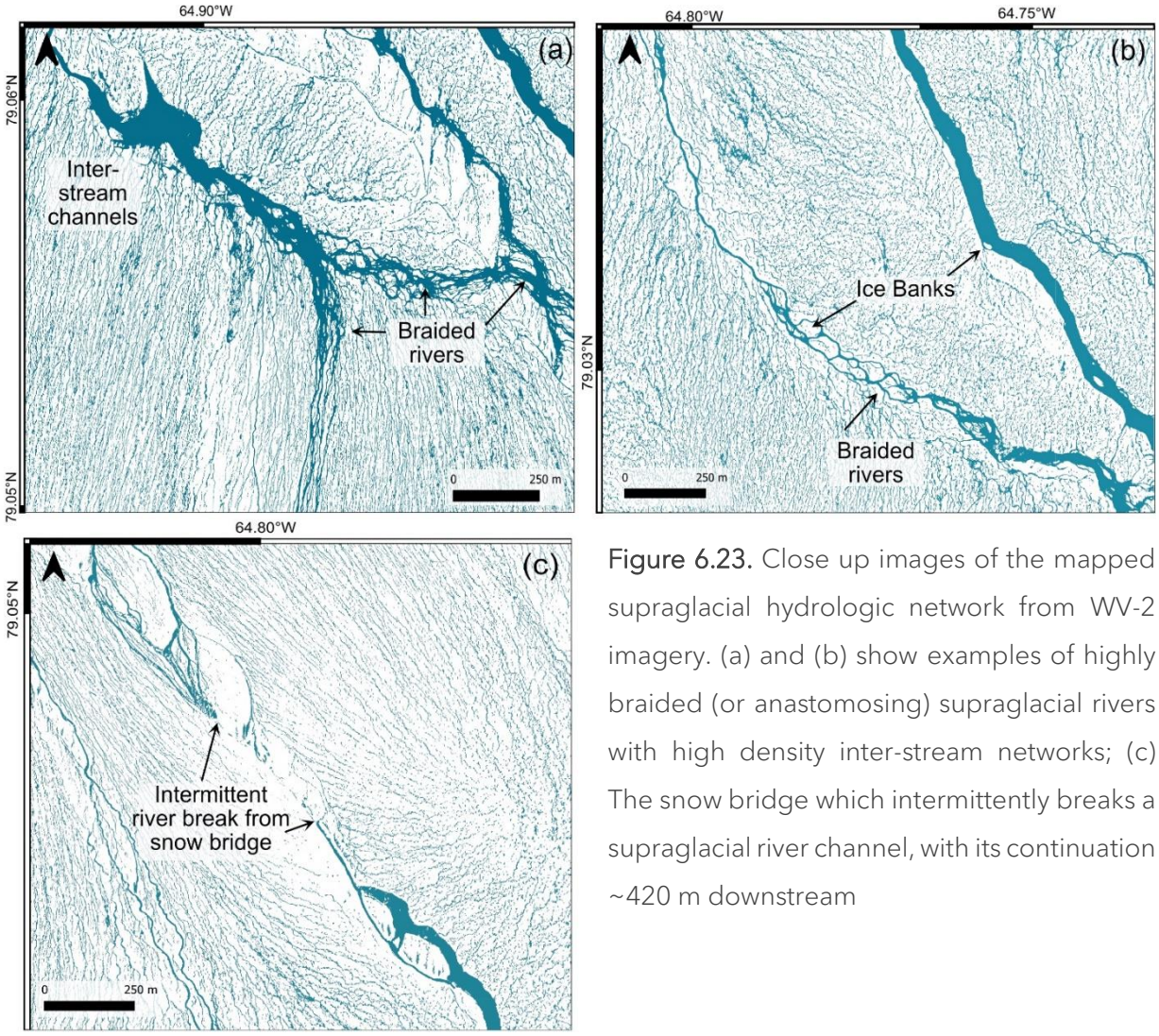

Figure 6.23. Close up images of the mapped supraglacial hydrologic network from WV-2 imagery. (a) and (b) show examples of highly braided (or anastomosing) supraglacial rivers with high density inter-stream networks; (c) The snow bridge which intermittently breaks a supraglacial river channel, with its continuation ~420 m downstream

6.7 Discussion of WV-2 results

The inter-stream networks mapped within the sampled bare ice area at Humboldt Glacier show their widespread presence confirming the further complexity of the supraglacial hydrologic system at this prominent northern glacier and the existence of such fine-scale features which do not appear in the mapped network shown in Chapters 4 and 5 of this thesis. Such narrow inter-stream networks are known to occur on the GrIS. They have been mapped in specific locations on the south-western GrIS (Yang and Smith, 2013; Smith *et al.*, 2015; Smith *et al.*, 2017) and can account for up to 66% of the supraglacial hydrologic network (Yang *et al.*, 2016). The expansive presence of such fine-scale supraglacial features has important implications for the production and movement of meltwater at both a large glacier-wide and smaller internally drained catchment scales (Yang and Smith, 2016; Smith *et al.*, 2017) as well as ice-albedo feedbacks (Ryan *et al.*, 2018; Skiles *et al.*, 2018).

Unlike main-stem supraglacial river channels, which are typically static and reoccur in the same location each year, finer-scale inter-stream networks are narrower, shallower and of lower-order (Pitcher and Smith, 2019), acting as feeder tributaries which also have the ability to change planform, pattern and abundance rapidly in response to both seasonal and diurnal meltwater supply and small-scale changes to surface elevation through ablating processes (Yang and Smith, 2016). Despite their narrower size, their collective area accounts for over 86% of the mapped network in this area, representing an important high-capacity mechanism for conveying meltwater across the Greenland surface into primary river channels that are otherwise undetectable or 'invisible' in coarser resolution imagery (Yang and Smith, 2016). Unlike supraglacial streams mapped in an area of western Greenland by Yang *et al.* (2016), mapped lower-order supraglacial streams accounted for up to 66% of the mapped network, with their lengths accounting for a small percentage of the total network length (13.8%). It should be stated that due to constraints with WV-2 imagery access in this

study at Humboldt Glacier, the full delineation of the primary and associated inter-stream network that continues downstream was unmapped. Therefore, whilst the supraglacial inter-stream network may still dominate total drainage area, drainage density calculations may be somewhat underestimated. However, whilst this hypothesis of underestimation is supported by findings in western Greenland, whereby lower-order streams were overall shorter in length and had lower drainage density calculations versus primary river segments also derived from WV-2 imagery (Yang *et al.*, 2016), inter-stream networks found in this study were generally longer in length and more complex in nature (parallel-style drainage and densely packed), which may further moderate the timing of melt to main river channels. This may be because more of the network was delineated in this study than Yang *et al.* (2016) However, it raises further important glacier-wide questions as to potential differences in lower-order streams across the GrIS and how important their role is in melt transport. A similarity, however, that is seen in the supraglacial channel morphology between north and western ice sheet regions when examining their morphology up-close is the occurrence of braided, or anastomosed segments, of primary river channels which are associated with low slopes (Yang *et al.*, 2016). Such features are likely the result of frequent variations in the large meltwater flows, inducing a stronger erosive control on ice banks (Knighton, 1981b; Jarosch and Gudmundsson, 2012; Yang *et al.*, 2016).

This expansive supraglacial hydrologic system derived from WV-2 imagery also has potential impacts on ice surface albedo and roughness. As shown in the UAV-derived research (Section 6.5) examining meltwater and surface facies characteristics in the ice marginal region of Russell Glacier, ice surface make-up is complex, with microscale features darkening the ice surface with the potential to generate a rougher ice surface. There is also a secondary role that the hydrologic system plays in albedo by consolidating and redistributing such sediments and impurities across the ice surface (Leidman *et al.*, 2023). As such, the existence

of these inter-stream networks is likely to further reduce ice albedo and increase surface roughness, interrupting the local surface energy balance in this bare ice zone.

Observations made in this chapter from both UAV and commercial WV-2 imagery also show the stark difference between the enhanced ability to capture the minutiae of the supraglacial network at micro-scale levels that is beyond possible to be seen or captured by coarser, freely-available imagery (e.g., Landsat and Sentinel-2 imagery; as further explored in Chapter 7.). Whilst these microscale networks are small and may look trivial, their combined action of meltwater movement across the ice surface to larger streams and rivers, as well as their secondary influence on surface reflectivity and roughness, further reveals their importance for continued quantification and understanding.

Whilst this research advances the link in understanding the hydrological-makeup of the ice surface in-detail, improvements in including these microscale features and such effects in climate and surface mass balance models are required.

6.8 Chapter synthesis and conclusion

Utilising two differing optical image platforms, a field-based UAV and commercial-based WV-2 satellite imagery, this chapter has explored the minutiae of the supraglacial hydrologic network, including microchannels, surface facies characteristics and inter-stream channels, to obtain further insights into the supraglacial network in (i) the spectrally-complex, dark ice marginal zone of western Greenland and (ii) the bare ice zone of Humboldt Glacier that coarser, freely-available satellite imagery cannot achieve. Results from both these platforms show the expansive presence of surface meltwater and the transport mechanisms by which melt is moved across the ice surface beyond large-scale river channels (<10 m wide); from shallow, slush-like microchannels measuring 0.04-0.5 m wide that flow from a highly

undulating surface near the ice margin to vast long inter-stream networks (3-5 m wide) feeding primary river channels in the mid-bare ice zone in the north. This chapter has also further quantified the surface morphology within the spectrally-complex and, subsequent, hard-to-map, darkened regions of southwestern Greenland to understand the complexities of this icy environment and some of the secondary influences, beyond incoming solar radiation, that can be responsible for driving surface melt. In particular, impacts of albedo and inferred enhancement of micro-scale roughness from such features, including microchannels and the widespread presence of cryoconite deposits and associated algal communities in a porous weathering crust, shows the complexities these features can play in affecting the surface energy balance, generating a rougher surface and increasing turbulent heat fluxes at the ice/atmosphere interface. Such insights across this small UAV-survey area are applicable ice-sheet wide, with the examination of small-scale features elsewhere, such as the extensive inter-stream network via WV-2 imagery at Humboldt Glacier, also likely to inherit some of these characteristics (i.e., reduced albedo, enhanced roughness, cryoconite deposits within channel beds) with melt-driven implications. These observations are an important stepping stone in providing both ground-truthing data and a more widespread overview of surface hydrologic system on the GrIS as well as ice surface complexities. There is a growing recognition that such accurate representations of surface characteristics and processes, including meltwater drainage and retention, are needed for realistically assessing the impact of climate variability on GrIS hydrological conditions, runoff and surface mass balance estimates that are currently lacking in modelling studies (van As *et al.*, 2016; van As *et al.*, 2017; Langen *et al.*, 2017; Mernild *et al.*, 2018), which will be further discussed in Chapter 7 of this thesis.

Chapter 7

Discussion

Synthesis, wider implications, future recommendations

7.1 Synthesis

The overall purpose of this thesis was to explore the complex and interconnected supraglacial hydrologic network of the GrIS that is expansive across the ablating margins during the summer melt season to provide further scientific contributions to (i) mapping the network in an understudied Greenlandic region as a collective system (i.e., rivers and lakes) and (ii) quantify and understand the distribution and evolution of the network across a range of temporal and spatial scales.

Recent studies of GrIS supraglacial hydrology have been primarily focussed on the western and southwestern regions with well-developed supraglacial hydrologic features strikingly observable in satellite imagery (Smith *et al.*, 2015; Yang and Smith, 2016; Smith *et al.*, 2017; Yang *et al.*, 2017; Smith *et al.*, 2021; Yang *et al.*, 2021). The Greenland-wide distribution of the network, however, remains less well known, with work conducted in this thesis motivated by the need to expand mapping efforts to other regions of the ice sheet where runoff has increased markedly in recent years and is expected to continue to expand with further warming (Noël *et al.*, 2019). This thesis has focussed on the supraglacial hydrologic network of the widest and largest marine-terminating outlet glacier in Greenland, Humboldt (Sermersuaq) Glacier, northern Greenland, which has lost the greatest area of grounded ice since 1992 of any GrIS outlet glacier (Box and Decker, 2011; Wood *et al.*, 2021) and is within a region that has undergone substantial ablation area expansion over the last two decades (Noël *et al.*, 2019). Unlike other investigations which have examined the GrIS supraglacial hydrologic network over a single melt year (Smith *et al.*, 2015; Lu *et al.*, 2021; Yang *et al.*, 2021) or a single date (King *et al.*, 2016; Yang *et al.*, 2019b), research conducted in this thesis has examined its distribution and evolution across a range of temporal and spatial scales, spanning three key research questions as introduced in Chapter 1. To review, these are outlined below:

RQ1: What does the surface hydrologic system look like at Humboldt Glacier, northern Greenland, and how does this network evolve over seasonal timescales?

RQ2: How has the supraglacial hydrologic network at Humboldt Glacier evolved over the last 30+ years?

RQ3: What does the minutiae of the supraglacial hydrologic network consist of in the (i) spectrally-complex ice marginal regions and (ii) the bare ice zone of the GrIS, beyond freely-available satellite imagery?

This chapter begins by summarising the key findings of this thesis, as reported in Chapters 4-6. These findings are then discussed within the wider context of the current and future projections of GrIS mass loss. The limitations of these findings are subsequently considered, and the chapter concludes with a discussion on recommendations for the future direction of supraglacial hydrologic research.

7.1.1 Summary of key research findings

Chapter 4 investigated, for the first time, the seasonal evolution of the supraglacial hydrologic network over multiple years Humboldt Glacier; the first to map the existence of the network here and examine its seasonal evolution over multiple years. A mapped record of the supraglacial hydrologic network was created for consecutive melt seasons of 2016 to 2020 using Sentinel-2 images and an automatic river detection algorithm by Yang *et al*. (2015a; 2017) to best extract the network retaining its narrow, linear form and connectivity; as introduced in Chapter 3. This work then quantified the hydrologic networks intra and inter-seasonal evolution.

An expansive supraglacial hydrologic network was found to exist extending up to 1440 m a.s.l., with a persistent and annually-recurrent network below 1000 m a.s.l (i.e., both rivers and SGLs) and a more transient network above 1000 m a.s.l whereby rapid planform

migration and reformation in space can occur if sufficient meltwater is available (Smith *et al.*, 2015; Pitcher and Smith, 2019). Seasonal evolution of the network was shown to transform from one dominated by unchannelised, inefficient flow in early-June to channelised, efficient flow as the snowline retreated upglacier at the end-of-July; consistent with other studies (Lampkin and VanderBerg, 2014; Yang *et al.*, 2017; Lu *et al.*, 2021; Yang *et al.*, 2021) and with modelled-runoff from MAR (Modèle Atmosphérique Régional). Much of the network persisted post-peak melt into August, likely due to the 'delay' effect, whereby residue melt may continue to be routed, stored or preserved in larger supraglacial rivers, SGLs or within the snowpack/firn at higher elevations prior to refreezing (Lu *et al.*, 2021). The timing, migration and inland expansion of the network, however, had large inter-annual variability due to dynamic links with the atmospheric circulation of the North Atlantic Oscillation (NAO) and Greenland Blocking Index (GBI). The exceptional melt years of 2016 and 2019 characterised by high areal and inland supraglacial hydrologic extents were influenced by a strong negative phase of the NAO and positive GBI which promoted warm southwestern-advected air, clear skies and enhanced solar radiation (Cullather *et al.*, 2020; Sasgen *et al.*, 2020; Tedesco and Fettweis, 2020; Hanna *et al.*, 2021). In particular, the lengthy melt season of 2019 favoured the formation of buried liquid water which remained unfrozen over winter (Schröder *et al.*, 2020). Combined with a drier-than-average spring into 2020 (Tedesco and Fettweis, 2020), this caused swift bare ice exposure and an anomalously early-spike in supraglacial meltwater area early into the 2020 melt season. This raised further questions as to how extreme and lengthy melt years may precondition the ice surface for subsequent melt seasons (Culberg *et al.*, 2021). Conversely, the onset and evolution of the melt seasons in 2017 and 2018 were delayed by ~1 month compared to other years examined, with meltwater area peak and inland expansion not occurring until August and being confined to 1150 m a.s.l in 2017 and 1050 m a.s.l in 2018; the result of a positive NAO and negative GBI

which promoted anomalously-cold summers with inhibited melt and increased summertime snowfall (Ruan *et al.*, 2019; Sasgen *et al.*, 2020).

Intra-catchment variation of the hydrologic network configuration was also shown, with a dendritic-style of drainage and the abrupt termination of larger primary rivers in the northern sector and a parallel-style of drainage with continuously-flowing rivers draining from the slush zone (~1500 m a.s.l) to lower elevations (200 m a.s.l) in the southern sector. Such differences were attributed to the increased interception of runoff by crevasses and moulins in the northern sector and the difference in bed-to-surface topographic wavelength transfer controlled by differing flow regimes, preconditioning the large-scale spatial structure of the surface system, as shown by Lu *et al.* (2021) at Nioghalvfjerdsbrae (the '79°N Glacier'). Additionally, multiple basal structures, including two geological structures, which run southwest to northeast identified by Livingstone *et al.* (2017), were expressed on the ice surface as depressions and shown to control the multi-year surface drainage configuration within their vicinity.

The findings from this Chapter contribute to advancing the scientific understanding of supraglacial hydrologic processes across the GrIS, in particular within unmapped regions and its behaviour across multiple melt seasons, in particular during a high versus low melt year. Additionally, work into the behaviour of the network in high melt seasons suggested that such rapid and extensive inland development, persistence, and the knock-on effects of extreme melt years preconditioning the ice surface for future seasons, will likely become representative of network behaviour with continued warming and enhanced runoff into the future.

The aim of Chapter 5 was to be the first to investigate the multi-annual evolution of the generalised structure of the supraglacial hydrologic network (i.e., primary river channels and lakes) on an extended timescale using the longest-running Earth observation satellite,

Landsat. Through Google Earth Engines (GEE) Landsat archive, annual meltwater maps were derived between 1985 and 2021 using mean NDWI pixel values between the melt season months of June, July and August (JJA), with the network subsequently extracted via the same automatic river detection algorithm used in Chapter 4 (Yang *et al.*, 2015a; 2017). The opportunity was also undertaken to utilise this imagery to assess terminus change, in particular the retreat behaviour of the northern and southern sectors of Humboldt Glacier, as per Carr *et al.* (2015). Changes to the areal extent and inland evolution of the supraglacial network were also compared to regional climate modelled temperature and runoff data from MAR to assess long-term controls.

The terminus of Humboldt Glacier retreated by an average of 4.7 ± 0.09 km and maximum of 13.4 ± 0.03 km over 37 years, with retreat between 2000 and 2021 being 2.8 times greater than between 1985 and 1999; consistent with the onset of rapid warming post-2000 and Greenland-wide observations of increased marine-terminating glacial retreat during the same period (Moon and Joughin, 2008; Howat and Eddy, 2011; Murray *et al.*, 2015; King *et al.*, 2020). This response of Greenlandic outlet glaciers, including Humboldt Glacier, to external forcing was likely due to (i) enhanced availability of surface meltwater and therefore hydrofracture potential promoting calving (Nick *et al.*, 2013; Carr *et al.*, 2015); (ii) increased submarine melt rates from oceanic warming and increased plume activity from subglacial discharge (Carr *et al.*, 2015; Rignot *et al.*, 2021; Slater and Straneo, 2022); (iii) enhanced surface ablation, which combined with increased submarine melt thinned the near-terminus region of marine-terminating glaciers reducing their basal friction, particularly in southwestern Greenland (Howat *et al.*, 2008) and (iv) earlier seasonal break-up and overall reduction of ice melange with greater and longer exposure of the terminus to external pressures (Carr *et al.*, 2015; Cassotto *et al.*, 2015; Moon *et al.*, 2015). Of the retreat at Humboldt Glacier between 1985 and 2021, 87% of its total loss in length occurred in the northern sector post-1999, with average retreat rates an order of magnitude higher than in

the southern sector, attributed to differences in bed geometry (Bunce *et al.*, 2018) and the promotion of many internal and external factors in the northern sector due to greater terminus exposure and its deep-seated position in its subglacial trough.

Between 1985 and 2021, Humboldt's supraglacial hydrologic network doubled in areal coverage (98%) and expanded inland by a mean and maximum elevation of 293 m (7.9 m a^{-1}) and 432 m (11.7 m a^{-1}), respectively, reaching a maximum recorded elevation of 1464 m a.s.l in 2021. Such trends were consistent with other observations (predominately of SGLs) from western and northern Greenland (Gledhill and Williamson, 2018; Otto *et al.*, 2022; Zhu *et al.*, 2022). The expansion of the network coincided with an 80% increase in runoff at Humboldt Glacier and trends of ablation area expansion, snowline retreat and runoff amplification in northern Greenland post-2000 (Noël *et al.*, 2019; Tedesco and Fettweis, 2020; Slater *et al.*, 2021). The largest network expansion occurred between 2010 and 2021, in-line with increased air temperature and runoff anomalies, with this period experiencing a number of notable extreme melt events including 2012, 2016 and 2019, promoted by strong atmospheric conditions of the NAO and GBI (Bevis *et al.*, 2019). Large interannual variability from such atmospheric circulation is highly likely to play a role in the response and behaviour of this surface network now and more so into the future.

The expansion of the network over the study period largely involved the lengthening of already-existing channels to higher elevations, with the generalised network below 1000 m a.s.l remaining stable overtime. The expansion of the network inland (>1200 m a.s.l) into the *'transient zone'*, as coined in Chapter 4, was found to be highly variable due to the short lifespan of such channels which have only consistently appeared at such elevations post-2008 and their ability to only form and change planform here if meltwater is readily available (Pitcher and Smith, 2019; Rawlins *et al.*, *in review*). Additionally, the makeup of the network varied over time, with supraglacial channels becoming increasingly dominant in the

network's composition (80%) as they extended inland, with SGLs playing a less dominant role (20%) linked to reduced transfer of bed topography to ice surface where ice is thicker and there is less basal sliding surface topographic constraints (Igneczi *et al.*, 2016) and the rare distribution of lakes >800 m a.s.l. However, it can be postulated that with ice thinning in the future, more depressions may become available for SGL formation. Additionally, two parallel basal structures expressed on the ice surface identified in Chapter 4 from Livingstone *et al*. (2017), were shown by this work to be a significant control on supraglacial hydrology, with many rivers and lakes aligned to the structures dating back to 1985. These observations have demonstrated the long-term significant role such structures play in the configuration and stability of the network and the potential for further bedrock controls inland influencing the future configuration of the network when ice thickness permits their expression at the surface.

Assessment of SGL change overtime found that whilst the overall number of SGLs did not significantly change due to the loss of SGLs at the retreating terminus and their gain at higher elevations, total SGL area and mean individual SGL size did significantly increase by 81% and 174%, respectively. The inland expansion of SGLs followed the pattern of available ice surface depressions, which are required for lake formation (Ignéczi *et al.*, 2018; Otto *et al.*, 2022), with their size increasing with elevation due to longer wavelength bed undulations being favourably transferred to the ice surface through thicker ice (Ng *et al.*, 2018). Unlike smaller SGLs <400 m a.s.l which have likely reached their maximum available melt area, higher-elevation lakes are not yet topographically constrained (Krawczynski *et al.*, 2009). As SGLs are already forming at progressively higher elevations and covering greater extents, particularly within the mid-to-upper ablation zone, the likelihood of SGLs that have not drained before becoming drain-active in the future will undoubtedly supply meltwater to new areas of the bed with potential ice dynamic implications (Christoffersen *et al.*, 2018).

Finally, Chapter 6 used ultra-high-resolution imagery from both field-based UAV surveys (0.009 – 0.18 m) and commercial-based platforms (Worldview-2; 0.4 m) to assess the minutiae of the supraglacial network beyond what is visible in freely available satellite imagery (i.e., Sentinel-2 and Landsat, covered in Chapters 4 and 5). This chapter focussed upon the presence of microchannels, surface facies and inter-stream networks in two distinctive areas of the ablation zone; (i) the spectrally-complex ice marginal region (<1 km from the margin) where debris-laden, crevassed surfaces dominate and (ii) an inland zone (25 km) where main-stem river channels are shown to dominate.

A UAV survey covering 7414 m^2 was conducted on rugged, undulating icy terrain of the ice marginal zone of Russell Glacier, southwest Greenland, with Structure-from-Motion (SfM) photogrammetric models reconstructing the survey scene in 2D and 3D (orthomosaic at 0.009 m pix^{-1} and DEM at 0.18 m pix^{-1}). Supraglacial streams and microchannel networks (<0.5 m wide) were manually mapped from the orthomosaic model and supervised classification performed to classify the ice surface into four key facies; (i) water (+cryoconite), (ii) slush, (iii) algae and/or surface cryoconite, and (iv) bare ice. A further proxy for albedo was determined using the digital numbers from individual red, green and blue image channels to infer surface reflectivity (Rippin *et al.*, 2015). For WV-2 imagery, a 20.3 km^2 section of the bare ice zone (~790 m a.s.l) at Humboldt Glacier, was examined using the panchromatic band (0.4 m) passed through the automatic linear detection algorithm (Yang *et al.*, 2015a; Yang *et al.*, 2017) to extract the supraglacial hydrologic network with a particular focus on inter-stream networks which are too narrow for conventionally-available imagery (i.e., Landsat and Sentinel-2).

Three prominent streams (0.59 ± 0.44 m wide) flowed between topographic undulations and beyond the surveyed scene, with a number of finer-scale microchannels (0.06-0.5 m wide) flowing down the side of topographical hummocks as shallow, slush-like flows through

a porous weathering crust; a substrate vulnerable to the initiation of rill-type flow (Schuster, 2001). In total, streams with extensive cryoconite channel bed coverage (and any additional areas of water and cryoconite) accounted for 4.5% of the survey scene and had a lower proxy albedo value than any other surface facies, with such wetted cryoconite able to absorb 23% more incoming solar radiation (Boggild *et al.*, 2010) used to increase water temperatures and thus provide more thermal energy for expansion of the channel (Karlstrom *et al.*, 2013; Leidman *et al.*, 2023). As the survey was conducted in August, post peak-melt, stream-based cryoconite has been shown to increase in cover by 0.75% a day despite an overall reduction in melt, which simultaneously drives a more negative SMB with the potential to extend the number of melt days (Leidman *et al.*, 2023). Cryoconite deposits and algal communities were the dominant surface facies, covering 49% of the survey area, with particular abundance on northern and western facing slopes hypothesised to be the result of uneven diurnal melting promoting shallower slopes and accumulation of cryoconite-based deposits which facilitate microbial activity (Yallop *et al.*, 2012). These facies also had the second lowest proxy albedo values which were 21% lower than bare ice; bare ice of which covered 44% of the scene and was predominately found on the steeper, southern facing slopes of topographical hummocks. Reduced cryoconite presence on these slopes was likely due to enhanced diurnal exposure of incoming solar radiation driving increased melt and higher redistribution of melt-out cryoconite downslope into the microchannel beds below.

The widespread occurrence of micro-scale features, including streams, microchannels and cryoconite-based surface deposits with associated algal communities, were also discussed in relation to the surface energy balance. They not only affect the albedo of the ice surface as their darker nature absorbs more incoming radiation driving further melt (i.e., a positive feedback loop), but their presence is also known to drive roughness variations across the surface, generating more turbulence in the ice/atmosphere boundary layer, affecting

turbulent heat fluxes and enhancing melt rates (Cathles *et al.*, 2011; Rippin *et al.*, 2015; Irvine-Fynn *et al.*, 2022).

From WV-2 imagery, main-stem river channels with highly-braided segments were present alongside an extensive inter-stream network which do not appear in the mapped networks of Humboldt Glacier in Chapters 4 and 5. These inter-stream networks were 1-2 m wide and exhibited sinuous characteristics, which anastomose with each other and ultimately feed into the main river channels. These inter-stream networks accounted for 86% of the mapped network, representing a high-capacity mechanism for the transportation of melt across the GrIS surface. Collectively, these fine-scale features from UAV and WV-2 imagery have shown the complexity of the supraglacial hydrologic network beyond that of coarser, freely available imagery and highlighted the need to have a holistic understanding of the network, not only for meltwater transport but its secondary, localised effects on the surface energy balance with subsequent SMB implications.

7.2 Wider implications

Drawing together these findings, collectively the three results chapters of this thesis (Chapters 4-6) show a range of wider implications for the current understanding of the supraglacial hydrologic network and SMB of the GrIS. Even though this work has been primarily centred around northern Greenland, with the exception of Chapter 6 which also touches upon the spectrally-complex and, subsequent, hard-to-map ice marginal zone of southwestern Greenland, findings presented in this thesis motivate further remote sensing and field-based studies. In particular, understanding into the past, present and future extent of the supraglacial hydrologic network is key for assessing its influence on the SMB of the GrIS and other large ice bodies, such as the Antarctic Ice Sheet (AIS).

The response of the GrIS to future warming will vary in relation to different shared socioeconomic pathways (SSPs), as per the recent IPCC report (IPCC, 2021). Surface temperatures will continue to rise on a global scale for all SSP scenarios, with a projected 1–1.8°C for the lowest scenarios (SSP1-1.9), 2.1–3.5°C for intermediate scenarios (SSP2-4.5) and 3.3–5.7°C for high emission scenarios (SSP5-8.5) up to the year 2100 (compared to 1850–1900; IPCC, 2021). For Arctic regions, warming will be significantly greater than these global mean values due to the effects of Arctic Amplification, which has already resulted in Arctic surface temperatures increasing by more than double the global average, with projections of up to 6°C for SSP8.5 by the end of the century (Overland *et al.*, 2019; IPCC, 2021). Even limiting the warming to 1.5°C, which is the most ambitious goal of the Paris Climate Agreement (UNFCCC, 2015), the Arctic is projected to still warm by up to 4°C with the GrIS entering a phase of irreversible loss this century (Overland *et al.*, 2019). With continued warming and the likelihood of extreme melt events becoming more frequent, severe, and persistent (Beckmann and Winkelmann, 2022; Mattingly *et al.*, 2023) driving lengthier melt seasons (Cook *et al.*, 2020), the GrIS snow line is likely to start migrating earlier in the melt season and continue shifting to higher elevations (Ryan *et al.*, 2019). This will continue expanding the bare ice ablating zone, which currently produces a large proportion of Greenland's total runoff (78%; Steger *et al.*, 2017b). An increased bare ice zone will increase the areal extent of melt and subsequent runoff (Cuffey and Paterson, 2010; Tedesco *et al.*, 2011; Lampkin and VanderBerg, 2014; Noël *et al.*, 2019), with implications for the supraglacial hydrologic network, including (i) earlier initiation for years with greater melt which precondition the ice surface for such early and rapid transport of melt in following years, as reported in Chapter 4 and (ii) becoming more areally extensive and transporting melt greater distances from higher elevations, as seen with inland expansion of the network in Chapter 5 over the period 1985 to 2021. What is currently denoted as an 'extreme' melt year during years examined in Chapters 4 and 5 (i.e., 2016 and 2019) with the areal and

inland expansive-response of the supraglacial hydrologic network, may become the 'norm' for future melt seasons, with subsequent findings in these chapters acting as an analogue for the future behaviour of this system. The supraglacial network also supplies as much as 40-98% of total proglacial river discharge from Greenland (Smith *et al.*, 2015), making it vital for understanding the hydrology of glacial systems and the associated impacts of Greenland on large-scale ocean circulations and global sea level rise (Fettweis *et al.*, 2013; Albert *et al.*, 2016; Muntjewerf *et al.*, 2020).

During the 21st century, surface processes are projected to continue to be the primary contributor of mass loss across the GrIS for all SSP scenarios, rather than ice discharge (Goelzer *et al.*, 2020; Fox-Kemper *et al.*, 2021 in IPCC, 2021; Payne *et al.*, 2021). This is not only due to the increasing amount of surface melting and runoff in the expanding bare ice zone, but ice sheet thinning, darkening of the ice surface and the loss of refreezing capacity in the lower-accumulation firn zone (Machguth *et al.*, 2016; Cooper *et al.*, 2018; MacFerrin *et al.*, 2019; Noël *et al.*, 2019; Noël *et al.*, 2022). Thinning of the ice sheet due to increasing ablation is affected by a positive feedback loop between SMB and elevation: as surface elevation falls, surface air temperature rises driving surface melt increase and the magnification of ablation (Gregory *et al.*, 2020). However, due to differences in ice sheet hypsometry (i.e., area-elevation distribution) and climate, such impacts will be regionally-dependent (Ryan *et al.*, 2019). Additionally, a wider ablation zone, which is characteristically darker and consists of semi-impermeable bare ice, strongly enhances the melt-feedback with the magnitude of darkening likely to be driven by earlier and higher migration of the snowline, which will drive increasing meltwater features (i.e., expanse and duration of the network), concentrations of light absorbing impurities (i.e., cryoconite deposits) and biologically-active habitats for algal growth (Benning *et al.*, 2014; Tedesco *et al.*, 2016). Snowline increasing in elevation and additional melting into the percolation zone will also cause snow grain size to increase, which if not replenished by fresh snow, can promote

metamorphism and lead to further reductions in albedo (Brun, 1989; Moustafa *et al.*, 2015; Lewis *et al.*, 2021; Box *et al.*, 2022b).

In the lower accumulation zone, which is comprised of firn that currently acts a 'buffer' for meltwater runoff, this capacity could be significantly reduced as a result of increasing temperatures and expansion of the ablation zone, with knock-on effects to the amount of liquid-water subsequently transported and evacuated each summer (Noël *et al.*, 2022). Recent studies already indicate that the meltwater retention capacity of this zone has already decreased in the western GrIS between 1998-2008 and 2010-2017, with the rapid expansion of low-permeability ice slabs, formed from the refreezing of meltwater, rapidly expanding and increasing runoff here since 2001 (MacFerrin *et al.*, 2019). The firn layer currently retains ~45% of liquid water from surface meltwater and rain, or ~230 Gt yr^{-1} (1960–2014; Steger *et al.*, 2017a). However, due to (i) runoff increasing quadratically with atmospheric warming (Trusel *et al.*, 2018), (ii) firn retreating and the exposure of dark bare ice (Noël *et al.*, 2019; Ryan *et al.*, 2019) and (iii) increased rainfall events over snowfall limiting the recovery of the firn layer (Doyle *et al.*, 2015; Lenaerts *et al.*, 2020), pore space is progressively depleting within this zone with its projected loss in next 100 years marking a 'tipping point' for GrIS mass loss (Noël *et al.*, 2022). Under the lowest SSP (1-2.6), it is projected SMB is expected to contribute 0.03 (0.01-0.07) m to SLR by 2100 and for the highest SSP (5-8.5), a SLR contribution of 0.07 (0.03–0.16) m (Fox-Kemper *et al.*, 2021 in IPCC, 2021). Upon Greenland passing its 'tipping point', its contribution to global SLR could increase over twenty-fold compared to the last three decades (Noël *et al.*, 2022).

In particular, northern sectors of Greenland are expected to be major contributors to ice sheet mass loss and SLR by the end of this century through decreasing SMB (Muntjewerf *et al.*, 2020). At northern margins, the ablation zone is expected to progress faster inland than southern margins, as a result of low meltwater buffering capacity of the snow pack (Lenaerts

et al., 2015) and hypsometric amplification; the flattening of the ice surface towards higher elevations which will promote a gain in the net surface area of the ice surface exposed to such melt conditions (Mikkelsen *et al.*, 2016). Already this region has experienced the fastest atmospheric warming in Greenland and upward migration of the runoff line since 1990 as a result of their wide ablating zones and gently sloping ice sheet margins (Albert *et al.*, 2016; Noël *et al.*, 2019; Noël *et al.*, 2022). In projections by Muntjewerf *et al.* (2020), northern basins compounded by the marine-terminating margin could contribute 43% to total SMB decrease by the end of the century and 45% to total SLR, showing the importance of this region to overall GrIS mass loss and SLR now and into the future (Figure 7.1).

Ice discharge will still play a major role in GrIS mass loss in the coming decades, particularly within this region, due to the dominance of marine-terminating glaciers. However, with mass changes due to SMB, including thinning margins, inland retreat and hydrologic links with outlet glacier dynamics, mass loss through ice discharge is likely to decline over longer timescales as the ice retreats onto land above sea level, becoming isolated from marine influences (Nick *et al.*, 2013; Fürst *et al.*, 2015; Aschwanden *et al.*, 2019).

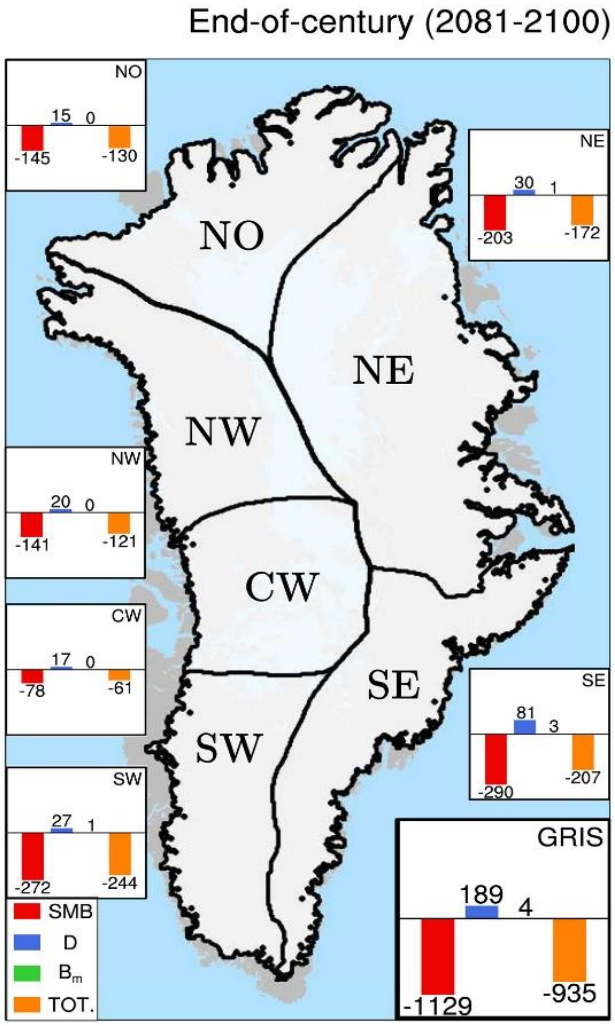

Figure 7.1. Change in GrIS mass balance and the components that comprise it with respect to the contemporary budget (1995 – 2014) and end of Century (2081 – 2100), expressed in Gt yr^{-1}. GrIS mass balance (TOT; orange), surface mass balance (SMB; red), ice discharge (D; blue) and basal melt (B_m; green). Figure taken from Muntjewerf *et al.* (2020).

7.3 Limitations

There are several limitations associated with the approaches and methods used within this thesis, primarily surrounding the automatic river detection algorithm developed by Yang *et al.* (2015a; 2017) and satellite imagery used in Chapters 4-6, which are discussed further below.

As shown in performance accuracy results in the respective data chapters (Chapter 4 and 5), the automatic river detection method produces supraglacial rivers and streams that are shorter (5.4%) than those from manual digitisation. Whilst overall performance accuracy is better than in other studies (e.g., Lu *et al.* (2020) who found delineated channels were 16.3% shorter than manual digitisation) and automated mapping is quicker to achieve than manual digitisation, connectivity due to varying pixel intensity (i.e., NDWI) within channel networks still poses an issue. This then presents additional issues for using such networks in further morphometric analysis, for example deriving stream orders and bifurcation ratios, which require seamless flow (King *et al.*, 2016). To account for such connectivity issues, surface hydrologic mapping via DEMs whereby network connectivity is implicit in flow routing, could be combined with satellite-mapped networks to reconnect and fill such gaps. DEM-derived supraglacial mapping of river and stream networks has had varying successes at varying scales (Yang *et al.*, 2015b; Karlstrom and Yang, 2016; Bash *et al.*, 2022). As shown by Karlstrom and Yang (2016) and King *et al.* (2016), when terminal points (i.e., moulins, terminal SGLs and crevasses) or 'sinks' as known in flow routing, are preserved rather than filled, the resultant network is more realistic and comparable to those by satellite-derivation, particularly for higher-order channels and broad-scale drainage patterns. DEM-derived networks could therefore be utilised to fill connectivity gaps in satellite-derived channels. Caution and manual intervention would, however, be required as DEM flow routing accuracy has been shown to decrease with stream order and elevation, particularly for lower resolution DEMs where difficulties in specifying channel heads occurs due to slushy headwater zones (King *et al.*, 2016). Additionally, some temporary gaps in channel networks are the result of snow bridges or moulin capture, which should be considered. Therefore, selecting site and time-specific channel initiation thresholds from DEM flow routing is required to best extract the most-realistic and comparable network possible as well as

careful implementation of connectivity filling for river and stream channels where there is high confidence that DEM-derived networks overlap.

Mapping conducted in this thesis has also shown the effect image resolution can have on the extraction of the supraglacial hydrologic network, in particular discerning different sized channels. As shown in Figure 7.2, which compares a section of mapped imagery from Landsat, Sentinel-2 and WV-2 from Chapters 4-6, clear differences in how much of the overall network has been extracted can be seen. Sentinel-2 imagery has a resolution that is three times higher than Landsat imagery, and panchromatic imagery from WV-2 has a resolution that is twenty-five times higher than Sentinel-2 imagery and seventy-five times higher than Landsat imagery, therefore providing a much greater ability to identify small scale features, even if it is over a reduced area. Sentinel-2 images are able to partially discern short, often braided river networks, whereas these features were difficult to identify or discern in Landsat images. Landsat imagery was able to primarily discern large scale, main-stem, primary supraglacial rivers which is important for understanding the generalised structure of the network, but anything smaller is imperceptible. Of course, for WV-2 imagery, narrow, braided or anastomosing channels were easily identifiable and delineated with a whole host of additional, narrow (1-10 m), inter-stream networks visible. In terms of the quantification of the supraglacial hydrologic network between these differing resolutions, the area (area fraction, %) within each Landsat, Sentinel-2 and WV-2 image panels are 1.39 km^2 (6.8%), 1.63 km^2 (8%) and 3.74 km^2 (18.4%), respectively. The delineation and quantification of networks therefore requires careful consideration and planning in mapping studies, taking into account sensor-specific characteristics with the acknowledgement that with coarser resolution imagery, intricate channel characteristics and underrepresentation of the full network will occur, but broader-scale network insights such as drainage configuration and primary river channels which transport the largest melt volumes will remain valuable, particularly in unmapped regions and for exploring long-term evolution (Yang *et al.*, 2021).

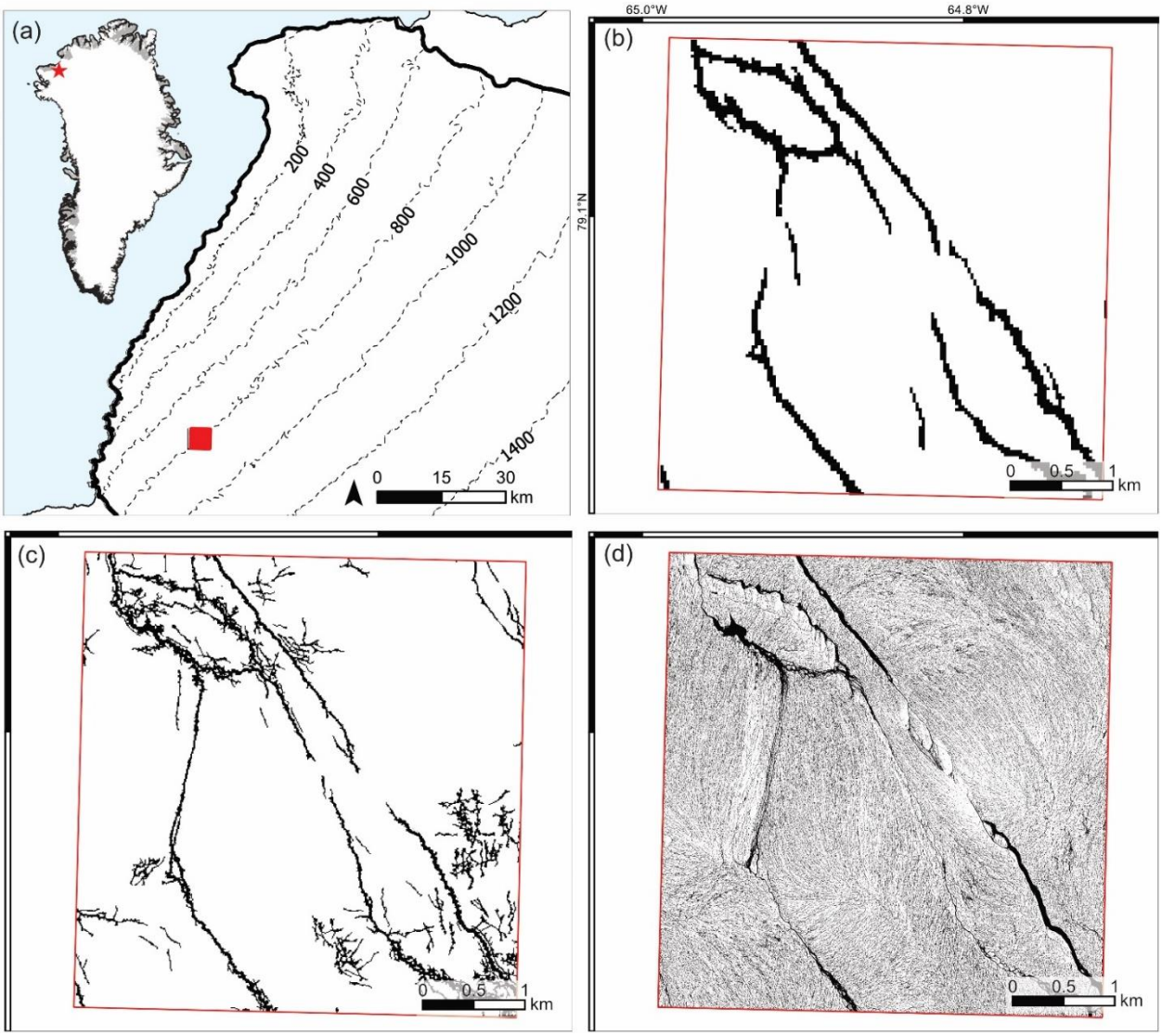

Figure 7.2. Comparison of the extracted supraglacial hydrologic network from a section of the mapped Humboldt Glacier (a) in this thesis; (b) Landsat image (30 m); (c) Sentinel-2 image (10 m); (d) Worldview-2 image (0.4 m)

Additionally, research conducted in this thesis, as well as much for the supraglacial hydrologic mapping on the GrIS to-date (Smith *et al.*, 2015; Karlstrom and Yang, 2016; Karlstrom and Yang, 2016; Yang *et al.*, 2016; Yang *et al.*, 2016; Smith *et al.*, 2017; Lu *et al.*, 2020; Lu *et al.*, 2021; Yang *et al.*, 2021; Rawlins *et al., in review*), has used multispectral (optical) imagery-only alongside automated methods (i.e., NDWI, automatic river detection

algorithms and supervised classifications). A wealth of other active remotely-sensed platforms are available to enhance the mapping capabilities of supraglacial features that cannot be detected or monitored by optical imagery alone. For example, optical sensors cannot detect features during the polar night, are easily disturbed by clouds, rain, fog and snow and light conditions (Jiang *et al.*, 2022). In contrast, the additional use of Synthetic Aperture Radar (SAR) imagery, such as Sentinel-1, can operate all-day in all-weather conditions and has been used to closely monitor the drainage of SGLs (Miles *et al.*, 2017; Schröder *et al.*, 2020) as well as reveal snow-buried liquid water bodies at high elevations (up to ~1700 m a.s.l), even during winter (Koenig *et al.*, 2015). Sentinel-1 has been used for multiple SGL mapping studies both across the GrIS and AIS (Miles *et al.*, 2017; Dirscherl *et al.*, 2020; Benedek and Willis, 2021; Jiang *et al.*, 2022). However, it has been highlighted that such surface features are not always clear in SAR imagery and can experience fuzzy edges, low visual contrast and speckling, making features difficult to differentiate with no additional image information (e.g., different radar polarisations, temporal information, elevation data; (Dirscherl *et al.*, 2020)). As SAR detection is also heavily influenced by liquid water, including high water content in snow during the melt season (Schröder *et al.*, 2020), there is the potential for overestimation of meltwater area (Hochreuther *et al.*, 2021). Therefore, such considerations in using SAR as well as fine-tuning of its thresholds for supraglacial mapping should be accounted for based on local conditions (Williamson *et al.*, 2017). Future work assessing high temporal and spatial resolution evolutionary behaviour of the network may therefore find it beneficial to use a multi-sensor approach to reliably assess diurnal-to-seasonal behaviour, such as SGL drainages, and seasonal network evolution.

A final limitation to be addressed here is the restricted areal coverage of the UAV survey and commercial-based WV-2 imagery used in Chapter 6 at Russell Glacier and Humboldt Glacier, respectively, to assess the minutiae of the supraglacial hydrologic network. Field-based studies are an important component not only within supraglacial hydrologic research,

but cryospheric research as a whole. In this thesis, field-based optical imaging in Chapter 6 enabled microchannel networks and surface facies characteristics to be explored in great detail, despite limited coverage, which could potentially be scaled-up to provide further larger-scale insights into the complexities of the hydrologic network and detailed composition of the ice surface. Other supraglacial hydrologic studies have also utilised field-based data to assess small-scale features and for the validation of models. For example, Leidman *et al*. (2023) assessed the variability of cryoconite-based deposits in supraglacial streams and its flux with seasonal meltwater flow to explore the influence of stream expansion and impacts on the surface energy balance. Smith *et al*. (2015) used in-situ supraglacial channel hydraulic measurements to calibrate two empirical remote-sensing algorithms for the estimation of water depth and discharge in WV-2 images in southwest Greenland. Whilst studies that utilise both field-based and ultra-high-resolution imagery, such as WV-2, may not be as spatially or temporally extensive, they can ultimately be used to 'ground-truth' other coarser, remotely-sensed datasets as shown in Figure 7.2, to provide validation that a certain feature is present before the potential for misclassification or removal in automated methods (e.g., thresholding). In particular, field data are incredibly valuable for validating, calibrating and realistically representing various components of the supraglacial network in modelling studies. As reviewed by Pitcher and Smith (2019), field data and observations are lacking for a number of hydrologic processes. This includes (i) evolution of channel geometry (i.e., meandering and incision rates), (ii) flow rates through open channel vs interfluve flow which modulates water velocity and (iii) discharge estimates for monitoring diurnal and seasonal discharge, typically via hydrographs, to better constrain the timing and volume of meltwater delivery to moulins, with Smith *et al*. (2017) converting modelled runoff with in-situ hydrograph coefficients to represent internally drained catchment discharge into a moulin. Such field observations are continually required to provide model parameters and better represent a multitude of surface processes.

7.4 Directions for future research

In this final discussion, recommendations for future research are advocated, based on the wider findings, implications and limitations discussed throughout this Chapter.

Research conducted in this thesis has provided an important stepping-stone in supraglacial hydrologic research on the GrIS, with each Chapter and its associated aims and objectives not only helping to expand network mapping to other regions of the ice sheet, but in furthering understanding into the seasonal and long-term evolution of the supraglacial hydrologic network. Nevertheless, findings presented in this thesis motivate further field and remote sensing observations, together with improving model simulations, to continue increasing our understanding of the current and future expansion of the supraglacial hydrologic network with increasing runoff and the influence this will have on future dynamic ice loss.

Firstly, the detailed supraglacial hydrology of large areas of the GrIS remain unmapped and, indeed, the global distribution of the supraglacial hydrologic network, is largely incomplete due to the fact the cryosphere is largely harsh and inaccessible for field-based studies and the resolution of satellite imagery can be difficult in resolving narrow channel features (Chu, 2014; Pitcher and Smith, 2019); as explored in this thesis. The advent of new high resolution satellite data, including the Planet constellation (3-5 m) which has a daily revisit rate, offers exciting prospects in the mapping of such networks at both a finer spatial and temporal scale, which combined with other datasets in a 'multi-satellite sensor approach' makes global supraglacial mapping and understanding into their distribution and behaviour evermore feasible (Pitcher and Smith, 2019). Additionally, such datasets can also be used to provide further, higher-resolution estimates of meltwater volume within the supraglacial hydrologic network. Whilst meltwater volume was not a calculated metric in work conducted in this thesis, it is important for assessing the relative storage capacity of lakes and rivers as well

helping to reduce uncertainties in surface runoff simulations and ice flow modelling (Smith *et al.*, 2017; Yang *et al.*, 2018; Yang *et al.*, 2021). A commonly used method for calculating meltwater volume from satellite-acquired imagery is a workflow developed by Pope *et al.* (2016) which uses spectral reflectance properties of water alongside an empirical relationship with its depth multiplied by meltwater area from Landsat 8 to derive estimated volume. A wealth of studies have utilised and adapted this method, predominately for the calculation of SGL volumes on both the GrIS and AIS (Williamson *et al.*, 2017; Yang *et al.*, 2019a; Arthur *et al.*, 2020b; Moussavi *et al.*, 2020). However, recently this method was also used for volume estimation of the supraglacial network (i.e., both rivers and lakes) by Yang *et al.* (2021). Further developments utilising work conducted in this thesis could therefore be made, including meltwater volume estimates as well as further hydrologic metrics (e.g., stream order), once network connectivity has been improved (as suggested in Section 7.3).

Recent advances in cloud-computing technology, for example GEE, utilised in Chapter 5 which hosts a wealth of geospatial datasets, is yet to be fully utilised for hydrologic mapping purposes, predominately driving understanding into the long-term evolution of broad-scale generalised network structures. Research conducted in Chapter 5 was the first to explore the long-term evolution of the supraglacial hydrologic network as an integrated system over 30+ years using Landsat-era imagery. Further exploitation of this imagery is necessary to understand the long-term behavioural evolution of this network, despite its resolution, not only on an annual basis (i.e., annual meltwater masks produced in Chapter 5) but the long-term seasonal evolution of the network; i.e., the length of melt seasons and the time for a seasonally efficient network to develop. Exploration of the inland expansion of such systems, including metrics such as rate of change, are required to ascertain the long-term response of the network to warming to-date, and to project such inland migration rates into the future.

Mapping of the supraglacial hydrologic network as an integrated network, rather than as independent features (rivers and lakes), is further required not only to assess active meltwater production and transportation across an ice surface, but to assess the speed and efficacy of potential inputs of meltwater into the englacial and subglacial systems via surface-to-bed connections such as moulins and SGL drainages. As mentioned in Chapter 2 of this thesis, it is currently contested as to whether such surface-to-bed connections (i.e., moulins via SGL drainages) will occur at higher elevations in the future leading to increased mass flux towards the ocean and associated SLR. To recap, Poinar *et al.* (2015) and Stevens *et al.* (2015) suggest a low likelihood of moulin formation at inland locations (>1600 m a.s.l) due to the inability to create large-scale hydrofracture events which require a sufficient meltwater reservoir and high tensile strain rates. Yet, due to longer-wavelength surface topography at inland locations and shallow SGLs (Lampkin and VanderBerg, 2011; Ignéczi *et al.*, 2018), fracturing will be less likely and melt will continue to be routed through long overflow streams to distant, nonlocal moulins. However, opposing research suggests such inland surface-to-bed connections could be viable from isolated SGL drainages due to locally favourable stress conditions which can propagate up-glacier and generate cascading lake drainages by as much as 135 km inland (Doyle *et al.*, 2014; Christoffersen *et al.*, 2018; Hoffman *et al.*, 2018). Additionally, Yang *et al.* (2021) have recently shown the presence of moulins at high elevation locations above 1600 m a.s.l, even in the colder-than-average year of 2015, alongside well-developed elongated supraglacial rivers, confirming such connections at this elevation do already exist and should be considered in the future. SGLs are predicted to expand 200 km inland from the margin over the next 50 years (Leeson *et al.*, 2015), which will also mean the simultaneous migration of the whole interconnected network (i.e., rivers and streams). It is critical to understand where such lakes and potential drainages may occur in delivering surface melt to the interior bed, where subglacial drainage will be largely inefficient and ice velocity impacts sustained (Doyle *et al.*, 2014).

Therefore, additional supraglacial hydrologic modelling using up-to-date topographic information (i.e., DEMs) would allow assessment of the future distribution of surface networks and SGL locations which may be susceptible to receiving inputs of heat and water from surface melt. An example of such DEM-derived supraglacial hydrologic modelling for Humboldt Glacier is presented in Figure 7.3, using the 10 m mosaic ArcticDEM product and flow route modelling following Karlstrom and Yang (2016) and as per Section 3.4 in Chapter 3, to provide some additional initial insights into its future network configuration and complexity. This modelling alone postulates the density of high elevation networks and further structural elements that may play an important physical role in the configuration of the system as it expands inland, including SGL location and topographically-influenced long supraglacial rivers. As surface melt also plays a critical role in controlling outlet glacier dynamics, such insights are particularly important for marine-terminating glaciers, especially those which lie in deep troughs below sea level (such as in northern Greenland), which are more susceptible to inland thinning, runaway terminus retreat (Hillebrand *et al.*, 2022) and associated acceleration.

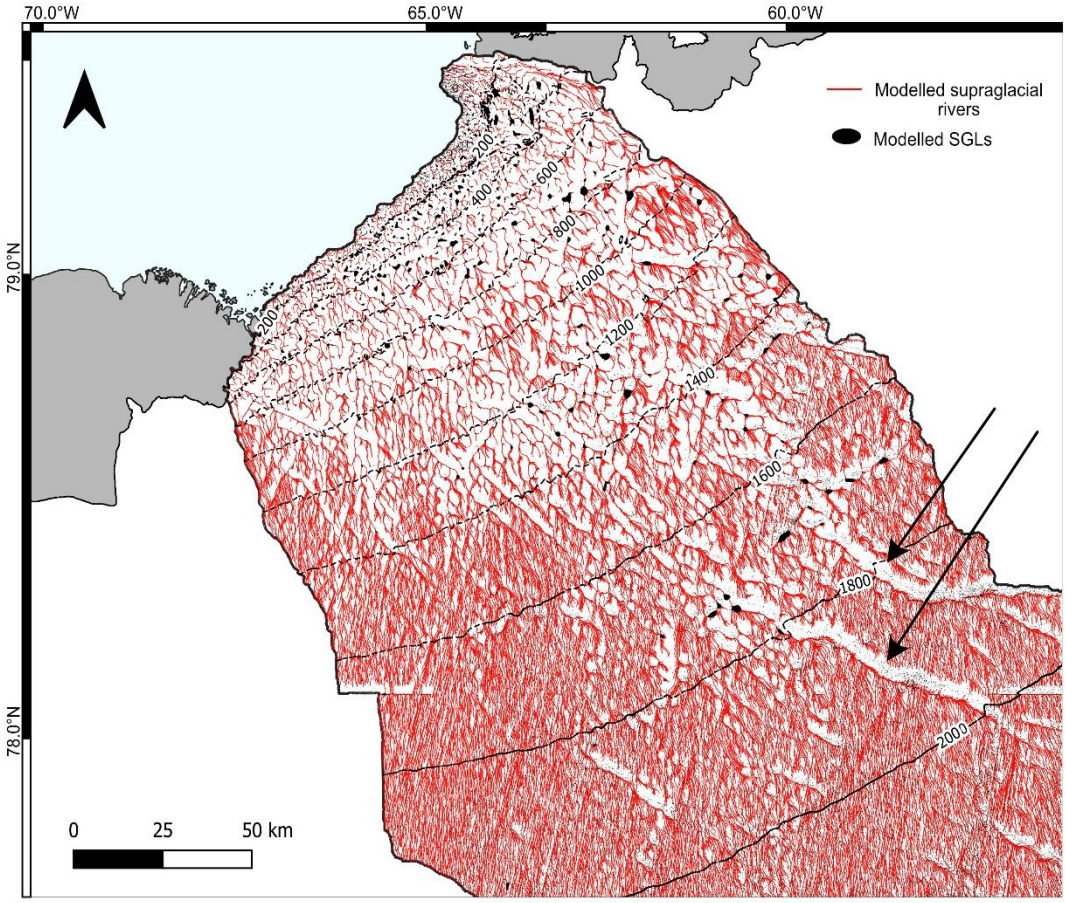

Figure 7.3. Supraglacial hydrologic modelling derived from the ArcticDEM (10 m mosaic product https://www.pgc.umn.edu/data/arcticdem/) to show the potential expansion, distribution and configuration of the network at Humboldt Glacier into the future. SGLs are shown to form further inland where depressions occur and the network consisting of rivers and tributary streams becomes dense. Long rivers (denoted by black arrows) are shown to be influenced by topographic structures between 1700-2000 m a.s.l, which correspond to bed depressions as deep as 224 m.

Such increased mapping and modelling studies and further behavioural insights gleaned of the supraglacial hydrologic network will additionally aid in their employment into various modelling simulations of the GrIS (and beyond) which currently do not account for or lack representation in model estimates, enhancing uncertainties associated with such projections. For example, SMB models which use regional atmospheric forcing to simulate GrIS SMB components, including meltwater production and runoff, are poorly constrained,

and have low spatial resolution compared to the dimensions of surface rivers (Gleason *et al.*, 2021). They therefore lack regional-to-catchment scale flow characteristics, as well as the coupling of surface water processes whereby (i) the network evolves seasonally, (ii) not all meltwater is routed immediately across the surface and can become impounded in SGLs, (iii) melt may diffusely flow through the weathering crust or in slush flows, (iv) the supraglacial network configuration may therefore modify the timing and magnitude of meltwater reaching moulins and subsequently influencing subglacial hydrologic processes or when exiting the system proglacially (Smith *et al.*, 2017; Lenaerts *et al.*, 2019). The inclusion of such coupling processes, as well as projected surface processes with continued warming such as (i) loss of firn pore space for meltwater retention, (ii) enhancement of the melt-albedo feedback as the ablation area grows and (iii) hypsometric-driven melt amplification is required to accurately estimate GrIS SMB and improve subsequent predictions of ice sheet loss and its behaviour into the future (Lenaerts *et al.*, 2019). Additionally, integration of supraglacial hydrologic processes and ice dynamics needs to be better represented in coupled hydrology-ice flow models, in particular understanding the distribution of Greenland-wide SGL drainage events and the input of meltwater runoff into the subglacial system, aiding in predicting future ice-sheet dynamics with greater certainty (Williamson *et al.*, 2018).

Although not explicitly explored in this thesis, large-scale climatic variability has been shown to influence the near-surface climate (i.e., surface air temperature and albedo) and hence the extent of the surface hydrologic network. In recent decades, the most extreme melt seasons have been associated with significant high-pressure blocking anomalies over Greenland linked to negative phases of the NAO and positive GBI, with significant increases in summer GBI since 1981. From results in Chapters 4 and 5, inter-annual variability of the hydrologic network was attributed to the behaviour of the NAO and GBI. Further work should aim to investigate the intrinsic links between the interannual variability of the

supraglacial hydrologic area and behaviour to the NAO and GBI, particularly over long-term timescales combined with improved projections of future circulatory behaviour with greenhouse gas forcing, which are expected to enhance ice sheet melt more than they already do (Hahn *et al.*, 2018; Ryan *et al.*, 2022).

Finally, whilst most of this 'directions for future research' section has favoured further research interests on the GrIS, it is also important to consider other large ice bodies which are similarly undergoing widespread mass loss and the effects of climatic warming. Despite surface melt rates on the GrIS being an order of magnitude greater than over the AIS (Lenaerts *et al.*, 2019), supraglacial hydrology represents a growing component of Antarctic mass loss. Whilst ice discharge and basal melting currently dominate AIS mass loss, surface melting is likely to become an increasingly important component of its mass budget under a warming climate (Shepherd *et al.*, 2019; Gudmundsson *et al.*, 2019; Gilbert and Kittel, 2021; Johnson *et al.*, 2021). Implications like many of those discussed for the GrIS, including increased meltwater runoff and ponding, melt-driven albedo feedbacks and hydro-dynamic implications, are all areas that require additional research to inform subsequent future evolution. Of particular concern for AIS is the effect meltwater accumulation and ocean warming will have on ice shelf stability, which could induce the collapse of ice shelf in a short period of time (Banwell *et al.*, 2014) and act as a precursor for the onset of marine ice sheet and cliff instability (Li, 2022). It is hypothesised that melt rates in regions of Antarctica that currently experience the most intense melting, like the Antarctic Peninsula and parts of the East AIS, could approach levels seen across the ablating margins of Greenland (Trusel *et al.*, 2015; Bell *et al.*, 2018). As reviewed by Arthur *et al.* (2020), whilst remote sensing capabilities since the 1970s have significantly improved the understanding of SGLs in Antarctica, much uncertainty still remains regarding continental-wide observations of AIS supraglacial hydrology, including meltwater area, volume and distribution (Arthur, 2022). As per recommendations for future research across the GrIS, further high spatial and temporal

resolution work and model validation is required to not only understand the current behaviour and evolution of ice sheets to increased surface melting, but assessing the future impacts of continued mass loss under a warming climate.

7.4.1 Summary

Collectively this results in a number of key themes for future recommendations within the study of supraglacial hydrology that are further synthesised below:

- The utilisation of high-resolution remotely sensed imagery from a range of satellites to derive Greenland-wide and globally-extensive supraglacial hydrologic network maps, including that of the AIS.

- The importance of mapping the supraglacial hydrologic network as an integrated system, including both rivers and lakes to assess meltwater transport and storage. Terminal points (i.e., moulins and confirmed drainages of lakes) should also play a part in such mapping to assess the speed, efficacy and input location of heat and water from the surface into the en- and sub-glacial network.

- Supraglacial hydrologic modelling based on up-to-date topographic information (i.e., DEMs) to assess the future pattern, distribution, and input of melt beyond the current melt extent. Such mapping could also be used to assist with network connectivity issues from satellite-derived mapping.

- Further field investigations to assist with ground truthing of remotely-sensed data and providing representative model parameters.

- Examination of additional meteorological (i.e., rain and cloud) and climate modes (i.e., NAO and GBI) to further investigate the intrinsic links between external variables, meltwater runoff and the interannual variability of the supraglacial hydrologic

network, which can additionally assist improved climate, SMB and coupled-hydrologic modelling.

Chapter 8

Conclusion

8.1 Concluding Remarks

The primary aim of this thesis was to expand supraglacial hydrologic mapping to understudied areas of the GrIS to explore the networks evolutionary behaviour at a range of spatial and temporal scales utilising both remotely-sensed and field-acquired imagery. Whilst a number of studies have explored the supraglacial hydrologic network, including channels and lakes collectively as a network, across the large melt-producing western and southwestern regions of the GrIS across a single date or melt year, only recently has exploration of this system begun at other areas of the GrIS. As surface meltwater runoff continues to amplify under climatic warming, understanding how quickly this melt is transported across the ice surface and where it may enter other hydrologic systems (i.e., subglacial) is crucial for assessing (i) hydro-dynamical implications and (ii) continued ice sheet contributions to global sea level rise.

Humboldt (Sermersuaq) Glacier, north Greenland, was the primary focus of satellite-based work (Chapters 4-6) of this thesis; a major marine-terminating northern Greenlandic outlet glacier. Large-scale supraglacial hydrologic mapping was conducted here for the first time, exploring the networks evolution across consecutive melt years (2016-2020) and over long timescales (1985-2021). An extensive supraglacial hydrologic network was found to exist here up to ~1400 m a.s.l and seasonally evolved from a network dominated by inefficient, slush-mobilised flows to an efficient, interconnected network as the snowline retreated and bare ice was exposed. Such evolution was highly variable between years (2016-2020) due to atmospheric circulatory behaviour, with high melt years and an extensive hydrologic network (e.g., 2019) providing an analogue for the 'future norm' under continued warming.

On a long-term scale (1985-2021), the supraglacial hydrologic network was shown to have expanded inland by a maximum elevation of 432 m a.s.l, as well as the network doubling in areal extent. Whilst annually-recurrent supraglacial river channels became lengthier and

more complex (i.e., tributary channels and slush zones) at higher elevations over time, some supraglacial lakes were lost due to terminus retreat. However, they were compensated for due the formation of new SGLs at higher elevations (>1000 m a.s.l), where they were larger in size. Basal topography was found to play a significant role in the long-term configuration of the network, with identifiable bed topographical features expressed on the surface with implications for channel orientation and termination.

Further, detailed observations of the supraglacial hydrologic network were undertaken in (i) the spectrally-complex ice marginal region of Russell Glacier, southwest Greenland, via an uncrewed aerial vehicle (UAV), whereby the dark ablation zone can hinder hydrologic mapping and (ii) the bare ice zone of Humboldt Glacier via ultra-high-resolution commercial-based imagery. UAV-derived models found a complex network of small-scale supraglacial streams and microchannels across the debris-laden ablating margin, with cryoconite deposits and algal communities dominating the surface facies, particularly on northern and western facing topographical slopes. Such small-scale features have the potential to drive further albedo-reduction and rougher surfaces, further enhancing turbulent heat fluxes and local melt. Inter-stream networks of 1-5 m wide from ultra-high-resolution commercial imagery were prevalent across the bare ice zone of Humboldt Glacier, providing evidence of this complex system beyond what is visible from conventional (freely) satellite imagery.

There is no doubt that, into the future, ablation zones will continue to migrate inland, which will play an important role in the speed, efficiency and development of ice sheet hydrologic systems. With less accumulated snow and firn, which would otherwise aid in buffering meltwater runoff through the porous medium, there will be extensive, semi-impermeable bare ice zones which will promote overland meltwater runoff, with the potential for supraglacial hydrologic networks to (i) become highly efficient at transporting melt earlier, quicker and for longer during the melt season and (ii) supply meltwater to new, isolated areas of the frozen bed.

This thesis has made important progress in furthering understanding into the supraglacial hydrologic network of the GrIS and motivates further work on the GrIS and beyond, which could utilise the ever-improving satellite datasets to develop Greenland and worldwide supraglacial hydrologic maps required to understand and better predict the future vulnerabilities of the changing cryosphere.

References

Abdalati, W. and Krabill, W.B. (1999) 'Calculation of ice velocities in the Jakobshavn Isbrae area using airborne laser altimetry'. *Remote Sensing of Environment* 67(2), pp. 194–204. doi: /10.1016/S0034-4257(98)00086-8

Abermann, J., Fischer, A., Lambrecht, A. and Geist, T. (2010) 'On the potential of very high-resolution repeat DEMs in glacial and periglacial environments'. *The Cryosphere* 4(1), pp. 53–65. doi: 10.5194/tc-4-53-2010

Agisoft Metashape Professional Edition, V1.6 (2020) 'Agisoft Metashape User Manual - Professional Edition, Version 1.6'.

Ahmed, J., Constantine, J.A. and Dunne, T. (2019) 'The role of sediment supply in the adjustment of channel sinuosity across the Amazon Basin'. *Geology* 47(9), pp. 807–810. doi: 10.1130/G46319.1.

Al Zaid, E., Shalash, W.M. and Abulkhair, M.F. (2018) 'Retinal Blood Vessels Segmentation using Gabor Filters'. in *2018 1st International Conference on Computer Applications & Information Security (ICCAIS).*, pp. 1–6. doi: 10.1109/CAIS.2018.8441937.

Ali, A., Hussain, A. and W Zaki, W.M.D. (2018) 'Segmenting Retinal Blood Vessels with Gabor Filter and Automatic Binarization'. *International Journal of Engineering and Technology(UAE)* 7, pp. 163–167. doi: 10.14419/ijet.v7i4.11.20794.

Alvarez-Vanhard, E., Corpetti, T. and Houet, T. (2021) 'UAV & satellite synergies for optical remote sensing applications: A literature review'. *Science of Remote Sensing* 3, p. 100019. doi: 10.1016/j.srs.2021.100019.

Amani, M., Ghorbanian, A., Ahmadi, S.A., Kakooei, M., Moghimi, A., Mirmazloumi, S.M., Moghaddam, S.H.A., Mahdavi, S., Ghahremanloo, M., Parsian, S. and Wu, Q., (2020). Google earth engine cloud computing platform for remote sensing big data applications: A comprehensive review. IEEE Journal of Selected Topics in Applied Earth Observations and Remote Sensing, 13, pp.5326-5350. doi: 10.1109/JSTARS.2020.3021052.

Amundson, J.M., Fahnestock, M., Truffer, M., Brown, J., Lüthi, M.P. and Motyka, R.J. (2010) 'Ice mélange dynamics and implications for terminus stability, Jakobshavn Isbræ, Greenland'. *Journal of Geophysical Research: Earth Surface* 115(F1). doi: 10.1029/2009JF001405.

Anderson, N.J., Saros, J.E., Bullard, J.E., Cahoon, S.M., McGowan, S., Bagshaw, E.A., Barry, C.D., Bindler, R., Burpee, B.T., Carrivick, J.L. and Fowler, R.A., (2017). The Arctic in the twenty-first century: Changing biogeochemical linkages across a paraglacial landscape of Greenland. BioScience, 67(2), pp.118-133. doi: 10.1093/biosci/biw158.

Andreassen, L.M., Paul, F., Kääb, A. and Hausberg, J.E. (2008) 'Landsat-derived glacier inventory for Jotunheimen, Norway, and deduced glacier changes since the 1930s'. *The Cryosphere* 2(2), pp. 131–145. doi: 10.5194/tc-2-131-2008

Andreassen, L.M., Winsvold, S.H., Paul, F. and Hausberg, J.E. (2012) 'Inventory of Norwegian glaciers'. Available at: https://www.zora.uzh.ch/id/eprint/73855.

Andrews, L.C., Catania, G.A., Hoffman, M.J., Gulley, J.D., Lüthi, M.P., Ryser, C., Hawley, R.L. and Neumann, T.A., 2014. Direct observations of evolving subglacial drainage beneath the Greenland Ice Sheet. Nature, 514(7520), pp.80-83. doi: 10.1038/nature13796

Andrews, L.C. et al. (2018) 'Seasonal Evolution of the Subglacial Hydrologic System Modified by Supraglacial Lake Drainage in Western Greenland'. *Journal of Geophysical Research: Earth Surface* 123(6), pp. 1479–1496. doi: 10.1029/2017JF004585.

Andrews, L.C., Poinar, K. and Trunz, C. (2022) 'Controls on Greenland moulin geometry and evolution from the Moulin Shape model'. *The Cryosphere* 16(6), pp. 2421–2448. doi: 10.5194/tc-16-2421-2022.

Arnold, N.S., Rees, W.G., Hodson, A.J. and Kohler, J. (2006) 'Topographic controls on the surface energy balance of a high Arctic valley glacier'. *Journal of Geophysical Research: Earth Surface* 111(F2). doi: 10.1029/2005JF000426.

Arthur, J.F. (2022) *Satellite remote sensing of supraglacial lakes in East Antarctica*. Doctoral Thesis, University of Durham.

Arthur, J.F., Stokes, C., Jamieson, S.S., Carr, J.R. and Leeson, A.A. (2020a) 'Recent understanding of Antarctic supraglacial lakes using satellite remote sensing'. *Progress in Physical Geography: Earth and Environment* 44(6), pp. 837–869. doi: 10.1177/0309133320916114

Arthur, J.F., Stokes, C.R., Jamieson, S.S.R., Carr, J.R. and Leeson, A.A. (2020b) 'Distribution and seasonal evolution of supraglacial lakes on Shackleton Ice Shelf, East Antarctica'. *The Cryosphere* 14(11), pp. 4103–4120. doi: 10.5194/tc-14-4103-2020.

Aschwanden, A., Fahnestock, M.A., Truffer, M., Brinkerhoff, D.J., Hock, R., Khroulev, C., Mottram, R. and Khan, S.A., (2019) 'Contribution of the Greenland Ice Sheet to sea level over the next millennium'. *Science Advances* 5(6), p. eaav9396. doi: 10.1126/sciadv.aav9396.

Ashmore, D.W., Mair, D.W.F. and Burgess, D.O. (2020) 'Meltwater percolation, impermeable layer formation and runoff buffering on Devon Ice Cap, Canada'. *Journal of Glaciology* 66(255), pp. 61–73. doi: 10.1017/jog.2019.80.

Avinash, S., Manjunath, K. and Kumar, S.S. (2016) 'An improved image processing analysis for the detection of lung cancer using Gabor filters and watershed segmentation technique'. in *2016 International Conference on Inventive Computation Technologies (ICICT).*, pp. 1–6. doi: 10.1109/INVENTIVE.2016.7830084.

Baillarin, S.J. et al. (2012) 'SENTINEL-2 LEVEL 1 PRODUCTS AND IMAGE PROCESSING PERFORMANCES'. *The International Archives of the Photogrammetry, Remote Sensing and*

Spatial Information Sciences XXXIX-B1, pp. 197–202. doi: 10.5194/isprsarchives-XXXIX-B1-197-2012.

Bajjali, W. (2018) 'ArcScan'. *ArcGIS for Environmental and Water Issues* , pp. 89–102.

Bamber, J.L., Griggs, J.A., Hurkmans, R.T.W.L., Dowdeswell, J.A., Gogineni, S.P., Howat, I., Mouginot, J., Paden, J., Palmer, S., Rignot, E. and Steinhage, D. (2013) 'A new bed elevation dataset for Greenland'. *The Cryosphere* 7(2), pp. 499–510. doi: 10.5194/tc-7-499-2013.

Banwell, A.F., Arnold, N.S., Willis, I.C., Tedesco, M. and Ahlstrøm, A.P. (2012) 'Modeling supraglacial water routing and lake filling on the Greenland Ice Sheet'. *Journal of Geophysical Research: Earth Surface* 117(F4). doi: 10.1029/2012JF002393.

Banwell, A.F., Caballero, M., Arnold, N.S., Glasser, N.F., Cathles, L.M. and MacAyeal, D.R. (2014) 'Supraglacial lakes on the Larsen B ice shelf, Antarctica, and at Paakitsoq, West Greenland: a comparative study'. *Annals of Glaciology* 55(66), pp. 1–8. doi: 10.3189/2014AoG66A049.

Barr, W. (2015) 'Alfred de Quervain's Swiss Greenland expeditions, 1909 and 1912'. *Polar Record* 51(4), pp. 366–385. doi: 10.1017/S0032247414000199.

Bartholomew, I., Nienow, P., Mair, D., Hubbard, A., King, M.A. and Sole, A. (2010) 'Seasonal evolution of subglacial drainage and acceleration in a Greenland outlet glacier'. *Nature Geoscience* 3(6), pp. 408–411. doi: 10.1038/ngeo863.

Bartholomew, I., Nienow, P., Sole, A., Mair, D., Cowton, T., Palmer, S. and Wadham, J. (2011) 'Supraglacial forcing of subglacial drainage in the ablation zone of the Greenland ice sheet'. *Geophysical Research Letters* 38(8). doi: 10.1029/2011GL047063

Bash, E.A. and Moorman, B.J. (2020) 'Surface melt and the importance of water flow – an analysis based on high-resolution unmanned aerial vehicle (UAV) data for an Arctic glacier'. *The Cryosphere* 14(2), pp. 549–563. doi: 10.5194/tc-14-549-2020.

Bash, E.A., Moorman, B.J. and Gunther, A. (2018) 'Detecting Short-Term Surface Melt on an Arctic Glacier Using UAV Surveys'. *Remote Sensing* 10(10), p. 1547. doi: 10.3390/rs10101547.

Bash, E.A., Shellian, C., Dow, C.F., Mcdermid, G., Kochtitzky, W., Medrzycka, D. and Copland, L. (2022) 'A semi-automated, GIS-based framework for the mapping of supraglacial hydrology'. *Journal of Glaciology* , pp. 1–15. doi: 10.1017/jog.2022.92.

Baumann, S. et al. (2021) 'Updated inventory of glacier ice in New Zealand based on 2016 satellite imagery'. *Journal of Glaciology* 67(261), pp. 13–26. doi: 10.1017/jog.2020.78.

Baumhoer, C.A., Dietz, A.J., Dech, S. and Kuenzer, C. (2018) 'Remote sensing of Antarctic glacier and ice-shelf front dynamics—A review'. *Remote Sensing* 10(9), p. 1445. doi: 10.3390/rs10091445

Baurley, N. (2022) *Insights into the seasonal dynamics of the lake-terminating glacier Fjallsjökull, South-East Iceland, inferred using ultra-high resolution repeat UAV imagery*. phd, University of Southampton. Available at: https://eprints.soton.ac.uk/471220/ (Accessed: 1 June 2023).

Beckmann, J. and Winkelmann, R. (2022) 'Effects of extreme melt events on ice flow and sea level rise of the Greenland Ice Sheet'. *The Cryosphere Discussions* , pp. 1–23. doi: 10.5194/tc-2022-145.

Bemis, S.P., Micklethwaite, S., Turner, D., James, M.R., Akciz, S., Thiele, S.T. and Bangash, H.A. (2014) 'Ground-based and UAV-Based photogrammetry: A multi-scale, high-resolution mapping tool for structural geology and paleoseismology'. *Journal of Structural Geology* 69, pp. 163–178. doi: 10.1016/j.jsg.2014.10.007.

Benedek, C.L. and Willis, I.C. (2021) 'Winter drainage of surface lakes on the Greenland Ice Sheet from Sentinel-1 SAR imagery'. *The Cryosphere* 15(3), pp. 1587–1606. doi: 10.5194/tc-15-1587-2021

Bennartz, R., Shupe, M.D., Turner, D.D., Walden, V.P., Steffen, K., Cox, C.J., Kulie, M.S., Miller, N.B. and Pettersen, C. (2013) 'July 2012 Greenland melt extent enhanced by low-level liquid clouds'. *Nature* 496(7443), pp. 83–86. doi: 10.1038/nature12002. doi: 10.1038/nature12002

Benning, L.G., Anesio, A.M., Lutz, S. and Tranter, M. (2014) 'Biological impact on Greenland's albedo'. *Nature Geoscience* 7(10), pp. 691–691. doi: 10.1038/ngeo2260.

Berra, E.F. and Peppa, M.V. (2020) 'Advances and Challenges of UAV SFM MVS Photogrammetry and Remote Sensing: Short Review'. in *2020 IEEE Latin American GRSS & ISPRS Remote Sensing Conference (LAGIRS).*, pp. 533–538. doi: 10.1109/LAGIRS48042.2020.9285975.

Bevan, S.L., Luckman, A.J., Benn, D.I., Cowton, T. and Todd, J. (2019) 'Impact of warming shelf waters on ice mélange and terminus retreat at a large SE Greenland glacier'. *The Cryosphere* 13(9), pp. 2303–2315. doi: 10.5194/tc-13-2303-2019.

Bevis, M. et al. (2019) 'Accelerating changes in ice mass within Greenland, and the ice sheet's sensitivity to atmospheric forcing'. *Proceedings of the National Academy of Sciences* 116(6), pp. 1934–1939. doi: 10.1073/pnas.1806562116.

Bhardwaj, A., Sam, L., Akanksha, Martín-Torres, F.J. and Kumar, R. (2016) 'UAVs as remote sensing platform in glaciology: Present applications and future prospects'. *Remote Sensing of Environment* 175, pp. 196–204. doi: 10.1016/j.rse.2015.12.029.

Bindschadler, R.A., Jezek, K.C. and Crawford, J. (1987) 'Glaciological investigations using the synthetic aperture radar imaging system'. *Annals of Glaciology* 9, pp. 11–19. doi:10.3189/S0260305500200694

Boggild, C.E., Brandt, R.E., Brown, K.J. and Warren, S.G. (2010) 'The ablation zone in northeast Greenland: ice types, albedos and impurities'. *Journal of Glaciology* 56(195), pp. 101–113. doi: 10.3189/002214310791190776.

Boghosian, A.L., Pitcher, L.H., Smith, L.C., Kosh, E., Alexander, P.M., Tedesco, M. and Bell, R.E. (2021) 'Development of Ice-Shelf Estuaries Promotes Fractures and Calving'. *Nature geoscience* 14, pp. 899–905. doi: 10.1038/s41561-021-00837-7.

Bolch, T. and Christiansen, H.H. (2021) 'Mountains, lowlands, and coasts: The physiography of cold landscapes'. in *Snow and Ice-Related Hazards, Risks, and Disasters*. Elsevier, pp. 199–213. doi: 10.1016/B978-0-12-817129-5.00020-2

Bolch, T., Menounos, B. and Wheate, R. (2010) 'Landsat-based inventory of glaciers in western Canada, 1985–2005'. *Remote sensing of Environment* 114(1), pp. 127–137. doi: 10.1016/j.rse.2009.08.015

Box, J.E. et al. (2022a) 'Greenland ice sheet climate disequilibrium and committed sea-level rise'. *Nature Climate Change* 12(9), pp. 808–813. doi: 10.1038/s41558-022-01441-2.

Box, J.E. et al. (2022b) 'Greenland Ice Sheet Rainfall, Heat and Albedo Feedback Impacts From the Mid-August 2021 Atmospheric River'. *Geophysical Research Letters* 49(11), p. e2021GL097356. doi: 10.1029/2021GL097356.

Box, J.E. and Decker, D.T. (2011) 'Greenland marine-terminating glacier area changes: 2000–2010'. *Annals of Glaciology* 52(59), pp. 91–98. doi: 10.3189/172756411799096312.

Box, J.E., Fettweis, X., Stroeve, J.C., Tedesco, M., Hall, D.K. and Steffen, K. (2012) 'Greenland ice sheet albedo feedback: thermodynamics and atmospheric drivers'. *The Cryosphere* 6(4), pp. 821–839. doi: 10.5194/tc-6-821-2012.

Box, J.E. and Ski, K. (2007) 'Remote sounding of Greenland supraglacial melt lakes: implications for subglacial hydraulics'. *Journal of glaciology* 53(181), pp. 257–265. doi:10.3189/172756507782202883

Bray, E.N., Dozier, J. and Dunne, T. (2017) 'Mechanics of the energy balance in large lowland rivers, and why the bed matters'. *Geophysical Research Letters* 44(17), pp. 8910–8918. doi: 10.1002/2017GL075317

Breiman, L. (2001) 'Random Forests'. *Machine Learning* 45(1), pp. 5–32. doi: 10.1023/A:1010933404324.

Brenning, A., Long, S. and Fieguth, P. (2012) 'Detecting rock glacier flow structures using Gabor filters and IKONOS imagery'. *Remote Sensing of environment* 125, pp. 227–237. doi: 10.1016/j.rse.2012.07.005

Brough, S., Carr, J.R., Ross, N. and Lea, J.M. (2023) 'Ocean-Forcing and Glacier-Specific Factors Drive Differing Glacier Response Across the 69°N Boundary, East Greenland'. *Journal of Geophysical Research: Earth Surface* 128(4), p. e2022JF006857. doi: 10.1029/2022JF006857.

Brun, E. (1989) 'Investigation on Wet-Snow Metamorphism in Respect of Liquid-Water Content'. *Annals of Glaciology* 13, pp. 22–26. doi: 10.3189/S0260305500007576.

Bunce, C., Carr, J.R., Nienow, P.W., Ross, N. and Killick, R. (2018) 'Ice front change of marine-terminating outlet glaciers in northwest and southeast Greenland during the 21st century'. *Journal of Glaciology* 64(246), pp. 523–535. doi: 10.1017/jog.2018.44.

Callaghan, T.V., Johansson, M., Key, J., Prowse, T., Ananicheva, M. and Klepikov, A. (2011) 'Feedbacks and interactions: From the Arctic cryosphere to the climate system'. *Ambio* 40, pp. 75–86. doi: 10.1007/s13280-011-0215-8

Carr, J.R. et al. (2015) 'Basal topographic controls on rapid retreat of Humboldt Glacier, northern Greenland'. *Journal of Glaciology* 61(225), pp. 137–150. doi: 10.3189/2015JoG14J128.

Carrivick, J.L. (2011) 'Jökulhlaups: geological importance, deglacial association and hazard management'. *Geology Today* 27(4), pp. 133–140. doi: 10.1111/j.1365-2451.2011.00800.x.

Carrivick, J.L. et al. (2017) 'Ice-Dammed Lake Drainage Evolution at Russell Glacier, West Greenland'. *Frontiers in Earth Science* 5. doi: 10.3389/feart.2017.00100.

Carrivick, J.L. and Quincey, D.J. (2014) 'Progressive increase in number and volume of ice-marginal lakes on the western margin of the Greenland Ice Sheet'. *Global and Planetary Change* 116, pp. 156–163. doi: 10.1016/j.gloplacha.2014.02.009.

Carrivick, J.L., Turner, A.G.D., Russell, A.J., Ingeman-Nielsen, T. and Yde, J.C. (2013) 'Outburst flood evolution at Russell Glacier, western Greenland: effects of a bedrock channel cascade with intermediary lakes'. *Quaternary Science Reviews* 67, pp. 39–58. doi: 10.1016/j.quascirev.2013.01.023.

Cassotto, R., Fahnestock, M., Amundson, J.M., Truffer, M. and Joughin, I. (2015) 'Seasonal and interannual variations in ice melange and its impact on terminus stability, Jakobshavn Isbræ, Greenland'. *Journal of Glaciology* 61(225), pp. 76–88. doi: 10.3189/2015JoG13J235.

Cassotto, R.K., Burton, J.C., Amundson, J.M., Fahnestock, M.A. and Truffer, M. (2021) 'Granular decoherence precedes ice mélange failure and glacier calving at Jakobshavn Isbræ'. *Nature Geoscience* 14(6), pp. 417–422. doi: 10.1038/s41561-021-00754-9.

Catania, G.A., Neumann, T.A. and Price, S.F. (2008) 'Characterizing englacial drainage in the ablation zone of the Greenland ice sheet'. *Journal of Glaciology* 54(187), pp. 567–578. doi: 10.3189/002214308786570854.

Cathles, L.M., Abbot, D.S., Bassis, J.N. and MacAyeal, D.R. (2011) 'Modeling surface-roughness/solar-ablation feedback: application to small-scale surface channels and crevasses of the Greenland ice sheet'. *Annals of Glaciology* 52(59), pp. 99–108. doi: 10.3189/172756411799096268.

Chandler, D.M. et al. (2013) 'Evolution of the subglacial drainage system beneath the Greenland Ice Sheet revealed by tracers'. *Nature Geoscience* 6(3), pp. 195–198. doi: 10.1038/ngeo1737.

Chen, J.L., Wilson, C.R. and Tapley, B.D. (2011) 'Interannual variability of Greenland ice losses from satellite gravimetry'. *Journal of Geophysical Research: Solid Earth* 116(B7). doi: 10.1029/2010JB007789.

Chen, X. et al. (2017) 'The increasing rate of global mean sea-level rise during 1993–2014'. *Nature Climate Change* 7(7), pp. 492–495. doi: 10.1038/nclimate3325.

Chi, M., Plaza, A., Benediktsson, J.A., Sun, Z., Shen, J. and Zhu, Y. (2016) 'Big Data for Remote Sensing: Challenges and Opportunities'. *Proceedings of the IEEE* 104(11), pp. 2207–2219. doi: 10.1109/JPROC.2016.2598228.

Christoffersen, P., Bougamont, M., Hubbard, A., Doyle, S.H., Grigsby, S. and Pettersson, R. (2018) 'Cascading lake drainage on the Greenland Ice Sheet triggered by tensile shock and fracture'. *Nature Communications* 9(1), p. 1064. doi: 10.1038/s41467-018-03420-8.

Chu, V.W. (2014) 'Greenland ice sheet hydrology: A review'. *Progress in Physical Geography* 38(1), pp. 19–54. doi: 10.1177/0309133313507075

Chudley, T.R. et al. (2021) 'Controls on Water Storage and Drainage in Crevasses on the Greenland Ice Sheet'. *Journal of Geophysical Research: Earth Surface* 126(9), p. e2021JF006287. doi: 10.1029/2021JF006287.

Chudley, T.R., Christoffersen, P., Doyle, S.H., Abellan, A. and Snooke, N. (2019) 'High-accuracy UAV photogrammetry of ice sheet dynamics with no ground control'. *The Cryosphere* 13(3), pp. 955–968. doi: 10.5194/tc-13-955-2019.

Clason, C., Rangecroft, S., Owens, P.N., Łokas, E., Baccolo, G., Selmes, N., Beard, D., Kitch, J., Dextre, R.M., Morera, S. and Blake, W., 2023. Contribution of glaciers to water, energy and food security in mountain regions: current perspectives and future priorities. Annals of Glaciology, pp.1-6. doi:10.1017/aog.2023.14

Colgan, W. et al. (2011) 'An increase in crevasse extent, West Greenland: Hydrologic implications: Increased Crevasse Extent West Greenland'. *Geophysical Research Letters* 38(18), p. n/a-n/a. doi: 10.1029/2011GL048491.

Collins, M. et al. (2019) 'IPCC SROCC—Extremes, Abrupt Changes and Managing Risks'.

Cook, J., Edwards, A., Takeuchi, N. and Irvine-Fynn, T. (2016) 'Cryoconite: The dark biological secret of the cryosphere'. *Progress in Physical Geography: Earth and Environment* 40(1), pp. 66–111. doi: 10.1177/0309133315616574.

Cook, J.M. et al. (2020) 'Glacier algae accelerate melt rates on the south-western Greenland Ice Sheet'. *The Cryosphere* 14(1), pp. 309–330. doi: 10.5194/tc-14-309-2020.

Cook, J.M., Sweet, M., Cavalli, O., Taggart, A. and Edwards, A. (2018) 'Topographic shading influences cryoconite morphodynamics and carbon exchange'. *Arctic, Antarctic, and Alpine Research* 50(1). doi: 10.1080/15230430.2017.1414463.

Cooper, M.G. et al. (2018) 'Meltwater storage in low-density near-surface bare ice in the Greenland ice sheet ablation zone'. *The Cryosphere* 12(3), pp. 955–970. doi: 10.5194/tc-12-955-2018.

Corr, D., Leeson, A., McMillan, M., Zhang, C. and Barnes, T. (2022) 'An inventory of supraglacial lakes and channels across the West Antarctic Ice Sheet'. *Earth System Science Data* 14(1), pp. 209–228. doi: 10.5194/essd-14-209-2022

Corripio, J.G. (2004) 'Snow surface albedo estimation using terrestrial photography'. *International Journal of Remote Sensing* 25(24), pp. 5705–5729. doi: 10.1080/01431160410001709002.

Cowton, T. et al. (2013) 'Evolution of drainage system morphology at a land-terminating Greenlandic outlet glacier'. *Journal of Geophysical Research: Earth Surface* 118(1), pp. 29–41. doi: 10.1029/2012JF002540.

Crozier, J., Karlstrom, L. and Yang, K. (2018) 'Basal control of supraglacial meltwater catchments on the Greenland Ice Sheet'. *The Cryosphere* 12(10), pp. 3383–3407. doi: 10.5194/tc-12-3383-2018.

Cuffey, K.M. and Paterson, W.S.B. (2010) *The physics of glaciers*. Academic Press.

Culberg, R., Chu, W. and Schroeder, D.M. (2022) 'Shallow Fracture Buffers High Elevation Runoff in Northwest Greenland'. *Geophysical Research Letters* 49(23), p. e2022GL101151. doi: 10.1029/2022GL101151.

Culberg, R., Schroeder, D.M. and Chu, W. (2021) 'Extreme melt season ice layers reduce firn permeability across Greenland'. *Nature Communications* 12(1), p. 2336. doi: 10.1038/s41467-021-22656-5.

Cullather, R.I. et al. (2020) 'Anomalous Circulation in July 2019 Resulting in Mass Loss on the Greenland Ice Sheet'. *Geophysical Research Letters* 47(17), p. e2020GL087263. doi: 10.1029/2020GL087263.

Dall'Asta, E., Thoeni, K., Santise, M., Forlani, G., Giacomini, A. and Roncella, R. (2015) 'Network Design and Quality Checks in Automatic Orientation of Close-Range Photogrammetric Blocks'. *Sensors* 15(4), pp. 7985–8008. doi: 10.3390/s150407985.

Dandois, J.P., Olano, M. and Ellis, E.C. (2015) 'Optimal Altitude, Overlap, and Weather Conditions for Computer Vision UAV Estimates of Forest Structure'. *Remote Sensing* 7(10), pp. 13895–13920. doi: 10.3390/rs71013895.

Das, S.B., Joughin, I., Behn, M.D., Howat, I.M., King, M.A., Lizarralde, D. and Bhatia, M.P. (2008) 'Fracture Propagation to the Base of the Greenland Ice Sheet During Supraglacial Lake Drainage'. *Science* 320(5877), pp. 778–781. doi: 10.1126/science.1153360.

Datta, R.T. and Wouters, B. (2021) 'Supraglacial lake bathymetry automatically derived from ICESat-2 constraining lake depth estimates from multi-source satellite imagery'. *The Cryosphere* 15(11), pp. 5115–5132. doi: 10.5194/tc-15-5115-2021

Davison, B.J., Sole, A.J., Cowton, T.R., Lea, J.M., Slater, D.A., Fahrner, D. and Nienow, P.W. (2020) 'Subglacial Drainage Evolution Modulates Seasonal Ice Flow Variability of Three Tidewater Glaciers in Southwest Greenland'. *Journal of Geophysical Research: Earth Surface* 125(9). doi: 10.1029/2019JF005492.

Davison, B.J., Sole, A.J., Livingstone, S.J., Cowton, T.R. and Nienow, P.W. (2019) 'The Influence of Hydrology on the Dynamics of Land-Terminating Sectors of the Greenland Ice Sheet'. *Frontiers in Earth Science* 7. doi: 10.3389/feart.2019.00010.

Dell, R., Arnold, N., Willis, I., Banwell, A., Williamson, A., Pritchard, H. and Orr, A. (2020) 'Lateral meltwater transfer across an Antarctic ice shelf'. *The Cryosphere* 14(7), pp. 2313–2330. 10.5194/tc-14-2313-2020

Dell, R.L., Banwell, A.F., Willis, I.C., Arnold, N.S., Halberstadt, A.R.W., Chudley, T.R. and Pritchard, H.D. (2022) 'Supervised classification of slush and ponded water on Antarctic ice shelves using Landsat 8 imagery'. *Journal of Glaciology* 68(268), pp. 401–414. doi:10.1017/jog.2021.114

Delworth, T.L. et al. (2008) 'The Potential for Abrupt Change in the Atlantic Meridional Overturning Circulation'. *NOAA SAP3.4*

Delworth, T.L. and Zeng, F. (2016) 'The impact of the North Atlantic Oscillation on climate through its influence on the Atlantic meridional overturning circulation'. *Journal of Climate* 29(3), pp. 941–962. doi: 10.1175/JCLI-D-15-0396.1

Denis, G., Claverie, A., Pasco, X., Darnis, J.-P., de Maupeou, B., Lafaye, M. and Morel, E. (2017) 'Towards disruptions in Earth observation? New Earth Observation systems and markets evolution: Possible scenarios and impacts'. *Acta Astronautica* 137, pp. 415–433. doi: 10.1016/j.actaastro.2017.04.034

Di Mauro, B. et al. (2020) 'Glacier algae foster ice-albedo feedback in the European Alps'. *Scientific Reports* 10(1), p. 4739. doi: 10.1038/s41598-020-61762-0.

Dirscherl, M., Dietz, A.J., Kneisel, C. and Kuenzer, C. (2020) 'Automated mapping of Antarctic supraglacial lakes using a machine learning approach'. *Remote Sensing* 12(7), p. 1203. doi: 10.3390/rs12071203

Djoumna, G., Mernild, S.H. and Holland, D.M. (2021) 'Meteorological Conditions and Cloud Effects on Surface Radiation Balance Near Helheim Glacier and Jakobshavn Isbræ (Greenland) Using Ground-Based Observations'. *Frontiers in Earth Science* 8. doi: 10.3389/feart.2020.616105.

Dow, C.F., Kulessa, B., Rutt, I.C., Doyle, S.H. and Hubbard, A. (2014) 'Upper bounds on subglacial channel development for interior regions of the Greenland ice sheet'. *Journal of Glaciology* 60(224), pp. 1044–1052. doi: 10.3189/2014JoG14J093.

Doyle, S.H. et al. (2013) 'Ice tectonic deformation during the rapid in situ drainage of a supraglacial lake on the Greenland Ice Sheet'. *The Cryosphere* 7(1), pp. 129–140. doi: 10.5194/tc-7-129-2013

Doyle, S.H. et al. (2015) 'Amplified melt and flow of the Greenland ice sheet driven by late-summer cyclonic rainfall'. *Nature Geoscience* 8(8), pp. 647–653. doi: 10.1038/ngeo2482.

Doyle, S.H., Hubbard, A., Fitzpatrick, A.A.W., van As, D., Mikkelsen, A.B., Pettersson, R. and Hubbard, B. (2014) 'Persistent flow acceleration within the interior of the Greenland ice sheet'. *Geophysical Research Letters* 41(3), pp. 899–905. doi: 10.1002/2013GL058933.

Dozier, J. (1989) 'Spectral signature of alpine snow cover from the Landsat Thematic Mapper'. *Remote sensing of environment* 28, pp. 9–22.

Dunmire, D., Banwell, A.F., Wever, N., Lenaerts, J.T.M. and Datta, R.T. (2021) 'Contrasting regional variability of buried meltwater extent over 2 years across the Greenland Ice Sheet'. *The Cryosphere* 15(6), pp. 2983–3005. doi: 10.5194/tc-15-2983-2021.

Elachi, C. and Van Zyl, J.J. (2021) *Introduction to the physics and techniques of remote sensing*. John Wiley & Sons.

Elmes, A., Levy, C., Erb, A., Hall, D.K., Scambos, T.A., DiGirolamo, N. and Schaaf, C. (2021) 'Consequences of the 2019 Greenland Ice Sheet Melt Episode on Albedo'. *Remote Sensing* 13(2), p. 227. doi: 10.3390/rs13020227.

Enderlin, E.M., Howat, I.M., Jeong, S., Noh, M.-J., van Angelen, J.H. and van den Broeke, M.R. (2014) 'An improved mass budget for the Greenland ice sheet'. *Geophysical Research Letters* 41(3), pp. 866–872. doi: 10.1002/2013GL059010.

Esri Inc. (2022). *ArcGIS Pro* (Version 2.4). Esri Inc. https://www.esri.com/en-us/arcgis/products/arcgis-pro/overview

Esri Inc. (2023). *ArcGIS Pro* (Version 3.0). Esri Inc. https://www.esri.com/en-us/arcgis/products/arcgis-pro/overviewa

Fahrner, D., Lea, J.M., Brough, S., Mair, D.W.F. and Abermann, J. (2021) 'Linear response of the Greenland ice sheet's tidewater glacier terminus positions to climate'. *Journal of Glaciology* 67(262), pp. 193–203. doi: 10.1017/jog.2021.13.

Fausto, R.S. et al. (2021) 'Programme for Monitoring of the Greenland Ice Sheet (PROMICE) automatic weather station data'. *Earth System Science Data* 13(8), pp. 3819–3845. doi: 10.5194/essd-13-3819-2021.

Fausto, R.S., van As, D., Box, J.E., Colgan, W., Langen, P.L. and Mottram, R.H. (2016) 'The implication of nonradiative energy fluxes dominating Greenland ice sheet exceptional ablation area surface melt in 2012'. *Geophysical Research Letters* 43(6), pp. 2649–2658. doi: 10.1002/2016GL067720.

Ferguson, R.I. (1973) 'Sinuosity of Supraglacial Streams'. *GSA Bulletin* 84(1), pp. 251–256. doi: 10.1130/0016-7606(1973)84<251:SOSS>2.0.CO;2.

Fettweis, X. et al. (2020) 'GrSMBMIP: intercomparison of the modelled 1980–2012 surface mass balance over the Greenland Ice Sheet'. *The Cryosphere* 14(11), pp. 3935–3958. doi: 10.5194/tc-14-3935-2020.

Fettweis, X. et al. (2021) 'Brief communication: Reduction in the future Greenland ice sheet surface melt with the help of solar geoengineering'. *The Cryosphere* 15(6), pp. 3013–3019. doi: 10.5194/tc-15-3013-2021.

Fettweis, X., Franco, B., Tedesco, M., van Angelen, J.H., Lenaerts, J.T.M., van den Broeke, M.R. and Gallée, H. (2013) 'Estimating the Greenland ice sheet surface mass balance contribution to future sea level rise using the regional atmospheric climate model MAR'. *The Cryosphere* 7(2), pp. 469–489. doi: 10.5194/tc-7-469-2013.

Fettweis, X., Tedesco, M., van den Broeke, M. and Ettema, J. (2011) 'Melting trends over the Greenland ice sheet (1958–2009) from spaceborne microwave data and regional climate models'. *The Cryosphere* 5(2), pp. 359–375. doi: 10.5194/tc-5-359-2011

Fitzpatrick, A. a. W. et al. (2014) 'A decade (2002-2012) of supraglacial lake volume estimates across Russell Glacier, West Greenland'. *The Cryosphere* 8(1), pp. 107–121. doi: 10.5194/tc-8-107-2014.

Flowers, G.E. (2018) 'Hydrology and the future of the Greenland Ice Sheet'. *Nature Communications* 9(1), p. 2729. doi: 10.1038/s41467-018-05002-0.

Foga, S., Stearns, L.A. and van der Veen, C.J. (2014) 'Application of Satellite Remote Sensing Techniques to Quantify Terminus and Ice Mélange Behavior at Helheim Glacier, East Greenland'. *Marine Technology Society Journal* 48(5), pp. 81–91. doi: 10.4031/MTSJ.48.5.3.

Fonstad, M.A., Dietrich, J.T., Courville, B.C., Jensen, J.L. and Carbonneau, P.E. (2013) 'Topographic structure from motion: a new development in photogrammetric measurement'. *Earth Surface Processes and Landforms* 38(4), pp. 421–430. doi: 10.1002/esp.3366.

Fountain, A.G. and Walder, J.S. (1998) 'Water flow through temperate glaciers'. *Reviews of Geophysics* 36(3), pp. 299–328. doi: 10.1029/97RG03579.

Fox-Kemper, B. et al. (2021) 'Ocean, Cryosphere and Sea Level Change. In Climate Change 2021: The Physical Science Basis. Contribution of Working Group I to the Sixth Assessment Report of the Intergovernmental Panel on Climate Change [Masson-Delmotte, V., P. Zhai, A. Pirani, S.L. Connors, C. Péan, S. Berger, N. Caud, Y. Chen, L. Goldfarb, M.I. Gomis, M. Huang, K. Leitzell, E. Lonnoy, J.B.R. Matthews, T.K. Maycock, T. Waterfield, O. Yelekçi, R. Yu, and B. Zhou (eds.)]'. . *Cambridge University Press, Cambridge, United Kingdom and New York, NY, USA,* , pp. 1211–1362. doi: :10.1017/9781009157896.011.

Fugazza, D. et al. (2018) 'Combination of UAV and terrestrial photogrammetry to assess rapid glacier evolution and map glacier hazards'. *Natural Hazards and Earth System Sciences* 18(4), pp. 1055–1071. doi: 10.5194/nhess-18-1055-2018.

Fürst, J.J., Goelzer, H. and Huybrechts, P. (2015) 'Ice-dynamic projections of the Greenland ice sheet in response to atmospheric and oceanic warming'. *The Cryosphere* 9(3), pp. 1039–1062. doi: 10.5194/tc-9-1039-2015.

Gao, H., Wang, L., Jing, L. and Xu, J. (2016) 'An effective modified water extraction method for Landsat-8 OLI imagery of mountainous plateau regions'. in *IOP conference series: earth and environmental science*. IOP Publishing, p. 012010.

Gao, J. and Liu, Y. (2001) 'Applications of remote sensing, GIS and GPS in glaciology: a review'. *Progress in Physical Geography* 25(4), pp. 520–540.

Gardner, A. S., M. A. Fahnestock, and T. A. Scambos, 2019: ITS_LIVE Regional Glacier and Ice Sheet Surface Velocities. Data archived at National Snow and Ice Data Center; doi:10.5067/6II6VW8LLWJ7

Germain, S.L.S. and Moorman, B.J. (2019) 'Long-term observations of supraglacial streams on an Arctic glacier'. *Journal of Glaciology* 65(254), pp. 900–911. doi: 10.1017/jog.2019.60.

Gindraux, S., Boesch, R. and Farinotti, D. (2017) 'Accuracy Assessment of Digital Surface Models from Unmanned Aerial Vehicles' Imagery on Glaciers'. *Remote Sensing* 9(2), p. 186. doi: 10.3390/rs9020186.

Glasser, N.F. et al. (2009) 'Surface structure and stability of the Larsen C ice shelf, Antarctic Peninsula'. *Journal of Glaciology* 55(191), pp. 400–410. doi:10.3189/002214309788816597

Gleason, C.J. et al. (2016) 'Characterizing supraglacial meltwater channel hydraulics on the Greenland Ice Sheet from in situ observations'. *Earth Surface Processes and Landforms* 41(14), pp. 2111–2122. doi: 10.1002/esp.3977.

Gleason, C.J. et al. (2021) 'Hourly surface meltwater routing for a Greenlandic supraglacial catchment across hillslopes and through a dense topological channel network'. *The Cryosphere* 15(5), pp. 2315–2331. doi: 10.5194/tc-15-2315-2021

Gledhill, L.A. and Williamson, A.G. (2018) 'Inland advance of supraglacial lakes in north-west Greenland under recent climatic warming'. *Annals of Glaciology* 59(76pt1), pp. 66–82. doi: 10.1017/aog.2017.31.

Goelzer, H. et al. (2013) 'Sensitivity of Greenland Ice Sheet Projections to Model Formulations'. *Journal of Glaciology* 59(216), pp. 733–749. doi: 10.3189/2013JoG12J182.

Goelzer, H. et al. (2020) 'The future sea-level contribution of the Greenland ice sheet: a multi-model ensemble study of ISMIP6'. *The Cryosphere* 14(9), pp. 3071–3096. doi: 10.5194/tc-14-3071-2020. doi: 10.5194/tc-14-3071-2020

Goldstein, R.M., Engelhardt, H., Kamb, B. and Frolich, R.M. (1993) 'Satellite radar interferometry for monitoring ice sheet motion: application to an Antarctic ice stream'. *Science* 262(5139), pp. 1525–1530. doi: 10.1126/science.262.5139.1525

Goodison, B., Brown, J., Jezek, K., Key, J., Prowse, T., Snorrason, A. and Worby, T. (2007) 'State and fate of the polar cryosphere, including variability of the Arctic hydrological cycle'. *Bulletin of the World Meteorological Organization* 56(4), pp. 284–292.

Gorelick, N., Hancher, M., Dixon, M., Ilyushchenko, S., Thau, D. and Moore, R. (2017) 'Google Earth Engine: Planetary-scale geospatial analysis for everyone'. *Remote sensing of Environment* 202, pp. 18–27. doi: 10.1016/j.rse.2017.06.031

Gray, L. (2021) 'Brief communication: Glacier run-off estimation using altimetry-derived basin volume change: case study at Humboldt Glacier, northwest Greenland'. *The Cryosphere* 15(2), pp. 1005–1014. doi: 10.5194/tc-15-1005-2021.

Greenwood, S.L., Clason, C.C., Helanow, C. and Margold, M. (2016) 'Theoretical, contemporary observational and palaeo-perspectives on ice sheet hydrology: Processes and products'. *Earth-Science Reviews* 155, pp. 1–27. doi: 10.1016/j.earscirev.2016.01.010.

Gregory, J.M., George, S.E. and Smith, R.S. (2020) 'Large and irreversible future decline of the Greenland ice sheet'. *The Cryosphere* 14(12), pp. 4299–4322. doi: 10.5194/tc-14-4299-2020.

Greuell, W. and Knap, W.H. (2000) 'Remote sensing of the albedo and detection of the slush line on the Greenland ice sheet'. *Journal of Geophysical Research: Atmospheres* 105(D12), pp. 15567–15576. doi: 10.1029/1999JD901162.

Griffiths, T.M. (1960) 'Glaciological investigations in the TUTO area of Greenland'.

Gudmundsson, G.H. (2003) 'Transmission of basal variability to a glacier surface'. *Journal of Geophysical Research: Solid Earth* 108(B5). doi: 10.1029/2002JB002107.

Gulley, J.D., Benn, D.I., Screaton, E. and Martin, J. (2009) 'Mechanisms of englacial conduit formation and their implications for subglacial recharge'. *Quaternary Science Reviews* 28(19), pp. 1984–1999. doi: 10.1016/j.quascirev.2009.04.002.

Gupta, R.P., Haritashya, U.K. and Singh, P. (2005) 'Mapping dry/wet snow cover in the Indian Himalayas using IRS multispectral imagery'. *Remote Sensing of Environment* 97(4), pp. 458–469. doi: 10.1016/j.rse.2005.05.010

Hahn, L., Ummenhofer, C.C. and Kwon, Y.-O. (2018) 'North Atlantic Natural Variability Modulates Emergence of Widespread Greenland Melt in a Warming Climate'. *Geophysical Research Letters* 45(17), pp. 9171–9178. doi: 10.1029/2018GL079682.

Halberstadt, A.R.W., Gleason, C.J., Moussavi, M.S., Pope, A., Trusel, L.D. and DeConto, R.M. (2020) 'Antarctic Supraglacial Lake Identification Using Landsat-8 Image Classification'. *Remote Sensing* 12(8), p. 1327. doi: 10.3390/rs12081327.

Hambrey, M.J. (1977) 'Supraglacial drainage and its relationship to structure, with particular reference to Charles Rabots Bre, Okstindan, Norway'. *Norsk Geografisk Tidsskrift - Norwegian Journal of Geography* 31(2), pp. 69–77. doi: 10.1080/00291957708545319.

Hanna, E. et al. (2008) 'Increased Runoff from Melt from the Greenland Ice Sheet: A Response to Global Warming'. *Journal of Climate* 21(2), pp. 331–341. doi: 10.1175/2007JCLI1964.1.

Hanna, E. et al. (2013) 'Ice-sheet mass balance and climate change'. *Nature* 498(7452), pp. 51–59. doi: 10.1038/nature12238.

Hanna, E. et al. (2020) 'Mass balance of the ice sheets and glaciers – Progress since AR5 and challenges'. *Earth-Science Reviews* 201, p. 102976. doi: 10.1016/j.earscirev.2019.102976.

Hanna, E. et al. (2021) 'Greenland surface air temperature changes from 1981 to 2019 and implications for ice-sheet melt and mass-balance change'. *International Journal of Climatology* 41(S1), pp. E1336–E1352. doi: 10.1002/joc.6771.

Hanna, E., Cropper, T.E., Hall, R.J. and Cappelen, J. (2016) 'Greenland Blocking Index 1851–2015: a regional climate change signal'. *International Journal of Climatology* 36(15), pp. 4847–4861. doi: 10.1002/joc.4673.

Hanna, E., Hall, R.J., Cropper, T.E., Ballinger, T.J., Wake, L., Mote, T. and Cappelen, J. (2018) 'Greenland blocking index daily series 1851–2015: Analysis of changes in extremes and links with

North Atlantic and UK climate variability and change'. *International Journal of Climatology* 38(9), pp. 3546–3564. doi: 10.1002/joc.5516.

Hanna, E., Mernild, S.H., Cappelen, J. and Steffen, K. (2012) 'Recent warming in Greenland in a long-term instrumental (1881–2012) climatic context: I. Evaluation of surface air temperature records'. *Environmental Research Letters* 7(4), p. 045404. doi: 10.1088/1748-9326/7/4/045404.

Härer, S., Bernhardt, M., Siebers, M. and Schulz, K. (2018) 'On the need for a time-and location-dependent estimation of the NDSI threshold value for reducing existing uncertainties in snow cover maps at different scales'. *Cryosphere* 12(5), pp. doi: 10.5194/tc-2017-177

Harper, J., Humphrey, N., Pfeffer, W.T., Brown, J. and Fettweis, X. (2012) 'Greenland ice-sheet contribution to sea-level rise buffered by meltwater storage in firn'. *Nature* 491(7423), pp. 240–243. doi: 10.1038/nature11566

Haran, T., J. Bohlander, T. Scambos, T. Painter, and M. Fahnestock. MEaSUREs MODIS Mosaic of Greenland (MOG) 2005, 2010, and 2015 Image Maps, Version 2. Boulder, Colorado USA. NASA National Snow and Ice Data Center Distributed Active Archive Center. https://doi.org/10.5067/9ZO79PHOTYE5, 2018, last access 21st November 2022.

Hartley, R.I. and Sturm, P. (1997) 'Triangulation'. *Computer vision and image understanding* 68(2), pp. 146–157.

Hill, E.A., Carr, J.R. and Stokes, C.R. (2017) 'A Review of Recent Changes in Major Marine-Terminating Outlet Glaciers in Northern Greenland'. *Frontiers in Earth Science* 4. doi: 10.3389/feart.2016.00111.

Hill, E.A., Carr, J.R., Stokes, C.R. and Gudmundsson, G.H., 2018. Dynamic changes in outlet glaciers in northern Greenland from 1948 to 2015. The Cryosphere, 12(10), pp.3243-3263. doi: 10.5194/tc-12-3243-2018

Hillebrand, T.R., Hoffman, M.J., Perego, M., Price, S.F. and Howat, I.M. (2022) 'The contribution of Humboldt Glacier, northern Greenland, to sea-level rise through 2100 constrained by recent observations of speedup and retreat'. *The Cryosphere* 16(11), pp. 4679–4700. doi: 10.5194/tc-16-4679-2022.

Hochreuther, P., Neckel, N., Reimann, N., Humbert, A. and Braun, M. (2021) 'Fully Automated Detection of Supraglacial Lake Area for Northeast Greenland Using Sentinel-2 Time-Series'. *Remote Sensing* 13(2), p. 205. doi: 10.3390/rs13020205.

Hock, R. (2005) 'Glacier melt: a review of processes and their modelling'. *Progress in physical geography* 29(3), pp. 362–391.

Hock, R. (2010) 'Glacier Meteorology Energy Balance'. *Summer School in Glaciology Fairbanks/McCarthy* , pp. 7–17.

Hodson, A. et al. (2007) 'A glacier respires: Quantifying the distribution and respiration CO2 flux of cryoconite across an entire Arctic supraglacial ecosystem'. *Journal of Geophysical Research: Biogeosciences* 112(G4). doi: 10.1029/2007JG000452.

Hofer, S., Lang, C., Amory, C., Kittel, C., Delhasse, A., Tedstone, A. and Fettweis, X. (2020) 'Greater Greenland Ice Sheet contribution to global sea level rise in CMIP6'. *Nature Communications* 11(1), p. 6289. doi: 10.1038/s41467-020-20011-8.

Hoffman, M.J. et al. (2018) 'Widespread Moulin Formation During Supraglacial Lake Drainages in Greenland'. *Geophysical Research Letters* 45(2), pp. 778–788. doi: 10.1002/2017GL075659.

Hoffman, M.J., Catania, G.A., Neumann, T.A., Andrews, L.C. and Rumrill, J.A. (2011) 'Links between acceleration, melting, and supraglacial lake drainage of the western Greenland Ice Sheet'. *Journal of Geophysical Research: Earth Surface* 116(F4). doi: 10.1029/2010JF001934.

Holland, D.M., Thomas, R.H., de Young, B., Ribergaard, M.H. and Lyberth, B. (2008) 'Acceleration of Jakobshavn Isbræ triggered by warm subsurface ocean waters'. *Nature Geoscience* 1(10), pp. 659–664. doi: 10.1038/ngeo316.

Hörhold, M. et al. (2023) 'Modern temperatures in central–north Greenland warmest in past millennium'. *Nature* 613(7944), pp. 503–507. doi: 10.1038/s41586-022-05517-z.

How, P., Messerli, A., Mätzler, E., Santoro, M., Wiesmann, A., Caduff, R., Langley, K., Bojesen, M.H., Paul, F., Kääb, A. and Carrivick, J.L., 2021. Greenland-wide inventory of ice marginal lakes using a multi-method approach. Scientific reports, 11(1), p.4481. doi: 10.1038/s41598-021-83509-1

Howat, I.M., Box, J.E., Ahn, Y., Herrington, A. and McFadden, E.M. (2010) 'Seasonal variability in the dynamics of marine-terminating outlet glaciers in Greenland'. *Journal of Glaciology* 56(198), pp. 601–613. doi: 10.3189/002214310793146232.

Howat, I.M., De la Pena, S., Van Angelen, J.H., Lenaerts, J.T.M. and Van den Broeke, M.R. (2013) 'Brief Communication" Expansion of meltwater lakes on the Greenland ice sheet"'. *The Cryosphere* 7(1), pp. 201–204. doi: 10.5194/tc-7-201-2013

Howat, I.M. and Eddy, A. (2011) 'Multi-decadal retreat of Greenland's marine-terminating glaciers'. *Journal of Glaciology* 57(203), pp. 389–396. doi: 10.3189/002214311796905631.

Howat, I.M., Joughin, I., Fahnestock, M., Smith, B.E. and Scambos, T.A. (2008) 'Synchronous retreat and acceleration of southeast Greenland outlet glaciers 2000–06: ice dynamics and coupling to climate'. *Journal of Glaciology* 54(187), pp. 646–660. doi: 10.3189/002214308786570908.

Howat, I.M., Joughin, I., Tulaczyk, S. and Gogineni, S. (2005) 'Rapid retreat and acceleration of Helheim Glacier, east Greenland'. *Geophysical Research Letters* 32(22). doi: 10.1029/2005GL024737.

Howat, I.M., Negrete, A. and Smith, B.E. (2014) 'The Greenland Ice Mapping Project (GIMP) land classification and surface elevation data sets'. *The Cryosphere* 8(4), pp. 1509–1518. doi: 10.5194/tc-8-1509-2014.

Hu, J. et al. (2022) 'Distribution and Evolution of Supraglacial Lakes in Greenland during the 2016–2018 Melt Seasons'. *Remote Sensing* 14(1), p. 55. doi: 10.3390/rs14010055.

Huggel, C., Carey, M. and Clague, J.J. (2015) *The high-mountain cryosphere*. Cambridge University Press.

Huggel, C., Kääb, A., Haeberli, W., Teysseire, P. and Paul, F. (2002) 'Remote sensing based assessment of hazards from glacier lake outbursts: a case study in the Swiss Alps'. *Canadian Geotechnical Journal* 39(2), pp. 316–330. doi: 10.1139/t01-099.

Humphrey, N.F., Harper, J.T. and Pfeffer, W.T. (2012) 'Thermal tracking of meltwater retention in Greenland's accumulation area'. *Journal of Geophysical Research: Earth Surface* 117(F1). doi: 10.1029/2011JF002083.

Igneczi, A. et al. (2016) 'Northeast sector of the Greenland Ice Sheet to undergo the greatest inland expansion of supraglacial lakes during the 21st Century'. *Geophysical Research Letters* 43(18), pp. 9729–9738. doi: 10.1002/2016GL070338

Ignéczi, Á., Sole, A.J., Livingstone, S.J., Ng, F.S.L. and Yang, K. (2018) 'Greenland Ice Sheet Surface Topography and Drainage Structure Controlled by the Transfer of Basal Variability'. *Frontiers in Earth Science* 6. doi: 10.3389/feart.2018.00101.

IPCC (2019) 'IPCC Special Report on the Ocean and Cryosphere in a Changing Climate [H.-O. Pörtner, D.C. Roberts, V. Masson-Delmotte, P. Zhai, M. Tignor, E. Poloczanska, K. Mintenbeck, A. Alegría, M. Nicolai, A. Okem, J. Petzold, B. Rama, N.M. Weyer (eds.)].' *Cambridge University Press, Cambridge, UK and New York, NY, USA,* .

IPCC (2021) 'Climate Change 2021: The Physical Science Basis. Contribution of Working Group I to the Sixth Assessment Report of the Intergovernmental Panel on Climate Change [Masson-Delmotte, V., P. Zhai, A. Pirani, S.L. Connors, C. Péan, S. Berger, N. Caud, Y. Chen, L. Goldfarb, M.I. Gomis, M. Huang, K. Leitzell, E. Lonnoy, J.B.R. Matthews, T.K. Maycock, T. Waterfield, O. Yelekçi, R. Yu, and B. Zhou (eds.)].' . *Cambridge University Press, Cambridge, United Kingdom and New York, NY, USA,* . doi: 10.1017/9781009157896.

Irvine-Fynn, T.D.L., Hodson, A.J., Moorman, B.J., Vatne, G. and Hubbard, A.L. (2011) 'POLYTHERMAL GLACIER HYDROLOGY: A REVIEW'. *Reviews of Geophysics* 49(4), p. RG4002. doi: 10.1029/2010RG000350.

Irvine-Fynn, T.D.L., Holt, T.O., James, T.D., Smith, M.W., Rutter, N., Porter, P.R. and Hodson, A.J. (2022) 'Time-lapse photogrammetry reveals hydrological controls of fine-scale High-Arctic glacier surface roughness evolution'. *Earth Surface Processes and Landforms* 47(6), pp. 1635–1652. doi: 10.1002/esp.5339.

Isenko, E. and Mavlydov, B. (2002) 'On the intensity of ice melting in supraglacial and englacial channels'. *Bulletin of glaciological research* 19, pp. 93–99.

Isenko, E., Naruse, R. and Mavlyudov, B. (2005) 'Water temperature in englacial and supraglacial channels: Change along the flow and contribution to ice melting on the channel wall'. *Cold regions science and technology* 42(1), pp. 53–62. doi: 10.1016/j.coldregions.2004.12.003

James, M.R., Antoniazza, G., Robson, S. and Lane, S.N. (2020) 'Mitigating systematic error in topographic models for geomorphic change detection: accuracy, precision and considerations

beyond off-nadir imagery'. *Earth Surface Processes and Landforms* 45(10), pp. 2251–2271. doi: 10.1002/esp.4878.

James, M.R. and Robson, S. (2012) 'Straightforward reconstruction of 3D surfaces and topography with a camera: Accuracy and geoscience application'. *Journal of Geophysical Research: Earth Surface* 117(F3). doi: 10.1029/2011JF002289.

Jansson, P., Naslund, J.-O. and Rodhe, L. (2007) 'Ice sheet hydrology - a review'. *Technical Report. Geological Survey of Sweden*

Jarosch, A.H. and Gudmundsson, M.T. (2012) 'A numerical model for meltwater channel evolution in glaciers'. *The Cryosphere* 6(2), pp. 493–503. doi: 10.5194/tc-6-493-2012.

Javernick, L., Brasington, J. and Caruso, B. (2014) 'Modeling the topography of shallow braided rivers using Structure-from-Motion photogrammetry'. *Geomorphology* 213, pp. 166–182. doi: 10.1016/j.geomorph.2014.01.006.

Jawak, S.D., Bidawe, T.G. and Luis, A.J. (2015) 'A review on applications of imaging synthetic aperture radar with a special focus on cryospheric studies'. *Advances in Remote Sensing* 4(02), p. 163. doi: 10.4236/ars.2015.42014

Jawak, S.D., Wankhede, S.F. and Luis, A.J. (2019) 'Explorative Study on Mapping Surface Facies of Selected Glaciers from Chandra Basin, Himalaya Using WorldView-2 Data'. *Remote Sensing* 11(10), p. 1207. doi: 10.3390/rs11101207.

Jenkins, A., 2011. Convection-driven melting near the grounding lines of ice shelves and tidewater glaciers. Journal of Physical Oceanography, 41(12), pp.2279-2294.Jensen, C.D. (2022) 'Weather Observations from Greenland 1958'. *DMI Report 22-08*. doi: 10.1175/JPO-D-11-03.1

Jevrejeva, S., Jackson, L.P., Riva, R.E.M., Grinsted, A. and Moore, J.C. (2016) 'Coastal sea level rise with warming above 2 °C'. *Proceedings of the National Academy of Sciences* 113(47), pp. 13342–13347. doi: 10.1073/pnas.1605312113.

Jezek, K.C. (2003) 'Observing the Antarctic ice sheet using the RADARSAT-1 synthetic aperture radar'. *Polar Geography* 27(3), pp. 197–209. doi: 10.1080/789610167

Jiang, D., Li, X., Zhang, K., Marinsek, S., Hong, W. and Wu, Y. (2022) 'Automatic Supraglacial Lake Extraction in Greenland Using Sentinel-1 SAR Images and Attention-Based U-Net'. *Remote Sensing* 14(19), p. 4998. doi: 10.3390/rs14194998.

Johansson, A.M. and Brown, I.A. (2013) 'Adaptive Classification of Supra-Glacial Lakes on the West Greenland Ice Sheet'. *IEEE Journal of Selected Topics in Applied Earth Observations and Remote Sensing* 6(4), pp. 1998–2007. doi: 10.1109/JSTARS.2012.2233722.

Joughin, I. et al. (2013) 'Influence of ice-sheet geometry and supraglacial lakes on seasonal ice-flow variability'. *The Cryosphere* 7(4), pp. 1185–1192. doi: 10.5194/tc-7-1185-2013.

Joughin, I., Das, S.B., King, M.A., Smith, B.E., Howat, I.M. and Moon, T. (2008) 'Seasonal Speedup Along the Western Flank of the Greenland Ice Sheet'. *Science* 320(5877), pp. 781–783. doi: 10.1126/science.1153288.

Joughin, I., Kwok, R. and Fahnestock, M. (1996a) 'Estimation of ice-sheet motion using satellite radar interferometry: method and error analysis with application to Humboldt Glacier, Greenland'. *Journal of Glaciology* 42(142), pp. 564–575. doi:10.3189/S0022143000003543

Joughin, I., Smith, B.E. and Holland, D.M. (2010) 'Sensitivity of 21st century sea level to ocean-induced thinning of Pine Island Glacier, Antarctica'. *Geophysical Research Letters* 37(20). doi: 10.1029/2010GL044819

Joughin, I., Tulaczyk, S., Fahnestock, M. and Kwok, R. (1996b) 'A mini-surge on the Ryder Glacier, Greenland, observed by satellite radar interferometry'. *Science* 274(5285), pp. 228–230. doi: 10.1126/science.274.5285.228

Jouvet, G., Weidmann, Y., van Dongen, E., Lüthi, M.P., Vieli, A. and Ryan, J.C. (2019) 'High-Endurance UAV for Monitoring Calving Glaciers: Application to the Inglefield Bredning and Eqip Sermia, Greenland'. *Frontiers in Earth Science* 7. doi: 10.3389/feart.2019.00206.

Jullien, N., Tedstone, A.J., Machguth, H., Karlsson, N.B. and Helm, V. (2023) 'Greenland Ice Sheet Ice Slab Expansion and Thickening'. *Geophysical Research Letters* 50(10), p. e2022GL100911. doi: 10.1029/2022GL100911.

Kääb, A. et al. (2014) 'Glacier mapping and monitoring using multispectral data'. *Global land ice measurements from space* , pp. 75–112.

Kääb, A., Paul, F., Maisch, M., Hoelzle, M. and Haeberli, W. (2002) 'The new remote-sensing-derived Swiss glacier inventory: II. First results'. *Annals of Glaciology* 34, pp. 362–366. doi: 10.3189/172756402781817473.

Kamb, B. (1987) 'Glacier surge mechanism based on linked cavity configuration of the basal water conduit system'. *Journal of Geophysical Research* 92(B9), p. 9083. doi: 10.1029/JB092iB09p09083.

Kamintzis, J.E. (2015) 'The spatial dynamics of an annual supraglacial meltwater channel in the ablation zone of Haut Glacier d'Arolla, Switzerland.'

Kamp, U. and Pan, C.G. (2015) 'Inventory of glaciers in Mongolia, derived from Landsat imagery from 1989 to 2011'. *Geografiska Annaler: Series A, Physical Geography* 97(4), pp. 653–669. doi: 10.1111/geoa.12105

Karlstrom, L., Gajjar, P. and Manga, M. (2013) 'Meander formation in supraglacial streams'. *Journal of Geophysical Research: Earth Surface* 118(3), pp. 1897–1907. doi: 10.1002/jgrf.20135

Karlstrom, L. and Yang, K. (2016) 'Fluvial supraglacial landscape evolution on the Greenland Ice Sheet'. *Geophysical Research Letters* 43(6), pp. 2683–2692. doi: 10.1002/2016GL067697.

Karlstrom, L., Zok, A. and Manga, M. (2014) 'Near-surface permeability in a supraglacial drainage basin on the Llewellyn Glacier, Juneau Icefield, British Columbia'. *The Cryosphere* 8(2), pp. 537–546. doi: 10.5194/tc-8-537-2014

Kattsov, V.M. et al. (2010) 'Arctic sea-ice change: a grand challenge of climate science'. *Journal of Glaciology* 56(200), pp. 1115–1121. doi:10.3189/002214311796406176

Kellerer-Pirklbauer, A., Lieb, G.K. and Kleinferchner, H. (2012) 'A NEW ROCK GLACIER INVENTORY OF THE EASTERN EUROPEAN ALPS.' *Austrian Journal of Earth Sciences* 105(2)

Keshri, A.K., Shukla, A. and Gupta, R.P. (2009) 'ASTER ratio indices for supraglacial terrain mapping'. *International Journal of Remote Sensing* 30(2), pp. 519–524. doi: 10.1080/01431160802385459

Khalid, H.W., Khalil, R.M.Z. and Qureshi, M.A. (2021) 'Evaluating spectral indices for water bodies extraction in western Tibetan Plateau'. *The Egyptian Journal of Remote Sensing and Space Science* 24(3), pp. 619–634. doi: 10.1016/j.ejrs.2021.09.003

Khan, S.A., Aschwanden, A., Bjørk, A.A., Wahr, J., Kjeldsen, K.K. and Kjær, K.H. (2015) 'Greenland ice sheet mass balance: a review'. *Reports on Progress in Physics* 78(4), p. 046801. doi: 10.1088/0034-4885/78/4/046801.

King, L., Hassan, M.A., Yang, K. and Flowers, G. (2016) 'Flow Routing for Delineating Supraglacial Meltwater Channel Networks'. *Remote Sensing* 8(12), p. 988. doi: 10.3390/rs8120988.

King, M.D. et al. (2020) 'Dynamic ice loss from the Greenland Ice Sheet driven by sustained glacier retreat'. *Communications Earth & Environment* 1(1), pp. 1–7. doi: 10.1038/s43247-020-0001-2.

King, M.D., Howat, I.M., Jeong, S., Noh, M.J., Wouters, B., Noël, B. and van den Broeke, M.R. (2018) 'Seasonal to decadal variability in ice discharge from the Greenland Ice Sheet'. *The Cryosphere* 12(12), pp. 3813–3825. doi: 10.5194/tc-12-3813-2018.

Kingslake, J., Ng, F. and Sole, A. (2015) 'Modelling channelized surface drainage of supraglacial lakes'. *Journal of Glaciology* 61(225), pp. 185–199. doi: 10.3189/2015JoG14J158.

Knighton, A.D. (1972) 'Changes in a braided reach'. *Geological Society of America Bulletin* 83(12), pp. 3813–3822.

Knighton, A.D. (1981a) 'Asymmetry of river channel cross-sections: Part I. Quantitative indices'. *Earth Surface Processes and Landforms* 6(6), pp. 581–588. doi: 10.1002/esp.3290060607.

Knighton, A.D. (1981b) 'Channel form and flow characteristics of supraglacial streams, Austre Okstindbreen, Norway'. *Arctic and Alpine Research* 13(3), pp. 295–306.

Knighton, A.D. (1985) 'Channel form adjustment in supraglacial streams, Austre Okstindbreen, Norway'. *Arctic and Alpine Research* 17(4), pp. 451–466.

Koenig, L.S. et al. (2015) 'Wintertime storage of water in buried supraglacial lakes across the Greenland Ice Sheet'. *The Cryosphere* 9(4), pp. 1333–1342. doi: 10.5194/tc-9-1333-2015

König, M., Winther, J.-G. and Isaksson, E. (2001) 'Measuring snow and glacier ice properties from satellite'. *Reviews of Geophysics* 39(1), pp. 1–27. doi: 10.1029/1999RG000076

Kostrzewski, A. and Zwolinski, Z. (1995) 'Hydraulic geometry of a supraglacial stream, Ragnarbreen, Spitsbergen'. *Quaestiones Geographicae. Zeszyt Specjalny* 4

Kour, R., Patel, N. and Krishna, A.P. (2015) 'Assessment of relationship between snow cover characteristics (SGI and SCI) and snow cover indices (NDSI and S3)'. *Earth Science Informatics* 8, pp. 317–326. doi: 10.1007/s12145-015-0216-4

Koziol, C., Arnold, N., Pope, A. and Colgan, W. (2017) 'Quantifying supraglacial meltwater pathways in the Paakitsoq region, West Greenland'. *Journal of Glaciology* 63(239), pp. 464–476. doi: 10.1017/jog.2017.5.

Koziol, C.P. (2018) 'Modelling the impact of surface melt on the hydrology and dynamics of the Greenland Ice Sheet'. Available at: https://www.repository.cam.ac.uk/handle/1810/273345. doi: 10.17863/CAM.20372

Koziol, C.P. and Arnold, N. (2018) 'Modelling seasonal meltwater forcing of the velocity of land-terminating margins of the Greenland Ice Sheet'. *The Cryosphere* 12(3), pp. 971–991. doi: 10.5194/tc-12-971-2018.

Kraaijenbrink, P., Meijer, S.W., Shea, J.M., Pellicciotti, F., Jong, S.M.D. and Immerzeel, W.W. (2016) 'Seasonal surface velocities of a Himalayan glacier derived by automated correlation of unmanned aerial vehicle imagery'. *Annals of Glaciology* 57(71), pp. 103–113. doi: 10.3189/2016AoG71A072.

Krabill, W.B., Thomas, R.H., Martin, C.F., Swift, R.N. and Frederick, E.B. (1995) 'Accuracy of airborne laser altimetry over the Greenland ice sheet'. *International Journal of Remote Sensing* 16(7), pp. 1211–1222. doi: 10.1080/01431169508954472

Krawczynski, M.J., Behn, M.D., Das, S.B. and Joughin, I. (2009) 'Constraints on the lake volume required for hydro-fracture through ice sheets'. *Geophysical Research Letters* 36(10). doi: 10.1029/2008GL036765.

Krieger, L. and Floricioiu, D. (2017) 'Automatic glacier calving front delineation on TerraSAR-X and Sentinel-1 SAR imagery'. in *2017 IEEE International Geoscience and Remote Sensing Symposium (IGARSS)*. IEEE, pp. 2817–2820. doi: 10.1109/IGARSS.2017.8127584.

Lampkin, D.J. (2011) 'Supraglacial lake spatial structure in western Greenland during the 2007 ablation season'. *Journal of Geophysical Research: Earth Surface* 116(F4). doi: 10.1029/2010JF001725.

Lampkin, D.J. and VanderBerg, J. (2011) 'A preliminary investigation of the influence of basal and surface topography on supraglacial lake distribution near Jakobshavn Isbrae, western Greenland'. *Hydrological Processes* 25(21), pp. 3347–3355. doi: 10.1002/hyp.8170.

Lampkin, D.J. and VanderBerg, J. (2014) 'Supraglacial melt channel networks in the Jakobshavn Isbræ region during the 2007 melt season'. *Hydrological Processes* 28(25), pp. 6038–6053. doi: 10.1002/hyp.10085.

Langen, P.L., Fausto, R.S., Vandecrux, B., Mottram, R.H. and Box, J.E. (2017) 'Liquid Water Flow and Retention on the Greenland Ice Sheet in the Regional Climate Model HIRHAM5: Local and Large-Scale Impacts'. *Frontiers in Earth Science* 4. doi: 10.3389/feart.2016.00110.

Law, R., Arnold, N., Benedek, C., Tedesco, M., Banwell, A. and Willis, I. (2020) 'Over-winter persistence of supraglacial lakes on the Greenland Ice Sheet: results and insights from a new model'. *Journal of Glaciology* 66(257), pp. 362–372. doi: 10.1017/jog.2020.7.

Lea, J.M. (2018) 'The Google Earth Engine Digitisation Tool (GEEDiT) and the Margin change Quantification Tool (MaQiT) – simple tools for the rapid mapping and quantification of changing Earth surface margins'. *Earth Surface Dynamics* 6(3), pp. 551–561. doi: 10.5194/esurf-6-551-2018.

Leclercq, P.W., Kääb, A. and Altena, B. (2021) 'Brief communication: Detection of glacier surge activity using cloud computing of Sentinel-1 radar data'. *The Cryosphere* 15(10), pp. 4901–4907. doi: 10.5194/tc-15-4901-2021

Leeson, A.A., Shepherd, A., Briggs, K., Howat, I., Fettweis, X., Morlighem, M. and Rignot, E. (2015) 'Supraglacial lakes on the Greenland ice sheet advance inland under warming climate'. *Nature Climate Change* 5(1), pp. 51–55. doi: 10.1038/nclimate2463

Leeson, A.A., Shepherd, A., Palmer, S., Sundal, A. and Fettweis, X. (2012) 'Simulating the growth of supraglacial lakes at the western margin of the Greenland ice sheet'. *The Cryosphere* 6(5), pp. 1077–1086. doi: 10.5194/tc-6-1077-2012.

Leidman, S., Rennermalm, Å.K., Lathrop, R.G. and Cooper, M. (2021a) 'Terrain-Based Shadow Correction Method for Assessing Supraglacial Features on the Greenland Ice Sheet'. *Frontiers in Remote Sensing* , p. 20. doi: 10.3389/frsen.2021.690474

Leidman, S.Z., Rennermalm, Å.K., Muthyala, R., Guo, Q. and Overeem, I. (2021b) 'The presence and widespread distribution of dark sediment in Greenland ice sheet supraglacial streams implies substantial impact of microbial communities on sediment deposition and albedo'. *Geophysical Research Letters* 48(1). doi: 10.1029/2020GL088444

Leidman, S.Z., Rennermalm, Å.K., Muthyala, R., Skiles, S.M. and Getraer, A. (2023) 'Intra-seasonal variability in supraglacial stream sediment on the Greenland Ice Sheet'. *Frontiers in Earth Science* 11, p. 969629. doi: 10.3389/feart.2023.969629

Lenaerts, J.T.M., Camron, M.D., Wyburn-Powell, C.R. and Kay, J.E. (2020) 'Present-day and future Greenland Ice Sheet precipitation frequency from CloudSat observations and the Community Earth System Model'. *The Cryosphere* 14(7), pp. 2253–2265. doi: 10.5194/tc-14-2253-2020.

Lenaerts, J.T.M., Le Bars, D., van Kampenhout, L., Vizcaino, M., Enderlin, E.M. and van den Broeke, M.R. (2015) 'Representing Greenland ice sheet freshwater fluxes in climate models'. *Geophysical Research Letters* 42(15), pp. 6373–6381. doi: 10.1002/2015GL064738.

Lenaerts, J.T.M., Medley, B., van den Broeke, M.R. and Wouters, B. (2019) 'Observing and Modeling Ice Sheet Surface Mass Balance'. *Reviews of Geophysics* 57(2), pp. 376–420. doi: 10.1029/2018RG000622.

Leopold, L.B. and Wolman, M.G. (1960) 'River meanders'. *Geological Society of America Bulletin* 71(6), pp. 769–793. doi: 10.1130/0016-7606(1960)71[769:RM]2.0.CO;2

Lettang, F.J., Crocker, R.I., Emery, W.J. and Maslanik, J.A. (2013) 'Estimating the extent of drained supraglacial lakes on the Greenland Ice Sheet'. *International Journal of Remote Sensing* 34(13), pp. 4754–4768. doi: 10.1080/01431161.2013.782118.

Lewis, G. et al. (2021) 'Atmospheric Blocking Drives Recent Albedo Change Across the Western Greenland Ice Sheet Percolation Zone'. *Geophysical Research Letters* 48(10), p. e2021GL092814. doi: 10.1029/2021GL092814.

Lewis, S.M. and Smith, L.C. (2009) 'Hydrologic drainage of the Greenland Ice Sheet'. *Hydrological Processes* 23(14), pp. 2004–2011. doi: 10.1002/hyp.7343.

Li, D. (2022) 'Physical processes and feedbacks obscuring the future of the Antarctic Ice Sheet'. *Geosystems and Geoenvironment* 1(4), p. 100084. doi: 10.1016/j.geogeo.2022.100084.

Li, D., Shan, J. and Gong, J. (2009) *Geospatial technology for earth observation*. Springer Science & Business Media.

Li, Y., Yang, K., Gao, S., Smith, L.C., Fettweis, X. and Li, M. (2022) 'Surface meltwater runoff routing through a coupled supraglacial-proglacial drainage system, Inglefield Land, northwest Greenland'. *International Journal of Applied Earth Observation and Geoinformation* 106, p. 102647. doi: 10.1016/j.jag.2021.102647

Li, Z.-Q., Ma, H.-M. and Liu, Z.-Y. (2016) 'Road Lane Detection with Gabor Filters'. in *2016 International Conference on Information System and Artificial Intelligence (ISAI)*., pp. 436–440. doi: 10.1109/ISAI.2016.0099.

Liang, Y.-L. et al. (2012) 'A decadal investigation of supraglacial lakes in West Greenland using a fully automatic detection and tracking algorithm'. *Remote Sensing of Environment* 123, pp. 127–138. doi: 10.1016/j.rse.2012.03.020.

Lim, Y.-K. et al. (2016) 'Atmospheric summer teleconnections and Greenland Ice Sheet surface mass variations: Insights from MERRA-2'. *Environmental Research Letters* 11(2), p. 024002. doi: 10.1088/1748-9326/11/2/024002

Lindbäck, K., Pettersson, R., Hubbard, A.L., Doyle, S.H., van As, D., Mikkelsen, A.B. and Fitzpatrick, A.A. (2015) 'Subglacial water drainage, storage, and piracy beneath the Greenland ice sheet'. *Geophysical Research Letters* 42(18), pp. 7606–7614. doi: 10.1002/2015GL065393.

Liu, X., Lian, X., Yang, W., Wang, F., Han, Y. and Zhang, Y. (2022) 'Accuracy Assessment of a UAV Direct Georeferencing Method and Impact of the Configuration of Ground Control Points'. *Drones* 6(2), p. 30. doi: 10.3390/drones6020030.

Livingstone, S.J., Chu, W., Ely, J.C. and Kingslake, J. (2017) 'Paleofluvial and subglacial channel networks beneath Humboldt Glacier, Greenland'. *Geology* 45(6), pp. 551–554. doi: 10.1130/G38860.1

Lowe, D.G. (2004) 'Distinctive Image Features from Scale-Invariant Keypoints'. *International Journal of Computer Vision* 60(2), pp. 91–110. doi: 10.1023/B:VISI.0000029664.99615.94.

Lu, Y. et al. (2020) 'Diverse supraglacial drainage patterns on the Devon ice Cap, Arctic Canada'. *Journal of Maps* 16(2), pp. 834–846. doi: 10.1080/17445647.2020.1838353

Lu, Y., Yang, K., Lu, X., Li, Y., Gao, S., Mao, W. and Li, M. (2021) 'Response of supraglacial rivers and lakes to ice flow and surface melt on the northeast Greenland ice sheet during the 2017 melt season'. *Journal of Hydrology* 602, p. 126750. 10.1016/j.jhydrol.2021.126750

Luckman, A., Murray, T., Jiskoot, H., Pritchard, H. and Strozzi, T. (2003) 'ERS SAR feature-tracking measurement of outlet glacier velocities on a regional scale in East Greenland'. *Annals of Glaciology* 36, pp. 129–134. doi:10.3189/172756403781816428

Luthcke, S.B. et al. (2006) 'Recent Greenland Ice Mass Loss by Drainage System from Satellite Gravity Observations'. *Science* 314(5803), pp. 1286–1289. doi: 10.1126/science.1130776.

Lüthje, M., Pedersen, L.T., Reeh, N. and Greuell, W. (2006) 'Modelling the evolution of supraglacial lakes on the West Greenland ice-sheet margin'. *Journal of Glaciology* 52(179), pp. 608–618. doi: 10.3189/172756506781828386.

Lutz, S., Anesio, A.M., Raiswell, R., Edwards, A., Newton, R.J., Gill, F. and Benning, L.G. (2016) 'The biogeography of red snow microbiomes and their role in melting arctic glaciers'. *Nature Communications* 7(1), p. 11968. doi: 10.1038/ncomms11968.

Macdonald, G.J., Banwell, A.F. and MacAyeal, D.R. (2018) 'Seasonal evolution of supraglacial lakes on a floating ice tongue, Petermann Glacier, Greenland'. *Annals of Glaciology* 59(76pt1), pp. 56–65. doi: 10.1017/aog.2018.9.

MacDonell, S. and Fitzsimons, S. (2008) 'The formation and hydrological significance of cryoconite holes'. *Progress in Physical Geography: Earth and Environment* 32(6), pp. 595–610. doi: 10.1177/0309133308101382.

MacFerrin, M., Machguth, H., As, D.V., Charalampidis, C., Stevens, C.M., Heilig, A., Vandecrux, B., Langen, P.L., Mottram, R., Fettweis, X. and Van Den Broeke, M.R., (2019). Rapid expansion of Greenland's low-permeability ice slabs. Nature, 573(7774), pp.403-407. doi: 10.1038/s41586-019-1550-3

Machguth, H., MacFerrin, M., van As, D., Box, J.E., Charalampidis, C., Colgan, W., Fausto, R.S., Meijer, H.A.J., Mosley-Thompson, E. and van de Wal, R.S.W., (2016). Greenland meltwater storage in rn limited by near-surface ice formation, Nature Clim. Change, 6, p.390393. doi: 10.1038/nclimate2899.

Mankoff, K.D., Ahlstrøm, A.P., Colgan, W., Fausto, R.S., Fettweis, X., Kondo, K., Langley, K., Noël, B., Sugiyama, S. and van As, D., (2020). Greenland liquid water runoff from 1979 through 2017. Earth System Science Data Discussions, 2020, pp.1-44. doi:10.5194/essd-2020-47

Mantelli, E., Camporeale, C. and Ridolfi, L. (2015) 'Supraglacial channel inception: Modeling and processes'. *Water Resources Research* 51(9), pp. 7044–7063. doi: 10.1002/2015WR017075.

Marston, R.A. (1983) 'Supraglacial stream dynamics on the Juneau Icefield'. *Annals of the Association of American Geographers* 73(4), pp. 597–608. doi: 10.1111/j.1467-8306.1983.tb01861.x

Martínez-Carricondo, P., Agüera-Vega, F., Carvajal-Ramírez, F., Mesas-Carrascosa, F.-J., García-Ferrer, A. and Pérez-Porras, F.-J. (2018) 'Assessment of UAV-photogrammetric mapping accuracy based on variation of ground control points'. *International Journal of Applied Earth Observation and Geoinformation* 72, pp. 1–10. doi: 10.1016/j.jag.2018.05.015.

Masson-Delmotte, V. et al. (2018) 'Global warming of 1.5 C'. *An IPCC Special Report on the impacts of global warming of* 1(5), pp. 43–50.

Mattingly, K.S., Turton, J.V., Wille, J.D., Noël, B., Fettweis, X., Rennermalm, Å.K. and Mote, T.L. (2023) 'Increasing extreme melt in northeast Greenland linked to foehn winds and atmospheric rivers'. *Nature Communications* 14(1), p. 1743. doi: 10.1038/s41467-023-37434-8.

McCutcheon, J. et al. (2021) 'Mineral phosphorus drives glacier algal blooms on the Greenland Ice Sheet'. *Nature Communications* 12(1), p. 570. doi: 10.1038/s41467-020-20627-w.

McFeeters, S.K. (1996) 'The use of the Normalized Difference Water Index (NDWI) in the delineation of open water features'. *International journal of remote sensing* 17(7), pp. 1425–1432. doi: 10.1080/01431169608948714

McGrath, D., Colgan, W., Steffen, K., Lauffenburger, P. and Balog, J. (2011) 'Assessing the summer water budget of a moulin basin in the Sermeq Avannarleq ablation region, Greenland ice sheet'. *Journal of Glaciology* 57(205), pp. 954–964. doi: 10.3189/002214311798043735.

McLeod, J.T. and Mote, T.L. (2016) 'Linking interannual variability in extreme Greenland blocking episodes to the recent increase in summer melting across the Greenland ice sheet'. *International Journal of Climatology* 36(3), pp. 1484–1499. doi: 10.1002/joc.4440

McMillan, M., Nienow, P., Shepherd, A., Benham, T. and Sole, A. (2007) 'Seasonal evolution of supra-glacial lakes on the Greenland Ice Sheet'. *Earth and Planetary Science Letters* 262(3), pp. 484–492. doi: 10.1016/j.epsl.2007.08.002.

Medina, R., Llamas, J., Gómez-García-Bermejo, J., Zalama, E. and Segarra, M.J. (2017) 'Crack Detection in Concrete Tunnels Using a Gabor Filter Invariant to Rotation'. *Sensors* 17(7), p. 1670. doi: 10.3390/s17071670.

Meierbachtol, T., Harper, J. and Humphrey, N. (2013) 'Basal Drainage System Response to Increasing Surface Melt on the Greenland Ice Sheet'. *Science* 341(6147), pp. 777–779. doi: 10.1126/science.1235905.

Mejia, J.Z. et al. (2022) 'Moulin density controls the timing of peak pressurization within the Greenland Ice Sheet's subglacial drainage system'. *Geophysical Research Letters* 49(22), p. e2022GL100058. doi: 10.1029/2022GL100058

Mernild, S.H. and Hasholt, B. (2009) 'Observed runoff, jökulhlaups and suspended sediment load from the Greenland ice sheet at Kangerlussuaq, West Greenland, 2007 and 2008'. *Journal of Glaciology* 55(193), pp. 855–858. doi: 10.3189/002214309790152465.

Mernild, S.H. and Liston, G.E. (2012) 'Surface melt extent for the Greenland Ice Sheet, 2011'. *Geografisk Tidsskrift-Danish Journal of Geography* 112(1), pp. 84–88. doi: 10.1080/00167223.2012.707808.

Mernild, S.H., Liston, G.E., van As, D., Hasholt, B. and Yde, J.C. (2018) 'High-resolution ice sheet surface mass-balance and spatiotemporal runoff simulations: Kangerlussuaq, west Greenland'. *Arctic, Antarctic, and Alpine Research* 50(1), p. S100008. doi: 10.1080/15230430.2017.1415856.

Mikkelsen, A.B. et al. (2016) 'Extraordinary runoff from the Greenland ice sheet in 2012 amplified by hypsometry and depleted firn retention'. *The Cryosphere* 10(3), pp. 1147–1159. doi: 10.5194/tc-10-1147-2016

Miles, K.E., Willis, I.C., Benedek, C.L., Williamson, A.G. and Tedesco, M. (2017) 'Toward Monitoring Surface and Subsurface Lakes on the Greenland Ice Sheet Using Sentinel-1 SAR and Landsat-8 OLI Imagery'. *Frontiers in Earth Science* 5. doi: 10.3389/feart.2017.00058.

Mölg, N., Bolch, T., Rastner, P., Strozzi, T. and Paul, F. (2018) 'A consistent glacier inventory for Karakoram and Pamir derived from Landsat data: distribution of debris cover and mapping challenges'. *Earth System Science Data* 10(4), pp. 1807–1827. doi: 10.5194/essd-10-1807-2018

Moon, T. and Joughin, I. (2008) 'Changes in ice front position on Greenland's outlet glaciers from 1992 to 2007'. *Journal of Geophysical Research: Earth Surface* 113(F2). doi: 10.1029/2007JF000927.

Moon, T., Joughin, I. and Smith, B. (2015) 'Seasonal to multiyear variability of glacier surface velocity, terminus position, and sea ice/ice mélange in northwest Greenland'. *Journal of Geophysical Research: Earth Surface* 120(5), pp. 818–833. doi: 10.1002/2015JF003494.

Moon, T., Joughin, I., Smith, B., van den Broeke, M.R., van de Berg, W.J., Noël, B. and Usher, M. (2014) 'Distinct patterns of seasonal Greenland glacier velocity'. *Geophysical Research Letters* 41(20), pp. 7209–7216. doi: 10.1002/2014GL061836.

Moon, T.A. et al. (2020) 'Arctic Report Card 2020: Greenland Ice Sheet'.

Morard, V., Dokládal, P. and Decencière, E. (2014) 'Parsimonious Path Openings and Closings'. *IEEE Transactions on Image Processing* 23(4), pp. 1543–1555. doi: 10.1109/TIP.2014.2303647.

Morlighem, M. et al. IceBridge BedMachine Greenland, Version 4. [Bed Topography]. Boulder, Colorado USA. NASA National Snow and Ice Data Center Distributed Active Archive Center. https://doi.org/10.5067/VLJ5YXKCNGXO, 2021, last access 30th February 2021.

Morriss, B.F. et al. (2013) 'A ten-year record of supraglacial lake evolution and rapid drainage in West Greenland using an automated processing algorithm for multispectral imagery'. *The Cryosphere* 7(6), pp. 1869–1877. doi: 10.5194/tc-7-1869-2013.

Mouginot, J. et al. (2019) 'Forty-six years of Greenland Ice Sheet mass balance from 1972 to 2018'. *Proceedings of the National Academy of Sciences* 116(19), pp. 9239–9244. doi: 10.1073/pnas.1904242116.

Mouginot, J. and Rignot, E. (2019) 'Glacier catchments/basins for the Greenland Ice Sheet'. doi:10.7280/D1WT11.

Mouragnon, E., Lhuillier, M., Dhome, M., Dekeyser, F. and Sayd, P. (2006) '3D reconstruction of complex structures with bundle adjustment: an incremental approach'. in *Proceedings 2006 IEEE*

International Conference on Robotics and Automation, 2006. ICRA 2006. IEEE, pp. 3055–3061. doi: 10.1109/ROBOT.2006.1642166.

Moussavi, M., Pope, A., Halberstadt, A.R.W., Trusel, L.D., Cioffi, L. and Abdalati, W. (2020) 'Antarctic Supraglacial Lake Detection Using Landsat 8 and Sentinel-2 Imagery: Towards Continental Generation of Lake Volumes'. *Remote Sensing* 12(1), p. 134. doi: 10.3390/rs12010134.

Moussavi, M.S., Abdalati, W., Pope, A., Scambos, T., Tedesco, M., MacFerrin, M. and Grigsby, S. (2016) 'Derivation and validation of supraglacial lake volumes on the Greenland Ice Sheet from high-resolution satellite imagery'. *Remote sensing of environment* 183, pp. 294–303. doi: 10.1016/j.rse.2016.05.024

Moustafa, S.E. et al. (2015) 'Multi-modal albedo distributions in the ablation area of the southwestern Greenland Ice Sheet'. *The Cryosphere* 9(3), pp. 905–923. doi: 10.5194/tc-9-905-2015.

Munawar, H.S., Aggarwal, R., Qadir, Z., Khan, S.I., Kouzani, A.Z. and Mahmud, M.A.P. (2021) 'A Gabor Filter-Based Protocol for Automated Image-Based Building Detection'. *Buildings* 11(7), p. 302. doi: 10.3390/buildings11070302.

Muntjewerf, L. et al. (2020) 'Greenland Ice Sheet contribution to 21st century sea level rise as simulated by the coupled CESM2. 1-CISM2. 1'. *Geophysical Research Letters* 47(9), p. e2019GL086836. doi: 10.1029/2019GL086836

Murray, T. et al. (2015) 'Extensive retreat of Greenland tidewater glaciers 2000-2010'. *Arctic, Antarctic and Alpine Research* 47(3), pp. 427–447. doi: 10.1657/AAAR0014-049

Muthyala, R., Rennermalm, Å.K., Leidman, S.Z., Cooper, M.G., Cooley, S.W., Smith, L.C. and van As, D. (2022) 'Supraglacial streamflow and meteorological drivers from southwest Greenland'. *The Cryosphere* 16(6), pp. 2245–2263. doi: 10.5194/tc-16-2245-2022.

Nex, F. et al. (2022) 'UAV in the advent of the twenties: Where we stand and what is next'. *ISPRS Journal of Photogrammetry and Remote Sensing* 184, pp. 215–242. doi: 10.1016/j.isprsjprs.2021.12.006.

Ng, F.S., Ignéczi, Á., Sole, A.J. and Livingstone, S.J. (2018) 'Response of surface topography to basal variability along glacial flowlines'. *Journal of Geophysical Research: Earth Surface* 123(10), pp. 2319–2340. doi: 10.1029/2017JF004555

Nghiem, S.V. et al. (2012) 'The extreme melt across the Greenland ice sheet in 2012'. *Geophysical Research Letters* 39(20). doi: 10.1029/2012GL053611.

Nick, F.M. et al. (2013) 'Future sea-level rise from Greenland's main outlet glaciers in a warming climate'. *Nature* 497(7448), pp. 235–238. doi: 10.1038/nature12068.

Nick, F.M., Vieli, A., Howat, I.M. and Joughin, I. (2009) 'Large-scale changes in Greenland outlet glacier dynamics triggered at the terminus'. *Nature Geoscience* 2(2), pp. 110–114. doi: 10.1038/ngeo394.

Nielsen, M.S., Nikolov, I., Kruse, E.K., Garnæs, J. and Madsen, C.B. (2023) 'Quantifying the Influence of Surface Texture and Shape on Structure from Motion 3D Reconstructions'. *Sensors* 23(1), p. 178. doi: 10.3390/s23010178.

Nienow, P.W., Sole, A.J., Slater, D.A. and Cowton, T.R. (2017) 'Recent advances in our understanding of the role of meltwater in the Greenland Ice Sheet system'. *Current Climate Change Reports* 3, pp. 330–344. doi: 10.1007/s40641-017-0083-9

Nobles, L.H. (1960) 'Glaciological investigations, Nunatarssuaq ice ramp, northwestern Greenland'.

Noël, B., van de Berg, W.J., Lhermitte, S. and van den Broeke, M.R. (2019) 'Rapid ablation zone expansion amplifies north Greenland mass loss'. *Science Advances* 5(9), p. eaaw0123. doi: 10.1126/sciadv.aaw0123.

Noël, B., van Kampenhout, L., Lenaerts, J.T.M., van de Berg, W.J. and van den Broeke, M.R. (2021) 'A 21st Century Warming Threshold for Sustained Greenland Ice Sheet Mass Loss'. *Geophysical Research Letters* 48(5), p. e2020GL090471. doi: 10.1029/2020GL090471.

Noël, B., Lenaerts, J.T.M., Lipscomb, W.H., Thayer-Calder, K. and van den Broeke, M.R. (2022) 'Peak refreezing in the Greenland firn layer under future warming scenarios'. *Nature Communications* 13(1), p. 6870. doi: 10.1038/s41467-022-34524-x.

O'Callaghan, J.F. and Mark, D.M. (1984) 'The Extraction of Drainage Networks from Digital Elevation Data'. *Computer vision, graphics, and image processing* 28(3)

Ohmura, A. (2015) 'Snow and Ice in the Climate System'. in *Snow and Ice-Related Hazards, Risks, and Disasters*., pp. 77–98. doi: 10.1016/B978-0-12-394849-6.00003-2.

Oniga, V.-E., Breaban, A.-I., Pfeifer, N. and Chirila, C. (2020) 'Determining the Suitable Number of Ground Control Points for UAS Images Georeferencing by Varying Number and Spatial Distribution'. *Remote Sensing* 12(5), p. 876. doi: 10.3390/rs12050876.

Orsi, A.J. et al. (2017) 'The recent warming trend in North Greenland'. *Geophysical Research Letters* 44(12), pp. 6235–6243. doi: 10.1002/2016GL072212.

Oswald, G.K.A. and Gogineni, S.P. (2012) 'Mapping Basal Melt Under the Northern Greenland Ice Sheet'. *IEEE Transactions on Geoscience and Remote Sensing* 50(2), pp. 585–592. doi: 10.1109/TGRS.2011.2162072.

Otto, J., Holmes, F.A. and Kirchner, N. (2022) 'Supraglacial lake expansion, intensified lake drainage frequency, and first observation of coupled lake drainage, during 1985–2020 at Ryder Glacier, Northern Greenland'. *Frontiers in Earth Science* 10. doi: 10.3389/feart.2022.978137.

Overland, J. et al. (2019) 'The urgency of Arctic change'. *Polar Science* 21, pp. 6–13. doi: 10.1016/j.polar.2018.11.008.

Palmer, S., Shepherd, A., Nienow, P. and Joughin, I. (2011) 'Seasonal speedup of the Greenland Ice Sheet linked to routing of surface water'. *Earth and Planetary Science Letters* 302(3–4), pp. 423–428. doi: 10.1016/j.epsl.2010.12.037

Parizek, B.R. and Alley, R.B. (2004) 'Implications of increased Greenland surface melt under global-warming scenarios: ice-sheet simulations'. *Quaternary Science Reviews* 23(9), pp. 1013–1027. doi: 10.1016/j.quascirev.2003.12.024.

Parker, G. (1975) 'Meandering of supraglacial melt streams'. *Water Resources Research* 11(4), pp. 551–552. doi: 10.1029/WR011i004p00551

Pattyn, F. et al. (2018) 'The Greenland and Antarctic ice sheets under 1.5 C global warming'. *Nature climate change* 8(12), pp. 1053–1061. doi: 10.1038/s41558-018-0305-8

Paul, F., Baumann, S., Anderson, B. and Rastner, P. (2023) 'Deriving a year 2000 glacier inventory for New Zealand from the existing 2016 inventory'. *Annals of Glaciology* , pp. 1–11. doi:10.1017/aog.2023.20

Paul, F., Frey, H. and Le Bris, R. (2011) 'A new glacier inventory for the European Alps from Landsat TM scenes of 2003: challenges and results'. *Annals of Glaciology* 52(59), pp. 144–152. doi:10.3189/172756411799096295

Paul, F., Kääb, A., Maisch, M., Haeberli, W. and Herren, E.R. (2008) 'The new Swiss glacier inventory 2000'. *Glaciological report* (123/12), pp. 51–58.

Payne, A.J. et al. (2021) 'Future Sea Level Change Under Coupled Model Intercomparison Project Phase 5 and Phase 6 Scenarios From the Greenland and Antarctic Ice Sheets'. *Geophysical Research Letters* 48(16), p. e2020GL091741. doi: 10.1029/2020GL091741.

Pfeffer, W.T. et al. (2014) 'The Randolph Glacier Inventory: a globally complete inventory of glaciers'. *Journal of Glaciology* 60(221), pp. 537–552. doi: 10.3189/2014JoG13J176.

Pitcher, L.H. and Smith, L.C. (2019) 'Supraglacial streams and rivers'. *Annual Review of Earth and Planetary Sciences* 47, pp. 421–452. doi: 10.1146/annurev-earth-053018-060212

PIX4Dcapture (2019). Available at: https://support.pix4d.com/hc/en-us/articles/202557269-Getting-Started-PIX4Dcapture (Accessed: 5 June 2023).

Poinar, K., Joughin, I., Das, S.B., Behn, M.D., Lenaerts, J.T. and Van Den Broeke, M.R. (2015) 'Limits to future expansion of surface-melt-enhanced ice flow into the interior of western Greenland'. *Geophysical Research Letters* 42(6), pp. 1800–1807. doi: 10.1002/2015GL063192

Pope, A., Rees, W.G., Fox, A.J. and Fleming, A. (2014) 'Open access data in polar and cryospheric remote sensing'. *Remote Sensing* 6(7), pp. 6183–6220. doi: 10.3390/rs6076183

Pope, A., Scambos, T.A., Moussavi, M., Tedesco, M., Willis, M., Shean, D. and Grigsby, S. (2016) 'Estimating supraglacial lake depth in West Greenland using Landsat 8 and comparison with other multispectral methods'. *The Cryosphere* 10(1), pp. 15–27. doi: 10.5194/tc-10-15-2016

Price, J.C. (1994) 'How unique are spectral signatures?'. *Remote sensing of environment* 49(3), pp. 181–186. doi: 10.1016/0034-4257(94)90013-2

Pritchard, H.D., Arthern, R.J., Vaughan, D.G. and Edwards, L.A. (2009) 'Extensive dynamic thinning on the margins of the Greenland and Antarctic ice sheets'. *Nature* 461(7266), pp. 971–975. doi: 10.1038/nature08471.

QGIS.org, 2023 . QGIS Geographic Information System. QGIS Association. http://www.qgis.org

Racoviteanu, A.E., Williams, M.W. and Barry, R.G. (2008) 'Optical remote sensing of glacier characteristics: a review with focus on the Himalaya'. *Sensors* 8(5), pp. 3355–3383. doi: 10.3390/s8053355

Rahmstorf, S. and Coumou, D. (2011) 'Increase of extreme events in a warming world'. *Proceedings of the National Academy of Sciences* 108(44), pp. 17905–17909. doi: 10.1073/pnas.1101766108

Rawlins, L.D., Rippin, D.M., Sole, A.J., Livingstone, S.J. and Yang, K. (2023) *Seasonal evolution of the supraglacial drainage network at Humboldt Glacier, northern Greenland, between 2016 and 2020*. doi: 10.5194/tc-17-4729-2023

Raymond, M.J. and Gudmundsson, G.H. (2005) 'On the relationship between surface and basal properties on glaciers, ice sheets, and ice streams'. *Journal of Geophysical Research: Solid Earth* 110(B8). doi: 10.1029/2005JB003681

Rees, W.G. (2005) *Remote Sensing of Snow and Ice*. CRC Press.

Rennermalm, A.K. et al. (2013) 'Evidence of meltwater retention within the Greenland ice sheet'. *The Cryosphere* 7(5), pp. 1433–1445. doi: 10.5194/tc-7-1433-2013

Rignot, E. et al. (2021) 'Retreat of Humboldt Gletscher, North Greenland, driven by undercutting from a warmer ocean'. *Geophysical research letters* 48(6), p. e2020GL091342. doi: 10.1029/2020GL091342

Rignot, E., Box, J.E., Burgess, E. and Hanna, E. (2008) 'Mass balance of the Greenland ice sheet from 1958 to 2007'. *Geophysical Research Letters* 35(20). doi: 10.1029/2008GL035417.

Rignot, E., Gogineni, S., Joughin, I. and Krabill, W. (2001) 'Contribution to the glaciology of northern Greenland from satellite radar interferometry'. *Journal of Geophysical Research: Atmospheres* 106(D24), pp. 34007–34019. doi: 10.1029/2001JD900071.

Rignot, E. and Kanagaratnam, P. (2006) 'Changes in the Velocity Structure of the Greenland Ice Sheet'. *Science* 311(5763), pp. 986–990. doi: 10.1126/science.1121381.

Rignot, E., Koppes, M. and Velicogna, I. (2010) 'Rapid submarine melting of the calving faces of West Greenland glaciers'. *Nature Geoscience* 3(3), pp. 187–191. doi: 10.1038/ngeo765.

Rignot, E. and MacAyeal, D.R. (1998) 'Ice-shelf dynamics near the front of the Filchner–Ronne Ice Shelf, Antarctica, revealed by SAR interferometry'. *Journal of Glaciology* 44(147), pp. 405–418. doi:10.3189/S0022143000002732

Rignot, E., Velicogna, I., van den Broeke, M.R., Monaghan, A. and Lenaerts, J.T.M. (2011) 'Acceleration of the contribution of the Greenland and Antarctic ice sheets to sea level rise'. *Geophysical Research Letters* 38(5). doi: 10.1029/2011GL046583.

Rignot, E.J., Gogineni, S.P., Krabill, W.B. and Ekholm, S. (1997) 'North and northeast Greenland ice discharge from satellite radar interferometry'. *Science* 276(5314), pp. 934–937. doi: 10.1126/science.276.5314.934

Riihelä, A., King, M.D. and Anttila, K. (2019) 'The surface albedo of the Greenland Ice Sheet between 1982 and 2015 from the CLARA-A2 dataset and its relationship to the ice sheet's surface mass balance'. *The Cryosphere* 13(10), pp. 2597–2614. doi: 10.5194/tc-13-2597-2019

Rippin, D. and Rawlins, L. (2021) *Supraglacial River Networks*. Wiley-Blackwell. doi: 10.1002/9781118786352.wbieg2072.

Rippin, D.M., Pomfret, A. and King, N. (2015) 'High resolution mapping of supra-glacial drainage pathways reveals link between micro-channel drainage density, surface roughness and surface reflectance'. *Earth Surface Processes and Landforms* 40(10), pp. 1279–1290. doi: 10.1002/esp.3719.

Rothlisberger, H. and H. Lang. 1987. Glacial hydrology. In Gurnell, A. M. and M. J. Clark, eds. Glacio 7flurial sedinzent transfer: an alpine perspective. Chichester, etc., John Wiley and Sons, 207-284.

Roy, D.P., Huang, H., Houborg, R. and Martins, V.S. (2021) 'A global analysis of the temporal availability of PlanetScope high spatial resolution multi-spectral imagery'. *Remote Sensing of Environment* 264, p. 112586. doi: 10.1016/j.rse.2021.112586.

Ruan, R. et al. (2019) 'Decelerated Greenland Ice Sheet melt driven by positive summer North Atlantic oscillation'. *Journal of Geophysical Research: Atmospheres* 124(14), pp. 7633–7646. doi: 0.1029/2019JD030689

Rupnik, E., Daakir, M. and Pierrot Deseilligny, M. (2017) 'MicMac – a free, open-source solution for photogrammetry'. *Open Geospatial Data, Software and Standards* 2(1), p. 14. doi: 10.1186/s40965-017-0027-2.

Russell, A. (1989) 'A Comparison of two Recent Jökulhlaups from An Ice-dammed Lake, Søndre Strømfjord, West Greenland'. *Journal of Glaciology - J GLACIOLOGY* 35, pp. 157–162. doi: 10.3189/S0022143000004433.

Russell, A.J., Carrivick, J.L., Ingeman-Nielsen, T., Yde, J.C. and Williams, M. (2011) 'A new cycle of jökulhlaups at Russell Glacier, Kangerlussuaq, West Greenland'. *Journal of Glaciology* 57(202), pp. 238–246. doi: 10.3189/002214311796405997.

Ryan, J.C. et al. (2018) 'Dark zone of the Greenland Ice Sheet controlled by distributed biologically-active impurities'. *Nature communications* 9(1), p. 1065. doi: 10.1038/s41467-018-03353-2

Ryan, J.C., Smith, L.C., Cooley, S.W., Pearson, B., Wever, N., Keenan, E. and Lenaerts, J.T.M. (2022) 'Decreasing surface albedo signifies a growing importance of clouds for Greenland Ice Sheet meltwater production'. *Nature Communications* 13(1), p. 4205. doi: 10.1038/s41467-022-31434-w.

Ryan, J.C., Smith, L.C., Van As, D., Cooley, S.W., Cooper, M.G., Pitcher, L.H. and Hubbard, A. (2019) 'Greenland Ice Sheet surface melt amplified by snowline migration and bare ice exposure'. *Science Advances* 5(3), p. eaav3738. doi: 10.1126/sciadv.aav3738

Sadeq, H.A. (2019) 'Accuracy assessment using different UAV image overlaps'. *Journal of Unmanned Vehicle Systems* 7(3), pp. 175–193. doi: 10.1139/juvs-2018-0014.

Sasgen, I. et al. (2012) 'Timing and origin of recent regional ice-mass loss in Greenland'. *Earth and Planetary Science Letters* 333–334, pp. 293–303. doi: 10.1016/j.epsl.2012.03.033.

Sasgen, I. et al. (2020) 'Return to rapid ice loss in Greenland and record loss in 2019 detected by the GRACE-FO satellites'. *Communications Earth & Environment* 1(1), pp. 1–8. doi: 10.1038/s43247-020-0010-1

Schoof, C. (2010) 'Ice-sheet acceleration driven by melt supply variability'. *Nature* 468(7325), pp. 803–806. doi: 10.1038/nature09618

Schröder, L., Neckel, N., Zindler, R. and Humbert, A. (2020) 'Perennial supraglacial lakes in Northeast Greenland observed by polarimetric SAR'. *Remote Sensing* 12(17), p. 2798. doi: 10.3390/rs12172798

Schuster, C.J. (2001) *Weathering crust processes on melting glacier ice (Alberta, Canada)*. Theses and Dissertations (Comprehensive). 489., Wilfrid Laurier University. Available at: https://scholars.wlu.ca/etd/489.

Schytt, V. (1955) *Glaciological investigations in the Thule Ramp area*. Snow, Ice and Permafrost Research Establishment, Corps of Engineers, US Army.

Screen, J.A. and Simmonds, I. (2010) 'The central role of diminishing sea ice in recent Arctic temperature amplification'. *Nature* 464(7293), pp. 1334–1337. doi: 10.1038/nature09051.

Selmes, N., Murray, T. and James, T.D. (2011) 'Fast draining lakes on the Greenland Ice Sheet'. *Geophysical Research Letters* 38(15). doi: 10.1029/2011GL047872

Selmes, N., Murray, T. and James, T.D. (2013) 'Characterizing supraglacial lake drainage and freezing on the Greenland Ice Sheet'. *The Cryosphere Discussions* 7(1), pp. 475–505. doi: 10.5194/tcd-7-475-2013

Serreze, M.C. and Francis, J.A. (2006) 'The Arctic Amplification Debate'. *Climatic Change* 76(3), pp. 241–264. doi: 10.1007/s10584-005-9017-y.

Sévellec, F., Fedorov, A.V. and Liu, W. (2017) 'Arctic sea-ice decline weakens the Atlantic Meridional Overturning Circulation'. *Nature Climate Change* 7(8), pp. 604–610. doi: 10.1038/nclimate3353.

Shaw, G.A. and Burke, H.K. (2003) 'Spectral imaging for remote sensing'. *Lincoln laboratory journal* 14(1), pp. 3–28.

Shepherd, A. et al. (2012) 'A Reconciled Estimate of Ice-Sheet Mass Balance'. *Science* 338(6111), pp. 1183–1189. doi: 10.1126/science.1228102.

Shiggins, C.J., Lea, J.M. and Brough, S. (2023) 'Automated ArcticDEM iceberg detection tool: insights into area and volume distributions, and their potential application to satellite imagery and modelling of glacier–iceberg–ocean systems'. *The Cryosphere* 17(1), pp. 15–32. doi: 10.5194/tc-17-15-2023.

Shukla, A. and Ali, I. (2016) 'A hierarchical knowledge-based classification for glacier terrain mapping: a case study from Kolahoi Glacier, Kashmir Himalaya'. *Annals of Glaciology* 57(71), pp. 1–10. doi:10.3189/2016AoG71A046

Shum, H.-Y., Ke, Q. and Zhang, Z. (1999) 'Efficient bundle adjustment with virtual key frames: A hierarchical approach to multi-frame structure from motion'. in *Proceedings. 1999 IEEE computer society conference on computer vision and pattern recognition (Cat. No PR00149)*. IEEE, pp. 538–543. doi: 10.1109/CVPR.1999.784733

Sidjak, R.W. (1999) 'Glacier mapping of the Illecillewaet icefield, British Columbia, Canada, using Landsat TM and digital elevation data'. *International Journal of Remote Sensing* 20(2), pp. 273–284. doi: 10.1080/014311699213442

Sieberth, T., Wackrow, R. and Chandler, J.H. (2016) 'Automatic detection of blurred images in UAV image sets'. *ISPRS Journal of Photogrammetry and Remote Sensing* 122, pp. 1–16. doi: 10.1016/j.isprsjprs.2016.09.010.

Singh, A.K. and Singla, R. (2020) 'Different approaches of classification of brain tumor in MRI using gabor filters for feature extraction'. in *Soft Computing: Theories and Applications: Proceedings of SoCTA 2018*. Springer, pp. 1175–1188.

Singh, K.K. and Frazier, A.E. (2018) 'A meta-analysis and review of unmanned aircraft system (UAS) imagery for terrestrial applications'. *International Journal of Remote Sensing* 39(15–16), pp. 5078–5098. doi: 10.1080/01431161.2017.1420941.

Skiles, S.M., Flanner, M., Cook, J.M., Dumont, M. and Painter, T.H. (2018) 'Radiative forcing by light-absorbing particles in snow | Nature Climate Change'. *Nature Climate Change* 8(11), pp. 964–971. doi: 10.1038/s41558-018-0296-5.

Slater, D.A. et al. (2022) 'Characteristic Depths, Fluxes, and Timescales for Greenland's Tidewater Glacier Fjords From Subglacial Discharge-Driven Upwelling During Summer'. *Geophysical Research Letters* 49(10), p. e2021GL097081. doi: 10.1029/2021GL097081.

Slater, D.A., Goldberg, D.N., Nienow, P.W. and Cowton, T.R. (2016) 'Scalings for submarine melting at tidewater glaciers from buoyant plume theory'. *Journal of Physical Oceanography* 46(6), pp. 1839–1855. doi: 10.1175/JPO-D-15-0132.1

Slater, D.A. and Straneo, F. (2022) 'Submarine melting of glaciers in Greenland amplified by atmospheric warming'. *Nature Geoscience* 15(10), pp. 794–799. doi: 10.1038/s41561-022-01035-9.

Slater, T. et al. (2021) 'Increased variability in Greenland Ice Sheet runoff from satellite observations'. *Nature Communications* 12(1), p. 6069. doi: 10.1038/s41467-021-26229-4

Smith, L.C. et al. (2015) 'Efficient meltwater drainage through supraglacial streams and rivers on the southwest Greenland ice sheet'. *Proceedings of the National Academy of Sciences* 112(4), pp. 1001–1006. doi: 10.1073/pnas.1413024112

Smith, L.C. et al. (2017) 'Direct measurements of meltwater runoff on the Greenland ice sheet surface'. *Proceedings of the National Academy of Sciences* 114(50), pp. E10622–E10631. doi: 10.1073/pnas.1707743114

Smith, L.C. et al. (2021) 'Supraglacial river forcing of subglacial water storage and diurnal ice sheet motion'. *Geophysical Research Letters* 48(7), p. e2020GL091418. doi: 10.1029/2020GL091418

Smith, M.W., Carrivick, J.L., Hooke, J. and Kirkby, M.J. (2014) 'Reconstructing flash flood magnitudes using "Structure-from-Motion": A rapid assessment tool'. *Journal of Hydrology* 519, pp. 1914–1927. doi: 10.1016/j.jhydrol.2014.09.078.

Smith, M.W., Carrivick, J.L. and Quincey, D.J. (2016) 'Structure from motion photogrammetry in physical geography'. *Progress in physical geography* 40(2), pp. 247–275.

Smith, W.D., Dunning, S.A., Brough, S., Ross, N. and Telling, J. (2020) 'GERALDINE (Google Earth Engine supRaglAciaL Debris INput dEtector): a new tool for identifying and monitoring supraglacial landslide inputs'. *Earth Surface Dynamics* 8(4), pp. 1053–1065. doi: 10.5194/esurf-8-1053-2020.

Sohn, H.-G., Jezek, K.C. and van der Veen, C.J. (1998) 'Jakobshavn Glacier, west Greenland: 30 years of spaceborne observations'. *Geophysical Research Letters* 25(14), pp. 2699–2702. doi: 10.1029/98GL01973.

Sole, A.J., Mair, D.W.F., Nienow, P.W., Bartholomew, I.D., King, M.A., Burke, M.J. and Joughin, I. (2011) 'Seasonal speedup of a Greenland marine-terminating outlet glacier forced by surface melt-induced changes in subglacial hydrology'. *Journal of Geophysical Research Earth Surface* 116(3). doi: 10.1029/2010JF001948.

Sood, V., Singh, S., Taloor, A.K., Prashar, S. and Kaur, R. (2020) 'Monitoring and mapping of snow cover variability using topographically derived NDSI model over north Indian Himalayas during the period 2008–19'. *Applied Computing and Geosciences* 8, p. 100040. doi: 10.1016/j.acags.2020.100040

Steffen, K., Nghiem, S.V., Huff, R. and Neumann, G. (2004) 'The melt anomaly of 2002 on the Greenland Ice Sheet from active and passive microwave satellite observations'. *Geophysical Research Letters* 31(20). doi:10.1029/2004GL020444.

Steger, C.R. et al. (2017a) 'Firn Meltwater Retention on the Greenland Ice Sheet: A Model Comparison'. *Frontiers in Earth Science* 5. doi: 10.3389/feart.2017.00003.

Steger, C.R., Reijmer, C.H. and van den Broeke, M.R. (2017b) 'The modelled liquid water balance of the Greenland Ice Sheet'. *The Cryosphere* 11(6), pp. 2507–2526. doi: 10.5194/tc-11-2507-2017.

Stevens, L.A. et al. (2015) 'Greenland supraglacial lake drainages triggered by hydrologically induced basal slip'. *Nature* 522(7554), pp. 73–76. doi: 10.1038/nature14480.

Stibal, M. et al. (2017) 'Algae Drive Enhanced Darkening of Bare Ice on the Greenland Ice Sheet'. *Geophysical Research Letters* 44(22), p. 11,463-11,471. doi: 10.1002/2017GL075958.

Stokes, C.R., Sanderson, J.E., Miles, B.W., Jamieson, S.S. and Leeson, A.A. (2019) 'Widespread distribution of supraglacial lakes around the margin of the East Antarctic Ice Sheet'. *Scientific reports* 9(1), p. 13823. doi: 10.1038/s41598-019-50343-5

Storey, J., Scaramuzza, P., Schmidt, G. and Barsi, J. (2005) 'LANDSAT 7 SCAN LINE CORRECTOR-OFF GAP-FILLED PRODUCT DEVELOPMENT'.

Stroeve, J. (2001) 'Assessment of Greenland albedo variability from the advanced very high resolution radiometer Polar Pathfinder data set'. *Journal of Geophysical Research: Atmospheres* 106(D24), pp. 33989–34006. doi: 10.1029/2001JD900072.

Sugden, D.E., Clapperton, C.M. and Knight, P.G. (1985) 'A Jökulhlaup Near Søndre Strømfjord, West GreenLand, and Some Effects on the Ice-Sheet Margin'. *Journal of Glaciology* 31(109), pp. 366–368. doi: 10.3189/S0022143000006729.

Sundal, A.V., Shepherd, A., Nienow, P., Hanna, E., Palmer, S. and Huybrechts, P. (2009) 'Evolution of supra-glacial lakes across the Greenland Ice Sheet'. *Remote Sensing of Environment* 113(10), pp. 2164–2171. doi: 10.1016/j.rse.2009.05.018.

Sundal, A.V., Shepherd, A., Nienow, P., Hanna, E., Palmer, S. and Huybrechts, P. (2011) 'Melt-induced speed-up of Greenland ice sheet offset by efficient subglacial drainage'. *Nature* 469(7331), pp. 521–524. doi: 10.1038/nature09740.

Takeuchi, N., Sakaki, R., Uetake, J., Nagatsuka, N., Shimada, R., Niwano, M. and Aoki, T. (2018) 'Temporal variations of cryoconite holes and cryoconite coverage on the ablation ice surface of Qaanaaq Glacier in northwest Greenland'. *Annals of Glaciology* 59(77), pp. 21–30. doi: 10.1017/aog.2018.19.

Tarboton, D.G., Bras, R.L. and Rodriguez-Iturbe, I. (1991) 'On the extraction of channel networks from digital elevation data'. *Hydrological Processes* 5(1), pp. 81–100. doi: 10.1002/hyp.3360050107.

Taylor, L.S., Quincey, D.J., Smith, M.W., Baumhoer, C.A., McMillan, M. and Mansell, D.T. (2021) 'Remote sensing of the mountain cryosphere: Current capabilities and future opportunities for research'. *Progress in Physical Geography: Earth and Environment* 45(6), pp. 931–964. doi: 10.1177/03091333211023690.

Tedesco, M. et al. (2011) 'The role of albedo and accumulation in the 2010 melting record in Greenland'. *Environmental Research Letters* 6(1), p. 014005. doi: 10.1088/1748-9326/6/1/014005.

Tedesco, M. (2015) 'Remote sensing and the cryosphere'. *Remote Sensing of the Cryosphere* , pp. 1–16.

Tedesco, M., Box, J.E., Cappelen, J., Fausto, R.S., Fettweis, X., Anderson, J.K., Mote, T., Smeets, C.J.P.P., van As, D., van de Wal, R.S.W. (2018). NOAA Arctic Report Card 2018: Greenland Ice Sheet in Arctic Report Card 2018. Available online: https://arctic.noaa.gov/Report-Card/Report-Card-2018, last access 20th November 2022.

Tedesco, M., Box, J.E., Capplelen, J., Fausto, R.S., Fettweis, X., Hansen, K., Mote, T., Sasgen, I., Smeets, C.J.P.P., van As, D., van de Wal, R.S.W., Velicogna, I. (2017) NOAA Arctic Report Card 2017: Greenland Ice Sheet in Arctic Report Card 2017. Available online: https://arctic.noaa.gov/Report-Card/Report-Card-2017, last access 20th November 2022.

Tedesco, M., Moon. T., Box, J.E., Cappelen, J., Fauto, R.S., Fettweis, X., Loomis, B., Mankoff. K.D., Mote, T., Smeets, C.J.P.P., van As, D., van de Wal, R.S.W., (2019) 'Arctic Report Card 2019'. Available at: https://arctic.noaa.gov/Portals/7/ArcticReportCard/Documents/ArcticReportCard_full_report2019.pdf.

Tedesco, M., Doherty, S., Fettweis, X., Alexander, P., Jeyaratnam, J. and Stroeve, J. (2016) 'The darkening of the Greenland ice sheet: trends, drivers, and projections (1981–2100)'. *The Cryosphere* 10(2), pp. 477–496. doi: 10.5194/tc-10-477-2016

Tedesco, M. and Fettweis, X. (2020) 'Unprecedented atmospheric conditions (1948–2019) drive the 2019 exceptional melting season over the Greenland ice sheet'. *The Cryosphere* 14(4), pp. 1209–1223. doi: 10.5194/tc-14-1209-2020

Tedesco, M., Fettweis, X., Mote, T., Wahr, J., Alexander, P., Box, J.E. and Wouters, B. (2013) 'Evidence and analysis of 2012 Greenland records from spaceborne observations, a regional climate model and reanalysis data'. *The Cryosphere* 7(2), pp. 615–630. doi: 10.5194/tc-7-615-2013.

Tedstone, A.J., Bamber, J.L., Cook, J.M., Williamson, C.J., Fettweis, X., Hodson, A.J. and Tranter, M. (2017) 'Dark ice dynamics of the south-west Greenland Ice Sheet'. *The Cryosphere* 11(6), pp. 2491–2506. doi: 10.5194/tc-11-2491-2017.

Tedstone, A.J. and Machguth, H. (2022) 'Increasing surface runoff from Greenland's firn areas'. *Nature climate change* 12(7), pp. 672–676. doi: 10.1038/s41558-022-01371-z.

The IMBIE Team (2020) 'Mass balance of the Greenland Ice Sheet from 1992 to 2018'. *Nature* 579(7798), pp. 233–239. doi: 10.1038/s41586-019-1855-2

Thomas, R.H., Abdalati, W., Frederick, E., Krabill, W.B., Manizade, S. and Steffen, K. (2003) 'Investigation of surface melting and dynamic thinning on Jakobshavn Isbræ, Greenland'. *Journal of Glaciology* 49(165), pp. 231–239. doi: 10.3189/172756503781830764.

Thomsen, H.H. (1986) 'Photogrammetric and satellite mapping of the margin of the inland ice, West Greenland'. *Annals of glaciology* 8, pp. 164–167.

Triggs, B., McLauchlan, P.F., Hartley, R.I. and Fitzgibbon, A.W. (2000) 'Bundle adjustment—a modern synthesis'. in *Vision Algorithms: Theory and Practice: International Workshop on Vision Algorithms Corfu, Greece, September 21–22, 1999 Proceedings*. Springer, pp. 298–372.

Trusel, L.D. et al. (2018) 'Nonlinear rise in Greenland runoff in response to post-industrial Arctic warming'. *Nature* 564(7734), pp. 104–108. doi: 10.1038/s41586-018-0752-4

Tuckett, P.A., Ely, J.C., Sole, A.J., Lea, J.M., Livingstone, S.J., Jones, J.M. and van Wessem, J.M. (2021) 'Automated mapping of the seasonal evolution of surface meltwater and its links to climate on the Amery Ice Shelf, Antarctica'. *The Cryosphere* 15(12), pp. 5785–5804. doi: 10.5194/tc-15-5785-2021

Turner, M.R. (1986) 'Texture discrimination by Gabor functions'. *Biological cybernetics* 55(2–3), pp. 71–82.

Turton, J.V., Hochreuther, P., Reimann, N. and Blau, M.T. (2021) 'The distribution and evolution of supraglacial lakes on 79 N Glacier (north-eastern Greenland) and interannual climatic controls'. *The Cryosphere* 15(8), pp. 3877–3896. doi: 10.5194/tc-15-3877-2021

Van Angelen, J.H., van den Broeke, M.R., Wouters, B. and Lenaerts, J.T.M. (2014) 'Contemporary (1960–2012) Evolution of the Climate and Surface Mass Balance of the Greenland Ice Sheet'. *Surveys in Geophysics* 35(5), pp. 1155–1174. doi: 10.1007/s10712-013-9261-z.

Van As, D., Bech Mikkelsen, A., Holtegaard Nielsen, M., Box, J.E., Claesson Liljedahl, L., Lindbäck, K., Pitcher, L. and Hasholt, B., 2017. Hypsometric amplification and routing moderation of Greenland ice sheet meltwater release. The Cryosphere, 11(3), pp.1371-1386.. doi: 10.5194/tc-11-1371-2017.

Van As, D., Box, J.E. and Fausto, R.S. (2016) 'Challenges of Quantifying Meltwater Retention in Snow and Firn: An Expert Elicitation'. *Frontiers in Earth Science* 4. doi: 10.3389/feart.2016.00101

Van den Broeke, M., Bamber, J., Ettema, J., Rignot, E., Schrama, E., van de Berg, W.J., van Meijgaard, E., Velicogna, I. and Wouters, B (2009) 'Partitioning Recent Greenland Mass Loss'. *Science* 326(5955), pp. 984–986. doi: 10.1126/science.1178176. doi: 10.1126/science.1178176

Van den Broeke, M., Box, J., Fettweis, X., Hanna, E., Noël, B., Tedesco, M., van As, D., van de Berg, W.J. and van Kampenhout, L., 2017. Greenland ice sheet surface mass loss: recent developments in observation and modeling. Current Climate Change Reports, 3, pp.345-356. doi: 10.1007/s40641-017-0084-8

Van den Broeke, M.R., Enderlin, E.M., Howat, I.M., Kuipers Munneke, P., Noël, B.P., Van De Berg, W.J., Van Meijgaard, E. and Wouters, B., 2016. On the recent contribution of the Greenland ice sheet to sea level change. The Cryosphere, 10(5), pp.1933-1946. doi: 10.5194/tc-10-1933-2016

Van den Broeke, M.R., Smeets, C. and Van de Wal, R.S.W. (2011) 'The seasonal cycle and interannual variability of surface energy balance and melt in the ablation zone of the west Greenland ice sheet'. *The Cryosphere* 5(2), pp. 377–390. doi: 10.5194/tc-5-377-2011

Van den Broeke, M., Smeets, P., Ettema, J. and Munneke, P.K. (2008) 'Surface radiation balance in the ablation zone of the west Greenland ice sheet'. Journal of Geophysical Research: Atmospheres 113(D13).doi: 10.1029/2007JD009283.

Van Tricht, K. et al. (2016) 'Clouds enhance Greenland ice sheet meltwater runoff'. *Nature Communications* 7(1), p. 10266. doi: 10.1038/ncomms10266.

Vaughan D G et al. (2013) Climate Change 2013: The Physical Science Basis. Contribution of Working Group I to the Fifth Assessment Report of the Intergovernmental Panel on Climate Change ed T F Stocker, D Qin, G-K Plattner, M Tignor, S K Allen, J Boschung, A Nauels, Y Xia, V Bex and P M Midgley (Cambridge: Cambridge University Press). Observations: cryosphere. pp 317–382

van der Veen, C.J. (1998) 'Fracture mechanics approach to penetration of surface crevasses on glaciers'. *Cold Regions Science and Technology* 27(1), pp. 31–47. doi: 10.1016/S0165-232X(97)00022-0.

Velicogna, I., Wahr, J., Hanna, E. and Huybrechts, P. (2005) 'Short term mass variability in Greenland, from GRACE'. *Geophysical Research Letters* 32(5). Available at: https://onlinelibrary.wiley.com/doi/abs/10.1029/2004GL021948.

Vizcaino, M. (2014) 'Ice sheets as interactive components of Earth System Models: progress and challenges'. *Wiley Interdisciplinary Reviews: Climate Change* 5(4), pp. 557–568. doi: 10.1002/wcc.285

van de Wal, R.S.W., Boot, W., van den Broeke, M.R., Smeets, C.J.P.P., Reijmer, C.H., Donker, J.J.A. and Oerlemans, J. (2008) 'Large and Rapid Melt-Induced Velocity Changes in the Ablation Zone of the Greenland Ice Sheet'. *Science* 321(5885), pp. 111–113. doi: 10.1126/science.1158540.

Wang, W., Zender, C.S. and van As, D. (2018) 'Temporal Characteristics of Cloud Radiative Effects on the Greenland Ice Sheet: Discoveries From Multiyear Automatic Weather Station Measurements'. *Journal of Geophysical Research: Atmospheres* 123(20), p. 11,348-11,361. doi: 10.1029/2018JD028540.

Wang, W., Zender, C.S., van As, D., Fausto, R.S. and Laffin, M.K. (2021) 'Greenland Surface Melt Dominated by Solar and Sensible Heating'. *Geophysical Research Letters* 48(7), p. e2020GL090653. doi: 10.1029/2020GL090653.

Wang, X. and Zender, C.S. (2010) 'Constraining MODIS snow albedo at large solar zenith angles: Implications for the surface energy budget in Greenland'. *Journal of Geophysical Research: Earth Surface* 115(F4). doi:10.1029/2009JF00143.

Watson, C.S., King, O., Miles, E.S. and Quincey, D.J. (2018) 'Optimising NDWI supraglacial pond classification on Himalayan debris-covered glaciers'. *Remote sensing of environment* 217, pp. 414–425. doi: 10.1016/j.rse.2018.08.020

Wehrlé, A., Box, J.E., Niwano, M., Anesio, A.M. and Fausto, R.S. (2021) 'Greenland bare-ice albedo from PROMICE automatic weather station measurements and Sentinel-3 satellite observations'. *GEUS Bulletin* 47.

Wesche, C., Jansen, D. and Dierking, W. (2013) 'Calving fronts of Antarctica: Mapping and classification'. *Remote Sensing* 5(12), pp. 6305–6322. doi: 10.3390/rs5126305

Westoby, M., Brasington, J., Glasser, N., Hambrey, M. and Reynolds, J. (2012) 'Structure-from-Motion photogrammetry: a novel, low-cost tool for geomorphological applications'., p. 936.

Wheate, R.D., Berthier, E., Bolch, T., Menounos, B.P., Shea, J.M., Clague, J.J. and Schiefer, E. (2014) 'Remote Sensing of Glaciers in the Canadian Cordillera, Western Canada'. in Kargel, J. S., Leonard, G. J., Bishop, M. P., Kääb, A., and Raup, B. H. (eds.) *Global Land Ice Measurements from Space*. Springer Praxis Books. Berlin, Heidelberg: Springer, pp. 333–352. doi:10.1007/978-3-540-79818-7_14.

Wientjes, I.G.M. and Oerlemans, J. (2010) 'An explanation for the dark region in the western melt zone of the Greenland ice sheet'. *The Cryosphere* 4(3), pp. 261–268. doi: 10.5194/tc-4-261-2010.

Wientjes, I.G.M., Van de Wal, R.S.W., Reichart, G.J., Sluijs, A. and Oerlemans, J. (2011) 'Dust from the dark region in the western ablation zone of the Greenland ice sheet'. *The Cryosphere* 5(3), pp. 589–601. doi: 10.5194/tc-5-589-2011.

Williamson, A.G., Arnold, N.S., Banwell, A.F. and Willis, I.C. (2017) 'A Fully Automated Supraglacial lake area and volume Tracking ("FAST") algorithm: Development and application using MODIS imagery of West Greenland'. *Remote Sensing of Environment* 196, pp. 113–133. doi: 10.1016/j.rse.2017.04.032

Williamson, A.G., Banwell, A.F., Willis, I.C. and Arnold, N.S. (2018) 'Dual-satellite (Sentinel-2 and Landsat 8) remote sensing of supraglacial lakes in Greenland'. *The Cryosphere* 12(9), pp. 3045–3065. doi: 10.5194/tc-12-3045-2018

Williamson, Christopher.J. et al. (2020) *Algal photophysiology drives darkening and melt of the Greenland Ice Sheet*. doi:10.1073/pnas.1918412117.

Willis, I.C., Arnold, N.S. and Brock, B.W. (2002) 'Effect of snowpack removal on energy balance, melt and runoff in a small supraglacial catchment'. *Hydrological Processes* 16(14), pp. 2721–2749. doi: 10.1002/hyp.1067.

Wiscombe, W.J. and Warren, S.G. (1980) 'A Model for the Spectral Albedo of Snow. I: Pure Snow'. *Journal of the Atmospheric Sciences* 37(12), pp. 2712–2733. doi: 10.1175/1520-0469(1980)037<2712:AMFTSA>2.0.CO;2.

Wolf, P.R., Dewitt, B.A. and Wilkinson, B.E. (2014) *Elements of Photogrammetry with Applications in GIS*. 4th Edition. McGraw-Hill Education. Available at: https://www.accessengineeringlibrary.com/content/book/9780071761123.

Woods, T. and Hewitt, I.J. (2022) *A model of the weathering crust and microbial activity on an ice-sheet surface*. EHUsphere. pp. 1-30. doi:10.5194/egusphere-2022-1086.

Wouters, B., Chambers, D. and Schrama, E.J.O. (2008) 'GRACE observes small-scale mass loss in Greenland'. *Geophysical Research Letters* 35(20). doi:10.1029/2008GL034816

Wu, C., Song, J., Ma, G., Zhang, Y., Sun, J. and Zhang, F. (2021) 'Dense stereo matching in depth discontinuity areas based on edge detection and nearest valid point search'. *Remote Sensing Letters* 12(9), pp. 869–878. doi: 10.1080/2150704X.2021.1944690.

Wulder, M.A. et al. (2019) 'Current status of Landsat program, science, and applications'. *Remote sensing of environment* 225, pp. 127–147. doi: 10.1016/j.rse.2019.02.015

Wyatt, F.R. and Sharp, M.J. (2015) 'Linking surface hydrology to flow regimes and patterns of velocity variability on Devon Ice Cap, Nunavut'. *Journal of Glaciology* 61(226), pp. 387–399. doi: 10.3189/2015JoG14J109

Xin, S., Wenchang, L., Hong, X. and Qing, Z. (2019) 'Image detection method for the exposed area of overhead cable based on Gabor filter'., pp. 425–433. doi: 10.1109/ICEMI46757.2019.9101513.

Xu, H. (2005) 'A study on information extraction of water body with the modified normalized difference water index (MNDWI)'. *JOURNAL OF REMOTE SENSING-BEIJING-* 9(5), p. 595.

Xu, Y., Rignot, E., Menemenlis, D. and Koppes, M. (2012) 'Numerical experiments on subaqueous melting of Greenland tidewater glaciers in response to ocean warming and enhanced subglacial runoff'. *Annals of Glaciology* 53. doi: 10.3189/2012AoG60A139.

Yallop, M.L. et al. (2012) 'Photophysiology and albedo-changing potential of the ice algal community on the surface of the Greenland ice sheet'. *The ISME Journal* 6(12), pp. 2302–2313. doi: 10.1038/ismej.2012.107.

Yang, K. et al. (2018) 'A new surface meltwater routing model for use on the Greenland Ice Sheet surface'. *The Cryosphere* 12(12), pp. 3791–3811. doi: 10.5194/tc-12-3791-2018.

Yang, K. et al. (2021) 'Seasonal evolution of supraglacial lakes and rivers on the southwest Greenland Ice Sheet'. *Journal of Glaciology* 67(264), pp. 592–602. doi: 10.1017/jog.2021.10

Yang, K., Karlstrom, L., Smith, L.C. and Li, M. (2017) 'Automated high-resolution satellite image registration using supraglacial rivers on the Greenland Ice Sheet'. *IEEE Journal of Selected Topics in Applied Earth Observations and Remote Sensing* 10(3), pp. 845–856. doi: 10.1109/JSTARS.2016.2617822

Yang, K. and Li, M. (2014) 'Greenland Ice Sheet surface melt: A review'. *Sciences in Cold and Arid Regions* 6, pp. 0099–0106. doi: 10.3724/SP.J.1226.2014.00099.

Yang, K., Li, M., Liu, Y., Cheng, L., Huang, Q. and Chen, Y. (2015a) 'River detection in remotely sensed imagery using Gabor filtering and path opening'. *Remote Sensing* 7(7), pp. 8779–8802. doi: /10.3390/rs70708779

Yang, K. and Smith, L.C. (2013) 'Supraglacial streams on the Greenland Ice Sheet delineated from combined spectral–shape information in high-resolution satellite imagery'. *IEEE Geoscience and Remote Sensing Letters* 10(4), pp. 801–805. doi: 10.1109/LGRS.2012.2224316

Yang, K. and Smith, L.C. (2016) 'Internally drained catchments dominate supraglacial hydrology of the southwest Greenland Ice Sheet'. *Journal of Geophysical Research: Earth Surface* 121(10), pp. 1891–1910. doi:10.1002/2016JF003927

Yang, K., Smith, L.C., Andrews, L.C., Fettweis, X. and Li, M. (2022) 'Supraglacial drainage efficiency of the Greenland Ice Sheet estimated from remote sensing and climate models'. *Journal of Geophysical Research: Earth Surface* 127(2). doi: 10.1029/2021JF006269

Yang, K., Smith, L.C., Chu, V.W., Gleason, C.J. and Li, M. (2015b) 'A caution on the use of surface digital elevation models to simulate supraglacial hydrology of the Greenland ice sheet'. *IEEE Journal of Selected Topics in Applied Earth Observations and Remote Sensing* 8(11), pp. 5212–5224. doi: 10.1109/JSTARS.2015.2483483

Yang, K., Smith, L.C., Chu, V.W., Pitcher, L.H., Gleason, C.J., Rennermalm, A.K. and Li, M. (2016) 'Fluvial morphometry of supraglacial river networks on the southwest Greenland Ice Sheet'. *GIScience & Remote Sensing* 53(4), pp. 459–482. doi: 10.1080/15481603.2016.1162345

Yang, K., Smith, L.C., Fettweis, X., Gleason, C.J., Lu, Y. and Li, M. (2019a) 'Surface meltwater runoff on the Greenland ice sheet estimated from remotely sensed supraglacial lake infilling rate'. *Remote Sensing of Environment* 234, p. 111459. doi: 10.1016/j.rse.2019.111459

Yang, K., Smith, L.C., Sole, A., Livingstone, S.J., Cheng, X., Chen, Z. and Li, M. (2019b) 'Supraglacial rivers on the northwest Greenland Ice Sheet, Devon Ice Cap, and Barnes Ice Cap mapped using Sentinel-2 imagery'. *International Journal of Applied Earth Observation and Geoinformation* 78, pp. 1–13. doi: 10.1016/j.jag.2019.01.008

Young, N.E., Anderson, R.S., Chignell, S.M., Vorster, A.G., Lawrence, R. and Evangelista, P.H. (2017) 'A survival guide to Landsat preprocessing'. *Ecology* 98(4), pp. 920–932.

Zhang, E., Liu, L., Huang, L. and Ng, K.S. (2021) 'An automated, generalized, deep-learning-based method for delineating the calving fronts of Greenland glaciers from multi-sensor remote sensing imagery'. *Remote Sensing of Environment* 254, p. 112265. doi: 10.1016/j.rse.2020.112265

Zhu, D., Zhou, C., Zhu, Y. and Peng, B. (2022) 'Evolution of supraglacial lakes on Sermeq Avannarleq glacier, Greenland using Google Earth Engine'. *Journal of Hydrology: Regional Studies* 44, p. 101246. doi: 10.1016/j.ejrh.2022.101246. doi: 10.1016/j.ejrh.2022.101246

Zwally, H.J., Abdalati, W., Herring, T., Larson, K., Saba, J. and Steffen, K. (2002) 'Surface melt-induced acceleration of Greenland ice-sheet flow'. *Science* 297(5579), pp. 218–222. doi: 10.1126/science.1072708

Appendix A

Table A1. Details of the various data sources used for this study, including Sentinel-2 imagery sourced from the European Space Agency (ESA) Copernicus Open Access Hub available at https://scihub.copernicus.eu/ with associated tile IDs (*tile IDs were downloaded for each of the study dates). Information is also provided for the ArcticDEM 10m tile IDs sourced from the Polar Geospatial Centre available at https://www.pgc.umn.edu/data/arcticdem/.

Image Type	Acquisition Date	Tile ID	Source
Sentinel-2 L1C	22/05/2016	T20XMN*	ESA
		T20XMP*	ESA
		T20XNN*	ESA
		T20XNP*	ESA
	12/06/2016		
	28/06/2016		
	08/07/2016		
	18/07/2016		
	29/07/2016		
	07/08/2016		
	25/08/2016		
	03/09/2016		
	30/05/2017		
	10/06/2017		
	22/06/2017		
	06/07/2017		
	19/07/2017		
	24/07/2017		
	06/08/2017		
	22/08/2017		
	05/09/2017		
	15/06/2018		
	22/06/2018		
	29/06/2018		
	05/07/2018		
	25/07/2018		
	02/08/2018		
	20/08/2018		
	17/05/2019		
	04/06/2019		
	24/06/2019		
	30/06/2019		
	07/07/2019		
	17/07/2019		
	27/07/2019		
	05/08/2019		
	13/08/2019		
	02/09/2019		

	15/06/2020 23/06/2020 28/06/2020 25/07/2020 30/07/2020 07/08/2020 17/08/2020 29/08/2020 05/09/2020		
ArcticDEM (10m)		28_36 28_37 28_38 29_36 29_37 29_38 30_36 30_37 30_38	PGC

Table A2. Table showing the satellite-derived water metrics and extracted MAR melt production and runoff values for each study date across the study period (2016 – 2020).

Date	Meltwater Area (km^2)	Meltwater Area Fraction (%)	River Fraction (%)	No. Lakes	Lake Size (km^2)	Lake Fraction (%)	Daily RCM Surface Runoff (mm w.e d^{-1})	Cumulative MAR Runoff (mm w.e d^{-1})
2016-05-22	17.48	0.13	0.13	0	0	0	0.01	0.69
2016-06-12	419.08	3.11	3.11	0	0	0	1.97	3.82
2016-06-28	1538.60	11.41	11.28	73	17.40	0.13	7.12	59.96
2016-07-08	1533.06	11.37	11.22	53	19.10	0.14	14.74	180.89
2016-07-18	1539.78	11.42	11.30	48	15.53	0.12	15.70	338.05
2016-07-29	1021.35	7.57	7.46	37	15.12	0.11	7.44	531.41
2016-08-07	639.77	4.74	4.71	13	4.90	0.04	2.90	624.71
2016-08-25	197.79	1.47	1.45	6	2.03	0.02	0.22	659.19
2016-09-03	122.24	0.91	0.91	0	0	0	0.04	662.11
2017-05-30	10.69	0.08	0.08	0	0	0	0.03	0.37
2017-06-10	15.13	0.11	0.11	0	0	0	0.01	0.60
2017-06-22	28.61	0.21	0.21	0	0	0	1.92	6.98
2017-07-06	131.89	0.98	0.96	15	1.98	0.01	3.56	38.05
2017-07-19	349.65	2.59	2.49	53	13.31	0.10	3.82	98.65
2017-07-24	1039.68	7.71	7.59	54	15.81	0.12	5.68	124.22
2017-08-06	1247.27	9.25	9.13	46	15.30	0.11	4.03	255.56
2017-08-22	1373.33	10.18	10.18	1	0.15	0	0.28	322.40
2017-09-05	195.25	1.45	1.45	0	0	0	0.01	322.89
2018-06-15	16.72	0.12	0.12	0	0	0	0.53	2.15
2018-06-22	86.23	0.64	0.64	0	0	0	1.01	9.66

2018-06-29	230.75	1.71	1.70	12	1.48	0.01	4.28	27.74
2018-07-05	365.10	2.71	2.64	48	8.69	0.06	4.74	55.03
2018-07-25	384.60	2.85	2.77	38	11.29	0.08	0.79	111.69
2018-08-02	905.39	6.71	6.56	74	20.08	0.15	7.09	141.68
2018-08-20	965.73	7.16	7.12	20	5.20	0.04	2.23	235.51
2019-05-17	18.43	0.14	0.14	0	0	0	0.05	0.88
2019-06-04	136.99	1.02	1.02	0	0	0	0.05	1.83
2019-06-24	636.04	4.72	4.51	108	27.65	0.20	1.18	100.54
2019-06-30	2684.99	19.91	19.70	111	27.35	0.20	19.37	147.26
2019-07-07	1659.37	12.30	12.13	95	22.61	0.17	21.46	286.49
2019-07-17	1870.99	13.87	13.70	79	23.11	0.17	16.80	473.14
2019-07-27	1566.27	11.61	11.49	45	16.77	0.12	12.62	617.05
2019-08-05	1031.83	7.65	7.53	45	16.73	0.12	11.22	764.95
2019-08-13	1595.78	11.83	11.71	41	16.48	0.12	8.20	858.76
2019-09-02	1506.69	11.17	11.16	3	1.08	0.01	0.78	924.32
2020-06-15	1572.85	11.66	11.58	57	11.19	0.08	0.57	6.36
2020-06-23	526.47	3.90	3.77	63	17.78	0.13	6.94	36.46
2020-06-28	1637.63	12.14	12.02	70	16.10	0.12	19.60	102.56
2020-07-25	1213.84	9.00	8.91	43	12.53	0.09	14.57	572.35
2020-07-30	560.86	4.16	4.10	37	8.30	0.06	11.41	642.56
2020-08-07	312.61	2.32	2.30	8	2.08	0.02	1.16	681.21
2020-08-17	349.44	2.59	2.58	3	1.01	0.01	0.95	694.33
2020-08-29	371.43	2.75	2.75	2	0.78	0.01	0.29	751.94
2020-09-05	156.02	1.16	1.16	0	0	0	0.01	752.52

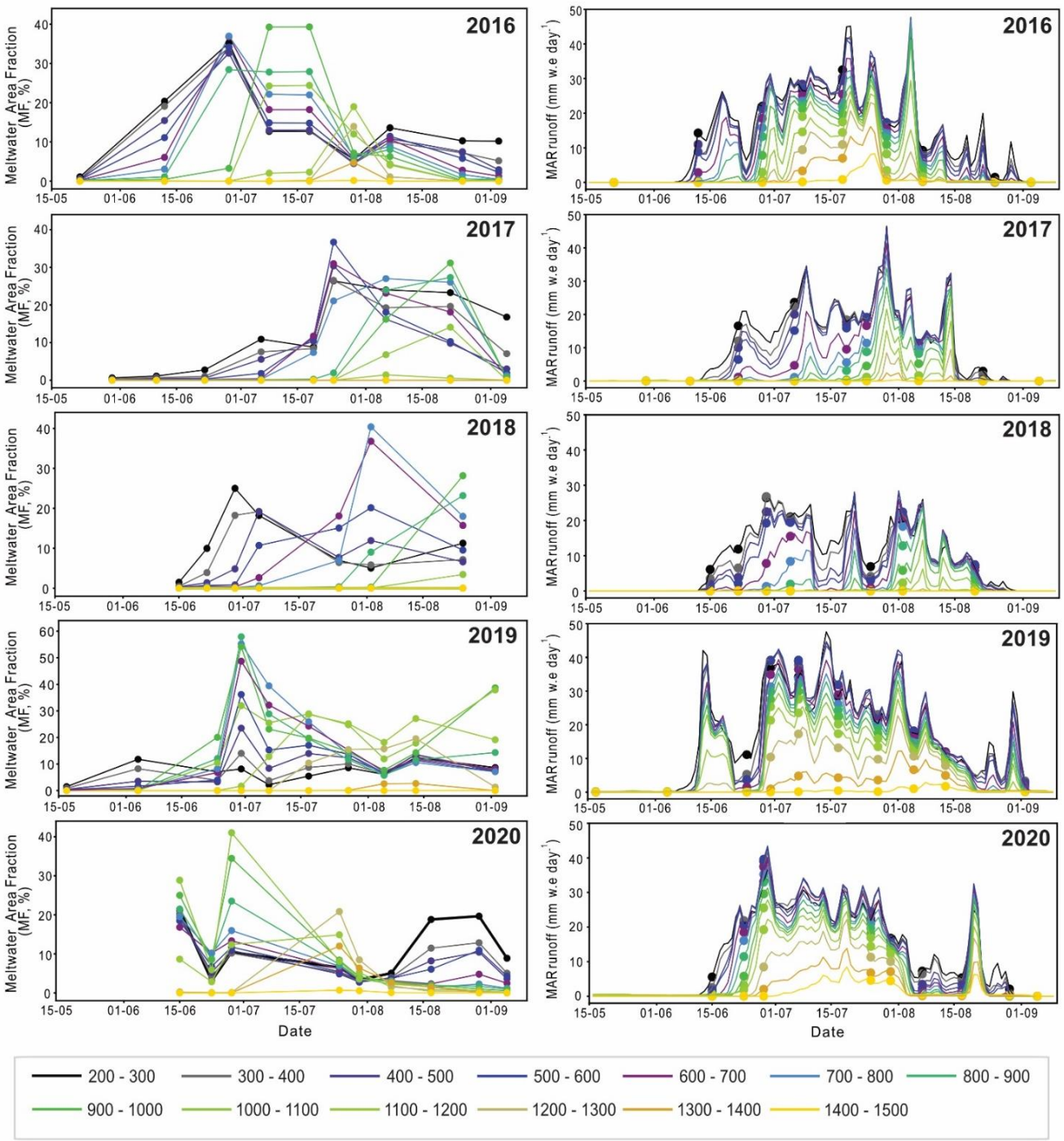

Figure A1. Meltwater area fraction (%) and MAR runoff (mm w.e day^{-1}) per 100 m contour band from 200 m a.s.l to 1500 m a.s.l (conservative limit of maximum mapped network extent) across the Humboldt Glacier catchment for each mapped date across the study period

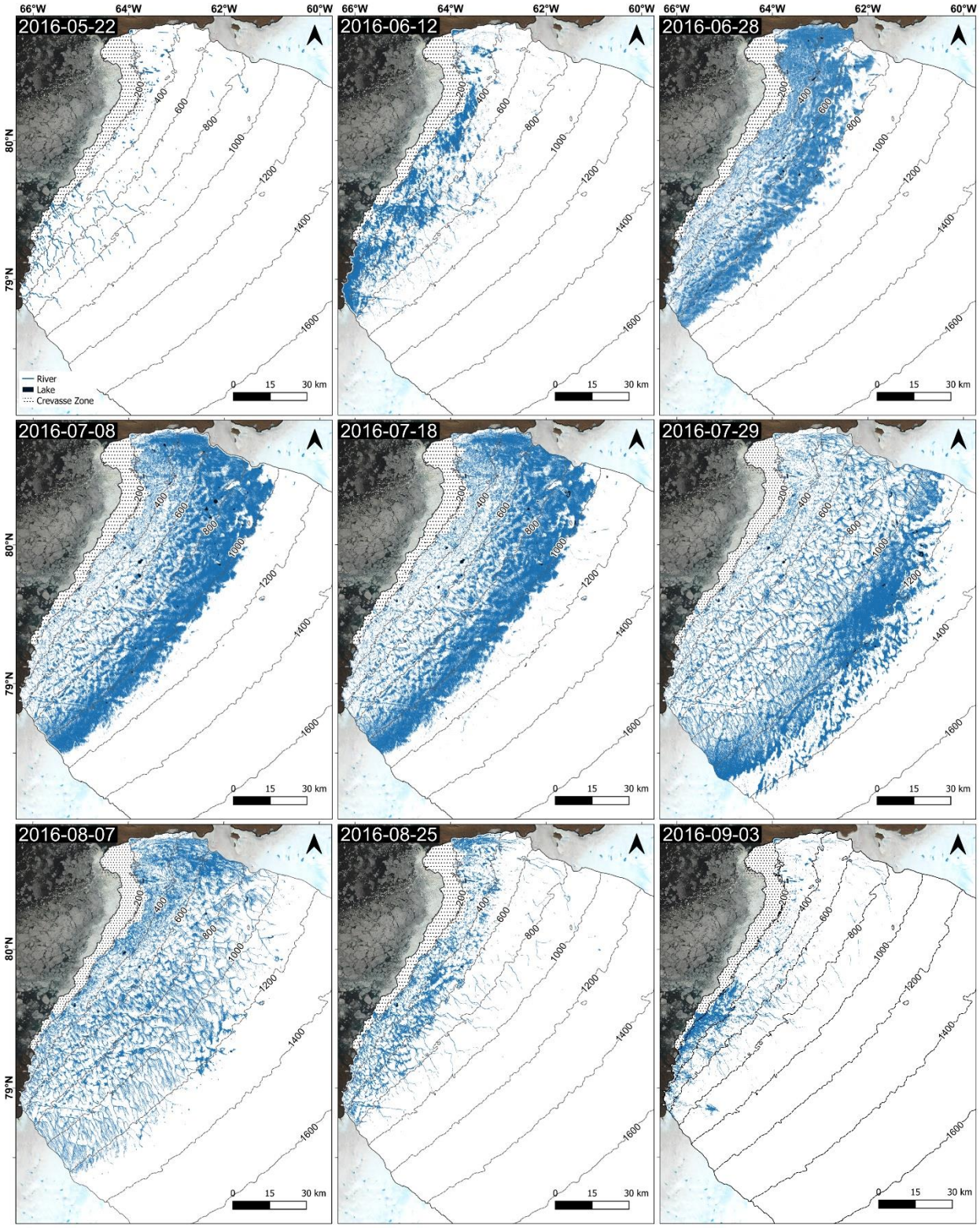
2016-05-22
2016-06-12
2016-06-28
2016-07-08
2016-07-18
2016-07-29
2016-08-07
2016-08-25
2016-09-03
66°W
64°W
62°W
60°W
80°N
79°N
River
Lake
Crevasse Zone
0
15
30 km

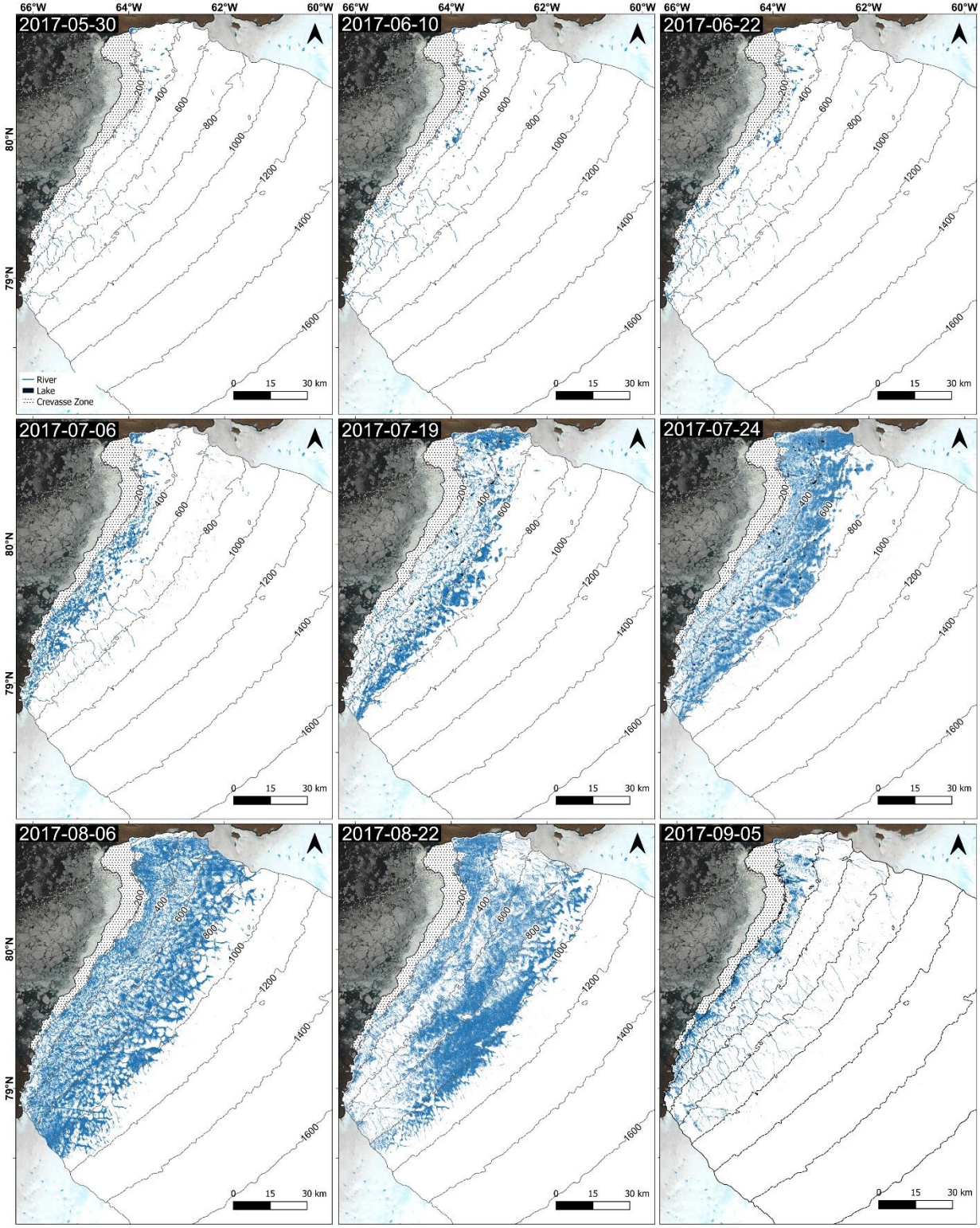
66°W
64°W
62°W
60°W
80°N
79°N
2017-05-30
2017-06-10
2017-06-22
2017-07-06
2017-07-19
2017-07-24
2017-08-06
2017-08-22
2017-09-05
200
400
600
800
1000
1200
1400
1600
River
Lake
Crevasse Zone
0
15
30 km

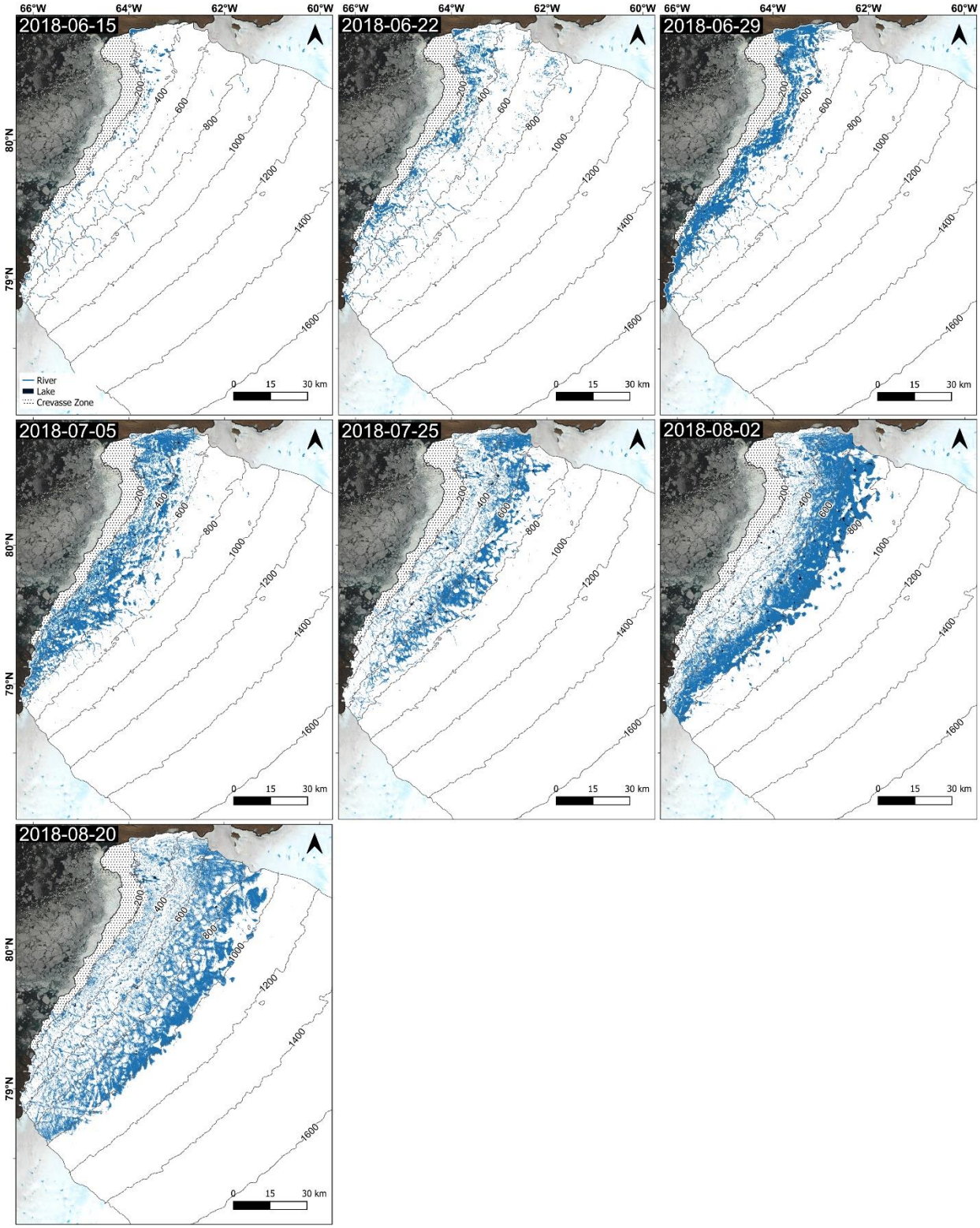
66°W
64°W
62°W
60°W
80°N
79°N
2018-06-15
2018-06-22
2018-06-29
2018-07-05
2018-07-25
2018-08-02
2018-08-20
River
Lake
Crevasse Zone
0
15
30 km
200
400
600
800
1000
1200
1400
1600

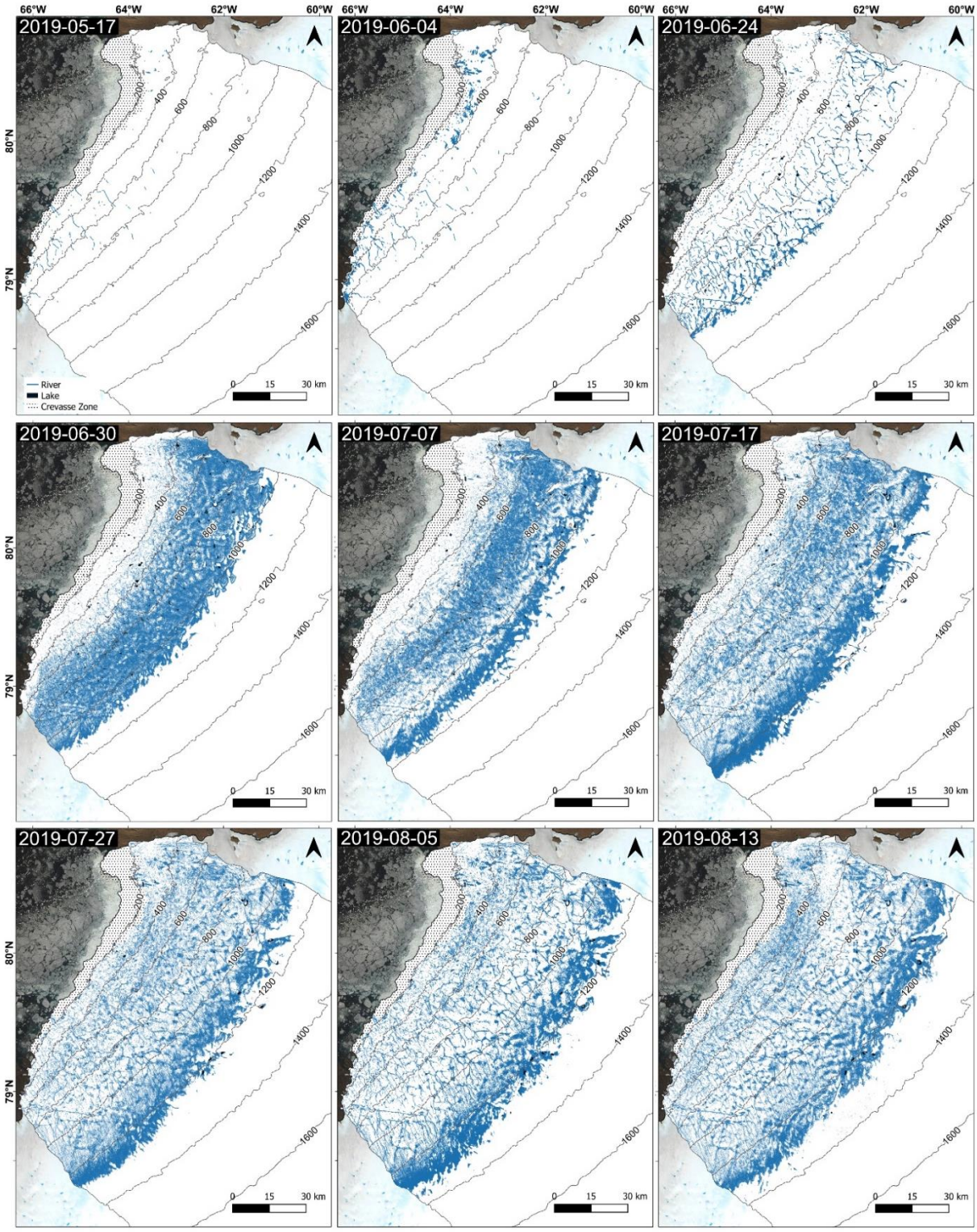
66°W
64°W
62°W
60°W
80°N
79°N
2019-05-17
2019-06-04
2019-06-24
2019-06-30
2019-07-07
2019-07-17
2019-07-27
2019-08-05
2019-08-13
River
Lake
Crevasse Zone
0 15 30 km

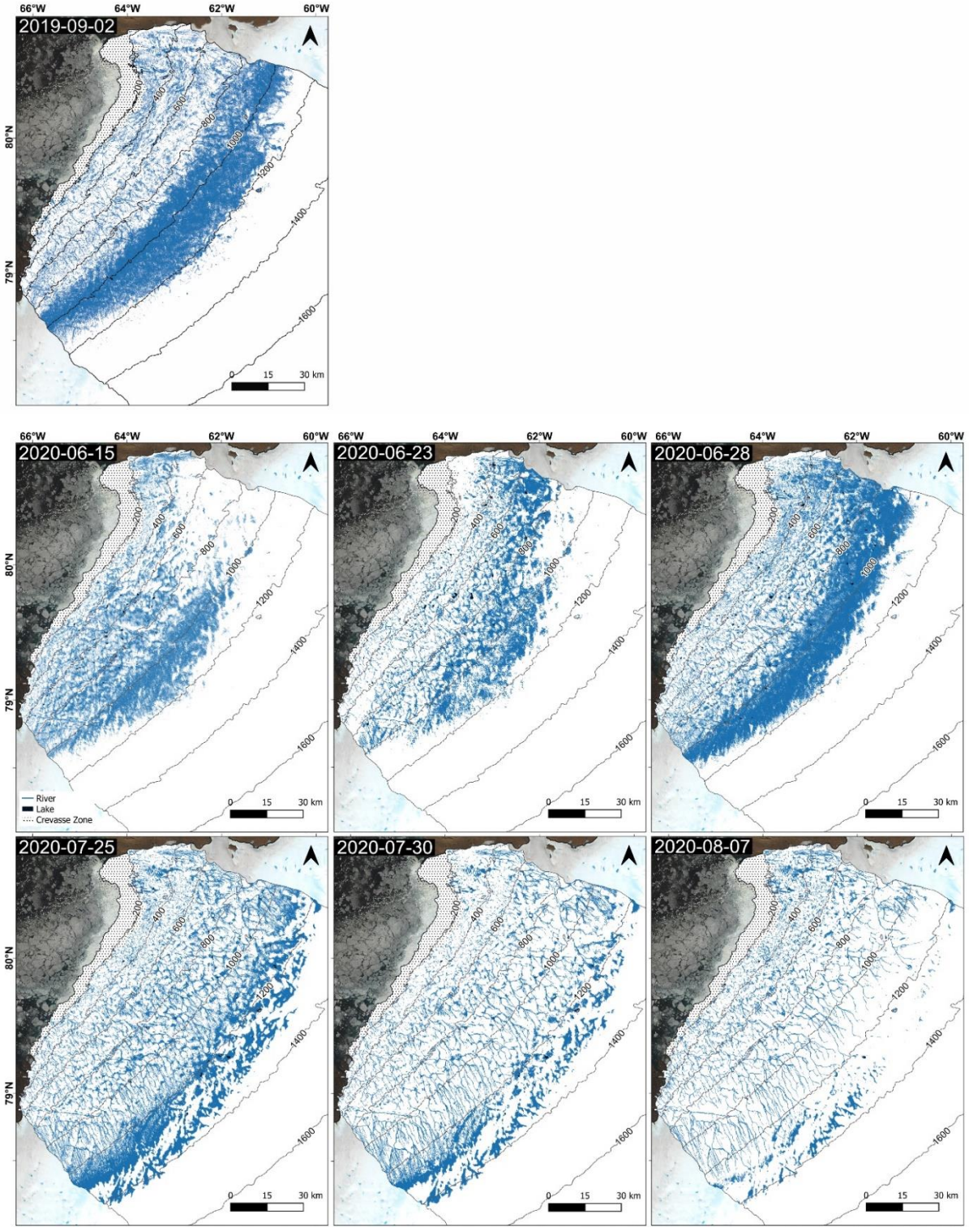
66°W
64°W
62°W
60°W
80°N
79°N
2019-09-02
2020-06-15
2020-06-23
2020-06-28
2020-07-25
2020-07-30
2020-08-07
River
Lake
Crevasse Zone
0
15
30 km

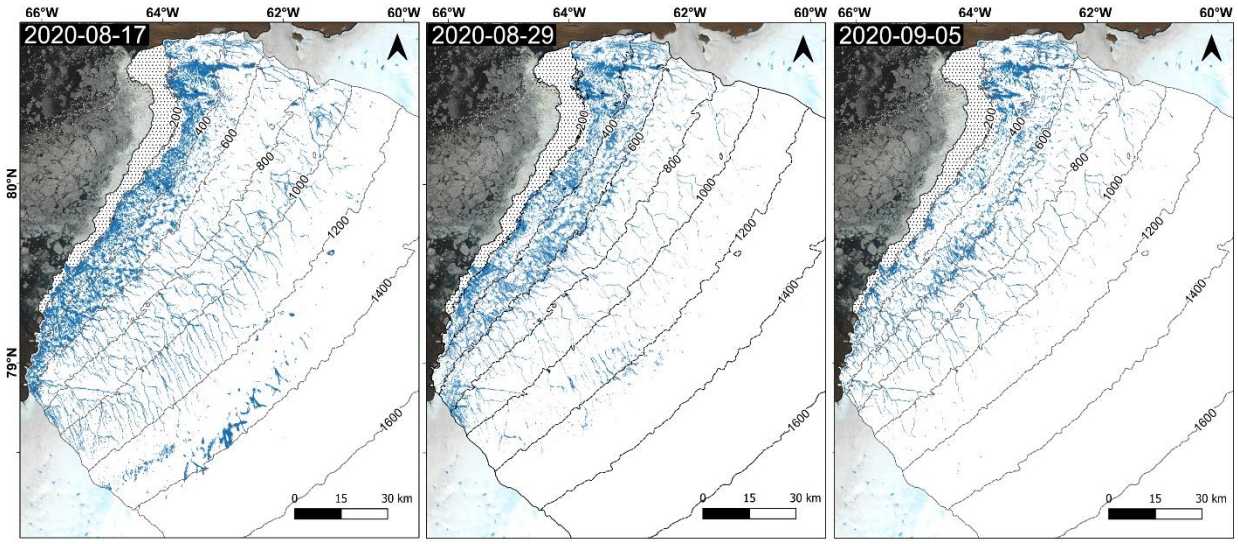

Figure A2. Supraglacial drainage network maps for all mapped study dates between 2016-2020. Blue lines represent delineated supraglacial rivers, black polygons represent SGLs (>0.1 km2) and the crevasse zone within the lower 25 km of the glacier is denoted by black and white dots. Elevation contours extracted from the 10 m ArcticDEM mosaic are presented for every 200 m a.s.l up to 1600 m a.s.l. The background Sentinel-2 image is courtesy of the Copernicus Open Access Hub (https://scihub.copernicus.eu).

The Cryosphere, 17, 4729–4750, 2023
https://doi.org/10.5194/tc-17-4729-2023
© Author(s) 2023. This work is distributed under
the Creative Commons Attribution 4.0 License.

The Cryosphere Open Access EGU

Seasonal evolution of the supraglacial drainage network at Humboldt Glacier, northern Greenland, between 2016 and 2020

Lauren D. Rawlins[1], David M. Rippin[1], Andrew J. Sole[2], Stephen J. Livingstone[2], and Kang Yang[3]

[1]Department of Environment and Geography, University of York, York, YO10 5NG, UK
[2]Department of Geography, University of Sheffield, Sheffield, S3 7ND, UK
[3]School of Geography and Ocean Science, Nanjing University, Nanjing, People's Republic of China

Correspondence: Lauren D. Rawlins (lauren.rawlins@york.ac.uk)

Received: 10 February 2023 – Discussion started: 22 February 2023
Revised: 9 September 2023 – Accepted: 12 September 2023 – Published: 9 November 2023

Abstract. Supraglacial rivers and lakes are important for the routing and storage of surface meltwater during the summer melt season across the Greenland Ice Sheet (GrIS) but remain poorly mapped and quantified across the northern part of the ice sheet, which is rapidly losing mass. Here we produce, for the first time, a high-resolution record of the supraglacial drainage network (including both rivers and lakes) and its seasonal behaviour at Humboldt Glacier, a wide-outlet glacier draining a large melt-prone hydrologic catchment (13 488 km^2), spanning the period 2016 to 2020 using 10 m spatial resolution Sentinel-2 imagery. Our results reveal a perennially extensive yet interannually variable supraglacial network extending from an elevation of 200 m a.s.l. to a maximum of ∼1440 m a.s.l. recorded in 2020, with limited development of the network observed in the low-melt years of 2017 and 2018. The supraglacial drainage network is shown to cover an area ranging between 966 km^2 (2018) and 1566 km^2 (2019) at its maximum seasonal extent, with spatial coverage of up to 2685 km^2 recorded during the early phases of the melt season when a slush zone is most prominent. Up-glacier expansion and the development of an efficient supraglacial drainage network as surface runoff increases and the snowline retreats is clearly visible. Preconditioning of the ice surface following a high-melt year is also observed, with an extreme and long-lasting 2019 melt season and over-winter persistence of liquid lakes, followed by low snow accumulation the following spring, culminating in earlier widespread exposure of the supraglacial drainage network in 2020 compared to other years. This preconditioning is predicted to become more common with persistent warmer years into the future. Overall, this study provides evidence of a persistent, yet dynamic, supraglacial drainage network at this prominent northern GrIS outlet glacier and advances our understanding of such hydrologic processes, particularly under ongoing climatic warming and enhanced runoff.

1 Introduction

The Greenland Ice Sheet (GrIS) has experienced significant mass loss throughout the 21st century and currently represents the largest single cryospheric component of global sea level rise, contributing an estimated 10.6 ± 0.9 mm since 1992 (The IMBIE Team, 2020). Over the last 2 decades, GrIS mass loss has become increasingly dominated by surface mass balance (SMB) processes, accounting for 60 % of ice loss annually since 1991, with the remainder attributed to dynamical mass losses from marine-terminating glaciers along the ice sheet periphery (van den Broeke et al., 2016). Such SMB losses are being increasingly revealed by the magnitude and spatial extent of seasonal surface melting and runoff (Trusel et al., 2018), attributed to climate-driven atmospheric warming (Hanna et al., 2012, 2021), summertime atmospheric circulatory behaviour (i.e. Greenland Blocking Index; Hanna et al., 2012, 2021; McLeod et al., 2016; van den Broeke, 2017), and the ongoing expansion (Noël et al., 2019) and darkening (Tedesco et al., 2016; Ryan et al., 2018, 2019; Riihelä et al., 2019) of the bare ice zone. Between 2011 and 2020, runoff was 21 % higher than any of the preceding 3 decades (Slater et al., 2021).

Published by Copernicus Publications on behalf of the European Geosciences Union.

Surface runoff is transported by an expansive and complex supraglacial drainage system that is activated during the summer season (Pitcher and Smith, 2019). This drainage system, made up of an ephemeral network of interconnected supraglacial rivers and lakes, transports and stores large volumes of surface meltwater on the ablating ice surface (Rippin and Rawlins, 2021). Such runoff can become intercepted by crevasses and moulins that provide connections to the ice sheet bed where the timing and delivery of such water has been shown to affect ice velocity (Zwally et al., 2002; Bartholomew et al., 2010, 2012; Hoffman et al., 2011; Sole et al., 2011; Andrews et al., 2014; Nienow et al., 2017). In particular, meltwater delivery into an inefficient subglacial configuration, such as linked cavities (Kamb, 1987), which typically occurs during the early period of the melt season, can temporarily overwhelm the subglacial hydrologic system, increasing water pressure and enhancing subsequent sliding (Andrews et al., 2014; Davison et al., 2019). In some regions where moulins and crevasses are absent, supraglacial rivers can extend undisturbed for tens of kilometres across the bare ice surface, flowing directly into the proglacial zone (Yang et al., 2019a; Li et al., 2022). Ultimately, much of this meltwater will end up in the ocean, contributing directly to global sea level rise (Pitcher and Smith, 2019).

Whilst many remote sensing studies have examined components of the supraglacial drainage network in-depth across the largest melt producing western and southwestern sectors of the GrIS (Smith et al., 2015; Gleason et al., 2016, 2021; Yang et al., 2021), it is only recently that other significant ice sheet sectors have begun to be mapped (Gledhill and Williamson, 2018; Macdonald et al., 2018; Yang et al., 2019a; Schröder et al., 2020; Turton et al., 2021; Lu et al., 2021; Boghosian et al., 2023). Focus has only recently shifted to the rapidly changing northern regions of the GrIS, with evidence of inland expansion of supraglacial lakes observed in northeastern Greenland (Turton et al., 2021) that aligns with climate model projections (Leeson et al., 2015) and the existence of a widespread supraglacial network (Lu et al., 2021). This study utilises Sentinel-2 satellite imagery to map the supraglacial drainage network, including both rivers and lakes, on a major northern outlet glacier of the GrIS – Humboldt Glacier (79°23.86° N, 64°20.60° W), here denoted as HG – to examine its seasonal behaviour at high spatial (10 m) and temporal resolution over 5 consecutive melt years (2016–2020).

2 Study location

The drainage basins of outlet glaciers in the northern sector of the GrIS comprise ∼ 14 % of the total ice sheet area, with 82 % of the northern sector predominately drained by 12 marine-terminating glaciers which together hold a sea level equivalent of 93 cm (Mouginot et al., 2019). Since 1990, this sector has experienced some of the most pronounced changes in surface melt and runoff, attributed to the rapid expansion of the ablation (46 %) and bare ice (33 %) zone at rates twice as fast as in southern Greenland, with this trend expected to continue with ongoing climatic warming (Noël et al., 2019). Of the northern outlet glaciers that drain the GrIS, HG, also known as Sermersuaq Glacier, is the widest marine-terminating outlet glacier (∼ 91 km wide) in Greenland and is responsible for draining ∼ 5 % of the ice sheet alone northwestward into the Kane Basin (Hill et al., 2017; Rignot and Kanagaratnam, 2006; Rignot et al., 2021; Fig. 1). Since the late 1990s, HG has experienced rapid rates of retreat (∼ 162 m yr^{-1}) attributed to increases in mean summer air temperatures and sea ice decline (Carr et al., 2015). Holding an ice volume equivalent of 19 cm of sea level rise, HG is the fourth-largest Greenland glacial contributor to sea level rise (Rignot et al., 2021), having lost 161 Gt since 1972 and 311 km^2 of its area between 2000 and 2010 (Box and Decker, 2011).

Until recently, few glaciological studies had focussed on HG (Joughin et al., 1996, 1999; Carr et al., 2015; Livingstone et al., 2017; Hill et al., 2017, 2018; Mouginot et al., 2019; Gray, 2021; Rignot et al., 2001, 2021, Hillebrand et al., 2022). Studies that have examined HG identified a distinctive ice velocity divide between the northern and southern sectors (Rignot et al., 2001, 2021; Carr et al., 2015; Fig. 1d); the northern sector has up to 4 times faster ice flow than the south. In terms of surface hydrology, several studies have noted the presence of supraglacial lakes (SGLs; Joughin et al., 1996; Selmes et al., 2011; Carr et al., 2015); however, none to-date have examined the overall drainage system, including both rivers and lakes, in detail.

3 Data and methodology

3.1 Data sources

Earth-observing satellites enable the study of supraglacial drainage features with broad spatial and temporal coverages (Rennermalm et al., 2013; Yang and Smith, 2012; Chu, 2014). Over the last 4 decades, the Landsat Program has provided a wealth of remotely sensed data for the mapping and quantification of a number of supraglacial features such as SGLs (Lampkin and VanderBerg, 2011; Banwell et al., 2014; Pope et al., 2016; Williamson et al., 2017; Gledhill and Williamson, 2018; Williamson et al., 2018; Yang et al., 2019b; Dell et al., 2022; Otto et al., 2022), as well as for exploring the generalised configuration (i.e. main river stems) of the supraglacial drainage system (Lampkin and VanderBerg, 2014; Yang et al., 2021). However, its spatial resolution in the visible spectrum (30 m) precludes the reliable delineation of numerous smaller supraglacial rivers (Yang et al., 2019a). This has resulted in these complex networks being unmapped and underrepresented (Chu, 2014). The application of the Multispectral Instrument (MSI) on Sentinel-

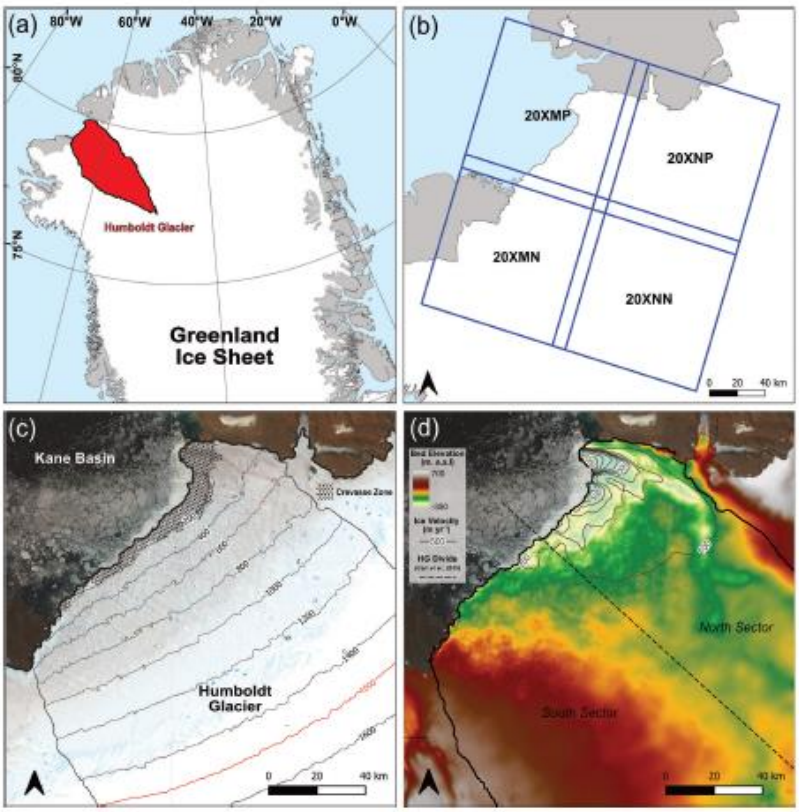

Figure 1. **(a)** Study location of HG, northern Greenland, and its highlighted drainage basin (shaded red). The dashed box shows the inset for other figure boxes **(b–d)**. **(b)** The four Sentinel-2 tiles used for extraction of the supraglacial drainage network across the study region. **(c)** True colour (R: band 4; G: band 3; B: band 2) Sentinel-2 image of HG acquired from 25 July 2020 courtesy of the Copernicus Open Access Hub (https://scihub.copernicus.eu, last access: 15 December 2022). HG denoted drainage basin and 200 m contour lines derived from ArcticDEM (10 m) are shown. The 1500 m a.s.l. contour denotes the maximum melt extent. The shaded section up to 200 m a.s.l. also shows the heavily crevassed zone that exists within the northern sector of the terminus. **(d)** Bed topography of HG and the surrounding area from BedMachine version 4 (Morlighem et al., 2021), ice velocity contours via NASAs MEaSUREs ITS_LIVE project (Gardner et al., 2019), and the division of Humboldt's north and south sectors (dashed line) as per Carr et al. (2015).

2 satellites (Sentinel-2A and -2B), which launched in 2015 and 2017, respectively, offers a higher-resolution (10 m) perspective of such systems (Yang et al., 2019a; Lu et al., 2020, 2021). Sentinel-2 imagery enables the detection and delineation of both wide, main-stem river channels, which have high stream orders and are perennially reoccupied (Pitcher and Smith, 2019), as well as narrower (one pixel, or 10 m) tributary-style channels that are of lower order and shallower in depth (Smith et al., 2015; Fig. 2). Sentinel-2 imagery has also been shown to better resolve supraglacial networks in general for mapping purposes at a glacier-wide scale, particularly in terms of river continuity (Yang et al., 2019a), which contributes to its preferred use in this study.

For the years 2016 to 2020, a total of 176 Sentinel-2 Level-1C (orthorectified top-of-atmosphere reflectance) images with sub-pixel multispectral registration (Baillarin et al., 2012) were acquired over HG (Fig. 1b; Table S1 in the Supplement) obtained from ESA's Scientific Data Hub (https://scihub.copernicus.eu/dhus/#/home, last access: 15 December 2022). These images covered the entirety of the study area on 44 d between the months of May and September across the study period, equating to 1–2 images per month, allowing us to gain a full melt season perspective of supraglacial drainage evolution for the HG drainage catchment. For scenes with cloud cover below a 20 % threshold, cloud coverage was typically restricted to the Kane Basin wa-

v

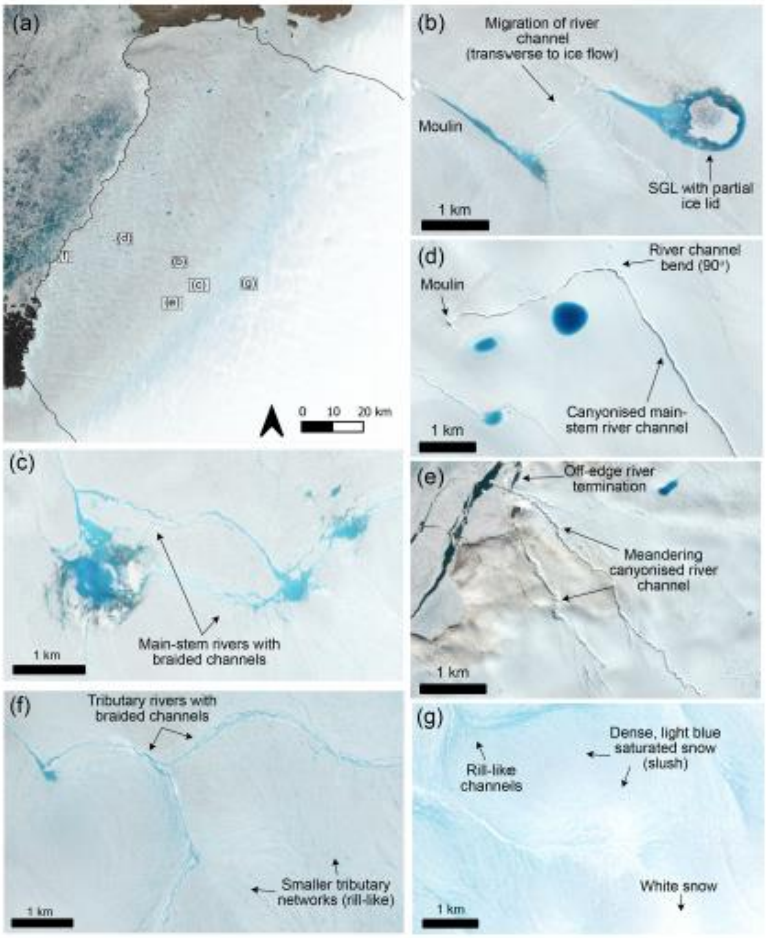

Figure 2. Example of the supraglacial drainage features found across the study region of HG, represented in panel **(a)**, from a Sentinel-2 image taken on 23 June 2020 (RGB). **(b)** A supraglacial lake with a central ice lid feeding an outlet supraglacial river, with evidence of river advection transverse to ice flow. **(c)** Braided supraglacial rivers flowing between supraglacial lakes, known as "connector" lakes. **(d)** A large canyonised supraglacial river with a 90° bend terminating abruptly in a moulin. **(e)** Deep, canyonised supraglacial rivers flowing off the ice edge. **(f)** Narrow supraglacial rivers with rill features seen in the higher-elevation regions of HG, flowing and coalescing into braided tributary rivers. **(g)** The slush zone, with dense areas of saturated snow (light blue) culminating in rill-like channels. The Sentinel-2 image is courtesy of the Copernicus Open Access Hub (https://scihub.copernicus.eu).

terway (Fig. 1c) or ice interior locations beyond the melt extent, and thus they did not pose any significant problems for river and lake mapping.

The HG drainage catchment was generated using the ArcticDEM 10 m mosaic product obtained from the Polar Geospatial Centre (https://www.pgc.umn.edu/data/arcticdem/, last access: 15 December 2022) and delineated following the method of Karlstrom and Yang (2016). Elevation contours at 100 m intervals were defined across the HG basin up to 1500 m a.s.l. (maximum limit of the melt-prone zone), equating to a size of 13 488 km^2. Daily surface meltwater production and runoff for the study area were extracted from the Modèle Atmosphérique Régional (MAR) regional climate model (RCM) v3.11 (available at ftp://ftp.climato.be/, last access: 15 December 2022; Fettweis et al., 2017, 2020, 2021). MAR is among the best RCM to cover the GrIS as it explicitly models important polar processes (i.e. SMB) forced with ERA5 reanalysis data and has been extensively evaluated against in situ automatic weather station and satellite data (for a detailed description of MAR v3.11, see

Amory et al., 2021; Fettweis et al., 2020, 2021). MAR has now been widely used in other GrIS-based supraglacial hydrologic studies (Smith et al., 2017; Yang et al., 2019b; Lu et al., 2020) for quantifying the relationship between modelled runoff and satellite-derived meltwater metrics for RCM accuracy validation. The version MAR 3.11 used in this study was run at high spatial (6 km) and temporal (daily) resolution to generate estimates of daily meltwater production and runoff (R) in millimetres of water equivalent per day (mm w.e. d^{-1}) within each grid cell to assess the spatial and temporal distribution of meltwater against mapped supraglacial rivers and lakes, similar to other studies (Yang et al., 2019b; Lu et al., 2020, 2021; Yang et al., 2021). MAR grid cells were also sampled at each 100 m interval to assess elevational gradients in both mapped drainage and runoff. A MAR uncertainty value of ±15 % was also calculated (Fettweis et al., 2020).

3.2 Supraglacial river and lake extraction

To effectively delineate supraglacial rivers from remotely sensed imagery, an automatic linear enhancement method developed by Yang et al. (2015) was used, which characterises supraglacial rivers according to their Gaussian-like brightness cross sections and longitudinal open-channel morphology. Firstly, a normalised difference water index was performed following McFeeters (1996) to differentiate active surface meltwater from the background ice and snow (Lu et al., 2020; Li et al., 2022). This equation (Eq. 1) utilises Band 3 ("Green") and Band 8 ("NIR") from Sentinel-2 imagery as follows:

$$\mathrm{NDWI} = \frac{(\mathrm{Green} - \mathrm{NIR})}{(\mathrm{Green} + \mathrm{NIR})}. \quad (1)$$

An ice-derived spectral index, $\mathrm{NDWI}_{\mathrm{ice}}$, has been widely applied to supraglacial mapping studies in recent years (Yang and Smith, 2012; Moussavi et al., 2016; Williamson et al., 2018; Yang et al., 2021), as it produces fewer false classifications of blue ice and slush areas. We use NDWI (McFeeters, 1996) here because of its successful implementation in other studies (Stokes et al., 2019; Lu et al., 2020, 2021; Corr et al., 2022) and its ability to map all active surface melt of interest, including slush zones. Additionally, preliminary testing of a small sample area found using NDWI (McFeeters, 1996) was able to map 16.3 % more regularly connected supraglacial river channels compared to those mapped by the alternate $\mathrm{NDWI}_{\mathrm{ice}}$ (Supplement Fig. S1). Next, an ice mask was applied, created from manually digitising the HG terminus from the latest, end-of-season image (late August–early September) in each of the study years to extract ice-only regions and remove surrounding land, rocky outcrops and the ocean of the Kane Basin. A separate crevasse mask was delineated from manually identifying the heavily crevassed zone known to extend up to 25 km from the northern sector of the terminus, with particular prevalence across the 7 km floating section (Carr et al., 2015). This mask was applied, and this section of the terminus removed to avoid the erroneous delineation of crevasses and crevasse shadows in this area during image processing and to reduce the effects of drainage overestimation in these ice marginal regions in further calculations (Ignéczi et al., 2018). A global NDWI threshold of 0.4 ($t_{0.4}$) was then applied to the masked NDWI image as it effectively captures SGL boundaries and wide, main-stem river segments (Lu et al., 2021). To aid in delineating narrower river segments and obtain a complete and continual supraglacial network, the automatic river detection algorithm for linear enhancement (Yang et al., 2015) was then applied. This involved the removal of the low-frequency image background and high-frequency image noise using a band-pass filter ramped between 1/200 and 1/40 m^{-1} (Yang et al., 2019a), before the application of a Gabor filter to enhance the cross sections of smaller rivers (< 2 pixel width). This was followed by a parsimonious path opening (PPO) operator, which is a flexible mathematical morphological operator, to stabilise linear brightness across river lengths and preserve connectivity, with a minimum path length of 20 pixels.

After Gabor–PPO filtering, the supraglacial river network becomes easier to differentiate and delineate from the surrounding icy background. A global pixel brightness threshold of 5 (out of 255) denoted t^5 was used to extract supraglacial rivers of varying widths from Gabor–PPO opened filtered images (Lu et al., 2020), i.e. from tributary-style rivers to main-stem, large river channels. Hydrologically connected slush zones, which is where the pore space of snow becomes entirely water saturated when temperatures permit melting (above freezing, 0 °C) and forms expansive fields of ponded surface water, were retained as they play an important role in the initial mobilisation of melt as slush flows or within rill-type channels and the inland expansion of the melt-prone zone as summer progresses (Holmes, 1955; Marston, 1983; Cuffey and Paterson, 2010; Chu, 2014; Rippin and Rawlins, 2021). Slush zones can be spectrally distinguished in true-colour satellite images as dense, light blue patches on the surface as snow becomes water saturated (Fig. 2g), and they can be partially distinguished in NDWI images as bright, dense features similar to that of individual linear river channels (Lu et al., 2021). For mapping conducted in this study, slush zones are mapped inclusively within the drainage network and not treated independently due to their overall hydrologic importance and spectral similarity to other hydrological components. Whilst dynamic thresholding techniques have been used in other studies, particularly in the identification and mapping of supraglacial lakes across independent dates and/or years (Selmes et al., 2011; Williamson et al., 2017), applying these two separate thresholds ($t_{0.4}$ and t^5) to all images across this study period is reasonable for exploring the seasonal behaviour over the available dates used. Finally, these masks were vectorised into separate river channel polylines and lake polygons for analysis, with a size threshold of 0.1 km^2 applied to SGLs. To assess the ability of the automated mapping technique to capture supraglacial rivers at

HG, a small area was manually digitised (Fig. 3). The overall spatial pattern extracted was similar, and the difference between manual vs. automated river area was 5.4 %, with automated rivers tending to have several gaps in the network compared to manual results. A similar finding was also produced by Lu et al. (2020), who found a difference of 13.6 % between manual vs. automated supraglacial rivers also using Sentinel-2 imagery.

3.3 Supraglacial river and lake quantification

To characterise the extracted supraglacial drainage system, metrics were calculated for both rivers and lakes. These metrics are summarised in Table S2 and include meltwater area (km^2), meltwater area fraction (MF, %), drainage density (D_d), the number of supraglacial lakes (L_n) and supraglacial lake area (L_a). MF is defined as the percentage total meltwater area across the drainage catchment below a conservative upper melt limit of 1500 m a.s.l. for each date mapped, which is then also further divided into separate feature ratios including river area fraction (RF) and lake area fraction (LF). MF was also calculated across 100 m elevation contours from above the heavily crevassed zone at 200 m a.s.l., to the maximum melt extent at 1500 m a.s.l. To explore the relationship between remotely mapped drainage and modelled RCM MAR runoff (R), a Spearman's rank correlation (r_s) was performed and linear regression analysis undertaken with subsequent R^2, r_s and P values reported.

4 Results

4.1 Spatial characteristics of the supraglacial drainage network

Supraglacial rivers and lakes were mapped from a total of 44 dates across the lower, melt-prone 13 488 km^2 HG drainage basin from the melt seasons of 2016 to 2020. The mapped supraglacial drainage network across HG is shown extend up to 1440 m a.s.l., with well-developed, main-stem river channels occurring up to 1000 m a.s.l., which we characterise as the persistent zone, and an ephemeral network of tributary-style rivers and slush zones extending beyond 1000 m a.s.l. in a transient zone up to maximum extent (Fig. 4a). Active supraglacial rivers and lakes form progressively upglacier from low elevations (200 m a.s.l.) to a maximum of 1440 m a.s.l. as the melt seasons progress across the study period, with interannual variability observed.

Within the lower-elevation regions (< 400 m a.s.l.) of HG, collectively the supraglacial drainage network is largely fragmented, with many short (< 750 m long), supraglacial rivers observed alongside small SGLs with an average size of 0.23 km^2, which is the smallest observed across all elevation bands. At greater elevations, beyond 400 m a.s.l., we observe large, main-stem supraglacial rivers, some with incised-canyon features (Fig. 2b), interconnected with increasingly larger SGLs. At elevations > 1000 m a.s.l., average SGL size is 0.41 km^2, with a maximum SGL size of 2.08 km^2. SGLs and rivers parallel to ice flow tend to be highly persistent year-on-year across the study period. In Fig. 4b, we also see some evidence of a potential main-river reconfigurations, with the northwestward advection of a river channel that runs transverse to ice flow. In the upper parts of the catchment, the supraglacial drainage network becomes increasingly dense, especially between 800–1000 m a.s.l., where we see a 120 % increase in average meltwater area (94.5 km^2) compared to 200–400 m a.s.l. (42.9 km^2), a 79 % increase compared to 400–600 m a.s.l. (54.2 km^2) and a 10 % increase compared to 600–800 m a.s.l. Not only are persistent main-stem rivers still present up to 1000 m a.s.l., but an extensively connected tributary river system is also observed within this persistent zone.

The drainage network up to 1000 m a.s.l., in particular within the central and northern reaches of HG, is dendritic in nature (Fig. 4c). This type of drainage, however, is not uniform across HG, with the supraglacial network to the south exhibiting a more sub-parallel drainage style (Fig. 4e), with this configuration extending beyond the persistent zone and into the more transient zone with slush zone development and inland evolution a key part of the temporal aspect of the network at higher elevations (Fig. 4a). Even though density remains high until 1300 m a.s.l., vastly transient tributary rivers and slush zones dominate, feeding meltwater from headwater regions downstream. In terms of SGLs, the maximum recorded elevation was 1346 m a.s.l. both in 2019 and 2020. Fewer SGLs are observed in the transient zone, accounting for 16 % of total SGL area across the study period. However, average SGL area increases with elevation, with lakes in this zone being 54 % larger (0.4 km^2) on average than those found below 1000 m a.s.l. (0.26 km^2). The single largest SGL size of 2.08 km^2 was recorded in 2016 at 1150 m a.s.l.

A key feature that is particularly prominent in the supraglacial drainage network is the presence of two parallel lines that track across glacier from the southwest to the northeast (Fig. 4a). Many supraglacial rivers and lakes are aligned along these two features, which appear as depressions in the ice surface, with the abrupt termination of many rivers indicating meltwater capture via moulins, indicating a strong structural element influencing drainage configuration.

4.2 Temporal evolution of the supraglacial drainage network

Typically, the supraglacial drainage network becomes active in early June with the onset of melt production and runoff in the region, with only a small number of large-stem supraglacial rivers becoming active and subsequently recorded (MF < 3.2 %) during this time within the mapped elevation bands of 200–950 m a.s.l. By late June a widespread (500 to 1150 m a.s.l.) slush zone develops and advances upglacier as the melt season progresses runoff in-

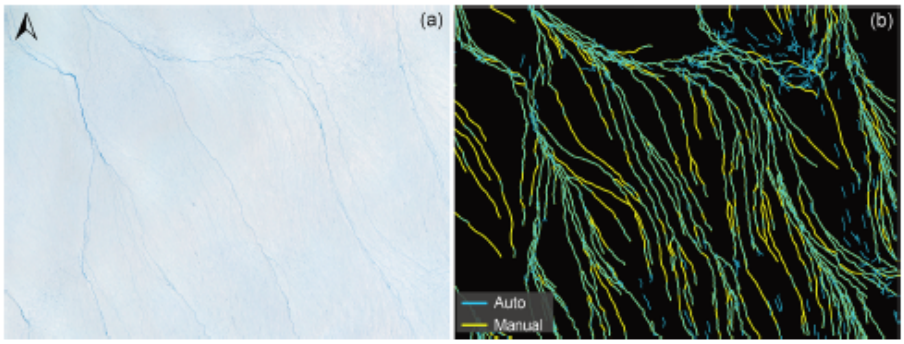

Figure 3. **(a)** RGB image of a sample area of HG with both main-stem and tributary supraglacial river channels present. **(b)** A performance accuracy assessment comparing the automatic river detection algorithm (blue) used in this study with manually digitised networks (yellow). Overall, automated rivers networks were 5.4 % shorter than those manually derived. The Sentinel-2 image in **(a)** is courtesy of the Copernicus Open Access Hub (https://scihub.copernicus.eu).

creases, with MF ranging between 11.4 % and 19.9 %. As bare ice is exposed below this slush zone, the drainage system becomes increasingly channelised (Fig. 5). The formation of the slush zone at the end of June typically coincides with maximum melt storage in SGLs (both numbers and size of lakes). The network with the largest expanse of slush zone and number of SGLs in this study was observed on 30 June 2019 (Fig. 5), with 2685 km^2 (19.9 %) of the HG ice surface comprised of a hydrologically connected, unchannelised system and 111 SGLs recorded (total area 27.4 km^2). As the season progresses, the slush zone shifts upglacier while reducing in size, with average June MF decreasing by up to 33 % before stagnating at a maximum inland extent, ranging between 1050 m a.s.l. (2018) and 1440 m a.s.l. (2020) across the study period. At this elevation, the slush zone operates thereafter as headwaters, feeding the complex, transient, tributary systems below and further supplying the larger, well-defined supraglacial rivers at lower elevations (< 1000 m a.s.l.).

Towards the end of the melt season, despite melt and runoff cessation, the supraglacial drainage network remains (Fig. 5).

The interannual variability in seasonal behaviour of the supraglacial drainage network between 2016 and 2020 (Fig. 5) corresponds to the length and intensity of the melt season. Drainage within the melt seasons of 2016, 2019 and 2020 follow a similar pattern characterised by a rapid increase and peak in MF in late June, yielding values of 11.4 % ($R = 7.1\,mm\,d^{-1}$), 19.9 % ($R = 19.4\,mm\,d^{-1}$) and 12.1 % ($R = 19.6\,mm\,d^{-1}$), respectively (Fig. 6), concurrent with early season melt production and runoff. These high MF values are largely associated with widespread slush zone initiation, with a subsequent peak in MF increasing the drainage network area by 267 % in 2016 (28 June) and 322 % in 2019 (30 June), with its spatial extent observed below 1000 m a.s.l. at this time (Fig. S3). The beginning of the melt season in 2020 is an exception, with an anomalously high MF (11.6 %) recorded on 15 June reaching 1100 m a.s.l., as well as a high number (57) and cumulative area of SGLs (11.2 km^2; Fig. 6). This high is followed by a 66 % reduction in MF by 23 June, after which the network behaviour is similar to that of other seasons, with a subsequent MF increase of 211 % to its peak at the end of June (28 June; Fig. 6). Despite high rates of melt production and runoff throughout July across these three melt seasons, MF plateaus and reduces, reaching a steady state of between 7.6 % and 13.9 %. The number of SGLs also reduces on average between 20 % and 27 % throughout July, with cumulative SGL area reducing between 9 % and 38 %.

By the end of July, the supraglacial drainage network consistently extends to 75–80 km inland (1440 m a.s.l.) at its maximum areal extent. As melt and runoff reaches declines into August, the drainage network reduces between 53 % (2016) and 9 % (2020). In 2019, persistent high rates of melt production and runoff result in persistence of the drainage networks maximum inland extent and even a late-season increase of 54 % in MF from the 5 August to 13 August. The year 2019 is registered as an exceptional year at HG, with an average meltwater area up to 75 % greater in June compared to 2016, between 25 % and 92 % greater in July compared to 2016 and 2020, and up to 3 times greater (300 %) in August compared to both 2016 and 2020. Additionally, 129 % and 86 % more lakes are recorded compared to 2016 and 2020, respectively, with SGLs persisting much later into the melt season (mid-August) than the other years.

The supraglacial drainage network in 2017 and 2018 behaves quite differently to the other melt years (Fig. S4). Until late July, MF remains low (< 7 %; Fig. 6) with runoff predominately occurring within the lower 700 m of the HG basin (Fig. S3). The number and area of SGLs is also low during this period, with an average of 15 lakes observed in June and July across 2017 and 2018 with a cumulative average area of 21.5 and 31.1 km^2, respectively; 280 % lower

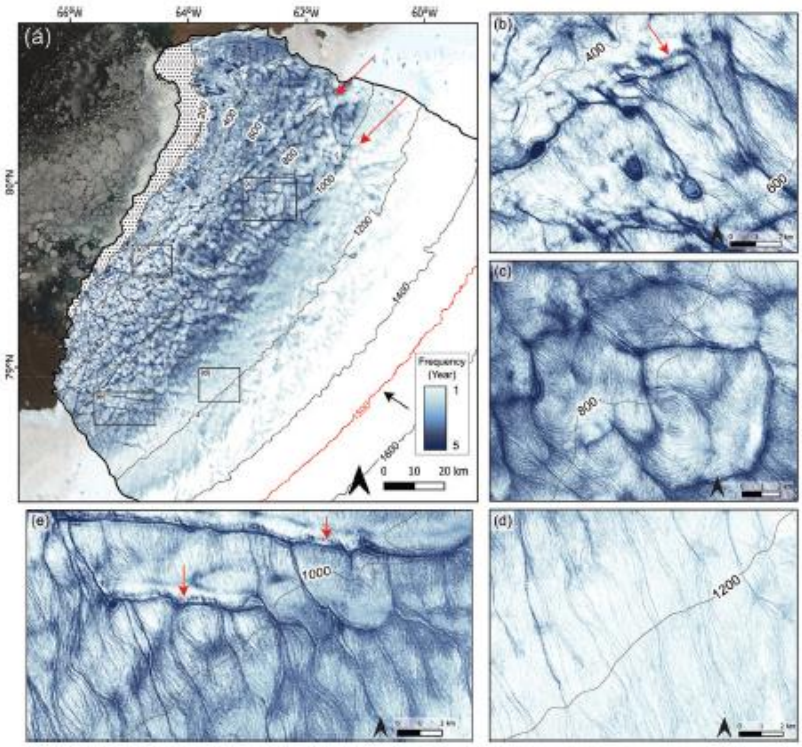

Figure 4. **(a)** Map showing the recurrence frequency of the supraglacial drainage network across the study period (2016 to 2020) at HG. Dark blue shades denote a higher frequency of occurrence, which is highly prominent in the persistent zone below 1000 m a.s.l., with rivers and lakes typically reforming in the same location each year. Red arrows denote the location and direction of two distinct parallel drainage structures. The black arrow represents ice flow direction. The background Sentinel-2 image is provided courtesy of the Copernicus Open Access Hub (https://scihub.copernicus.eu). **(b)** Close-up panel showing highly persistent rivers in the persistent zone with a prominent 90° angle in their channel form. The red arrow denotes some channel reconfiguration due to ice advection. **(c)** Close-up panel showing the dendritic supraglacial drainage structure typical in the northern sector of HG. **(d)** Close-up panel of the transient zone (> 1000 m a.s.l.), where yearly river persistence is lower and characterised by lengthy tributary river channels. **(e)** Close-up panel showing the more parallel form of supraglacial drainage structure in the southern sector of HG, with red arrows denoting some channel advection with ice motion.

than average lake counts and 218 % lower than cumulative average area for the same monthly periods across 2016, 2019 and 2020. Unlike the other study years, peak MF does not occur until much later in the melt season, reaching 10.2 % on 22 August 2017 and 7.2 % on 20 August 2018 with a 690 km^2 (197 %) and 521 km^2 (135 %) increase in meltwater area to its prior mapped date, respectively; concurrent with peak runoff and the widespread occurrence of a late slush zone. Similarly, SGL numbers and area also peak on these dates, with 54 (15.8 km^2) and 74 (20 km^2) lakes recorded, comprising 32 % and 39 % of total lakes recorded per year, respectively. Examination of the maximum extent of the supraglacial drainage network is also revealed to be limited, with a maximum elevation of ~ 1150 m in 2017 and ~ 1050 m in 2018, equivalent to between 48 and 51 km inland.

When comparing what could be considered high-melt vs. low-melt year seasonal patterns, the supraglacial drainage network is twice as large during high-melt years (2016, 2019 and 2020) and is seen to form at elevations ~ 300 m higher than in low-melt years (2017, 2018; Figs. S2 and S3). In terms of the average number of SGLs, there is almost double the number of SGLs observed (92 %) in the high-melt years compared to low-melt years, with average SGL area also being 111 % higher, showing large year-on-year variability in this system.

The contribution of rivers and SGLs to the supraglacial drainage network follows the same general seasonal trend as MF. RF and LF (%) peak at the end of June in the high-

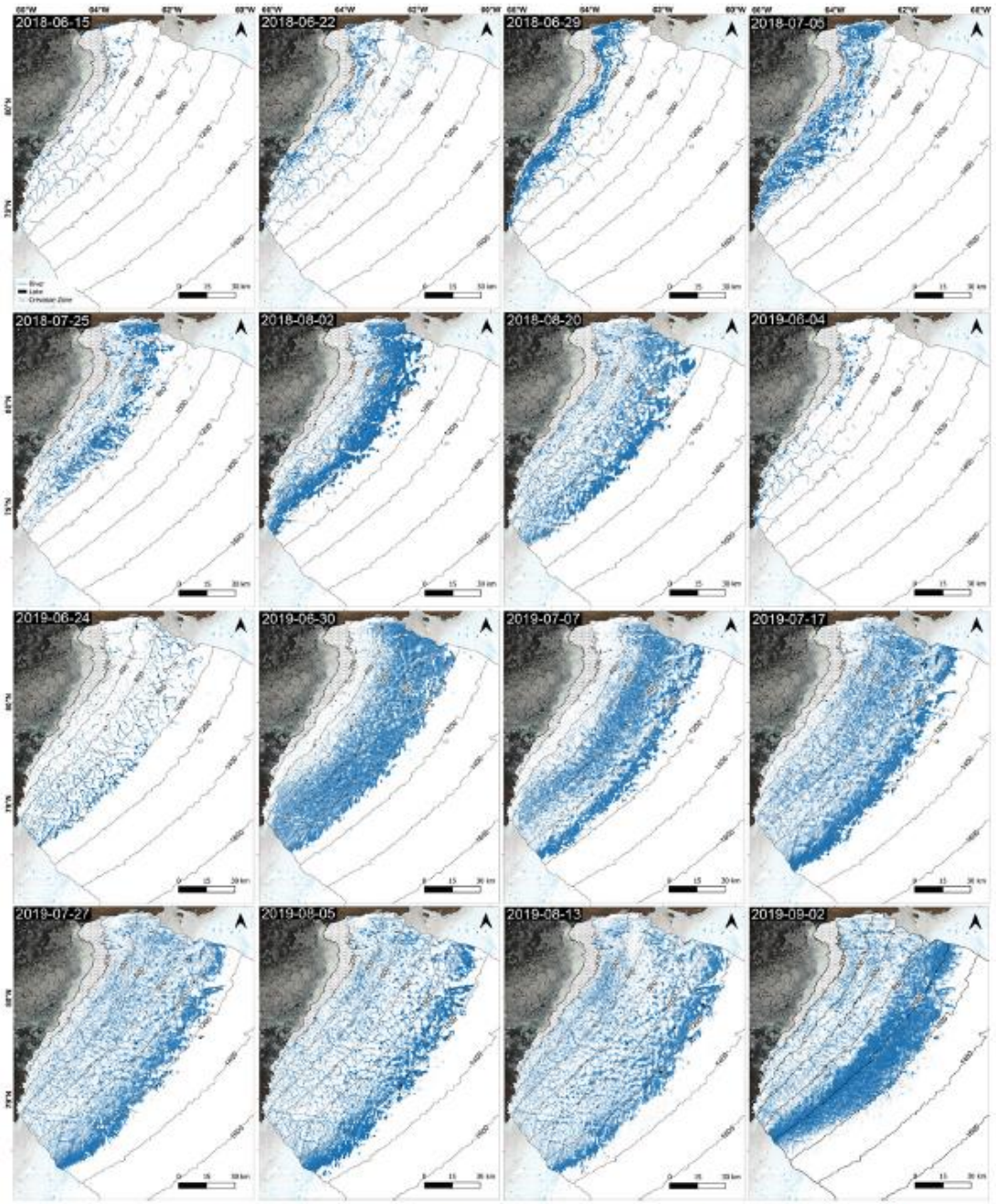

Figure 5. Satellite-derived mapping of the temporal evolution of the supraglacial drainage network, including rivers and lakes, across the HG drainage basin from 2 melt years during the study period, with 2018 showing the typical behaviour of a low-melt year and 2019 the behaviour during a high-melt year. The background image is a Sentinel-2 image courtesy of the Copernicus Open Access Hub (https://scihub.copernicus.eu). For all mapped study dates, please refer to Fig. S3.

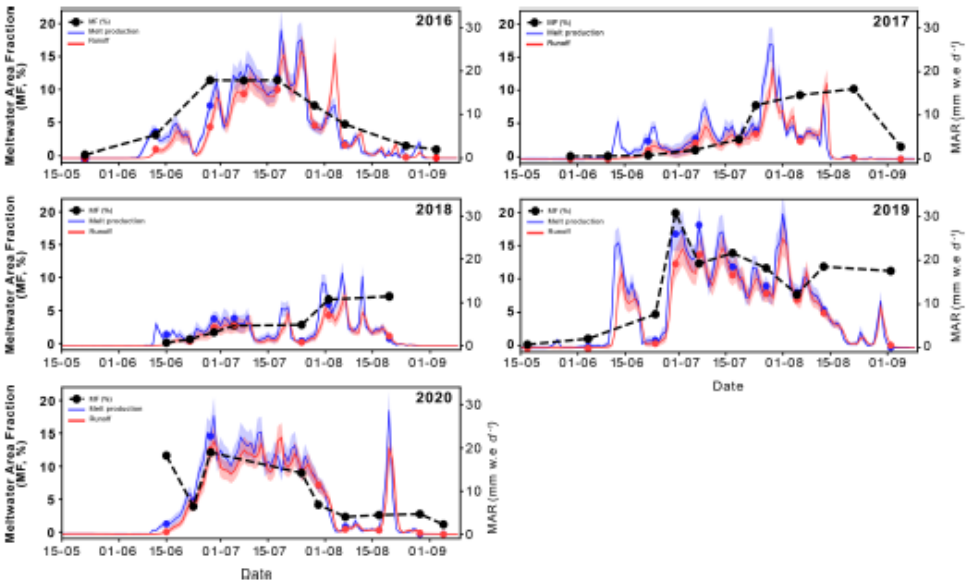

Figure 6. The satellite-derived water metric meltwater area fraction (MF, %) for each mapped date across the study period (2016–2020) alongside melt production and runoff values (mm w.e d^{-1}) derived from MAR v3.11 for the HG catchment. The ±15 % uncertainty envelopes are provided for MAR-derived values (Fettweis et al., 2020).

melt years of 2016, 2019 and 2020 and in mid-August for the low-melt years of 2017 and 2018 (Fig. 7), i.e. when hydrologically connected slush zones are most prominent and SGL numbers are shown to peak. Overall, the network is largely composed of supraglacial rivers, with RF accounting for an average of 6.2 % ± 5.6 % (mean ± SD) of the HG catchment across the study dates and is higher during high-melt years (7.8 % ± 6.0 %) compared to low-melt years (3.5 % ± 3.4 %). The highest RF recorded occurred on the 7 July 2019 and measured 24.5 %; the highest RF measured in a supraglacial hydrologic study. For SGLs, average LF was much lower, accounting for an average of 0.07 % ± 0.06 % of the melt-prone area of the catchment, with slightly higher LF in high-melt years (0.08 % ± 0.07 %) compared to low-melt years (0.05 % ± 0.04 %). In terms of the overall contribution of supraglacial rivers and SGLs to peak meltwater area fraction, 98 % of the network is dominated by supraglacial rivers across all study years, with SGLs playing a less dominant role in HG's drainage network. In comparison, rivers contribute ∼62 % to the drainage network in southwestern Greenland, with SGLs contributing ∼38 % (Yang et al., 2021).

4.3 Supraglacial hydrology and MAR runoff

A strong positive linear relationship was identified between satellite-derived MF and regional climate model MAR surface R for the HG catchment across the study period 2016 to 2020 (Fig. 8; $R^2 = 0.77$, $R_s = 0.91$, $p = < 0.001$) up until peak MF values and rapid surface runoff decline at the end of the melt season. Both MF and R increased concurrently each year as the melt season progressed, with peak runoff often coinciding with the existence of expansive slush fields across the upper part of the catchment. Runoff remained high until maximum extent occurred, particularly for high-melt years: 2016 (2 July, $R = 7.5\,\mathrm{mm\,d^{-1}}$), 2019 (13 August, $R = 8.2\,\mathrm{mm\,d^{-1}}$) and 2020 (30 July, $R = 11.4\,\mathrm{mm\,d^{-1}}$). For low-melt years, runoff remained relatively high until early August (6 August 2017, $R = 4.0\,\mathrm{mm\,d^{-1}}$; 2 August 2018, $R = 7.1\,\mathrm{mm\,d^{-1}}$), with maximum extent occurring within 2 weeks (the next mapped date). This relationship between MF and R shows the reliability of simulated variations in seasonal surface meltwater runoff in capturing the behaviour of the supraglacial drainage network via satellite-derived water metrics, particularly during high-melt years and until runoff declines each melt season.

5 Discussion

5.1 Spatial characteristics of the supraglacial drainage network

Our satellite-derived mapping reveals a complex supraglacial drainage network at HG that reaches a maximum elevation of 1440 m a.s.l., recorded in 2020. This maximum elevation

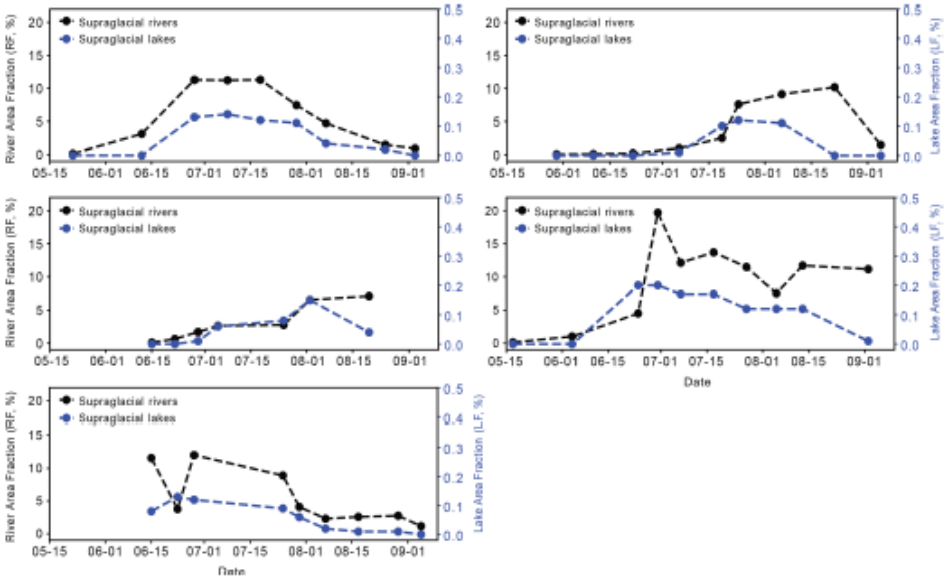

Figure 7. River area fraction (RF, %) and lake area fraction (LF, %) across the melt-prone zone of HG for each mapped date across the study period. On average, 98 % of the supraglacial drainage network across the study period at HG is comprised of RF.

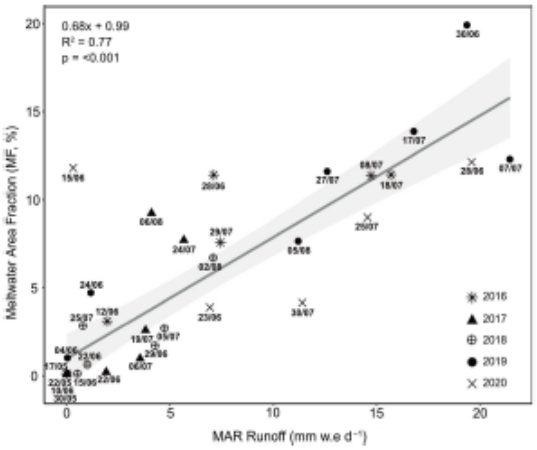

Figure 8. Linear relationship between the satellite-derived water metric meltwater area fraction (MF, %) and RCM-derived runoff from MAR v3.11 for each year studied up until runoff declines.

is 400 m lower than supraglacial drainage observations in southwestern Greenland (~ 1800 m a.s.l.; Yang et al., 2021), consistent with observations by Ryan et al. (2019), who found the maximum snowline elevation to be 400 m lower in northern Greenland than southwestern Greenland. Up to elevations of 1000 m a.s.l., the supraglacial drainage network is highly persistent across the study period, with a variable system beyond this elevation observed within the transient zone; defined in this study as a high-elevation region where drainage is transient in time but not necessarily space. The recurrence frequency of meltwater pixels in the supraglacial drainage network (Fig. 4) demonstrates the stability of SGLs in particular, which re-occupy the same location year-on-year despite ice advection (Smith et al., 2015; Pitcher and Smith, 2019). SGLs increase in size with elevation, with higher-elevation lakes persisting for longer (i.e. incapable of draining) and undergoing greater season expansion (Gledhill and Williamson, 2018; Yang et al., 2021). Larger lakes at higher elevations are the result of longer wavelength bed undulations being favourably transferred to the ice surface through thicker ice, creating large, shallow surface depressions (Ng et al., 2018). Unlike SGLs found < 400 m a.s.l., which are smaller and have likely reached their maximum available melt area, higher-elevation lakes are not yet topographically constrained (Krawczynski et al., 2009). This is similar to observations in southwestern Greenland where SGL size was larger and more variable > 1400 m a.s.l., with 21 % of these lakes draining via hydrofracture (Yang et al., 2021).

Whilst SGL location is known to be largely controlled by bed topography (Lampkin and VanderBerg, 2011; Ignéczi et al., 2018), this study also notes that many well-established rivers that are longitudinal to ice flow, including many with canyonised features, also reoccupy locations. Supraglacial rivers that are transverse to ice flow or have a transverse el-

ement to their channel, however, may be less stable in some areas by up ~ 300 m (Fig. 4a) over the study period, probably due to the impact of ice advection. In the transient zone, the recurrence frequency is reduced, with tributary rivers and slush zones dominating at higher elevations. Here, their persistence is highly reliant on there being enough melt at higher elevations to initiate and sustain channel formation, which in 2017 and 2018 was limited, and therefore drainage occurrence was much reduced in this zone. Also, tributary rivers are typically lower order, with narrower channels and shallower depths (Smith et al., 2015; Pitcher and Smith, 2019), meaning their form has the potential to migrate, close and reform quickly if melt is available. The transient zone is therefore not only influenced by melt availability over time but also the potential for migration in space. In agreement with previous studies (Joughin et al., 2013; Poinar et al., 2015), we also show that rivers tend to be longer at higher elevations (> 25 km long), consistent with observations in SW GrIS (> 40 km long), likely due to the basal transfer of only long-wavelength basal undulations to the surface due to thicker ice and the reduced presence of surface crevassing (Gudmundsson, 2003; Lampkin and VanderBerg, 2011; Crozier et al., 2018).

Drainage patterns are also shown to vary across HG, with a dendritic style of drainage observed in the northern sector and a parallel style of drainage observed in the southern sector. These differing patterns highlight not only variations across different hydrologic catchments of the GrIS but also intra-catchment variations, which may stem from local variations in surface topography via the transmission of basal topography (Raymond and Gudmundsson, 2005; Ng et al., 2018) controlled by bed roughness and structure, wavelength transfer, and differing ice flow regimes (Gudmundsson et al., 1998; Gudmundsson, 2003; Lampkin and VanderBerg, 2011; Crozier et al., 2018; Ignéczi et al., 2018). This has been shown to play an important role in mapped rivers and lake hydromorphology at both the 79° N Glacier (Lu et al., 2021) and across the Devon Ice Cap (Wyatt and Sharp, 2015).

In the northern sector of HG, we observed short supraglacial rivers and small SGLs at lower elevations (200–400 m a.s.l.) and a prominent dendritic-style drainage pattern of interconnected rivers and lakes up to 1000 m a.s.l., with some larger rivers abruptly terminating. Such characteristics suggest the interception of runoff by crevasses and moulins, with such capture directed to the englacial and subglacial system with the potential for pronounced impacts on localised flow rates (Catania et al., 2008; Schoof, 2010; Mejia et al., 2022). This drainage style is typical of that observed within the western and southwestern sectors of GrIS, whereby structurally controlled drainage of supraglacial rivers flowing between SGLs promote shorter river channels, while high rates of crevassing at lower elevations (< 1000 m a.s.l.) means virtually all surface meltwater is captured and diverted before reaching the ice edge. This more compact style of drainage is likely to create a "flashier" response in hydrographs, with a greater runoff peak and shorter rising limb (Smith et al., 2017). Additionally, as shown by Carr et al. (2015) and Rignot et al. (2021), this sector of HG sits within a 475 m deep basal trough that extends ~ 45 km wide and > 70 km inland and is characterised by fast rates of flow (200–600 m yr^{-1}). Faster basal sliding has the ability to promote the more efficient transfer of basal topography to the surface and can subsequently precondition the large-scale spatial structure of the surface drainage system, including drainage fragmentation due to higher rates of crevassing and moulin formation, which can further supply meltwater to this faster-flowing sector (Crozier et al., 2018; Ignéczi et al., 2018).

In comparison, the sub-parallel drainage structure of the supraglacial network in the southern sector differs greatly to that of the northern sector of HG and observed drainage in western and southwestern regions of the GrIS. Drainage largely consists of continuously flowing rivers that drain surface meltwater from the slush zone at ~ 1500 m a.s.l. to much lower elevations (200 m a.s.l.), with some rivers directly terminating off the ice sheet edge. This suggests limited opportunities for meltwater to penetrate to the ice sheet bed, with meltwater having longer transport times to travel to the catchment outlet (i.e. proglacial zone/Kane Basin) with the hydrograph expected to have a more subdued and longer rising limb (Karamouz et al., 2013; Yang et al., 2019a). Within this southern sector of HG, ice velocity is significantly slower (< 100 m yr^{-1}; Rignot et al., 2021) than its northern counterpart, with relatively thick ice contributing to the absence of crevasses and moulins (Oswald and Gogineni, 2011; Yang et al., 2019a; Andrews et al., 2022), as well as controlling the hydromorphology of the drainage network found here. Similar drainage hydromorphology was also mapped at the neighbouring glacier at Inglefield Land (Yang et al., 2019a; Li et al., 2022), with supraglacial rivers flowing uninterrupted into the proglacial zone, with discharge into terrestrial rivers directly reflecting the timing and intensity of surface meltwater runoff from the outlet glacier catchment without modification from englacial and/or subglacial processes.

The supraglacial drainage configuration is also further influenced by significant structural elements that were identified by Livingstone et al. (2017) via the Moderate-Resolution Imaging Spectroradiometer (MODIS) mosaic of Greenland (Haran et al., 2013). Two linear structures expressed as depressions on the ice surface that run in a southwest to northeast direction across HG are clearly visible on the mapped glacier surface in this study (Figs. 4a, 9), with many supraglacial rivers and SGLs aligned-to or terminating at them. Some longitudinal rivers are also shown to suddenly change direction when encountering these structures, with subsequent channels diverting at a 90° angle, transverse to ice flow (Fig. 4a, b). It is at the intersection of such structures we observe some channel advection with spacing of 300 m (Fig. 4a), broadly representing the ice displacement over the study period. Other basal structures are also reflected

within the supraglacial drainage system, including many V- and X-shaped patterns clearly controlled by depressions in the bed. There is a strong glacier-wide emphasis here on the influential control of these structures on drainage, which are shown here in Fig. 7 based on Livingstone et al. (2017) from MODIS imagery (MOG2015, Haran et al., 2018) and also within bed topography data from BedMachine (version 4; Morlighem et al., 2017, 2021). This identification provides independent confirmation of the existence of these depressions in the bed and their subsequent expression on the surface, as well as how they significantly control the multi-year surface drainage configuration within the vicinity of such structures.

The supraglacial drainage network at HG is also shown to be largely dominated by supraglacial rivers (98 %), consistent with findings by Lu et al. (2021) in northeastern Greenland where supraglacial rivers also dominate the surface drainage network (83.8 %). Such river contributions in northern Greenland are significantly higher than southwestern GrIS, whereby supraglacial rivers account for an average of 62 % of the network (Yang et al., 2021). The difference in contribution of rivers and SGLs to the drainage network between northern and southwestern Greenland is likely the result of (i) reduced lake distributions and storage > 800 m a.s.l. in northern Greenland due to surface topographic constraints (i.e. reduced number of available depressions due to ice thickness; Ignéczi et al., 2016; Lu et al., 2021) and (ii) steeper northern surface slopes promoting meltwater runoff over storage, with gentler elevation gradients in southwestern Greenland promoting a wider, more susceptible ablation zone to melt and meltwater ponding (Mikkelsen et al., 2016; van As et al., 2017). At HG, the maximum supraglacial RF recorded for a single date across the melt-prone zone reached 24.5 %, the largest RF value recorded to date from a supraglacial drainage mapping study (e.g. 5.3 % in northeastern Greenland, 5.5 % at the Devon Ice Cap and ∼ 14 % for southwestern Greenland). A reason for this large value is likely due to the inclusion of expansive hydrologically connected slush zones within hydrologic mapping, which are prevalent during the early-to-middle melt season when snow becomes water saturated. This slush zone progressively moves upglacier and is removed to reveal the bare ice below. Additionally, a lower river threshold (t^5) was used in this study compared to other studies (e.g. t^{20}, Lu et al., 2021), allowing narrower supraglacial rivers and slush zones to be captured, increasing the overall supraglacial drainage and river components. Whilst supraglacial rivers are likely to dominate the drainage network here, similar to northeastern Greenland (Lu et al., 2021), regardless of the threshold used due to reduced lake presence, care should be taken when directly comparing drainage network statistics between mapping studies from differing regions of the GrIS.

5.2 Temporal evolution of the supraglacial drainage network

Across the study period (2016–2020), we observe the seasonal development and inland evolution of the supraglacial drainage network as the melt season progresses and runoff increases up to the maximum melt extent, which typically occurs at the end of July. During the early melt season and at higher elevations as melt progresses, we observe the growth and inland migration of a large, poorly channelised slush zone (Greuell and Knap, 2000). Within this zone, slush flows can occur as surface melt percolates and saturates the snowpack, promoting slush mobilisation into topographical lows and initiating the reopening of perennially occupied channels (Cuffey and Paterson, 2010; Irvine-Fynn et al., 2011). On higher-draining slopes, such mobilisation can form slush-filled rills, which coalesce into networks of arborescent tributary channels, efficiently transporting melt to larger, primary river channels and subsequently the transportation of melt downglacier (Marston, 1983; Cuffey and Paterson, 2010; Chu, 2014; Rippin and Rawlins, 2021). The seasonal development of the drainage network is shown to transform from a system initially dominated by water percolation to one dominated by channelised, efficient flow (Fig. 5), further confirming behaviour identified across multiple supraglacial drainage mapping studies across the GrIS (Lu et al., 2021; Yang et al., 2021; Li et al., 2022).

The rate and extent of the spatial and temporal evolution of the supraglacial drainage network is highly variable between years. Several years within the last decade have been characterised by high air temperatures and extreme melt events, including 2 years represented within this study: 2016 and 2019. Both years, in particular 2019, experienced a strong negative North Atlantic Oscillation and simultaneously a positive East Atlantic Index and Greenland Blocking Index phase, which are associated with persistent, anticyclonic conditions over Greenland driving enhanced surface mass loss (Lim et al., 2016; Cullather et al., 2020; Zhang et al., 2022). Mass loss during summer 2019 in particular was promoted by enhanced solar radiation, reduced cloud cover and the northwestward advection of warm, moist air from the western margins as a result of such atmospheric variability (Hanna et al., 2021; Cullather et al., 2020; Tedesco and Fettweis, 2020; Elmes et al., 2021). Combined with low snow accumulation in the 2018/19 winter (Sasgen et al., 2020), extensive melting occurred along much of the Greenland coast, with surface melt experienced in the north being the highest on the record since 1948 (Tedesco and Fettweis, 2020). It was during this exceptional and long melt year that we observed the highest MF values (19.9 % or 2685 km^2 recorded on the 30 June 2019) and second highest areal extent of supraglacial drainage network (1375 m a.s.l.; Fig. 5). Ablation continued throughout September (Sasgen et al., 2020; Tedesco et al., 2019; Tedesco and Fettweis, 2020); however, this was beyond our mapped time frame. The year 2019 also recorded the largest number

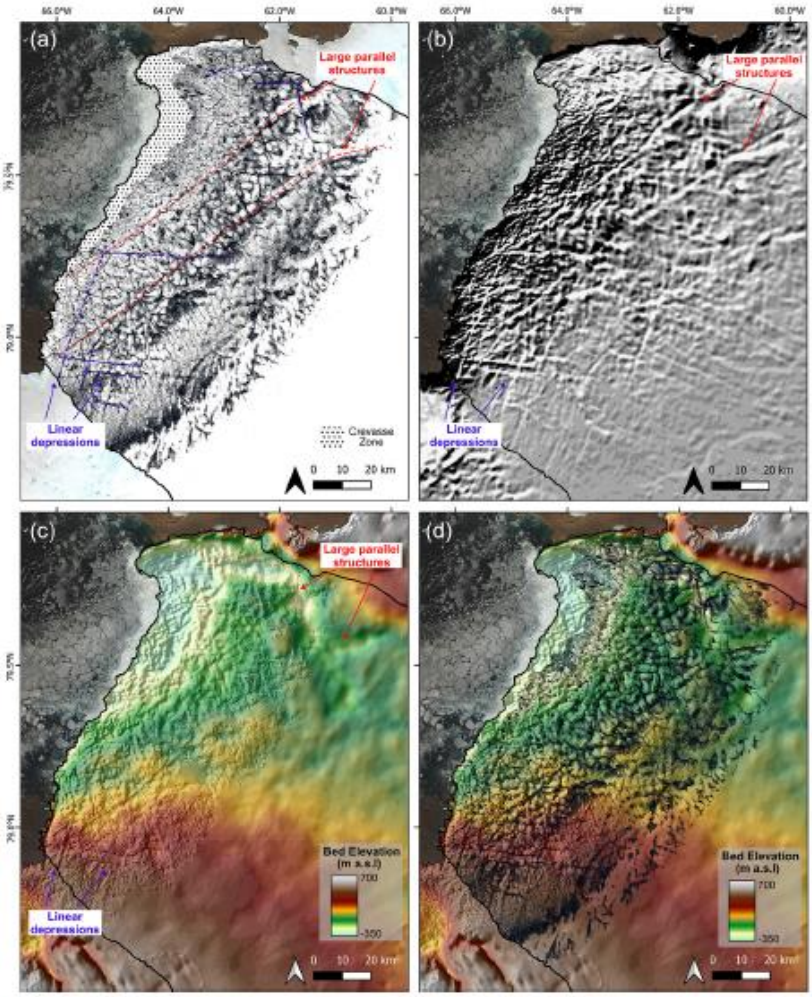

Figure 9. **(a)** Combined map of the supraglacial drainage network at its maximum extent across 2016 to 2020 showing the two parallel structures orientated southwest to northeast identified by dashed red lines. Other V- and X-shaped structures in the drainage network are also highlighted by dashed purple lines. **(b)** Moderate-Resolution Imaging Spectroradiometer (MODIS) Mosaic of Greenland (MOG2015, Haran et al., 2018) showing evidence of the these structures on the ice surface. **(c)** Bed topography via BedMachine (Morlighem et al., 2021) showing the structures as depressions within the bed. **(d)** The supraglacial drainage network as presented in **(a)** overlain on top of bed topography presented in **(c)** showing the overall influence bed topography has on the surface drainage structure at HG.

of SGLs (527) and cumulative lake areas (151.8 km^2). The hydrologic expansion of the drainage network was also rapid, in-line with a record early melt season event that, combined with low snow accumulation (Tedesco and Fettweis, 2020), promoted rapid snowpack warming, disintegration and exposure of the bare ice zone, resulting in an enhanced melt–albedo feedback mechanism (Tedesco and Fettweis, 2020). Similar findings by Turton et al. (2021) and Hochreuther et al. (2021) at 79° N Glacier recorded the largest SGL numbers and extents of their study periods in 2019, indicating the widespread impact of this extreme melt event, particularly across the GrIS northern sector.

Similar seasonal and multi-annual behavioural patterns during 2017 and 2018 were again also observed by Turton et al. (2021) and Lu et al. (2021) on the northeastern glacier of 79° N and Otto et al. (2022) on the northern Ry-

der Glacier. These findings all record a slow rate of SGL increase and late area peak (early-August) in 2017 and 2018, with Lu et al. (2021) confirming the late area peak in combined supraglacial drainage mapping of both lakes and rivers during August 2017. SGL mapping by Turton et al. (2021) also identified the delayed development and lower SGL presence during the 2018 melt season, with SGLs largely limited to < 900 m a.s.l. Such findings are consistent with observations in this study, with the onset and inland evolution of the supraglacial network, including both rivers and lakes, delayed by ~ 1 month compared to other the other study years (2016, 2019, 2020) and the limited areal development of the network (< 1150 m a.s.l.). Both the melt seasons of 2017 and 2018 recorded below-average melt (1981–2010 reference period) and melt extents (32.9 % and 44 %, respectively) across the GrIS (Tedesco et al., 2017, 2018; Sasgen et al., 2020). There was heavy springtime snowfall and late surviving snow in bare-ice areas (Tedesco et al., 2017, 2018), consistent with a strongly positive average summer (JJA) North Atlantic Oscillation and a negative Greenland Blocking Index, hypothesised to inhibit surface melt and promote increased summertime snowfall (Ruan et al., 2019; Sasgen et al., 2020), leading to these anomalously cold summers.

The anomalously early spike in satellite-derived meltwater area recorded in early June 2020 raises questions as to how extreme melt years, such as 2019, may precondition the ice surface (Cullather et al., 2020) and affect surface conditions and subsequent surface hydrologic behaviour the following year (Culberg et al., 2021). Some SGLs on the GrIS have been found to persist throughout the winter months due to insulation from a layer of ice and/or snow (Koenig et al., 2015; Law et al., 2020; Schröder et al., 2020). This lake persistence includes the winter of 2019/2020, when late summer surface melt and high autumnal temperatures (August–November) are believed to have increased subsurface firn temperatures, delaying and even decreasing the ability for subsurface meltwater freezing in northern Greenland, contributing to higher totals of liquid-buried SGLs (Dunmire et al., 2021). This, alongside a drier than average (1981–2020) winter and spring (Tedesco and Fettweis, 2020; Moon et al., 2020), has the potential to cause the rapid disintegration of limited snow present and the subsequent swift exposure of the bare ice zone the following summer. This swift exposure would also include that of perennial rivers and lakes much earlier in the melt season than expected, leading to/ the increased MF value observed in this study despite low MAR-derived melt production and runoff values.

5.3 Satellite-derived MF and runoff simulations

We found a positive linear relationship between satellite-derived MF and MAR simulated R before runoff declined (Fig. 8), showing how the MF–R relationship can be used to reliably simulate seasonal surface meltwater variation and provide further understanding into how runoff is routed and stored, at least up to peak melt events. This finding supports other studies that have used satellite-derived meltwater metrics and RCM-modelled runoff which have focussed on the southwestern GrIS (Yang et al., 2021), Northern GrIS (Lu et al., 2021; Li et al., 2022) and the Devon Ice Cap (Lu et al., 2020). In terms of post-peak melt events, surface meltwater can still cover a substantially large area even after surface runoff has reduced and ceased, as seen in this study. This is known as the "delay" effect (Lu et al., 2021), whereby meltwater may continue to be routed or stored on the ice surface via the slow routing of melt out of snowpack or firn at higher elevations, the stagnation and subsequent preservation of transported meltwater in large supraglacial rivers, or the storage of melt in SGLs. Therefore, while this MF–R relationship is promising in providing comparative assessments between satellite observations and RCM-modelled runoff at HG, calculated runoff volume via satellite-based (Yang et al., 2021) or field-based measurements (Smith et al., 2017) are required to provide further validation of such relationships, particularly over space and time across a full melt season.

5.4 Future implications

Substantial changes have taken place at HG over the last 2 decades driven by atmospheric and oceanic change (Carr et al., 2015; Rignot et al., 2021). It is therefore important to consider HG and the overall northern region sensitivity to such warming under present climate scenarios. Northern Greenland is expected to undergo the greatest warming of the 21st century across the GrIS (Hill et al., 2017), and given its already low rates of winter accumulation compared to other ice sheet sectors (Goelzer et al., 2013), this region is likely to become ever more sensitive to climatic change in the future. Mapping performed within this study illustrates the multi-annual persistence of the supraglacial drainage network within this high-latitude region (Fig. 4a) and the rapid and extensive response of this system to high-melt years (Fig. 5). This response, particularly in the extreme melt year of 2019, can precondition the ice surface for the following melt season, resulting in earlier but widespread hydrologic activity and longer-lasting melt season. This preconditioning and subsequent behaviour is likely to become increasingly normalised as melt events and atmospheric variability, such as persistent blocking events, increase in frequency and intensity (Rahmstorf and Coumou, 2011; McLeod and Mote, 2016).

Inland migration of the supraglacial drainage network is also projected with continued warming (Leeson et al., 2015), with recent work already showing ablation area expansion and amplification of melt and runoff post-1990 across northern Greenland (Noël et al., 2019). Many more surface depressions for future SGL locations are present above the current northern equlibrium line altitude (Ignéczi et al., 2016), with the potential to accumulate high volumes of meltwater and feed lengthening overflow supraglacial rivers that

extend tens of kilometres downstream to non-local, low-elevation moulins (Poinar et al., 2015). For ponded water, if ice becomes thin enough (Poinar et al., 2015) or localised ice columns become vulnerable to fracture from refrozen ice complexities within firn (ice blobs; Culberg et al., 2022), new hydrofracture events will bring such meltwater to isolated areas of the ice sheet bed. This could have knock-on impacts on ice flow, with the likely delivery of water and heat to a persistent inefficient subglacial system, where thicker, flatter ice may prohibit the development of an efficient subglacial system (Dow et al., 2014), enhancing ice flow (Christoffersen et al., 2018).

Persistent low-permeability ice slabs that block vertical percolation have continued to thicken over time in the lower-accumulation zone. Ice slabs are expected to enhance runoff from Greenland's interior, particularly in consecutive warm summers (MacFerrin et al., 2019). Enhanced runoff and inland expansion of the supraglacial drainage network will impact meltwater feedback processes, not only in driving overall SMB decline (Noël et al., 2021) but further impacting dynamical behaviour, including hydrofracture potential. At HG, a particular concern is the vulnerability of its northern terminus to increased hydrofracture events from greater melt runoff (Carr et al., 2015). Such events at HG have the potential to promote future rapid runaway retreat of HG, especially if the northern sector of the terminus retreats beyond its pinning point into the deepened bed (below sea level) in which is sits (Carr et al., 2015; Hillebrand et al., 2022).

As the northern region mainly consists of fast-flowing, marine-terminating outlet glaciers like HG that drain a large proportion of the GrIS, further understanding of the mechanisms that drive their dynamical behaviour, in particular those related to enhanced runoff, are required for predicting their future contribution to GrIS mass loss and subsequent sea level rise.

6 Conclusion

In this study, we mapped and quantified for the first time the spatial and temporal evolution of the supraglacial drainage network, including both rivers and lakes, using 10 m Sentinel-2 images from the melt seasons of 2016 to 2020 at Humboldt Glacier, northern Greenland. We identify an extensive supraglacial drainage network at Humboldt Glacier that is particularly prevalent up to 1000 m a.s.l. with a further variable transient zone extending up to ∼1440 m a.s.l. The seasonal evolutionary behaviour of this network migrates upglacier in response to increasing runoff as air temperatures rise throughout the melt season, with the network transforming from an inefficient system dominated by water percolation and slush flows to one dominated by channelised, efficient flow. Interannual variability in the extent and behaviour of the system is associated with high- and low-melt years across the study period, with the low-melt years of 2017 and 2018 having both limited and delayed spatial development. The extreme melt year of 2019 showed the extensive development and persistence of the supraglacial drainage network into September, which followed by low snow accumulation during the subsequent winter and spring, preconditioned the ice sheet for earlier hydrologic activity in 2020. This behaviour may become more representative with extreme melt events and longer-lasting melt seasons into the future. This work ultimately contributes to advancing our understanding of supraglacial hydrologic processes across the Greenland Ice Sheet by expanding detailed drainage mapping to other understudied regions of the ice sheet, in particular to Greenland's rapidly changing northern region, aiding in projections of future mass loss as enhanced runoff continues with climatic warming.

Data availability. Supraglacial river and lake shapefiles can be requested by contacting the lead author. Regional climate model MAR v3.11 datasets (Amory et al., 2021; Fettweis et al., 2021) were provided by Xavier Fettweis and are freely available via (ftp://ftp.climato.be/, Amory et al., 2021, Fettweis et al., 2021). Sentinel-2 imagery is available from the Copernicus Open Access Hub (https://scihub.copernicus.eu, Copernicus, 2022). The automatic river detection algorithm (Yang et al., 2015, 2017) to generate supraglacial network datasets is freely available on the GitHub site (https://github.com/njuRS/River_detection, njuRS, 2022).

Supplement. The supplement related to this article is available online at: https://doi.org/10.5194/tc-17-4729-2023-supplement.

Author contributions. LDR designed the study, conducted data collection and analysis, and prepared the manuscript. KY provided the source code for the automatic detection algorithm for automatic river mapping in MATLAB. AJS aided with MAR data extraction for the Humboldt Glacier catchment. DMR, AJS, SJL, and KY provided comments on draft versions of the manuscript produced by LDR.

Competing interests. At least one of the (co-)authors is a member of the editorial board of *The Cryosphere*. The peer-review process was guided by an independent editor, and the authors also have no other competing interests to declare.

Disclaimer. Publisher's note: Copernicus Publications remains neutral with regard to jurisdictional claims made in the text, published maps, institutional affiliations, or any other geographical representation in this paper. While Copernicus Publications makes every effort to include appropriate place names, the final responsibility lies with the authors.

Acknowledgements. Lauren D. Rawlins acknowledges financial support from a Natural Environmental Research Council (NERC) Doctoral Training Partnership (grant no. NE/L002450/1). The authors would like to acknowledge the Copernicus Open Access Hub for providing free access to the satellite imagery used in this study and also thank Xavier Fettweis for the availability of MAR data. We also thank the Polar Geospatial Center for the availability of the ArcticDEM. The authors would like to thank the two anonymous reviewers for providing constructive comments that led to improvements to the manuscript and to the editor (Caroline Clason) for handling the manuscript.

Financial support. Lauren D. Rawlins was supported by a PhD studentship via the Natural Environment Research Council (NERC) Doctoral Training Partnership (grant no. NE/L002450/1).

Review statement. This paper was edited by Caroline Clason and reviewed by two anonymous referees.

References

Amory, C., Kittel, C., Le Toumelin, L., Agosta, C., Delhasse, A., Favier, V., and Fettweis, X.: Performance of MAR (v3.11) in simulating the drifting-snow climate and surface mass balance of Adélie Land, East Antarctica, Geosci. Model Dev., 14, 3487–3510, https://doi.org/10.5194/gmd-14-3487-2021, 2021 (data available at: ftp://ftp.climato.be/).

Andrews, L. C., Catania, G. A., Hoffman, M. J., Gulley, J. D., Lüthi, M. P., Ryser, C., Hawley, R. L., and Neumann, T. A.: Direct observations of evolving subglacial drainage beneath the Greenland Ice Sheet, Nature, 514, 80–83, https://doi.org/10.1038/nature13796, 2014.

Andrews, L. C., Poinar, K., and Trunz, C.: Controls on Greenland moulin geometry and evolution from the Moulin Shape model, The Cryosphere, 16, 2421–2448, https://doi.org/10.5194/tc-16-2421-2022, 2022.

Baillarin, S., Meygret, A., Dechoz, C., Petrucci, B., Lacherade, S.,Trémas, T., Isola, C., Martimort, P., and Spoto, F.: Sentinel-2 level 1 products and image processing performances, IEEE international geoscience and remote sensing symposium, Munich, Germany, 22–27 July 2012, 7003–7006, https://doi.org/10.1109/IGARSS.2012.6351959, 2012.

Banwell, A. F., Cabellero, M., Arnold, N., Glasser, N., Cathles, L. M., and MacAyeal, D.: Supraglacial lakes on the Larsen B Ice Shelf, Antarctica, and Paakitsoq Region, Greenland: a comparative study, Ann. Glaciol., 55, 66, https://doi.org/10.3189/2014AoG66A049, 2014.

Bartholomew, I., Nienow, P., Mair, D., Hubbard, A., King, M. A., and Sole, A.: Seasonal evolution of subglacial drainage and acceleration in a Greenland outlet glacier, Nat. Geosci., 3, 408–411, https://doi.org/10.1038/ngeo863, 2010.

Bartholomew, I., Nienow, P., Sole, A., Mair, D., Cowton, T., and King, M. A.: Short-term variability in Greenland Ice Sheet motion forced by time-varying meltwater drainage: Implications for the relationship between subglacial drainage system behavior and ice velocity, J. Geophys. Res.-Earth, 117, F03002,, https://doi.org/10.1029/2011JF002220, 2012.

Boghosian, A. L., Pitcher, L. H., Smith, L. C., Kosh, E., Alexander, P. M., Tedesco, M., and Bell, R. E.: Development of ice-shelf estuaries promotes fractures and calving, Nat. Geosci., 14, 899–905, https://doi.org/10.1038/s41561-021-00837-7, 2021.

Box, J. E. and Decker, D. T.: Greenland marine-terminating glacier area changes: 2000–2010, Ann. Glaciol., 52, 91–98, https://doi.org/10.3189/172756411799096312, 2011.

Carr, J. R., Vieli, A., Stokes, C., Jamieson, S., Palmer, S., Christoffersen, P., Dowdeswell, J., Nick, F., Blankenship, D., and Young, D.: Basal topographic controls on rapid retreat of Humboldt Glacier, northern Greenland, J. Glaciol., 61, 137–150, https://doi.org/10.3189/2015JoG14J128, 2015.

Catania, G. A., Neumann, T. A., and Price, S. F.: Characterizing englacial drainage in the ablation zone of the Greenland ice sheet, J. Glaciol., 54, 567–578, https://doi.org/10.3189/002214308786570854, 2008.

Christoffersen, P., Bougamont, M., Hubbard, A., Doyle, S. H., Grigsby, S., and Pettersson, R.: Cascading lake drainage on the Greenland Ice Sheet triggered by tensile shock and fracture, Nat. Commun., 9, 1064, https://doi.org/10.1038/s41467-018-03420-8, 2018.

Chu, V. W.: Greenland ice sheet hydrology: A review, Prog. Phys. Geogr., 38, 19–54, https://doi.org/10.1177/0309133313507075, 2014.

Copernicus: Copernicus Open Access Hub, https://scihub.copernicus.eu, last access: 15 December 2022.

Corr, D., Leeson, A., McMillan, M., Zhang, C., and Barnes, T.: An inventory of supraglacial lakes and channels across the West Antarctic Ice Sheet, Earth Syst. Sci. Data, 14, 209–228, https://doi.org/10.5194/essd-14-209-2022, 2022.

Crozier, J., Karlstrom, L., and Yang, K.: Basal control of supraglacial meltwater catchments on the Greenland Ice Sheet, The Cryosphere, 12, 3383–3407, https://doi.org/10.5194/tc-12-3383-2018, 2018.

Cuffey, K. M. and Paterson, W. S. B.: The physics of glaciers, Academic Press, ISBN 978-0-12-369461-4, 2010.

Culberg, R., Schroeder, D. M., and Chu, W.: Extreme melt season ice layers reduce firn permeability across Greenland, Nat. Commun., 12, 2336, https://doi.org/10.1038/s41467-021-22656-5, 2021.

Culberg, R., Chu, W., and Schroeder, D. M.: Shallow Fracture Buffers High Elevation Runoff in Northwest Greenland, Geophys. Res. Lett., 49, e2022GL101151, https://doi.org/10.1029/2022GL101151, 2022.

Cullather, R. I., Andrews, L. C., Croteau, M. J., Digirolamo, N. E., Hall, D. K., Lim, Y. K., Loomis, B. D., Shuman, C. A., and Nowicki, S. M.: Anomalous circulation in July 2019 resulting in mass loss on the Greenland Ice Sheet, Geophys. Res. Lett., 47, e2020GL087263, https://doi.org/10.1029/2020GL087263, 2020.

Davison, B. J., Sole, A. J., Livingstone, S. J., Cowton, T. R., and Nienow, P. W.: The influence of hydrology on the dynamics of land-terminating sectors of the Greenland ice sheet, Front. Earth Sci., 7, 10, https://doi.org/10.3389/feart.2019.00010, 2019.

Dell, R., Banwell, A. F., Willis, I., Arnold, N., Halberstadt, A. R. W., Chudley, T. R., and Pritchard, H.: Supervised classification of slush and ponded water on Antarctic ice

shelves using Landsat 8 imagery, J. Glaciol., 68, 401–414, https://doi.org/10.1017/jog.2021.114, 2022.

Dow, C., Kulessa, B., Rutt, I., Doyle, S. H., and Hubbard, A.: Upper bounds on subglacial channel development for interior regions of the Greenland ice sheet, J. Glaciol., 60, 1044–1052, https://doi.org/10.3189/2014JoG14J093, 2014.

Dunmire, D., Banwell, A. F., Wever, N., Lenaerts, J. T. M., and Datta, R. T.: Contrasting regional variability of buried meltwater extent over 2 years across the Greenland Ice Sheet, The Cryosphere, 15, 2983–3005, https://doi.org/10.5194/tc-15-2983-2021, 2021.

Elmes, A., Levy, C., Erb, A., Hall, D. K., Scambos, T. A., DiGirolamo, N., and Schaaf, C.: Consequences of the 2019 greenland ice sheet melt episode on albedo, Remote Sensing, 13, 227, https://doi.org/10.3390/rs13020227, 2021.

Fettweis, X., Box, J. E., Agosta, C., Amory, C., Kittel, C., Lang, C., van As, D., Machguth, H., and Gallée, H.: Reconstructions of the 1900–2015 Greenland ice sheet surface mass balance using the regional climate MAR model, The Cryosphere, 11, 1015–1033, https://doi.org/10.5194/tc-11-1015-2017, 2017.

Fettweis, X., Hofer, S., Krebs-Kanzow, U., Amory, C., Aoki, T., Berends, C. J., Born, A., Box, J. E., Delhasse, A., Fujita, K., Gierz, P., Goelzer, H., Hanna, E., Hashimoto, A., Huybrechts, P., Kapsch, M.-L., King, M. D., Kittel, C., Lang, C., Langen, P. L., Lenaerts, J. T. M., Liston, G. E., Lohmann, G., Mernild, S. H., Mikolajewicz, U., Modali, K., Mottram, R. H., Niwano, M., Noël, B., Ryan, J. C., Smith, A., Streffing, J., Tedesco, M., van de Berg, W. J., van den Broeke, M., van de Wal, R. S. W., van Kampenhout, L., Wilton, D., Wouters, B., Ziemen, F., and Zolles, T.: GrSMBMIP: intercomparison of the modelled 1980–2012 surface mass balance over the Greenland Ice Sheet, The Cryosphere, 14, 3935–3958, https://doi.org/10.5194/tc-14-3935-2020, 2020.

Fettweis, X., Hofer, S., Séférian, R., Amory, C., Delhasse, A., Doutreloup, S., Kittel, C., Lang, C., Van Bever, J., Veillon, F., and Irvine, P.: Brief communication: Reduction in the future Greenland ice sheet surface melt with the help of solar geoengineering , The Cryosphere, 15, 3013–3019, https://doi.org/10.5194/tc-15-3013-2021, 2021 (data available at: ftp://ftp.climato.be/).

Gardner, A. S., Fahnestock, M. A., and Scambos, T. A.: ITS_LIVE Regional Glacier and Ice Sheet Surface Velocities, National Snow and Ice Data Center [data set], https://doi.org/10.5067/6II6VW8LLWJ7, 2019.

Gleason, C. J., Smith, L. C., Chu, V. W., Legleiter, C. J., Pitcher, L. H., Overstreet, B. T., Rennermalm, A. K., Forster, R. R., and Yang, K.: Characterizing supraglacial meltwater channel hydraulics on the Greenland Ice Sheet from in situ observations, Earth Surf. Proc. Land., 41, 2111–2122, https://doi.org/10.1002/esp.3977, 2016.

Gleason, C. J., Yang, K., Feng, D., Smith, L. C., Liu, K., Pitcher, L. H., Chu, V. W., Cooper, M. G., Overstreet, B. T., and Rennermalm, A. K.: Hourly surface meltwater routing for a Greenlandic supraglacial catchment across hillslopes and through a dense topological channel network, The Cryosphere, 15, 2315–2331, https://doi.org/10.5194/tc-15-2315-2021, 2021.

Gledhill, L. A. and Williamson, A. G.: Inland advance of supraglacial lakes in north-west Greenland under recent climatic warming, Ann. Glaciol., 59, 66–82, https://doi.org/10.1017/aog.2017.31, 2018.

Goelzer, H., Huybrechts, P., Fürst, J. J., Nick, F. M., Andersen, M. L., Edwards, T. L., Fettweis, X., Payne, A. J., and Shannon, S.: Sensitivity of Greenland ice sheet projections to model formulations, J. Glaciol., 59, 733–749, https://doi.org/10.3189/2013JoG12J182, 2013.

Gray, L.: Brief communication: Glacier run-off estimation using altimetry-derived basin volume change: case study at Humboldt Glacier, northwest Greenland, The Cryosphere, 15, 1005–1014, https://doi.org/10.5194/tc-15-1005-2021, 2021.

Greuell, W. and Knap, W. H.: Remote sensing of the albedo and detection of the slush line on the Greenland ice sheet, J. Geophys. Res.-Atmos., 105, 15567–15576, https://doi.org/10.1029/1999JD901162, 2000.

Gudmundsson, G. H.: Transmission of basal variability to a glacier surface, J. Geophys. Res.-Sol. Ea., 108, 2253, https://doi.org/10.1029/2002JB002107, 2003.

Gudmundsson, G. H., Raymond, C. F., and Bindschadler, R.: The origin and longevity of flow stripes on Antarctic ice streams, Ann. Glaciol., 27, 145–152, https://doi.org/10.3189/1998AoG27-1-145-152, 1998.

Hanna, E., Mernild, S. H., Cappelen, J., and Steffen, K.: Recent warming in Greenland in a long-term instrumental (1881–2012) climatic context: I. Evaluation of surface air temperature records, Environ. Res. Lett., 7, 045404, https://doi.org/10.1088/1748-9326/7/4/045404, 2012.

Hanna, E., Cappelen, J., Fettweis, X., Mernild, S. H., Mote, T. L., Mottram, R., Steffen, K., Ballinger, T. J., and Hall, R. J.: Greenland surface air temperature changes from 1981 to 2019 and implications for ice-sheet melt and mass-balance change, Int. J. Climatol., 41, E1336–E1352, https://doi.org/10.1002/joc.6771, 2021.

Haran, T., Bohlander, J., Scambos, T., Painter, T., and Fahnestock, M.: MEaSUREs MODIS Mosaic of Greenland 2005 (MOG2005) Image Map, Version 1, Boulder, Colorado, NSIDC: National Snow and Ice Data Center [data set] , https://doi.org/10.5067/IAGYM8Q26QRE, 2013.

Haran, T., Bohlander, J., Scambos, T., Painter, T., and Fahnestock, M.: MEaSUREs MODIS Mosaic of Greenland (MOG) 2005, 2010, and 2015 Image Maps, Version 2, Boulder, Colorado USA, NASA National Snow and Ice Data Center Distributed Active Archive Center [data set], https://doi.org/10.5067/9ZO79PHOTYE5, 2018.

Hill, E. A., Carr, J. R., and Stokes, C. R.: A review of recent changes in major marine-terminating outlet glaciers in Northern Greenland, Front. Earth Sci., 4, 111, https://doi.org/10.3389/feart.2016.00111, 2017.

Hill, E. A., Carr, J. R., Stokes, C. R., and Gudmundsson, G. H.: Dynamic changes in outlet glaciers in northern Greenland from 1948 to 2015, The Cryosphere, 12, 3243–3263, https://doi.org/10.5194/tc-12-3243-2018, 2018.

Hillebrand, T. R., Hoffman, M. J., Perego, M., Price, S. F., and Howat, I. M.: The contribution of Humboldt Glacier, northern Greenland, to sea-level rise through 2100 constrained by recent observations of speedup and retreat, The Cryosphere, 16, 4679–4700, https://doi.org/10.5194/tc-16-4679-2022, 2022.

Hochreuther, P., Neckel, N., Reimann, N., Humbert, A., and Braun, M.: Fully automated detection of supraglacial lake area for Northeast Greenland using sentinel-2 time-series, Remote Sensing, 13, 205, https://doi.org/10.3390/rs13020205, 2021.

Hoffman, M., Catania, G., Neumann, T., Andrews, L., and Rumrill, J.: Links between acceleration, melting, and supraglacial lake drainage of the western Greenland Ice Sheet, J. Geophys. Res.-Earth, 116, F04035, https://doi.org/10.1029/2010JF001934, 2011.

Holmes, G. W.: Morphology and hydrology of the Mint Julep area, southwest Greenland, in: Project Mint Julep Investigation of Smooth Ice Areas of the Greenland Ice Cap, 1953, Part II Special Scientific Reports, Arctic, Desert, Tropic Information Center, Research Studies Institute, Air University, 1955

Ignéczi, Á., Sole, A. J., Livingstone, S. J., Leeson, A. A., Fettweis, X., Selmes, N., Gourmelen, N., and Briggs, K.: Northeast sector of the Greenland Ice Sheet to undergo the greatest inland expansion of supraglacial lakes during the 21st century, Geophys. Res. Lett., 43, 9729–9738, https://doi.org/10.1002/2016GL070338, 2016.

Ignéczi, Á., Sole, A. J., Livingstone, S. J., Ng, F. S., and Yang, K.: Greenland Ice Sheet surface topography and drainage structure controlled by the transfer of basal variability, Front. Earth Sci., 6, 101, https://doi.org/10.3389/feart.2018.00101, 2018.

Irvine-Fynn, T. D., Hodson, A. J., Moorman, B. J., Vatne, G., and Hubbard, A. L.: Polythermal glacier hydrology: A review, Rev. Geophys., 49, RG4002, https://doi.org/10.1029/2010RG000350, 2011.

Joughin, I., Kwok, R., and Fahnestock, M.: Estimation of ice-sheet motion using satellite radar interferometry: method and error analysis with application to Humboldt Glacier, Greenland, J. Glaciol., 42, 564–575, https://doi.org/10.3189/S0022143000003543, 1996.

Joughin, I., Fahnestock, M., Kwok, R., Gogineni, P., and Allen, C.: Ice flow in the Humboldt, Petermann, and Ryder Glaciers, North Greenland, J. Glaciol., 45, 231–341, https://doi.org/10.3189/S0022143000001738, 1999.

Joughin, I., Das, S. B., Flowers, G. E., Behn, M. D., Alley, R. B., King, M. A., Smith, B. E., Bamber, J. L., van den Broeke, M. R., and van Angelen, J. H.: Influence of ice-sheet geometry and supraglacial lakes on seasonal ice-flow variability, The Cryosphere, 7, 1185–1192, https://doi.org/10.5194/tc-7-1185-2013, 2013.

Kamb, B.: Glacier surge mechanism based on linked cavity configuration of the basal water conduit system, J. Geophys. Res.-Sol. Ea., 92, 9083–9100, https://doi.org/10.1029/JB092iB09p09083, 1987.

Karamouz, M., Nazif, S., and Falahi, M.:. Hydrology and hydroclimatology: principles and applications, CRC Press, ISBN 978-1-4665-1220-7, https://doi.org/10.1201/b13771, 2013.

Karlstrom, L. and Yang, K.: Fluvial supraglacial landscape evolution on the Greenland Ice Sheet, Geophys. Res. Lett., 43, 2683–2692, https://doi.org/10.1002/2016GL067697, 2016.

Koenig, L. S., Lampkin, D. J., Montgomery, L. N., Hamilton, S. L., Turrin, J. B., Joseph, C. A., Moutsafa, S. E., Panzer, B., Casey, K. A., Paden, J. D., Leuschen, C., and Gogineni, P.: Wintertime storage of water in buried supraglacial lakes across the Greenland Ice Sheet, The Cryosphere, 9, 1333–1342, https://doi.org/10.5194/tc-9-1333-2015, 2015.

Krawczynski, M. J., Behn, M. D., Das, S. B., and Joughin, I.: Constraints on the lake volume required for hydrofracture through ice sheets, Geophys. Res. Lett., 36, L10501, https://doi.org/10.1029/2008GL036765, 2009.

Lampkin, D. and VanderBerg, J.: A preliminary investigation of the influence of basal and surface topography on supraglacial lake distribution near Jakobshavn Isbrae, western Greenland, Hydrol. Process., 25, 3347–3355, https://doi.org/10.1002/hyp.8170, 2011.

Lampkin, D. and VanderBerg, J.: Supraglacial melt channel networks in the Jakobshavn Isbræ region during the 2007 melt season, Hydrol. Process., 28, 6038–6053, https://doi.org/10.1002/hyp.10085, 2014.

Law, R., Arnold, N., Benedek, C., Tedesco, M., Banwell, A., and Willis, I.: Over-winter persistence of supraglacial lakes on the Greenland Ice Sheet: results and insights from a new model, J. Glaciol., 66, 362–372, https://doi.org/10.1017/jog.2020.7, 2020.

Leeson, A., Shepherd, A., Briggs, K., Howat, I., Fettweis, X., Morlighem, M., and Rignot, E.: Supraglacial lakes on the Greenland ice sheet advance inland under warming climate, Nat. Clim. Change, 5, 51–55, https://doi.org/10.1038/nclimate2463, 2015.

Li, Y., Yang, K., Gao, S., Smith, L. C., Fettweis, X., and Li, M.: Surface meltwater runoff routing through a coupled supraglacial-proglacial drainage system, Inglefield Land, northwest Greenland, Int. J. Appl. Earth Obs., 106, 102647, https://doi.org/10.1016/j.jag.2021.102647, 2022.

Lim, Y.-K., Schubert, S. D., Nowicki, S. M., Lee, J. N., Molod, A. M., Cullather, R. I., Zhao, B., and Velicogna, I.: Atmospheric summer teleconnections and Greenland Ice Sheet surface mass variations: Insights from MERRA-2, Environ. Res. Lett., 11, 024002, https://doi.org/10.1088/1748-9326/11/2/024002, 2016.

Livingstone, S. J., Chu, W., Ely, J. C., and Kingslake, J.: Paleofluvial and subglacial channel networks beneath Humboldt Glacier, Greenland, Geology, 45, 551–554, https://doi.org/10.1130/G38860.1, 2017.

Lu, Y., Yang, K., Lu, X., Smith, L. C., Sole, A. J., Livingstone, S. J., Fettweis, X., and Li, M.: Diverse supraglacial drainage patterns on the Devon ice Cap, Arctic Canada, J. Maps, 16, 834–846, https://doi.org/10.1080/17445647.2020.1838353, 2020.

Lu, Y., Yang, K., Lu, X., Li, Y., Gao, S., Mao, W., and Li, M.: Response of supraglacial rivers and lakes to ice flow and surface melt on the northeast Greenland ice sheet during the 2017 melt season, J. Hydrol., 602, 126750, https://doi.org/10.1016/j.jhydrol.2021.126750, 2021.

Macdonald, G., Banwell, A., and MacAyeal, D.: Seasonal evolution of supraglacial lakes on a floating ice tongue, Petermann Glacier, Greenland, Ann. Glaciol., 59, 56–65, https://https://doi.org/10.1017/aog.2018.9, 2018.

MacFerrin, M., Machguth, H., As, D. v., Charalampidis, C., Stevens, C., Heilig, A., Vandecrux, B., Langen, P., Mottram, R., and Fettweis, X.: Rapid expansion of Greenland's low-permeability ice slabs, Nature, 573, 403–407, https://doi.org/10.1038/s41586-019-1550-3, 2019.

Marston, R. A.: Supraglacial stream dynamics on the Juneau Icefield, Ann. Assoc. Am. Geogr., 73, 597-608, https://doi.org/10.1111/j.1467-8306.1983.tb01861.x, 1983.

McFeeters, S. K.: The use of the Normalized Difference Water Index (NDWI) in the delineation of open water features, Int. J. Remote Sens., 17, 1425–1432, https://doi.org/10.1080/01431169608948714, 1996.

McLeod, J. T. and Mote, T. L.: Linking interannual variability in extreme Greenland blocking episodes to the recent increase in

summer melting across the Greenland ice sheet, Int. J. Climatol., 36, 1484–1499, https://doi.org/10.1002/joc.4440, 2016.

Mejia, J., Gulley, J., Trunz, C., Covington, M. D., Bartholomaus, T., Breithaupt, C., Xie, S., and Dixon, T. H.: Moulin density controls the timing of peak pressurization within the Greenland Ice Sheet's subglacial drainage system, Geophys. Res. Lett., 49, e2022GL100058, https://doi.org/10.1029/2022GL100058, 2022.

Mikkelsen, A. B., Hubbard, A., MacFerrin, M., Box, J. E., Doyle, S. H., Fitzpatrick, A., Hasholt, B., Bailey, H. L., Lindbäck, K., and Pettersson, R.: Extraordinary runoff from the Greenland ice sheet in 2012 amplified by hypsometry and depleted firn retention, The Cryosphere, 10, 1147–1159, https://doi.org/10.5194/tc-10-1147-2016, 2016.

Moon, T. A., Tedesco, M., Box, J., Cappelen, J., Fausto, R., Fettweis, X., Korsgaard, N., Loomis, B., Mankoff, K., and Mote, T.: Arctic Report Card 2020: Greenland Ice Sheet, National Snow and Ice Data Center (U.S.), University of Colorado Boulder, United States, National Oceanic and Atmospheric Administration. Office of Oceanic and Atmospheric Research, https://doi.org/10.25923/ms78-g612, 2020

Morlighem, M., Williams, C. N., Rignot, E., An, L., Arndt, J. E., Bamber, J. L., Catania, G., Chauché, N., Dowdeswell, J. A., and Dorschel, B.: BedMachine v3: Complete bed topography and ocean bathymetry mapping of Greenland from multibeam echo sounding combined with mass conservation, Geophys. Res. Lett., 44, 11051–11061, https://doi.org/10.1002/2017GL074954, 2017.

Morlighem, M., et al.: IceBridge BedMachine Greenland, Version 4. [Bed Topography], Boulder, Colorado USA, NASA National Snow and Ice Data Center Distributed Active Archive Center [data set], https://doi.org/10.5067/VLJ5YXKCNGXO, 2021

Mouginot, J., Rignot, E., Bjørk, A. A., Van den Broeke, M., Millan, R., Morlighem, M., Noël, B., Scheuchl, B., and Wood, M.: Forty-six years of Greenland Ice Sheet mass balance from 1972 to 2018, P. Natl. Acad. Sci. USA, 116, 9239–9244, https://doi.org/10.1073/pnas.1904242116, 2019.

Moussavi, M. S., Abdalati, W., Pope, A., Scambos, T., Tedesco, M., MacFerrin, M., and Grigsby, S.: Derivation and validation of supraglacial lake volumes on the Greenland Ice Sheet from high-resolution satellite imagery, Remote Sens. Environ., 183, 294–303, https://doi.org/10.1016/j.rse.2016.05.024, 2016.

Ng, F. S., Ignéczi, Á., Sole, A. J., and Livingstone, S. J.: Response of surface topography to basal variability along glacial flowlines, J. Geophys. Res.-Earth, 123, 2319–2340, https://doi.org/10.1029/2017JF004555, 2018.

Nienow, P., Sole, A., Slater, D. A., and Cowton, T.: Recent advances in our understanding of the role of meltwater in the Greenland Ice Sheet system, Current Climate Change Reports, 3, 330–344, https://doi.org/10.1007/s40641-017-0083-9, 2017.

Noël, B., van de Berg, W. J., Lhermitte, S., and van den Broeke, M. R.: Rapid ablation zone expansion amplifies north Greenland mass loss, Science Advances, 5, eaaw0123, https://doi.org/10.1126/sciadv.aaw0123, 2019.

Noël, B., van Kampenhout, L., Lenaerts, J. T. M., van de Berg, W. J., and van den Broeke, M. R.: A 21st century warming threshold for sustained Greenland ice sheet mass loss, Geophys. Res. Lett., 48, e2020GL090471, https://doi.org/10.1029/2020GL090471, 2021.

njuRS: River_detection, GitHub [data set], https://github.com/njuRS/River_detection, last access: 15 December 2022.

Oswald, G. K. and Gogineni, S.: Mapping basal melt under the northern Greenland Ice Sheet, IEEE T. Geosci. Remote, 50, 585–592, https://doi.org/10.1109/TGRS.2011.2162072, 2011.

Otto, J., Holmes, F. A., and Kirchner, N.: Supraglacial lake expansion, intensified lake drainage frequency, and first observation of coupled lake drainage, during 1985–2020 at Ryder Glacier, Northern Greenland, Front. Earth Sci., 10, 978137, https://doi.org/10.3389/feart.2022.978137, 2022.

Pitcher, L. H. and Smith, L. C.: Supraglacial streams and rivers, Annu. Rev. Earth Planet. Sci., 47, 421–452, https://doi.org/10.1146/annurev-earth-053018-060212, 2019.

Poinar, K., Joughin, I., Das, S. B., Behn, M. D., Lenaerts, J. T., and Van Den Broeke, M. R.: Limits to future expansion of surface-melt-enhanced ice flow into the interior of western Greenland, Geophys. Res. Lett., 42, 1800–1807, https://doi.org/10.1002/2015GL063192, 2015.

Pope, A., Scambos, T. A., Moussavi, M., Tedesco, M., Willis, M., Shean, D., and Grigsby, S.: Estimating supraglacial lake depth in West Greenland using Landsat 8 and comparison with other multispectral methods, The Cryosphere, 10, 15–27, https://doi.org/10.5194/tc-10-15-2016, 2016.

Rahmstorf, S. and Coumou, D.: Increase of extreme events in a warming world, P. Natl. Acad. Sci. USA, 108, 17905–17909, https://doi.org/10.1073/pnas.1101766108, 2011.

Raymond, M. J. and Gudmundsson, G. H.: On the relationship between surface and basal properties on glaciers, ice sheets, and ice streams, J. Geophys. Res.-Sol. Ea., 110, B08411, https://doi.org/10.1029/2005JB003681, 2005.

Rennermalm, A. K., Smith, L. C., Chu, V. W., Box, J. E., Forster, R. R., Van den Broeke, M. R., Van As, D., and Moustafa, S. E.: Evidence of meltwater retention within the Greenland ice sheet, The Cryosphere, 7, 1433–1445, https://doi.org/10.5194/tc-7-1433-2013, 2013.

Rignot, E. and Kanagaratnam, P.: Changes in the velocity structure of the Greenland Ice Sheet, Science, 311, 986–990, https://doi.org/10.1126/science.1121381, 2006.

Rignot, E., Gogineni, S., Joughin, I., and Krabill, W.: Contribution to the glaciology of northern Greenland from satellite radar interferometry, J. Geophys. Res., 106, 34007–34019, https://doi.org/10.1029/2001JD900071, 2001.

Rignot, E., An, L., Chauche, N., Morlighem, M., Jeong, S., Wood, M., Mouginot, J., Willis, J. K., Klaucke, I., and Weinrebe, W.: Retreat of Humboldt Gletscher, North Greenland, driven by undercutting from a warmer ocean, Geophys. Res. Lett., 48, e2020GL091342, https://doi.org/10.1029/2020GL091342, 2021.

Riihelä, A., King, M. D., and Anttila, K.: The surface albedo of the Greenland Ice Sheet between 1982 and 2015 from the CLARA-A2 dataset and its relationship to the ice sheet's surface mass balance, The Cryosphere, 13, 2597–2614, https://doi.org/10.5194/tc-13-2597-2019, 2019.

Rippin, D. and Rawlins, L.: Supraglacial River Networks, In International Encyclopedia of Geography, edited by: Richardson, D., Castree, N., Goodchild, M. F., Kobayashi, A., Liu, W., and Marston, R. A., https://doi.org/10.1002/9781118786352.wbieg2072, 2021.

Ruan, R., Chen, X., Zhao, J., Perrie, W., Mottram, R., Zhang, M., Diao, Y., Du, L., and Wu, L.: Decelerated Greenland Ice Sheet melt driven by positive summer North At-

lantic oscillation, J. Geophys. Res.-Atmos., 124, 7633–7646, https://doi.org/10.1029/2019JD030689, 2019.

Ryan, J., Smith, L., Van As, D., Cooley, S., Cooper, M., Pitcher, L., and Hubbard, A.: Greenland Ice Sheet surface melt amplified by snowline migration and bare ice exposure, Science Advances, 5, eaav3738, https://doi.org/10.1126/sciadv.aav3738, 2019.

Ryan, J. C., Hubbard, A., Stibal, M., Irvine-Fynn, T. D., Cook, J., Smith, L. C., Cameron, K., and Box, J.: Dark zone of the Greenland Ice Sheet controlled by distributed biologically-active impurities, Nat. Commun., 9, 1065, https://doi.org/10.1038/s41467-018-03353-2, 2018.

Sasgen, I., Wouters, B., Gardner, A. S., King, M. D., Tedesco, M., Landerer, F. W., Dahle, C., Save, H., and Fettweis, X.: Return to rapid ice loss in Greenland and record loss in 2019 detected by the GRACE-FO satellites, Commun. Earth Environ., 1, 1–8, https://doi.org/10.1038/s43247-020-0010-1, 2020.

Schoof, C.: Ice-sheet acceleration driven by melt supply variability, Nature, 468, 803–806, https://doi.org/10.1038/nature09618, 2010.

Schröder, L., Neckel, N., Zindler, R., and Humbert, A.: Perennial supraglacial lakes in Northeast Greenland observed by polarimetric SAR, Remote Sensing, 12, 2798, https://doi.org/10.3390/rs12172798, 2020.

Selmes, N., Murray, T., and James, T.: Fast draining lakes on the Greenland Ice Sheet, Geophys. Res. Lett., 38, L15501, https://doi.org/10.1029/2011GL047872, 2011.

Slater, T., Shepherd, A., McMillan, M., Leeson, A., Gilbert, L., Muir, A., Munneke, P. K., Noël, B., Fettweis, X., and van den Broeke, M.: Increased variability in Greenland Ice Sheet runoff from satellite observations, Nat. Commun., 12, 6069, https://doi.org/10.1038/s41467-021-26229-4, 2021.

Smith, L. C., Chu, V. W., Yang, K., Gleason, C. J., Pitcher, L. H., Rennermalm, A. K., Legleiter, C. J., Behar, A. E., Overstreet, B. T., and Moustafa, S. E.: Efficient meltwater drainage through supraglacial streams and rivers on the southwest Greenland ice sheet, P. Natl. Acad. Sci. USA, 112, 1001–1006, https://doi.org/10.1073/pnas.1413024112, 2015.

Smith, L. C., Yang, K., Pitcher, L. H., Overstreet, B. T., Chu, V. W., Rennermalm, Å. K., Ryan, J. C., Cooper, M. G., Gleason, C. J., and Tedesco, M.: Direct measurements of meltwater runoff on the Greenland ice sheet surface, P. Natl. Acad. Sci. USA, 114, E10622–E10631, https://doi.org/10.1073/pnas.1707743114, 2017.

Sole, A. J., Mair, D. W. F., Nienow, P. W., Bartholomew, I., King, M., Burke, M. J., and Joughin, I.: Seasonal speedup of a Greenland marine-terminating outlet glacier forced by surface melt–induced changes in subglacial hydrology, J. Geophys. Res.-Earth, 116, F03014, https://doi.org/10.1029/2010JF001948, 2011.

Stokes, C. R., Sanderson, J. E., Miles, B. W. J. Jamieson, S. S., and Leeson, A. A.: Widespread distribution of supraglacial lakes around the margin of the East Antarctic Ice Sheet, Sci. Rep., 9, 13823, https://doi.org/10.1038/s41598-019-50343-5, 2019.

Tedesco, M. and Fettweis, X.: Unprecedented atmospheric conditions (1948–2019) drive the 2019 exceptional melting season over the Greenland ice sheet, The Cryosphere, 14, 1209–1223, https://doi.org/10.5194/tc-14-1209-2020, 2020.

Tedesco, M., Doherty, S., Fettweis, X., Alexander, P., Jeyaratnam, J., and Stroeve, J.: The darkening of the Greenland ice sheet: trends, drivers, and projections (1981–2100), The Cryosphere, 10, 477–496, https://doi.org/10.5194/tc-10- 477-2016, 2016.

Tedesco, M., Box, J. E., Capplelen, J., Fausto, R. S., Fettweis, X., Hansen, K., Mote, T., Sasgen, I., Smeets, C. J. P. P., van As, D., van de Wal, R. S. W., and Velicogna, I.: NOAA Arctic Report Card 2018: Greenland Ice Sheet in Arctic Report Card 2017, https://arctic.noaa.gov/Report-Card/Report-Card-2017 (last access: 20 November 2022), 2017.

Tedesco, M., Box, J. E., Cappelen, J., Fausto, R. S., Fettweis, X., Anderson, J. K., Mote, T., Smeets, C. J. P. P., van As, D., and van de Wal, R. S. W.: NOAA Arctic Report Card 2018: Greenland Ice Sheet in Arctic Report Card 2018, https://arctic.noaa.gov/Report-Card/Report-Card-2018 (last access: 20 November 2022), 2018.

Tedesco, M., Moon, T., Anderson, J. K., Box, J. E., Cappelen, J., Fausto, R. S., Fettweis, X., Loomis, B., Mankoff, K. D., Mote, T., Smeets, C. J. P. P., van As, D., and van de Wal, R. S. W.: Greenland Ice Sheet in Arctic Report Card 2019, https://arctic.noaa.gov/Report-Card/Report-Card-2019 (last access: 21 November 2022), 2019.

The IMBIE Team: Mass balance of the Greenland Ice Sheet from 1992 to 2018, Nature, 579, 233–239, https://doi.org/10.1038/s41586-019-1855-2, 2020.

Trusel, L. D., Das, S. B., Osman, M. B., Evans, M. J., Smith, B. E., Fettweis, X., McConnell, J. R., Noël, B. P., and van den Broeke, M. R.: Nonlinear rise in Greenland runoff in response to post-industrial Arctic warming, Nature, 564, 104–108, https://doi.org/10.1038/s41586-018-0752-4, 2018.

Turton, J. V., Hochreuther, P., Reimann, N., and Blau, M. T.: The distribution and evolution of supraglacial lakes on 79° N Glacier (north-eastern Greenland) and interannual climatic controls, The Cryosphere, 15, 3877–3896, https://doi.org/10.5194/tc-15-3877-2021, 2021.

van As, D., Bech Mikkelsen, A., Holtegaard Nielsen, M., Box, J. E., Claesson Liljedahl, L., Lindbäck, K., Pitcher, L., and Hasholt, B.: Hypsometric amplification and routing moderation of Greenland ice sheet meltwater release, The Cryosphere, 11, 1371–1386, https://doi.org/10.5194/tc-11-1371-2017, 2017.

van den Broeke, M., Box, J., Fettweis, X., Hanna, E., Noël, B., Tedesco, M., van As, D., van de Berg, W. J., and van Kampenhout, L.: Greenland ice sheet surface mass loss: recent developments in observation and modeling, Current Climate Change Reports, 3, 345–356, https://doi.org/10.1007/s40641-017-0084-8, 2017.

van den Broeke, M. R., Enderlin, E. M., Howat, I. M., Kuipers Munneke, P., Noël, B. P. Y., van de Berg, W. J., van Meijgaard, E., and Wouters, B.: On the recent contribution of the Greenland ice sheet to sea level change, The Cryosphere, 10, 1933–1946, https://doi.org/10.5194/tc-10-1933-2016, 2016.

Williamson, A. G., Arnold, N. S., Banwell, A. F., and Willis, I. C.: A Fully Automated Supraglacial lake area and volume Tracking ("FAST") algorithm: Development and application using MODIS imagery of West Greenland, Remote Sens. Environ., 196, 113–133, https://doi.org/10.1016/j.rse.2017.04.032, 2017.

Williamson, A. G., Banwell, A. F., Willis, I. C., and Arnold, N. S.: Dual-satellite (Sentinel-2 and Landsat 8) remote sensing of supraglacial lakes in Greenland, The Cryosphere, 12, 3045–3065, https://doi.org/10.5194/tc-12-3045-2018, 2018.

Wyatt, F. R. and Sharp, M. J.: Linking surface hydrology to flow regimes and patterns of velocity variability on Devon Ice Cap, Nunavut, J. Glaciol., 61, 387–399, https://doi.org/10.3189/2015JoG14J109, 2015.

Yang, K. and Smith, L. C.: Supraglacial streams on the Greenland Ice Sheet delineated from combined spectral–shape information in high-resolution satellite imagery, IEEE Geosci. Remote Se., 10, 801–805, https://doi.org/10.1109/LGRS.2012.2224316., 2012.

Yang, K., Smith, L. C., Chu, V. W., Gleason, C. J., and Li, M.: A caution on the use of surface digital elevation models to simulate supraglacial hydrology of the Greenland ice sheet, IEEE J. Sel. Top. Appl., 8, 5212–5224, https://doi.org/10.1109/JSTARS.2015.2483483., 2015.

Yang, K., Smith, L. C., Sole, A., Livingstone, S. J., Cheng, X., Chen, Z., and Li, M.: Supraglacial rivers on the northwest Greenland Ice Sheet, Devon Ice Cap, and Barnes Ice Cap mapped using Sentinel-2 imagery, Int. J. Appl. Earth Obs., 78, 1–13, https://doi.org/10.1016/j.jag.2019.01.008, 2019a.

Yang, K., Smith, L. C., Fettweis, X., Gleason, C. J., Lu, Y., and Li, M.: Surface meltwater runoff on the Greenland ice sheet estimated from remotely sensed supraglacial lake infilling rate, Remote Sens. Environ., 234, 111459, https://doi.org/10.1016/j.rse.2019.111459, 2019b.

Yang, K., Smith, L. C., Cooper, M. G., Pitcher, L. H., Van As, D., Lu, Y., Lu, X., and Li, M.: Seasonal evolution of supraglacial lakes and rivers on the southwest Greenland Ice Sheet, J. Glaciol., 67, 592–602, https://doi.org/10.1017/jog.2021.10, 2021.

Zhang, Q., Huai, B., van Den Broeke, M. R., Cappelen, J., Ding, M., Wang, Y., and Sun, W.: Temporal and Spatial Variability in Contemporary Greenland Warming (1958–2020), J. Climate, 35, 2755–2767, https://doi.org/10.1175/JCLI-D-21-0313.1, 2022.

Zwally, H. J., Abdalati, W., Herring, T., Larson, K., Saba, J., and Steffen, K.: Surface melt-induced acceleration of Greenland ice-sheet flow, Science, 297, 218–222, https://doi.org/10.1126/science.1072708, 2002.

Appendix B

Table B1 – Supraglacial drainage network water metrics derived from Landsat mapping for the Humboldt Glacier catchment between 1985-2021, including drainage area (km^2), meltwater area fraction (%), mean drainage elevation (m a.s.l) and maximum drainage elevation (m a.s.l).

Year	*Drainage Area (km^2)*	*Meltwater Area Fraction (%)*	*Mean Drainage Elevation (m)*	*Maximum Drainage Elevation (m)*
1985	328.0	2.26	592	1032
1986	58.8	0.41	317	672
1987	310.3	2.14	626	1036
1988	400.2	2.76	529	1064
1989	173.7	1.2	484	945
1990	411.2	2.83	712	1136
1991	190.9	1.32	649	1120
1992	153.4	1.06	434	836
1994	385.2	2.66	696	1133
1995	210.2	1.45	620	1148
1998	526.1	3.62	754	1184
1999	279.1	1.92	745	1158
2000	146.8	1.01	383	912
2003	255.7	1.76	248	1213
2004	87.2	0.60	655	1140
2005	298.8	2.06	593	1190
2006	96.0	0.66	399	957
2007	383.0	2.64	786	1275
2008	489.6	3.37	902	1322
2009	328.5	2.26	614	1278
2010	288.4	1.99	686	1246
2011	363.8	2.51	707	1292
2012	320.6	2.21	821	1389
2013	189.7	1.31	635	1110
2014	728.9	5.16	820	1315
2015	381.3	2.63	816	1414
2016	332.9	2.29	703	1411
2017	235.3	1.62	461	1109
2018	351.8	2.42	557	1040
2019	577.7	3.98	778	1324
2020	323.1	2.23	790	1418
2021	650.9	4.48	885.7	1464

Table B2. Satellite mapping-derived metrics for supraglacial lakes (SGLs) at Humboldt Glacier (1985–2021), including metrics split between all SGLs >0.01 km2 and SGLs >0.1 km2 only.

	Lake Size >0.01km²						*Lake Size >0.1km²*				
Year	SGL No	Total SGL Area (km²)	Mean SGL Area (km²)	Max SGL Area (km²)	Mean Elevation (m)	Max Elevation (m)	SGL No	Total SGL area (km²)	Mean individual SGL area (km²)	Mean elevation (m)	Max Elevation (m)
1985	388	37.4	0.19	1.06	383.2	1022.4	121	28	0.23	472.7	998.7
1986	346	26.5	0.08	0.82	261.1	673.9	85	17.2	0.2	304.1	566.8
1987	467	63.8	0.34	1.67	375.3	1026.1	160	52.3	0.33	520	1024.4
1988	591	68.6	0.25	1.48	326.5	1025.3	204	52.4	0.26	450.8	1024.8
1989	334	36.6	0.19	0.93	357.7	951	107	28.3	0.27	437.3	901.5
1990	484	36.9	0.21	1.11	357.7	1036.5	95	22.6	0.24	525.7	1024.2
1991	347	54.3	0.34	1.34	427.5	1030.4	146	47.7	0.32	568.9	1024.5
1992	341	34.5	0.19	1.78	319.5	816.2	86	26	0.3	410	706.6
1994	542	61.8	0.29	1.83	335.1	1026.8	167	47.4	0.28	484.5	1024.9
1995	457	58.6	0.33	2.1	383.4	1081.4	151	46.7	0.31	531.1	1076.2
1998	526	65.4	0.40	1.9	463.3	1123.2	148	52.4	0.35	271.5	1123.2
1999	500	69.0	0.35	1.9	369.1	1160.8	183	56.6	0.31	518.6	1122
2000	471	38.0	0.1	0.81	282.1	870.6	122	24.5	0.2	375.3	752.5
2003	177	18.3	0.30	1.9	582.5	1212	48	13.8	0.29	691.3	1211.9
2004	266	32.1	0.30	1.63	530.2	1120	81	25.3	0.31	604.2	1024.9
2005	528	70.8	0.42	1.58	384	1189.5	171	56.7	0.33	537.7	1099.7
2006	482	51.3	0.30	1.61	327.9	949.7	141	37.8	0.27	423.3	946.2
2007	516	71.6	0.45	2.86	424.9	1222	176	58.4	0.33	562.2	1211.6

2008	490	72.7	0.53	2.21	422.2	1222	187	60.6	0.32	582.3	1221.8
2009	426	68.5	0.45	1.44	457.1	1227.6	159	58	0.37	605.2	1220.4
2010	431	43.8	0.28	1.2	415.3	1239	128	31.7	0.25	523.8	1161.8
2011	250	42.9	0.58	1.86	586.6	1289.7	93	36.7	0.4	729.3	1220.4
2012	345	55.9	0.58	2.11	489.3	1304	141	48	0.34	646	1288.7
2013	288	33.4	0.25	1.38	419.6	1031.5	88	25.6	0.29	527.3	1024.5
2014	434	76.5	0.65	2.5	498.1	1034	171	65.5	0.38	606.3	1220.5
2015	372	67.7	0.71	3.5	547.9	1352	153	60.9	0.4	691.7	1351.8
2016	547	75.2	0.64	2.56	473.3	1317	180	61.8	0.34	613.8	1303.8
2017	419	49.8	0.25	1.71	390.6	1034.1	152	43.1	0.28	510.8	1024.6
2018	447	59.8	0.31	2.29	418.6	1022.4	158	49.4	0.31	554.7	1025.3
2019	394	70.4	0.60	3.2	524.1	1304	160	60	0.38	688.6	1248.2
2020	502	73.4	0.55	1.89	505.7	1373	187	61.7	0.33	670.3	1349.6
2021	464	67.7	0.52	2.11	484.9	1329.9	171	56.8	0.33	645.5	1329.4

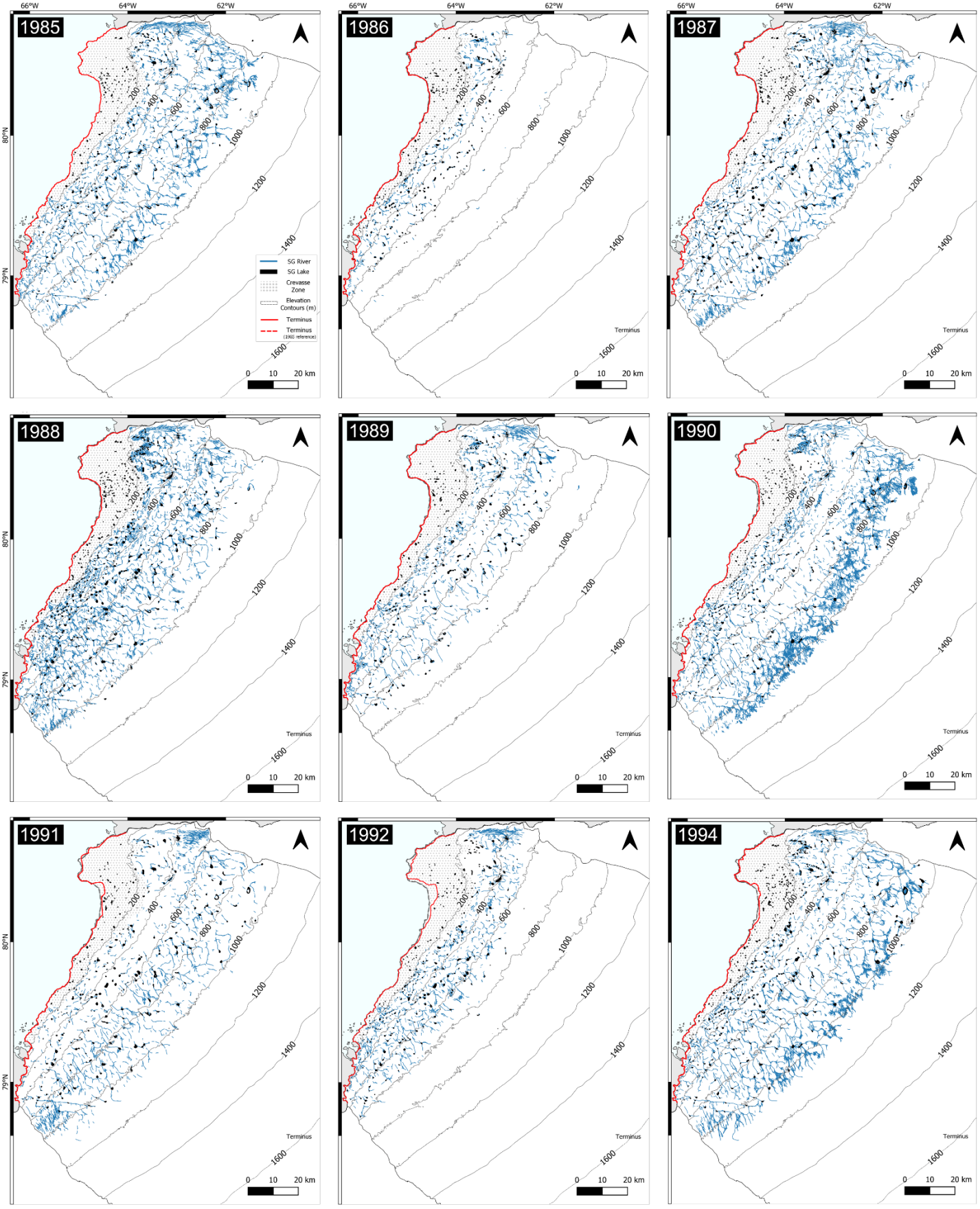
1985
1986
1987
1988
1989
1990
1991
1992
1994
66°W
64°W
62°W
80°N
76°N
SG River
SG Lake
Crevasse Zone
Elevation Contours (m)
Terminus
Terminus (1985 reference)
Terminus
0 10 20 km

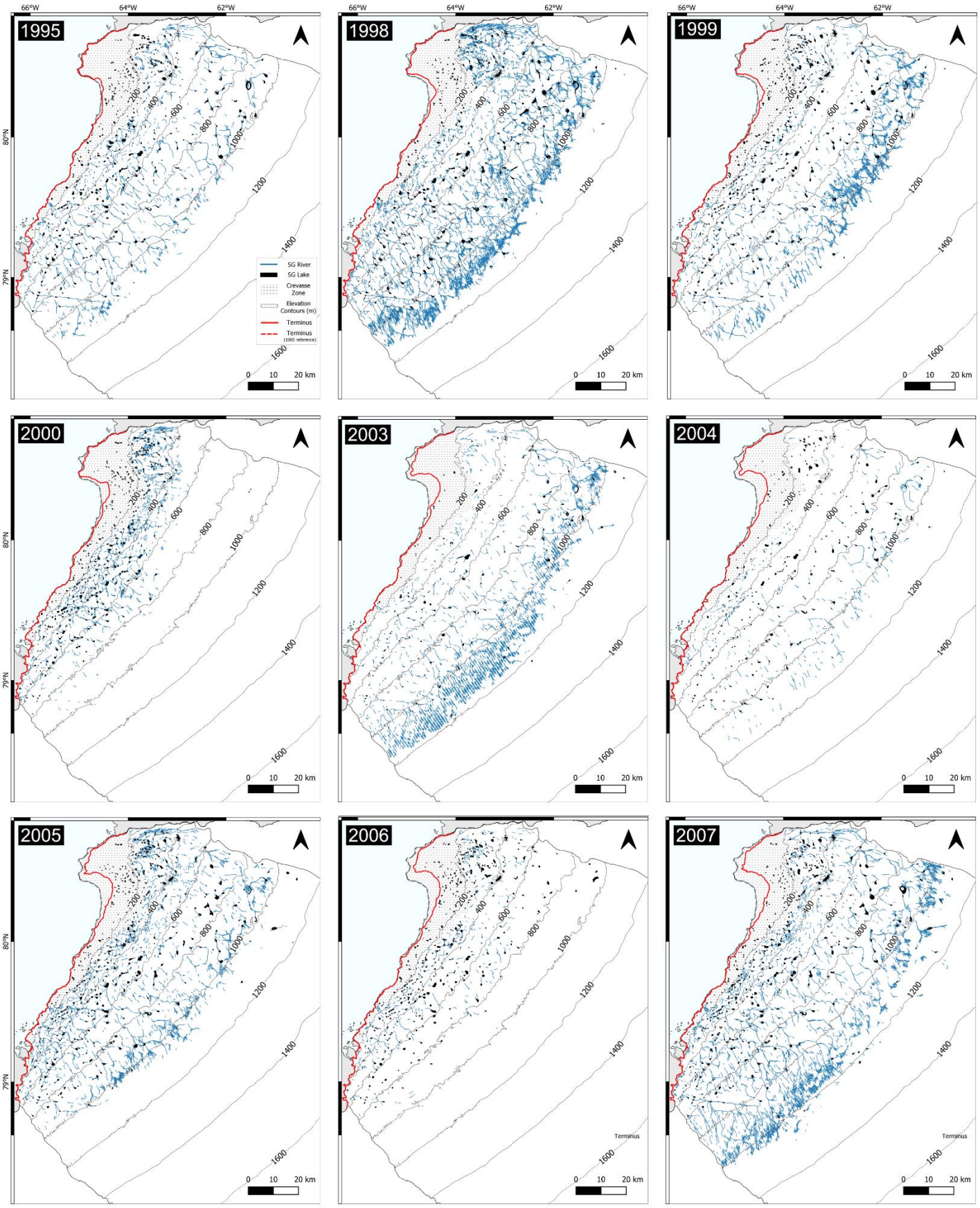
66°W
64°W
62°W
80°N
79°N
1995
1998
1999
2000
2003
2004
2005
2006
2007
200
400
600
800
1000
1200
1400
1600
SG River
SG Lake
Crevasse Zone
Elevation Contours (m)
Terminus
Terminus (1985 reference)
0 10 20 km
Terminus

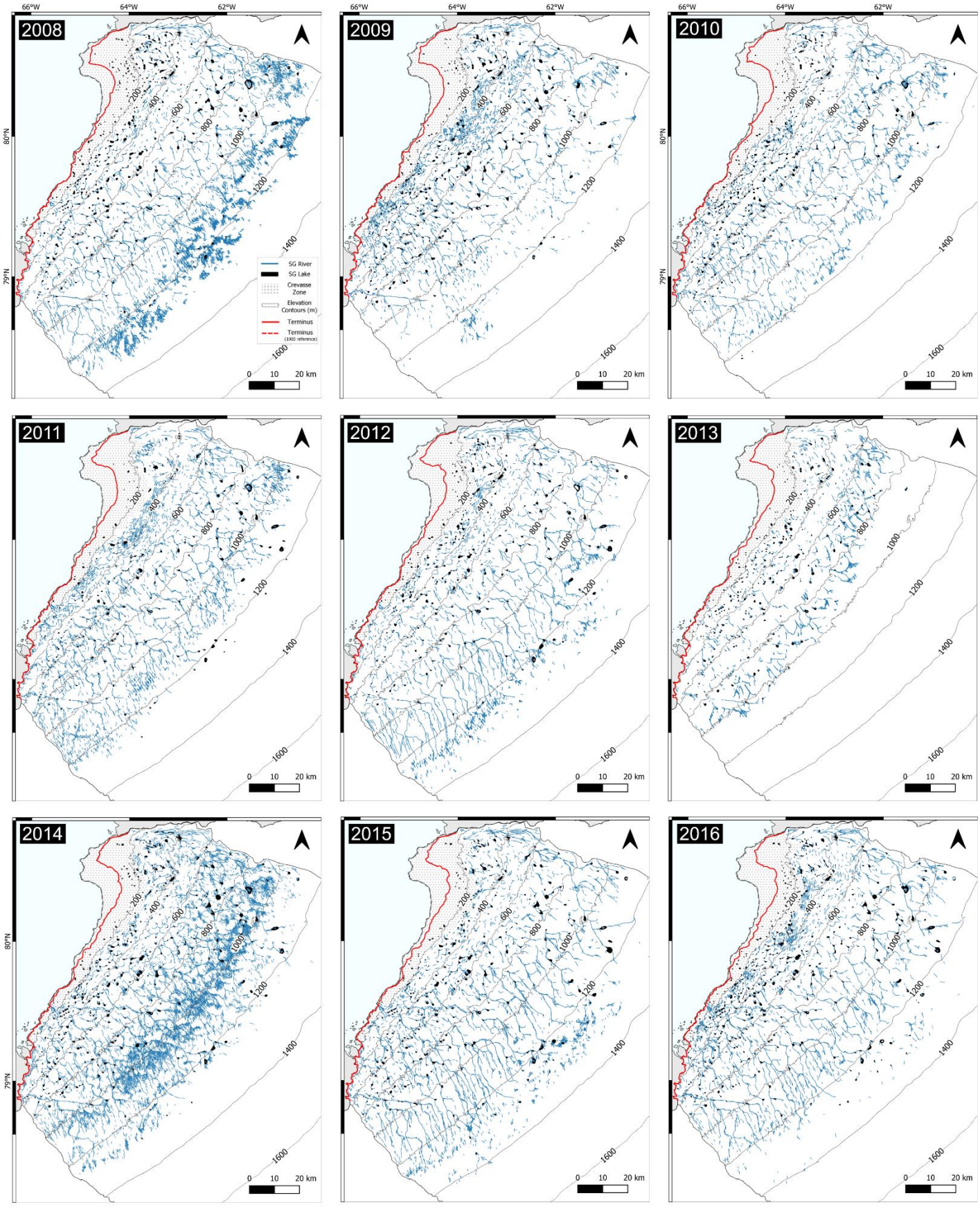
2008
2009
2010
2011
2012
2013
2014
2015
2016
66°W
64°W
62°W
80°N
79°N
SG River
SG Lake
Crevasse Zone
Elevation Contours (m)
Terminus
Terminus (1985 reference)
0 10 20 km

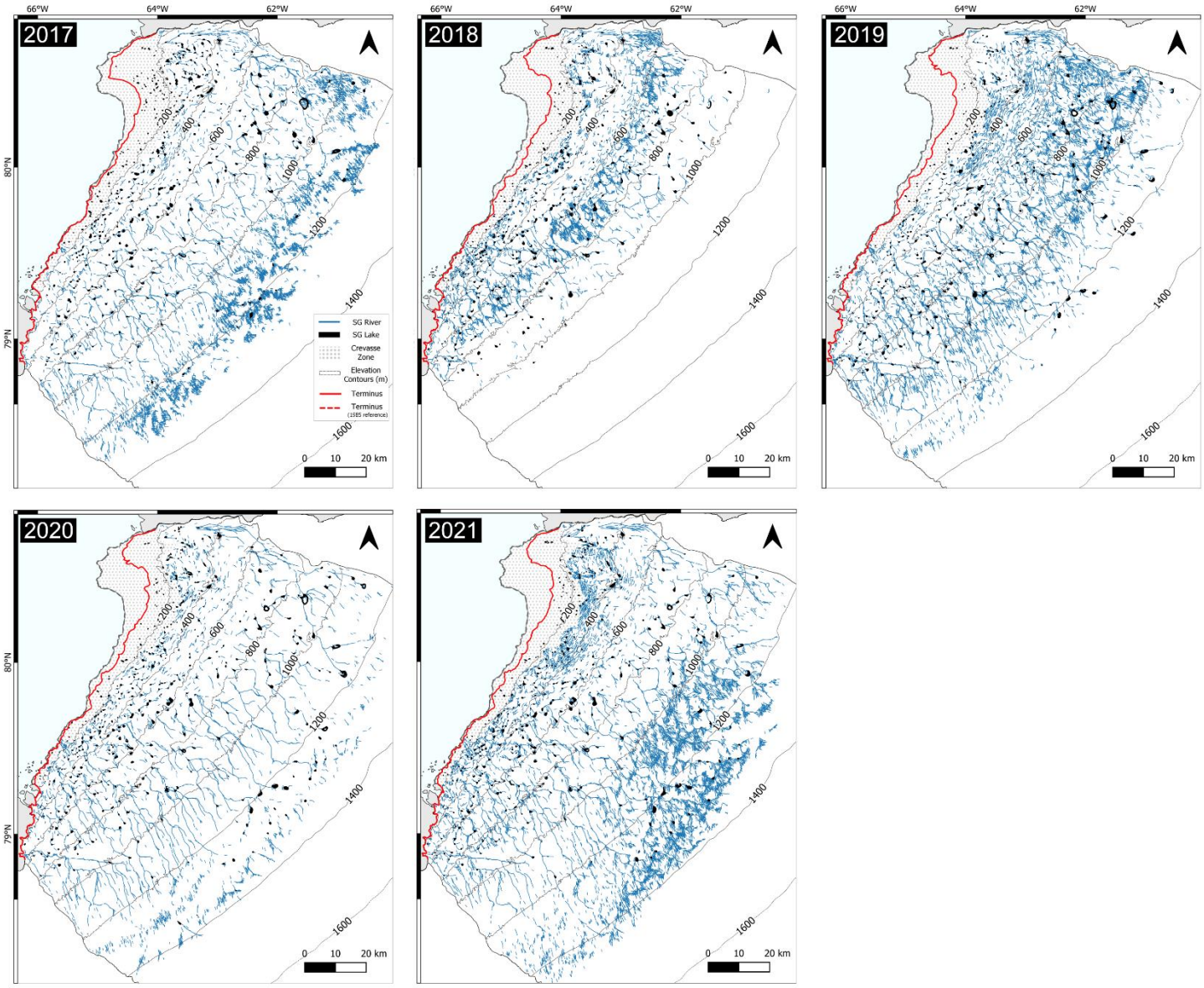

Figure B1. Additional 32 maps for supplementary information showing the supraglacial drainage inland advance over the 37-year study period (1985 – 2021), excluding years where imagery was unavailable. Supraglacial (SG) rivers are represented by blue lines and supraglacial (SG) lakes shown in black. Red lines represent the terminus position of the associated year, with the grey dashed line showing the 1985 terminus reference. The crevasse zone is shown via grey dots below 200m and this area was removed from supraglacial river mapping and quantification due to the potential for erroneous crevasse capture. Supraglacial lakes, however, were retained in this area as a size threshold (>0.01km2) was applied.

Appendix C

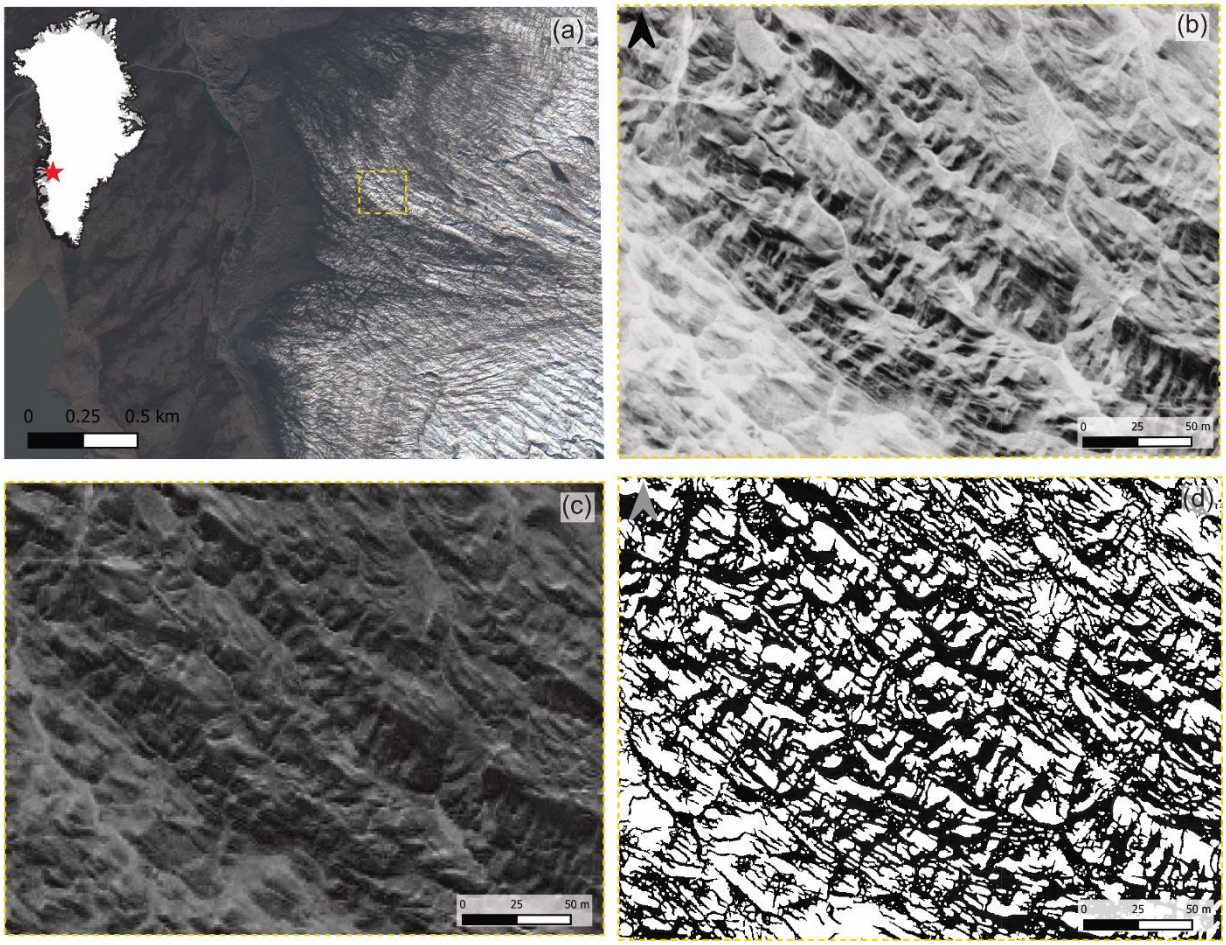

Figure C1. (a) Worldview-2 (WV-2) RGB image of the ice marginal region of Russell Glacier, southwestern Greenland. Yellow box denotes location of (b-d); (b-c) panchromatic WV-2 imagery of the ice surface covering the area surveying by the UAV. Supraglacial meltwater features are not well resolved in such imagery; (d) results from the automatic river detection algorithm from higher resolution panchromatic imagery (0.4 m) with over-estimation of the supraglacial network due to poor contrast between the ice surface and meltwater features.

A Worldview-2 (WV-2) image was also sought for a 15 km^2 area of the southwestern region of the GrIS covering the UAV-survey scene of the on-ice ice marginal region of Russell Glacier, ~300 m from the ice edge. Originally, the WV-2 image was going to be used to assess the minutiae of the supraglacial network in this region where UAV imagery was

acquired utilising the automatic river detection algorithm by (Yang *et al.*, 2015a; Yang *et al.*, 2017). However, as this requires a strong contrast between the snow/ice background and meltwater features (i.e., rivers, streams and lakes), due to the darkened- and high-undulating surface as well as instances of fractures, the supraglacial hydrology could not be successfully mapped from satellite-acquired data. As shown in Figure C1, supraglacial streams are not well resolved in panchromatic (0.4 m; Figure C1b) or NDWI (0.18 m; Figure C1c) images and are unsuccessful at being extracted by the algorithm (Figure C1d). Instead, overestimation occurs due to the complexity of the ice surface. Such factors also led to difficulties with alternate manual digitisation of the network.

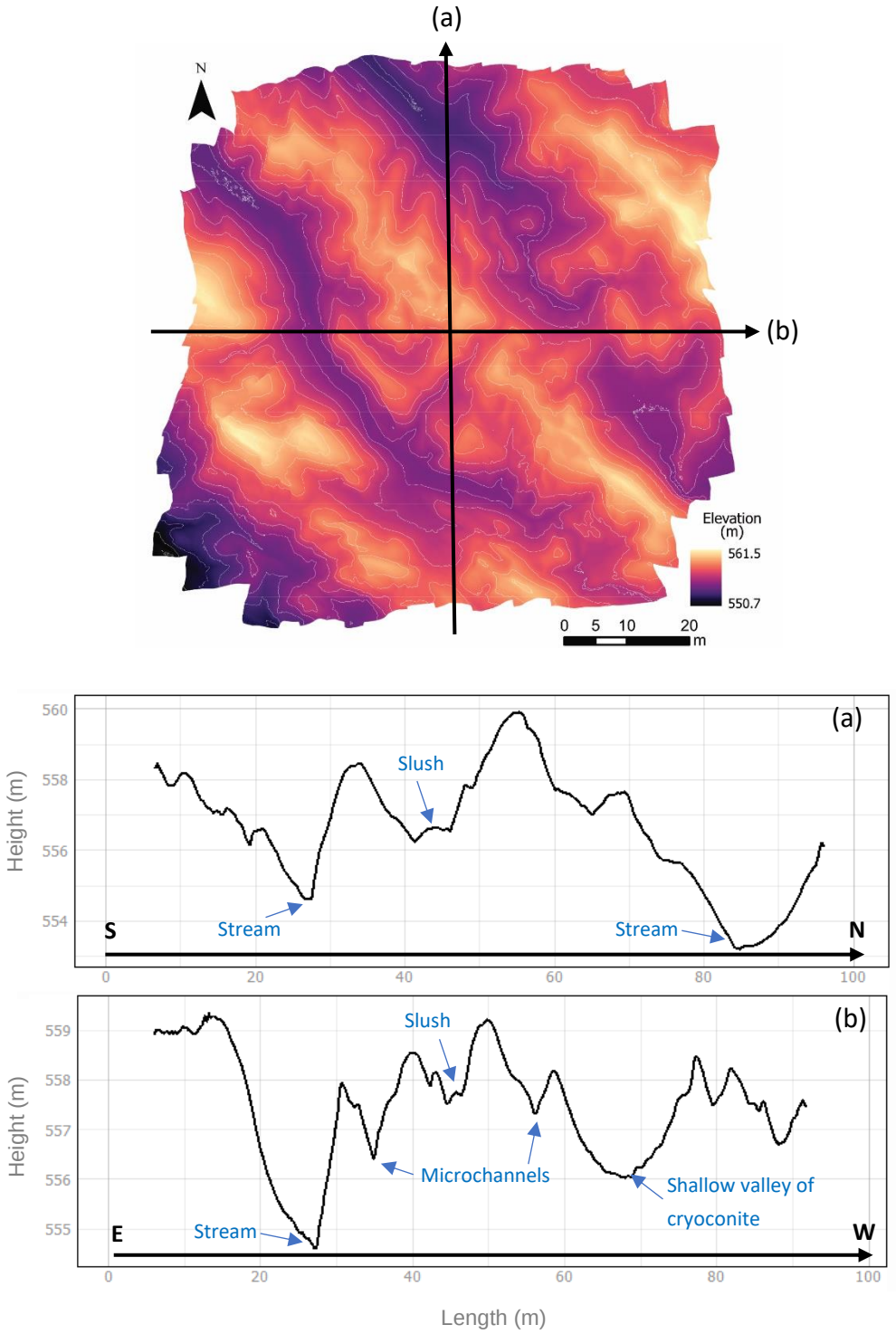

Figure C2. Elevation profiles of the UAV survey scene from north-to-south and east-to-west, as shown by lines on the DEM. (a) Elevation profile from south-to-north (left-to-right) with supraglacial features denoted for interest; (b) elevation profile from east-to-west (left-to-right) with supraglacial features denoted for interest.

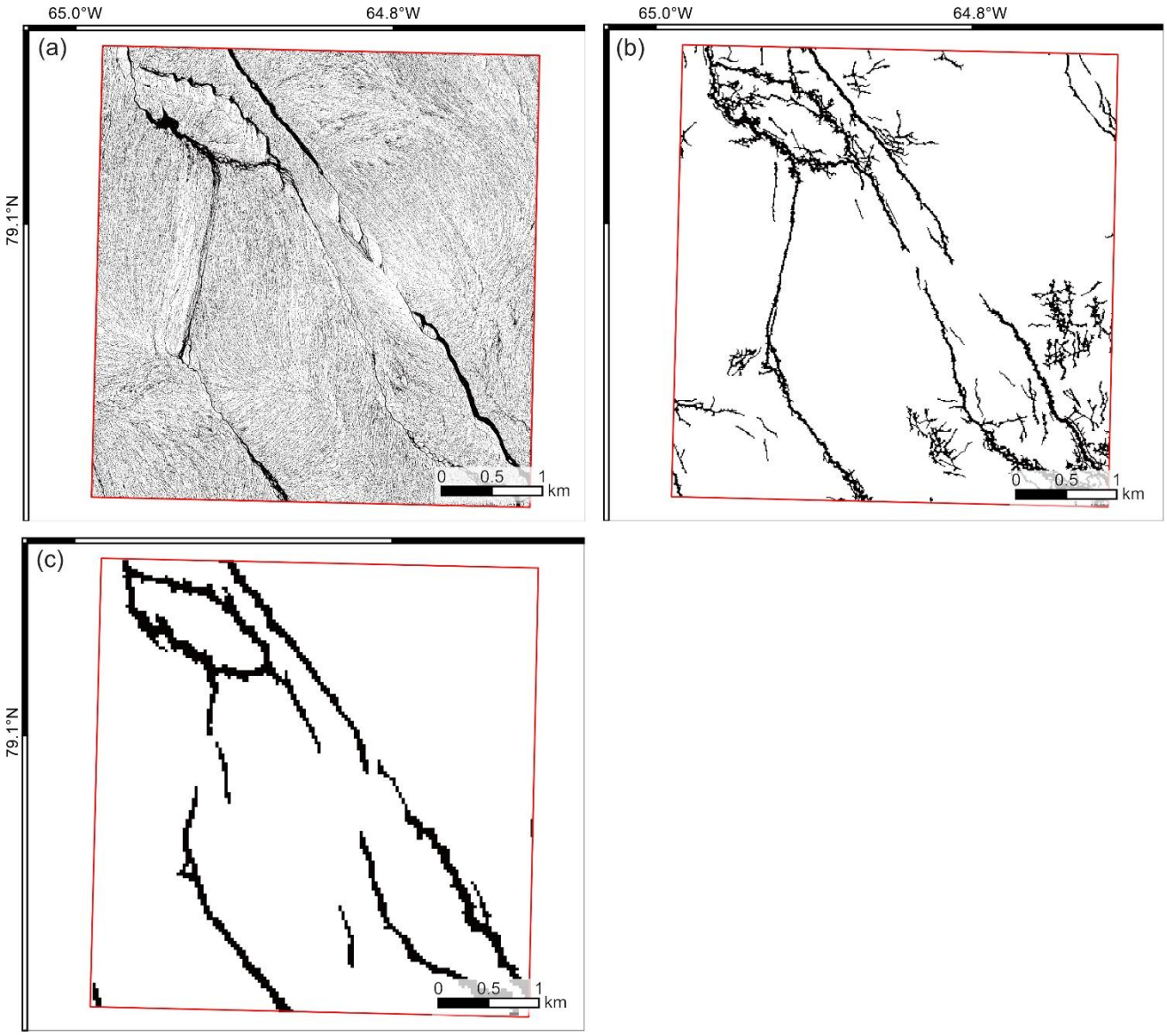

Figure C3. The supraglacial hydrologic network delineated from different satellite-acquired imagery for a small 20.3 km^2 region of Humboldt Glacier, northern Greenland. (a) The network derived via WV-2 imagery (30th June 2020) including main river channels with clear braiding characteristics and a vast expanse of narrow, tributary inter-stream networks; (b) the network derived from Sentinel-2 (Chapter 4; 23rd June 2020) showing the main river channels and some evidence of tributary channels; (c) the network derived from Landsat imagery (Chapter 5; JJA 2020) showing the main river channels only. The general structure and hydrologic network is retained across image resolutions, however the ability to extract narrow, expansive streams (inter-stream networks) is resolution-dependent.